U.S.NRC
United States Nuclear Regulatory Commission
Protecting People and the Environment

Technical Letter Report
TLR-RES/DE/REB-2021-03

Fracture Analysis of Vessels – Oak Ridge
FAVOR v20.1.12
Theory and Implementation of Algorithms, Methods, and Correlations

Date:

Drafted: September 2020

Updated: June 2021

Completed: June 2021

NUMARK Associates, Inc:

Terry Dickson	*Marvin Smith*	*Andrew Dyszel*
Subject Matter Expert	Project Manager	Senior Technical Reviewer

NRC Contributors:

Patrick Raynaud
Senior Materials Engineer
Component Integrity Branch

Division of Engineering
Office of Nuclear Regulatory Research
U.S. Nuclear Regulatory Commission
Washington, DC 20555–0001

DISCLAIMER

This report was prepared as an account of work sponsored by an agency of the U.S. Government. Neither the U.S. Government nor any agency thereof, nor any employee, makes any warranty, expressed or implied, or assumes any legal liability or responsibility for any third party's use, or the results of such use, of any information, apparatus, product, or process disclosed in this publication, or represents that its use by such third party complies with applicable law.

This report does not contain or imply legally binding requirements. Nor does this report establish or modify any regulatory guidance or positions of the U.S. Nuclear Regulatory Commission and is not binding on the Commission.

CONTENTS

Page

LIST OF TABLES

Table **Page**

LIST OF FIGURES

Figure **Page**

EXECUTIVE SUMMARY

The **F**racture **A**nalysis of **V**essels – **O**ak **R**idge (**FAVOR**) computer program has been developed to perform deterministic and probabilistic risk-informed analyses of the structural integrity of a nuclear reactor pressure vessel (RPV) when subjected to a range of thermal-hydraulic events. The focus of these analyses is on the beltline region of the RPV. Development of FAVOR originated under the NRC-sponsored Heavy Section Steel Technology (HSST) program and, more recently, continued under the Probabilistic Structural and Material Modeling (ProSaMM) Program, both at Oak Ridge National Laboratory (ORNL).

Thermal-hydraulic events addressed by the FAVOR code include both overcooling accidents and normal operating transients. Overcooling events, where the temperature of the coolant in contact with the inner surface of the RPV wall rapidly decreases with time, produce time-dependent temperature gradients that induce biaxial stress states varying in magnitude through the vessel wall. Near the inner surface and through most of the wall thickness, the stresses are tensile, thus generating Mode I opening driving forces that can act on possible existing internal surface-breaking or embedded flaws near the wetted inner surface. If the internal pressure of the coolant is sufficiently high, then the combined thermal plus mechanical loading results in a transient condition known as a pressurized-thermal shock (PTS) event. Normal planned reactor operational transients, such as start-up, cool-down, and leak-test can also present challenges to the structural integrity of the RPV.

In 1999 ORNL, working in cooperation with the NRC staff and with other NRC contractors, illustrated that the application of fracture-related technology developed since the derivation of the current pressurized-thermal-shock (PTS) regulations (established in the early-mid 1980s) had the potential for providing a technical basis for a re-evaluation of the then-current PTS regulations. Motivated by these findings, the U.S. Nuclear Regulatory Commission (NRC) began the PTS Re-evaluation Project to develop a technical basis to support a revision to the rule within the framework established by modern probabilistic risk assessment techniques and advances in the technologies associated with the physics of PTS events.

An updated computational methodology was developed through research and interactions among experts in the relevant disciplines of thermal-hydraulics, probabilistic risk assessment (PRA), materials embrittlement, probabilistic fracture mechanics (PFM), and inspection (flaw characterization). Major differences between this methodology and that used to establish the technical basis for the original PTS rule (10 CFR 50.61) include the following:

- **the ability to incorporate new detailed flaw-characterization distributions from NRC research obtained via work performed at Pacific Northwest National Laboratory, PNNL,**
- **the ability to incorporate detailed neutron fluence maps,**
- **the ability to incorporate warm-prestressing effects into the analysis,**
- **the ability to include temperature-dependencies in the thermo-elastic properties of base and cladding,**
- **the ability to include crack-face pressure loading for surface-breaking flaws,**
- **the addition of a new ductile-fracture model simulating stable and unstable ductile tearing,**
- **the addition of a new embrittlement correlation,**
- **the ability to include multiple transients in one execution of FAVOR,**

- **the ability to include input from the Reactor Vessel Integrity Database, Revision 2, (RVID2) of relevant RPV material properties,**
- **the addition of new fracture-toughness models based on extended databases and improved statistical distributions,**
- **the addition of a variable failure criterion, i.e., how far must a flaw propagate into the RPV wall for the vessel simulation to be considered as "failed",**
- **the addition of semi-elliptic surface-breaking and embedded-flaw models,**
- **the addition of through-wall weld stresses,**
- **the addition of SIFIC(s) for base material from ASME code, Section XI, Appendix A, Article A-3000, *Method of K_I Determination*, for finite, semi-elliptical, axial, and circumferential surface flaws and infinite axial and 360° continuous circumferential surface flaws flaws into the FAVOR SIFIC database, and**
- **the implementation of an improved PFM methodology that incorporates modern PRA procedures for the classification and propagation of input uncertainties and the characterization of output uncertainties as statistical distributions.**

These updated methodologies were implemented into the FAVOR computer code, which was then subjected to extensive verification studies. A specific version, FAVOR, v06.1, was used to develop the PTS TWCF estimates reported in NUREG-1806 and NUREG-1874, which were published in 2006 and 2007, respectively. The TWCF estimates in NUREG-1874 formed part of the technical basis for the alternate PTS rule (10 CFR 50.61a).

The FAVOR computer code has continued to evolve and to be extensively applied by analysts from the nuclear industry, both nationally and internationally, and by regulators at the NRC. After FAVOR v16.1 was released, a new option to add the capability of analyzing as-found flaws to create FAVOR, v20.1, the latest version[1] of this tool. FAVOR version 20.1 is backwards compatible with version 16.1 and both versions will produce the same results for flaws inout in the VFLAW format. Version 20.1 adds an option to evaluate as-found flaws. This report documents the technical bases for the assumptions, algorithms, methods, and correlations employed in the development of the FAVOR code.

[1] The differences between the various versions of FAVOR are detailed in the FAVOR revision history presented in Chapter 2 (see Appendix A for additional historical information).

ACRONYMS

API	American Petroleum Institute
ASME	American Society of Mechanical Engineers
ASTM	American Society for Testing and Materials (ASTM International since 2001)
BNL	Brookhaven National Laboratory
BPVC	ASME Boiler and Pressure Vessel Code
BWR	boiling water reactor
CCA	compact crack-arrest test specimen
C(T)	compact tension fracture-toughness test specimen
CDF	cumulative distribution function
CPI	conditional probability of initiation
CPF	conditional probability of failure (as indicated by through-wall cracking)
CRP	copper-rich precipitate
CVN	Charpy V-Notch test specimen
DTE	differential-thermal expansion
EFPY	effective full-power years
EPFM	elastic-plastic fracture mechanics
EPRI	Electric Power Research Institute
EOL	end-of-licensing
FAVLoad	FAVOR's load module
FAVOR	Fracture Analysis of Vessels – Oak Ridge
$FAVOR^{HT}$	a special version of FAVOR developed for heat-up transients
FAVPFM	FAVOR's PFM module
FAVPost	FAVOR's post-processing module
FEM	finite-element method
GPS	generalized plane strain
HAZ	heat-affected zone
HR	human reliability
HSST	Heavy Section Steel Technology Program
IGA	initiation, growth, and arrest module within FAVPFM
IPTS	Integrated Pressurized Thermal Shock Program
LEFM	linear-elastic fracture mechanics
LOCA	loss-of-coolant accident
NESC	Network for Evaluating Structural Components
NIST	National Institute for Standards and Technology
NRC	United States Nuclear Regulatory Commission
ODR	orthogonal distance regression
ORNL	Oak Ridge National Laboratory
PDF	probability density function
PFM	probabilistic fracture mechanics
PNNL	Pacific Northwest National Laboratory
PRA	Probabilistic Risk Assessment
ProSaMM	Probabilistic Structural and Material Modeling Program
PTS	pressurized thermal shock
PWHT	post-weld heat treatment
PWR	pressurized water reactor
RCW	recirculating primary cooling water system
RG1.99	NRC Regulatory Guide 1.99, Revision 2, ref. [17]
RG1.154	NRC Regulatory Guide 1.154, ref. [16]
RPV	reactor pressure vessel
RMSD	root-mean-square deviation

RVID2	Reactor Vessel Integrity Database, Version 2, ref. [155]
SIFIC	stress-intensity-factor influence coefficients
SMD	stable matrix defect
SQA	software quality assurance
10CFR50.61	Title 10 of the *Code of Federal Regulations*, Part 50, Section 50.61, ref. [15]
10CFR50.61a	Title 10 of the *Code of Federal Regulations,* Part 50, Section 50.61a, ref.[18, 20]
TMI	Three-Mile-Island nuclear reactor
T-E	thermo-elastic
T-H	thermal-hydraulic
UMD	unstable matrix defect
WGFE	ASME Working Group on Flaw Evaluation
WOL	wedge-open loading test specimen for fracture toughness
WPS	warm prestressing

ACKNOWLEDGMENTS

FAVOR 20.1.12 was developed in a collaborative manner by a team composed of:

- Terry Dickson, Andrew Dyszel, and Marvin Smith, of NUMARK Associates, Inc.
- Brad Richardson, Karla Morris, Kate Rasmussen, and Damian Rouson, of Sourcery Inc.
- Giovanni Facco, James Burke, and Patrick Raynaud, of the NRC's Office of Nuclear Regulatory Research.

This work was sponsored by the U.S. NRC.

This page is intentionally left blank.

.

1. Introduction

In 1999, Dickson et al. [1] illustrated that the application of fracture-related technology, developed since the derivation of the original pressurized-thermal-shock (PTS) rules established in the 1980s, had the potential to better inform the basis of the then-existent PTS regulations. An updated computational methodology was developed over several years through research and interactions among experts in the relevant disciplines of thermal-hydraulics, probabilistic risk assessment (PRA), materials embrittlement, probabilistic fracture mechanics (PFM), and inspection (flaw characterization).

This updated methodology has been implemented into the Fracture Analysis of Vessels – Oak Ridge (FAVOR) computer code developed at Oak Ridge National Laboratory (ORNL) for the U.S. Nuclear Regulatory Commission (NRC). FAVOR was applied in the PTS Re-evaluation Project to successfully establish a technical basis supporting a revision to the original PTS Rule (Title 10 of the Code of Federal Regulations, Chapter I, Part 50, Section 50.61, 10CFR50.61) within the framework established by modern probabilistic risk assessment techniques and advances in the technologies associated with the physics of PTS events.

The FAVOR computer code continues to evolve. Extensively applied by analysts from the nuclear industry and regulators at the NRC, FAVOR incorporates fracture mechanics and risk-informed methodologies to assess and update regulations designed to insure that the structural integrity of aging nuclear reactor pressure vessels (RPVs) is maintained throughout the licensing period of the reactor.

The analysis of PTS was the primary motivation in the development of FAVOR; however, the problem class for which FAVOR is applicable encompasses a broad range of events that include normal operational transients (such as start-up and shut-down) as well as upset conditions beyond PTS. Essentially any event in which the RPV wall is exposed to time-varying thermal-hydraulic boundary conditions would be an appropriate candidate for a FAVOR analysis of the vessel's structural integrity.

Earlier versions of FAVOR were developed to perform deterministic and risk-informed probabilistic analyses of the structural integrity of a nuclear reactor pressure vessel (RPV) when subjected to overcooling events such as PTS accidental transients and normal cool-down transients such as those associated with reactor shutdown. *Overcooling events*, where the temperature of the coolant in contact with the inner surface of the RPV wall *decreases* with time, produce temporally-dependent temperature and stress gradients. These stresses are tensile on and near the RPV inner surface, thus

generating Mode I opening driving forces that tend to open inner surface-breaking or embedded flaws located near the inner surface of the RPV wall.

The **F**racture **A**nalysis of **V**essels – **O**ak **R**idge **H**ea**t**-Up (FAVOR^{HT}) computer program was previously developed to perform deterministic and probabilistic fracture analyses of a nuclear RPV subjected to heat-up events, such as those transients associated with the start-up of reactors. *Heat-up events*, where the temperature of the coolant in contact with the inner surface of the RPV wall *increases* with time, produce temporally-dependent temperature and stress gradients that are tensile on and near the RPV external surface, thus generating Mode I opening driving forces that tend to open external surface-breaking or embedded flaws located near the external surface of the reactor vessel wall. The focus of these analyses of both *overcooling* and *heat-up* events is the *beltline* region of the RPV wall as shown in Fig. 1.

A limitation of the versions of FAVOR released before v09.1 is that they performed analyses of reactor vessels with an internal radius, R_i, to wall thickness, t, (R_i/t), ratio of approximately 10, this being characteristic of pressurized water reactors (PWRs). Most boiling water reactors (BWRs) have R_i/t ratios of approximately 20, although a few BWRs in the United States have R_i/t ratios between 10 and 20. This limitation was removed in FAVOR, v09.1.

A later version of FAVOR, v12.1, consolidated and expanded the modeling and analysis capabilities of the previous versions of FAVOR and FAVOR^{HT} discussed above into a single computer program. Thus, FAVOR was generalized to provide the capability to perform deterministic and probabilistic fracture analyses of PWRs and BWRs vessels subjected to cool-down and /or heat-up transients.

The FAVOR, v16.1, code represents the final release of the NRC applications tool for performing deterministic and risk-informed probabilistic fracture analyses of RPVs. The principal changes in FAVOR, v16.1, involve revisions to the logic for keeping track of flaws.

This report documents the technical bases for the assumptions, algorithms, methods, and correlations employed in the development of the FAVOR code. A user's guide to computer system requirements, installation, and execution of the FAVOR deterministic and probabilistic fracture mechanics code is presented in the companion report *Fracture Analysis of Vessels – FAVOR, v16.1, Computer Code: User's Guide* [2].

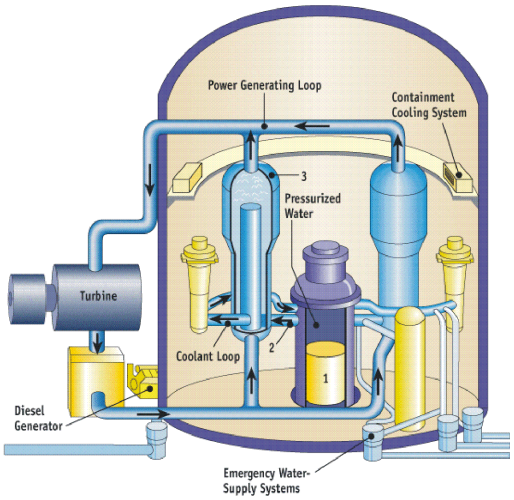

Source: Nuclear Regulatory Commission

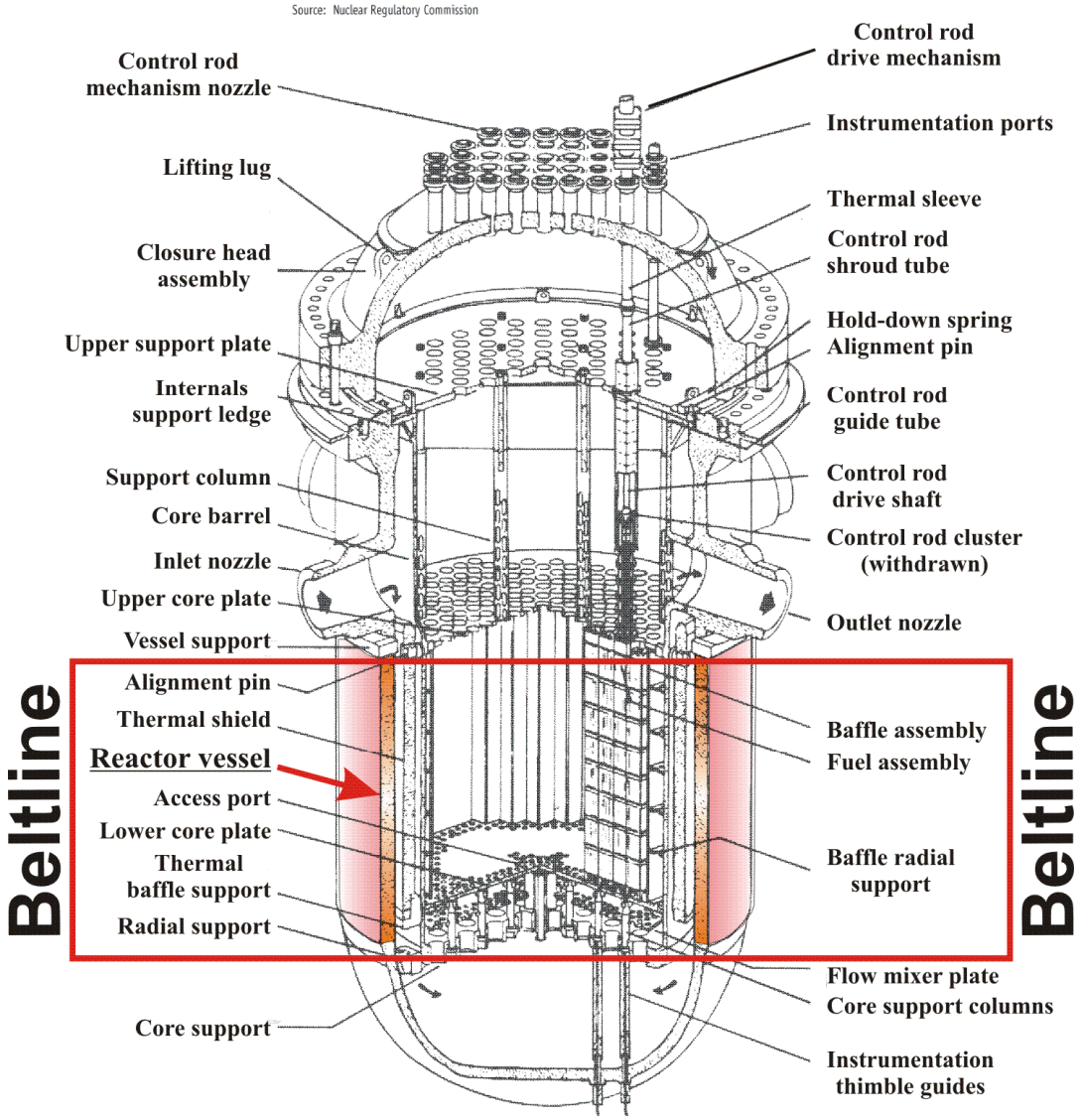

Fig. 1. The beltline region of the reactor pressure vessel wall extends from approximately one foot above the active reactor core to one foot below the core (adapted from [3]).

Some of the elements of the updated technologies and computational methodology that have been incorporated into FAVOR (from v01.1 to the current release) are as follows:

- **the ability to incorporate new detailed flaw-characterization distributions from NRC research (with Pacific Northwest National Laboratory, PNNL),**
- **the ability to incorporate detailed neutron fluence maps,**
- **the ability to incorporate warm-prestressing effects into the analysis,**
- **the ability to include temperature-dependencies in the thermo-elastic properties of base and cladding,**
- **the ability to include crack-face pressure loading for surface-breaking flaws,**
- **the addition of a new ductile-fracture model simulating stable and unstable ductile tearing,**
- **the addition of a new embrittlement correlation,**
- **the ability to include multiple transients in one execution of FAVOR,**
- **the ability to include input from the Reactor Vessel Integrity Database, Revision 2, (RVID2) of relevant RPV material properties,**
- **the addition of new fracture-toughness models based on extended databases and improved statistical distributions,**
- **the addition of a variable failure criterion, i.e., how far must a flaw propagate into the RPV wall for the vessel simulation to be considered as "failed" ?**
- **the addition of semi-elliptic surface-breaking and embedded-flaw models,**
- **the addition of through-wall weld stresses,**
- **the addition of base material SIFIC(s) from ASME code, Section XI, Appendix A, Article A-3000, *Method of K_I Determination*, for (a) finite semi-elliptical axial and circumferential inside surface flaws and (b) infinite axial and 360° continuous circumferential inside surface flaws into the FAVOR SIFIC database, and**
- **the implementation of an improved PFM methodology that incorporates modern PRA procedures for the classification and propagation of input uncertainties and the characterization of output uncertainties as statistical distributions.**

The revision history in Chapter 2 lists major changes made to FAVOR as it has evolved from Version 01.1, released in 2001, to release, v20.1. Chapter 3 of this report provides a short historical perspective for viewing the pressurized-thermal-shock problem, including a summary of events leading to the current (as of this writing in 2016) regulations. This chapter is followed by a full description of the analytical models employed in the FAVOR code, described in Chapters 4 and 5. In that presentation, particular emphasis is given to the new features of the code that were highlighted above. A summary and conclusions are given in Chapter 6. Appendix A presents a summary of the development history of FAVOR and its antecedents, and Appendix B presents the database of stress-intensity-factor influence coefficients that has been implemented in FAVOR for its surface-breaking flaw models. The database of plane-strain static initiation fracture toughness, K_{Ic}, and plane-strain crack arrest, K_{Ia}, properties for pressure vessel steels is given in Appendix C. This fracture-toughness

database was used in the construction of the statistical models for crack initiation and arrest that are implemented in FAVOR. Appendix D presents a summary of RVID2 data to be used in FAVOR analyses for the PTS Re-evaluation Project. The point-estimation techniques applied in the development of the Weibull cumulative distribution functions that estimate the epistemic uncertainty in the fracture initiation and arrest reference temperatures are given in Appendix E. The development of the sampling protocols for the epistemic uncertainties in two important reference temperatures is given in Appendix F. Appendix G in this report describes the verification and validation efforts that have been ongoing throughout the lifecycle of the FAVOR code. Appendix H describes the changes to FAVOR to add an option to evaluate as-found flaws that may be identified during RPV in-service inspections.

2. FAVOR Revision History

2.1 Summary of Modifications to the v20.1 Release of FAVOR (Relative to v16.1)

An as-found flaw analysis capability was added as an option to FAVOR version 16.1 to create FAVOR version 20.1. FAVOR version 20.1 is backwards compatible with version 16.1 and FAVOR 20.1 can perform analysis of flaws files generated by VFLAW and produce the same results for these analyses as FAVOR version 16.1. Appendix H provides a detailed discussion of the as-found flaw option added to create FAVOR version 20.1.

2.2 Summary of Modifications to the v16.1 Release of FAVOR (Relative to v15.3)

(1) In the subroutine PFM in the FAVPFM module, logic was added such that when the total number of flaws is less than 1.0 for any of the 1000 flaw cases, the appropriate arrays are filled with zeros, and the analysis continues. In subroutine FLWDIS also in FAVPFM, logic was added for the case where there is a fractional part of Category 1 surface-breaking flaws, i.e., greater than 0.0, but less than 1.0. For this case, the fractional part should be subtracted out of the total number of flaws. This logic ensures that the number of flaws and the PDF and CDF used in the determination of flaw category are identical with the case with no Category 1 surface-breaking flaws (i.e., embedded flaws only).

(2) A complete review was carried out of the influence coefficients for cladding in the FAVOR SIFIC database. Some errors were identified and corrected, specifically for the case of cladding with R/t = 20, $2c/a$ = 10, and t_{clad} = 0.25 in. The corrected cladding data are shown below and compared to cladding influence coefficients for aspect ratios of $2c/a$ = 2 and 6.

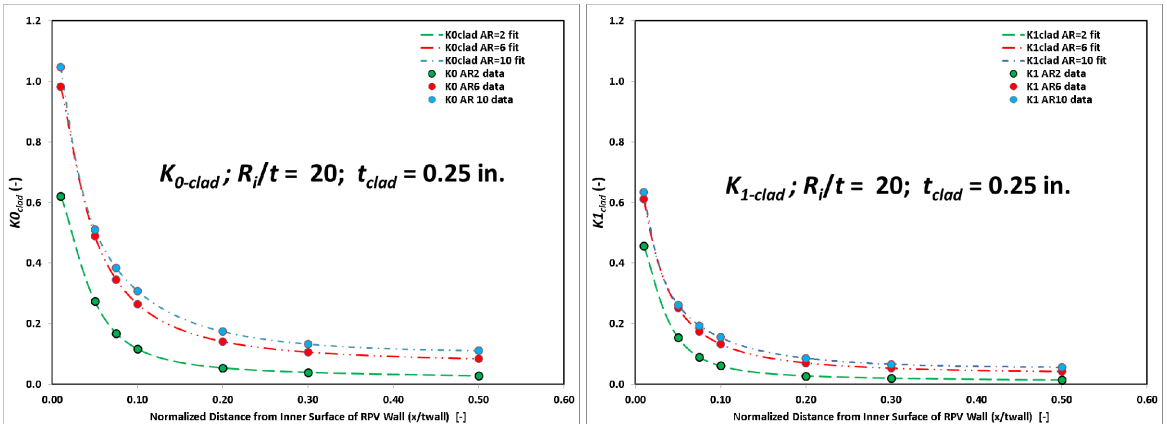

(3) Reviewer comments regarding the description of the treatment of weld fusion lines have been incorporated into the FAVOR theory manual (see Sect. 4.3.3) and user's guide.

2.3 Summary of Modifications to the v15.3 Candidate Release (released to ORNL and NRC Only) of FAVOR (Relative to v12.1)

(1) For finite-length surface breaking flaws, revised SIFIC(s) provide consistency in the normalized flaw depths used in the databases for nominal R_i/t values[2] of 10 and 20. Specifically, in the tables for R_i/t = 20, SIFIC(s) are now given for the second relative flaw depth at a/t =0.0184 (see Table B37); the latter relative flaw depth at the second position in the tabulation for R_i/t = 20 now matches that for R_i/t= 10 at the second position (see Table B2). In the original SIFIC tables, the relative flaw-depth values of a/t for R_i/t = 10 and 20 differed only in the second normalized flaw depth position in the tabulations (see Tables B2 and B11). This change was made to simplify interpolation of applied K_I factors for those intermediate values of R_i/t between 10 and 20, and to correct an error found in previous versions of FAVOR.

(2) For infinite axial and 360° continuous circumferential internal surface-breaking flaws, the entire database of SIFIC(s) was regenerated using the same scheme employed for finite-length, semi-elliptical internal surface-breaking flaws (see Section 5.1.3.2 for a detailed description of that methodology which explicitly models the clad layer); the revised SIFIC database is given in Tables B38 – B41. This change from previous versions (v01.1 through v12.1) of FAVOR was made to address issues identified for very shallow flaws where the effects of the cladding layer play a more significant role than is the case with deeper flaws. The motivation for this change is due to the fact that the original SIFIC database for infinite axial and 360° continuous circumferential internal surface-breaking flaws was generated in the early 1980s using a technique (see Section 5.1.3.2) that did not explicitly account for the effects of cladding. The revised SIFIC database now includes cladding effects consistent with the technique used for finite-length flaws.

(3) The methodology for the calculation of K_I for inner-surface breaking flaws was modified to include a component due to the crack face pressure acting on the clad in addition to the component due to the crack face pressure acting on the base metal. This modification applies to (a) finite semi-elliptical axial flaws, (b) infinite axial flaws, (c) finite semi-elliptical circumferential flaws, and (d) 360° circumferential flaws. These changes are for inner-surface breaking flaws only. Previous releases of the code (i.e., v12.1 and earlier) included only the component due to crack face pressure acting on the base metal.

(4) Closed-form curve fits based on tabular influence coefficient data from API 579-1/ASME FFS-1 (2007 edition) [4] for both finite/infinite axially-oriented flaws and finite/360° circumferentially-

[2] R_i is the inner radius of the vessel, t is the RPV wall thickness (inclusive of the cladding layer thickness) at the beltline, and a is the flaw depth. Actual value for nominal 10 is 10.118 and for nominal 20 is 20.637.

oriented flaws were developed by the ASME Working Group on Flaw Evaluation (WGFE) for the ASME Boiler and Pressure Vessel Code 2015 (BPVC), Section XI, Appendix A, Article A-3000, *Method of K_I Determination*.[5] These curve fits [6, 7] were implemented into the FAVLoad , v15.3, release. See Appendix G of this report for details. In addition, a new Fortran subroutine (*get_A3000_SIFIC(s)*) was developed and installed in the FAVLoad code, where the required inputs are the R_i/t ratio for the RPV under study, the flaw orientation (*axial* or *circumferential*) , and an array of relative flaw depths, a/t. The subroutine returns an array of SIFIC(s) corresponding to the input array of a/t values.

2.4 Summary of Modifications to the v12.1 Release of FAVOR (Relative to v09.1)

(1) Fixed a source for potential error in the FAVLoad module such that the last time in any of the three thermal hydraulic time histories (convective heat transfer, coolant temperature, and coolant pressure) must correspond to the user-specified total time for the which the load analyses (finite element thermal, stress, and applied K_I analyses) are to be performed. Modifications were made to FAVLoad such that it performs checks to insure that the last transient time for all three time histories for each transient corresponds exactly to the user-specified total time. If inconsistencies are found, execution is stopped; the user is notified of the inconsistency and told to correct and resubmit.

Before this fix, if the last time in one of the three time histories was less than the total time, FAVLoad used the last time-history value for all additional discrete time steps. If the last time of any of the three time histories exceeded the total time, then FAVLoad interpolated to determine the value at the total time.

(2) Modified an equality requirement for the warm prestress models 1 and 3. For these warm-prestress options, one of the requirements for brittle fracture is that the applied K_I must be greater than that at any previous transient times. FAVOR, v09.1 and earlier versions required only that the applied K_I be greater than or equal to that at any previous transient times.

(3) External surface breaking and embedded flaws in the outer half of the vessel wall thickness that initiate in brittle fracture are considered to also have failed, i.e., the conditional probability of vessel failure is equal to the conditional probability of initiation. There is no incremental through-wall crack propagation (toward the wetted inner surface) performed.

2.5 Summary of Modifications to the v09.1 Release of FAVOR (Relative to v07.1)

(1) Consolidated capabilities of previous versions of FAVOR and FAVORHT to have the capability to model embedded flaws at any through-wall location of the RPV wall thickness.

(2) Developed, implemented, and verified stress intensity factor influence coefficients (SIFIC(s)) for infinite-length and finite-length semi-elliptical (with aspect ratios of 2, 6, and 10) axially- and circumferentially-oriented external surface-breaking flaws applicable to a reactor vessel with an internal radius to wall thickness (R_i/t) ratio of 10, characteristic of PWR pressure vessels.

(3) Developed, implemented, and verified SIFIC(s) for infinite length- and finite-length semi-elliptical (with aspect ratios of 2, 6, and 10) axially- and circumferentially-oriented inner surface-breaking flaws applicable to a reactor pressure vessel with an R_i/t ratio of 20, characteristic of BWR pressure vessels.

(4) Developed, implemented, and verified SIFIC(s) for infinite-length and finite-length semi-elliptical (with aspect ratios of 2, 6, and 10) axially- and circumferentially-oriented external surface-breaking flaws applicable to a reactor vessel with an R_i/t ratio of 20, characteristic of BWR pressure vessels.

(5) Added user options to choose from three flaw populations: (1) inner surface-breaking flaws and embedded flaws near the RPV inner surface as required in the analysis of cool-down transients, (2) external surface-breaking flaws and embedded flaws near the RPV external surface, and (3) inner and external surface-breaking flaws and embedded flaws through the entire RPV wall thickness as might be required in the analysis of a hydro-test.

(6) Developed, implemented, and verified algorithms such that the SIFIC databases for $R_i/t = 10$ (nominal, actual value is $R_i/t = 10.118$) and BWR geometry $R_i/t = 20$ (nominal, actual value is $R_i/t = 20.637$) for internal and external surface breaking flaws are appropriately interpolated for application to RPVs for which $10 < R_i/t < 20$.

(7) The additional capabilities specified in (1) – (6) above collectively provide the capability for FAVOR,(starting with v09.1), to perform deterministic and PFM analyses of BWRs and PWRs subjected to heat-up, cool-down, and hydro-test transients.

(8) Added two additional warm-prestress options to FAVPFM.

(9) Added an optional convergence check option to FAVPost.

(10) Fixed one minor bug in FAVLoad and one in FAVPFM (from version 07.1).

2.6 Summary of Modifications to the v07.1 Release of FAVOR (Relative to v06.1)

(1) Changed the procedures in FAVPost to estimate percentiles for the random variates reported in the FAVPost output. These percentiles are now calculated from a mixed empirical/exponential

distribution function constructed using order statistics and the Kaplan-Meier rank estimator. A shifted exponential distribution is fitted to the extreme right tail to correct known problems associated with estimated percentiles based on a purely empirical distribution function.

(2) Added three new radiation shift correlations (see Sect. 5.2.2).

2.7 Summary of Modifications to the v06.1 Release of FAVOR (Relative to v05.1)

(1) Changed the data basis for $\Delta RT_{epistemic}$ which results in a new cumulative distribution function from which to sample $\Delta RT_{epistemic}$.

(2) Added the Eason 2006 radiation-shift correlation, which is also a function of manganese, in addition to the input variables for the Eason 2000 correlation.

(3) Changed the Monte Carlo looping structure where uncertainty in $RT_{NDT}(u)$, $\Delta RT_{epistemic}$, and the standard deviation of copper (Cu), nickel (Ni), phosphorus (P), and manganese (Mn) are sampled.

(4) Changed the coefficients for the upper-shelf ductile tearing model.

(5) Refined the treatment of temperature dependencies of thermal expansion coefficients in accordance with ref. [108].

(6) Enhanced output data reports as requested by Steve Long (of NRR).

(7) Changed the flaw accounting procedures in the 05.1 version of FAVPFM to correct inconsistencies discovered during an independent check and review exercise conducted by Dr. R. M. Gamble.

2.8 Summary of Modifications to the v05.1 Release of FAVOR (Relative to v04.1)

(1) Provided the capability to predict a non-zero conditional probability of vessel failure at a transient time of zero. In previous versions of FAVOR, an implicit assumption had been that steady-state conditions exist at a transient time of zero and that fracture would not be predicted to occur at steady state conditions; this assumption was removed by making the needed changes to the code were developed, tested, and implemented

(2) Modified the ductile tearing model such that it no longer executes an inappropriate double-sampling of the epistemic uncertainty in $RT_{NDT(u)}$.

2.9 Summary of Modifications to the v04.1 Release of FAVOR (Relative to v03.1)

(1) Added the ability to include temperature-dependent, thermo-elastic properties in the thermal and stress analysis sections of the FAVLoad module. These thermo-elastic properties include the thermal conductivity, k, mass-specific heat, c_p, coefficient of thermal expansion, α, Young's modulus of elasticity, E, and Poisson's ratio, ν.

(2) Added the optional ability to include the crack-face pressure as an additional load for inner surface-breaking flaws.

(3) Added a restart capability such that at regular, user-defined check points in the FAVPFM analysis, the FAVPFM module creates a binary restart file. If the FAVPFM run should fail during execution, or if, at the normal end of a run, it is determined that additional RPV trials are required to reach convergence, then the run may be restarted using the most recent random number generator seeds as recorded in the restart file. The use of the restart seeds ensures that the restart will continue with the same random number sequence that it would have used if the run had not been terminated.

(4) Implemented a new upper-shelf ductile-tearing model. This new model has three stochastically sampled variables.

(5) Removed the limitation on the number of time history pairs (of 1000) for convective heat transfer coefficient, coolant temperature, and pressure for each transient. The arrays into which these data are read are now dynamically dimensioned.

(6) Replaced the compiler-specific intrinsic random number (uniform distribution) generator available with the LAHEY Fortran 90 compiler utilized in previous releases of FAVOR with a portable (coded in Fortran) composite generator with a reported minimum theoretical period of 2.3×10^{18} (see ref. [78]). The intent was to insure that FAVOR generated identical solutions, regardless of the Fortran compiler used. Also a portable random number generator, with explicit control on its seeds, is a necessity for restart capability.

(7) Replaced the Box-Müller Method for sampling from a normal distribution with an extension of Forsythe's method as presented in ref. [83]. Ahrens and Dieter (1973) in ref. [83] have experienced a 27 percent reduction in computational time relative to the older Box-Müller method. The intent of this modification is to increase the computational efficiency of FAVOR.

(8) Various modifications and enhancements were made to FAVPOST reports.

2.10 Summary of Modifications to the v03.1 Release of FAVOR (Relative to v02.4)

(1) Implemented initial ductile tearing model into the FAVPFM model. This model had a single sampled variable.

(2) Fixed two minor bugs in the v0.2.4 version of the FAVPFM module

(3) Modified FAVPost so that the solutions (distributions of frequency of crack initiation and RPV failure) have no dependency on the ordering of the transients.

2.11 Summary of Modifications to the v02.4 Release of FAVOR (Relative to v01.1)

(1) Extended dynamic memory management in all three FAVOR modules.

(2) For thermal analysis in FAVLoad, the quadrature was extended to full-Gaussian integration, instead of the previously applied reduced integration as in the stress analysis.

(3) Added SLATEC error-handling package in all three FAVOR modules.

(4) Added warm-prestressing as an option for both initiation and re-initiation in FAVPFM.

(5) Added T-H Transient time-windowing capability in FAVPFM.

(6) Added Parent-Child reporting in FAVPFM.

(7) Fixed problem with stress discontinuity calculation at clad/base interface.

(8) Added user-input to specify a failure criterion for through-wall flaw growth.

3. Pressurized Thermal Shock Events

Overcooling events, where the temperature of the coolant in contact with the inner surface of the reactor pressure vessel (RPV) wall rapidly decreases with time, produce temporally dependent temperature gradients that induce biaxial stress states varying in magnitude through the vessel wall. Near the inner surface of the RPV wall, the stresses are tensile, thus presenting Mode I opening driving forces that can act on possible surface-breaking or embedded flaws. The combined thermal plus mechanical loading results in a transient condition known as a pressurized thermal shock (PTS) event.

PTS can potentially challenge the integrity of a nuclear RPV due to the combined effects of (1) the combination of pressure and thermal-shock loadings, (2) embrittlement of the vessel material due to cumulative irradiation exposure over the operating history of the vessel, and (3) the possible existence of crack-like defects at the inner surface of or embedded within the RPV heavy-section wall. The decrease in vessel temperature associated with a thermal shock reduces the fracture toughness of the vessel material and introduces the possibility of flaw propagation. Inner surface-breaking flaws and embedded flaws near the inner surface have the greatest risk significance, because at the inner surface the temperature is at its minimum and the stress and radiation-induced embrittlement are at their maximum.

3.1 Historical Review

The designers of the first pressurized-water reactor (PWR) vessels in the late 1950s and early 1960s were cognizant of thermal shock events as a reactor vessel integrity issue where nonductile fracture was evaluated as a part of the design basis using a transition-temperature approach [8].The need to ensure the high reliability and fracture safety of nuclear RPVs under all operational and postulated accident conditions motivated a number of advances in fracture mechanics technology in the 1960s and the 1970s. Before the 1970s, it was postulated that the most severe thermal shock challenging a PWR vessel would occur during a large-break loss-of-coolant accident (LOCA), where room-temperature emergency core-cooling water would flood the reactor vessel within a few minutes, rapidly cooling the wall and inducing tensile thermal stresses near the inner surface of the vessel [9]. However, the addition of pressure loading to the thermal loading was not typically considered, since it was expected that during a large-break LOCA the system would remain at low pressure. Two events in 1978-1979 served to highlight the importance of addressing the structural integrity challenges posed by a *pressurized* thermal shock.

In 1978, the occurrence of an off-normal event at the Rancho Seco Nuclear Power Plant in California showed that during some types of overcooling transients, the rapid cooldown could be accompanied

by repressurization of the primary recirculating cooling water (RCW) system, thus adding pressure stresses to the already existent thermal stresses produced by the cool-down. The Three-Mile-Island (TMI) incident in 1979, which also involved a cooldown event at high RCW system pressure, drew additional attention to the impact of operator action and control system effects on transient temperature and pressure characteristics for PTS events [8].

Following these two events, the U.S. Nuclear Regulatory Commission (NRC) designated PTS as an *Unresolved Safety Issue* (USI) A-49, December 1981, *Pressurized Thermal Shock*. Questions also arose concerning the stratification (or lack of mixing) of cold safety injection water with reactor coolant in the vessel, leading to an amplification of the PTS effect. In 1980, the NRC issued NUREG 0737-Item II.K.2.13, which required that the operators of all PWRs and all applicants for licenses evaluate reactor vessel integrity following a small-break LOCA as part of the TMI action plan [10]. Additional potential transients were added in March of 1981. At the end of 1981, the nuclear power industry submitted its response to NUREG 0737 to the NRC. These submittals were based primarily on deterministic analyses using conservative thermal-hydraulic and fracture-mechanics models of postulated design-basis transients and the temperature and pressure time-histories from some of the PTS events that had actually been experienced in operating PWR plants [8]. On the basis of these analyses, the NRC concluded that no event having a significant probability of occurring could cause a PWR vessel to fail at that time or within the next few years. To address the potential for other events with more limiting transient characteristics in combination with the impact of operator action and control system effects, the NRC subsequently placed greater emphasis on Probabilistic Risk Assessment (PRA) combined with thermal-hydraulic (T-H) analysis and probabilistic fracture mechanics (PFM) as primary vessel-integrity assessment tools.

3.2 NRC Regulatory Approach to PTS and Proposed Amendment

During the 1980s, in an effort to establish generic screening limits quantified in terms of vessel embrittlement, the NRC funded the Integrated Pressurized Thermal Shock (IPTS) Program [9, 11, 12] which developed a comprehensive probabilistic approach to risk assessment. The regulatory requirements expressed in 10 CFR 50.61 are based on the resulting risk-informed probabilistic methodology. In the early 1980s, extensive analyses were performed by the NRC and others to estimate the likelihood of vessel failure due to PTS events in PWRs. Though a large number of parameters governing vessel failure were identified, the single most significant parameter was a correlative index of the material that also serves as a measure of embrittlement. This material index is the reference nil-ductility transition temperature, RT_{NDT}. The NRC staff and others performed analyses of PTS risks on a conservative and generic basis to bound the risk of vessel failure for any PWR reactor. The NRC staff approach to the selection of the RT_{NDT} screening criteria is described in

SECY 82 465 [13]. Reference [14] is a short review of the derivation of the PTS *screening criteria* from both deterministic and probabilistic fracture mechanics considerations. The analyses discussed in SECY-82-465 led to the establishment of the *PTS Rule* [15], promulgated in Title 10 of the *Code of Federal Regulations*, Chapter I, Part 50, Section 50.61 (10CFR50.61), and the issuance of NRC Regulatory Guide 1.154 (RG1.154) [16][3].

The original *PTS Rule* specifies *screening criteria* in the form of irradiated values of RT_{NDT} (designated by the rule as RT_{PTS}) of 270 °F for axially oriented welds, plates, and forgings and 300 °F for circumferentially oriented welds. The PTS rule also prescribes a method to estimate RT_{PTS} . Although not explicitly cited by the rule, this method is based on the prescription given in Regulatory Guide 1.99, Revision 2 [17]. To justify plant operation for RT_{PTS} values that exceed the screening criteria, licensees must submit a plant-specific safety analysis to the NRC three years before the screening limit is anticipated to be reached.

In 2007, the NRC initiated rulemaking to provide an alternative PTS screening criteria [18] (10CFR50.61a). This rulemaking was completed in 2010 [Federal Register /Vol. 75, No. 1 /Monday, January 4, 2010, pp. 13-29]. The 10CFR50.61a requirements are voluntary and provide one means by which a PWR licensee can comply with the existing requirements in 10CFR50.61. The technical bases for 10 CFR 50.61a are reported in ref. [19] in which the FAVOR code played a critical role. The recommended reference temperature screening criteria for PTS in 10CFR50.61a are discussed in ref. [20] which includes the following description:

> The NRC staff recommends using different reference temperature (*RT*) metrics to characterize the resistance of an RPV to fractures initiating from different flaws at different locations in the vessel. Specifically, the staff recommends an *RT* for flaws occurring along axial weld fusion lines ($RT_{MAX\text{-}AW}$), another for the embedded flaws occurring in plates ($RT_{MAX\text{-}PL}$), a third for flaws occurring along circumferential weld fusion lines ($RT_{MAX\text{-}CW}$), and a fourth for embedded and/or underclad cracks in forgings ($RT_{MAX\text{-}FO}$). These values can be estimated based mostly on the information in the NRC's Reactor Vessel Integrity Database (RVID). The staff also recommends using these different *RT* values together to characterize the fracture resistance of the vessel's beltline region, recognizing that the probability of a vessel fracture initiating from different flaw populations varies considerably in response to factors that are both understood and predictable. Correlations between these *RT* values and the through-wall cracking frequency attributable to different flaw populations show little plant-to-plant variability because of the general similarity of PTS challenges among plants.

[3] As stated in the Federal Register, Vol. 26, No. 10, Friday, on January 14, 2011, Regulatory Guide 1.154 was withdrawn from use by the NRC. According to the notice [NRC-2011-0010], "withdrawal means that the guide should not be used for future NRC licensing activities. Changes to existing licenses would be accomplished using other regulatory products."

3.3 Contributions of Large-Scale Experiments to the Technical Basis for PTS Assessment

A number of large-scale experiments, conducted internationally over the past 30 years, have contributed significantly to a better understanding of the factors influencing the behavior of RPVs subjected to postulated PTS scenarios [21]. These experiments, several of which are summarized in Table 1, reflect different objectives that range from studies of "separate effects" to others that integrate several features into a single experiment. In Table 1, the experiments are organized in terms of four specimen groups: (1) pressure-vessel specimens, (2) cylindrical specimens, (3) plate specimens, and (4) beam specimens. The actual test specimens were fabricated from prototypical RPV steels, including plate, forgings, and weld product forms. Some of the specimens included prototypical cladding, and others used steels that had been heat-treated or were fabricated with a special chemistry to simulate near-end-of-licensing (degraded properties) conditions.

These large-scale experiments have provided a catalyst in western Europe and the United States for intensive international collaboration and for the formation of multinational networks to assess and extend RPV/PTS technology. Project FALSIRE [22-25] was initiated in 1989 through support provided by governmental agencies within Germany and the U. S., under sponsorship of the OECD/Nuclear Energy Agency. Within FALSIRE, researchers from a large number of international organizations used selected large-scale experiments to evaluate levels of conservatism in RPV integrity assessment methodologies. In 1993, the Joint Research Centre of the European Commission launched the Network for Evaluating Structural Components (NESC) to study the entire process of RPV integrity assessment. The NESC projects brought together a large number of leading international research organizations to evaluate all aspects of the assessment process (i.e., fracture methodologies, material properties characterization, inspection trials, and experimental techniques) through a large-scale PTS spinning cylinder experiment [26, 44]. Issues receiving special attention in the NESC experiment included (1) effects of constraint, (2) effects of cladding and HAZ regions, and (3) behavior of sub-clad flaws under simulated PTS loading.

The large-scale experimental database and extensive body of associated analytical interpretations have provided support for the technical basis that underpins various elements of the fracture models implemented in the FAVOR code. In particular, these results have contributed significantly to confirming the applicability of fracture methodologies to cleavage fracture events in RPV steels, including crack initiation and crack arrest. References [22-26, 44] (and references given therein) provide comprehensive evaluations of RPV integrity assessment methodologies applied to a broad selection of experiments.

Within the NRC-funded Heavy Section Steel Technology (HSST) program and its successors, the Probabilistic Pressure Boundary Integrity Safety Assessment (PISA) program and the Probabilistic Structural and Material Modeling (ProSaMM) program (all at ORNL), the large-scale experiments continue to contribute to a framework for future integration of advanced fracture techniques into RPV integrity assessment methodology.

Table 1. Large-Scale PTS Experiments and Performing Organizations

ID No.	Experiment Title	Research Organization	Country	Refs.
Tests with Pressurized Vessels				
ITV 1-8	Intermediate Test Vessels	Oak Ridge National Laboratory	USA	27-33
PTSE-1	Pressurized Thermal Shock Experiments	Oak Ridge National Laboratory	USA	34
PTSE-2	Pressurized Thermal Shock Experiments	Oak Ridge National Laboratory	USA	35
PTS I/6	Pressurized Thermal Shock Experiment I/6	Central Research Institute for Structural Materials (CRISM)	Russia	36, 37
Tests with Cylindrical Specimens				
NKS-3	Thermal Shock Experiment 3	Materialprüfungsanstalt (MPA)	Germany	38
NKS-4	Thermal Shock Experiment 4	Materialprüfungsanstalt (MPA)	Germany	38
NKS-5	Thermal Shock Experiment 5	Materialprüfungsanstalt (MPA)	Germany	39
NKS-6	Thermal Shock Experiment 6	Materialprüfungsanstalt (MPA)	Germany	37, 39
SC-1	Spinning Cylinder PTS Experiment 1	AEA Technology	UK	40
SC-2	Spinning Cylinder PTS Experiment 2	AEA Technology	UK	40
SC-4	Spinning Cylinder PTS Experiment 4	AEA Technology	UK	41
TSE-6	Thermal Shock Cylinders (Cylinder with Short Flaws)	Oak Ridge National Laboratory (ORNL)	USA	42
TSE-7	Thermal Shock Cylinders (Clad Cylinder)	Oak Ridge National Laboratory (ORNL)	USA	43
TSE-8	Thermal Shock Cylinders (Clad Cylinder)	Oak Ridge National Laboratory (ORNL)	USA	43
NESC-1	NESC-1 Spinning Cylinder PTS Experiment	Network for Evaluating Steel Components (NESC)	International Network	44
Tests with Plate Specimens				
PTS Step B	Wide-Plate PTS Step B Experiment	Japan Power and Engineering Inspection Corporation (JAPEIC)	Japan	45
WP-1 & 2	Wide-Plate Crack Arrest Tests of A533B and LUS Steels	Oak Ridge National Laboratory (ORNL)	USA	46, 47
GP-1	Wide Plate Test	Materialprüfungsanstalt (MPA)	Germany	48
Tests with Beam Specimens				
DD-2 & DSR-3	Clad-beam experiments	Electricité de France (EdF)	France	37, 49
SE(B) RPV Steel	Full-Thickness Clad Beam Experiments	National Institute of Standards and Testing (NIST) and ORNL	USA	50, 51
CB	Cruciform Beam (CB) Experiments	Oak Ridge National Laboratory (ORNL)	USA	52

4. Structure and Organization of the FAVOR Code

4.1 FAVOR – Computational Modules and Data Streams

As shown in Fig. 2, FAVOR, written in Fortran 90/95, is composed of three computational modules: (1) a deterministic load generator (**FAVLoad**), (2) a Monte Carlo PFM module (**FAVPFM**), and (3) a post-processor (**FAVPost**). Figure 2 also indicates the nature of the data streams that flow through these modules.

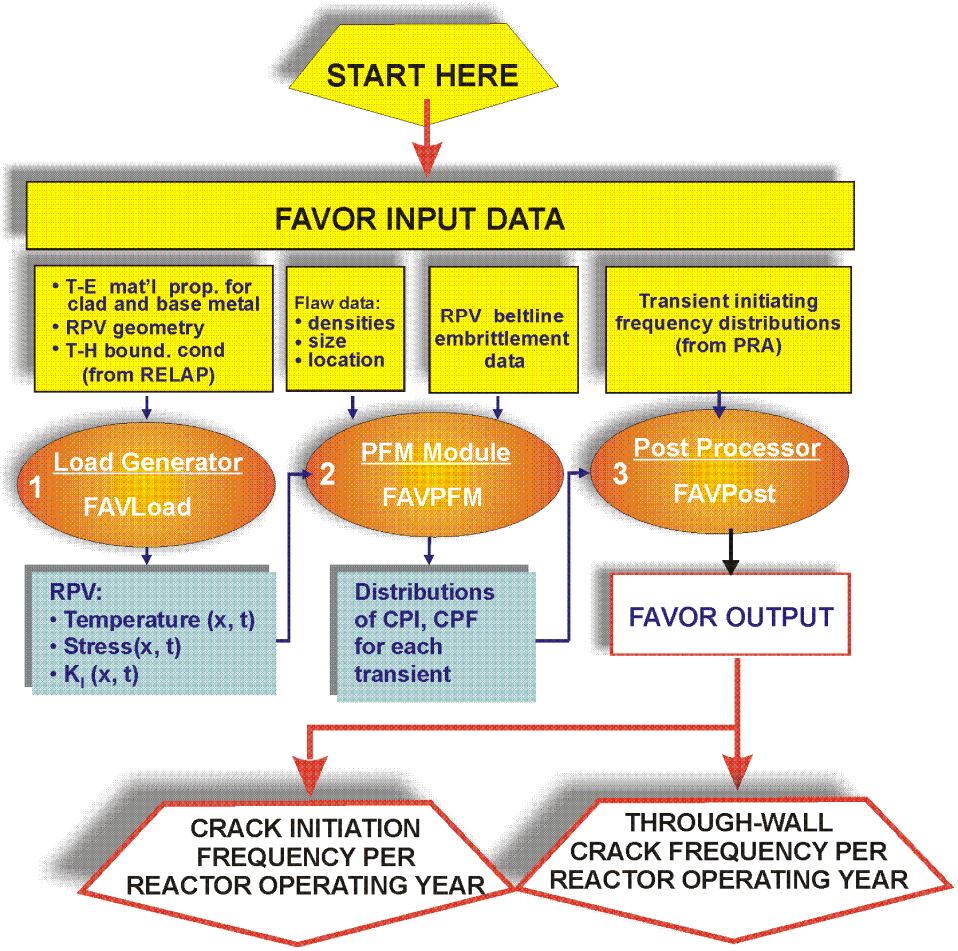

Fig. 2. FAVOR data streams flow through three modules: (1) FAVLoad, (2) FAVPFM, and (3) FAVPost.

The formats of the required user-input data files are discussed in detail in the companion report *FAVOR, v16.1: User's Guide* [2].

4.2 FAVOR Load Module (FAVLoad)

The functional structure of the FAVOR load module, FAVLoad, is shown in Fig. 3, where multiple thermal-hydraulic transients are defined in the input data. The number of transients that can be analyzed in a single execution of FAVLoad is dependent upon the memory capacity of the computer being used for the analysis. For each transient, deterministic calculations are performed to produce a load-definition input file for FAVPFM. These load-definition files include time-dependent through-wall temperature profiles, through-wall circumferential and axial stress profiles, and stress-intensity factors for a range of axially and circumferentially oriented inner and external surface-breaking flaw geometries (both infinite- and finite-length).

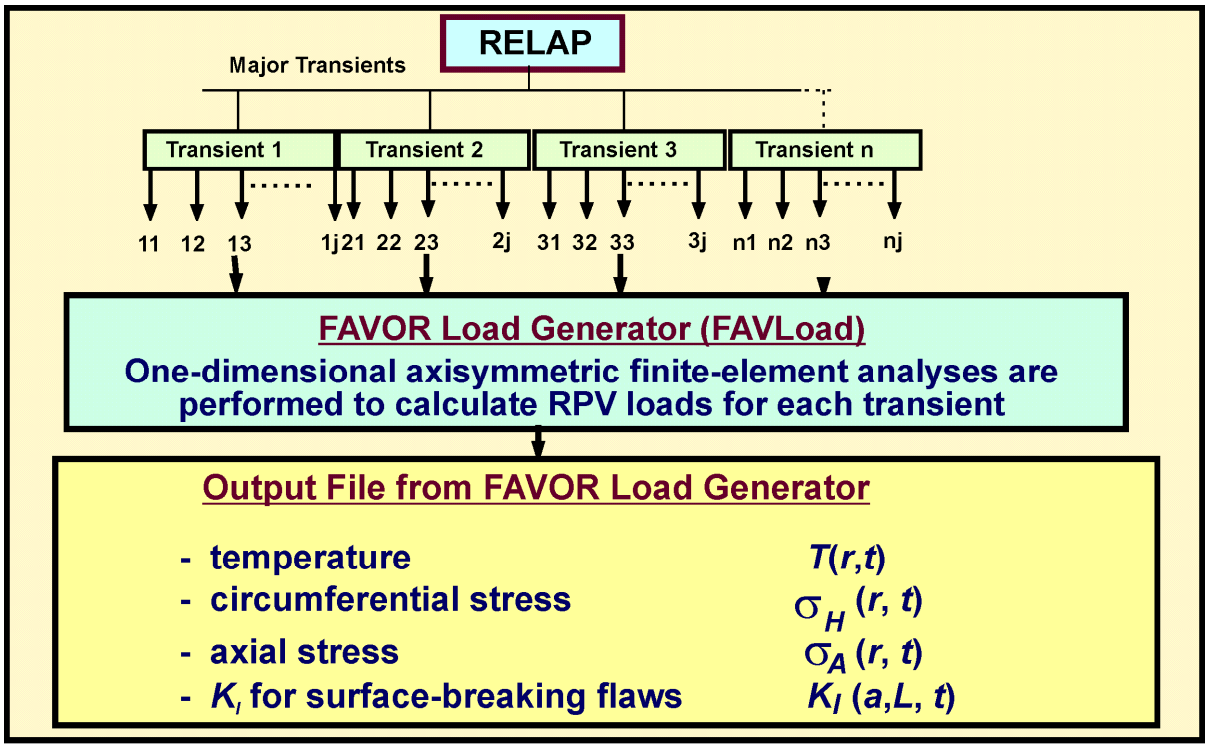

Fig. 3. The FAVOR load generator module FAVLoad performs deterministic analyses for a range of thermal-hydraulic transients.

4.2.1 Thermal-Hydraulic Transient Definitions

The thermal-hydraulic (T-H) definitions required by FAVLoad are supplied by the user in the form of digitized tables of bulk coolant temperature, convective heat-transfer coefficient, and internal pressure, all as functions of elapsed time for the transient. Time-history data pairs can be input for each of the three variables, allowing a very detailed definition of the thermal-hydraulic loading imposed on the RPV internal wall. An option is also available to specify a stylized exponentially decaying coolant temperature-time history.

4.2.2 Required Vessel Geometry and Thermo-Elastic Property Data

The FAVLoad module requires fundamental vessel geometry data, including the vessel's inner radius, wall thickness, and cladding thickness. Temperature-dependent thermo-elastic properties are also input for the cladding and base materials. These geometric descriptions and property data for the RPV are treated as fixed parameters in all subsequent analyses.

4.2.3 Deterministic Analyses

Finite-element analyses are carried out on a one-dimensional axisymmetric model of the vessel wall. The transient heat conduction equation with temperature-dependent properties is solved for the combined cladding and base materials to produce time-varying temperature profiles through the wall. The finite-element stress analysis calculates radial displacements and then, through strain-displacement and linear-elastic stress-strain relationships, time-varying axial and hoop stress profiles are also calculated. These stresses include the effects of thermal and mechanical loading (internal pressure applied to the inner vessel surface and exposed crack face) along with the option of superimposed weld-residual stress profiles developed by the HSST program. The steep stress gradient at the clad-base interface is also captured by the finite-element stress model. Through the specification of a selected stress-free temperature by the user, the effects of an initial thermal-differential expansion between the cladding and base materials can also be included in the quasi-static load path. The finite-element thermal and stress models use the same quadratic elements and graded-mesh discretization.

The finite-element method (FEM), together with the very detailed definition of the thermal-hydraulic boundary conditions, provides the capability to generate accurate 1-dimensional, thermal, stress, and applied stress-intensity factor, K_I, solutions as a function of transient elapsed time and radial position in the wall. The application of FEM in this way allows the resolution of complex thermal-hydraulic transients that exhibit discontinuities in the boundary condition time-histories, e.g., transients with late repressurizations.

Time-dependent stress-intensity factors for infinite- and finite-length, internal and external, surface-breaking flaws are calculated for a range of flaw depths, sizes, and aspect ratios. Due to its generality, the embedded-flaw model was implemented in the FAVPFM module, rather than FAVLoad. The details of these deterministic analyses are given in Chapter 5. See Fig. 4 for a summary of the flaw models available in FAVOR.

4.2.4 Flaw Populations and Models Used in FAVOR

A significant part of the generalization included in FAVOR is (1) the capability to model different flaw populations depending on the problem and (2) the capability to model BWR vessel geometries as well as PWR geometries.

FAVOR was originally developed to perform deterministic and probabilistic fracture mechanics (PFM) analyses of reactor pressure vessels subjected to cool-down thermal hydraulic transients imposed on the inner (wetted) surface of the reactor such as those associated with accidental PTS conditions and normal transients associated with reactor shutdown.

For such cool-down transients, the flaw population of interest are those flaws on and/or near the inner surface of the reactor vessel wall, because at the inner surface, the temperature is at its minimum and the tensile stress and radiation-induced embrittlement are at their maximum. These tensile stresses tend to open existing cracks located on or near the internal surface of the RPV wall.

Therefore, earlier versions of FAVOR were limited to modeling internal surface-breaking flaws and/or embedded flaws that reside near the inner surface of the vessel wall. The embedded flaws (quantified in the embedded flaw characterization files) are assumed to be distributed uniformly throughout the entire vessel wall; however, for computational efficiency, only those postulated to reside in the first 3/8 of the base metal (wall thickness exclusive of clad thickness) were included in the analysis. For cool-down transients, the applied-K_I driving force for embedded flaws postulated to reside in the vessel wall beyond the inner 3/8 of the wall thickness is too small to have a conditional probability of initiating an embedded flaw in cleavage fracture.

For heat-up transients, such as normal transients associated with reactor start-up, flaws on or near the external surface of the reactor vessel are the most risk-significant because the tensile stresses are at their maximum there. The FAVOR^{HT} code was designed to perform analyses of these heat-up transients; i.e., however, it was limited to the modeling of embedded flaws in the outer 3/8 of the RPV wall thickness. FAVOR^{HT} did not have the capability of modeling external surface-breaking flaws.

FAVOR, v09.1, consolidated the capabilities of the previous versions of FAVOR and FAVOR^{HT} as discussed above as well as added additional capabilities. Since v09.1, FAVOR has the user-specified optional ability to model three different flaw populations as follows:

Flaw Population Option 1 – (Identical to previous versions of FAVOR.) All surface-breaking flaws (quantified in the surface flaw characterization input file) are internal surface breaking flaws and only

those embedded flaws in the first 3/8 of the RPV wall thickness are included in the model. The primary application of this option is for modeling cool-down transients. Through-wall flaw propagation is included in this option

Flaw Population Option 2 – (Similar to previous versions of FAVOR^{HT}, however, it includes the capability to model external surface breaking flaws.) All surface-breaking flaws (quantified in the surface flaw characterization input file) are external surface-breaking flaws and those embedded flaws in the outer 3/8 of the RPV wall thickness are included in the model. The primary application of this option is for modeling heat-up transients. Through-wall flaw propagation is not yet included in this option.

Flaw Population Option 3 – This additional population includes internal and external surface-breaking flaws; all of the embedded flaws are uniformly distributed through the RPV wall (approximately 8/3 times the number of embedded flaws postulated in Options 1 and 2). The number of postulated surface breaking flaws is double that of Options 1 or 2; and they are evenly divided between internal and external surface breaking flaws. The application of Option 3 is for modeling transients in which the pressure-induced loading is dominant (e.g., hydro-testing, etc.), since the applied-K_I for all flaws has a smaller dependence on their respective locations. Through-wall flaw propagation is not yet included in this option.

Flaw Population Options 1 and 2 are available for computational efficiency. If the dominant loading is thermally induced, only those populations of flaws on or near the relevant RPV surface would likely ever initiate (and subsequently fail), so the other flaws are excluded from the analysis because their presence would not change the PFM solution(s), but could dramatically increase the computational resources (memory and time) to complete a PFM analysis. When in doubt, Option 3 is suggested; however, this option will require considerably more computational resources in terms of memory and computational time to reach a converged solution.

Another limitation of versions before FAVOR v09.1 is that the analysis of internal surface-breaking flaws was restricted to reactor vessels with an internal radius to wall thickness (R_i/t) ratio of approximately 10, characteristic of PWRs. This limitation occurred because the stress intensity factor-influence coefficients (SIFIC(s)), applied by FAVOR to calculate values of applied-K_I for surface-breaking flaws, were applicable only to this specific geometry. Most BWRs have an R_i/t ratio of approximately 20, although a few BWRs in the United States have R_i/t ratios between 10 and 20.

FAVOR has the capability of modeling 16 surface-breaking flaw types for PWR and BWR geometries as shown in Table 2.

Table 2. Surface-Breaking Flaw Geometries

Flaw type	Aspect ratio	Surface breaking	Orientation
1	**2**	Internal	Axial
2	**6**	Internal	Axial
3	**10**	Internal	Axial
4	**Infinite**	Internal	Axial
5	**2**	Internal	Circumferential
6	**6**	Internal	Circumferential
7	**10**	Internal	Circumferential
8	**Infinite**	Internal	Circumferential
9	**2**	External	Axial
10	**6**	External	Axial
11	**10**	External	Axial
12	**Infinite**	External	Axial
13	**2**	External	Circumferential
14	**6**	External	Circumferential
15	**10**	External	Circumferential
16	**Infinite**	External	Circumferential

The SIFIC databases for BWR vessel geometry ($R_i/t \approx 20$) are distinctly different from those generated for the PWR geometry ($R_i/t \approx 10$); therefore, there are two SIFIC databases for each of the 16 surface breaking flaw types in FAVOR; one each for PWR geometry $R_i/t \approx 10$ and BWR geometry $R_i/t \approx 20$. The generalization of FAVOR to include the capability to calculate applied-K_I 's for the 16 axially- and circumferentially-oriented internal and external surface breaking flaw types for both BWR and PWR required the creation, implementation, and verification of a total 32 SIFIC databases, compared to eight SIFIC databases in previous versions of FAVOR. Also, algorithms have been developed and verified such that the SIFIC databases for $R_i/t \approx 10$ and BWR geometry $R_i/t \approx 20$ for internal and external surface-breaking flaws are appropriately interpolated for application to RPVs for which $10 < R_i/t < 20$; therefore, FAVOR can be applied to those BWRs having R_i/t ratios between 10 and 20.

Regarding flaw orientation, all pre-existing inner-surface breaking flaws are assumed to be circumferentially oriented. Pre-existing external surface-breaking flaws in axial welds are axially

oriented; external surface-breaking flaws in circumferential welds are circumferentially oriented; and external surface-breaking flaws in plates are evenly divided between axial and circumferential orientations. As in previous versions of FAVOR, embedded flaws in welds assume the orientation of the weld, i.e., embedded flaws in axial welds are axially oriented, and embedded flaws in circumferential welds are circumferentially oriented. Embedded flaws in plates are evenly divided between axial and circumferential orientations.

For the finite-length, semi-elliptical flaw geometries, the SIFIC databases contain values corresponding to multiple angular positions around the semielliptical crack front; however, currently FAVOR only applies those values that correspond to the deepest point of the flaw.

The flaw models shown in Fig. 4 are included in the three categories of flaws identified by FAVOR:

Category 1:

Includes Flaw Population Option 1 – internal surface-breaking flaws only (flaw types 1-8)

Includes Flaw Population Option 2 – external surface-breaking flaws only (flaw types 9-16)

Includes Flaw Population Option 3 – internal and external surface-breaking flaws only (flaw types 1-16)

Category 2:

Includes Flaw Population Option 1 with embedded flaws having fully elliptic geometry with the crack tip nearest the wetted inner surface located between the clad / base interface and the inner $1/8^{th}$ of the base metal thickness

Includes Flaw Population Option 2 with embedded flaws having fully elliptic geometry with crack tip nearest the external surface located in the outer $1/8^{th}$ of the base metal thickness

Includes Flaw Population Option 3 with embedded flaws having fully elliptic geometry with crack tip nearest the external surface located between the clad base interface and the outer half of the total wall thickness.

Note: base metal thickness = total vessel wall thickness – clad thickness

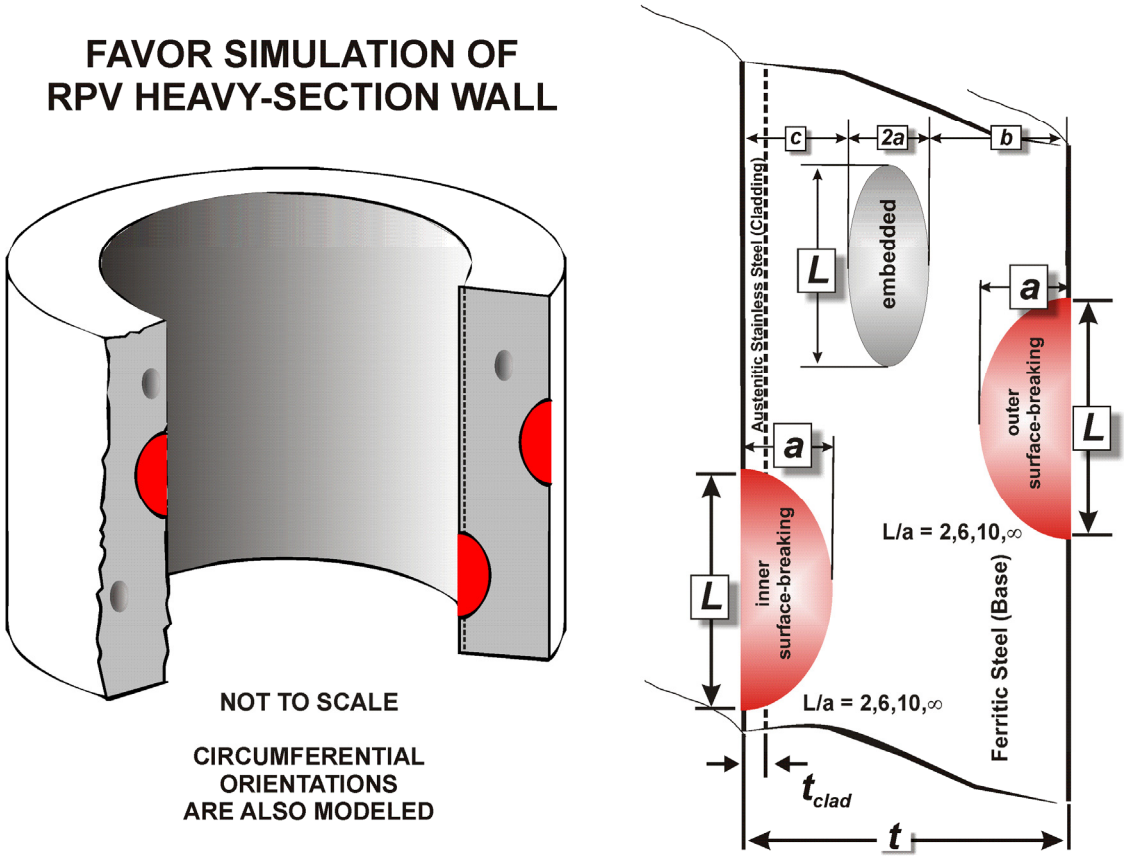

Fig. 4. Flaw models in FAVOR

Category 3:

Includes Flaw Population Option 1 with embedded flaws having fully elliptic geometry with the crack tip nearest the wetted inner surface located between 1/8th and 3/8th of the base metal thickness

Includes Flaw Population Option 2 with embedded flaws having fully elliptic geometry with crack tip nearest the external surface located between 1/8th and 3/8th of the outer base metal thickness

Includes Flaw Population Option 3 with embedded flaws having fully elliptic geometry with crack tip nearest the external surface located in the outer half of the total wall thickness.

4.3 FAVOR PFM Module (FAVPFM)

The FAVOR PFM model is based on the Monte Carlo technique, where deterministic fracture analyses are performed on a large number of stochastically generated RPV *trials* or *realizations*. Each vessel realization can be considered a perturbation of the *uncertain* condition of the specific RPV under analysis. The condition of the RPV is considered uncertain in the sense that a number of the vessel's properties (specifically, material chemistry composition and irradiation fluence) along with the postulated flaw population have uncertainties associated with them. These input uncertainties are described by statistical distributions. The RPV trials propagate the input uncertainties with their interactions through the model, thereby determining the probabilities of crack initiation and through-wall cracking for a set of postulated PTS events at a selected time in the vessel's operating history. The improved PFM model also provides estimates of the uncertainties in its outputs in terms of discrete statistical distributions. By repeating the RPV trials a large number of times, the output values constitute a random sample from the probability distribution over the output induced by the combined probability distributions over the several input variables [53].

The assumed fracture mechanism is stress-controlled cleavage initiation (in the transition-temperature region of the vessel material) modeled under the assumptions of linear-elastic fracture mechanics (LEFM). The failure mechanism by through-wall cracking is the prediction of sufficient flaw growth either (1) to produce a net-section plastic collapse of the remaining ligament or (2) to advance the crack tip through a user-specified fraction of the wall thickness. Flaw growth can be due to either cleavage propagation or stable ductile tearing. In addition, if the conditions for unstable ductile tearing are satisfied, then vessel failure by through-wall cracking is assumed to occur.

The Monte Carlo method involves sampling from appropriate probability distributions to simulate many possible combinations of flaw geometry and RPV material embrittlement subjected to transient loading conditions. The PFM analysis is performed for the beltline of the RPV as defined by the input data and typically assumed to extend from one foot below the reactor core to one foot above the reactor core. The RPV beltline can be divided into *major regions* such as axial welds, circumferential welds, and plates or forgings that may have their own embrittlement-sensitive chemistries. The major regions may be further discretized into *subregions* to accommodate detailed neutron fluence maps that can include significant details regarding azimuthal and axial variations in neutron fluence. The general data streams that flow through the FAVPFM module are depicted in Fig. 5.

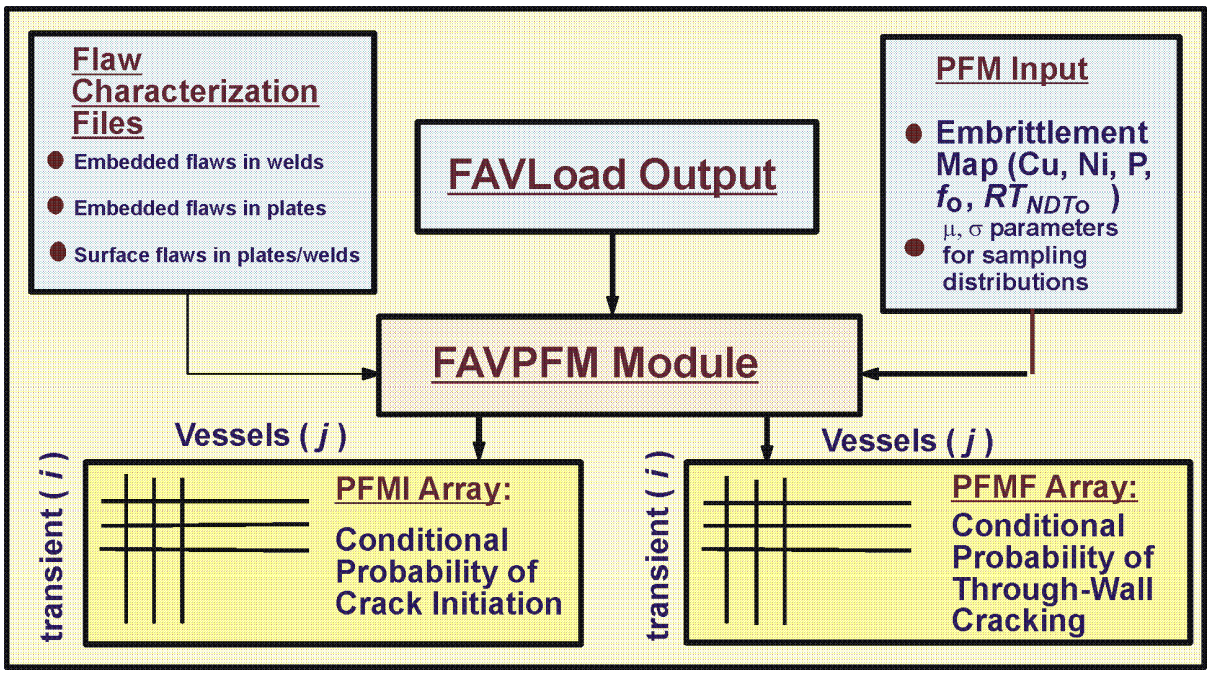

Fig. 5. The FAVPFM module takes output from FAVLoad and user-supplied data on flaw distributions and embrittlement of the RPV beltline and generates PFMI and PFMF arrays.

As shown in Fig. 5, the FAVPFM module requires, as input, load-definition data from FAVLoad and user-supplied data on flaw distributions and embrittlement of the RPV beltline. FAVPFM then generates two matrices: (1) the conditional probability of crack initiation (PFMI) matrix and (2) conditional probability of through-wall cracking (PFMF) matrix. The $(i, j)^{th}$ entry in each array contains the results of the PFM analysis for the j^{th} vessel simulation subjected to the i^{th} transient.

The original PTS rule was developed in part from PFM models that calculated a Bernoulli sequence of boolean results (either true or false) for cleavage fracture initiation and RPV failure by through-wall cracking; i.e., the outcome for each RPV trial in the Monte Carlo analysis was either crack initiation (true) or no crack initiation (false) and either failure (true) or no failure (false). The conditional probability of initiation, $P(I|E)$, was calculated simply by dividing the number of RPV trials predicted to experience cleavage fracture by the total number of trials. Similarly, the conditional probability of failure, $P(F|E)$, was calculated by dividing the number of RPV trials predicted to fail the vessel by the total number of trials. The final results were discrete values for $P(I|E)$ and $P(F|E)$, without any quantification of the uncertainty in the solution. Starting with the initial release of FAVOR, v01.1, and continuing on with all subsequent releases of FAVOR, the improved PFM module provides for the calculation of discrete probability *distributions* of RPV fracture and failure along with the estimation of uncertainties in the results. In this improved PFM model, values for the conditional probability of initiation ($0 \le CPI \le 1$) and conditional probability of failure ($0 \le CPF \le 1$) by through-wall cracking are calculated for each flaw subjected to each transient.

4.3.1 FAVPFM Flowchart

Figure 6 presents a flowchart illustrating the essential elements of the nested-loop structure of the PFM Monte Carlo model – (1) *RPV Trial Loop*, (2) *Flaw Loop*, (3) *Transient Loop*, and (4) *Time-integration Loop*. The outermost *RPV Trial Loop* is indexed for each RPV trial included in the analysis, where the number of RPV trials is specified by the user in the FAVPFM input stream. Since each RPV trial can be postulated to contain multiple flaws, the next innermost loop (the *Flaw Loop*) is indexed for the number of flaws for this trial. Each postulated flaw is positioned (through sampling) in a particular RPV beltline subregion having its own distinguishing embrittlement-related parameters. Next, the flaw geometry (depth, length, aspect ratio, and location within the RPV wall) is determined by sampling from appropriate distributions derived from expert judgment [54] and non-destructive and destructive examinations [55-57] of RPV steels. Each of the embrittlement-related parameters [nickel and manganese (alloying elements), copper and phosphorus (contaminants), neutron fluence, and an estimate of the *epistemic* and *aleatory* uncertainties in the unirradiated $RT_{NDT(0)}$] are sampled from appropriate distributions.[4] The neutron fluence is attenuated to the crack-tip location, and a value for the irradiated reference index, RT_{NDT} (serving as a quantitative estimate of radiation damage), is calculated.

A deterministic fracture analysis is then performed on the current flaw for each of the postulated PTS transients; thus, the deterministic component of the analysis involves two inner nested loops – a *Transient Loop* and a *Time-integration Loop*. The temporal relationship between the applied Mode I stress intensity factor (K_I) and the static cleavage fracture initiation toughness (K_{Ic}) at the crack tip is calculated at discrete transient time steps. The fracture-toughness, K_{Ic}, statistical model is a function of the normalized temperature, $T(\tau) - RT_{NDT}$, where $T(\tau)$ is the time-dependent temperature at the crack tip. Analysis results are used to calculate the conditional probability of crack initiation (*CPI*)[5], i.e., the probability that pre-existing fabrication flaws will initiate in cleavage fracture. Also, the PFM model calculates the conditional probability of failure (*CPF*)[2] by through-wall cracking, i.e., the probability that an initiated flaw will propagate through the RPV wall. These probabilities are conditional in the sense that the thermal-hydraulic transients are assumed to occur. In the treatment of postulated multiple flaws to be discussed in Sect. 4.3.10, the values of *CPI* and *CPF* calculated for individual flaws become the *statistically-independent marginal* probabilities used in the construction of the joint conditional probabilities of initiation and failure.

[4] The details of the protocols and statistical distributions for all sampled parameters are given in Chapter 5.

[5] The notations of *CPI* and *CPF* are used here rather than the older $P(I|E)$ and $P(F|E)$ notations in order to highlight the fact that a new PFM methodology is being applied.

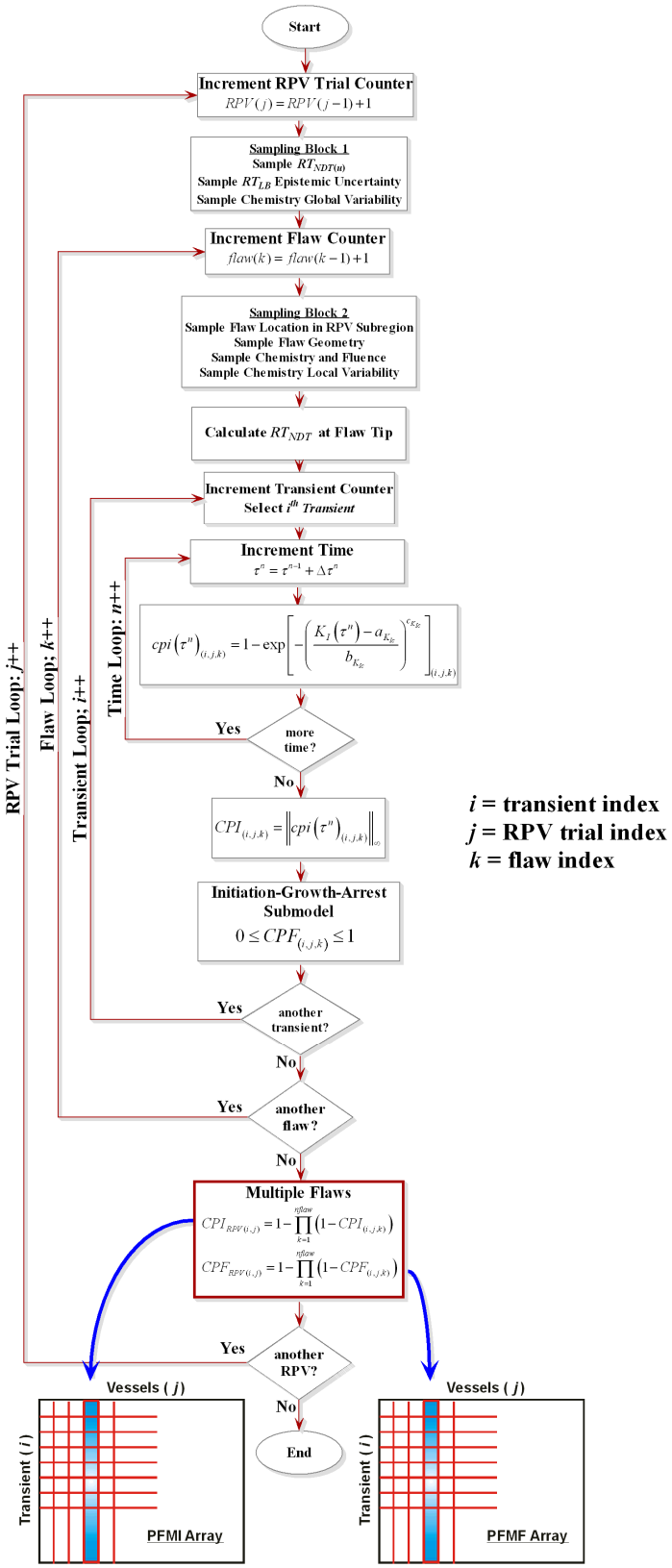

Fig. 6. Flow chart for improved PFM model implemented in FAVPFM showing the four primary nested loops – (1) *RPV Trial Loop*, (2) *Flaw Loop*, (3) *Transient Loop*, and (4) *Time Loop*. Note: ++ notation indicates increment index by 1, e.g., *i*++ means *i*=*i*+1.

Great care was taken in the construction of the nested-loop structure shown in Fig. 6 to preclude the introduction of a bias in the results due to the arbitrary ordering of the transients. Consequently, for a given RPV trial, flaw, and transient, the same value of *CPI* and *CPF* will be calculated irrespective of the position of the transient (or the number of transients) in the load-definition transient stack. This objective was accomplished by confining all random sampling to two *sampling blocks*, the first block at the top of the RPV Trial Loop and the second located at the top of the Flaw Loop. Any sampling required in the crack *Initiation-Growth-Arrest* submodel[6] draws from sets of random number sequences created in the second sampling block. These set-aside random number sequences remain fixed for the current flaw and are reset to the start of the sequence as each transient is incremented in the *Transient Loop*. New random number sequences are constructed (resampled) for each increment in the *Flaw Loop*. The above approach involves an implementation of a variance reduction technique called *common random numbers* (CRN) which, in the terminology of classical experimental design, is a form of *blocking*. CRN has also been called *correlated sampling* or *matched streams* in some statistical simulation contexts [58].

4.3.2 Beltline Configurations and Region Discretization

The FAVOR code provides the capability to model the variation of radiation damage in the *beltline region* of an RPV with as much detail as the analyst considers necessary. In this section, a description of the beltline region is given, focusing on those aspects that are relevant to a FAVOR PFM analysis.

The beltline region of an RPV is fabricated using either forged-ring segments or rolled-plate segments [9]. The vessels are constructed of a pressure vessel-grade ferritic steel (e.g., A533-B, Class 1 plate or A508, Class 2 forging) as the base material. The heavy-section steel wall is lined with an internal cladding of austenitic stainless steel for corrosion protection. Vessels made with forgings have only circumferential welds, and plate-type vessels have both circumferential welds and axial welds, as shown in Fig. 7. Therefore, beltline shells of a plate-type vessel contain three *major region* categories to model: (1) axial welds, (2) circumferential welds, and (3) plate segments. Only that portion of a weld that is within the axial bounds of the core need be considered, because the fast-neutron flux (and thus the radiation damage) decreases considerably beyond the fuel region. The extended surface length of an axially oriented flaw in a plate segment is modeled in FAVOR as being limited by the height of the core but not by the height of the shell course; therefore, the surface length of axial flaws in plate segments can be greater than those in axial welds [9]. Circumferential flaws in circumferential welds are limited to the full 360° arc-length of the weld. Due to the fabrication procedures

[6] As will be discussed in Chapter 5, resampling of weld chemistry is required in the through-wall crack growth protocol as the crack front advances into a different weld layer.

for applying the cladding on the inner surface of the vessel, FAVOR assumes all pre-existing surface-breaking flaws (in plate or weld subregions) are oriented circumferentially. Embedded flaws can be either axially or circumferentially oriented.

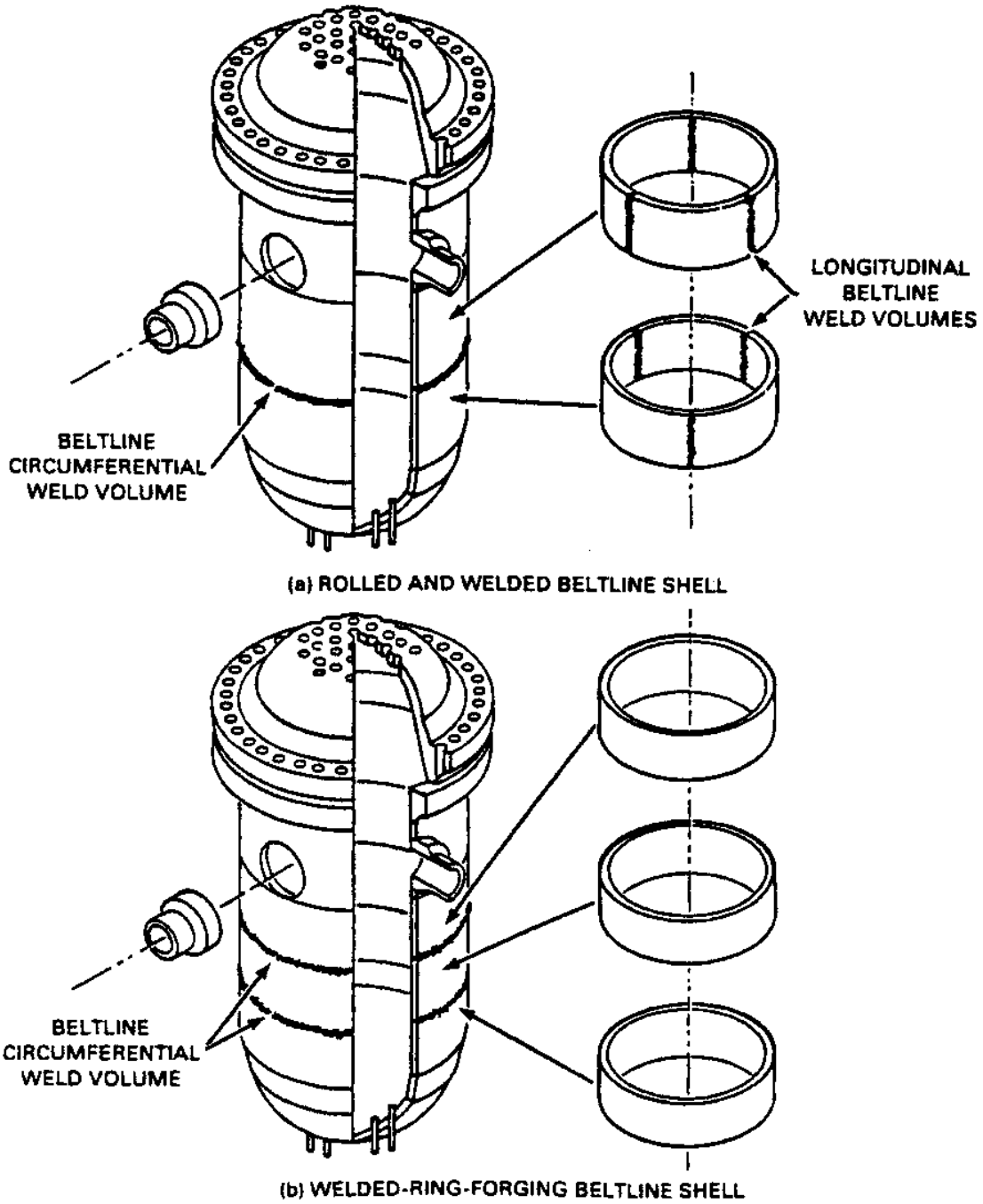

Fig. 7. Fabrication configurations of PWR beltline shells (adapted from [8]): (a) rolled-plate construction with axial and circumferential welds and (b) ring-forging construction with circumferential welds only.

Given the above considerations, the beltline region in FAVOR is defined as that portion of the RPV shell (including plate segments and welds) that extends from one foot below the bottom of the active core to one foot above the core. It is this region of the RPV wall that is explicitly modeled in FAVOR. As will be discussed in later sections, the assumption applied in the crack *Initiation-Growth-Arrest* submodel is that all finite-length flaws (both surface-breaking and embedded) upon initiation instantly become infinite-length flaws at depths corresponding to the locations of their outer crack tips at the time of initiation. This assumption is supported by experimental observations made during large-scale PTS experiments (discussed in Chapter 3) conducted at ORNL in the 1980s.

Figure 8 shows a rollout section of the beltline region of a boiling water reactor (BWR). The user is required to discretize (subdivide) the beltline into several major regions that contain plates (or forgings), axial welds, and circumferential welds. These major regions are further discretized into subregions for greater resolution of the variation in radiation-induced embrittlement. An embrittlement-distribution map is defined in the input data for FAVPFM using these major region and subregion definitions.

4.3.3 Treatment of the Fusion Line Along Welds

In a FAVOR PFM analysis, flaws that are postulated to be associated with a weld are assumed to reside on the *fusion line* between the weld and the adjacent plate or forging. Thus, decisions must be made as to how properties (chemistry and neutron fluence) of the weld or adjacent plate (or forging) should be assigned for the calculation of RT_{NDT} and the fracture toughness K_{Ic}.

Controlling Region

The discretization of the major regions and sub-regions of the RPV embrittlement model of the beltline includes a special treatment of these weld fusion lines. These fusion lines can be visualized as boundaries between a weld sub-region and its neighboring plate (or forging) sub-regions. Each weld sub-region will have at most two adjacent plate (or forging) sub-regions. FAVOR checks to determine if the value of RT_{NDT} of the weld sub-region of interest is higher than the corresponding values of the adjacent plate (or forging) sub-regions.

This determination of whether the weld sub-region or an adjacent plate (or forging) sub-region is controlling (i.e., has the higher RT_{NDT}) is performed one time before entering the PFM Monte Carlo looping structure. For each sub-region, the calculation uses the user-specified mean values of chemistry, RT_{NDTo}, and neutron fluence. Furthermore, the computation of RT_{NDT} for each sub-region includes the correction factors (i.e., 0.99 and 1.10) for weld and plate, respectively, as discussed in Sect. 5.2.2. The latter is necessary for consistency, since those factors are applied for all crack tip RT_{NDT} computations performed inside of the Monte Carlo looping structure.

The output file "RTNDT.out" contains a summary of the one-time computation to determine which sub-region (weld or adjacent plate) is controlling for flaws analyzed in that weld sub-region. That file does not include results for each weld / adjacent plate, but only for the sub-region with the higher RT_{NDT}.

Also, values found in the file RTNDT.out will not correspond to values of RT_{NDT} reported in the FAVPFM output report. The value of RT_{NDT} reported for each major region in the FAVPFM output report is the maximum value of RT_{NDT} of any sub-region in that major region, calculated without the 0.99 and 1.10 correction factors discussed above.

Restriction on Embrittlement Map

Inside the Monte Carlo looping analysis, when a flaw is postulated to reside in a weld, the values of chemistry (sampled from the appropriate distributions) of the controlling sub-region and the *sampled value of fluence of the weld***,** are used in the evaluation of RT_{NDT} at the crack tip. Flaw orientation is not transferred from a dominant plate sub-region to a weld sub-region.

To ensure that the FAVOR weld-fusion line methodology produces logically-consistent solutions, it is essential that the *same neutron fluence* of a weld be assigned to its two adjacent neighbor plate sub-regions. The latter restriction on the embrittlement map input to FAVOR necessitates special treatment for certain problems to be analyzed with FAVOR.

An example would be the use of an embrittlement map constructed based only on knowledge of the maximum value of fluence in any weld, plate, or forging, and where these maximum values are assigned to represent the fluence for the entire major region. If that maximum value of fluence in the plate or forging resides far from the adjacent weld, the resultant model is likely to have an unrealistic discontinuity of fluence between the weld sub-regions and adjacent plates sub-regions that will produce an illogical solution.

For this example, it is recommended that two thin (i.e., very small values $\Delta\theta$) plate sub-regions be modelled between the weld and adjacent plates, one on each side of the weld. These two sub-regions should be modelled with (1) the chemistry and $RT_{NDT(0)}$ of the respective adjacent plates and (2) a fluence equal (or close) to that of the weld, thus providing greater similarity of fluence between the weld and plate along the weld fusion line. This smoother transition in the fluence avoids a possibility of inconsistent results associated with discontinuities between fluences in welds and adjacent plates. Since the $\Delta\theta$ assigned to these regions is very small, they occupy negligible volume, have a negligible number of flaws, and thus have little or no other impact on the results of the PFM analysis.

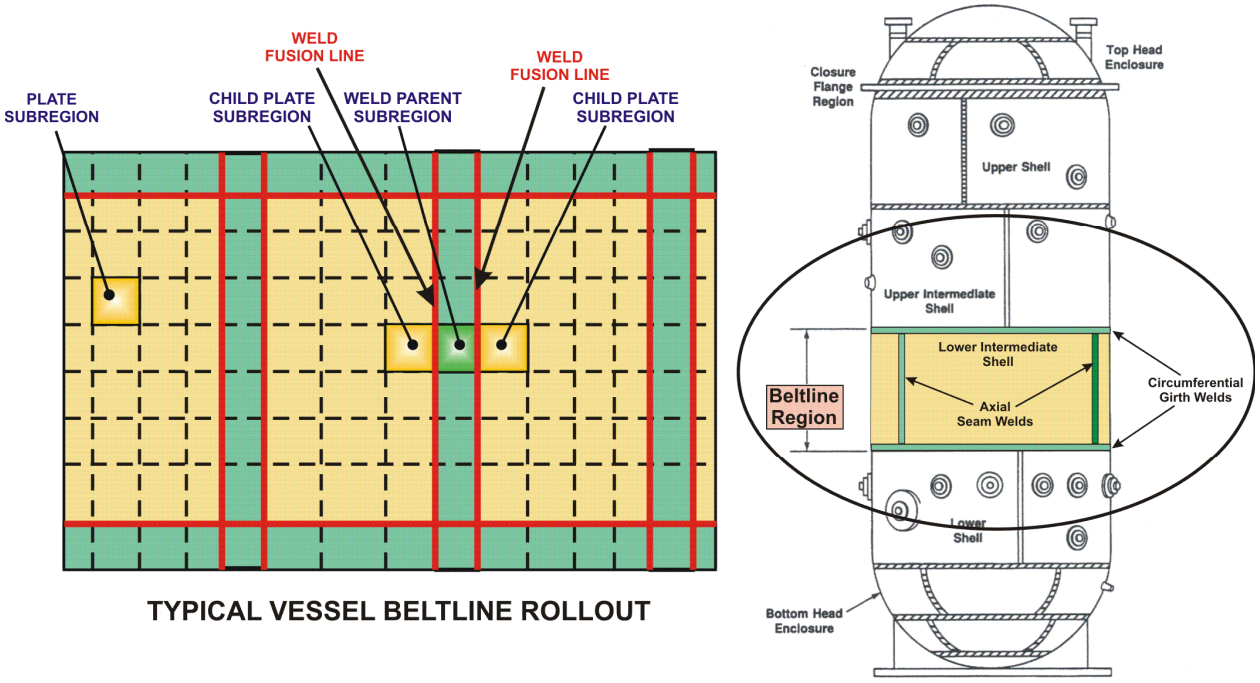

Fig. 8. FAVOR uses a discretization of the RPV beltline region to resolve the variation in radiation damage in terms of plate, axial weld, and circumferential weld major regions which are further discretized into multiple subregions. The above figure represents a boiling water reactor (BWR).

Weld-Fusion-Line Dependency for Ductile Tearing Model

For the Ductile Tearing Model No. 2, implemented in FAVOR, v03.1 (see the discussion in Sect. 4.3.11), a second *weld-fusion-line dependency structure* is created based on the irradiated upper-shelf energy, *USE*. This weld-fusion-line dependency structure for sampling ductile-tearing properties is independent of the embrittlement-related dependency structure discussed above. For Ductile-tearing Model No. 2, the ductile-tearing-related properties of the most limiting (either the weld or the adjacent plate subregion with the lowest value of irradiated *USE*) material are used when evaluating ductile-tearing of a flaw located in the weld subregion. As with the embrittlement-related weld-fusion-line treatment, the flaw type and pre- and post-initiation orientation of flaws are not transferred from a dominant plate subregion to a weld subregion. Ductile-Tearing Model No. 1, implemented in FAVOR, v07.1, this second weld-fusion-line dependency structure for sampling ductile-tearing properties is not required.

For those conditions in which plate embrittlement properties are used to characterize the weld subregion fracture toughness, the weld chemistry re-sampling protocols continue to be applied.

4.3.4 Warm Prestressing

Experimental evidence for the warm prestressing (WPS) effect in ferritic steels was first reported over 40 years ago [59]. Since then, this phenomena has been the subject of extensive research; e.g., see [60-69]. The technical basis for the inclusion of warm prestressing effects in FAVOR is presented in detail in [70] and repeated in Appendix B of [98]. The following is a summary of the discussion in Appendix B of ref. [98].

The WPS phenomena can be characterized as an increase in the apparent fracture toughness of a ferritic steel after first being "prestressed" at an elevated temperature. Three mechanisms have been identified [60, 64, 68] to produce the WPS phenomena:

1. Preloading at an elevated temperature *work-hardens the material ahead of the crack tip*. The increase in yield strength with decreasing temperature "immobilizes" the dislocations in the plastic zone [62,63]. Consequently, an increase in applied load is needed for additional plastic flow (a prerequisite for fracture) to occur at the lower temperature.
2. Preloading at an elevated temperature *blunts the crack tip*, reducing the geometric stress concentration making subsequent fracture more difficult.
3. Unloading after or during cooling from the elevated WPS temperature down to a reduced temperature *produces residual compressive stresses ahead of the crack tip*. The load applied at the reduced temperature must first overcome these compressive stresses before the loading can produce additional material damage and possibly fracture. The residual compressive stresses associated with the unloaded initial plastic zone can be viewed as protecting the crack tip, since higher applied loads are required to achieve a given level of crack driving force compared to the condition before preloading [66].

Before the introduction of WPS in FAVOR, v02.4, probabilistic fracture mechanics calculations performed in the United States typically did not include the WPS phenomena as part of the PFM model. This omission was based on the following considerations:

1. Thermal-hydraulic (TH) transients were often represented as smooth temporal variations of both pressure and coolant temperature; however, data taken from operating nuclear power plants demonstrate that actual overcooling events are not necessarily so well behaved. This non-smoothness of these fundamental mechanical and thermal loads created the possibility that, due to short-duration time-dependent fluctuations of pressure and/or coolant temperature, the criteria for WPS might be satisfied by the idealized transient but not satisfied by the real transient.
2. Previous PRA models of human reliability (HR) were typically not sufficiently sophisticated to capture the potential for plant operators to repressurize the primary coolant system as part of their response to an RPV-integrity challenge. Since such a repressurization would largely nullify the benefit of WPS, it was viewed as nonconservative to account for WPS within a model that may also ignore the potentially deleterious effects of operator actions.

FAVOR addresses both of these concerns by allowing as input data (1) more realistic and detailed representations of the postulated PTS transients and (2) more sophisticated PRA/HR models that explicitly consider both acts of omission and commission on the part of plant operators.

The FAVOR WPS model implements three variations (as user-specified options) on the *conservative WPS principle* first proposed by McGowan [61]. This principle states that for cleavage crack initiation to be possible the following criteria must be met: (1) the applied-K_I at the crack tip must exceed some minimum value of $K_{Ic(\min)}$ (designated as $a_{K_{Ic}}$ by Eqs. (112) and (113) in FAVOR) and (2) the applied-K_I must be increasing with time (i.e., $dK_I / d\tau > 0$) when the load path first enters the finite K_{Ic} probability space.

In FAVOR, a flaw is assumed to be in a state of WPS when the following condition is met:

- a falling applied-K_I field – the time-rate-of-change of the applied-K_I is nonpositive (≤ 0).

If a flaw is in a state of WPS, it is not eligible for initiation (or re-initiation if it has arrested) until it leaves the WPS state.

Three conditions can be stated for a flaw to not be in a state of WPS and, thereby, to be eligible for initiation. These three conditions are:

Condition (1): the applied-K_I is greater than $K_{Ic(\min)}$, where $K_{Ic(\min)}$ is defined by the fracture toughness model ($a_{K_{Ic}}$ in Eqs. (113)) for the temperature at the flaw tip;

Condition (2): a rising applied-K_I field – the time-rate-of-change of the applied-K_I is positive ($dK_I / d\tau > 0$);

Condition (3): in a rising applied-K_I field, the driving force at the flaw tip must exceed some portion of the previously-established maximum applied-K_I (designated as $K_{I(\max)}$) experienced by the flaw during the transient up to the current point in time under consideration –

$$\text{applied-}K_I(\tau) \geq \alpha\, K_{I(\max)}(\tau)$$

The three WPS options implemented in FAVOR refer to the different values of α applied in the 3rd condition above. These options are:

Baseline FAVOR Model $(\alpha = 1)$ **:**

The Baseline WPS model, first introduced in FAVOR, v02.4, sets $\alpha = 1$. As discussed in [71], the technical basis information available at the time FAVOR, v02.4, was released supported this approach.

Conservative Principle $(\alpha = 0)$**:**

The "conservative" WPS principle requires that only conditions (1) and (2) be met, and the parameter α is set to zero. Therefore, for this implementation, a non-zero cleavage fracture probability exists (a pre-existing flaw may initiate or an arrested flaw may re-initiate) whenever the applied-K_I is greater than $K_{Ic(\min)}$ and is increasing with time.

Best-Estimate Model (α **is sampled from a log-logistic distribution):**

In a recent publication, Moinereau et al. [72] summarized the results of an extensive European Commission funded investigation of WPS called SMILE. In their paper, a study of WPS conditions (e.g., Load-Cool-Fracture, Load-Unload-Cool-Fracture, Load-Transient-Fracture, etc.) was performed using three nuclear pressure vessel grade ferritic steels. Data from a total of 86 experiments were reported. One result from these experiments, specifically the ratio of the $K_{applied}$ at fracture ($K_{I\text{-}FRACTURE}$) to the maximum value of $K_{applied}$ ($K_{I\text{-}MAX}$) that had occurred previously during the transient, is summarized in Table 3. The ratio $K_{I-FRACTURE} / K_{I-MAX}$ quantifies the degree of re-loading that can occur before crack re-initiation again becomes possible. As discussed in [71], it is recognized that, by combining the results from all of the loading, temperature, and material conditions tested in [72] the distribution of $K_{I-FRACTURE} / K_{I-MAX}$ combines conditions that might be addressed separately in a more refined treatment. Nevertheless, PTS challenges also represent a spectrum of loading, temperature, and material conditions, thus providing some justification for adopting the $K_{I-FRACTURE} / K_{I-MAX}$ ratios as experimental estimates for the parameter α in the WPS Condition 3, above.

Applying the *Baseline* WPS option in FAVOR, Figures 9a-9c present an example of a PTS transient (Fig. 9a) applied to a flaw with its resulting load path (Fig. 9b). At Point 1 in Figs. 9b and 9c, the load path for the flaw enters finite K_{Ic} probability space, and, shortly thereafter, $dK_I / d\tau$ becomes negative. The flaw is in a state of WPS from Point 1 to Point 2b. At Point 2b, the applied-K_I at the crack tip exceeds the current $K_{I(max)}$ (established at Point 1). For the *Baseline* option, the parameter α is set to 1.0,

Along the load path between Points 2b and 3 in Fig. 9b, the flaw is no longer in a state of WPS and has a finite probability of crack initiation. At Point 3, a new $K_{I(max)}$ is established, and, since $dK_I / d\tau \le 0$ or $K_I < K_{I(max)}$ for the remainder of the load path, the flaw returns to and remains in a state of WPS. While the WPS condition is in effect, the instantaneous conditional probability of initiation, $cpi(\tau)$, for the flaw is set to zero, even though the applied K_I of the flaw is within the finite K_{Ic} probability space ($K_I > K_{Ic(min)}$).

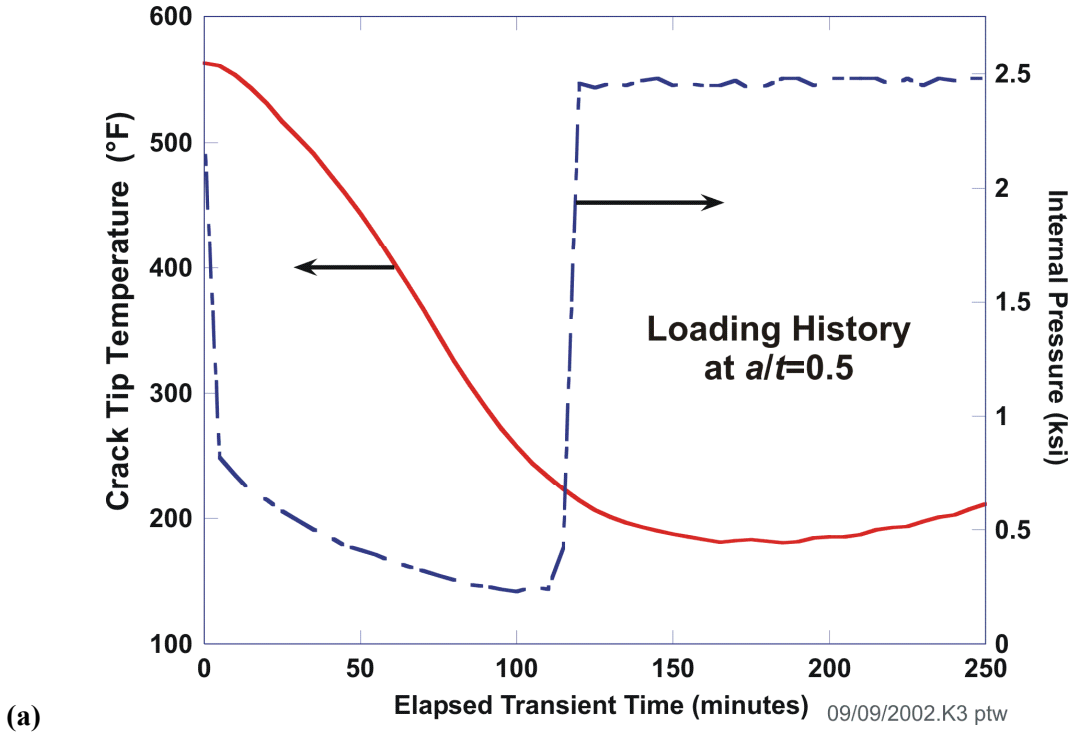

(a)

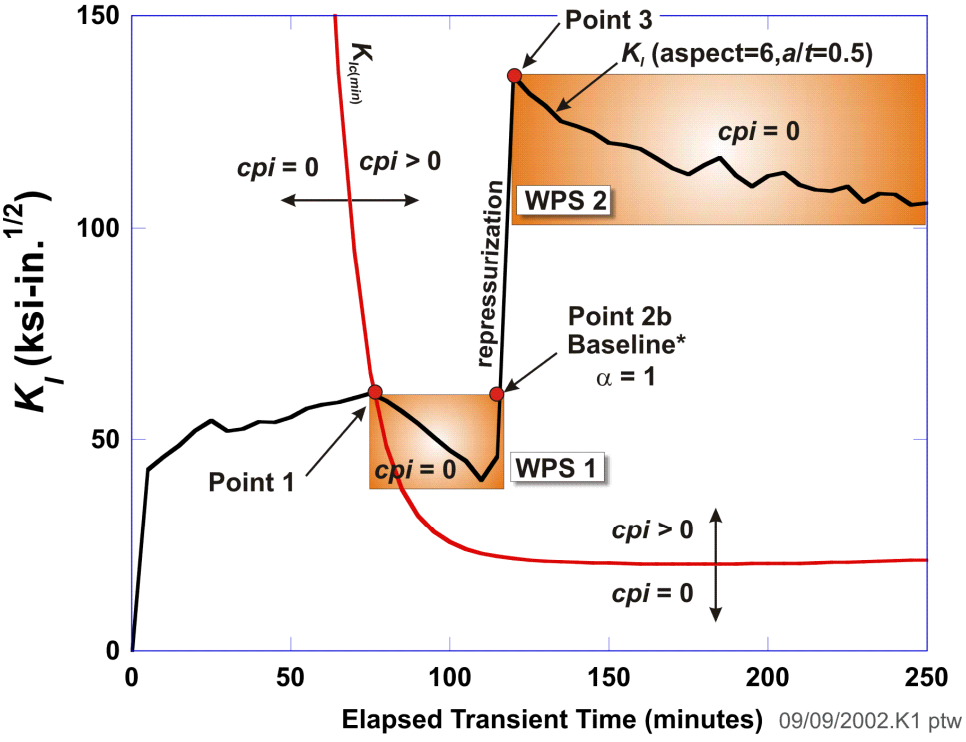

(b)

*Baseline WPS model implemented in FAVOR v02.4

Fig. 9. Example of warm prestressing: (a) loading history with pressure applied to the inner surface and the temperature at the crack tip, (b) load path for a flaw showing two WPS regions. (*cpi* is the instantaneous conditional probability of initiation).

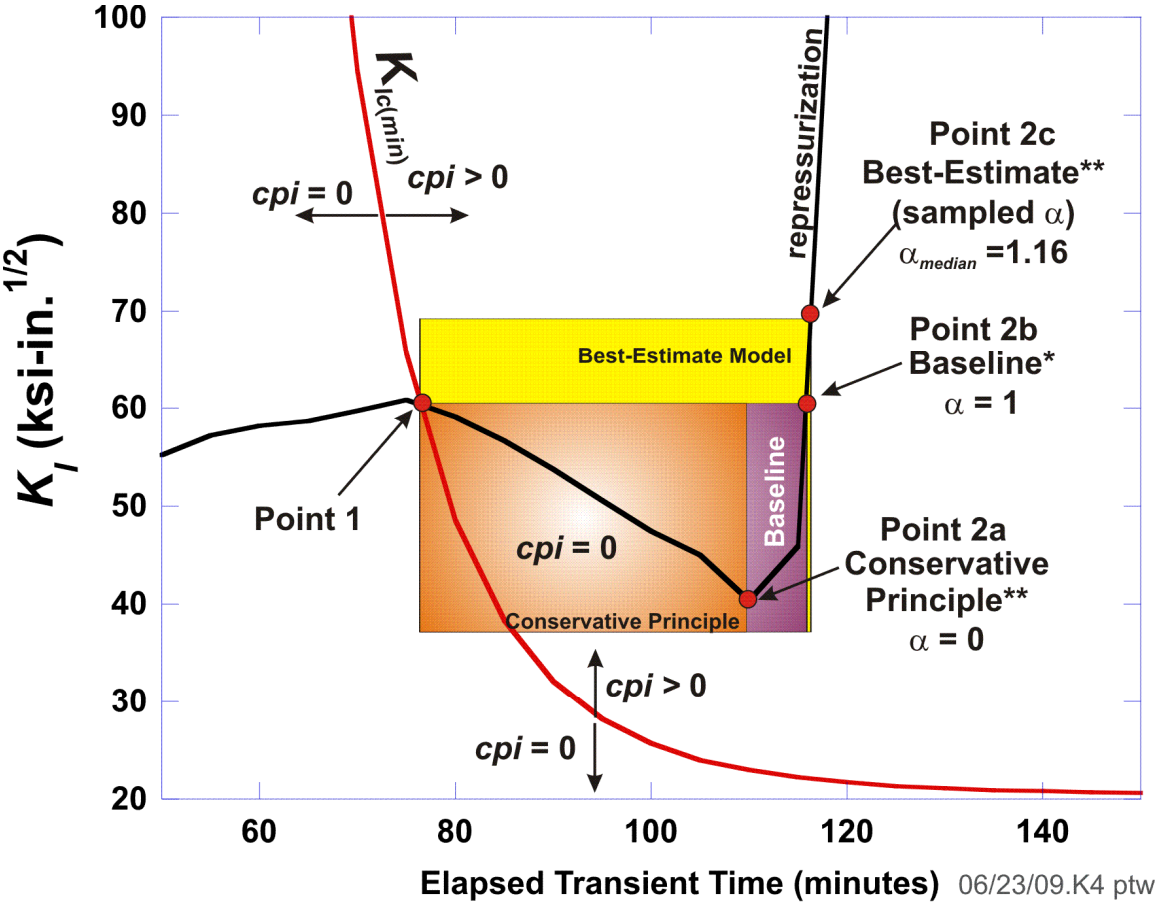

(c)

Fig. 9. (continued) Example of warm prestressing: (c) three options implemented in FAVOR, v09.1 for a flaw leaving the warm-prestress state allowing re-initiation. (*cpi* is the instantaneous conditional probability of initiation).

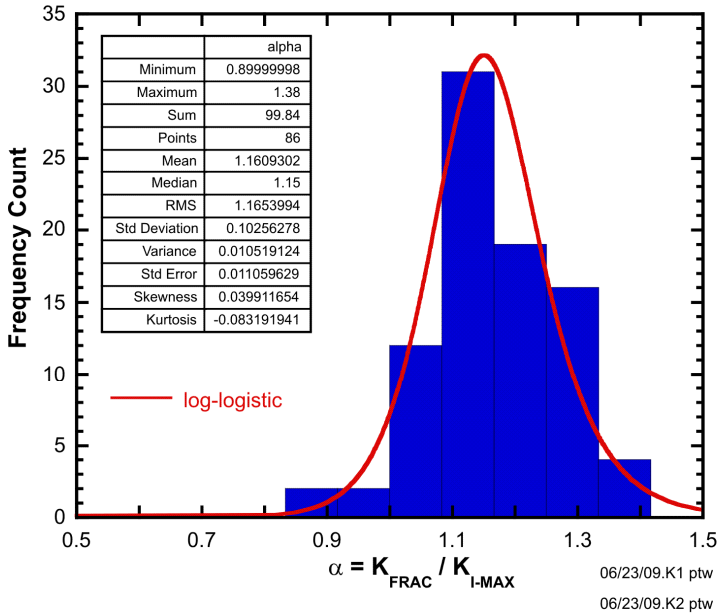

Log-Logistic(a,b,c)
probability density function

$$f(x\,|\,a,b,c)=\begin{cases}\dfrac{c\left(\dfrac{x-a}{b}\right)^{c-1}}{b\left[1+\left(\dfrac{x-a}{b}\right)^{c}\right]^{2}}; & x>a\\ 0; & x\le a\end{cases}$$

Fitted Parameters
a = location = 0
b = scale = 1.15643
c = shape = 20.12346

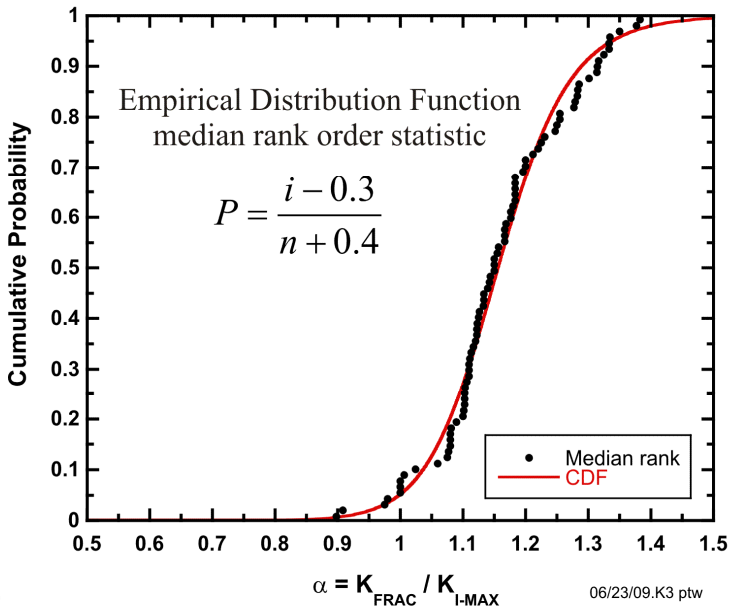

Log-Logistic(a,b,c)
cumulative distribution function

$$F(x\,|\,a,b,c)=\begin{cases}\dfrac{1}{1+\left(\dfrac{x-a}{b}\right)^{-c}}; & x>a\\ 0; & x\le a\end{cases}$$

Fitted Parameters
a = location = 0
b = scale = 1.15643
c = shape = 20.12346

(d)

Fig. 9. (continued) Example of warm prestressing: (d) log-logistic distribution fitted to data obtained from Moinereau et al. (2007) for a parameter in Best-Estimate Model for warm-prestress model implemented in FAVOR, v09.1.

Goodness-of-Fit Test Statistics for WPS Parameter α

Goodness-of-Fit Test	Distribution	Test Statistic	Level of Significance	Critical Values for Level of Significance 0.250	0.100	0.050	0.025	0.010	0.005
Anderson-Darling	Log-Logistic	0.691	0.040	0.425	0.561	0.658	**0.767**	**0.903**	**1.007**
	Lognormal	0.792	0.038	0.466	0.625	0.745	**0.865**	**1.026**	**1.149**
	Normal	0.888	0.022	0.466	0.625	0.745	0.865	**1.026**	**1.149**

Goodness-of-Fit Test	Distribution	Test Statistic	Level of Significance	Critical Values for Level of Significance 0.150	0.100	0.050	0.025	0.010
Kolmogorov-Smirnov	Log-Logistic	0.797	0.040		0.715	0.780	**0.827**	**0.886**
	Lognormal	0.962	0.030	0.768	0.812	0.887	**0.986**	**1.026**
	Normal	1.041	0.001	0.768	0.812	0.887	0.986	1.026

Goodness-of-Fit Test	Distribution	Test Statistic	Level of Significance	Critical Values for Level of Significance 0.250	0.150	0.100	0.050	0.010
Equi-Probable	Lognormal	16.791	0.399	**19.369**	**21.793**	**23.542**	**26.296**	**32**
Chi-Square	Log-Logistic	25.093	0.068	19.369	21.793	23.542	**26.296**	**32**
DOF = 16	Normal	32.605	0.008	19.369	21.793	23.542	26.296	32

When the *Conservative Principle* option is selected, the parameter α is set to zero, and the flaw will leave the WPS state at Point 2a in Fig. 9c and be eligible for initiation following the rising applied-K_I field up to Point 3 in Fig. 9b.

To implement the *Best Estimate* WPS model, a log-logistic statistical distribution (Fig. 9d) for the parameter α was fitted to the 86 data points given in Table 3 which were extracted from ref. [72] as reported in ref. [71]. The parameters for 31 statistical distributions were fitted to the data in Table 3, and test statistics from three *Goodness-of-Fit* tests (Anderson-Darling [73], Kolmogorov-Smirnov [74], Equi-Probable-Chi-Square [75]) for three representative statistical distributions are shown above. In *Goodness-of-Fit* testing, the higher the value of the test statistic the poorer the fit relative to other distributions being considered. For all of the 31 distributions examined, the log-logistic and lognormal distributions ranked the highest. The log-logistic was chosen over the lognormal, since the log-logistic distribution ranked higher than the lognormal in two out of the three *Goodness-of-Fit* of tests applied.

Table 3. Data on warm prestress from SMILE project Moinereau et al. (2007)

Source	Material	Specimen	$K_{I\text{-}MAX}$ [MPa√m]	$K_{I\text{-}FRAC}$ [MPa√m]	$\alpha = K_{I\text{-}FRAC} / K_{I\text{-}MAX}$	Source	Material	Specimen	$K_{I\text{-}MAX}$ [MPa√m]	$K_{I\text{-}FRAC}$ [MPa√m]	$\alpha = K_{I\text{-}FRAC} / K_{I\text{-}MAX}$
Fig 5	WPS	CT-25	80	90	1.125	Fig 7	18MND5	CT-50	60	71	1.183
Fig 5	WPS	CT-25	79	87	1.101	Fig 7	18MND5	CT-50	60	70	1.167
Fig 5	WPS	CT-25	79	89	1.127	Fig 7	18MND5	CT-50	98	110	1.122
Fig 5	WPS	CT-25	78	84	1.077	Fig 7	18MND5	CT-50	98	106	1.082
Fig 5	WPS	CT-25	77	85	1.104	Fig 7	18MND5	CT-50	60	70	1.167
Fig 5	WPS	CT-25	78	86	1.103	Fig 7	18MND5	CT-50	60	69	1.150
Fig 5	WPS	CT-25	78	86	1.103	Fig 7	18MND5	CT-50	98	88	0.898
Fig 5	WPS	CT-25	78	86	1.103	Fig 7	18MND5	CT-50	98	89	0.908
Fig 5	WPS	CT-25	77	88	1.143	Fig 9	18MND5	?	40	43	1.075
Fig 5	WPS	CT-25	77	90	1.169	Fig 9	18MND5	?	40	53	1.325
Fig 5	WPS	CT-50	81	91	1.123	Fig 9	18MND5	?	40	50	1.250
Fig 5	WPS	CT-50	80	78	0.975	Fig 9	18MND5	?	51	59	1.157
Fig 5	WPS	CT-50	80	88	1.100	Fig 9	18MND5	?	51	60	1.176
Fig 5	WPS	CT-100	81	90	1.111	Fig 9	18MND5	?	51	64	1.255
Fig 5	WPS	CT-100	103	114	1.107	Fig 9	18MND5	?	51	60	1.176
Fig 5	WPS	CT-101	80.5	81	1.006	Fig 9	18MND5	?	51	61	1.196
Fig 5	WPS	CT-102	81	83	1.025	Fig 9	18MND5	?	51	68	1.333
Fig 6	18MND5	CT-25	60	71	1.183	Fig 9	18MND5	?	60	77	1.283
Fig 6	18MND5	CT-25	60	69	1.150	Fig 9	18MND5	?	60	79	1.317
Fig 6	18MND5	CT-25	60	72	1.200	Fig 9	18MND5	?	60	81	1.350
Fig 6	18MND5	CT-25	100	111	1.110	Fig 9	18MND5	?	81	81	1.000
Fig 6	18MND5	CT-25	100	109	1.090	Fig 9	18MND5	?	100	100	1.000
Fig 6	18MND5	CT-25	100	114	1.140	Fig 9	18MND5	?	100	100	1.000
Fig 6	18MND5	CT-25	60	71	1.183	Fig 9	18MND5	?	102	128	1.255
Fig 6	18MND5	CT-25	60	71	1.183	Table 7	18MND5	?	60	70.8	1.180
Fig 6	18MND5	CT-25	60	68	1.133	Table 7	18MND5	?	60	78.9	1.315
Fig 6	18MND5	CT-25	100	108	1.080	Table 7	18MND5	?	100	111.7	1.117
Fig 6	18MND5	CT-25	100	108	1.080	Table 7	18MND5	?	100	115.5	1.155
Fig 6	18MND5	CT-25	100	111	1.110	Table 7	16MND5	?	100	123.1	1.231
Fig 6	18MND5	CT-25	60	69	1.150	Table 8	16MND6	?	100	122.5	1.225
Fig 6	18MND5	CT-25	60	68	1.133	Table 9	16MND7	?	100	128.3	1.283
Fig 6	18MND5	CT-25	62	69	1.113	Table 10	16MND8	?	100	124.7	1.247
Fig 6	18MND5	CT-25	100	98	0.980	Fig 12	?	CT(POR)	65.9	80.4	1.220
Fig 6	18MND5	CT-25	100	106	1.060	Fig 12	?	CT(POR)	86.7	110.9	1.279
Fig 6	18MND5	CT-25	100	111	1.110	Fig 13	?	CT(POR)	65.9	75.4	1.144
Fig 6	18MND5	CT-25	60	72	1.200	Fig 13	?	CT(POR)	86.4	104.7	1.212
Fig 6	18MND5	CT-25	60	80	1.333	Table 15	16MND5	CT12.7	61	84	1.377
Fig 6	18MND5	CT-25	100	108	1.080	Table 15	16MND5	CT12.7	72.8	93	1.277
Fig 6	18MND5	CT-25	100	112	1.120	Table 15	16MND5	CT12.7	68	94	1.382
Fig 7	18MND5	CT-50	60	71	1.183	Table 15	16MND5	CT12.5	82.2	107	1.302
Fig 7	18MND5	CT-50	60	70	1.167	Table 15	16MND5	CT12.5	79.4	106	1.335
Fig 7	18MND5	CT-50	98	110	1.122	Table 15	16MND5	CT12.5	70	90	1.286
Fig 7	18MND5	CT-50	98	111	1.133	Table 15	16MND5	CT12.5	70	92	1.314

Notes: $K_{I\text{-}FRAC}$ = applied K_I at fracture; $K_{I\text{-}MAX}$ = applied K_I that occurred previously during the transient from D. Moinereau et al. (2007) and Kirk and Dickson (2009).

Therefore, for each flaw that has entered the WPS state, the *Best-Estimate* WPS model draws a random sample value of α from the log-logistic distribution shown in Fig. 9d to establish the criterion for Condition 3, where Conditions 1, 2, and 3 must all be met before the flaw is assumed to leave the WPS state and be considered for initiation. From the value of $\alpha = 1$, it can be observed that the *Baseline* WPS model is a fairly conservative assumption. By the *Best-Estimate* WPS model, a value of $\alpha = 1$ is associated with an approximately 5% cumulative probability that the flaw has left the WPS state, i.e., there is a 95% probability that the flaw still remains in the WPS state by the *Best-Estimate* model when the *Baseline* model would consider the flaw to be eligible for initiation.

4.3.5 Probability Distributions

The sampled variables used in FAVPFM are drawn from a range of specified statistical distributions. The following presents general information about these distributions including, the form of their probability density function (PDF), cumulative distribution function (CDF), first and second moments, and sampling methods used in FAVOR. The notation $X_i \leftarrow N(\mu,\sigma)$ signifies that a random variate is drawn as a sample from a population described by the specified distribution. In this example, the population is described by a two-parameter normal distribution with mean, μ, and standard deviation, σ. Other distributions applied in FAVOR include the standard *uniform* distribution for a unit open interval, $U(0,1)$; the two-parameter *lognormal* distribution, $\Lambda(\mu_{\log},\sigma_{\log})$; the three-parameter *Weibull* distribution, $W(a,b,c)$; the two-parameter *logistic* distribution, $L(\alpha,\beta)$; the three-parameter *log-logistic* distribution, $LL(a,b,c)$; and the four-parameter *Johnson* S_B distribution, $JS_B(a,b,\alpha_1,\alpha_2)$.

A standard uniform distribution on the interval $U(0,1)$ is the starting point for all of the transformation methods that draw random variates from nonuniform continuous distributions. A uniform distribution is defined by the following:

Uniform Distribution – $U(a,b)$

PDF:
$$f_U(x \mid a,b) = \begin{cases} 0 & ; \quad x < a \\ \dfrac{1}{b-a} & ; \quad a \le x \le b \\ 0 & ; \quad x > b \end{cases}$$

CDF:
$$\Pr(X \le x) = F_U(x \mid a,b) = \begin{cases} 0 & ; \quad x < a \\ \dfrac{x-a}{b-a} & ; \quad a \le x \le b \\ 1 & ; \quad x > b \end{cases}$$

Moments:

Mean $\mu = \frac{a+b}{2}$

Variance $\sigma^2 = \frac{(b-a)^2}{12}$

Sampling from a Two-Parameter Uniform Distribution: $U_i \leftarrow U(0,1)$

Sampling from a standard uniform distribution, $U(0,1)$, is accomplished computationally with a *Random Number Generator* (RNG). A portable random number generator [76-78], written in Fortran, has been implemented and tested in FAVOR. This portable generator, based on a composite of two multiplicative linear congruential generators using 32 bit integer arithmetic, has a reported theoretical minimum period of 2.3×10^{18}. This implementation was successfully tested by the HSST Program at ORNL for statistical randomness using the NIST *Statistical Test Suite for Random and Pseudorandom Number Generators* [79].

<u>Normal Distribution</u> – $N(\mu,\sigma)$

PDF: $$f_N(x \mid \mu,\sigma) = \frac{1}{\sigma\sqrt{2\pi}} \exp\left[-\frac{(x-\mu)^2}{2\sigma^2}\right]; \quad -\infty < x < +\infty$$

CDF: $$\Pr(X \le x) = \Phi(z) = \frac{1}{\sqrt{2\pi}} \int_{-\infty}^{z} \exp\left(-\frac{\xi^2}{2}\right) d\xi \; ; \; z = \frac{x-\mu}{\sigma}; \quad -\infty < x < +\infty$$

Moments:

Mean μ

Variance σ^2

Sampling from a Two-Parameter Normal Distribution: $X_i \leftarrow N(\mu,\sigma)$

Earlier versions of FAVOR used the Box-Müller *Transformation Method* [80-82] to sample from a standard normal distribution, $N(0,1)$. Beginning with FAVOR, v04.1, the more computationally efficient Forsythe's method (as extended by Ahrens and Dieter [83]) for sampling from a standard normal distribution has been implemented. The sampled standard normal deviate, Z_i, is then scaled to the required random normal deviate with mean, μ, and standard deviation, σ, by

$$\begin{aligned} Z_i &\leftarrow N(0,1) \\ X_i &= Z_i\sigma + \mu \end{aligned} \tag{1}$$

The extended Forsythe's method is computationally very efficient; however, one problem with the method is that there is no direct connection between the standard normal deviate and its associated *p-value* in the normal cumulative distribution function. When this relationship between the *p-value* and the deviate is required, an alternative method for expressing the inverse of a standard normal CDF (also known as a percentile function) is applied in FAVOR. The following rational function [84] represents an accurate approximation of the standard normal percentile function:

$$
\begin{aligned}
x &= \begin{cases} p & \text{for } p < \dfrac{1}{2} \\ 1-p & \text{for } p \geq \dfrac{1}{2} \end{cases} \\
y &= \sqrt{-2\ln(x)} \\
Z_p &= \operatorname{sgn}\left(p - \frac{1}{2}\right)\left(y + \frac{a_0 + a_1 y + a_2 y^2 + a_3 y^3 + a_4 y^4}{b_0 + b_1 y + b_2 y^2 + b_3 y^3 + b_4 y^4}\right)
\end{aligned}
\tag{2}
$$

where

$$
\operatorname{sgn}(x) = \begin{cases} -1 & \text{if } x < 0 \\ +1 & \text{if } x \geq 0 \end{cases}
$$

and the coefficients of the rational function are:

$$
\begin{aligned}
a_0 &= \text{-}0.3222324310880000 & b_0 &= 0.0993484626060 \\
a_1 &= \text{-}1.0000000000000000 & b_1 &= 0.5885815704950 \\
a_2 &= \text{-}0.3422420885470000 & b_2 &= 0.5311034623660 \\
a_3 &= \text{-}0.0204231210245000 & b_3 &= 0.1035377528500 \\
a_4 &= \text{-}0.0000453642210148 & b_4 &= 0.0038560700634
\end{aligned}
$$

The standard normal deviate is then scaled to obtain the required quantile

$$
X_p = Z_p \sigma + \mu \tag{3}
$$

<u>Lognormal Distribution</u> – $\Lambda\left(\mu_{\log}, \sigma_{\log}\right)$

PDF:
$$
f_{\Lambda}(x \mid \mu_{\log}, \sigma_{\log}) = \begin{cases} 0 & ; \quad x \leq 0 \\ \dfrac{1}{\sigma_{\log} x \sqrt{2\pi}} \exp\left[-\dfrac{\left(\ln x - \mu_{\log}\right)^2}{2\sigma_{\log}^2} \right] & ; \quad 0 < x < \infty \end{cases}
$$

CDF: $$\Pr(X \le x) = \Phi(z) = \begin{cases} 0 & ; \quad x \le 0 \\ \dfrac{1}{\sqrt{2\pi}} \displaystyle\int_{-\infty}^{z} \exp\left(-\frac{\xi^2}{2}\right) d\xi \; ; \; z = \dfrac{\ln x - \mu_{\log}}{\sigma_{\log}}, & 0 < x < \infty \end{cases}$$

Moments:

Mean $$\mu = \exp\left(\mu_{\log} + \frac{\sigma_{\log}^2}{2}\right)$$

Variance $$\sigma^2 = \omega(\omega - 1)\exp(2\mu_{\log}); \quad \omega = \exp(\sigma_{\log}^2)$$

Equivalently, the parameters $\left(\mu_{\log}, \sigma_{\log}^2\right)$ can be calculated from the mean and variance $\left(\mu, \sigma^2\right)$ by $\mu_{\log} = \ln\left(\mu\right) - \frac{1}{2}\ln\left(1 + \frac{\sigma^2}{\mu^2}\right)$ and $\sigma_{\log}^2 = \ln\left(1 + \frac{\sigma^2}{\mu^2}\right)$, where $\exp\left(\mu_{\log}\right)$ and $\sigma_{\log}$ are the *median* and *multiplicative standard deviation* of the lognormal distribution.

Sampling from a Two-Parameter Lognormal Distribution: $X_i \leftarrow \Lambda(\mu_{\log}, \sigma_{\log})$

The log-transformed deviate is sampled from a normal distribution with mean equal to the lognormal mean, $\mu_{\log}$, and standard deviation equal to the lognormal standard deviation, $\sigma_{\log}$. The log-transformed deviate is then converted into the required random deviate by the exponential function.

$$\begin{aligned} Y_i &\leftarrow N(\mu_{\log}, \sigma_{\log}) \\ X_i &= \exp(Y_i) \end{aligned} \tag{4}$$

<u>Weibull Distribution</u> – $W(a,b,c)$

(a = location parameter, b = scale parameter, c = shape parameter)

PDF: $$f_W(x|a,b,c) = \begin{cases} 0 & ; \quad x \le a \\ \dfrac{c}{b} y^{c-1} \exp\left(-y^c\right); & (y = (x-a)/b, x > a,\ b,c > 0) \end{cases}$$

CDF: $$\Pr(X \le x) = F_W(x \mid a,b,c) = \begin{cases} 0 & ; \quad x \le a \\ 1 - \exp\left[-y^c\right]; & (y = (x-a)/b, x > a,\ b,c > 0) \end{cases}$$

Moments:

Mean $\mu = a + b\,\Gamma\left(1+\frac{1}{c}\right)$

Variance $\sigma^2 = b^2\left[\Gamma\left(1+\frac{2}{c}\right) - \Gamma^2\left(1+\frac{1}{c}\right)\right]$

where $\Gamma(x)$ is Euler's gamma function.

Sampling from a Three-Parameter Weibull Distribution: $X_i \leftarrow W(a,b,c)$

A random number is drawn from a uniform distribution on the open interval (0,1) and then transformed to a Weibull variate with the Weibull percentile function.

$$\begin{aligned} U_i &\leftarrow U(0,1) \\ X_i &= a + b\left[-\ln(1-U_i)\right]^{1/c} \end{aligned} \tag{5}$$

<u>Logistic Distribution</u> – $L(\alpha,\beta)$

PDF: $f_L(x \mid \alpha,\beta) = \frac{z}{\beta(1+z)^2}; \quad z = \exp\left[-\left(\frac{x-\alpha}{\beta}\right)\right], \quad -\infty < x < \infty$

CDF: $\Pr(X \le x) = F_L(x \mid \alpha,\beta) = \frac{1}{1+z}; \quad z = \exp\left[-\left(\frac{x-\alpha}{\beta}\right)\right], \quad -\infty < x < \infty$

Moments:

Mean $\mu = \alpha$

Variance $\sigma^2 = \frac{\pi^2\beta^2}{3}$

Sampling from a Two-Parameter Logistic Distribution $X_i \leftarrow L(\alpha,\beta)$

A random number is drawn from a uniform distribution on the open interval (0,1) and then transformed to a logistic variate by the logistic percentile function.

$$U_i \leftarrow U(0,1)$$
$$X_i = \alpha - \beta \ln\left(\frac{1}{U_i} - 1\right) \tag{6}$$

Log-Logistic Distribution – $LL(a,b,c)$

(a = location parameter, b = scale parameter, c = shape parameter)

PDF: $$f_L(x \mid a,b,c) = \begin{cases} \dfrac{c\, z^{c-1}}{b(1+z^c)^2}; & \text{for } z > 0 \\ 0; & \text{for } z \le 0 \end{cases} \quad \text{where } z \equiv \left(\frac{x-a}{b}\right), (b,c) > 0$$

CDF:

$$\Pr(X \le x) = F_L(x \mid a,b,c) = \begin{cases} \dfrac{1}{1+z^{-c}}; & \text{for } z > 0 \\ 0; & \text{for } z \le 0; \end{cases} \quad \text{where } z \equiv \left(\frac{x-a}{b}\right); (b,c) > 0$$

Moments:

Mean $$\mu = a + b\,\theta \csc(\theta) \text{ for } c > 1 \text{, where } \theta = \frac{\pi}{c}$$

Variance $$\sigma^2 = b^2\theta\left[2\csc(2\theta) - \theta \csc^2(\theta)\right] \text{ for } c > 2 \text{, where } \theta = \frac{\pi}{c}$$

Sampling from a Three-Parameter Log-Logistic Distribution $X_i \leftarrow LL(a,b,c)$

A random number is drawn from a uniform distribution on the open interval (0,1) and then transformed to a log-logistic variate by the log-logistic percentile function.

$$U_i \leftarrow U(0,1)$$
$$X_i = a + b\exp\left(\frac{\ln(U_i) - \ln(1-U_i)}{c}\right) \tag{7}$$

Johnson S_B Distribution [85, 86] – $JS_B(a,b,\alpha_1,\alpha_2)$

(a,b = upper and lower location parameters, b-a = scale parameter, (α_1,α_2) = shape parameters)

$$\text{PDF:}\quad f_{JSB}(x|a,b,\alpha_1,\alpha_2)=\begin{cases}0 & x\le a\\ \dfrac{\alpha_2(b-a)}{(x-a)(b-x)\sqrt{2\pi}}\exp\left\{-\dfrac{1}{2}\left[\alpha_1+\alpha_2\ln\left(\dfrac{x-a}{b-x}\right)\right]^2\right\} & a<x<b\\ 0 & x\ge b\end{cases}$$

$$\text{CDF:}\quad \Pr(X\le x)=F_{JS_B}(x\,|\,a,b,\alpha_1,\alpha_2)=\begin{cases}0 & x\le a\\ \Phi\left[\alpha_1+\alpha_2\ln\left(\dfrac{x-a}{b-x}\right)\right] & a<x<b\\ 1 & x\ge b\end{cases}$$

where $\Phi(z)$ is the cumulative distribution function of a standard normal random variate with $\mu=0;\sigma^2=1$.

Moments: all moments exist but are extremely complicated (see [87])

Sampling from a Four-Parameter Johnson S_B Distribution: $X_i \leftarrow JS_B(a,b,\alpha_1,\alpha_2)$

A random number is drawn from a uniform distribution on the open interval (0,1) and then transformed to a Johnson S_B variate with the Johnson S_B percentile function.

$$\begin{aligned}U_i &\leftarrow U(0,1)\\ Z_i &= \Phi^{-1}(U_i)\\ X_i &= \frac{a+b\exp\left[\dfrac{Z_i-\alpha_1}{\alpha_2}\right]}{1+\exp\left[\dfrac{Z_i-\alpha_1}{\alpha_2}\right]}\end{aligned}\qquad (8)$$

where $\Phi^{-1}(U_i)$ is calculated using the approximation of the standard normal percentile function of Eq. (2) from ref. [84].

Figure 10 gives examples of PDFs from each of these continuous probability distributions.

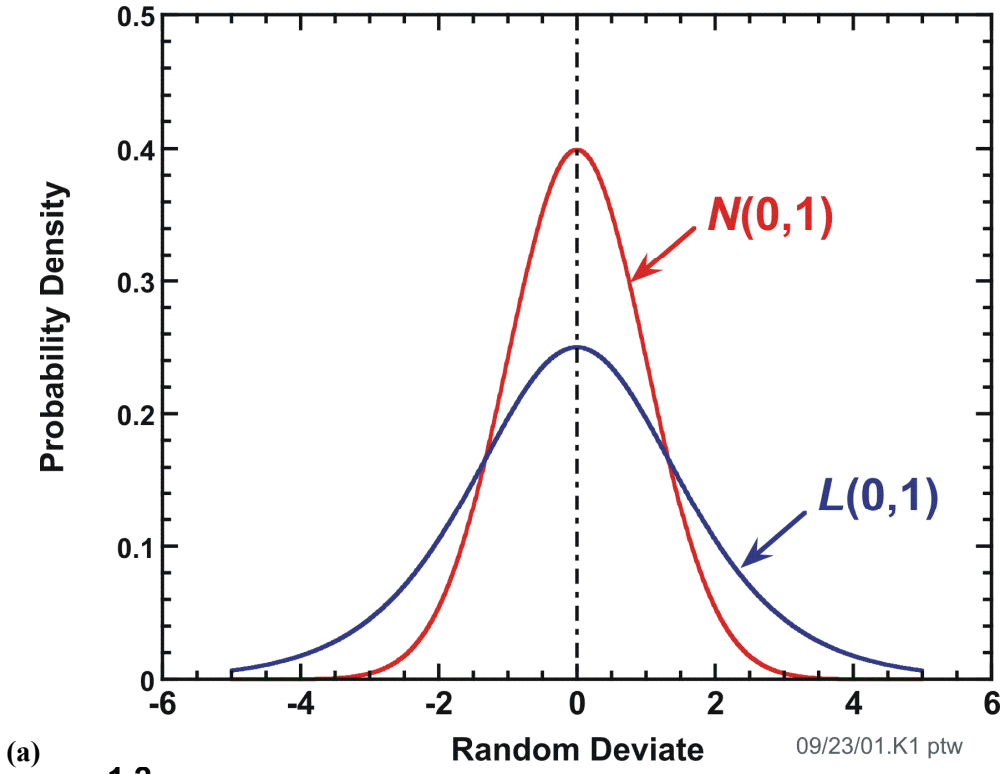

(a)

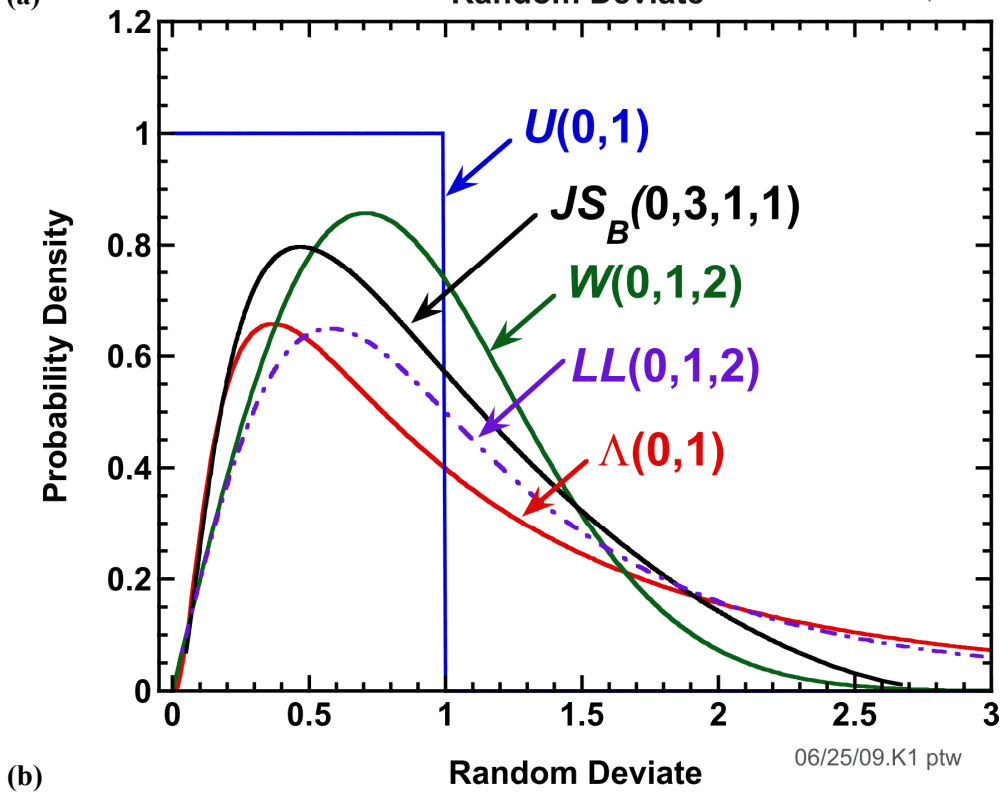

(b)

Fig. 10. Example probability density functions for (a) normal and logistic and (b) uniform, Johnson S_B ,Weibull, log-logistic, and lognormal continuous distributions.

4.3.6 Truncation Protocol

When sampling physical variables from statistical distributions, it is sometimes necessary to truncate the distribution to preclude the sampling of nonphysical values. When truncation is required in FAVOR, the truncation bounds, either symmetric or one-sided, are explicitly stated in the sampling protocols presented in Chapters 4 and 5. The truncation rule applied in FAVOR requires a sampled variable that exceeds its truncation bounds to be replaced by the boundary value. This exception-handling protocol ensures that the integrated area under the truncated probability density function remains equal to unity; however, the shape of the resulting sampled density distribution will have a step-function rise at the truncated boundary.

4.3.7 Conditional Probability of Initiation (*CPI*)

As discussed above, a deterministic fracture analysis is performed by stepping through discrete transient time steps to examine the temporal relationship between the applied Mode I stress intensity factor (K_I) and the static cleavage fracture initiation toughness (K_{Ic}) at the crack tip. The computational model for quantification of fracture-toughness uncertainty has been improved (relative to the models used in the 1980s that supported the PFM calculations that informed 10 CFR 50.61) in three ways: (1) the K_{Ic} and K_{Ia} databases were extended by 84 and 62 data values, respectively, relative to the databases in the EPRI NP-719-SR[7] report [88]; (2) the statistical representations for K_{Ic} and K_{Ia} were derived through the application of rigorous mathematical procedures; and (3) a method for estimating the *epistemic* uncertainty in the transition-reference temperature was developed. Bowman and Williams [89] provide details regarding the extended database and mathematical procedures employed in the derivation of a Weibull distribution for fracture-toughness data. Listings of the extended ORNL 99/27 K_{Ic} and K_{Ia} database are given in Appendix C. A Weibull distribution, in which the parameters were calculated by the *Method of Moments* point-estimation technique, forms the basis for the new statistical model of K_{Ic}. For the Weibull distribution, there are three parameters to estimate: the location parameter, a, of the random variate; the scale parameter, b, of the random variate; and the shape parameter, c. The Weibull probability density, f_W, is given by:

$$f_w(x|a,b,c) = \begin{cases} 0 \quad ; & x \le a \\ \dfrac{c}{b} y^{c-1} \exp\left(-y^c\right); & (y = (x-a)/b, x > a,\ b,c > 0) \end{cases} \tag{9}$$

[7] The fracture-toughness database given in EPRI NP-719-SR (1978) [88] served as the technical basis for the statistical K_{Ic} / K_{Ia} distributions used in the IPTS studies of the 1980s.

where the parameters of the K_{Ic} distribution are a function of $\widehat{\Delta T}_{RELATIVE}$:

$$\begin{aligned} a_{K_{Ic}}(\widehat{\Delta T}_{RELATIVE}) &= 19.35 + 8.335\exp\left[0.02254(\widehat{\Delta T}_{RELATIVE})\right] \text{ [ksi}\sqrt{\text{in.}}\text{]} \\ b_{K_{Ic}}(\widehat{\Delta T}_{RELATIVE}) &= 15.61 + 50.132\exp\left[0.008(\widehat{\Delta T}_{RELATIVE})\right] \text{ [ksi}\sqrt{\text{in.}}\text{]} \\ c_{K_{Ic}} &= 4 \end{aligned} \tag{10}$$

where $\widehat{\Delta T}_{RELATIVE} = (T(t) - \widehat{RT_{NDT}})$ in °F . The curve, "$\widehat{X}$", above a variable indicates that it is a randomly sampled value. The details of the development of Eq. (10) will be given in Chapter 5 along with a discussion of the sampling methods for $\widehat{RT_{NDT}}$.

For each postulated flaw, a deterministic fracture analysis is performed by stepping through the transient time history for each transient. At each time step, τ^n , for the i^{th} transient and j^{th} RPV trial, an instantaneous $cpi(\tau^n)_{(i,j,k)}$ is calculated for the k^{th} flaw from the Weibull K_{Ic} cumulative distribution function at time, τ, to determine the fractional part (or fractile) of the distribution that corresponds to the applied $K_I(\tau^n)_{(i,j,k)}$:

$$\Pr\left(K_{Ic} \le K_I(\tau^n)_{(i,j,k)}\right) = cpi(\tau)_{(i,j,k)} = \begin{cases} 0 \ ; & K_I(\tau^n)_{(i,j,k)} \le a_{K_{Ic}} \\ 1 - \exp\left\{-\left[\dfrac{K_I(\tau^n)_{(i,j,k)} - a_{K_{Ic}}}{b_{K_{Ic}}}\right]^{c_{K_{Ic}}}\right\} \ ; & K_I(\tau^n)_{(i,j,k)} > a_{K_{Ic}} \end{cases} \tag{11}$$

Here, $cpi(\tau^n)_{(i,j,k)}$ is the instantaneous conditional probability of initiation at the crack tip at time τ^n. Figure 11 illustrates the interaction of the applied K_I time history and the Weibull K_{Ic} distribution for an example case, in which an embedded flaw 0.67-in. in depth, 4.0-in. in length, with the inner crack tip located 0.5-in. from the inner surface, is subjected to a severe PTS transient. The RT_{NDT} of the RPV material is 270 °F. A Weibull distribution, as a lower-bounded continuous statistical distribution, has a lower limit (referred to as the *location parameter,* $a_{K_{Ic}}$) such that any value of K_I below the location parameter has a zero probability of initiation. As described in Fig. 11, the applied K_I must be greater than the local value of $a_{K_{Ic}}$ before $cpi > 0$. The region designated as $cpi > 0$ in the figure represents the finite probability K_{Ic} initiation space, and outside of this region $cpi = 0$.

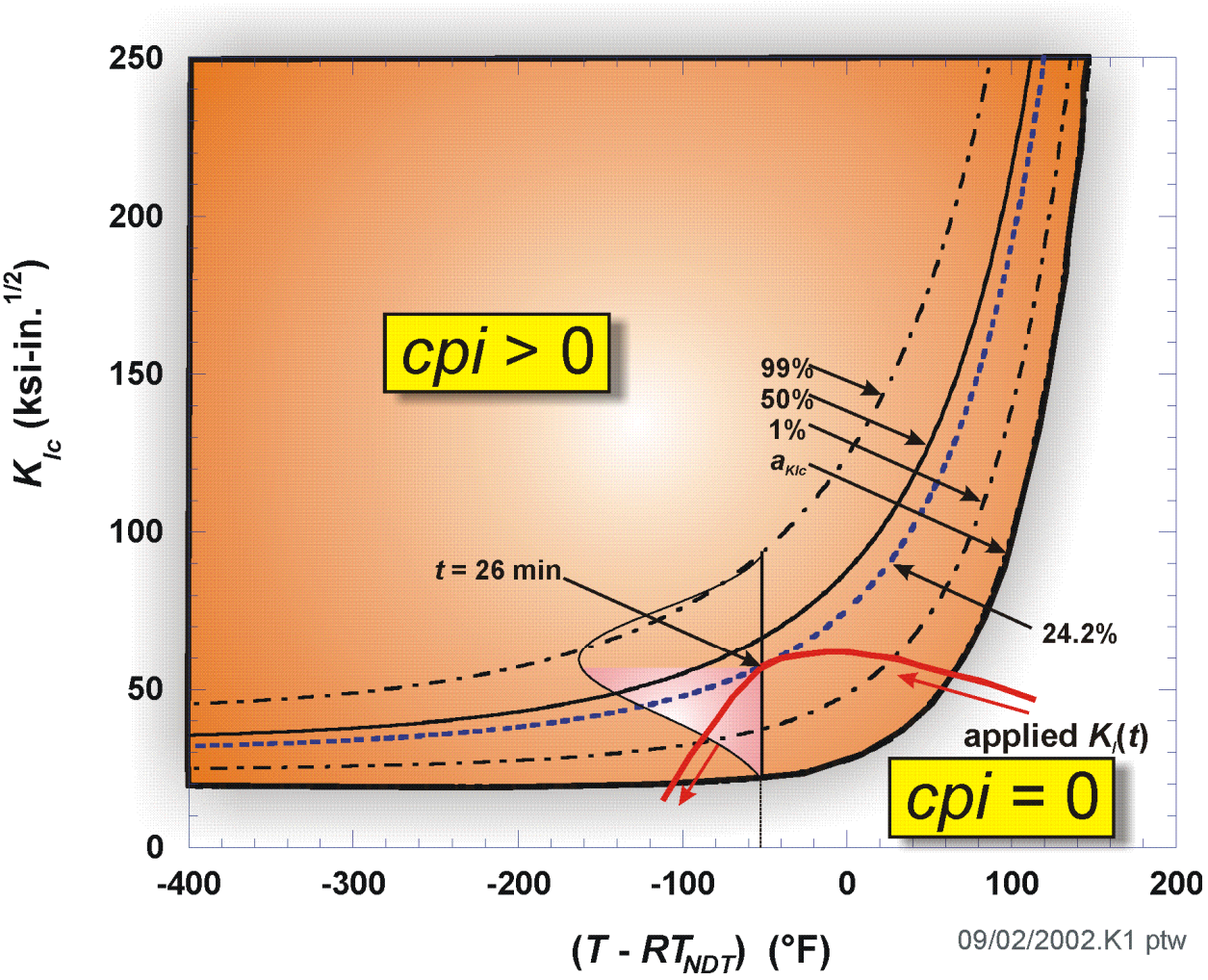

Fig. 11. Interaction of the applied K_I time history and the Weibull K_{Ic} statistical model for a postulated flaw.

Table 4. Illustration of Computational Procedure to Determine *CPI* and *CPF* for a Postulated Flaw (Warm Prestress Not Included)

Time(τ^n) (min)	$T(\tau^n)$ (°F)	RT_{NDT} (°F)	$T(\tau^n)$-RT_{NDT} (°F)	K_{Ic} Weibull Parameters a (ksi√in)	b (ksi√in)	c (-)	$K_I(\tau^n)$ (ksi√in)	$cpi(\tau^n)$ (-)	$\Delta cpi(\tau^n)$ (-)	$P(F\|I)$ (-)	$\Delta cpf(\tau^n)$ (-)	$cpf(\tau^n)$ (-)
8	360.68	270.0	90.68	83.70	119.16	4	50.90	0	0	0	0	0
10	328.28	270.0	58.28	50.35	95.52	4	55.70	9.82E-06	9.82E-06	0	0	0
12	302.18	270.0	32.18	36.57	80.46	4	59.20	6.24E-03	6.23E-03	0.20	0.0012	0.0012
14	281.48	270.0	11.48	30.15	70.56	4	61.00	3.59E-02	2.96E-02	0.25	0.0074	0.0087
16	264.74	270.0	-5.26	26.75	63.68	4	61.80	8.77E-02	5.18E-02	0.30	0.0155	0.0242
18	251.24	270.0	-18.76	24.81	58.76	4	61.70	1.44E-01	5.62E-02	0.40	0.0225	0.0467
20	240.44	270.0	-29.56	23.63	55.18	4	61.10	1.91E-01	4.76E-02	0.50	0.0238	0.0705
22	231.62	270.0	-38.38	22.86	52.49	4	60.10	2.24E-01	3.24E-02	0.60	0.0194	0.0899
24	224.24	270.0	-45.76	22.32	50.37	4	58.80	2.40E-01	1.66E-02	0.70	0.0116	0.1015
26	218.12	270.0	-51.88	21.94	48.71	4	57.30	2.42E-01	2.04E-03	0.80	0.0016	0.1031

Notes:
$cpi(\tau^n)$ – instantaneous conditional probability of initiation
$\Delta cpi(\tau^n)$ – incremental change in instantaneous conditional probability of initiation
$P(F|I)$ - the number of flaws that propagated through the wall thickness divided by the total number of initiated flaws
$\Delta cpf(\tau^n) = P(F|I) \times \Delta cpi(t^n)$
$cpf(\tau^n)$ = instantaneous conditional probability of failure by through-wall cracking
CPI = *sup*-norm[8] of the vector $\{cpi(\tau^n)\}$
CPF = *sup*-norm of the vector $\{cpf(\tau^n)\}$
The transient index, *i*, RPV trial index, *j*, and flaw index, *k*, are implied.

Table 4 summarizes results of the PFM model for the postulated flaw. The transient index, *i*, RPV trial index, *j*, and flaw index, *k*, are implied for all variables. The column headed $cpi(\tau^n)$ is the instantaneous value of the conditional probability of initiation determined from Eq. (11) (see Fig.12). The next column headed $\Delta cpi\ (\tau^n)$ is the increase in $cpi(\tau^n)$ that occurred during the discrete time step, $\Delta\tau^n$, as illustrated in Fig. 13. The current value of $CPI_{(i,j,k)}$ is

$$CPI_{(i,j,k)} = \left\| \left\{ cpi(\tau^m) \right\}_{(i,j,k)} \right\|_\infty \quad \text{for } 1 \le m \le n \tag{12}$$

For the example flaw in Table 4, *CPI* = 0.242 occurs at a transient time of 26 minutes. The last three columns in Table 4 are used in the determination of the conditional probability of vessel failure, *CPF*, by through-wall cracking, as will be discussed below.

[8] the *sup*-norm is the maximum-valued element (in absolute value) in the vector

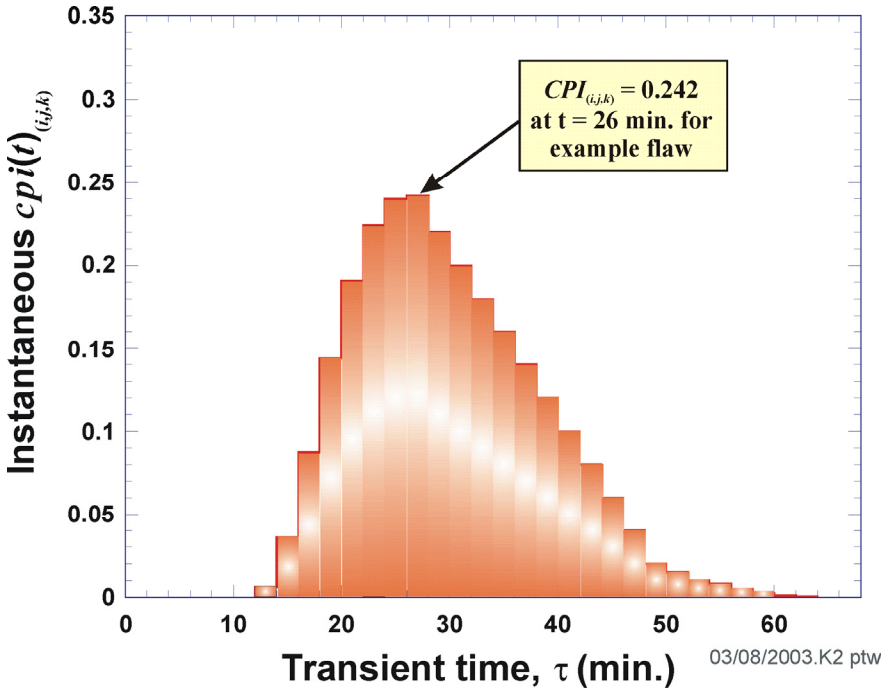

Fig. 12. The parameter $cpi(\tau)_{(i,j,k)}$ is the instantaneous conditional probability of initiation (*cleavage fracture*) obtained from the Weibull K_{Ic} cumulative distribution function. $CPI_{(i,j,k)}$ is the maximum value of $cpi(\tau)_{(i,j,k)}$. (Note: i = transient index, j = RPV trial index, and k = flaw index)

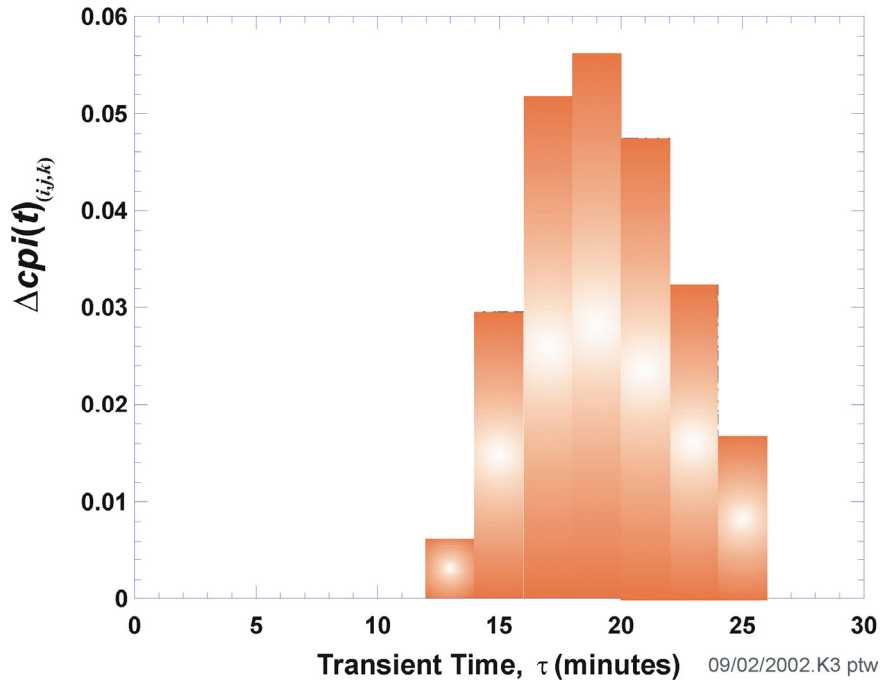

Fig. 13. $\Delta cpi(\tau^n)_{(i,j,k)}$ is the increase in $cpi(\tau^n)_{(i,j,k)}$ that occurs during each discrete time step. When the maximum value of $cpi(\tau^n)_{(i,j,k)}$ is reached, negative values of $\Delta cpi(\tau^n)_{(i,j,k)}$ are set to zero. (Note: i = transient index, j = RPV trial index, and k = flaw index)

4.3.8 Post-Initiation Flaw Geometries and Orientations

4.3.8.1 Internal Surface and Embedded Flaws in the Inner Half of the RPV Wall

All internal surface-breaking semi-elliptical flaws that initiate in cleavage fracture are assumed to become infinite length internal surface-breaking flaws (see Fig. 14). This assumption is consistent with the results of large-scale fracture experiments in which flaws, initiated in cleavage fracture, were observed to extend in length before propagating through the wall thickness [90]. For example, a circumferentially oriented semi-elliptical surface-breaking flaw ½-inch in depth is assumed to become a ½-inch deep, 360° circumferential flaw. As discussed in Section 4.2.4, FAVOR models all pre-existing internal surface breaking flaws as being circumferentially oriented. This restriction is based on the assumption that these flaws were created during vessel fabrication, as the austenitic stainless-steel cladding was being applied to the inner surface of the vessel.

Pre-existing embedded flaws in the inner half of the RPV may be oriented either axially or circumferentially. Upon initiation, the transformed infinite-length flaws retain the orientation of the parent initiating flaw i.e. become either an infinite-length (when axially-oriented) or a 360° (when circumferentially-oriented) internal surface breaking flaws. For example, an embedded flaw ½-inch in depth with its inner crack tip located at ½-inch from the RPV inner surface becomes a 1-inch deep infinite-length flaw, since it is assumed that an initiated embedded flaw first propagates through the clad, thus becoming an infinite-length surface-breaking flaw before advancing into the vessel wall.

4.3.8.2 External Surface and Embedded Flaws in the Outer Half of the RPV Wall

Through-wall propagation is not included by FAVOR for external-surface breaking flaws regardless of geometry and orientation. Therefore, any external surface-breaking flaws or embedded flaws in the outer half of the RPV wall upon initiating in cleavage fracture are directly assumed to propagate through the entire wall thickness causing RPV failure.

Table 5(a) summarizes different flaw orientations applied by FAVOR according to the major region where the flaw is located. Table 5(b) details various post-initiation flaw geometries and orientations for various kinds of flaws.

Table 5(a). Applied Flaw Orientations by Major Region

Major Region	Flaw Category 1	Flaw Category 2	Flaw Category 3
axial weld	circumferential	axial	axial
circumferential weld	circumferential	circumferential	circumferential
plate/forging	circumferential	axial/circumferential*	axial/circumferential*

Flaw Category 1 – surface-breaking flaw

Flaw Category 2 – embedded flaw in the base material between the clad/base interface and $\frac{1}{8}t$

Flaw Category 3 – embedded flaw in the base material between $\frac{1}{8}t$ and $\frac{3}{8}t$

*Flaw Categories 2 and 3 in plates/forgings are equally divided between axial and circumferential orientations

Table 5(b) Post-Initiation Flaw Geometries and Orientations

FLAW TYPE & GEOMETRY	LOCATION	ORIENTATION	AFTER INITIATION
surface-breaking (semi-elliptical)	RPV internal surface	*circumferential*	360º internal surface breaking flaw
surface-breaking (semi-elliptical)	RPV external surface	*axial*	failure of RPV
		circumferential	failure of RPV
embedded flaw (elliptical)	crack tip between (0 - λ.t) where: λ = 3/8 for flaw population 1; λ = 1/2 for flaw population 3	*axial*	surface-breaking infinite length flaw with nearly same depth as original crack-tip
		circumferential	surface-breaking 360º flaw with nearly same depth as original crack-tip
embedded flaw (elliptical)	crack tip between (λ.t – t) where: λ = 5/8 for flaw population 2 λ = 1/2 for flaw population 3	*axial*	failure of RPV
		circumferential	failure of RPV

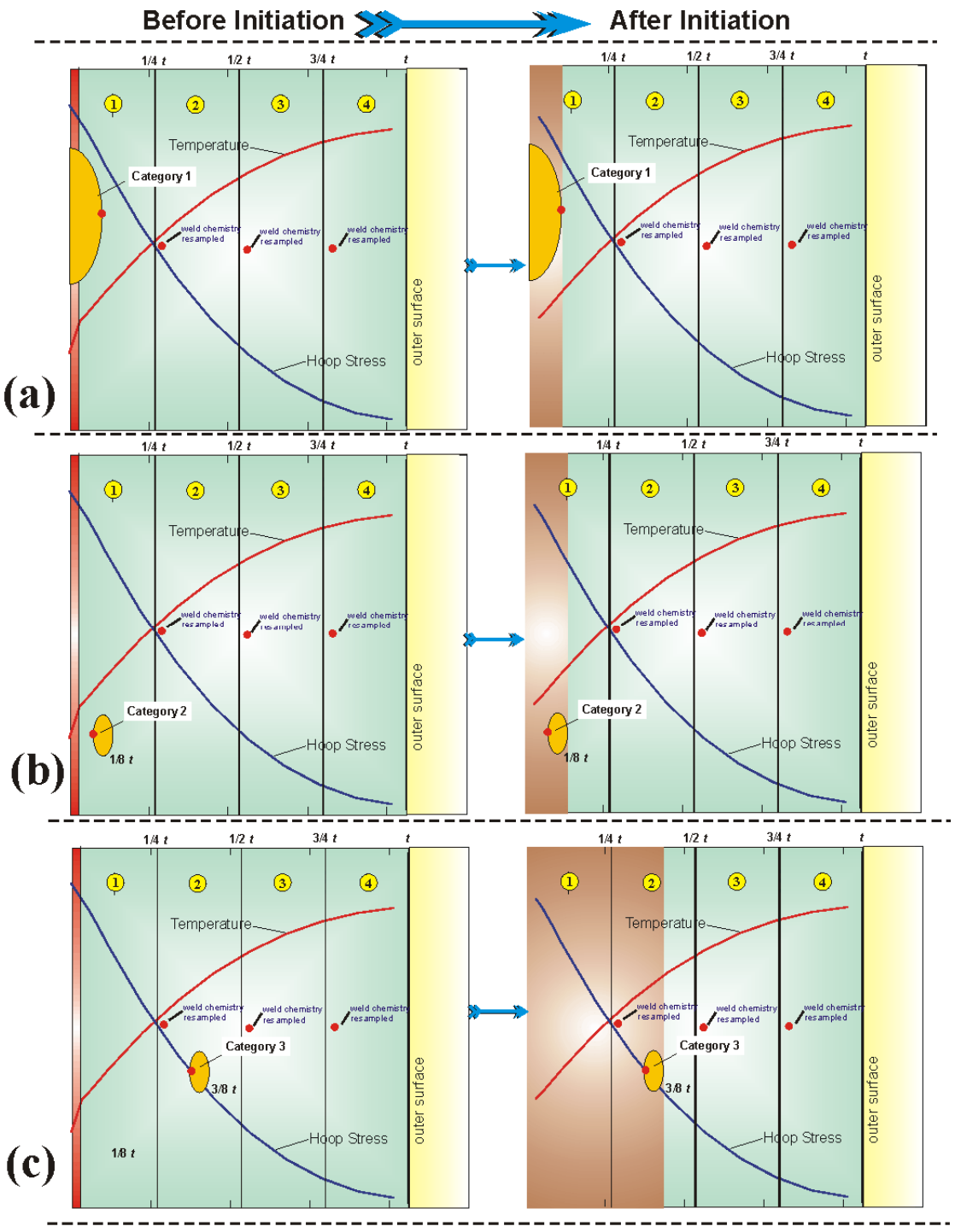

Fig. 14. At the time of initiation, the three categories of flaws are transformed into infinite-length flaws: (a) Category 1 semi-elliptic surface-breaking circumferential flaws become 360° circumferential flaws, (b) and (c) Category 2 and 3 embedded flaws become inifinite-length axial or 360° circumferential flaws at the same depth. Category 1 flaws are only oriented in the circumferential direction.

4.3.9 Conditional Probability of Failure (*CPF*) by Through-Wall Cracking

A flaw that has initiated in cleavage fracture has two possible outcomes for the time remaining in the transient. The newly-formed infinite-length flaw either propagates through the entire wall thickness causing RPV failure by through-wall cracking, or it experiences a stable arrest at some location in the wall. In either case, the advancement of the crack tip through the RPV wall may involve a sequence of *initiation* / *arrest* / *re-initiation* events as discussed in the following section. In the discussion in this section, the transient index, *i*, RPV trial index, *j*, and flaw index, *k*, are implied for all variables. They have been left off to simplify the notation.

Table 4 summarizes the calculation of RPV failure in the improved PFM model. The column headed $P(F \mid I)$ is the conditional probability of failure given initiation; $P(F \mid I)$ is equal to the fraction of initiated flaws that propagate through the wall thickness causing RPV failure. At the current time, τ^n, the increment in the conditional probability of failure, $\Delta cpf(\tau^n)$, is the product of $P(F \mid I)$ and $\Delta cpi(\tau^n)$. The instantaneous value of the conditional probability of failure at time τ^n, $cpf(\tau^n)$, is therefore

$$cpf(\tau^n) = \sum_{m=1}^{n_{\max}} P(F \mid I) \times \Delta cpi(\tau^m) = \sum_{m=1}^{n_{\max}} \Delta cpf(\tau^m) \tag{13}$$

where $n_{\max}$ is the time step at which the current value of *CPI* occurred, i.e., the time at which the maximum value of $cpi(\tau)$ occurred.

The fraction of flaws that would fail the RPV is determined (at each time step for each flaw) by performing a Monte Carlo analysis of through-wall propagation of the infinite-length flaw. In each analysis, the infinite-length flaw is incrementally propagated through the RPV wall until it either fails the RPV or experiences a stable arrest. In each analysis, a K_{Ia} curve is sampled from the lognormal K_{Ia} distribution (to be discussed in Sect. 5.2.8). The applied K_I for the growing infinite-length flaw is compared to K_{Ia} as the flaw propagates through the wall. If crack arrest does not occur ($K_I \geq K_{Ia}$), the crack tip advances another small increment, and again a check is made for arrest. If the crack does arrest ($K_I \leq K_{Ia}$), the simulation continues stepping through the transient time history checking for re-initiation of the arrested flaw. At the end of the Monte Carlo analysis, $P(F|I)$ is simply the number of flaws (that initiated at time τ^n) that propagated through the wall thickness causing RPV failure, divided by the total number of simulated flaws. See Sect. 4.3.12 for details of the Initiation-Growth-Arrest (*IGA*) submodel.

The *sup*-norm of the vector $\{cpf(\tau^n)\}$, *CPF*, occurs at the same time step as the *CPI*. In Table 4, for the example flaw, *CPF* is 0.103 and occurs at a transient elapsed time of 26 minutes.

4.3.10 Multiple Flaws

The technical basis for the treatment of multiple flaws in the beltline region of an RPV is given in [91,92]. For each j^{th} RPV trial and i^{th} transient, the process described above is repeated for all postulated flaws, resulting in an array of values of $CPI_{(i,j,k)}$, for each k^{th} flaw, where the value of $CPI_{(i,j,k)}$ is the *sup*-norm of the vector $\{cpi(\tau^n)_{(i,j,k)}\}$ (0.242 for the example in Table 4).

If $CPI_{(i,j,1)}$ is the *probability of initiation* of a flaw in an RPV trial that contains a single flaw, then $(1\text{-}CPI_{(i,j,1)})$ is the *probability of non-initiation*. If $CPI_{(i,j,1)}$ and $CPI_{(i,j,2)}$ are the *marginal* probabilities of initiation of two flaws in an RPV trial that contains two flaws, then $(1\text{-}CPI_{(i,j,1)})\times\ (1\text{-}CPI_{(i,j,2)})$ is the total probability of non-initiation, i.e., the joint probability that neither of the two flaws will fracture. This can be generalized to an RPV simulation with *nflaw* flaws, so that the total joint probability that none of the flaws will initiate is:

$$\left\{\begin{matrix}\text{Conditional probability} \\ \text{of non-initiation}\end{matrix}\right\}_{(i,j)} = \prod_{k=1}^{nflaw}(1-CPI_{(i,j,k)}) = (1-CPI_{(i,j,1)})(1-CPI_{(i,j,2)})\ldots(1-CPI_{(i,j,nflaw)}) \tag{14}$$

Therefore, for the i^{th} transient and j^{th} RPV trial with *nflaw* flaws, the total probability that at *least one of the flaws* will fracture is just the complement of Eq. (14):

$$CPI_{RPV(i,j)} = 1 - \prod_{k=1}^{nflaw}(1-CPI_{(i,j,k)}) = 1-\left[\left(1-CPI_{(i,j,1)}\right)(1-CPI_{(i,j,2)})\ldots(1-CPI_{(i,j,nflaw)})\right] \tag{15}$$

The method described here for combining the values of *CPI* for multiple flaws in an RPV is also used for combining the values of *nonfailure* to produce *CPFs* for multiple flaws.

4.3.11 Ductile-Tearing Models in FAVOR

Two ductile-tearing models have been implemented into FAVOR. Ductile-Tearing Model No. 1, implemented in the FAVOR, v05.1, is the recommended model to estimate the effects of ductile tearing in the *Initiation-Growth-Arrest* model. Ductile-Tearing Model No. 2 was implemented in FAVOR, v03.1, and is retained in the current release for the purposes of backward compatibility with previous analyses carried out using FAVOR, v03.1.

Ductile-tearing property data were obtained from the PTSE-1 [34] and PTSE-2 [35] studies carried out in the 1980s along with additional data collected in [97-99] and applied in the model development. A summary of the major materials and data sources is presented in Table 6 along with the chemistry composition and relevant ductile-tearing properties in Tables 7 and 8.

Table 6. Sources for Ductile-Tearing Data [34, 35, 93, 94, 95, 142]

Materials	Reference
61-67W	NUREG/CR-3506
Midland Weld	NUREG/CR-5736
P02, 68-71W	NUREG/CR-4880
PTSE-1 Post Test	NUREG/CR-4106
PTSE-2 Post Test	NUREG/CR-4888
W8A & W9A	NUREG/CR-5492

Table 7. Chemical Composition of Materials Used in the Ductile-Tearing Model Development

HSST	Weld Flux	Chemistry Composition (wt %)									
ID	Lot ID	C	Mn	P	S	Si	Cr	Ni	Mo	Cu	V
Plate 02	(-)	0.230	1.550	0.009	0.014	0.200	0.040	0.670	0.530	0.140	0.003
Midland Beltine	Linde 80	0.083	1.607	0.017	0.006	0.622	0.100	0.574	0.410	0.256	0.006
Midland Nozzle	Linde 80	0.083	1.604	0.016	0.007	0.605	0.110	0.574	0.390	0.290	0.008
W8A	Linde 80	0.083	1.330	0.011	0.016	0.770	0.120	0.590	0.470	0.390	0.003
W9A	Linde 0091	0.190	1.240	0.010	0.008	0.230	0.100	0.700	0.490	0.390	
68W	Linde 0091	0.150	1.380	0.008	0.009	0.160	0.040	0.130	0.600	0.040	0.007
69W	Linde 0091	0.140	1.190	0.010	0.009	0.190	0.090	0.100	0.540	0.120	0.005
70W	Linde 0124	0.100	1.480	0.011	0.011	0.440	0.130	0.630	0.470	0.056	0.004
71W	Linde 80	0.120	1.580	0.011	0.011	0.540	0.120	0.630	0.450	0.046	0.005
61W	Linde 80 btwn A533B	0.090	1.480	0.020	0.014	0.570	0.160	0.630	0.370	0.280	0.005
62W	Linde 80 btwn A508	0.083	1.510	0.160	0.007	0.590	0.120	0.537	0.377	0.210	0.010
63W	Linde 80 btwn A508	0.098	1.650	0.016	0.011	0.630	0.095	0.685	0.427	0.299	0.011
64W	Linde 80 btwn A508	0.085	1.590	0.014	0.015	0.520	0.092	0.660	0.420	0.350	0.007
65W	Linde 80 btwn A508	0.080	1.450	0.015	0.015	0.480	0.088	0.597	0.385	0.215	0.006
66W	Linde 80 btwn A508	0.092	1.630	0.018	0.009	0.540	0.105	0.595	0.400	0.420	0.009
67W	Linde 80 btwn A508	0.082	1.440	0.011	0.012	0.500	0.089	0.590	0.390	0.265	0.007

Table 8. Summary of Ductile-Tearing Data Used in the Ductile-Tearing Model Development

Material	Size	Fluence	Temp.	J_{Ic}	Avg. T_R	Avg. USE	Material	Size	Fluence	Temp.	J_{Ic}	Avg. T_R	Avg. USE	Material	Size	Fluence	Temp.	J_{Ic}	Avg. T_R	Avg. USE
ID		10^{19} n/cm^2	(°C)	(kJ/m^2)	(-)	(ft-lbf)	ID		10^{19} n/cm^2	(°C)	(kJ/m^2)	(-)	(ft-lbf)	ID		10^{19} n/cm^2	(°C)	(kJ/m^2)	(-)	(ft-lbf)
61W	0.8	0	75	142.3	89	62	64W	0.5	0.582	177	119.1	36	75	Mid-Belt	NA	0	21	167.4	71	65
61W	0.5	0	75	143.4	106	62	64W	4	0.66	200	78.7	50	75	Mid-Belt	NA	0	21	116.4	84	65
61W	0.8	0	121	123.9	74	62	64W	4	0.64	200	94.9	49	75	Mid-Belt	NA	0	21	131.4	76	65
61W	0.5	0	121	130.6	90	62	64W	1.6	0.623	200	57.3	46	75	Mid-Belt	NA	0	21	164.7	70	65
61W	4	0	200	97.4	100	62	64W	1.6	0.671	200	80.2	50	75	Mid-Belt	NA	0	150	133.4	41	65
61W	4	0	200	128.1	72	62	64W	0.8	0.773	200	101.9	31	75	Mid-Belt	NA	0	150	125.1	44	65
61W	1.6	0	200	78.3	70	62	64W	0.5	0.672	200	99.4	23	75	Mid-Belt	NA	0	150	141.1	60	65
61W	0.8	0	200	89.5	52	62	64W	0.8	0.773	288	46	15	75	Mid-Belt	NA	0	288	86.4	32	65
61W	0.5	0	200	89.1	66	62	64W	0.5	0.672	288	66.3	18	75	Mid-Belt	NA	0	288	103.3	33	65
61W	1.6	0	288	57.7	68	62	65W	1.6	0	132	123.4	120	108	Mid-Nozz	NA	0	21	126.6	47	64
61W	0.8	0	288	66.1	47	62	65W	0.8	0	132	147.2	97	108	Mid-Nozz	NA	0	21	113.0	57	64
61W	0.5	0	288	75	53	62	65W	0.5	0	132	118.5	130	108	Mid-Nozz	NA	0	150	102.8	39	64
61W	0.5	0	288	76.5	53	62	65W	4	0	177	80.4	138	108	Mid-Nozz	NA	0	150	89.9	43	64
61W	0.8	1.1	121	103.1	51	52	65W	0.8	0	177	117.6	76	108	Mid-Nozz	NA	0	288	69.1	32	64
61W	1.6	1.3	121	83	41	52	65W	0.5	0	177	114.8	102	108	Mid-Nozz	NA	0	288	64.5	39	64
61W	0.5	1.6	121	76.4	22	52	65W	4	0	200	69.3	114	108	Mid-Nozz	NA	0	288	64.3	37	64
61W	0.5	1	200	96.4	60	52	65W	1.6	0	200	104.1	72	108	Plate 02	NA	0	50	117.3	197	105
61W	4	1.1	200	52.4	38	52	65W	0.8	0	200	128.9	84	108	Plate 02	NA	0	50	189.9	164	105
61W	1.6	1.2	200	63.6	31	52	65W	0.5	0	200	94.8	111	108	Plate 02	NA	0	50	191.8	154	105
61W	0.8	1.2	200	69.5	44	52	65W	4	0	288	120.1	73	108	Plate 02	NA	0	50	205.1	141	105
61W	4	1.4	200	61.3	30	52	65W	1.6	0	288	71.9	73	108	Plate 02	NA	0	50	218.9	153	105
61W	0.8	1.1	288	46.4	15	52	65W	1.6	0	288	74.2	69	108	Plate 02	NA	0	121	111.0	156	105
61W	0.5	1.4	288	44.6	17	52	65W	0.8	0	288	73.5	56	108	Plate 02	NA	0	121	137.1	178	105
62W	0.5	0	75	121.7	119	93	65W	0.5	0	288	83.8	69	108	Plate 02	NA	0	121	161.7	147	105
62W	1.6	0	149	114.5	124	93	65W	1.6	0.67	132	106.2	77	72	Plate 02	NA	0	121	168.3	133	105
62W	0.8	0	149	150.1	139	93	65W	0.8	0.744	132	113.6	54	72	Plate 02	NA	0	121	171.4	138	105
62W	0.5	0	149	91.4	99	93	65W	0.5	0.767	132	110.3	48	72	Plate 02	NA	0	204	132.1	118	105
62W	4	0	177	107.6	154	93	65W	4	0.74	177	53.1	89	72	Plate 02	NA	0	204	134.7	99	105
62W	0.8	0	177	160.3	115	93	65W	0.8	0.744	177	104.8	45	72	Plate 02	NA	0	204	139.2	115	105
62W	0.5	0	177	101	94	93	65W	0.5	0.629	177	114.7	47	72	Plate 02	NA	0	204	140.4	113	105
62W	4	0	200	145.5	140	93	65W	4	0.61	200	85.6	61	72	Plate 02	NA	0	204	181.0	100	105
62W	1.6	0	200	154.4	117	93	65W	1.6	0.62	200	70.4	56	72	Plate 02	NA	0	288	111.8	81	105
62W	1.6	0	200	128.7	133	93	65W	0.8	0.756	200	91.5	41	72	Plate 02	NA	0	288	112.1	73	105
62W	0.8	0	200	150.8	99	93	65W	0.5	0.629	200	107	54	72	Plate 02	NA	0	288	118.1	92	105
62W	0.5	0	200	78.4	83	93	65W	0.8	0.756	288	41	23	72	Plate 02	NA	0	288	121.9	73	105
62W	0.5	0	200	113.8	87	93	65W	0.5	0.767	288	43.9	32	72	Plate 02	NA	0	288	132.6	89	105
62W	4	0	288	87.3	112	93	66W	0.5	0	100	94.4	41	76	68W	NA	0	23	160.1	219	147
62W	1.6	0	288	101	118	93	66W	1.6	0	200	67	55	76	68W	NA	0	121	151.1	204	147
62W	0.8	0	288	93.8	59	93	66W	0.8	0	200	103.6	50	76	68W	NA	0	121	196.9	204	147
62W	0.5	0	288	83.6	59	93	66W	0.5	0	200	73	42	76	68W	NA	0	200	223.5	111	147
62W	0.5	0	288	85	84	93	66W	0.8	0	288	73.8	40	76	68W	NA	0	288	121.3	132	147

Table 8. (cont.) Summary of Ductile-Tearing Data Used in the Ductile-Tearing Model Development

Material ID	Size	Fluence 10^{19} n/cm^2	Temp. (°C)	J_{Ic} (kJ/m^2)	Avg. T_R (-)	Avg. USE (ft-lbf)
62W	1.6	1.4	149	118.3	60	80
62W	0.8	1.3	149	118.7	91	80
62W	0.5	1.6	149	96.2	32	80
62W	0.5	1.3	176	94.1	50	80
62W	4	1.4	177	105.9	62	80
62W	0.8	1.5	177	127.4	45	80
62W	0.5	0.8	177	95.9	34	80
62W	4	1.5	200	90	62	80
62W	1.6	1.6	200	85	52	80
62W	0.8	1.3	200	115.9	69	80
62W	0.5	1	200	63.3	29	80
62W	0.8	1.5	288	60.9	24	80
62W	0.5	1.5	288	61.9	24	80
63W	1.6	0	100	118	120	87
63W	0.8	0	100	141.2	95	87
63W	0.5	0	100	131.1	86	87
63W	4	0	171	148.4	100	87
63W	1.6	0	171	103.5	97	87
63W	0.8	0	171	112.4	77	87
63W	0.5	0	171	113.2	88	87
63W	4	0	200	77.7	113	87
63W	1.6	0	200	79.6	94	87
63W	0.8	0	200	120.3	69	87
63W	0.5	0	200	89.2	70	87
63W	0.5	0	200	98.4	80	87
63W	4	0	288	88.4	62	87
63W	1.6	0	288	122.4	64	87
63W	0.8	0	288	66.8	57	87
63W	0.5	0	288	59.1	55	87
63W	0.5	0	288	66.7	52	87
63W	0.5	1.1	149	68.4	43	68
63W	1.6	1.3	171	79.2	49	68
63W	0.8	1.1	171	89.7	32	68
63W	0.5	1.3	171	78.9	27	68
63W	4	1.25	200	72.7	16	68
63W	1.6	1.4	200	62.2	29	68
63W	0.8	1.1	200	75.8	33	68
63W	0.5	0.9	200	77	49	68
63W	0.5	1	204	56.3	42	68
63W	0.8	1.4	288	42.7	19	68
63W	0.5	1.2	288	51.5	23	68
64W	1.6	0	100	105.7	148	100
64W	0.8	0	100	160.4	105	100
64W	0.5	0	100	116	89	100
64W	4	0	177	117.4	146	100
64W	1.6	0	177	134.6	103	100
64W	0.8	0	177	114.9	83	100
64W	0.5	0	177	125	73	100
64W	4	0	200	161.4	96	100
64W	1.6	0	200	67.8	97	100
64W	0.8	0	200	118.8	76	100
64W	0.5	0	200	115.8	54	100
64W	4	0	288	85.5	96	100
64W	1.6	0	288	76.6	83	100
64W	0.8	0	288	75.9	54	100
64W	0.5	0	288	74.2	44	100
64W	0.8	0.773	177	92.9	37	75
66W	0.5	0	288	61.9	25	76
66W	1.6	0.854	200	68.4	31	58
66W	1.6	0.944	200	66.4	29	58
66W	0.8	1.022	200	75.2	22	58
66W	0.5	0.896	200	67.4	18	58
66W	0.8	1.03	288	42.8	17	58
66W	0.5	0.896	288	51.6	16	58
67W	1.6	0	100	130.4	164	103
67W	0.8	0	100	166.5	112	103
67W	0.5	0	100	132.8	98	103
67W	4	0	200	97.4	121	103
67W	1.6	0	200	84.1	116	103
67W	0.8	0	200	118	85	103
67W	0.5	0	200	102.1	76	103
67W	0.5	0	200	92	69	103
67W	4	0	288	97.9	58	103
67W	1.6	0	288	63.4	83	103
67W	0.8	0	288	82.6	56	103
67W	0.5	0	288	80	51	103
67W	4	0.86	200	67.3	45	73
67W	4	0.96	200	56.7	57	73
67W	0.8	1.022	200	76.3	45	73
67W	0.5	0.834	200	92.2	32	73
67W	0.8	1.03	288	58.6	23	73
67W	0.5	0.617	288	80	24	73
W8A	1	0	0	104.4	72	58
W8A	1	0	75	94.4	81	58
W8A	1	0	200	79.7	57	58
W8A	1	0	288	58.6	34	58
W8A	1	2.1	125	69.9	16	36
W8A	1	2.1	200	54.1	14	36
W8A	1	2.1	288	38.6	9	36
W8A	1	1.5	30	80.8	54	40
W8A	1	1.5	75	84.6	28	40
W8A	1	1.5	200	60	17	40
W8A	1	1.5	200	57.4	18	40
W8A	1	1.5	288	41.6	11	40
W9A	1	0	-40	207.4	NA	115
W9A	1	0	0	255	173	115
W9A	1	0	75	195.9	170	115
W9A	1	0	200	147.9	130	115
W9A	1	0	288	92.9	120	115
W9A	1	0	288	116	97	115
W9A	1	2.1	75	156.2	42	74
W9A	1	2.1	200	124.1	37	74
W9A	1	2.1	200	147.7	40	74
W9A	1	2.1	288	81.5	31	74
W9A	1	1.5	75	167.7	52	84
W9A	1	1.5	200	146.4	46	84
W9A	1	1.5	200	127.2	47	84
W9A	1	1.5	288	96.1	36	84
PTSE-2	NA	0	100	64	120	46.4
PTSE-2	NA	0	100	55.6	145	46.4
PTSE-2	NA	0	175	58.3	106	46.4
PTSE-2	NA	0	175	68.4	105	46.4
PTSE-2	NA	0	250	52.8	67	46.4
PTSE-2	NA	0	250	52.2	61	46.4
68W	NA	0	288	190.7	138	147
69W	NA	0	50	143.0	87	147
69W	NA	0	50	147.9	80	147
69W	NA	0	50	163.7	70	147
69W	NA	0	121	139.5	89	147
69W	NA	0	121	141.7	93	147
69W	NA	0	121	142.7	82	147
69W	NA	0	121	158.9	88	147
69W	NA	0	200	174.5	54	147
69W	NA	0	204	98.9	76	147
69W	NA	0	204	117.5	61	147
69W	NA	0	288	89.7	56	147
69W	NA	0	288	94.1	49	147
69W	NA	0	288	103.8	56	147
69W	NA	0	288	129.4	56	147
70W	NA	0	50	106.2	188	74
70W	NA	0	50	177.8	163	74
70W	NA	0	121	127.5	159	74
70W	NA	0	121	131.1	148	74
70W	NA	0	121	142.8	140	74
70W	NA	0	204	103.3	108	74
70W	NA	0	204	112.0	133	74
70W	NA	0	204	121.0	110	74
70W	NA	0	288	89.0	79	74
70W	NA	0	288	105.6	93	74
70W	NA	0	288	106.2	88	74
71W	NA	0	30	128.0	186	81
71W	NA	0	50	97.9	144	81
71W	NA	0	50	121.0	98	81
71W	NA	0	121	110.8	153	81
71W	NA	0	121	126.7	105	81
71W	NA	0	121	131.0	155	81
71W	NA	0	204	77.6	66	81
71W	NA	0	204	84.7	87	81
71W	NA	0	204	115.4	90	81
71W	NA	0	288	64.5	72	81
71W	NA	0	288	77.4	71	81
71W	NA	0	288	80.2	61	81

In conjunction with the ductile-tearing model development, a revised fracture arrest toughness stochastic model has also been implemented in FAVOR. A discussion of this new arrest model is given in Sect. 5.2.8.

One of the constraints in developing a ductile-tearing model for FAVOR is that the required material properties should currently be available for the four plants being studied in the PTS Re-evaluation project. The relevant information available from RVID2 [155] includes Cu, Ni, Mn, and P content; the upper-shelf Charpy V-notch (CVN) energy, *USE*; and the unirradiated flow stress of the RPV steels. Consequently, all ductile fracture toughness properties used in FAVOR need to be derived from this information.

The following models are required:

- **a model for the variation of ductile crack initiation toughness, J_{Ic}, with temperature and irradiation, and**
- **a model for the variation of ductile-tearing resistance as a function of temperature, irradiation, and accumulated ductile tearing, Δa.**

These two models are connected in that they both can be derived from a J_R curve, expressed in a power-law model form by:

$$J_R = C(\Delta a^m) \tag{16}$$

where the tearing resistance is characterized by the material's local tearing modulus, T_R, defined by

$$T_R = \left(\frac{E}{\sigma_f^2}\right)\left(\frac{dJ_R}{da}\right) = \left(\frac{E}{\sigma_f^2}\right) \times m \times C \times \Delta a^{(m-1)} \tag{17}$$

Given the elastic modulus, E, and sampled irradiated flow stress, σ_f, the remaining three variables required by the ductile-tearing model are J_{Ic}, C, and m, where all three are a function of temperature and level of irradiation damage.

Applying the definition of J_{Ic} in ASTM E-1820 [96], estimates of two of the variables allows the calculation of the third. In Fig. 15, the ductile-tearing initiation toughness, J_{Ic}, is defined in ASTM E-1820 as the intersection of the J_R curve with a 0.2 mm offset blunting line given by

$$J_{(0.2\text{ mm offset})} = 2\sigma_f(\Delta a - \Delta a_0) \tag{18}$$

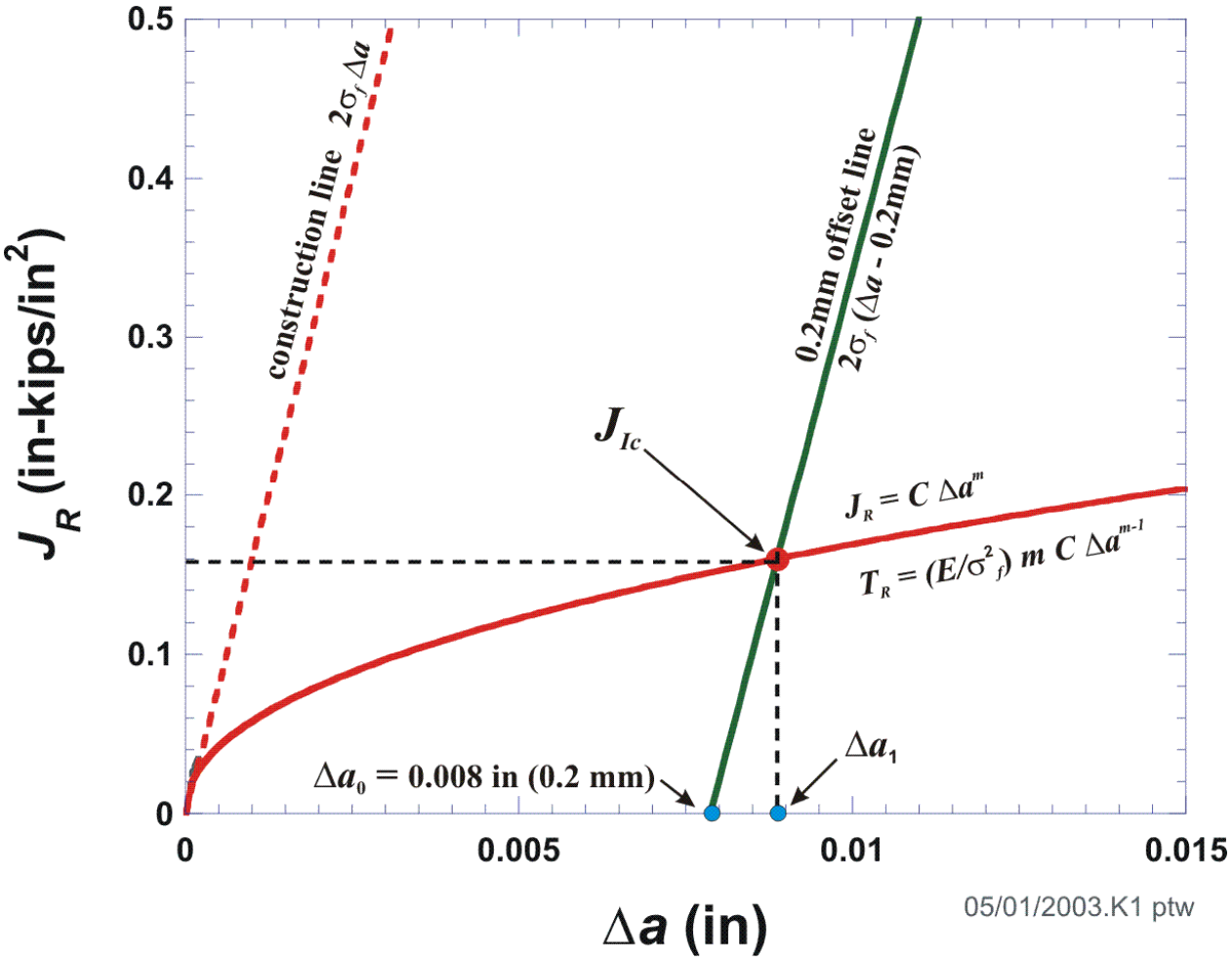

Fig. 15. Given a J_R curve in power-law model form and current flow stress, σ_f, the initiation toughness, J_{Ic}, and local tearing modulus, T_R, are uniquely defined (see ASTM E-1820 [96]).

where the prescribed offset is $\Delta a_0 = 0.2$ mm (0.008 in). Therefore, with an estimate of J_{Ic} and the power-law exponent, m, the power-law coefficient, C, is

$$J_{Ic} = C\Delta a^m \Rightarrow C = \frac{J_{Ic}}{\Delta a^m}$$

$$J_{Ic} = 2\sigma_f(\Delta a - \Delta a_0) \Rightarrow \Delta a = \frac{J_{Ic}}{2\sigma_f} + \Delta a_0 \qquad (19)$$

$$\therefore \quad C = \frac{J_{Ic}}{\left(\frac{J_{Ic}}{2\sigma_f} + \Delta a_0\right)^m}$$

The local tearing modulus then follows from Eq. (17). The focus of model development was, therefore, placed on providing methods of estimating the initiation fracture toughness, J_{Ic}, and the power-law exponent, m, as a function of temperature and irradiation damage.

4.3.11.1 Ductile-Tearing Model No. 1 (implemented in FAVOR, v05.1)

The recommended Ductile-Tearing Model No. 1 was developed from the research described in [97,98]. The following is a summary of the model described in these references.

A model of ferritic steel toughness that accounts for fracture mode transition behavior, upper shelf behavior, and the interaction between these two different fracture modes can be constructed based on Wallin's Master Curve [150], the relationship between the upper-shelf temperature, T_{US}, the Master Curve reference temperature, T_0, and the upper-shelf Master Curve. Using these relationships it is possible, as described below, to estimate the complete variation of initiation fracture toughness, J_{Ic}, with temperature in both the transition regime and on the upper shelf based only on an estimate of T_0.

The following sampling protocols are taken from [98]:

Step 1. – Estimate a Value for T_0

Given a sampled value of $\widehat{RT}_{NDT(0)}\left[°\mathrm{F}\right]$ and an adjustment for the effects of irradiation damage, $\widehat{\Delta RT}_{NDT}\left(r,\ldots\right)$, an estimate for T_0 (for a reference size of 1T) can be sampled using Eq. (102) (see Sect. 5.2.5)

$$\widehat{T}_0 = \frac{\left\langle \widehat{RT}_{NDT-DT} + 8.28 - \left\{ 100.43 \left[\left(-\ln(1-P_{T_0}) \right)^{\frac{1}{2.036}} \right] \right\} \right\rangle - 32}{1.8} \quad \left[°\mathrm{C}\right] \tag{20}$$

Where $\widehat{RT}_{NDT-DT}\left(r,\ldots\right) = \widehat{RT}_{NDT0} + \widehat{\Delta RT}_{NDT}\left(r,\ldots\right)$, (see Eq. (104)) with $\widehat{RT}_{NDT0}$ equal to the sampled unirradiated value of $RT_{NDT,}$ $\widehat{\Delta RT}_{NDT}\left(r,\ldots\right)$ equal to the shift due to radiation embrittlement, and $P_{T_0} = \Phi$ is the fractile drawn for the epistemic uncertainty in RT_{NDT} in Eq. (103).

Step 2. – Estimate a Value for the Upper-Shelf Temperature, T_{US}

From the relationship developed in [98], an estimate for the upper-shelf temperature associated with this sampled value for T_0 can be calculated from

$$\widehat{T_{US}} = 48.843 + \left(0.7985\ \widehat{T_0}\right) \quad [°\text{C}] \tag{21}$$

Step 3. – Calculate a Value for J_C Using the Master Curve at T_{US}

Using a plane strain conversion from K_{Jc} to J_c, we have, from the Master Curve model [150]

$$J_{c(med)} = \frac{1000\left\{30 + 70\exp\left[0.019\left(T_{US} - T_0\right)\right]\right\}^2\left(1-\nu^2\right)}{E} \quad \left[\frac{\text{kJ}}{\text{m}^2}\right]$$

where (22)

$$E = 207200 - \left(57.1\ T_{US}\right) \ \ [\text{MPa}] \text{ and } \nu = 0.3$$

Step 4. – Calculate an Estimate for ΔJ_{Ic} at T_{US}

Using the relationship derived in [98] to characterize the temperature dependence of J_{Ic}

$$\Delta J_{Ic} = J_{Ic}^{meas} - J_{Ic}^{288°\text{C}} = 1.75\left\{C_1 \exp\left[-C_2\left(T_{US} + 273.15\right) + C_3\left(T_{US} + 273.15\right)\ln\left(\dot{\varepsilon}\right)\right] - \sigma_{ref}\right\}$$

$$\text{where} \quad C_1 = 1033 \text{ MPa}, \quad C_2 = 0.00698 \text{ K}^{-1}, \quad C_3 = 0.000415 \text{ K}^{-1}, \quad \dot{\varepsilon} = 0.0004 \text{ sec}^{-1}, \quad \sigma_{ref} = 3.3318 \text{ MPa} \tag{23}$$

Step 5. – Calculate an Estimated Mean and Standard Deviation for the Aleatory Uncertainty in J_{Ic}

At a given wall temperature, $T_{wall}(R,t)$ $[°\text{C}]$, an estimated mean value for J_{Ic} can now be estimated by

$$\overline{J_{Ic}} = J_{c(med)} - \Delta J_{Ic} + 1.75\left\{C_1 \exp\left[-C_2\left(T_{wall} + 273.15\right) + C_3\left(T_{wall} + 273.15\right)\ln\left(\dot{\varepsilon}\right)\right] - \sigma_{ref}\right\} \quad \left[\frac{\text{kJ}}{\text{m}^2}\right] \tag{24}$$

Where an estimate for the standard deviation is given in [98] by

$$\sigma_{J_{Ic}} = 51.199\exp\left(-0.0056\ T_{wall}\right) \quad \left[\frac{\text{kJ}}{\text{m}^2}\right] \tag{25}$$

Step 6. – Sample a Value for J_{Ic} from a Normal Distribution

The aleatory uncertainty in J_{Ic} is now estimated by sampling from the following normal distribution

$$\widehat{J}_{Ic} \leftarrow N\left(\overline{J_{Ic}}, \sigma_{J_{Ic}}\right) \quad \left[\frac{\text{kJ}}{\text{m}^2}\right] \tag{26}$$

where the sampled value is truncated at $\overline{J_{Ic}} - 2\sigma_{J_{Ic}} \le \widehat{J_{Ic}} \le \overline{J_{Ic}} + 2\sigma_{J_{Ic}}$ using the truncation protocol of Sect. 4.3.6.

Step 7. – Calculate an Estimate for the Power-Law Exponent, *m*, and Coefficient, *C*

The mean value of the *J-R* curve exponent *m* (as in $J_R = C\left(\Delta a^m\right)$) is estimated based on the sampled value of $\widehat{J_{Ic}}$ and the local value of the wall temperature, $T_{wall}(R,t)$, from the following equation (developed from the data given in [98])

$$\overline{m} = a + b\exp\left(\frac{T_{wall}\left[^{\circ}\mathrm{C}\right]}{d}\right) + c\left(\widehat{J_{Ic}}\left[\mathrm{kJ/m^2}\right]\right)^3$$
$$a = 0.1117 \quad c = 5.8701\times10^{-09}$$
$$b = 0.4696 \quad d = -758.19 \qquad (27)$$
$$\sigma_{\text{std-error}} = 0.08425$$
$$R^2 = 0.2992$$

The *J-R* curve exponent *m* with aleatory uncertainty can then be sampled from the following normal distribution:

$$\widehat{m} \leftarrow N(\overline{m}, 0.08425) \qquad (28)$$

The *J-R* curve coefficient, *C*, then follows from

$$\widehat{C} = \frac{\widehat{J_{Ic\,(\text{at } T_{wall})}}}{\left(\frac{\widehat{J_{Ic\,(\text{at } T_{wall})}}}{2\widehat{\sigma_f}} + \Delta a_0\right)^{\widehat{m}}} \qquad (29)$$

where $\widehat{\sigma_f}$ is the sampled flow stress and $\Delta a_0 = 0.2$ mm.

4.3.11.2 Ductile-Tearing Model No. 2 (implemented in FAVOR, v03.1)

Following the development in [99], a preliminary ductile-tearing model was created and implemented into FAVOR, v03.1, for a scoping study of the effects of tearing resistance associated with RPV materials.

4.3.11.2.1 Upper-Shelf Irradiation Effects Model

The following discussion is taken from [99]:

To date, efforts to trend the effects of irradiation damage on RPV steels have focused predominantly on predicting the joint effects of radiation (as quantified by the fast-neutron fluence, energy > 1 MEv)

and chemical composition on the energy absorbed by a Charpy V-notch (CVN) specimen on the upper shelf (i.e., the upper shelf energy, or *USE*). This focus occurs because CVN specimens are placed into surveillance capsules that are used to assess the effect of irradiation damage on the RPV steel. It should be emphasized that the *USE* is ***not*** the initiation fracture toughness (J_{Ic}) or the tearing modulus (T_R) information needed by FAVOR to assess the probability of through-wall cracking of the RPV arising from a PTS event. Nevertheless, without significant additional research the only way to predict the effect of irradiation on J_{Ic} and T_R is to first predict the effect of irradiation on *USE* and then correlate J_{Ic} and T_R with *USE*.

In 1998, Eason, Wright, and Odette [100, 101] proposed the following relation between *USE*, chemical composition, and fluence based on the *USE* data available from domestic nuclear RPV surveillance programs at that time (692 data records) (NUREG/CR-6551) [101]. This model is given by the following equation

$$USE_{(i)} = A + 0.0570 \cdot USE_{(u)}^{1.456} - \left[17.5 \cdot f\left(Cu\right) \cdot \left(1 + 1.17 Ni^{0.8894}\right) + 305P\right]\left(\frac{f_0(r)}{10^{19}}\right)^{0.2223} \quad \text{[ft-lbf]} \qquad (30)$$

where USE_u is the unirradiated upper-shelf energy in ft-lbf; *Cu*, *Ni*, and *P* are the copper, nickel, and phosphorous content in wt %; $f_0(r)$ is the attenuated fast-neutron fluence in neutrons/cm^2; *A* is a product-form constant; and *f*(*Cu*) is a function of copper content defined as

$$A = \begin{cases} 55.4 & \text{for welds} \\ 61.0 & \text{for plates} \\ 66.3 & \text{for forgings} \end{cases}$$

$$f\left(Cu\right) = \frac{1}{2} + \frac{1}{2}\tanh\left[\frac{Cu - 0.138}{0.0846}\right]$$

Reference [99] proposes the following method to simulate upper-shelf energies and address uncertainties in $USE_{(u)}$:

Step 1. Input a best-estimate value for the unirradiated upper-shelf energy for a given major region in the FAVOR embrittlement map of the beltline. Treat this value as the mean of a normal distribution of $USE_{(u)}$ values, $\mu_{USE_{(u)}}$.

Step 2. At this value of $\mu_{USE_{(u)}}$, sample a value for the standard deviation from a normal distribution given by

$$\begin{aligned} &\sigma_{USE_{(u)}(mean)} = 4.3296 - 0.0857\mu_{USE_{(u)}} + 0.0012\mu^2_{USE_{(u)}} \\ &\widehat{\sigma}_{USE_{(u)}} \leftarrow N(\sigma_{USE_{(u)}(mean)}, 2.2789) \end{aligned} \qquad (31)$$

Step 3. Sample a value for the unirradiated upper-shelf energy, $\widehat{USE_{(u)}}$, from the following normal distribution

$$\widehat{USE_{(u)}} \leftarrow N(\mu_{USE_{(u)}}, \widehat{\sigma}_{USE_{(u)}}) \tag{32}$$

Step 4. The irradiated value for the upper-shelf energy is then estimated from Eq. (30), or, applying sampling notation:

$$\widehat{USE}_{(i)} = A + 0.0570 \cdot \widehat{USE}_{(u)}^{1.456} - \left[17.5 \cdot f\left(\widehat{Cu}\right) \cdot \left(1 + 1.17\widehat{Ni}^{0.8894}\right) + 305\widehat{P}\right]\left(\frac{\widehat{f_0}(r)}{10^{19}}\right)^{0.2223} \quad \text{[ft-lbf]} \tag{33}$$

where the chemistry and attenuated fluence have been previously sampled.

4.3.11.2.2 Model for Initiation Ductile Fracture Toughness, J_{Ic}

The sampling protocol for J_{Ic} developed in [99] is as follows:

Step 1. Determine a value of $\widehat{USE}_{(u)}$ using the sampling protocol outlined in Sect. 4.3.11.2.1 and Eqs. (31) and (32).

Step 2. Apply this sampled value of $\widehat{USE}_{(u)}$ along with sampled values of $\widehat{Cu}$, $\widehat{Ni}$, $\widehat{P}$ and $\widehat{\phi t}$ to estimate a value of $\widehat{USE}_{(i)}$ using Eq. (33).

Step 3. Convert this estimate of $\widehat{USE}_{(i)}$ value to a value of $\widehat{K}_{J_{Ic}(i)(\text{at } 550°\text{F})}$ at 550°F using the mean curve established in [99], where the uncertainty in $\widehat{K}_{J_{Ic}(i)(\text{at } 550°\text{F})}$ is ***not*** sampled,

$$\widehat{K}_{J_{Ic}(i)(\text{at } 550°\text{F})} = 70.855 + \left(0.5784 \times \widehat{USE}_{(i)}\right) \quad [\text{ksi}\sqrt{\text{in}}] \tag{34}$$

Step 4. Convert the $\widehat{K}_{J_{Ic}(i)(\text{at } 550°\text{F})}$ value to a $\widehat{K}_{J_{Ic}(i)(\text{at } T_{wall})}$ value at the wall temperature of interest using the mean curve from [99]:

$$\begin{aligned}\widehat{\Delta K}_{J_{Ic}} &= K_{J_{Ic}(\text{at } T_{wall})} - \widehat{K}_{J_{Ic}(\text{at } 550°\text{F})} = \\ &= 1.35\left\{1033 \cdot \exp\left[\begin{array}{c} 0.000415\left(\frac{T_{wall} + 459.69}{1.8}\right) \cdot \ln\left(0.0004\right) \\ -0.00698\left(\frac{T_{wall} + 459.69}{1.8}\right) \end{array}\right] - \sigma_{ref}\right\} \quad [\text{ksi}\sqrt{\text{in}}]\end{aligned} \tag{35}$$

where σ_{ref} is

$$\sigma_{ref} = 1033 \cdot \exp\left[\begin{array}{c} 0.000415\left(\frac{550 + 459.69}{1.8}\right) \cdot \ln\left(0.0004\right) \\ -0.00698\left(\frac{550 + 459.69}{1.8}\right) \end{array}\right] = 3.331798 \tag{36}$$

and T_{wall} is the wall temperature at the crack tip in °F. Therefore

$$\widehat{K}_{J_{Ic}(\text{at } T_{wall})} = \widehat{K}_{J_{Ic}(\text{at } 550°\text{F})} + \widehat{\Delta K}_{J_{Ic}} \qquad [\text{ksi}\sqrt{\text{in}}] \tag{37}$$

The required sampled value of J_{Ic} follows from the plane strain conversion

$$\widehat{J}_{Ic(\text{at } T_{wall})} = \left(\frac{1-\nu^2}{E}\right)\widehat{K}^2_{J_{Ic}(\text{at } T_{wall})} \quad [\text{in-kips/in}^2] \tag{38}$$

4.3.11.2.3 Model for Normalized Average Tearing Resistance, T_{mat} , and J_R Curve Power-Law Exponent, m

In the analysis of ductile-tearing data in [99], the exponent, m, of the J_R power-law curve (see Eq. (16)) has been correlated with the material's estimated value for the average tearing modulus, T_{mat}, which is the normalized linear slope of all the J-Δa data between the 0.15 and 1.5 mm exclusion lines in the ASTM E-1820 determination of J_{Ic}.

The sampling protocol for estimating a value for T_{mat} is the following:

Step 1. Determine a value of $\widehat{USE}_{(u)}$ using the sampling protocol outlined in Sect. 4.3.11.2.1 and Eqs. (31) and (32).
Step 2. Apply this sampled value of $\widehat{USE}_{(u)}$ along with sampled values of $\widehat{Cu}$, $\widehat{Ni}$, $\widehat{P}$ and $\widehat{\phi t}$ to estimate a value of $\widehat{USE}_{(i)}$ using Eq. (33).
Step 3. Convert this estimate of $\widehat{USE}_{(i)}$ value to a value of $\widehat{T}_{mat(i)(\text{at } 550°\text{F})}$ at 550 °F using the mean curve established in [99], where the uncertainty in $\widehat{T}_{mat(i)(\text{at } 550°\text{F})}$ is ***not*** sampled

$$\widehat{T}_{mat(i)(\text{at } 550°\text{F})} = 3.9389 + \left(0.5721 \times \widehat{USE}_{(i)}\right) \tag{39}$$

Step 4. Convert the $\widehat{T}_{mat(i)(\text{at } 550°\text{F})}$ value to a $\widehat{T}_{mat(i)(\text{at } T_{wall})}$ value at the wall temperature of interest using the mean curve from [99]:

$$\begin{aligned}\widehat{\Delta T}_{mat} &= T_{mat(i)(\text{at } T_{wall})} - \widehat{T}_{mat(i)(\text{at } 550°\text{F})} = \\ &= 1.38\left\{1033 \cdot \exp\left[\begin{array}{c} 0.000415\left(\dfrac{T_{wall}+459.69}{1.8}\right)\cdot \ln\left(0.0004\right) \\ -0.00698\left(\dfrac{T_{wall}+459.69}{1.8}\right)\end{array}\right] - \sigma_{ref}\right\} \quad [-]\end{aligned} \tag{40}$$

where σ_{ref} is

$$\sigma_{ref} = 1033 \cdot \exp\left[\begin{array}{c} 0.000415\left(\dfrac{550+459.69}{1.8}\right)\cdot \ln\left(0.0004\right) \\ -0.00698\left(\dfrac{550+459.69}{1.8}\right)\end{array}\right] = 3.331798 \tag{41}$$

and T_{wall} is the wall temperature at the crack tip in °F. Therefore

$$\widehat{T}_{mat(i)(\text{at } T_{wall})} = \widehat{T}_{mat(i)(\text{at } 550°\text{F})} + \widehat{\Delta T}_{mat} \quad [-] \tag{42}$$

Step 5. Calculate an estimated value of the J_R power-law exponent, m, using the correlation developed in [99], where the uncertainty in $\widehat{m}$ is not sampled.

$$\widehat{m} = 0.3214 + \left(0.0019 \times \widehat{T}_{mat(i)}\right) \tag{43}$$

Step 6. Calculate a value for the J_R power-law coefficient, C, from the definition of J_{Ic} in ASTM E-1820

$$\widehat{C} = \frac{\widehat{J}_{Ic(i)(\text{at } T_{wall})}}{\left(\frac{\widehat{J}_{Ic(i)(\text{at } T_{wall})}}{2\widehat{\sigma}_f} + \Delta a_0\right)^{\widehat{m}}} \tag{44}$$

where $\Delta a_0 = 0.2$ mm (0.008 in) and $\widehat{\sigma_f}$ is the sampled flow stress.

4.3.12 Initiation-Growth-Arrest (*IGA*) Submodel

As shown in Fig. 16, after the value of *CPI* has been calculated for the current flaw and transient, the conditional probability of vessel failure, *CPF*, by through-wall cracking is determined by the flaw Initiation-Growth-Arrest (*IGA*) submodel. The *IGA* submodel may be viewed as a small Monte Carlo model nested within the larger PFM Monte Carlo model. The following steps in the *IGA* submodel are shown in Fig. 17a:

Step G1. The *IGA* submodel is entered from the *PFM* model with a given flaw and transient. The *IGA* trial counter, *NTRIAL*, is initialized to zero. The pointer to the vector holding the random number sequence containing the values of P_f [9] is reset to 1. Each transient for this flaw will start with the same random number sequence for internal sampling; however, each flaw has a different vector of random numbers. Go to Step G2.

Step G2. The *NTRIAL* counter is incremented; the time-step counter *NTSTEP* is initialized to zero; and a random number P_f is drawn from a uniform distribution on the open interval (0,1). Go to Step G3.

Step G3. The time-step counter is incremented up to the time step corresponding to when CPI occurred; time advances to the next time step. Go to Step G4.

Step G4. For the given flaw, subjected to the current transient, the change in *cpi* with respect to time is checked. If $\mathrm{d}cpi/dt > 0$, then the flaw becomes a candidate for propagation through the wall. (This submodel will be described in detail in the following.) If $\mathrm{d}cpi/\mathrm{d}t \le 0$, then control branches to Step G8.

[9] The value of P_f represents the percentile used in sampling $\widehat{\Delta RT}_{ARREST}$ (see Step 11 in Sect. 5.5) and $\widehat{K_{Ia}}$ (see Step 15 in Sect. 5.5) in Step P6 and in sampling $\widehat{K_{Ic}}$ in Step P8 of the *IGA Propagation Submodel*, and is used to ensure that the calculated initiation and failure probabilities are not affected by the order in which transients are analyzed. The *IGA Propagation Submodel* is an embedded Monte Carlo model that is repeated a user-set number of times using a different value of P_f each time. See the discussion in the final paragraph of Sect. 4.3.1.

Step G5. The *IGA Propagation* submodel is entered for this flaw, providing the submodel with the current time step, flaw depth, and value of P_f. Go to Step G6.

Step G6. Control returns from the *IGA Propagation* submodel with the fate of the flaw, either a vessel failure or a stable arrest (no failure). If a vessel failure occurred, control is transferred to Step G7. If a stable arrest occurred, control is transferred to Step G8.

Step G7. The vessel failure counter, *NFAIL*(*NTSTEP*), for this time step is incremented. Go to Step G8.

Step G8. If the transient has completed, i.e., $NTSTEP > NTSTEP_{CPI}$, branch to Step G9. If the transient is not finished, cycle to Step G3. Note that $NTSTEP_{CPI} = NTSTEP$ at which $cpi(t) = \|cpi(t)\|_{\infty} = CPI$.

Step G9. A check is made to see if the required number of trials has been completed. If there are more *NTRIALS* to be run, control is transferred to Step G2. If the *IGA* submodel has completed its sample trials for the current transient, then control is transferred to Step G10.

Step G10. The $CPF_{(i,j,k)}$ for the *i*th transient, and *j*th RPV trial, and *k*th flaw is calculated by the following:

$$CPF_{(i,j,k)} = \sum_{m=1}^{NTSTEP_{CPI}} \Delta cpi(t^m)_{(i,j,k)} P(F \mid I)^m$$
$$P(F \mid I)^m = \frac{NFAIL(m)}{NTRIALS} \tag{45}$$

where $NTSTEP_{CPI}$ is the time step at which the value of $CPI_{(i,j,k)}$ was calculated for this *i*th transient, *j*th RPV trial, and *k*th flaw.

Steps G2 through G9 are repeated *NTRIAL* cycles through the *IGA* submodel.

Figure 17b presents the control structure of the *IGA Propagation* submodel. This submodel proceeds in the following manner:

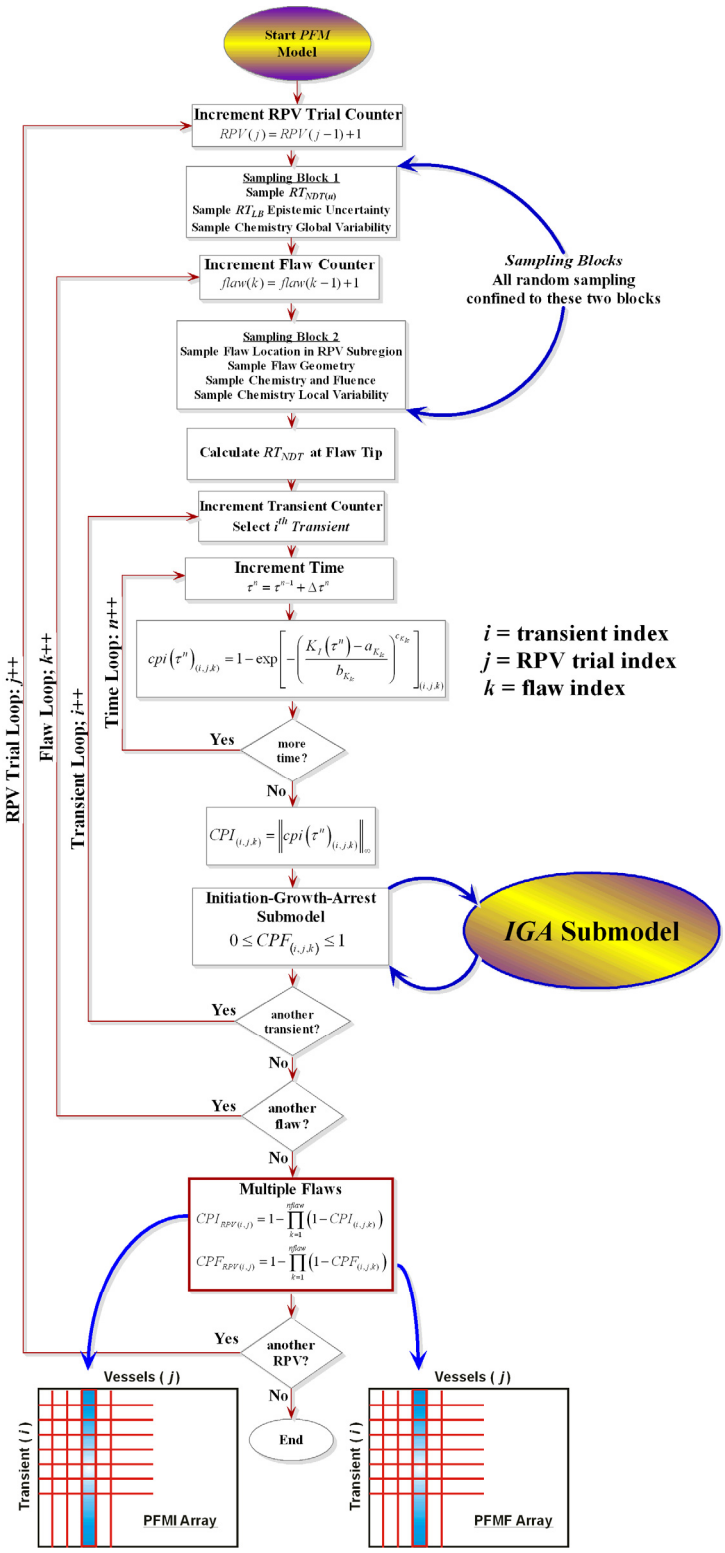

Fig. 16. Flowchart for PFM model – the Initiation-Growth-Arrest (*IGA*) submodel can be viewed as a Monte Carlo model nested within the larger PFM Monte Carlo model. For a given flaw, the *IGA* submodel is called after the *CPI* for the current transient has been calculated. Note: ++ notation indicates increment index by 1; e.g., *i*++ means *i*=*i*+1.

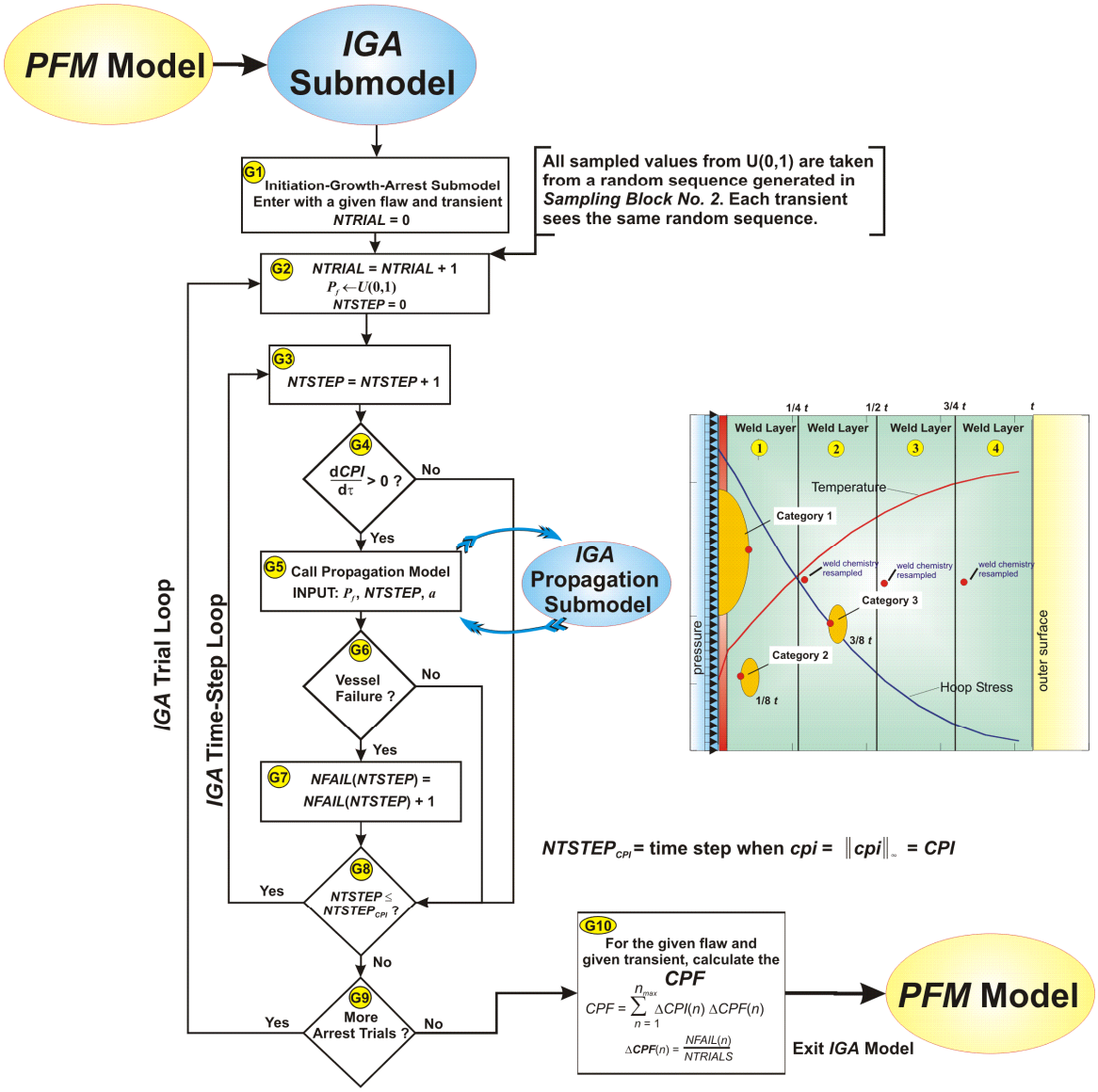

(a)

Fig 17. (a) Flow chart for Initiation-Growth-Arrest Submodel – The *IGA Propagation* submodel is only called for flaws with increasing *CPIs*. The weld-layering scheme is also shown for *Initiation-Growth-Arrest* Model. No through-wall resampling is carried out for plates or forgings.

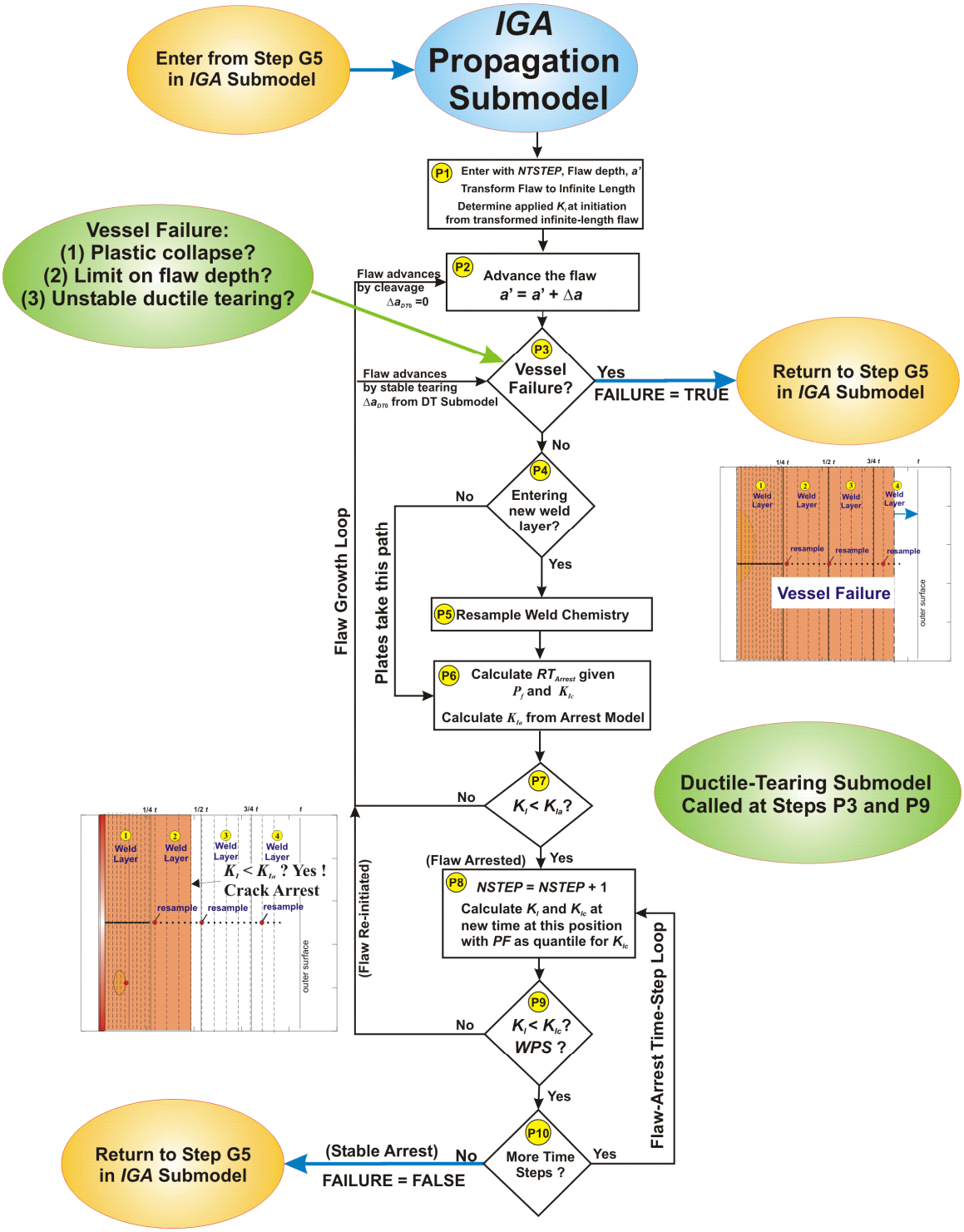

(b)

Fig. 17 (continued) (b) *IGA Propagation* submodel to test for Stable Arrest (no failure) and Vessel Failure.

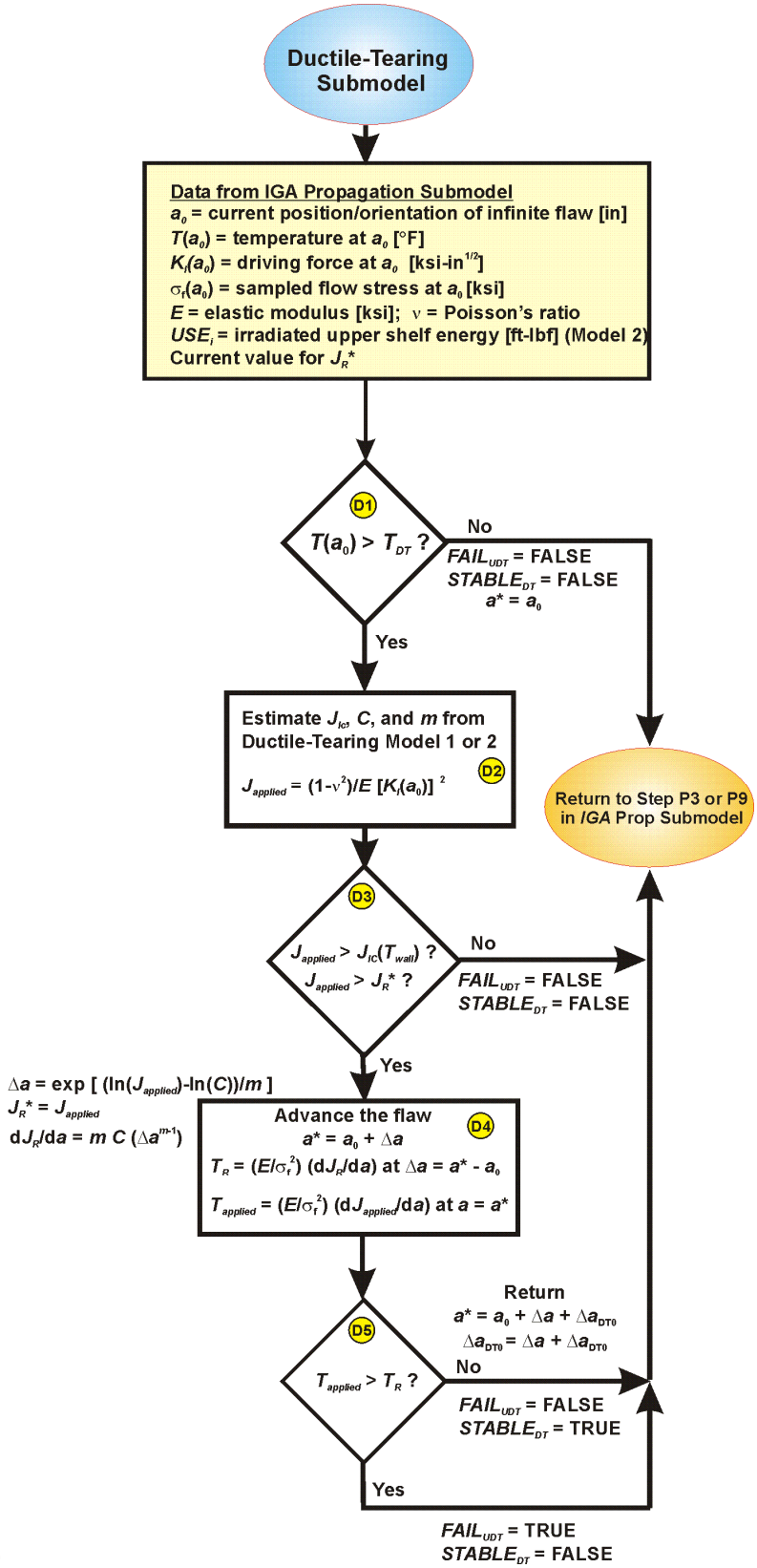

(c)

Fig. 17 (continued) (c) *Unstable-Ductile-Tearing* submodel to test for either stable tearing to a new flaw position, *a, or unstable ductile tearing that fails the vessel.**

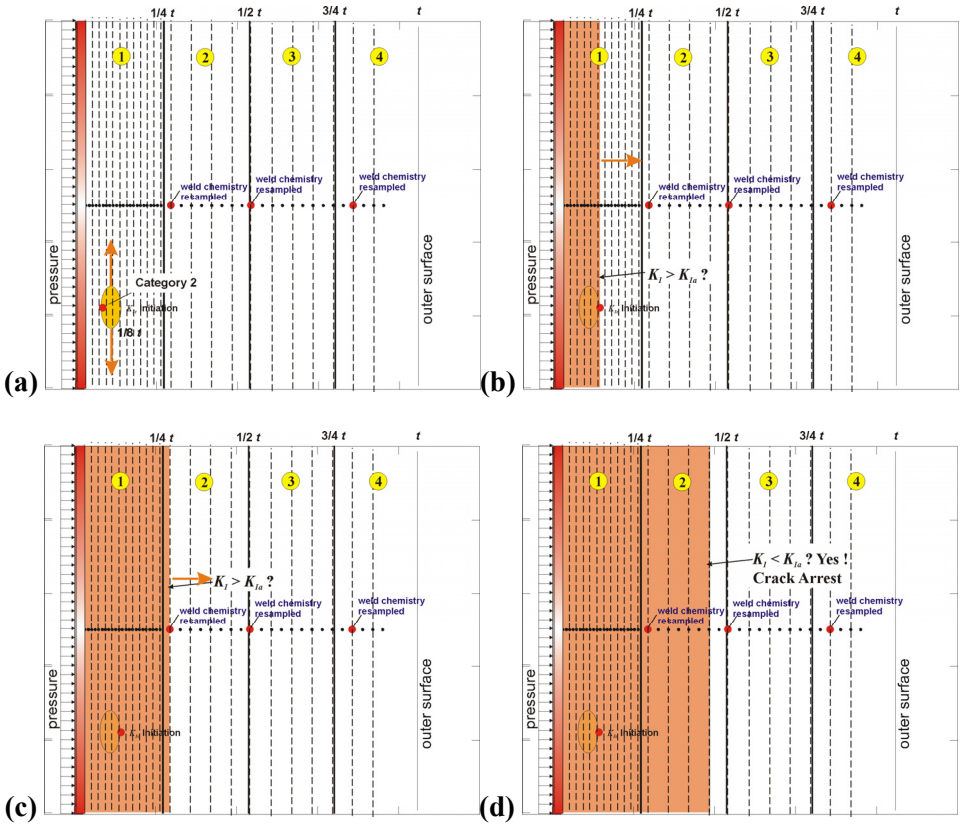

Fig. 18. An example Category 2 flaw (a) initiates, (b) expands into an infinite-length flaw, (c) advances to new weld layer and resamples chemistry content to calculate new RT_{NDT}, (d) continues growth until either failure by net-section plastic collapse of remaining ligament or stable crack arrest. The potential for arrest and subsequent re-initiation is also modeled.

IGA Propagation Submodel

Step P1. Enter the submodel with the initiating time step, *NTSTEP*, and the flaw depth. Set the *IGA Propagation Submodel* time-step counter *NSTEP* = *NTSTEP*. Transform the Category 1, 2, or 3 flaw into its corresponding infinite-length flaw, and calculate the applied stress-intensity factor, K_I, for the transformed flaw at this time and designate it $K_{I\text{-}initiation}$. This value of K_I will be higher than the K_I for the finite-flaw at initiation. Go to Step P2.

Step P2. Advance the infinite-length flaw to its next position in the *IGA* mesh (see Fig. 18). Proceed to Step P3.

Step P3. Check for vessel failure by through-wall cracking. At this new flaw depth and current time, calculate the current sampled estimate for the flow stress of the material. The current sampled value of $\widehat{\Delta T_{30}}$ (to be discussed in Chapter 5) is also used to estimate the effects of irradiation on the unirradiated flow stress, $\sigma_{flow(u)}$. After each resampling of $\widehat{\Delta T_{30}}$, the flow stress will have been adjusted by the following relation:

$$\widehat{\sigma_{flow}} = \sigma_{flow(u)} + \gamma\widehat{\Delta T_{30}} \text{ where } \gamma = \begin{cases} 0.112 \text{ ksi/°F for welds} \\ 0.131 \text{ ksi/°F for plates} \end{cases}$$

This sampled value of $\widehat{\sigma_{flow}}$ is then used in the vessel-failure test against the pressure-induced membrane stress in the remaining ligament, checking for net-section plastic collapse. The membrane stress is equal to

$$\sigma_m(t) = \frac{p_i(\tau)\left(R_i + a\right)}{\beta\left(R_o - R_i - a\right)}; \quad \beta = \begin{cases} 1 & \text{hoop stress} \\ 2 & \text{axial stress} \end{cases}$$

where $p_i(\tau)$ is the time-dependent internal pressure, R_i and R_o are the inner and external vessel radii, respectively, and a is the current flaw depth.

For the initial entry into the *IGA Propagation* submodel, the flaw is growing due to a cleavage initiation; therefore, the ductile-tearing model will not be applied until the flaw has experienced its first arrest event. After the flaw has arrested, the ductile-tearing model is called at this point to check for unstable ductile tearing. This check for unstable tearing is made only if the flaw has re-initiated in ductile tearing. If the flaw has re-initiated as a cleavage event, the ductile-tearing submodel is not called. If the conditions for unstable ductile tearing are encountered, the logical variable FAIL_UDT is set to TRUE in the ductile-tearing submodel and returned to the IGA Propagation Submodel.

The vessel failure criterion is

if REINITIATED_BY_DUCTILE_TEARING is TRUE then

if $\left\{ \begin{array}{c} \sigma_m > \widehat{\sigma_{flow}} \\ \text{or} \\ FAIL\_UDT \text{ is TRUE} \\ \text{or} \\ \left(\dfrac{a}{R_o - R_i}\right) > FAILCR \end{array} \right\}$ then

vessel failure = TRUE during ductile tearing

return to Step G5 in *IGA* Model

elseif $\left\{ \begin{array}{c} \sigma_m > \widehat{\sigma_{flow}} \\ or \\ \left(\dfrac{a}{R_o - R_i}\right) > FAILCR \end{array} \right\}$ then

vessel failure = TRUE during flaw growth by cleavage

return to Step G5 in *IGA* Model

else

vessel failure = FALSE

proceed to Step P4

where $0.25 \le FAILCR \le 0.95$ is a user-supplied failure criterion. A value of 0.95 is suggested.

Step P4. If the material is a plate or forging product form, proceed directly to Step P6. If the material is a weld, check to see if the flaw has advanced into the next quadrant of the weld through-wall thickness. Weld subregions are sectioned into through-wall quadrants to simulate, in an approximate manner, multiple weld layers. There can be more than one weld layer per quadrant. As the flaw advances from one quadrant into the next, the weld chemistry will be resampled with the attenuated fluence. If the flaw has just advanced into a new weld quadrant, go to Step P5. If not, then proceed to Step P6.

Step P5. Resample the weld chemistry $\left(\widehat{Cu}, \widehat{Ni}, \widehat{Mn}, \widehat{P}\right)$ using the sampling distributions given in Chapter 5. Update the irradiation shift, $\widehat{\Delta RT_{NDT}}$, and the irradiated value of the upper shelf energy, $\widehat{USE_{(i)}}$, using the resampled weld chemistry. If the weld-layer-resampling option is turned on and the flaw has just entered layer 2, 3, or 4, then resample for a new value of P_f to replace the value of P_f sampled in Step G2 of the *IGA* submodel. The random iterate P_f is drawn from a uniform distribution on the open interval $U(0,1)$.

Step P6. Using the current chemistry content and current value of P_f, recalculate the arrest reference temperature. Calculate the epistemic uncertainty in the arrest reference temperature by Eqs. (103) and (107) given in Sect. 5.5.

Retrieve the previously sampled unirradiated value of $\widehat{RT}_{NDT(0)}$ for this subregion and the sampled value of the irradiation shift for this flaw, $\widehat{\Delta RT_{NDT}}(r,\ldots)$, determined from the embrittlement model applied for this flaw at its current position in the RPV wall or from weld-chemistry resampling if Step P5 was executed. Calculate the shift in the arrest reference temperature, relative to the initiation reference temperature using Eqs. (139) in Step 11 of Sect. 5.5

$$\widehat{\Delta RT}_{ARREST} \leftarrow \Lambda(\widehat{\mu}_{\ln(\Delta RT_{ARREST})}, \widehat{\sigma}_{\ln(\Delta RT_{ARREST})}) \ \ [°\text{F}]$$

where (see Appendix F for the development of this protocol)

$$\widehat{\mu}_{\ln(\Delta RT_{ARREST})} = \ln\left[\widehat{\Delta RT}_{ARREST(mean)}\right] - \frac{\widehat{\sigma}^2_{\ln(\Delta RT_{ARREST})}}{2}$$

$$\widehat{\Delta RT}_{ARREST(mean)} = 44.122 \exp\left[-0.005971 \times \widehat{T}_0\right] \ \ [°\text{C}]$$

$$\widehat{T}_0 = \left(\widehat{RT}_{NDT_0} - \widehat{\Delta RT}_{epist-arrest} - 32\right)/1.8 \ \ [°\text{C}]$$

$$\widehat{\sigma}_{\ln(\Delta RT_{ARREST})} = \sqrt{\ln\left\{\exp\left[0.38998^2 + 2\ln(\widehat{\Delta RT}_{ARREST(mean)})\right] - \text{var}\left(\widehat{T}_0\right)\right\} - 2\ln\left[\widehat{\Delta RT}_{ARREST(mean)}\right]}$$

$$\text{var}(\widehat{T}_0) = \begin{cases} (12.778)^2 & \text{for } \widehat{T}_0 < -35.7 \ °\text{C} \\ 99.905972 - 1.7748073\widehat{T}_0 & \text{for } -35.7 \ °\text{C} \le \widehat{T}_0 \le 56 \ °\text{C} \\ 0 & \text{for } \widehat{T}_0 > 56 \ °\text{C} \end{cases}$$

Calculate the estimated arrest temperature[10] by Eq. (109) in Step 12 of Sect. 5.5

$$\widehat{RT}_{ARREST}(r,\ldots) = \widehat{RT}_{NDT_0} - \widehat{\Delta RT}_{epist-arrest} + \widehat{\Delta RT}_{ARREST} + \widehat{\Delta RT_{NDT}}(r,\ldots)$$

Calculate the normalized (relative to $\widehat{RT}_{ARREST}$) temperature of the vessel at the current location, *r*, in the RPV wall by Eq. (140) in Step 13 of Sect. 5.5

$$\widehat{\Delta T}_{RELATIVE}(r,\ldots) = T(r,t) - \widehat{RT}_{ARREST}(r,\ldots)$$

If this is the first pass through the submodel for this flaw, calculate (by Eqs. (118) or (119) and (141) in Steps 14 and 15 in Sect. 5.5) the fractile, $\Phi_{K_{I-initiation}}$, associated with this value of $K_{I\text{-}initiation}$ from the arrest model, given the current value of the applied $K_{I\text{-}initiation}$ from the infinite-length flaw in the *IGA* submodel

$$\Phi_{K_{I-initiation}} = \frac{1}{2}\left[\operatorname{erf}\left(\frac{\ln(K_{I-initiation}) - \mu_{\ln(K_{Ia})}(\widehat{\Delta T}_{RELATIVE})}{\sigma_{\ln(K_{Ia})}\sqrt{2}}\right) + 1\right]$$

where

$$\operatorname{erf}(x) = \text{ error function} = \frac{2}{\sqrt{\pi}}\int_0^x \exp(-\xi^2)\,\mathrm{d}\xi;\ \ \operatorname{erf}(-x) = -\operatorname{erf}(x)$$

if K_{Ia}_Model is equal to 1

$$K_{Ia(\text{mean})}(\widehat{\Delta T}_{RELATIVE}) = 27.302 + 69.962\exp\left[0.006057(\widehat{\Delta T}_{RELATIVE})\right] \ \ [\text{ksi}\sqrt{\text{in.}}]$$

$$\sigma_{\ln(K_{Ia})} = 0.18$$

else if K_{Ia}_Model is equal to 2

$$K_{Ia(\text{mean})}(\widehat{\Delta T}_{RELATIVE}) = 27.302 + 70.6998\exp\left[0.008991(\widehat{\Delta T}_{RELATIVE})\right] \ \ [\text{ksi}\sqrt{\text{in.}}]$$

$$\sigma_{\ln(K_{Ia})} = 0.34$$

$$\mu_{\ln(K_{Ia})}(\widehat{\Delta T}_{RELATIVE}) = \ln\left[K_{Ia(\text{mean})}(\widehat{\Delta T}_{RELATIVE})\right] - \frac{\sigma^2_{\ln(K_{Ia})}}{2}$$

In the above relation for $\Phi_{K_{I-initiation}}$, $\mu_{\ln(K_{Ia})}$ is calculated at the location of the initiation of the flaw. For this flaw, the value of $\Phi_{K_{I-initiation}}$ remains fixed in the *IGA Propagation* submodel until P_f is resampled in Step G2 of the *IGA* submodel. Using the current value of P_f, scale by $\Phi_{K_{I-initiation}}$ (if this is the weld layer in which the crack initiation originally occurred) such that (from Eq. (142) in Step 15 of Sect. 5.5)

$$\Phi_{K_{Ia}} = (P_f)(\Phi_{K_{I-initiation}})$$

For subsequent weld layers do not perform the above scaling. When the flaw advances into a new weld layer, any linkage between the flaw's initiation and its continued propagation is assumed to be broken.

[10] The major region variate $\widehat{RT_{NDTo}}$ is not re-sampled in this step.

With this $\Phi_{K_{Ia}}$ fractile, draw a value of K_{Ia} from its lognormal distribution as given by Eq. (143) of Step 15 in Sect. 5.5

$$K_{Ia}(\Phi_{K_{Ia}}, \widehat{\Delta T}_{RELATIVE}) = \exp\left[\sigma_{\ln(K_{Ia})} Z_{\Phi K_{Ia}} + \mu_{\ln(K_{Ia})}(\widehat{\Delta T}_{RELATIVE})\right]$$

$Z_{\Phi_{K_{Ia}}}$ = standard normal deviate corresponding to the $\Phi_{K_{Ia}}$ fractile

In the above relation for K_{Ia}, $\mu_{\ln(K_{Ia})}$ is calculated at the current location of the flaw. The scaling procedure in Step P6 ensures that the initial value of K_{Ia}, calculated immediately after initiation, does not exceed the initiating value of $K_{I\text{-}initiation}$, thus producing an initial extension. Once the value of $Z_{\Phi_{K_{Ia}}}$ has been determined for this *IGA* trial, the arrest toughness during flaw advancement through the wall changes due to changes in $\widehat{\Delta T}_{RELATIVE}$ only. These changes are caused by variations in $T(r,t)$ and RT_{Arrest} (due to the resampling of the weld chemistry when passing into new weld layers).

For Ductile-Tearing Model No. 2, update the current value of the irradiated upper-shelf energy by

$$\widehat{USE}_{(i)} = A + 0.0570 \cdot \widehat{USE}_{(u)}^{1.456} - \left[17.5 \cdot f\left(\widehat{Cu}\right) \cdot \left(1 + 1.17\widehat{Ni}^{0.8894}\right) + 305\widehat{P}\right]\left(\frac{\widehat{f}_0(r)}{10^{19}}\right)^{0.2223} \quad \text{[ft-lbf]}$$

Go to Step P7.

Step P7. Check the current applied K_I for the advancing flaw against the current value of the arrest fracture toughness K_{Ia}.

if $K_I < K_{Ia}$ then
  the flaw has arrested
  proceed to Step P8
else
  the flaw has not arrested
  proceed to Step P2

Step P8. Hold the flaw at this position, and advance the time to check for re-initiation or new ductile tearing.

$$NSTEP = NSTEP + 1$$

For this new time station, bring up the wall temperature, $T(r,\tau)$, at this position along with the current irradiated and attenuated value of RT_{NDT} to calculate

$$\widehat{\Delta T}_{RELATIVE}(r,\ldots) = T(r,\tau) - \widehat{RT}_{RTNDT}(r,\ldots)$$

Now calculate the parameters of the K_{Ic} model

$$a_{K_{Ic}}(\widehat{\Delta T}_{RELATIVE}) = 19.35 + 8.335\exp\left[0.02254(\widehat{\Delta T}_{RELATIVE})\right] \text{ [ksi}\sqrt{\text{in.}}\text{]}$$

$$b_{K_{Ic}}(\widehat{\Delta T}_{RELATIVE}) = 15.61 + 50.132\exp\left[0.008(\widehat{\Delta T}_{RELATIVE})\right] \text{ [ksi}\sqrt{\text{in.}}\text{]}$$

$$c_{K_{Ic}} = 4$$

with K_{Ic} in ksi$\sqrt{\text{in}}$ and $\Delta T = (T\text{-}RT_{NDT})$ in °F.

The static initiation toughness, K_{Ic}, is calculated from its Weibull distribution by

$$K_{Ic}(\widehat{\Delta T}_{RELATIVE}) = \widehat{a_{K_{Ic}}}(\widehat{\Delta T}_{RELATIVE}) + \widehat{b_{K_{Ic}}}(\widehat{\Delta T}_{RELATIVE})\left[-\ln(1-P_f)\right]^{1/c_{K_{Ic}}}$$

$$\text{for } a_{K_{Ic}}(\widehat{\Delta T}_{RELATIVE}) \le K_{Ic} \le K_{Ic(\max)}$$

Proceed to Step P9.

Step P9. If the warm prestressing (WPS) analysis option has been turned on by the user (see Sect. 4.3.4 for details on WPS effects as implemented in FAVOR), check to see if the flaw is in a state of WPS. If the ductile-tearing option is turned on, then call the ductile-tearing model to determine if there is stable or unstable ductile tearing. If the WPS option is on and WPS = TRUE, go to Step P10. If the WPS option is off or WPS = FALSE, check the current applied K_I for re-initiation by the test

if $K_I < K_{Ic}$ and $STABLE\_DT$ and $FAIL\_UDT$ are both FALSE then
  No re-initiation.
  Proceed to Step P10.
else if WPS_OPTION is on and WPS is TRUE then
  No re-initiation
  Proceed to Step P10
else if $FAIL\_UDT$ is TRUE then
  the vessel has failed by unstable ductile tearing
  set vessel failure to TRUE
  return to Step G5 of *IGA* model
else if $STABLE\_DT$ is TRUE and $K_{J_{Ic}}$ is less than K_{Ic} then
  the flaw has re-initiated by a ductile-tearing event
  REINITIATED_BY_DUCTILE_TEARING = TRUE
  the current level of tearing Δa_0 is set by the ductile-tearing model
  Proceed to Step P3
else
  The flaw has re-initiated by a cleavage event.
  REINITIATED_BY_DUCTILE_TEARING = FALSE
  Reset the current level of tearing $\Delta a_0 = 0$
  Proceed to Step P2 and advance the flaw

Step P10. If there are time steps remaining in the transient, proceed to Step P8 and advance the time. If the transient is complete, set vessel failure = FALSE, and return to Step 5 of the *IGA* submodel.

Note that in the *IGA Propagation* submodel, the flaw is assumed to advance instantaneously; i.e., the time station remains fixed during flaw growth, an assumption justified by the rapid crack growth rate associated with cleavage fracture relative to the time-scale of the RPV system transients typically modeled using FAVOR. Time will advance only if the flaw is in a state of arrest. If the flaw remains in arrest until the end of the transient, then the flaw is said to have experienced a *Stable Arrest*.

4.3.13 Ductile-Tearing Submodel

Figure 17c presents a flowchart of the *Ductile-Tearing Submodel*.

Step D1. The program enters the submodel with the current position and orientation of the crack tip and the time within the selected transient. The submodel first checks the current wall temperature at the crack tip with the ductile-tearing transition temperature, T_{DT}. Based on a previous study, the value of T_{DT} is set to $200\ °\text{F}$. If this is not the first entry into the model, a current value of J_R^* will be known, where J_R^* is a measure of the current deformation state due to tearing.

if $T_{wall} < T_{DT}$ then
$FAIL\_UDT = \text{FALSE}$
$STABLE\_DT = \text{FALSE}$
Return to Step P3 or P9 of *IGA* Submodel
else
Proceed to Step D2

Step D2. Given the location and orientation of the flaw tip, the submodel converts the known value of $K_{I\text{-}applied}$ to $J_{applied}$ using a plane-strain conversion. The submodel then proceeds to calculate/sample estimates for the J_R-curve parameters, J_{Ic}, C, and m.

$$J_{applied} = \frac{(1-\nu^2)}{E} K_{I-applied}^2 \quad [\text{in-kips/in}^2]$$

get $\widehat{J_{Ic}}$ from either Ductile-Tearing Model No. 1 or 2

get $\widehat{C}$, and $\widehat{m}$ from either Ductile-Tearing Model No. 1 or 2

Proceed to Step D3

Step D3. The submodel then compares the $J_{applied}$ to the estimated value of J_{Ic} obtained in Step D2 and the known value of J_R^*. If this is the first entry into the model or if a cleavage reinitiation has occurred since the last entry into the model, then $J_R^* = 0$. J_R^* is the value of $J_{applied}$ corresponding to a previous time step at which a stable ductile tear ocurred. For a ductile tear to occur at the current time, it is necessary for $J_{applied}$ to be equal to or greater than the current value of J_R^*.

if $(J_{applied} < J_{Ic})$ or $(J_{applied} \le J_R^*)$ then
  $FAIL\_UDT = \text{FALSE}$
  $STABLE\_DT = \text{FALSE}$
  Return to Step P3 or P9 of *IGA* Submodel
else
  Proceed to Step D4

Step D4. The submodel then advances the position of the flaw, a_0, by the amount of ductile crack extension, Δa, produced by the known value of $J_{applied}$, and the new flaw depth is $a^* = a_0 + \Delta a$. The flaw then is advanced to a depth a^{**}, which is the first nodal position deeper than a^*. It is at this nodal position, $a^{**} = x_n$, that the local material tearing modulus, T_R, and applied tearing modulus, $T_{applied}$, are calculated. The local tearing modulus, T_R, characterizes the tearing resistance of the material.

$$J_R^* = J_{applied}$$

$$\Delta a = \exp\left[\frac{\ln(J_R^*) - \ln(C)}{m}\right], \text{ [in]}$$

$$a^* = a_0 + \Delta a$$

The *IGA Propagation* submodel mesh is searched to find the closest node point, node n, that is deeper into the wall than the current flaw position at a^*. The flaw is then repositioned to this node point such that $a^{**} = x_n$ (see Fig. 19). Based on the new position of the flaw, the local material tearing modulus is calculated at a^{**} and the applied tearing modulus is estimated from a second-order finite-difference ratio.

$$\Delta a^{**} = a^{**} - a_0$$

$$T_R = \left(\frac{E}{\sigma_{flow}^2}\right)\left.\frac{dJ_R^*}{da}\right|_{\Delta a^{**}} = \left(\frac{E}{\sigma_{flow}^2}\right) \times m \times C \times \left(\Delta a^{**}\right)^{m-1}$$

and

$$\frac{dJ_{applied}}{da} \approx \frac{J_{n+1} + (\alpha - 1)J_n - \alpha^2 J_{n-1}}{\alpha(\alpha + 1)\Delta x} \quad , \quad \mathrm{O}\left(\Delta x^2\right)$$

where

$$\Delta x = x_n - x_{n-1}$$

$$\alpha = \frac{x_{n+1} - x_n}{x_n - x_{n-1}}$$

$$T_{applied} = \left(\frac{E}{\sigma_{flow}^2} \right) \left. \frac{dJ_{applied}}{da} \right|_{a=a^{**}}$$

Step D5. A check is now made for unstable ductile tearing. If the applied tearing modulus is greater than T_R, then a state of unstable ductile tearing is declared.

if $T_{applied} > T_R$ then

$FAIL\_UDT$ = TRUE

$STABLE\_DT$ = FALSE

Return to Step P3 or Step P9 in the *IGA Propagation* Submodel

else

$FAIL\_UDT$ = FALSE

$STABLE\_DT$ = TRUE

$\Delta a_0 = \Delta a$

$a_0 = a^*$

Return to Step P3 or Step P9 in the *IGA Propagation* Submodel

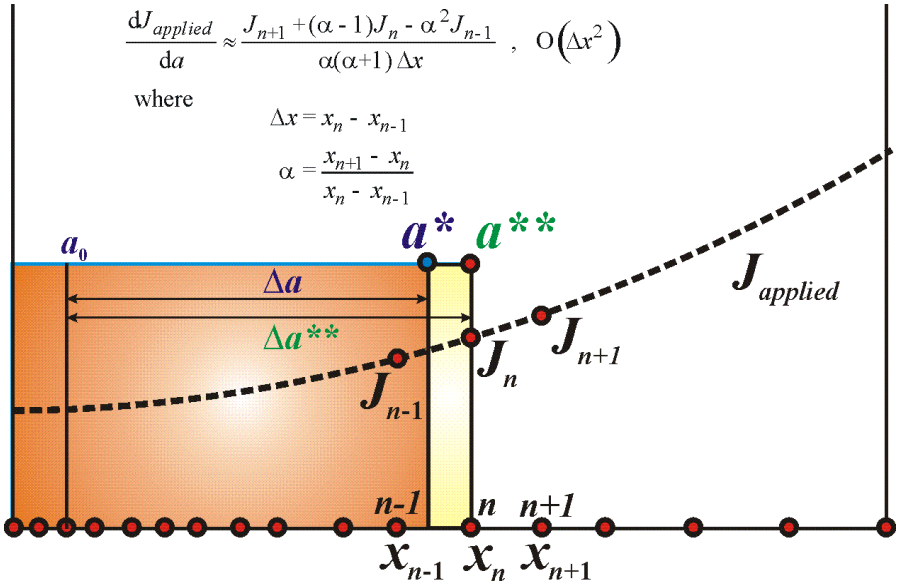

Fig. 19. *IGA Propagation* submodel mesh used to estimate d$J_{applied}$ / da using a second-order central finite-difference ratio.

4.3.14 Ductile Tearing as an Initiating Event

The ductile-tearing model, as implemented, should have no effect on the values of *CPI* produced by FAVOR, and this was verified in a preliminary scoping study. However, a counter was implemented into FAVOR at the point where the conditional probability of initiation, *cpi*, by cleavage is calculated to determine if initiation of flaw growth by ductile tearing was a potential issue. In all of the studies carried out to date using the ductile-tearing models described in Sect. 4.3.11, no predictions of ductile-tearing initiating events were discovered.

4.4 FAVOR Post Module – FAVPost

The distribution of the transient initiating frequencies obtained from PRA studies, the values of conditional probability of fracture (contained in the FAVPFM-generated matrix *PFMI*), and the values of the conditional probability of vessel failure (contained in the FAVPFM-generated matrix *PFMF*) are combined in the FAVPost module to generate discrete distributions of the frequency of vessel initiation, $\Phi(I)$, and frequency of vessel failure, $\Phi(F)$. This process is described by the following *pseudo code*:

For j = 1, N_{SIM} vessel simulations, increment by 1

For i = 1, N_{TRAN} transients, increment by 1

Sample the discrete cumulative distribution function of the transient-initiating frequency for this transient to generate a sample initiating frequency (in events per reactor year).

$\widehat{\phi(E)}_{(i)} \leftarrow CDF_{(i,j)}$ of transient-i initiating frequency

End of Transient Loop

The above loop generates a vector of transient-initiating frequencies for this vessel simulation, $\left\{\widehat{\phi(E)}\right\}_{(1\times N_{TRAN})}$.

For the jth vessel, take the inner product of the transient initiating frequencies vector times the jth column-vectors in the *PFMI* and *PFMF* matrices.

$$\Phi(I)_{(j)} = \sum_{i=1}^{N_{TRAN}} \widehat{\phi(E)}_{(i)} PFMI(i,j)$$

$$\Phi(F)_{(j)} = \sum_{i=1}^{N_{TRAN}} \widehat{\phi(E)}_{(i)} PFMF(i,j)$$

End of Vessel Simulation Loop

The inner product of the row-vector of the sampled transient initiating frequencies and the j^{th} column-vector of *PFMI* produces the frequency of crack initiation for the j^{th} vessel simulation, $\Phi(I)_{(j)}$. Likewise, the inner product of the row-vector of sampled transient initiating frequencies and the j^{th} column-vector of *PFMF* results in the frequency of vessel failure for the j^{th} vessel simulation, $\Phi(F)_{(j)}$. The (i, j) entry in matrix *PFMI* represents the conditional probability of crack initiation of the j^{th} vessel simulation subjected to the i^{th} transient. The units are *crack initiations per event*. Therefore, the frequency of crack initiation, as determined from the inner product of the transient-initiating frequency and the conditional probability of crack initiation, is the number of *crack initiations per reactor year*. Likewise, the frequency of vessel failure, as determined from the inner product of the transient-initiating frequency and the conditional probability of vessel failure is the number of vessel *failures per reactor year*.

At the end of this process, there are discrete distributions of sample size N_{SIM} for the frequency of crack initiation, $\{\Phi(I)\}_{N_{SIM}\times 1}$, and the frequency of vessel failure, $\{\Phi(F)\}_{N_{SIM}\times 1}$. The above process is described in Fig. 20.

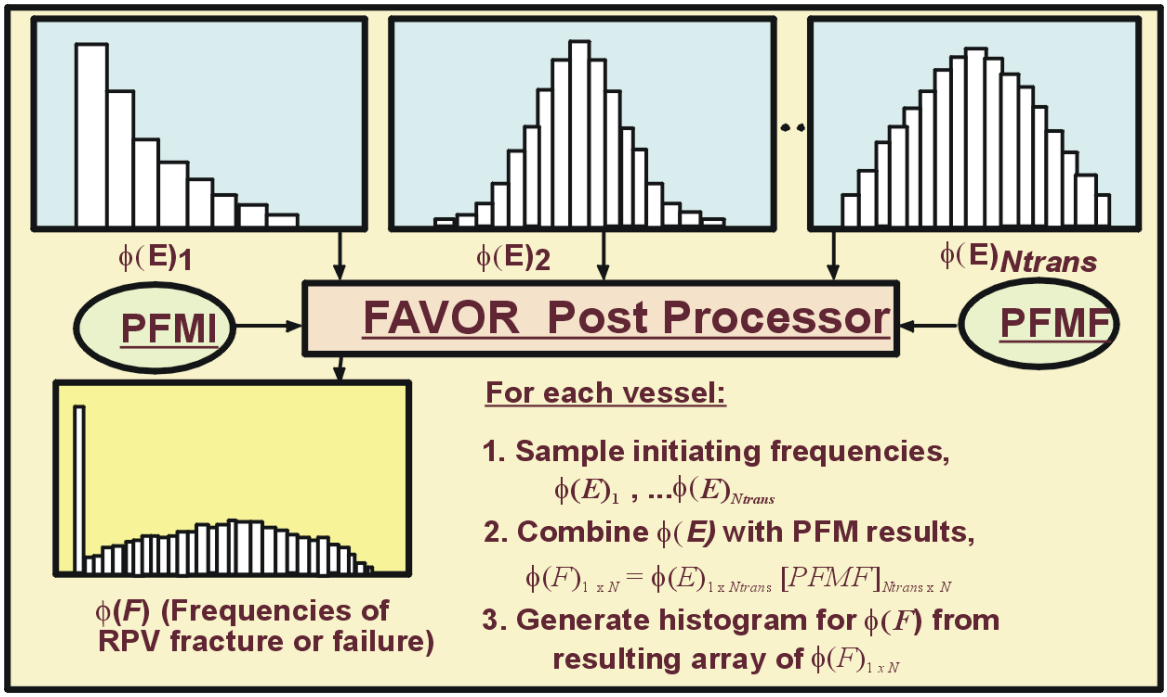

Fig. 20. The FAVOR post-processor FAVPost combines the distributions of conditional probabilities of initiation and failure calculated by FAVPFM with initiating frequency distributions for all of the transients under study to create distributions of frequencies of RPV fracture and failure.

The statistical data in the form of relative densities, cumulative probabilities, and estimated percentiles presented in tabulated histograms and summary tables for the various discrete distributions calculated by FAVOR are estimated through the construction of empirical distribution functions as described in Sects. 4.4.1 and 4.4.2.

4.4.1 Construction of Empirical Distribution Functions Using Order Statistics in FAVPost

Following the discussion in ref. [102], consider the observations $(x_1,\ldots,x_n)$ from an unknown population *assumed to have a probability density* $f(x)$. These sampled observations can be ordered by rank such that

$$\begin{aligned} x_{(1)} &= \text{ smallest of } (\mathrm{x}_1,\ldots,x_n), \\ x_{(2)} &= \text{ second smallest of } (\mathrm{x}_1,\ldots,x_n), \\ &\vdots \\ x_{(k)} &= \text{ k-th smallest of } (\mathrm{x}_1,\ldots,x_n), \\ &\vdots \\ x_{(n)} &= \text{ largest of } (\mathrm{x}_1,\ldots,x_n). \end{aligned}$$

where the quantities $x_{(1)}, x_{(2)}, \ldots x_{(n)}$ are random variates and are called the *order statistics* of the sample. The quantity $x_{(1)}$ is the *smallest* element in the sample, $x_{(n)}$ is the *largest*, $x_{(k)}$ is the *kth-order statistic*, and $x_{(m+1)}$ is the *median* of a sample size $n = 2m+1$. Since the probability density, $f(x)$, for the unknown population is assumed *a priori* to exist, the population's *cumulative distribution function,* c.d.f., $F(x)$, can, therefore, be defined by

$$F(x) = \int_{-\infty}^{x} f(x)\,dx \tag{46}$$

The estimator applied in FAVPost for $F(x)$ is the Kaplan-Meier estimate [103] $\hat{F}(x_{(i)}) = i/n$. [11]

Following the recommendations in ref. [104], FAVPost uses the data values (sorted by rank) for *CPI*, *CPF, Frequency of Crack Initiation,* and *Through-Wall Cracking Frequency* to construct mixed empirical-exponential distribution functions from which cumulative probabilities with their corresponding percentiles can be estimated. As discussed in [104], one difficulty with using a purely empirical c.d.f. based on the estimator $\hat{F}(x_{(i)}) = i/n$ is that it is discrete and when interpolated can possibly provide a poor fit to the true underlying distribution in the right or upper tail. Fitting a

[11] Other estimators are also in common use, including the *mean rank* $\hat{F}(x_{(i)}) = i/(n+1)$ and *median rank* $\hat{F}(x_{(i)}) = (i-0.3)/(n+0.4)$ estimators.

shifted exponential distribution to represent the extreme right tail alleviates this problem [104]. The shifted exponential distribution for the right tail also replaces the unrealistic estimate of $\hat{F}\left(x_{(n)}\right) = n/n = 1$. The following procedure is applied in FAVPost.

4.4.2 Construction of Mixed Empirical/Exponential Distribution Functions

(1) Order the data by rank such that $X_1 \le X_2 \le \cdots \le X_n$.

(2) Fit a piecewise linear c.d.f. to the first $n-k$ ordered data points and a shifted exponential to the *k* largest data points. Assuming $F(0) = 0$ and defining $X_0 = 0$, the constructed mixed empirical-exponential c.d.f. is

$$F(t) = \begin{cases} \dfrac{i}{n} + \dfrac{\left(t - X_{(i)}\right)}{n\left(X_{(i+1)} - X_{(i)}\right)} & \text{for } X_{(i)} \le t \le X_{(i+1)}, i = 0,1,\ldots,n-k-1 \\ 1 - \left(\dfrac{k}{n}\right)\exp\left[-\dfrac{\left(t - X_{(n-k)}\right)}{\theta}\right] & \text{for } t > X_{(n-k)} \end{cases}$$

where (47)

$$\theta = \frac{\left[\left(\dfrac{1}{2} - k\right)X_{(n-k)} + \displaystyle\sum_{i=n-k+1}^{n} X_{(i)}\right]}{k}$$

The value of *k* is selected automatically in FAVPost such that only cumulative probabilities greater than 0.999 are estimated by the fitted shifted-exponential distribution. The mean of this mixed distribution is $\left(X_{(1)} + X_{(2)} + \cdots + X_{(n)}\right)/n$ for $1 \le k \le n$, thus recovering the original sample mean. An estimator for the variance is

$$\begin{aligned} \operatorname{var}(X) = \frac{1}{3n}\left[2\sum_{i=1}^{n-k-1} X_{(i)}^2 + \sum_{i=1}^{n-k-1} X_{(i)}X_{(i+1)} + X_{(n-k)}^2\right] + \\ \frac{k}{n}\left[\left(\theta + X_{(n-k)}\right)^2 + \theta^2\right] - \left[\frac{1}{n}\sum_{i=1}^{n} X_{(i)}\right]^2 \end{aligned} \quad (48)$$

Given a specified probability $0 < P_i < 1$, then the corresponding percentile (quantile) is calculated by:

(1) if $P_i > 1 - \dfrac{k}{n}$, then estimate from the fitted exponential right tail

$$X_{P_i} = X_{n-k} - \theta \ln\left[\frac{n(1-P_i)}{k}\right] \quad (49)$$

(2) else if $P_i \le 1 - \frac{k}{n}$, then estimate from a piecewise linear interpolation within the empirical distribution

$$X_{P_i} = \left(P_i - \frac{I}{n} \right) \left(X_{I+1} - X_I \right) + X_I \tag{50}$$

where I satisfies the relation

$$I \le nP_i < I + 1$$

Figure 21 presents the mixed empirical/exponential distributions for the frequency of crack initiation and frequency of through-wall cracking calculated for the example problem presented in the FAVOR, v15.3, User's Guide [2].

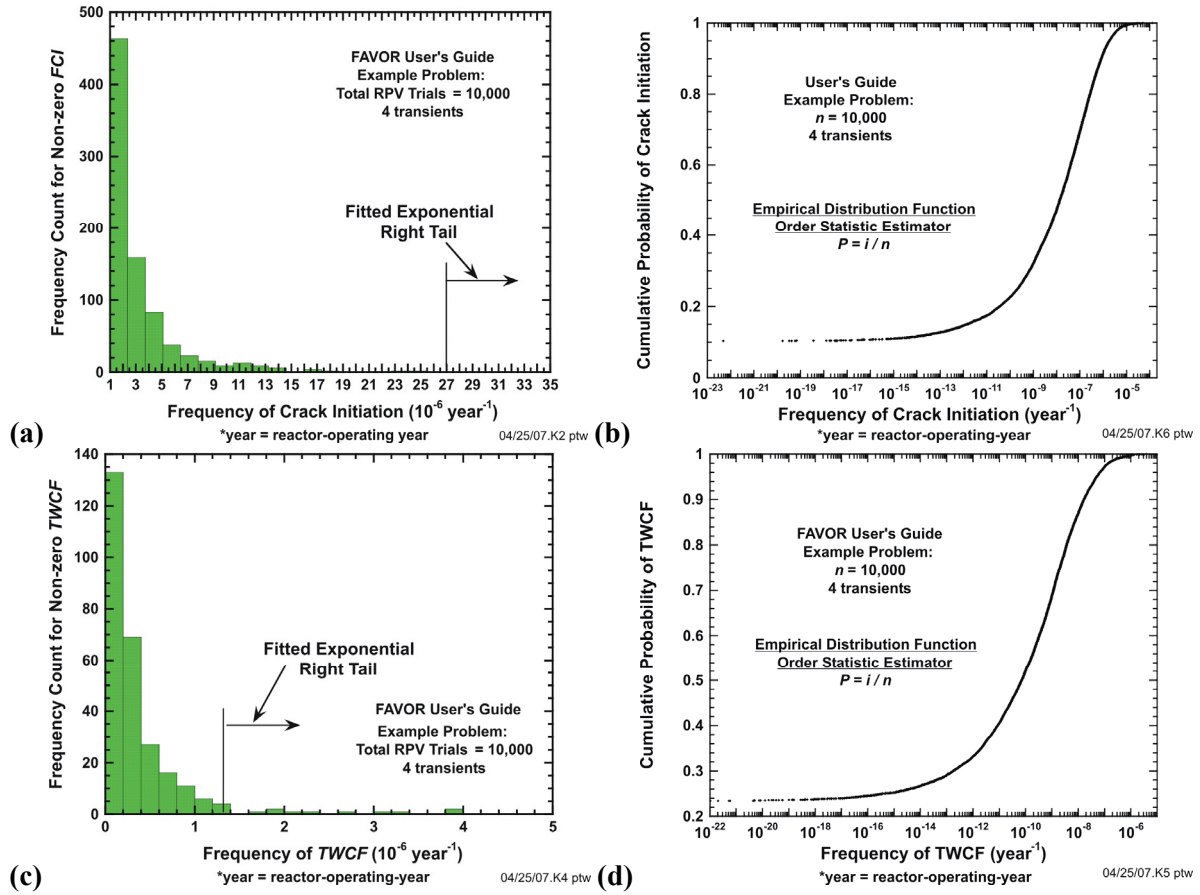

Fig. 21. Empirical distribution functions for *n* = 10,000 example problem: (a) histogram and (b) semi-log plot of empirical c.d.f. for frequency of crack initiation, (c) histogram and (d) semi-log plot empirical c.d.f. for through-wall cracking frequency.

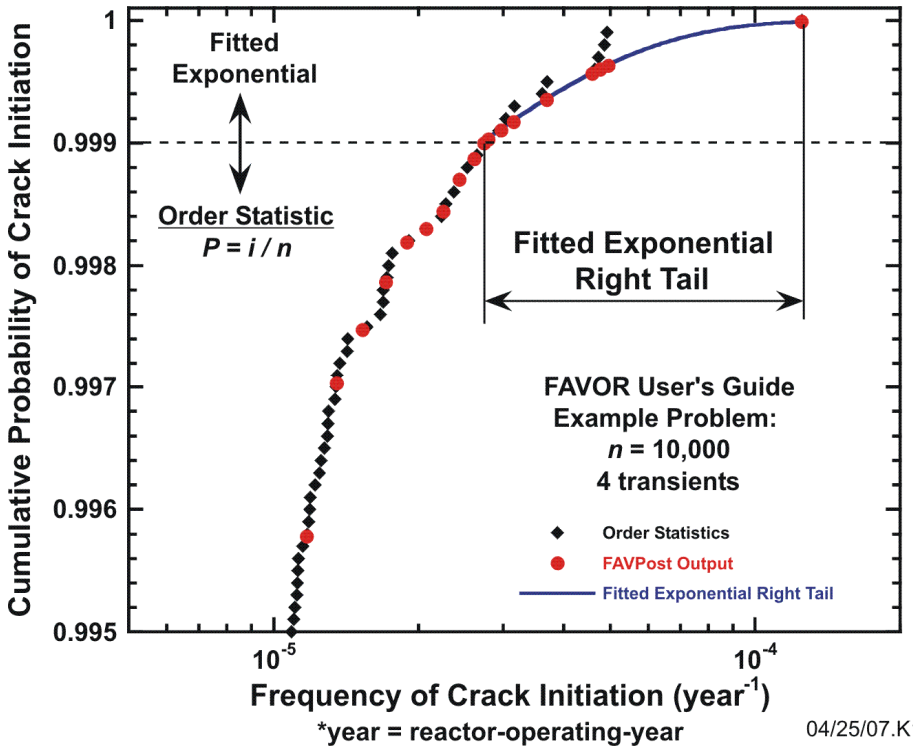

(e)

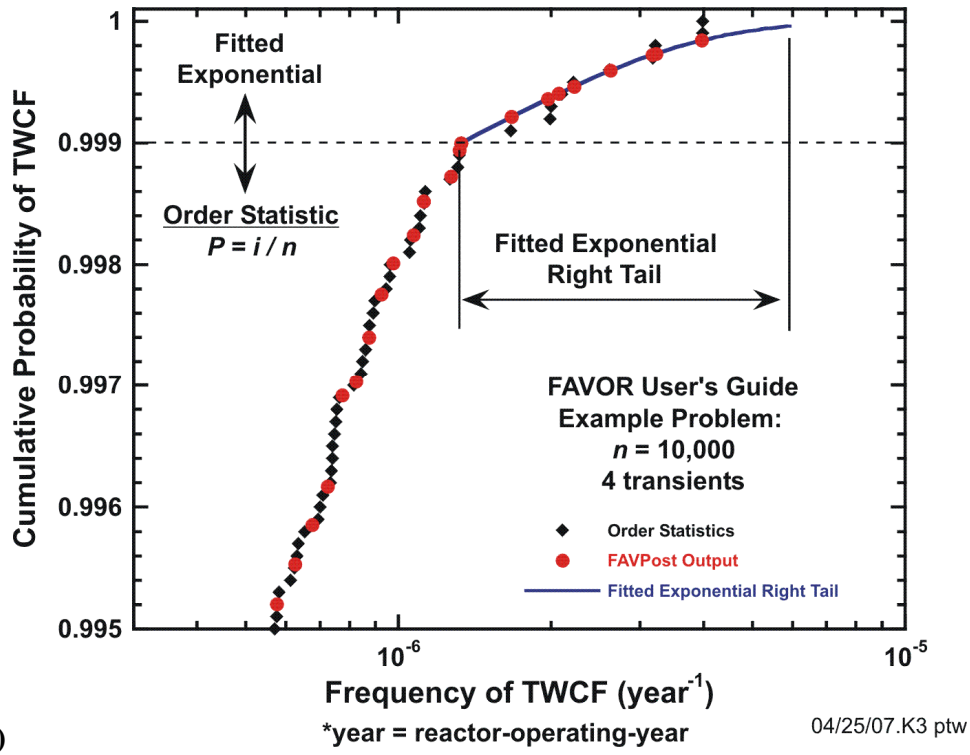

(f)

Fig. 21. (continued) Semi-log plots of empirical distribution functions with fitted exponential right tail for *n* = 10,000 example problem: (e) mixed empirical/exponential c.d.f. for frequency of crack initiation and (f) mixed empirical/exponential c.d.f. for through-wall cracking frequency.

5. Probabilistic Fracture Mechanics

A central feature of modern PRA/PFM analyses is an explicit treatment of model uncertainties with two types being distinguished, *aleatory* and *epistemic* [105]. *Aleatory uncertainties* arise due to the randomness inherent in any physical or human process, whereas *epistemic uncertainties* are caused by a limitation in the current state of knowledge (or understanding) of that process. Epistemic uncertainties can therefore, in principle, be reduced by an increased state of knowledge, whereas aleatory uncertainties are fundamentally irreducible. Playing a central role in the PTS Re-evaluation Project, the identification and classification of epistemic and aleatory uncertainties are crucial aspects of PRA/PFM analyses, because the mathematical procedures used to account for them are different. A major effort in the development of improved fracture mechanics models for FAVOR has been the attempt to identify and classify the uncertainties in these models. Sections 5.2 through 5.5 will present the results of this effort. The deterministic analyses carried out to create a *loading definition* for each PTS transient are first discussed in Section 5.1.

It should be noted that during the investigation of new models for the FAVOR code, the basic requirements of the PTS Re-evaluation Project played a key role in the development process. To enable all commercial operators of pressurized water reactors to assess the state of their RPV relative to the new PTS screening criteria without the need to make new material property measurements, the initiation fracture toughness of the RPV needed to be estimated using only currently available RT_{NDT} values. Moreover, to be consistent with the LEFM principals on which the FAVOR code is based, this RT_{NDT} -based model needed to estimate K_{Ic} values. These restrictions suggested that only very limited information, specifically a value of RT_{NDT}, would be available to define the initiation fracture-toughness model appropriate to a given steel in a plant-specific RPV.

5.1 Deterministic Analyses

The FAVLoad module carries out both thermal and stress analyses of a one-dimensional axisymmetric model of the RPV wall. The time-dependent temperature and stress distributions through the wall constitute the thermal and mechanical loading that will be applied to postulated flaws. In addition, Mode I stress-intensity factors are generated for a range of axially and circumferentially oriented infinite-length and finite-length (semi-elliptical) flaw geometries (flaw depths and lengths). The following subsections describe how these deterministic calculations are carried out in the FAVLoad module. The embedded-flaw model to be discussed has been implemented in the FAVPFM module.

5.1.1 Thermal Analysis

The temperature time-history, $T(r,\tau)$, for the vessel is determined by modeling the RPV wall as an axisymmetric one-dimensional structure with the temperature profile being dependent on the radial position, r, and elapsed time, τ, in the transient. In the absence of internal heat generation, the transient heat conduction equation is a second-order parabolic partial differential equation:

$$\rho\, c_p(T)\, \frac{\partial T}{\partial \tau} = \frac{1}{r}\frac{\partial}{\partial r}\left[k(T)\, r \frac{\partial T}{\partial r} \right] \tag{51}$$

where ρ is the mass density, $c_p(T)$ is the temperature-dependent mass-specific heat capacity, and $k(T)$ is the temperature-dependent thermal conductivity. Note that any temperature dependencies in the mass density should be included in the characterization of the mass-specific heat capacity, leaving the mass density as a constant in the problem formulation. Equation (51) can be expressed in the following canonical form

$$\frac{\partial T}{\partial \tau} - \frac{1}{r}\frac{\partial}{\partial r}\left[\lambda(T)\, r \frac{\partial T}{\partial r} \right] = 0 \text{ for } r \in \mathbb{R}^1; \tau \in (0,\infty) \tag{52}$$

where the property grouping $\lambda(T) = k(T) \big/ \rho\, c_p(T)$ is the temperature-dependent thermal diffusivity of the material. For Eq. (52) to be well posed, initial and boundary conditions must be applied.

$$\underline{\text{Initial Condition}}$$
$$T(r,0) = T_{initial} \text{ for } R_i \le r \le R_o \tag{53}$$

$$\underline{\text{Boundary Conditions}}$$
$$q(R_i,\tau) = h(\tau)\left(T_\infty(\tau) - T(R_i,\tau) \right) \text{ at } r = R_i \tag{54}$$
$$q(R_o,\tau) = 0 \text{ at } r = R_o$$

where in Eqs. (53)-(54), q is a prescribed boundary heat flux, $h(\tau)$ is the time-dependent convective film coefficient, $T_\infty(\tau)$ is the time-dependent bulk coolant temperature, and R_i and R_o are the inner and outer radii of the vessel wall, respectively. Input data to the thermal model include the mesh definition, property data, and prescribed time-histories for $h(\tau)$ and $T_\infty(\tau)$.

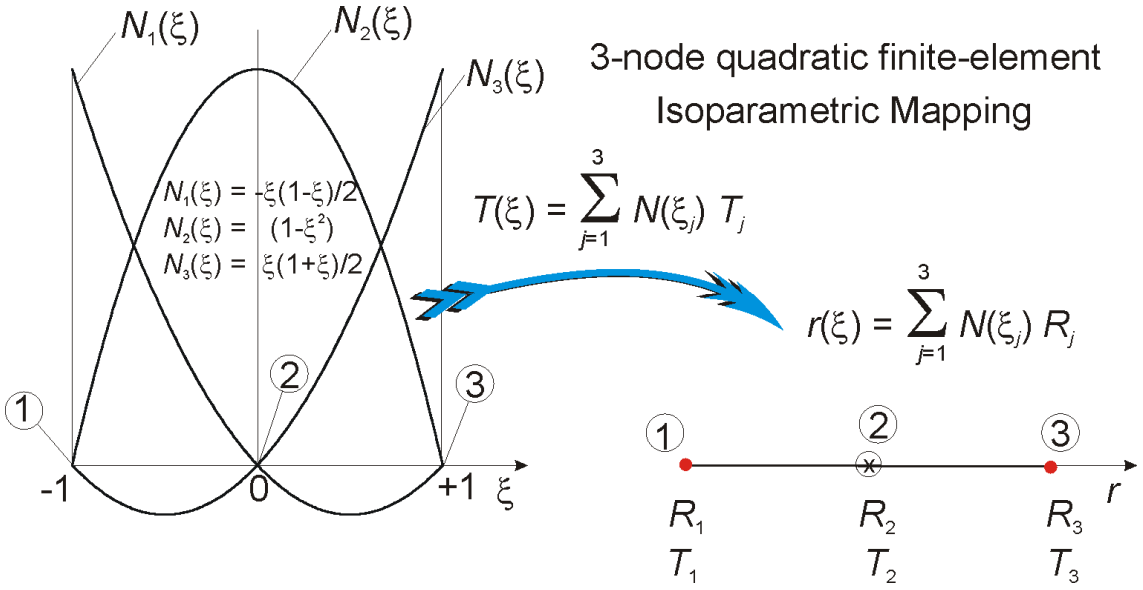

Fig. 22. Isoparametric mapping from parameter space to axisymmetric $\mathbb{R}^1$ Euclidean space using three-node quadratic basis functions.

Eqs. (52)-(54) can be solved using the finite-element method, where the variational formulation for the transient heat conduction equation is given in ref. [106]. The fundamental decisions required to implement the finite-element method are (1) choice of basis functions, (2) choice of mapping, and (3) choice of method for element integration. As shown in Fig. 22, FAVOR uses an isoparametric mapping with 3-node quadratic cardinal basis functions, specifically

$$\{N(\xi)\} = \begin{Bmatrix} N_1(\xi) \\ N_2(\xi) \\ N_3(\xi) \end{Bmatrix} = \frac{1}{2}\begin{Bmatrix} -\xi(1-\xi) \\ 2(1-\xi^2) \\ \xi(1+\xi) \end{Bmatrix}; \quad \left\{\frac{dN}{d\xi}\right\} = \begin{Bmatrix} \frac{dN_1}{d\xi} \\ \frac{dN_2}{d\xi} \\ \frac{dN_3}{d\xi} \end{Bmatrix} = \frac{1}{2}\begin{Bmatrix} (-1+2\xi) \\ -4\xi \\ (1+2\xi) \end{Bmatrix} \tag{55}$$

The elements of the thermal stiffness matrix [106] are calculated using a full-integration fourth-order Gauss-Legendre quadrature rule with the following weights, ω_i, and Gauss sampling points, ξ_i,

$$\int_{-1}^{+1} g(\xi)d\xi \approx \sum_{i=1}^{4} \omega_i g(\xi_i) \quad \text{where} \quad \{\xi_i\} = \begin{Bmatrix} -\sqrt{\frac{3+2\sqrt{6/5}}{7}} \\ -\sqrt{\frac{3-2\sqrt{6/5}}{7}} \\ \sqrt{\frac{3-2\sqrt{6/5}}{7}} \\ \sqrt{\frac{3+2\sqrt{6/5}}{7}} \end{Bmatrix}; \{\omega_i\} = \begin{Bmatrix} \frac{1}{2} - \frac{1}{6\sqrt{6/5}} \\ \frac{1}{2} + \frac{1}{6\sqrt{6/5}} \\ \frac{1}{2} + \frac{1}{6\sqrt{6/5}} \\ \frac{1}{2} - \frac{1}{6\sqrt{6/5}} \end{Bmatrix} \tag{56}$$

In FAVOR, a graded mesh (see Fig. 23) is generated through the wall thickness using ten three-noded quadratic isoparametric axisymmetric elements (21 nodes). Note that the FEM model does not use the same discretization applied in the *IGA* submodel. The first two elements represent the cladding, and the remaining eight elements model the base material. Explicit forward time integration is employed with a fixed time step of 1.0 second. Temperature and hoop-stress profiles are plotted in Fig. 23 for a fixed time in an example transient.

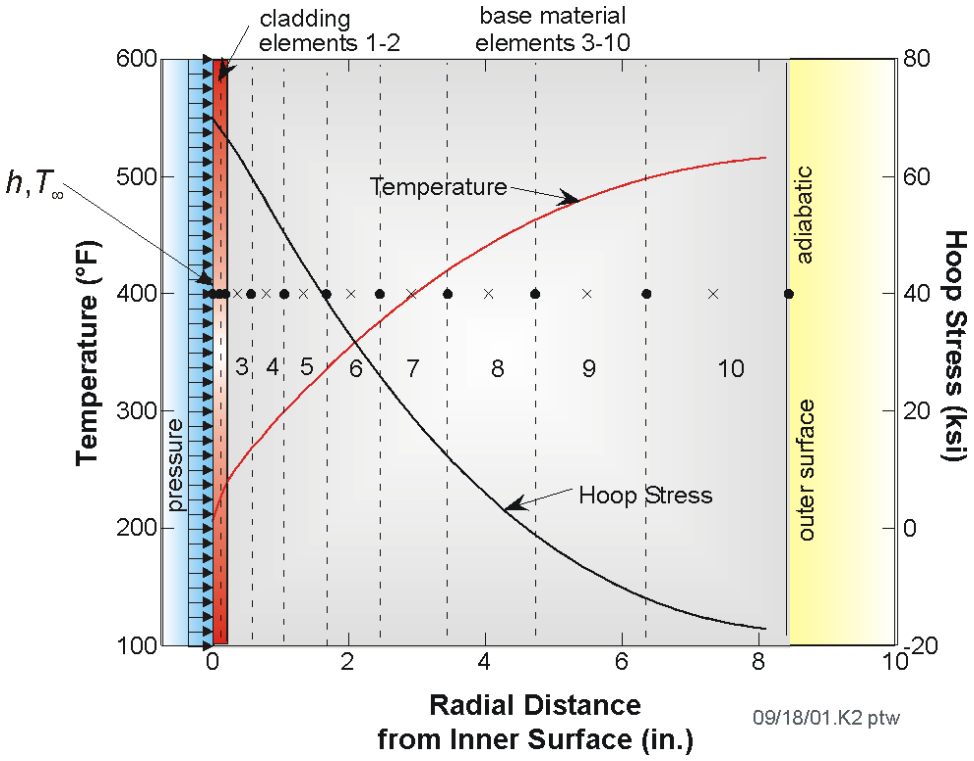

Fig. 23. One-dimensional axisymmetric finite-element model used in FAVOR to calculate both temperature and stress histories through the wall (beltline region) of an RPV.

5.1.2 Stress Analysis

FAVLoad carries out a displacement-based finite-element analysis of the vessel using a one-dimensional axisymmetric model of the vessel wall. The calculated displacements are converted into strains using strain-displacement relationships, and the associated stresses are then calculated using linear-elastic stress-strain relationships. At each time station during the transient, the structure is in a state of static equilibrium; thus the load history is considered *quasi-static.*

Let (u,v,w) be the radial, circumferential, and axial displacements, respectively, of a material point in a cylindrical (r,θ,z) coordinate system. The general two-dimensional axisymmetric case requires that

$$v=0;\tau_{r\theta}=\tau_{\theta z}=0;\gamma_{r\theta}=\gamma_{\theta z}=0 \tag{57}$$

where $\tau_{r\theta},\tau_{\theta z}$ are shear stresses and $\gamma_{r\theta},\gamma_{\theta z}$ are engineering shear strains. The strain-displacement relationships for the two-dimensional case are

$$\begin{Bmatrix}\varepsilon_{rr}\\ \varepsilon_{\theta\theta}\\ \varepsilon_{zz}\\ \gamma_{zr}\end{Bmatrix}=\begin{bmatrix}\frac{\partial}{\partial r} & 0\\ \frac{1}{r} & 0\\ 0 & \frac{\partial}{\partial z}\\ \frac{\partial}{\partial z} & \frac{\partial}{\partial r}\end{bmatrix}\begin{Bmatrix}u\\ w\end{Bmatrix} \tag{58}$$

For the one-dimensional axisymmetric case, (r,θ,z) are principal directions, and $w=0;\partial/\partial z=0;$ such that

$$\varepsilon_{rr}=\frac{\partial u}{\partial r};\quad \varepsilon_{\theta\theta}=\frac{u}{r};\quad \varepsilon_{zz}=\frac{\partial w}{\partial z}=0;\quad \gamma_{zr}=\frac{\partial u}{\partial z}+\frac{\partial w}{\partial r}=0 \tag{59}$$

For the case of a long cylinder with free ends and no axial or circumferential variations in temperature or material properties and with no radial variation in material properties, the radial and circumferential stresses for the one-dimensional axisymmetric case are calculated from the strains by

$$\sigma_{rr}=\frac{E}{(1+\nu)(1-2\nu)}\left[(1-\nu)\varepsilon_{rr}+\nu\varepsilon_{\theta\theta}\right]-\frac{\alpha E}{1-2\nu}(T-T_{ref}) \tag{60}$$

$$\sigma_{\theta\theta}=\frac{E}{(1+\nu)(1-2\nu)}\left[(1-\nu)\varepsilon_{\theta\theta}+\nu\varepsilon_{rr}\right]-\frac{\alpha E}{1-2\nu}(T-T_{ref}) \tag{61}$$

where

σ_{rr} = radial normal stress
$\sigma_{\theta\theta}$ = circumferential (hoop) normal stress
ε_{rr} = radial normal strain
$\varepsilon_{\theta\theta}$ = circumferential (hoop) normal strain
T = wall temperature as a function of r
T_{ref} = thermal stress-free reference temperature
r = radial position in wall
E = Young's modulus of elasticity
ν = Poisson's ratio
α = linear coefficient of thermal expansion

For generalized plane-strain conditions, the stress in the axial direction, σ_{zz}^{PS} , is given by

$$\sigma_{zz}^{PS} = \nu(\sigma_{rr} + \sigma_{\theta\theta}) - \alpha E(T - T_{ref}) \tag{62}$$

To obtain the axial stresses with the ends free (assuming no cap load), it is necessary to remove the net end force associated with the plane-strain condition. This net load is

$$f^{PS} = 2\pi \int_{R_i}^{R_o} \sigma_{zz}^{PS} r dr \tag{63}$$

where R_i and R_o are the inner and outer radii of the cylinder.

In FAVOR, the radial and hoop stresses are calculated using the finite-element method in which Eqs. (60) and (61) apply to each finite element, and thus radial variations in the material properties E, α, and ν can be included by letting the properties vary from one element material group to another. To account for radial variations in properties when calculating the axial stresses, Eq. (62) is applied to each element j such that

$$\sigma_{zz-j}^{PS} = \nu_j(\sigma_{rr-j} + \sigma_{\theta\theta-j}) - \alpha_j E_j(T_j - T_{ref}) \tag{64}$$

is the axial stress in each element under plane-strain conditions. To achieve a free-end condition, the force f_j^{PS} [Eq. (63)] must be released in such a manner that the change in axial strain (displacement) is the same for each element, because it is assumed that initial planes remain in plane under load (GPS condition) . If Δf_j is the reduction in the plane-strain force, f_j^{PS} , on element j, then

$$\frac{\Delta f_1}{A_1 E_1} = \frac{\Delta f_2}{A_2 E_2} = \cdots \frac{\Delta f_{nele}}{A_{nele} E_{nele}} \tag{65}$$

and

$$\sum_{j=1}^{nele} (f_j^{PS} + \Delta f_j) = 0 \tag{66}$$

where

$$f_j^{PS} = A_j\left[\nu_j\left(\sigma_{rr-j} + \sigma_{\theta\theta-j}\right) - \alpha_j E_j (T_j - T_{ref})\right]$$
$$A_j = \pi(r_{o-j}^2 - r_{i-j}^2) \tag{67}$$

where r_o and r_i are the outer and inner radii of element j, respectively. Let f_{p-j} be the axial forces that are the result of adding internal pressure, p. Specifying that the axial displacements for each element be the same gives

$$\frac{f_{p-1}}{A_1 E_1} = \frac{f_{p-2}}{A_2 E_2} = \cdots \frac{f_{p-nele}}{A_{nele} E_{nele}} \tag{68}$$

and

$$\sum_{j=1}^{nele} f_{p-j} = \pi R_o^2 p \tag{69}$$

where

$$f_j = \Delta f_j + f_{p-j}$$

Recalling that the uniform change in axial strain has no effect on either σ_{rr} or $\sigma_{\theta\theta}$, Eqs. (67), (68), and (69) can be solved for f_j after calculating values of σ_{rr-j} and $\sigma_{\theta\theta-j}$; then the axial stress is calculated from

$$\sigma_{zz-j} = \frac{\left(f_j^{PS} + f_j\right)}{A_j} \tag{70}$$

FAVOR uses a reduced-integration two-point Gauss-Legendre quadrature rule for the calculation of σ_{rr} and $\sigma_{\theta\theta}$ in each element. The Gauss sample points and weights for two-point quadrature are:

$$\int_{-1}^{+1} g(\xi)d\xi \approx \sum_{i=1}^{2} \omega_i g(\xi_i) \quad \text{where} \quad \{\xi_i\} = \begin{Bmatrix} -\sqrt{\frac{1}{3}} \\ +\sqrt{\frac{1}{3}} \end{Bmatrix}; \{\omega_i\} = \begin{Bmatrix} 1 \\ 1 \end{Bmatrix} \tag{71}$$

For the calculation of the axial stresses, each of the elements is divided into two sub-elements, each containing one of the two Gauss points, and the axial stresses are calculated at each of the Gauss points. Stresses at the nodes of the finite-element mesh are obtained by interpolation and extrapolation using a cubic spline fit of the stresses at the Gauss points. The stress analysis uses the same mesh and quadratic elements that are applied in the thermal analysis described in the previous section. Details regarding the formation and assembly of the stiffness matrix and load vector for a static stress analysis are given in any text on finite-element methods. See, for example, ref. [107].

When temperature-dependency is included in the thermal stress analysis, FAVLoad requires expansion coefficient data to be input that define the total thermal expansion from a specified reference temperature, T_{ref}. With $\overline{\alpha}_{(T_{ref},T)}$ data from handbook sources, this reference temperature is typically at room temperature, and the thermal strains should then be calculated by

$$\varepsilon^{th} = \overline{\alpha}_{(T_{ref},T)}\left(T - T_{ref}\right) - \overline{\alpha}_{(T_{ref},T_{s-free})}\left(T_{s-free} - T_{ref}\right) \tag{72}$$

where the second term in Eq. (72) represents the total thermal strain due to the difference between the reference temperature, T_{ref}, and RPV stress-free temperature, $T_{s\text{-}free}$. This term is necessary to enforce the assumption that there is no initial thermal strain at the RPV stress-free temperature.

The ability to include temperature-dependent thermo-physical properties in the FAVLoad deterministic analysis was added as a user-option in FAVOR, v04.1. A revision of the application of temperature-dependent thermal expansion coefficients has been implemented and verified in FAVOR, v06.1 Two revisions were required.

(1) Thermal expansion coefficient data available in the ASME BPVC, Sect. II, Part D, include both the *instantaneous* coefficient of linear thermal expansion, α_T, (or *thermal expansivity*) at a specified temperature T and the *mean* coefficient of linear thermal expansion, $\overline{\alpha}_{(T_{ref},T)}$, where the two are related by:

$$\overline{\alpha}_{(T_{ref},T)} = \frac{1}{(T - T_{ref})}\int_{T_{ref}}^{T} \alpha_T \, dT \tag{73}$$

For the implementation in FAVLoad, the correct data input should be the mean coefficient of linear thermal expansion. In verification studies, values for α_T and $\overline{\alpha}_{(T_{ref},T)}$ were obtained from Table TE-1 of the ASME Code, Sect. II, Part D, Material Group D (includes A533B) and High Alloy Steels (includes SS304).

(2) As noted in ref. [108], $\overline{\alpha}_{(T_{ref},T)}$ is based on a specified reference temperature, T_{ref} (typically $T_{ref} = 70\ °\text{F}$). For the thermal strain calculations in FAVLoad, it is assumed that there is no thermal strain at a user-input thermal stress-free temperature, T_{sfree}, where typically, $T_{ref} \neq T_{sfree}$. To insure that the thermal strain is in fact zero at T_{sfree}, a mapping of $\overline{\alpha}_{(T_{ref},T)}$ to $\overline{\alpha}_{(T_{sfree},T)}$ is required.

$$\overline{\alpha}_{(T_{sfree},T)} = \frac{\overline{\alpha}_{(T_{ref},T)}(T - T_{ref}) - \overline{\alpha}_{(T_{ref},T_{sfree})}(T_{sfree} - T_{ref})}{(T - T_{ref})\left[1 + \overline{\alpha}_{(T_{ref},T_{sfree})}(T_{sfree} - T_{ref})\right]} \tag{74}$$

Internally, FAVLoad scales the input thermal expansion coefficient data by the linear mapping of Eq. (74) such that

$$\alpha(T) = \frac{\overline{\alpha}_{(T_{ref},T)}(T - T_{ref}) - \overline{\alpha}_{(T_{ref},T_{sfree})}(T_{sfree} - T_{ref})}{(T - T_{ref})\left[1 + \overline{\alpha}_{(T_{ref},T_{sfree})}(T_{sfree} - T_{ref})\right]} \tag{75}$$

to ensure that the correct total thermal strain is being calculated with respect to $T_{s\text{-}free}$ in Eqs.(60)-(67).

Determination of the Stress-Free Temperature, $T_{s\text{-}free}$

The clad-base stress-free temperature of 468 °F, from which differential thermal expansion (DTE) stresses are calculated, was determined in a 1999 study [109] from a combination of experimental measurements taken from an RPV shell segment made available from a cancelled pressurized-water reactor plant and from finite element stress analyses using temperature-independent thermo-elastic material properties. Temperature-independent thermal elastic material properties were applied in v03.1 and earlier versions of FAVOR; however, to keep FAVOR models consistent with the same slot opening measurements, the clad-base stress-free temperature has been re-calculated using updated temperature dependencies.

The previously-derived stress-free temperature of 468 °F was calculated, using temperature-independent thermo-elastic material properties, based on producing a through-cladding average tensile DTE stress of 21.3 ksi at an assumed room temperature of 70 °F. This tensile DTE stress exactly offsets the 21.3 ksi compressive cladding hoop stress derived from finite element analyses in which the measured displacements taken on a test block from an RPV shell segment were used as boundary conditions. In other words, if the temperature of an unloaded vessel is assumed uniform at 70 °F, a stress-free temperature of 468 °F produces a tensile DTE stress of 21.3 ksi that exactly offsets the compressive stress derived from a combination of finite element analyses and experimental measurements.

The same method described above, except using the temperature-dependent thermo-elastic material proper obtained as input to FAVOR for the PTS Re-Evaluation Study were applied. In this case a stress-free temperature of 488 °F produces the tensile DTE stress of 21.3 ksi. Therefore, the stress-free temperature for the PTS Re-Evaluation Study when using the temperature-dependent properties presented in ref. [2] was 488 °F.

5.1.3 Linear-Elastic Fracture Mechanics (LEFM)

The FAVOR code's linear-elastic stress model treats axial flaws exposed to a one-dimensional axisymmetric stress field and circumferential flaws exposed to a generalized-plane-strain stress field. These flaws are, therefore, assumed to experience only a Mode I loading, where the principal load is applied normal to the crack plane, thus tending to open the crack. It is also assumed that the plastic zone around the crack tip is fully contained, and the overall deformation-load response of the structure is linear. For these high-constraint conditions, the principles of linear-elastic fracture mechanics (LEFM) apply when calculating driving forces for the crack.

5.1.3.1 Mode I Stress-Intensity Factors

For the cracked structure under LEFM conditions, the singular stress field in the vicinity of the crack tip can be characterized by a single parameter. This one-parameter model has the form

$$\begin{aligned} \sigma_{\theta\theta} &= \frac{K_I}{\sqrt{2\pi r}} \quad \text{for axial flaws} \\ \sigma_{zz} &= \frac{K_I}{\sqrt{2\pi r}} \quad \text{for circumferential flaws} \end{aligned} \tag{76}$$

where r is the radial distance from the crack tip, and the crack plane is assumed to be a principal plane. The critical fracture parameter in Eq. (76) is the Mode I stress-intensity factor, K_I. When the conditions for LEFM are met, the problem of calculating the stress-intensity factor can be formulated solely in terms of the flaw geometry and the stress distribution of the uncracked structure.

In a typical BWR [110], the pressure vessel has an inner radius of approximately 126 in. with a 6 in. thick stainless-steel clad wall of low-carbon pressure vessel steel, giving an inner radius (R_i) to wall thickness (t) ratio of approximately 20 ($R_i/t \approx 20$). The majority of BWR pressure vessels in the United States have a R_i/t of 20. By contrast, a typical PWR pressure vessel has an inner radius of from 78 to 118 in. with an 8 to 9 in. thick low-alloy carbon steel clad wall, giving an inner radius to wall thickness ratio of approximately 10, which is appropriate for the most of the PWRs in the United States.

Previous versions of FAVOR have an extensive stress-intensity-factor-influence coefficient (SIFIC) database for inner finite- and infinite-length surface flaws; however, these databases were implemented in the FAVLoad module for $R_i/t \approx 10$ only. The ProSaMM program at ORNL has also developed a similar database for $R_i/t \approx 20$ [111,112], which was implemented in FAVOR, v09.1. This extends the PWR ($R_i/t \approx 10$) database in FAVOR and gives the code the capability to compute fracture parameters for both PWR and BWR geometries.

Complete SIFIC databases were also developed for three flaw geometries often utilized in fracture analyses of BWRs ($R_i/t \approx 20$) and PWRs ($R_i/t \approx 10$) pressure vessels subjected to heat-up transients: (1) finite-length external surface flaws with aspect ratio of 2, 6, and 10; (2) infinite-length axial external surface flaws; and (3) 360º continuous circumferential external surface flaws [112]. Starting with v09.1, FAVOR, has the capability to perform PFM analyses on PWRs and BWRs for heat-up and/or cool-down transients in which the RPVs contain embedded and/or surface breaking (inner surface-breaking/external surface-breaking/or both) flaws.

5.1.3.2 Inner Surface-Breaking Flaw Models –Semi-Elliptical and Infinite Length

For inner surface-breaking flaws, the stress-intensity-factor, K_I, is calculated in FAVOR using a weighting-function approach originally introduced by Bückner [113] and applied by other researchers [114-117], including the developers of OCA-I [118] and OCA-P [119]. The HSST Program at ORNL generated a database of SIFIC(s) for axial infinite-length [120] and axial semi-elliptical [121] surface flaws along with circumferential 360° [120] and circumferential semi-elliptical [122] surface flaws. These databases have been implemented in the FAVLoad module.

Semi-Elliptical Finite Axial, Finite Circumferential, Infinite Axial, and 360° Continuous Circumferential Surface Flaws

As mentioned above, the stress-intensity factor, K_I, is calculated by a linear superposition technique proposed by Bückner [113], where, instead of analyzing the cracked structure using actual loads, the analysis is performed with a distributed pressure loading applied to the crack surfaces only. This pressure is opposite in sign, but equal in magnitude and distribution, to the stresses along the crack line that are calculated for the uncracked structure with the actual loads applied. For an arbitrary stress distribution and for the case of a three-dimensional semi-elliptical surface flaw, the stress distribution can be approximated by a third-order polynomial of the form

$$\sigma(a') = C_0 + C_1(a'/a) + C_2(a'/a)^2 + C_3(a'/a)^3 \tag{77}$$

where $\sigma(a')$ is the stress normal to the crack plane at radial position, a'. The variables a' and a are defined in Fig. 24, and the coefficients (C_0, C_1, C_2, C_3) are calculated by a generalized least squares regression analysis in the FAVLoad module for the stress distribution occurring in the uncracked structure across the crack depth. The K_I values are determined for each of the individual terms (stress distributions) in Eq. (77) and then added to obtain the total K_I value as follows:

$$K_I(a) = \sum_{j=0}^{3} K_{Ij}(a) = \sum_{j=0}^{3} C_j \sqrt{\pi a} K_j^*(a) \tag{78}$$

where

$$K_j^*(a) = \frac{K_{Ij}^{'}(a)}{C_j^{'}\sqrt{\pi a}} \tag{79}$$

Values of $K_{Ij}^{'}(a)/C_j^{'}\sqrt{\pi a}$ were calculated for each of the normalized stress distributions corresponding to each term in Eq. (77) (see Fig. 25), using three-dimensional finite-element analysis results and an arbitrary value of $C_j^{'} = 1$ (with units of stress). The dimensionless quantity $K_j^*(a)$ is referred to as the *stress-intensity-factor influence coefficient* (SIFIC). For semi-elliptic flaws, $K_j^*(a)$ values can be calculated for several points along the crack front, in which case Eq. (78) becomes

$$K_I(\phi) = \sum_{j=0}^{3} C_j \sqrt{\pi a} K_j^*(\phi) \tag{80}$$

where ϕ is the elliptical angle denoting the point on the crack front, and the crack-depth notation (a) has been dropped. Although SIFIC(s) are available in the database for a range of elliptical angles, this release of FAVOR only calculates the value of K_I at the deepest point along the flaw front (i.e., $\varphi = 90°$).

The presence of a thin layer of stainless steel cladding on the inner surface of reactor pressure vessels has a significant effect on the K_I values for inner-surface flaws because of very high thermal stresses and stress gradients generated in the cladding during a thermal transient. When using influence coefficients for three-dimensional flaws, it is necessary to represent the stress distribution in the uncracked cylinder with a third-order polynomial, and thus the discontinuity in the thermal stress at the clad-base material interface presents a problem. To accommodate the stress discontinuity associated with the cladding, influence coefficients were calculated for the cladding stresses alone; the corresponding K_I value can then be superimposed on the K_I value due to the stresses in the base material. This is accomplished by first calculating a K_I value for a continuous-function stress distribution obtained by a linear extrapolation of the stress distribution in the base material to the clad-base interface. Then a K_I value is calculated for the stress distribution in the cladding by subtracting the extrapolated distribution from the assumed-linear distribution in the cladding. The total K_I value is simply the sum of the two. Because the stress distribution in the cladding is essentially linear, only a first-order polynomial curve fit of the in-clad stress profile is needed for the determination of the cladding stress-intensity-factor-influence coefficients.

The influence coefficients implemented in FAVOR were calculated using the ABAQUS [123] finite-element code. Three-dimensional finite-element models were generated for a range of relative crack depths (a / t) and aspect ratios (L / a) (see Fig. 24). The analysis matrix included relative crack depths of $0.01 \le (a/t) \le 0.5$ and aspect ratios of $L/a = 2, 6, 10$ for finite semi-elliptic flaws and

$0.01 \le (a/t) \le 0.95$ for infinite[12] axial and 360° circumferential flaws. In the process of calculating the SIFIC(s) in [121-122], careful attention was paid to produce mesh-independent solutions with an appropriate cylinder length. The number of elements in the circumferential and axial directions and around the crack front was increased, one at a time, until the addition of one element changed the value of K_I by less than one percent. With regard to cylinder length, a minimum incremental length of the cylinder that could be added to the length of the flaw to negate end effects was estimated from Eq. (81) [124]

$$\ell = 2\pi \left[\frac{R_i^2 t^2}{3(1-\nu^2)} \right]^{1/4} \tag{81}$$

where ν is Poisson's ratio, R_i is the inner radius of the vessel, and t is the wall thickness.

The analysis results in ref. [122] demonstrated that there were essentially no differences in SIFIC(s) for finite flaws between the axial and circumferential orientations for relative flaw depths of $0.01 \le a/t < 0.5$ and flaw aspect ratios of $L/a = 2$, 6, and 10. This important finding implies that SIFIC(s) for axial flaws can be used for circumferential flaws up to a relative flaw depth of 0.5 with very little error. The greatest difference (~ 5%) between the two orientations occurs for flaw geometries with an $a/t = 0.5$ and $L/a = 10$. In Appendix B, SIFIC(s) for both axial and circumferential orientations for relative flaw depths of $a/t = 0.01$, 0.0184, 0.05, 0.075, 0.1, 0.2, and 0.3 are presented in Tables B1-B7, respectively. Table B8 presents the SIFIC(s) for an axial flaw with $a/t = 0.5$, and Table B9 presents the SIFIC(s) for a circumferential flaw with $a/t = 0.5$.

SIFIC(s) for both axial and circumferential orientations for relative flaw depths of $a/t = 0.01$, 0.0255, 0.05, 0.075, 0.1, 0.2, and 0.3 in BWRs ($R_i/t = 20$) are presented in Tables B10-B16, respectively. Table B17 presents the SIFIC(s) for an axial flaw with $a/t = 0.5$ in BWRs ($R_i/t = 20$), and Table B18 presents the SIFIC(s) for a circumferential flaw with $a/t = 0.5$ in BWRs ($R_i/t = 20$).

[12] SIFIC(s) for infinite axial and 360° circumferential flaws were determined as part of the development of the v15.3 release of FAVOR.

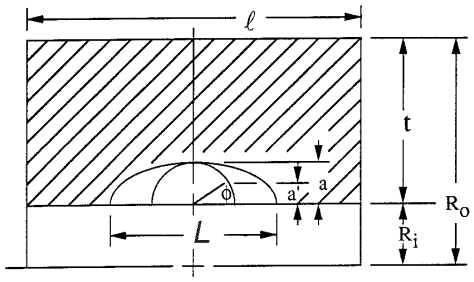

The truncated stress distribution is approximated with a third order polynomial

$$\sigma(a') = C_0 + C_1(a'/a) + C_2(a'/a)^2 + C_3(a'/a)^3$$

K_I values are calculated for each of the individual terms and then added to obtain the total K_I value

$$K_I(a) = \sum_{j=0}^{3} C_j \sqrt{\pi a} K_j^*(a)$$

for 3-D flaws

$$K_I(\phi) = \sum_{j=0}^{3} C_j \sqrt{\pi a} K_j^*(\phi)$$

Fig. 24. Influence coefficients, K^*, have been calculated for finite semi-elliptical flaws with aspect ratios $L / a = 2$, 6, and 10 for $R_i / t = 10$.

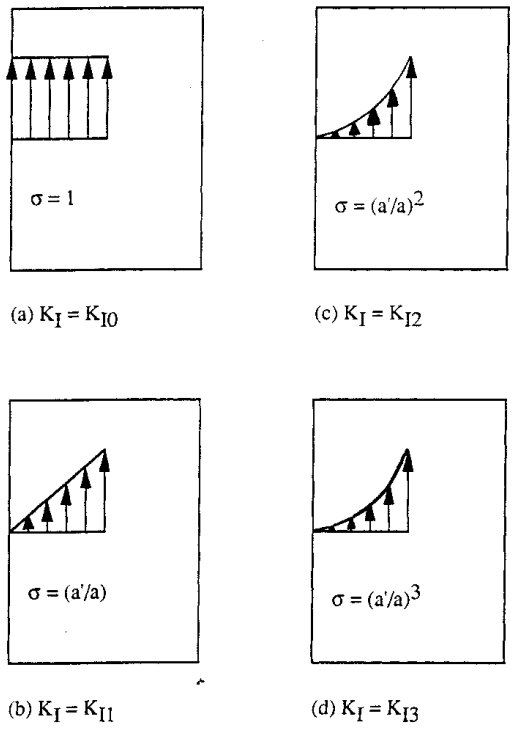

Fig. 25. Crack-surface loading cases for determining finite 3D flaw influence coefficients: (a) uniform unit load, (b) linear load, (c) quadratic load, and (d) cubic load.

Infinite-Length Surface Flaws (Methodology used through FAVOR v12.1)[13]

Figure 26 shows the geometries for the infinite-length axial and 360° continuous circumferential flaws. Figure 27 illustrates the decomposition of a cracked structure under actual loads into an equivalent problem with two components. One component is an uncracked structure under actual loads for which $K_I = 0$, since there is no crack. The second component is a cracked structure having a crack face loading equal in magnitude and opposite in direction to the stress distribution in the uncracked structure at the location of the crack. Therefore, the problem of interest reduces to the calculation of the K_I for the second component. This calculation can be accomplished by computing K^* values for each of several unit loads applied at specified points along the crack face (see Fig. 28) and then weighting them by the truncated crack-free stress distribution associated with the equivalent problem [118]. The procedure can be summarized as follows:

axial flaws

$$K_I(a) = \sum_{i=1}^{n} \sigma_i \Delta a_i K_i^*(a_i', a) \tag{82}$$

circumferential flaws

$$K_I(a) = \sum_{i=1}^{n} 2\pi(R + a_i')\sigma_i \Delta a_i K_i^*(a_i', a) \tag{83}$$

where

$\Delta a_i =$ an increment of a about a_i' such that $\sum_{i=1}^{n} \Delta a_i = a$

$a_i' =$ radial distance from open end of crack to point of application of unit load,

$\sigma_i =$ average crack-free stress over Δa_i for equivalent problem

$K_I =$ opening Mode I stress-intensity factor

$K_I^* =$ stress-intensity factor per unit load applied at a_i' , where load has dimensions of force/length for axial flaws and force for circumferential flaws

$n =$ number of points along length of crack for which K_i^* are available,

$R =$ inside radius of vessel.

The ABAQUS (version 4.9.1) finite-element code was used to calculate the influence coefficients for inner axial infinite-length surface flaws and inner circumferential 360° surface flaws in PWRs (R_i/t = 10) presented in Appendix B19 and B20. The general procedure consisted of developing a finite-element model for each crack depth and then individually applying unit loads at corner nodes located along the crack face. The axial stress-intensity-factor influence coefficients given in Table B19 have been nondimensionalized by multiplying by the factor ($0.1\ t^{1/2}$), where t is the wall thickness, and the

[13] See Sect. 5.1.3.2 for a description of the methodology used in FAVOR, v16.1.

circumferential stress-intensity-factor influence coefficients given in Table B20 have been nondimensionalized by multiplying by the factor ($10\ t^{3/2}$). These normalizing factors account for the fact that the applied load in the generalized plane-strain analyses for axial flaws is 1.0 kip/in. of model thickness, and the applied load in the axisymmetric analyses of the circumferential flaws is a 1.0 kip total "ring" load. For both orientations, the range of relative flaw depths are a/t = {0.01, 0.02, 0.03, 0.05, 0.075, 0.1, 0.2, 0.3, 0.4, 0.5, 0.6, 0.7, 0.8, 0.9, and 0.95}. It should be noted that values in Tables B10 and B11 for $a'/a \geq 0.95$ represent "fitted" or extrapolated values rather than directly computed ones.

The ABAQUS (version 6.8.1) finite-element code was also used to calculate the influence coefficients for inner axial infinite-length surface flaws and inner circumferential 360° surface flaws in BWRs (R_i/t = 20) presented in Appendices B21 and B22.

Finally, it should be pointed out that, as with the finite-surface flaws, great care was exercised in developing finite-element meshes that would produce mesh-independent solutions. Higher-order meshes were employed throughout the modeling. Starter finite-element meshes for each crack depth were examined for convergence by approximately doubling the mesh refinement, i.e., the number of nodes and elements, and performing a representative K^* calculation with the more refined model. This procedure was repeated until the difference in K^* values between successive models was less than one percent, at which time the more refined model was selected for the final computation.

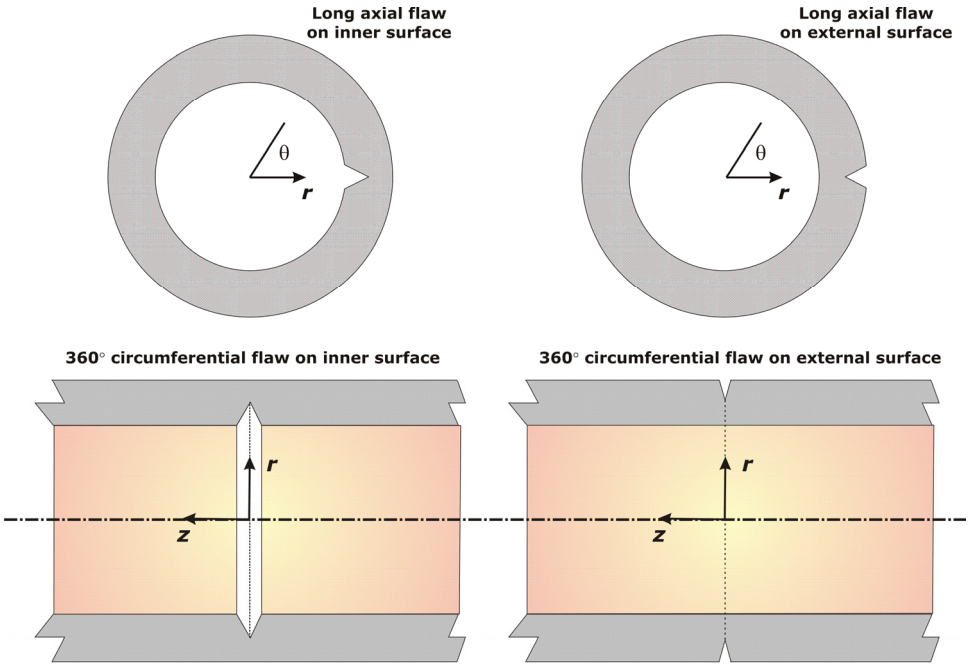

Fig. 26. – Illustration of infinite length internal and external-surface breaking flaws.

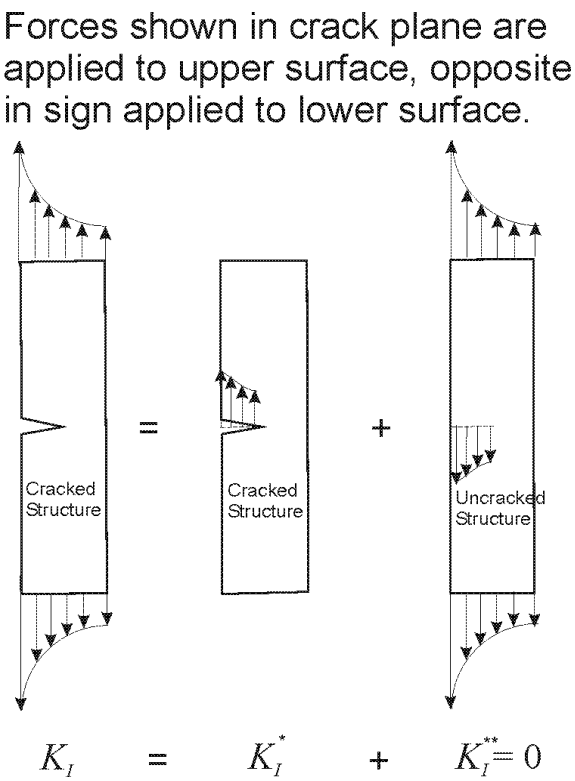

Fig. 27. Superposition allows the use of an equivalent problem to compute the stress intensity factor.

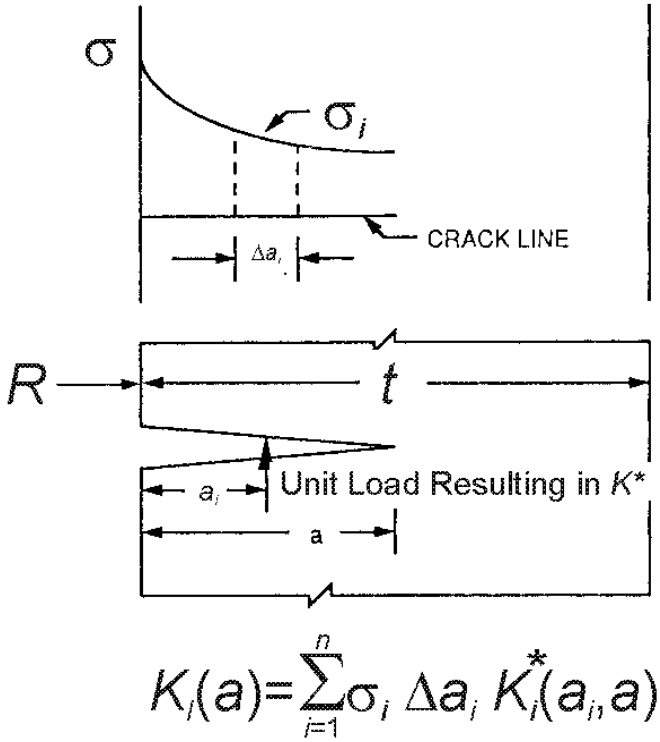

Fig. 28. Influence coefficients, *K, represent stress intensity factor per unit load applied to the crack face.**

5.1.3.3 Infinite-Length Inside Surface Flaws (starting with FAVOR, v15.3,, an internal release candidate)

Starting with the internal release candidate FAVOR, v15.3, the procedure for semi-elliptical internal flaws was also applied to infinite axial and 360° circumferential inside surface flaws. This change from previous FAVOR releases required that a new set of SIFIC(s) be generated for both base and clad materials. During this development, the results of the work carried out by the ASME Work Group for Flaw Evaluation (WGFE) was adopted into the 2015 ASME BPVC, Section XI, Appendix A, Article A-3000, for 360° continuous circumferential flaws (base material only). The proposed (but not yet adopted at the time of the release of FAVOR, v16.1) WGFE curve fits for infinite axial flaws also became available to the developers of FAVOR. Upon review of the WGFE curve fits for both infinite axial and 360° circumferential flaws, the decision was taken to incorporate these closed-form solutions into FAVOR for the four base material SIFIC(s). The required clad SIFIC(s) were calculated independently by the FAVOR developers. See Appendix G for details of these new A-3000 SIFIC solutions.

5.1.3.4 External Surface-Breaking Flaw Models – Semi-Elliptic and Infinite Length

SIFIC(s) were calculated to provide capabilities for the calculation of applied-K_I values using the weight-function technique for external surface breaking flaws for BWR and PWR geometries as required for the analysis of heat-up transients [125,126,154, 155]. A detailed description of the development of SIFIC(s) and superposition techniques to compute Mode I stress-intensity-factors is presented in the previous Section 5.1.3.2 and will not be repeated here.

External Semi-Elliptic Finite Surface Flaws

Tables B23-B27 give SIFIC(s) for axial external-surface semi-elliptical flaws for PWRs having $R/t = 10$. SIFIC(s) for $R/t = 10$ are tabulated for these aspect ratios (2:1, 6:1, and 10:1) for $a/t = 0.1$, 0.2, 0.3, 0.4, and 0.5. For BWRs ($R_i/t = 20$), SIFIC(s) for an axial orientation and for relative flaw depths of $a/t = 0.1$, 0.2, 0.3, 0.4, and 0.5 (with aspect ratios 2:1, 6:1, and 10:1) are presented in Tables B28-B32.

External Infinite-Length Surface Flaws

Table B33 presents SIFIC(s) for external axial infinite flaws for PWRs ($R_i/t = 10$). These SIFIC(s) have been non-dimensionalized by multiplying by the factor ($0.1t^{1/2}$), where t is the wall thickness. Table B34 displays SIFIC(s) for external 360° circumferential surface flaws for PWRs, and these SIFIC(s) have been non-dimensionalized by multiplying by the factor ($10t^{3/2}$). For both orientations, the range of relative flaw depths are a/t = {0.01, 0.02, 0.03, 0.05, 0.075, 0.1, 0.2, 0.3, 0.4, 0.5, 0.6,

0.7, 0.8, 0.9, and 0.95}. The non-dimensional SIFIC(s) make them applicable for all vessels with R_i/t = 10.

Table B35 presents SIFIC(s) for external axial infinite flaws for BWRs (R_i/t = 20). These SIFIC(s) have been non-dimensionalized by multiplying by the factor ($0.1t^{1/2}$), where t is the wall thickness. Table B36 displays SIFIC(s) for external 360° circumferential surface flaws for BWRs, and the SIFIC(s) have been non-dimensionalized by multiplying by the factor ($10t^{3/2}$). For both orientations, the range of relative flaw depths are a/t = {0.01, 0.02, 0.03, 0.05, 0.075, 0.1, 0.2, 0.3, 0.4, 0.5, 0.6, 0.7, 0.8, 0.9, and 0.95}. The non-dimensional SIFIC(s) make them applicable for all vessels with R_i/t = 20.

5.1.3.5 Embedded Flaw Model

The computational methodology implemented in FAVOR for calculating Mode I stress-intensity factors, K_I , for embedded flaws [127] is the EPRI NP-1181 analytical interpretation [128] of the ASME Section XI-Appendix A [129] model for embedded (or "subsurface" in the nomenclature of Ref. [129]) flaws. Previous versions of FAVOR included the capability to model embedded flaws that resided in the inner half of the vessel wall close to the inner (wetted) surface. FAVOR^{HT} modeled embedded flaws in the outer half of the vessel wall. FAVOR, v09.1, consolidated these capabilities such that embedded flaws can be positioned at any through-wall location. Figures 29a and 29b are schematics of the ASME embedded flaw model with the relevant descriptive variables, where Fig. 29a illustrates an embedded flaw located near the inner wetted surface of the vessel wall and Fig. 29b shows an embedded flaw near the external surface in the outer half of the vessel wall.

The procedure for calculating Mode I stress-intensity factors, K_I , is based on the resolution of nonlinear applied stresses through the RPV wall thickness into the linear superposition of approximate membrane and bending stress components. The K_I factor is thus computed from the following relation:

$$K_I = (M_m \sigma_m + M_b \sigma_b)\sqrt{\pi a / Q} \tag{84}$$

where:

$2a$ = the minor axis of the elliptical subsurface flaw
Q = flaw shape parameter
M_m = free-surface correction factor for membrane stresses
M_b = free-surface correction factor for bending stresses
σ_m = membrane stress
σ_b = bending stress

The stress-linearization procedure, depicted in Fig. 30a for a concave upward nonlinear stress profile (produced for example by a cool-down transient) near the vessel wall's inner (wetted) surface, involves the interpolation of the applied stresses at two points on the flaw crack front – point 1 at a distance x_1 from the inner surface and point 2 at a distance x_2 from the inner surface. The stress-linearization procedure illustrated in Fig. 30b is for a tensile stress field (produced for example by a heat-up transient) near the vessel wall's outer surface, and involves the interpolation of the applied stresses at two points on the flaw crack front – point 1 at a distance x_1 from the outer surface and point 2 at a distance x_2 from the outer surface. In each case, a straight line is passed through these two points which represents a linear approximation, $\hat{\sigma}(x)$, of the original nonlinear stress profile, $\sigma(x)$, where x is the distance from the inner surface in Fig. 30a and x is the distance from the outer surface in Fig. 30b.

For both cases, the effective membrane stress, σ_m, is located at $x = t/2$ along this line, and for embedded flaws in the inner half of the vessel wall, the bending stress, σ_b, is the stress at the inner surface ($x = 0$) minus the membrane stress, whereas for embedded flaws in the outer half of the vessel wall, the bending stress, σ_b, is the stress at the outer surface ($x = 0$) minus the membrane stress. The adaptation of the methodology to include calculating the applied-K_I for embedded flaws in the outer half of the RPV wall is accomplished by resolving the nonlinear through-wall stress profile at each time step into a linear superposition of effective membrane and bending stress in a coordinate system that has its origin at the RPV outer surface, as opposed to the RPV inner surface, as is done when calculating the applied K_I solutions for embedded flaws near the RPV inner surface.

For embedded flaws in the inner half of the vessel wall, K_I as evaluated by Eq. (84) is at point 1 (see Figs. 29a and 30a) at the crack tip nearest the vessel inner surface. For embedded flaws in the outer half of the vessel wall, K_I is also evaluated at point 1 (see Figs. 29b and 30b) at the crack tip nearest the vessel outer surface. In each case, this K_I is higher than at the other crack tip, point 2.

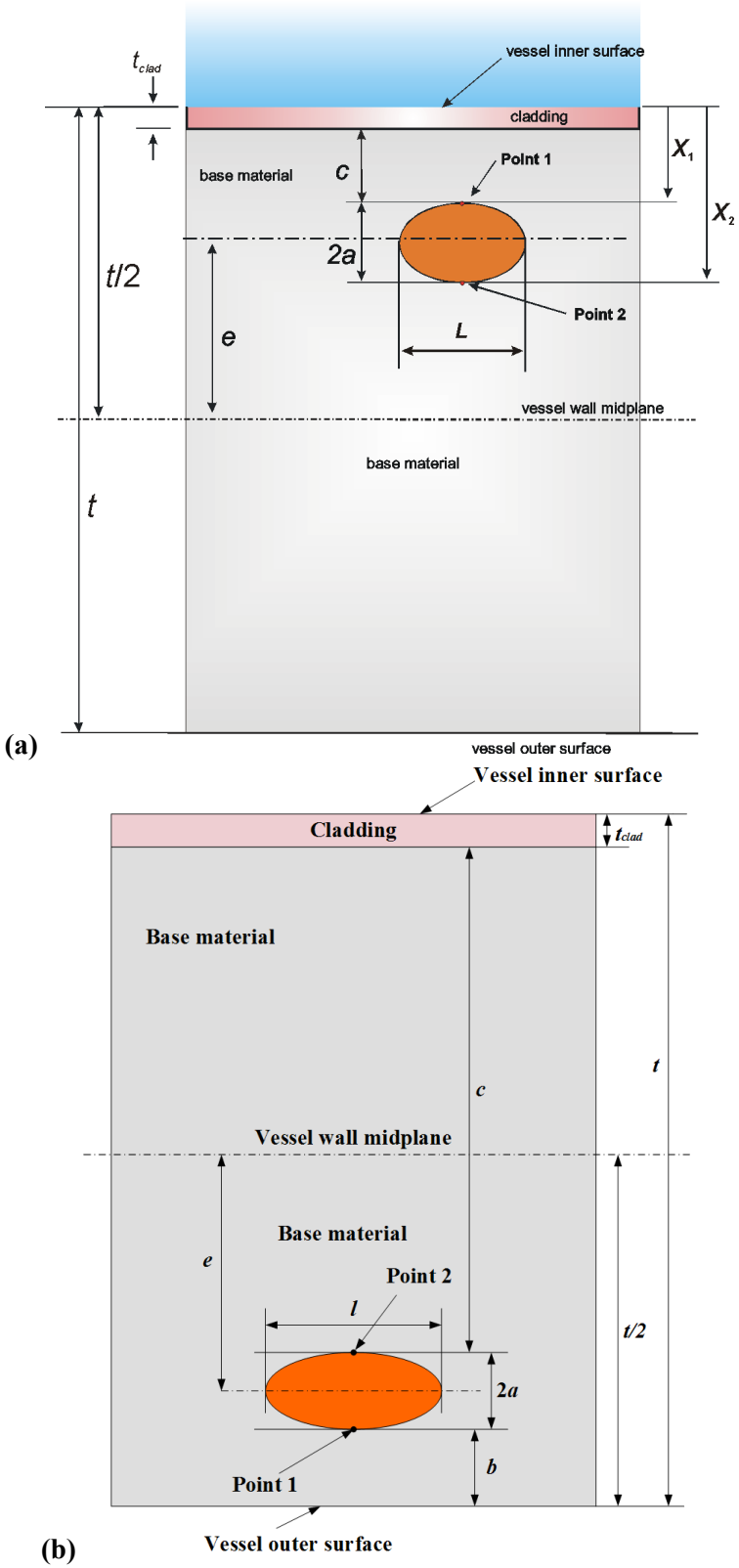

Fig. 29. Geometry and nomenclature used in embedded-flaw model: (a) embedded flaw near inner wetted surface and (b) embedded flaw near outer surface of vessel.

(a)

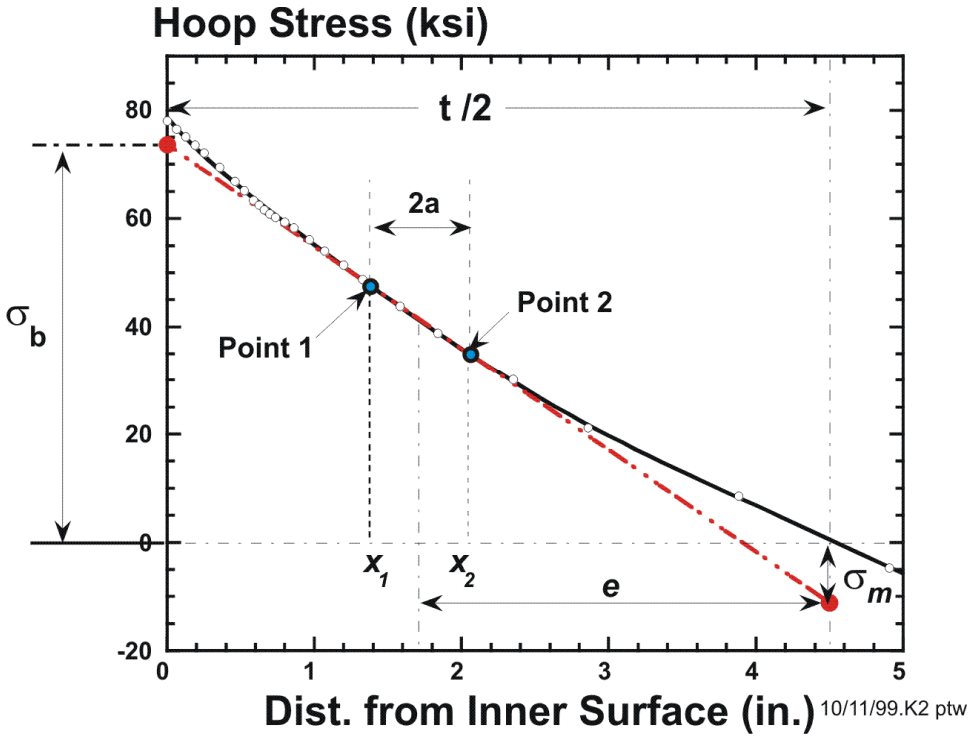
Hoop Stress (ksi)
t /2
2a
Point 1
Point 2
σb
σm
x1
x2
e
80
60
40
20
0
-20
0
1
2
3
4
5
Dist. from Inner Surface (in.)
10/11/99.K2 ptw

(b)

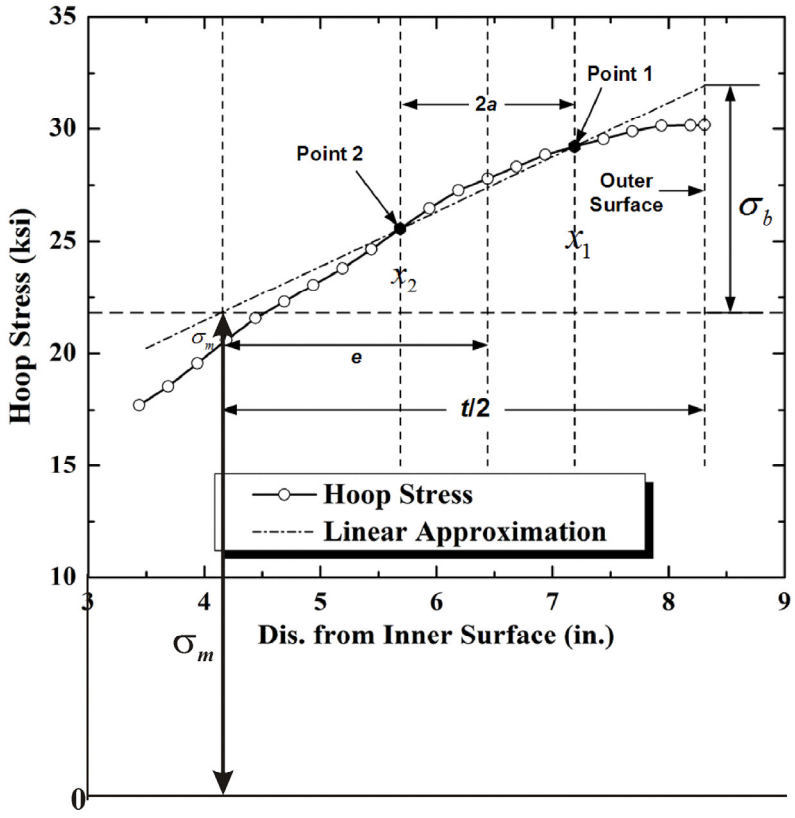
Hoop Stress (ksi)
Point 1
2a
Point 2
Outer Surface
σb
x1
x2
σm
e
t/2
Hoop Stress
Linear Approximation
σm
Dis. from Inner Surface (in.)
35
30
25
20
15
10
0
3
4
5
6
7
8
9

Fig. 30. Decomposition of computed nonlinear stress profile into the linear superposition of effective membrane and bending stresses: (a) embedded flaw near inner surface and (b) embedded flaw near outer surface of vessel wall.

The nonlinear stress profile, $\sigma(x)$, is resolved into the linear superposition of the membrane stress (σ_m) and bending stress (σ_b) (see Figs. 30a and 30b) as follows:

$$\sigma_m = \hat{\sigma}(t/2) = \frac{\left(\sigma(x_2) - \sigma(x_1)\right)}{2a} \times \left(t/2 - x_1\right) + \sigma(x_1) \tag{85}$$

$$\sigma_b = \hat{\sigma}(0) - \sigma_m = \frac{\left(\sigma(x_1) - \sigma(x_2)\right)}{2a} \times \left(t/2\right) \tag{86}$$

The formal definition of the shape parameter Q is based on the complete elliptic integral of the second kind, $E(x)$,

$$\begin{aligned} Q(x) &= E^2(x) \\ E(x) &= \int_0^{\pi/2} \sqrt{\left(1 - x\sin^2(\theta)\right)}\, d\theta \text{ for } 0 \le x \le 1 \\ x &= 1 - 4\left(\frac{a}{L}\right)^2 \end{aligned} \tag{87}$$

In ref. [128], the elliptic integral is replaced by an infinite-series approximation for Q of the form

$$Q \approx \frac{\pi^2}{4(1+m)^2}\left[1 + \frac{m^2}{4} + \frac{m^4}{64} + \frac{m^6}{256} + \left(\frac{5}{128}\right)^2 m^8 + \left(\frac{7}{256}\right)^2 m^{10}\right]^2 \tag{88}$$

where

$$m = \frac{1 - 2(a/L)}{1 + 2(a/L)}$$

Equation (88) has been implemented in FAVOR. The equation for the free-surface correction factor for the membrane stress (M_m) is as follows:

$$M_m = D_1 + D_2(2a/t)^2 + D_3(2a/t)^4 + D_4(2a/t)^6 + D_5(2a/t)^8 + \frac{D_6(2a/t)^{20}}{\left[1 - \left(2e/t\right) - \left(2a/t\right)\right]^{1/2}} \tag{89}$$

where:

$$D_1 = 1$$

$$D_2 = 0.5948$$

$$D_3 = 1.9502\left(e/a\right)^2 + 0.7816\left(e/a\right) + 0.4812$$

$$D_4 = 3.1913(e/a)^4 + 1.6026(e/a)^3 + 1.8806(e/a)^2 + 0.4207(e/a) + 0.3963$$

$$D_5 = 6.8410(e/a)^6 + 3.6902(e/a)^5 + 2.7301(e/a)^4 + 1.4472(e/a)^3 + 1.8104(e/a)^2 + 0.3199(e/a) + 0.3354$$

$$D_6 = 0.303$$

The equation for the free-surface correction factor for bending stresses (M_b) is:

$$M_b = E_1 + \frac{\left[\begin{array}{l} E_2(2e/t) + E_3(2e/t)^2 + E_4(2e/t)(2a/t) + \\ E_5(2a/t)(2e/t)^2 + E_6(2a/t) + \\ E_7(2a/t)^2 + E_8(2e/t)(2a/t)^2 + E_9 \end{array}\right]}{\left[1-(2e/t)-(2a/t)\right]^{1/2}} \quad (90)$$

where:

$$E_1 = 0.8408685,\ E_2 = 1.509002,\ E_3 = -0.603778,$$
$$E_4 = -0.7731469,\ E_5 = 0.1294097,\ E_6 = 0.8841685,$$
$$E_7 = -0.07410377,\ E_8 = 0.04428577\ E_9 = -0.8338377$$

5.1.3.6 Inclusion of Residual Stresses in Welds

The through-wall weld residual stress distribution currently used in FAVOR was derived in the HSST program from a combination of experimental measurements taken from an RPV shell segment made available from a cancelled pressurized-water reactor plant and finite-element thermal and stress analyses [109,130]. The residual stresses in an RPV structural weld are those remaining stresses that are not completely relaxed by the post-weld heat-treatment [131,132]. Data required for calculation of these residual stresses were obtained by cutting a radial slot in the longitudinal weld in a shell segment from an RPV and then measuring the deformation of the slot width after cutting. The measured slot openings were assumed to be the sums of the openings due to the clad-base material differential thermal expansion (DTE) and the weld residual stresses. To evaluate the residual stresses in an RPV structural weld, a combined experimental and analytical process was used. Slot opening measurements were made during the machining of full-thickness clad beam specimens with two-dimensional flaws. The blanks measured 54 inches long (circumferential direction), 9-inches wide (longitudinal direction), and 9 inches thick (radial direction). The blanks were cut so as to have a segment of a longitudinal seam weld from the original RPV at the mid-length of the blank. Using the

wire-EDM process, a slot was cut along the weld centerline in a radial direction from the inside (clad) surface of the blank. Measurements were made on three specimens having final slot depths of 0.045 inches, 0.90 inches, or 4.50 inches, respectively. After machining, the widths of the slots were measured along each radial face of the blanks. Finite-element analyses were used to develop a through-thickness stress distribution that gave a deformation profile matching the measured values.

A three-step analysis procedure was developed [132] to produce the estimated residual stress profile applied in FAVOR.

Step 1. – As discussed above, the first step was to measure the width of the a machined slot (flaw) cut into the axial weld, which was contained in a full-thickness beam taken from the RPV shell segment. The measured slot openings in the clad beam specimens are the result of relaxing the residual stresses from (1) the clad-/base-material differential thermal expansion (DTE) and (2) the residual stress generated by the structural welding process, which were not completely relaxed by postweld heat treatment. Therefore, the measured slot width is assumed to be the superposition of the deformation due to DTE and the deformation due to the residual stress.

Step 2. – Next, an ABAQUS finite-element analysis was performed to simulate the cooling of the clad beam from a stress-free state. The opening displacement of the notch resulting from this analysis is caused by DTE of the clad and base-material properties. The clad beam specimen was cooled uniformly from an assumed stress-free temperature of 600 °F (315.6 °C) to room temperature at 72 °F (22 °C). The difference between the slot displacement from the cooldown and the total measured slot width is then assumed to be caused by the residual stress alone.

Step 3. – The third step was to determine the through-wall stress distribution in the clad beam caused by the residual stress. An ABAQUS finite-element stress analysis was performed to impose the displacements from the residual stress on the crack plane. The resulting stress distribution is the estimated through-wall residual stress distribution.

The residual stress profile implemented in FAVOR, v05.1, (and earlier versions of FAVOR) is shown in Fig. 31(a), where the contributions from clad and base DTE have been removed. The residual stress profile is further modified in FAVLOAD to apply to an analysis of a vessel that has a wall thickness other than the one from which the stress distribution is derived. The through-wall weld residual stress distribution retains the shape and magnitude as derived from experiment/analysis; however, it is compressed or expanded to fit the current wall thickness by modifying the residual profile data by the ratio of the current RPV wall thickness to 8.936, i.e., the wall thickness from which the stress distribution was derived.

Temperature-independent properties were assumed in the analyses discussed above. The ProSaMM program at ORNL reviewed these calculations to determine the effect of using temperature-dependent properties consistent with the procedures now applied in the FAVOR deterministic load module. The first step in this review was to attempt to reproduce the analysis results reported in ref. [132] and then modify the analysis by applying temperature-dependent properties, specifically, a variable elastic modulus and thermal expansion coefficient for both the base and cladding materials. Figure 31(b) shows the finite-element model employed in the current study. Both the constant and temperature-dependent properties are presented in Figs. 31(c)-(d). The resulting vertical stresses in the test specimen are shown in Fig. 31(e) for the constant property case and Fig. 31(f) for the variable property case. The calculated slot displacements for both constant and variable properties are compared in Fig. 31(g). The displacement profile, C, calculated by subtracting B from A, is then applied to the slot (with an assumed temperature of 22 °C (72 °F). Finally the resulting through-wall residual stress profiles are compared in Fig. 31(h). As demonstrated in Figs. 31(e)-(h), the inclusion of temperature-dependent properties has a minimal impact on the estimated residual stress profile.

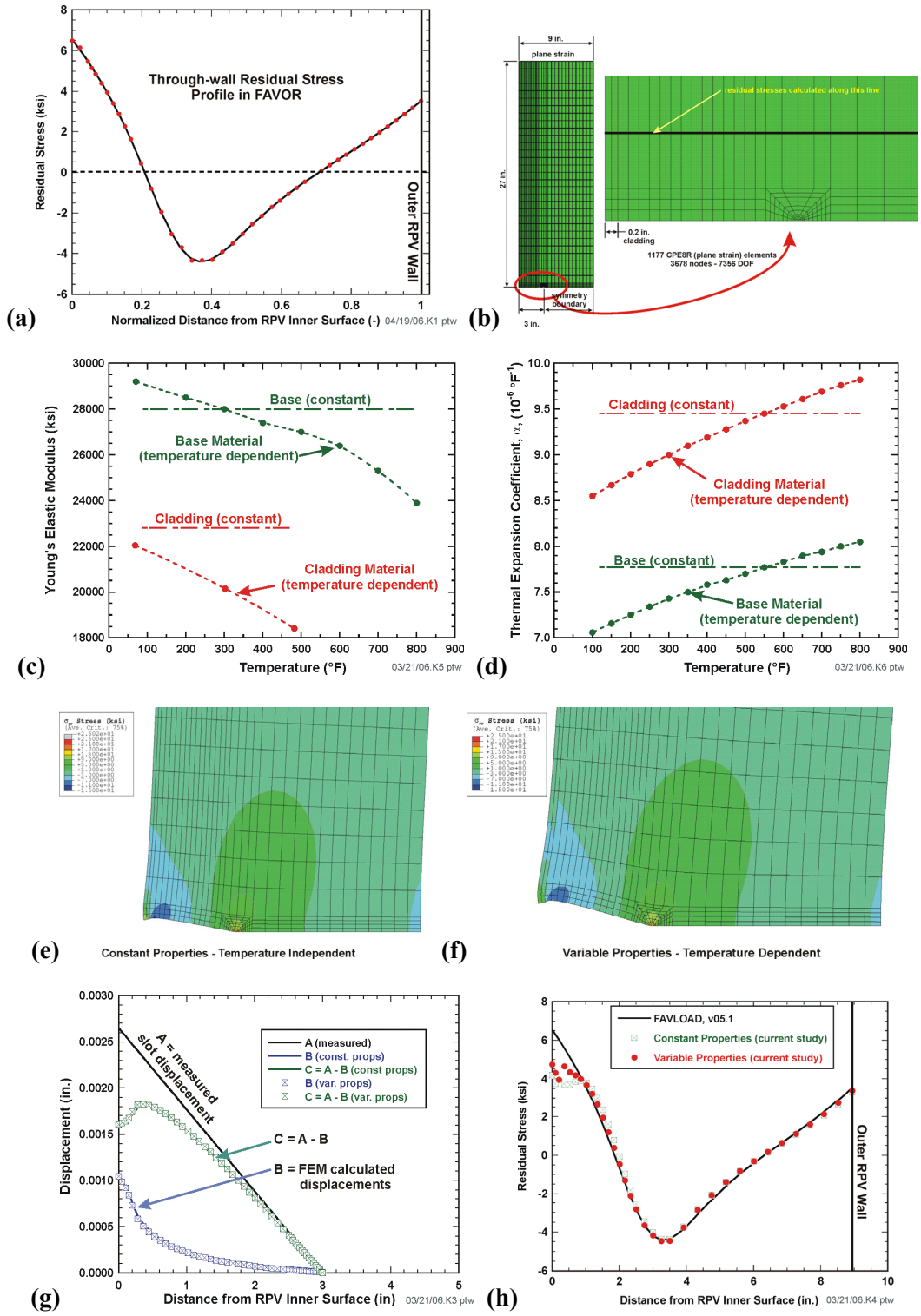

Fig. 31. Weld residual stress through-thickness distribution developed for use in RPV integrity analyses.

5.1.3.7 Inclusion of Crack-Face Pressure Loading for Surface-Breaking Flaws

Crack-face pressure loading on the exposed faces of internal surface-breaking flaws is included as an option in the mechanical loading of the family of surface-breaking flaws in a FAVLoad deterministic analysis. The Mode I Stress Intensity Factor database provides a convenient mechanism for including the effects of crack-face pressure loading.

Semi-Elliptic Finite and Infinite Surface Flaws

For semi-elliptic finite and infinite surface flaws, the uniform unit-load 3D-flaw influence coefficients can be applied to calculate the contribution, K_{I-cfp}, of the crack-face pressure loading to the total stress intensity factor (including cladding) at the deepest point of the flaw $(\phi = 90°)$ by

$$K_{I-cfp} = \sqrt{\pi a}\left(K^*_{0-base} + K^*_{0-clad}\right) p(\tau)$$

where $p(\tau)$ is the coolant pressure in ksi at time τ in the transient. By linear superposition, the crack-face pressure component, K_{I-cfp}, is then added to the total stress intensity factor.

Infinite-Length Surface Flaws (Methodology used through FAVOR, v12.1)

A similar procedure can be followed for infinite-length surface flaws.

for axial flaws

$$K_{I-cfp}(a) = \sum_{i=1}^{n} p(\tau)\,\Delta a_i K^*_i(a'_i, a)$$

for circumferential flaws

$$K_{I-cfp}(a) = \sum_{i=1}^{n} 2\pi(R + a'_i)\; p(\tau)\,\Delta a_i K^*_i(a'_i, a)$$

where

$\Delta a_i =$ an increment of a about a'_i such that $\sum_{i=1}^{n} \Delta a_i = a$

$a'_i =$ radial distance from open end of crack to point of application of unit load,

$p(\tau) =$ coolant pressure at time τ uniformly applied over the crack face

$K_{I-cfp} =$ opening Mode I stress-intensity factor contribution due to crack-face pressure

$K^*_I =$ stress-intensity factor per unit load applied at a'_i, where load has dimensions of force/length for axial flaws and force for circumferential flaws

$n =$ number of points along length of crack for which K^*_i are available,

$R =$ inside radius of vessel.

5.2 Sampled LEFM Material and Correlative Properties

A detailed description of the technical bases for the models in this section is presented in ref. [133]. A summary of the material in [133] is presented here with emphasis on the implementation of these models into FAVOR.

5.2.1 Reference Nil-Ductility Transition Temperature, RT_{NDT}

For each major region, FAVOR calculates and reports a value of $RT_{NDT.}$ This value of RT_{NDT} is the maximum of all the subregion RT_{NDT} values within the given major region. The major-region RT_{NDT} is not sampled from a distribution, is reported for comparison purposes only, and is not used in any subsequent analyses. Defined by

$$RT_{NDT(i)} \equiv \max\left(RT_{NDT(u)-(j)} + \Delta RT_{NDT(j)}\right);\ j \text{ subregion} \in \text{major region } i, \tag{91}$$

the major-region RT_{NDT} is the mean irradiated value corresponding to the irradiation shift, ΔRT_{NDT}, due to the neutron fluence at the inner surface of the vessel at the time in the operating life (typically designated in effective full-power years or EFPY) of the RPV for which the PFM analysis is being performed. Note that the major-region value for RT_{NDT} does not include any margin term.

Currently, in 10CFR50.61, the irradiation shift model is the same used in Regulatory Guide 1.99, Revision 2 [17], where

$$\Delta RT_{NDT} = (CF) f_0(\delta)^{(0.28-0.10\log_{10}(f_0(\delta)))}$$

$$\begin{aligned} CF &= \text{ chemistry factor, a continuous function of copper and nickel} \\ f_0(\delta) &= \text{ best-estimate neutron fluence } [10^{19}\ \text{n/cm}^2;\ E > 1\ \text{MeV}] \text{ attenuated} \\ &\quad \text{from the inner surface to the clad/base metal interface} \\ \delta &= \text{ distance from the inner surface to the clad/base metal interface [in.]} \end{aligned} \tag{92}$$

Look-up tables for the chemistry factor, *CF*, taken from 10CFR50.61 [15], are included in FAVOR for the calculation of ΔRT_{NDT}.

In FAVOR, the user has the option of calculating ΔRT_{NDT} by either Regulatory Guide 1.99, Rev 2 (RG 1.99, Rev 2) [17], as defined above, or by ΔT_{30} (see Eqs. (93) or (94)) as calculated by the selected irradiation-shift model [100, 101] to be discussed in the following section.

5.2.2 Radiation Embrittlement

Irradiation damage of RPV steels in U.S. PWRs occurs as a consequence of two hardening mechanisms: *matrix hardening* and *age hardening*. The following descriptions of these mechanisms are taken from [133]:

> **Matrix Hardening** – Matrix damage develops continuously during irradiation, producing hardening that has a square root dependence on fluence. Matrix damage can be divided into two components: unstable matrix defects (UMD), and stable matrix defects (SMD). Unstable matrix defects are formed at relatively low fluence and are small vacancy or interstitial clusters, complexed with solutes such as phosphorous. UMDs are produced in displacement cascades. Increasing flux causes increasing hardening due to these defects, but they occur relatively independently of alloy composition. In low copper alloys, at low fluence and high flux, UMD is the dominant source of hardening; however, in high copper steels, these defects delay the copper-rich precipitate contribution to hardening by reducing the efficiency of radiation-enhanced diffusion. Stable matrix features form at high fluence and include nanovoids and more highly complexed clusters. These defects cause hardening that increases with the square root of exposure and is especially important at high fluence levels.
>
> **Age Hardening** – Radiation accelerates the precipitation of copper held in solid solution, forming copper-rich precipitates (CRPs) that inhibit dislocation motion and, thereby, harden the material. This hardening rises to a peak value and is then unaffected by subsequent irradiation because no copper remains in solid solution to precipitate out and cause damage. The magnitude of this peak depends on the amount of copper initially in solution. This copper is available for subsequent precipitation. Post-weld heat treatment (PWHT) performed before the RPV is placed into service can also precipitate copper, removing its ability to cause further damage during irradiation. Thus, different materials are expected to have different peak hardening values due to differing pre-service thermal treatments. Additionally, the presence of nickel in the alloy further enhances its age-hardening capacity. Nickel precipitates together with copper, forming larger second-phase particles that present greater impediments to dislocation motion and, thereby, produce a greater hardening effect.

These insights helped to establish the functional form of a relationship between basic material composition, irradiation-condition variables, and measurable quantities such as yield-strength increase, Charpy-transition-temperature shift, and toughness-transition-temperature shift. A quantitative relationship was developed from the database of Charpy shift values, ΔT_{30}, generated in US commercial reactor surveillance programs. Two correlations were developed based on these data and implemented in FAVOR, v05.1 [101], and FAVOR, v06.1[134].[14] Three additional correlations were developed and implemented in FAVOR, v07.1.

[14] A curved overbar, $\widehat{X}$, indicates a sampled random variate.

Eason 2000 Correlation [101] Implemented in FAVOR, v05.1, and Earlier Versions

$$\widehat{\Delta T}_{30}(\widehat{Ni},\widehat{Cu},\widehat{P},\widehat{f_0}(r),\tau_{\text{exposure}},T_c,\text{product form})[^\circ\text{F}] =$$
$$A\exp\left(\frac{19310}{T_c+460}\right)\left(1+110\widehat{P}\right)\left(\widehat{f_0}(r)\right)^{0.4601}+B\left(1+2.40\widehat{Ni}^{1.250}\right)f(\widehat{Cu})g\left(\widehat{f_0}(r)\right)+Bias$$

$$A=\left\{\begin{matrix}8.86\times10^{-17}\ \text{for welds}\\ 9.30\times10^{-17}\ \text{for forgings}\\ 12.7\times10^{-17}\ \text{for plates}\end{matrix}\right\};B=\left\{\begin{matrix}230\ \text{for welds}\\ 132\ \text{for forgings}\\ 206\ \text{for plates in CE vessels}\\ 156\ \text{for other plates}\end{matrix}\right\}\left[\begin{matrix}\text{CE}\ \rightarrow\ \text{manufactured by}\\ \text{Combustion Engineering}\end{matrix}\right]$$

$$g\left(\widehat{f_0}(r)\right)=\frac{1}{2}+\frac{1}{2}\tanh\left[\frac{\log_{10}\left(\widehat{f_0}(r)+4.579\times10^{12}\tau_{\text{exposure}}\right)-18.265}{0.713}\right]$$

$$f\left(\widehat{Cu}\right)=\left\{\begin{matrix}0 & \text{for}\ \widehat{Cu}\le0.072\ \text{wt \%}\\ \left(\widehat{Cu}\text{-}0.072\right)^{0.659} & \text{for}\ \widehat{Cu}>0.072\ \text{wt \%}\end{matrix}\right\};\left[\begin{matrix}\text{subject to copper-saturation limit}\\ \widehat{Cu}=\min\left(\widehat{Cu},Cu_{\max}\right)\end{matrix}\right] \quad (93)$$

$$Cu_{\max}=\left\{\begin{matrix}0.25\ \text{for Linde 80 or Linde 0091 weld fluxes}\\ 0.305\ \text{for all other weld fluxes}\end{matrix}\right\}$$

and

$$Bias=\left\{\begin{matrix}0\ \text{for}\ \tau_{\text{exposure}}<97000\ \text{h}\\ 9.4\ \text{for}\ \tau_{\text{exposure}}\ge97000\ \text{h}\end{matrix}\right\}$$

Eason 2006 Correlation [134] Implemented in FAVOR, v06.1

$$\widehat{\Delta T}_{30}(\widehat{Ni},\widehat{Cu},\widehat{P},\widehat{Mn},\widehat{f_0}(r),\tau_{\text{exposure}},T_c,\text{product form})[^\circ\text{F}] =$$
$$A\left(1-0.001718\,T_c\right)\left(1+6.13\,\widehat{P}\,\widehat{Mn}^{2.471}\right)\sqrt{\widehat{f_0}(r)_{eff}}+ \quad (94)$$
$$B\left(1+3.769\,\widehat{Ni}^{1.191}\right)\left(\frac{T_c}{543.1}\right)^{1.100}f\left(\widehat{Cu},\widehat{P}\right)g\left(\widehat{Cu},\widehat{Ni},\widehat{f_0}(r)\right)$$

$$A = \begin{Bmatrix} 1.140\text{x}10^{-7} & \text{for forgings} \\ 1.561\text{x}10^{-7} & \text{for plates} \\ 1.417\text{x}10^{-7} & \text{for welds} \end{Bmatrix}; \quad B = \begin{Bmatrix} 102.3 & \text{for forgings} \\ 102.5 & \text{for plates in non-CE vessels} \\ 135.2 & \text{for plates in CE vessels} \\ 155.0 & \text{for welds} \end{Bmatrix};$$

$$\begin{bmatrix} \text{CE} \rightarrow \text{manufactured by} \\ \text{Combustion Engineering} \end{bmatrix}; \quad \widehat{f_0}(r) = \begin{Bmatrix} \text{sampled and attenuated} \\ \text{neutron fluence} \end{Bmatrix} \left[\frac{\text{neutrons}}{\text{cm}^2} \right];$$

$$\text{neutron flux: } \phi = \frac{\widehat{f_0}(r)}{3600\ \tau_{\text{exposure}}} \left[\frac{\text{neutrons}}{\text{cm}^2\text{-sec}} \right];$$

$$\widehat{f_0}(r)_{eff} = \begin{cases} \widehat{f_0}(r) & \text{for } \phi \geq 4.3925 \times 10^{10} \left[\dfrac{\text{neutrons}}{\text{cm}^2\text{-sec}} \right] \\ \widehat{f_0}(r) \left(\dfrac{4.3925 \times 10^{10}}{\phi} \right)^{0.2595} & \text{for } \phi < 4.3925 \times 10^{10} \left[\dfrac{\text{neutrons}}{\text{cm}^2\text{-sec}} \right] \end{cases}$$

$\widehat{f_0}(r)_{eff}$ is bounded from above by $3\widehat{f_0}(r) \rightarrow \ \widehat{f_0}(r)_{eff} = \min\left[\widehat{f_0}(r)_{eff}, \left(3\widehat{f_0}(r) \right) \right]$.

$$g\left(\widehat{Cu}, \widehat{Ni}, \widehat{f_0}(r) \right) = \frac{1}{2} + \frac{1}{2} \tanh \left[\frac{\log_{10}\left(\widehat{f_0}(r)_{eff} \right) + 1.139\widehat{Cu}_{eff} - 0.4483\widehat{Ni} - 18.12025}{0.6287} \right]$$

$$f\left(\widehat{Cu}, \widehat{P} \right) = \begin{Bmatrix} 0 & \widehat{Cu} \leq 0.072 \\ \left[\widehat{Cu}_{eff} - 0.072 \right]^{0.6679} & \text{for } \widehat{Cu} > 0.072 \text{ and } \widehat{P} \leq 0.008 \\ \left[\widehat{Cu}_{eff} - 0.072 + 1.359(\widehat{P}\text{-}0.008) \right]^{0.6679} & \text{for } \widehat{Cu} > 0.072 \text{ and } \widehat{P} > 0.008 \end{Bmatrix}$$

$$\text{where } \widehat{Cu}_{eff} = \begin{Bmatrix} 0 \quad \text{for } \widehat{Cu} \leq 0.072 \text{ wt\%} \\ \widehat{Cu} \quad \text{for } \widehat{Cu} > 0.072 \text{ wt\%} \end{Bmatrix}; \quad \begin{bmatrix} \text{subject to copper-saturation upper bound} \\ \widehat{Cu}_{eff} = \min\left(\widehat{Cu}_{eff}, Cu_{\max} \right) \end{bmatrix}$$

$$\text{with copper saturation defined by } Cu_{\max} \equiv \begin{Bmatrix} 0.3700 \text{ wt\%} & \text{for } \widehat{\text{Ni}} < 0.5 \text{ wt\%} \\ 0.2435 \text{ wt\%} & \text{for } 0.5 \leq \widehat{\text{Ni}} \leq 0.75 \text{ wt\%} \\ 0.3010 \text{ wt\%} & \text{for } \widehat{\text{Ni}} > 0.75 \text{ wt\%} \\ 0.3010 \text{ wt\%} & \text{all welds with L1092 flux} \end{Bmatrix}$$

Kirk 2007 Correlation Implemented in FAVOR, v07.1

$$\widehat{\Delta T}_{30}(\widehat{Ni},\widehat{Cu},\widehat{P},\widehat{f_0}(r),\tau_{\text{exposure}},T_c,\text{product form})\left[^\circ\text{F}\right]=\widehat{\Delta T}_{30(MD)}+\widehat{\Delta T}_{30(CRP)} \tag{95}$$

where

Matrix Damage

$$\widehat{\Delta T}_{30(MD)}=PF_{MD}\times\widehat{CF}_{MD}\times TF_{MD}\times\widehat{\phi F}_{MD}\times\widehat{f_0F}_{MD}$$

$$PF_{MD}=\begin{Bmatrix}6.70\ ; & \text{for welds}\\ 8.10\ ; & \text{for plates}\\ 4.75\ ; & \text{for forgings}\end{Bmatrix}\times 10^{-9}$$

$$\widehat{CF}_{MD}=\left[1+35\widehat{P}\right]$$

$$TF_{MD}=\left(\frac{T_c}{550}\right)^{-14.64}$$

$$\widehat{\phi F}_{MD}=\left(\frac{\log_{10}\left(\widehat{\phi}\right)}{10.7}\right)^{-3.44}$$

$$\widehat{f_0F}_{MD}=\sqrt{\widehat{f_0}(r)}$$

$$\text{neutron flux: }\phi=\frac{\widehat{f_0}(r)}{3600\ \tau_{\text{exposure}}}\left[\frac{\text{neutrons}}{\text{cm}^2\text{-sec}}\right]$$

Copper Rich Precipitation

$$\widehat{\Delta T}_{30(CRP)}=PF_{CRP}\times\widehat{CF}_{CRP}\times TF_{CRP}\times\widehat{f_0F}_{CRP}$$

$$PF_{CRP}=\begin{Bmatrix}0.301\ ; & \text{for welds}\\ 0.233\ ; & \text{for plates}\\ 0.233\ ; & \text{for forgings}\end{Bmatrix}$$

$$CF_{CRP}=f\left(\widehat{Cu}\right)_{eff}+2500.3\times\text{MIN}\left[0.32,\text{MAX}\left(0,\widehat{Cu}-0.048\right)\right]\times\widehat{Ni}$$

$$f\left(\widehat{Cu}\right)_{eff}=\begin{Bmatrix}0\ ; & \text{for } f\left(\widehat{Cu}\right)<0\\ f\left(\widehat{Cu}\right)\ ; & \text{for } 0\le f\left(\widehat{Cu}\right)\le 185\\ 118.5\ ; & \text{for } f\left(\widehat{Cu}\right)>185\end{Bmatrix}$$

$$\text{where } f\left(\widehat{Cu}\right)=-116.3+530.8\sqrt{\widehat{Cu}}$$

$$TF_{CRP} = \left(\frac{T_c}{550} \right)^{-1.74}$$

$$\widehat{f_0 F}_{CRP} = \left\{ 1 - \exp\left(\frac{-\widehat{f_0(r)}}{2.38 \times 10^{18}} \right) \right\}$$

RADAMO Correlation [Implemented in FAVOR, v07.1

$$\widehat{\Delta T}_{30}(\widehat{Ni}, \widehat{Cu}, \widehat{P}, \widehat{f_0}(r), \tau_{\text{exposure}}, T_c, \text{product form})[^\circ\text{F}] = \left\{ \begin{matrix} 1.39\ ; & \text{for welds} \\ 1.18\ ; & \text{for plates} \\ 0.84\ ; & \text{for forgings} \end{matrix} \right\} \times \Delta\widehat{YS} \qquad (96)$$

where

$$\Delta\widehat{YS}\ [\text{MPa}] = \Delta\widehat{YS}_{(MD)} + \sqrt{\Delta\widehat{YS}^2_{(CRP)} + \Delta\widehat{YS}^2_{(PRP)}}$$

Matrix Damage

$$\Delta\widehat{YS}_{(MD)} = \left\{ \begin{matrix} 0\ ; & \text{for } f_0(r) \le 10^{19}\ \text{n/cm}^2 \\ \left\{ 585 \exp\left[-1250 \exp\left(\frac{-0.345}{kT_{c(K)}} \right) \right] + \left(3880 - 6.3 T_{c(K)} \right) \widehat{Ni} \right\} \times \sqrt{1 - \exp\left[-0.01 \left(\frac{\widehat{f_0}(r)}{10^{19}} - 1 \right) \right]}; & \text{for } f_0(r) > 10^{19}\ \text{n/cm}^2 \end{matrix} \right\}$$

$$T_{c(K)} = \frac{(T_c - 32)}{1.8} + 273\ \ [\text{K}]$$

Copper Rich Precipitation

$$\Delta\widehat{YS}_{(CRP)} = \widehat{\Delta}_{CRP(PEAK)} \times f\left(\widehat{\phi}, \tau_{\text{exposure}}, T_c, \widehat{Cu}\right)$$

$$\widehat{\Delta}_{CRP(PEAK)} = \begin{Bmatrix} 0\ ; & \text{for } \widehat{Cu} \le Cu_{\min} \\ 215\left\{1 - \exp\left[-2.7\left(\widehat{Cu} - Cu_{\min}\right)\right]\right\}\ ; & \text{for } \widehat{Cu} > Cu_{\min} \end{Bmatrix}$$

$$f\left(\widehat{\phi}, \tau_{\text{exposure}}, T_c, \widehat{Cu}\right) = \begin{Bmatrix} 0\ ; & \text{for } \tau_{\text{exposure(EFPY)}} < \left(\tau_{peak}/20\right) \\ \dfrac{\ln\left(20 \times \tau_{\text{exposure(EFPY)}}/\tau_{peak}\right)}{\ln(20)}\ ; & \text{for } \left(\tau_{peak}/20\right) \le \tau_{\text{exposure(EFPY)}} < \tau_{peak} \\ 1\ ; & \text{for } \tau_{\text{exposure(EFPY)}} \ge \tau_{peak} \end{Bmatrix}$$

$$\widehat{\tau}_{peak} = \frac{10^{\left[\frac{10684}{T_{c(K)}} - \left(15.3 - \frac{0.3}{\widehat{Cu}}\right)\right]}}{1 + \dfrac{\widehat{\phi} \times 10^{-32}}{\exp\left(-\dfrac{\widehat{E}}{kT_{c(K)}}\right)}}$$

$$\widehat{E} = \begin{Bmatrix} \widehat{E_0}\ ; & \text{for } \widehat{\phi} < \phi_{LIM} \\ \widehat{E_0} - 0.03\ln\left(\dfrac{\widehat{\phi}}{\phi_{LIM}}\right); & \text{for } \widehat{\phi} \ge \phi_{LIM} \end{Bmatrix}$$

$$\widehat{E_0} = -kT_{c(K)} \ln\left\{\frac{\phi_{LIM} \times 10^{-32}}{\dfrac{10^{\left[\frac{10684}{T_{c(K)}} - \left(15.3 - \frac{0.3}{\widehat{Cu}}\right)\right]}}{\tau_{peak}^{Cu_{\max}}} - 1}\right\}$$

$$\tau_{peak}^{Cu_{\max}} = \frac{10^{\left[\frac{10684}{T_{c(K)}} - \left(15.3 - \frac{0.3}{Cu_{\max}}\right)\right]}}{1 + \dfrac{\phi_{LIM} \times 10^{-32}}{\exp\left(\dfrac{-2.8}{kT_{c(K)}}\right)}}$$

$$Cu_{\min} = 0.03 \text{ wt\%};\ Cu_{\max} = 0.425 \text{ wt\%};\ \phi_{LIM} = 6\times10^{12}\ \left[\text{n/cm}^2/\text{sec}\right];\ k = 8.617\times10^{-5}\ \left[\text{eV/K}\right]$$

$$\text{neutron flux: } \phi = \frac{\widehat{f_0}(r)}{3600\tau_{\text{exposure}}}\ \left[\frac{\text{neutrons}}{\text{cm}^2-\text{sec}}\right];\ T_{c(K)} = \frac{T_c - 32}{1.8} + 273\ \text{[K]}$$

Phosphorous Rich Precipitation

$$\Delta\widehat{YS}_{(PRP)} = \left\{\begin{array}{ll} 0\ ; & \text{for } \widehat{P} \le 0.012 \\ \min\left[\max\left(\frac{\log_{10}\left(\widehat{f_0}(r)\right)-16}{3}, 0\right), 1\right]\left(44470.5 - 70T_{c(K)}\right)\left(\widehat{P} - 0.012\right)\ ; & \text{for } \widehat{P} > 0.012 \end{array}\right\}$$

Kirk 2007 + RADAMO Correlation Implemented in FAVOR, v07.1

$$\widehat{\Delta T}_{30}(\widehat{Ni}, \widehat{Cu}, \widehat{P}, \widehat{f_0}(r), \tau_{\text{exposure}}, T_c, \text{product form})\left[^\circ\text{F}\right] = \left(1-\widehat{W}\right)\widehat{\Delta T}_{30}^{LOW} + \widehat{W}\,\widehat{\Delta T}_{30}^{HIGH} \qquad (97)$$

where

$$\widehat{W} = \left\{\begin{array}{ll} 0\ ; & \text{for } \widehat{f}_0(r) \le 2\times10^{19}\ \text{n/cm}^2 \\ \frac{1}{2}\left(\frac{\widehat{f}_0(r)}{10^{19}} - 2\right)\ ; & \text{for } 2\times10^{19} < \widehat{f_0}(r) \le 4\times10^{19}\ \text{n/cm}^2 \\ 1\ ; & \text{for } \widehat{f_0}(r) > 4\times10^{19}\ \text{n/cm}^2 \end{array}\right\}$$

for low fluences

$$\widehat{\Delta T}_{30}^{LOW} = \widehat{\Delta T}_{30(MD)} + \widehat{\Delta T}_{30(CRP)}$$

Matrix Damage

$$\widehat{\Delta T}_{30(MD)} = PF_{MD} \times \widehat{CF}_{MD} \times TF_{MD} \times \widehat{\phi F}_{MD} \times \widehat{f_0 F}_{MD}$$

$$PF_{MD} = \left\{ \begin{matrix} 6.70\ ; & \text{for welds} \\ 8.10\ ; & \text{for plates} \\ 4.75\ ; & \text{for forgings} \end{matrix} \right\} \times 10^{-9}$$

$$\widehat{CF}_{MD} = \left[1 + 35 \cdot \widehat{P} \right]$$

$$TF_{MD} = \left(\frac{T_c}{550} \right)^{-14.64}$$

$$\widehat{\phi F}_{MD} = \left(\frac{\log_{10}\left(\widehat{\phi}\right)}{10.7} \right)^{-3.44}$$

$$\widehat{f_0 F}_{MD} = \sqrt{\widehat{f_0}(r)}$$

$$\text{neutron flux: } \phi = \frac{\widehat{f_0}(r)}{3600\ \tau_{\text{exposure}}} \left[\frac{\text{neutrons}}{\text{cm}^2\text{-sec}} \right]$$

Copper Rich Precipitation

$$\widehat{\Delta T}_{30(CRP)} = PF_{CRP} \times \widehat{CF}_{CRP} \times TF_{CRP} \times \widehat{f_0 F}_{CRP}$$

$$PF_{CRP} = \left\{ \begin{matrix} 0.301\ ; & \text{for welds} \\ 0.233\ ; & \text{for plates} \\ 0.233\ ; & \text{for forgings} \end{matrix} \right\}$$

$$CF_{CRP} = f\left(\widehat{Cu}\right)_{eff} + 2500.3 \times \text{MIN}\left[0.32, \text{MAX}\left(0, \widehat{Cu} - 0.048\right) \right] \times \widehat{Ni}$$

$$f\left(\widehat{Cu}\right)_{eff} = \left\{ \begin{matrix} 0\ ; & \text{for } f\left(\widehat{Cu}\right) < 0 \\ f\left(\widehat{Cu}\right)\ ; & \text{for } 0 \le f\left(\widehat{Cu}\right) \le 185 \\ 118.5\ ; & \text{for } f\left(\widehat{Cu}\right) > 185 \end{matrix} \right\}$$

$$\text{where } f\left(\widehat{Cu}\right) = -116.3 + 530.8\sqrt{\widehat{Cu}}$$

$$TF_{CRP} = \left(\frac{T_c}{550} \right)^{-1.74}$$

$$\widehat{f_0 F}_{CRP} = \left\{ 1 - \exp\left(\frac{-\widehat{f_0(r)}}{2.38 \times 10^{18}} \right) \right\}$$

for high fluences

$$\widehat{\Delta T}_{30}^{HIGH} = \left\{ \begin{matrix} 1.39\ ; & \text{for welds} \\ 1.18\ ; & \text{for plates} \\ 0.84\ ; & \text{for forgings} \end{matrix} \right\} \times \Delta \widehat{YS}$$

where

$$\Delta \widehat{YS}\ [\text{MPa}] = \Delta \widehat{YS}_{(MD)} + \sqrt{\Delta \widehat{YS}_{(CRP)}^2 + \Delta \widehat{YS}_{(PRP)}^2}$$

Matrix Damage

$$\Delta \widehat{YS}_{(MD)} = \left\{ \begin{matrix} 0\ ; & \text{for } f_0(r) \le 10^{19}\ \text{n/cm}^2 \\ \left\{ 585 \exp\left[-1250 \exp\left(\dfrac{-0.345}{kT_{c(K)}} \right) \right] + \left(3880 - 6.3T_{c(K)} \right) \widehat{Ni} \right\} \times \sqrt{1 - \exp\left[-0.01 \left(\dfrac{\widehat{f_0(r)}}{10^{19}} - 1 \right) \right]}\ ; & \text{for } f_0(r) > 10^{19}\ \text{n/cm}^2 \end{matrix} \right\}$$

$$T_{c(K)} = \frac{\left(T_c - 32 \right)}{1.8} + 273\ \ [\text{K}]$$

Copper Rich Precipitation

$$\Delta \widehat{YS}_{(CRP)} = \widehat{\Delta}_{CRP(PEAK)} \times f\left(\widehat{\phi}, \tau_{\text{exposure}}, T_c, \widehat{Cu} \right)$$

$$\widehat{\Delta}_{CRP(PEAK)} = \left\{ \begin{matrix} 0\ ; & \text{for } \widehat{Cu} \le Cu_{\min} \\ 215 \left\{ 1 - \exp\left[-2.7 \left(\widehat{Cu} - Cu_{\min} \right) \right] \right\}\ ; & \text{for } \widehat{Cu} > Cu_{\min} \end{matrix} \right\}$$

$$f\left(\widehat{\phi}, \tau_{\text{exposure}}, T_c, \widehat{Cu} \right) = \left\{ \begin{matrix} 0\ ; & \text{for } \tau_{\text{exposure(EFPY)}} < \left(\tau_{peak} / 20 \right) \\ \dfrac{\ln\left(20 \times \tau_{\text{exposure(EFPY)}} / \tau_{peak} \right)}{\ln(20)}\ ; & \text{for } \left(\tau_{peak} / 20 \right) \le \tau_{\text{exposure(EFPY)}} < \tau_{peak} \\ 1\ ; & \text{for } \tau_{\text{exposure(EFPY)}} \ge \tau_{peak} \end{matrix} \right\}$$

$$\widehat{\tau}_{peak} = \frac{10^{\left[\frac{10684}{T_{c(K)}} - \left(15.3 - \frac{0.3}{\widehat{Cu}}\right)\right]}}{1 + \frac{\widehat{\phi} \times 10^{-32}}{\exp\left(-\frac{\widehat{E}}{kT_{c(K)}}\right)}}$$

$$\widehat{E} = \left\{ \begin{array}{ll} \widehat{E_0}\ ; & \text{for } \widehat{\phi} < \phi_{LIM} \\ \widehat{E_0} - 0.03\ln\left(\frac{\widehat{\phi}}{\phi_{LIM}}\right)\ ; & \text{for } \widehat{\phi} \geq \phi_{LIM} \end{array} \right\}$$

$$\widehat{E_0} = -kT_{c(K)} \ln\left\{ \frac{\phi_{LIM} \times 10^{-32}}{\frac{10^{\left[\frac{10684}{T_{c(K)}} - \left(15.3 - \frac{0.3}{\widehat{Cu}}\right)\right]}}{\tau_{peak}^{Cu_{\max}}} - 1} \right\}$$

$$\tau_{peak}^{Cu_{\max}} = \frac{10^{\left[\frac{10684}{T_{c(K)}} - \left(15.3 - \frac{0.3}{Cu_{\max}}\right)\right]}}{1 + \frac{\phi_{LIM} \times 10^{-32}}{\exp\left(\frac{-2.8}{kT_{c(K)}}\right)}}$$

$Cu_{\min} = 0.03$ wt%; $Cu_{\max} = 0.425$ wt%; $\phi_{LIM} = 6 \times 10^{12}$ $\left[\text{n/cm}^2/\text{sec}\right]$; $k = 8.617 \times 10^{-5}$ $\left[\text{eV/K}\right]$

neutron flux: $\phi = \frac{\widehat{f_0}(r)}{3600\tau_{\text{exposure}}}$ $\left[\frac{\text{neutrons}}{\text{cm}^2 - \text{sec}}\right]$; $T_{c(K)} = \frac{T_c - 32}{1.8} + 273$ [K]

Phosphorous Rich Precipitation

$$\Delta\widehat{YS}_{(PRP)} = \left\{ \begin{array}{ll} 0\ ; & \text{for } \widehat{P} \leq 0.012 \\ \min\left[\max\left(\frac{\log_{10}\left(\widehat{f_0}(r)\right) - 16}{3}, 0\right), 1\right]\left(44470.5 - 70T_{c(K)}\right)\left(\widehat{P} - 0.012\right)\ ; & \text{for } \widehat{P} > 0.012 \end{array} \right\}$$

where in all of the above correlations $\widehat{Cu}$ is the sampled copper content in wt%, $\widehat{Ni}$ is the sampled nickel content in wt%, $\widehat{P}$ is the sampled phosphorous content in wt%, $\widehat{Mn}$ is the sampled manganese content in wt%, $\hat{f}_0(r)$ is the sampled and then attenuated (see Eq. (99)) neutron fluence in neutrons/cm^2, r is the position from the inner surface of RPV wall, $\tau_{\text{exposure}(EFPY)}$ is the exposure time in effective-full-power-years (EFPY), τ_{exposure} is the exposure time in hours (calculated from $\tau_{\text{exposure}(EFPY)}$), and T_c is coolant temperature in °F. The fast-neutron fluence at the inner surface of the vessel, $f_0(0)$, is sampled using the protocol given in Sect. 5.2.3. The sampled neutron fluence for the flaw is then attenuated (again see Sect. 5.2.3) (but not resampled) as the crack grows through the wall. The sampling distributions and protocols for plate, forging, and weld chemistry are presented in Sect. 5.2.9.

Reference [133] recommends that the uncertainty in the sampled CVN transition shift values, $\widehat{\Delta T}_{30}$, be treated as *epistemic*. Having used information concerning composition and irradiation conditions to estimate the CVN transition temperature shift using Eqs. (93) or (94), it is necessary to transform these $\widehat{\Delta T}_{30}$ values into shifts in the fracture-toughness transition temperature. Figure 32 provides an empirical basis for the following least-squares fits for $\widehat{\Delta RT}_{NDT}$ using data extracted from the literature as discussed in [133].

$$\widehat{\Delta RT}_{NDT}(r,\ldots) = \begin{cases} 0.99\widehat{\Delta T_{30}}(r,\ldots) & \text{welds} \\ 1.10\widehat{\Delta T_{30}}(r,\ldots) & \text{plates and forgings} \end{cases} \tag{98}$$

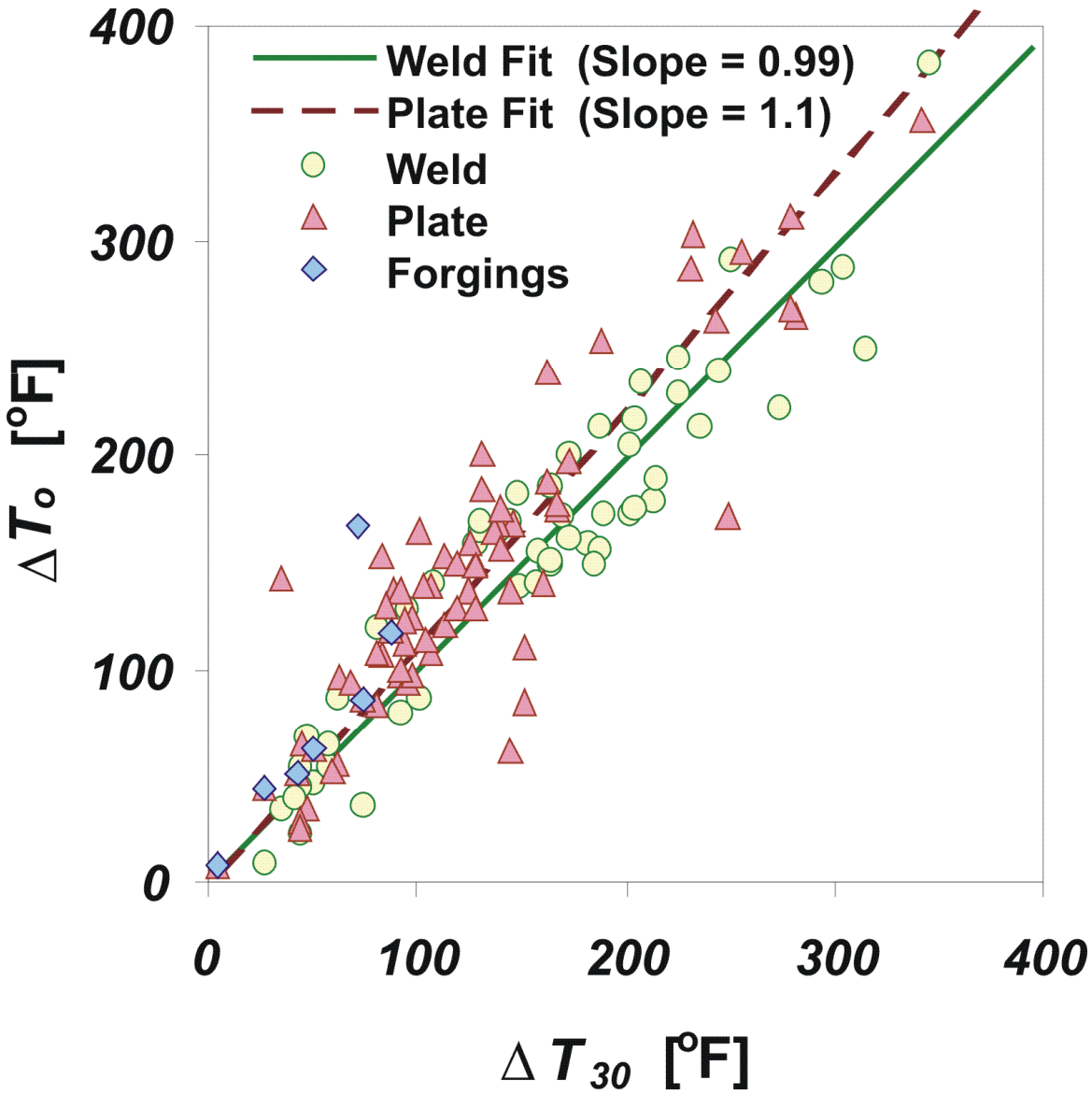

Fig. 32. Relationship between the change in the fracture-toughness index temperature ($\Delta T_0 \approx \Delta RT_{NDT}$) change in the 30 ft-lbf CVN transition temperature (ΔT_{30}) for welds and plates/forgings produced by irradiation. The difference in the best-fit slopes is statistically significant (from [133]).

5.2.3 Fast-Neutron Fluence Attenuation and Sampling Distribution

The sampled fast-neutron fluence at the crack tip depth is attenuated from its sampled reference value, $\widehat{f_0}(0)$, at the inner surface of the RPV wall. This attenuation takes the following form [17]

$$\widehat{f_0(a)} = \widehat{f}_0(0) \times \exp(-0.24a) \tag{99}$$

where a is the position of the flaw tip (in inches) relative to the inner surface.

The inner surface fluence is sampled from two normal distributions such that

$$\begin{aligned} \sigma_{global} &= SIGFGL \times fluence_{subregion} \\ \widehat{f}_{mean} &\leftarrow N(fluence_{subregion}, \sigma_{global}) \\ \widehat{\sigma_{local}} &= SIGFLC \times \widehat{f}_{mean} \\ \widehat{f_0}(0) &\leftarrow N(\widehat{f}_{mean}, \widehat{\sigma_{local}}) \end{aligned} \tag{100}$$

where the best-estimate fluence, $fluence_{subregion}$, is input by the user at the subregion level. The global *SIGFGL* and local *SIGFLC* multipliers are supplied as input by the user. Recommended values are *SIGFGL* = 0.118 and *SIGFLC* = 0.056. Negative values of sampled fast-neutron fluence are handled as nonphysical exceptions in FAVOR using the truncation protocol described in Sect. 4.3.6, with 0.0 as a one-sided truncation boundary.

5.2.4 ORNL 99/27 K_{Ic} and K_{Ia} Databases

The EPRI K_{Ic} database [88] as amended by Nanstad et al. [135] consists of 171 data points and includes data from 11 unirradiated pressure-vessel steels. These data were taken using compact tension C(T) and wedge-open-loading (WOL) test specimens ranging in size from 1T to 11T. A survey was conducted by ORNL to identify additional K_{Ic} and K_{Ia} data to augment the EPRI database. The result of this survey has been designated as the ORNL 99/27 extended K_{Ic}/K_{Ia} database [89].

The candidate K_{Ic} data were evaluated using the following criteria: (a) satisfaction of validity requirements given in ASTM Standard E-399 [136] to maintain consistency with the LEFM driving forces applied in the fracture model, (b) availability in tabular form, and (c) availability of unirradiated $RT_{NDT(0)}$, determined according to the *ASME Boiler and Pressure Vessel Code,* Section III, NB-2331 [137]. The ORNL survey produced an additional 84 K_{Ic} fracture-toughness values obtained from Refs. [138-142]. The extended K_{Ic} database, compiled from the amended EPRI data and from the ORNL survey, provided a total of 255 fracture-toughness data points from 18 materials for input to the statistical model development procedures described in Ref. [89] and applied

herein. A plot of the extended K_{Ic} database versus $(T - RT_{NDT(0)})$ is given in Fig. 33; the complete tabulation of the database is included in Appendix C of this report with a summary presented in Table 9.

A similar survey was carried out to compile an extended K_{Ia} database that would include those data in the EPRI report (see Fig. 34a). Because the ASTM Standard E 1221 [143] was relatively new at the time of survey, many of the existing data were generated before the adoption of the standard. Thus, it was agreed that candidate K_{Ia} data would be evaluated in a more general context, including engineering judgment of acknowledged experts and general acceptance by the nuclear technology community. The ORNL survey produced an additional 62 fracture-toughness, K_{Ia}, data points [144-146] to augment the existing 50 data points [147,148] in EPRI NP-719-SR. A complete tabulation of the 112 fracture-toughness values is given in Appendix C of this report with a summary presented in Table 10. A description of the chemistry and heat treatment of the principal steels in the ORNL 99/27 database is shown in Table 11.

In conjunction with the development of a ductile-tearing model, arrest data from large-specimen experiments carried out in the 1980s were also added to the K_{Ia} database (see Fig. 34b). These additional large-specimen arrest data came from the HSST Wide Plate test program (WP-1 [46] and WP2 [47]), the HSST Pressurized Thermal Shock Experiments (PTSE-1[34] and PTSE-2 [35]), and the HSST Thermal Shock Experiments (TSE) [149].

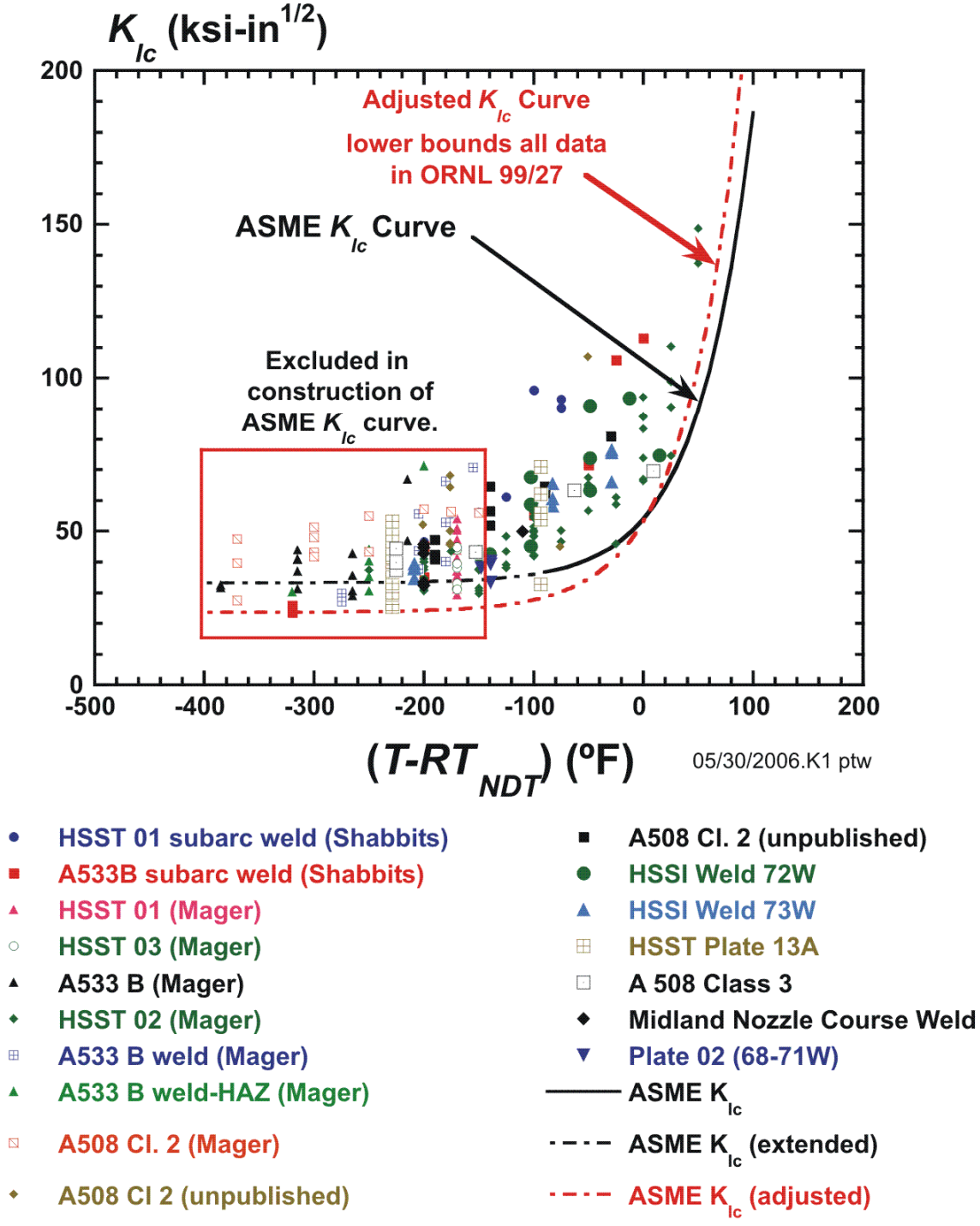

Fig. 33. ORNL 99/27 K_{Ic} database including modified ASME K_{Ic} curve that served as a lower-bounding reference curve in the development of a new transition index temperature.

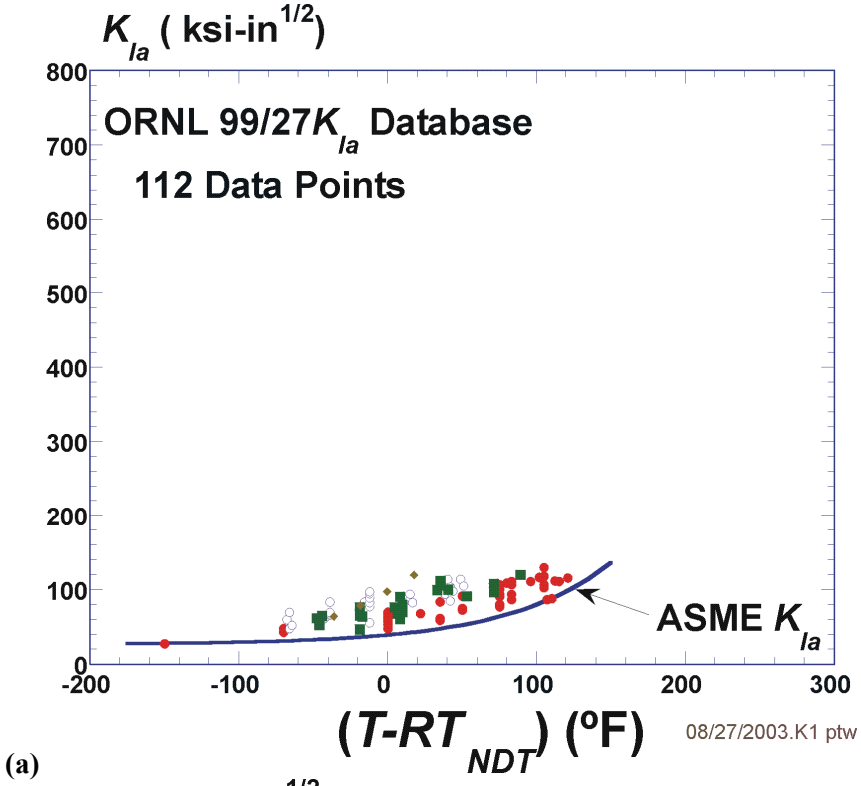

(a)

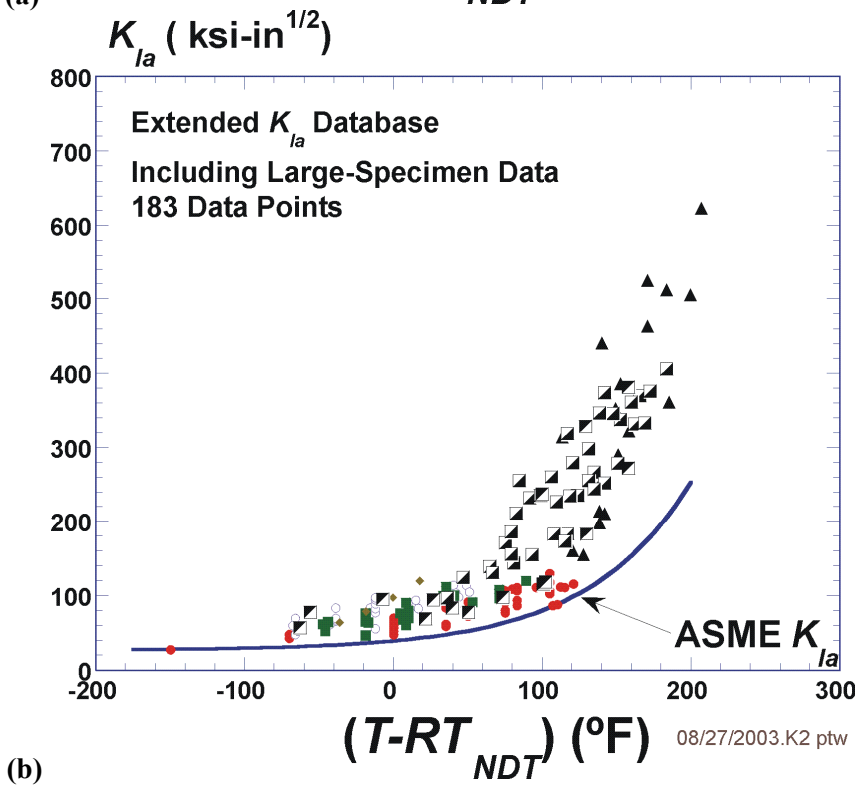

(b)

Fig. 34. K_{Ia} databases (a) ORNL 99/27 K_{Ia} database and (b) Extended K_{Ia} database.

Table 9. Summary of ORNL 99/27 K_{Ic} Extended Database

	Material	Source	Specimen Type	Size Range	Temp. Range (°F)	(T-RT_{NDT0}) Range (°F)	No. of Data Points
EPRI	**Database**	EPRI NP-719-SR					
1	HSST 01 subarc weldment	Shabbits (1969)	C(T)	1T - 6T	-200 to -50	-200 to -50	8
2	A533B Cl. 1 subarc weld	Shabbits (1969)	C(T)	1T - 8T	-200 to 0	-200 to 0	8
3	HSST 01	Mager (1970)	C(T)	1T	-150	-170	17
4	HSST 03	Mager (1970)	C(T)	1T	-150	-170	9
5	A533B Cl. 1	Mager (1969)	WOL	1T - 2T	-320 to -150	-385 to -215	13
6	HSST 02	Mager (1969)	WOL & C(T)	1T - 2T	-200 to 0	-200 to 0	41
6	HSST 02	Shabbits (1969)	C(T)	1T - 11T	-250 to 50	-250 to 50	28
7	A533B Cl. 1 weldment	Mager (1969)	WOL	1T - 2T	-320 to -200	-275 to -155	10
8	A533 B Cl. 1 weldment/HAZ	Mager (1969)	WOL	1T - 2T	-320 to -200	-320 to -200	6
9	A508 Cl.2 European Forging	Mager (1969)	WOL	1T - 2T	-320 to -100	-370 to -150	12
10	A508 Class 2	unpublished	C(T)	2T - 6T	-150 to 0	-201 to -51	9
11	A508 Class 2	unpublished	C(T)	2T - 8T	-125 to -75	-190 to -30	10
						Total	171
Additional	**Data**						
12	HSSI Weld 72W	NUREG/CR-5913.	C(T)	1T-6T	-238 to 50	-229 to 59	13
13	HSSI Weld 73W	NUREG/CR-5913	C(T)	1T-4T	-238 to -58	-209 to -29	10
14	HSST Plate 13A	NUREG/CR-5788	C(T)	½T-4T	-238 to -103	-229 to -94	43
15	A508 Cl. 3	ASTM STP 803	Bx2B C(T)	1T-4T	-238 to -4	-225 to 9	6
16	Midland Nozzle Course Weld	NUREG/CR-6249	C(T)	1T	-148 to -58	-200 to -110	6
17	Midland Beltline	NUREG/CR-6249	C(T)	1T	-148	-171	2
18	Plate 02 4th Irr. Series (68-71W)	NUREG/CR-4880	C(T)	1T	-148 to -139	-148 to -139	4
						Total	84
						Grand Total	255

Table 10. Summary of K_{Ia} Extended Database

	Material	Source	Specimen Type	Size Range	Test Temp. Range (°F)	(*T-RTNDT*) Range (°F)	No. of Data Points
EPRI	**Database**	**EPRI NP-719-SR**					
1	**HSST 02**	**Ripling (1971)**	**CCA crack arrest**	**1T-3T**	**-150 to 121**	**-150 to 121**	**50**
Additional Data	**Additional Data**						
2	**HSSI Weld 72W**	**NUREG/CR-5584**	**CCA crack arrest**		**-78 to 41**	**-68 to 51**	**32**
3	**HSSI Weld 73W**	**NUREG/CR-5584**	**CCA crack arrest**		**-78 to 59**	**-48 to 89**	**26**
4	**MW15J**	**NUREG/CR-6621**	**CCA crack arrest**		**-4 to 50**	**-36 to 18**	**4**
Large Specimen Data							
5	**HSST WP1**	**NUREG/CR-5330**	**Wide Plate Tests**	**(-)**	**84 to 198**	**94 to 207**	**18**
6	**HSST WP2**	**NUREG/CR-5451**	**Wide Plate Tests**	**(-)**	**142 tp 324**	**2 to 184**	**38**
7	**HSST PTSE-1**	**NUREG/CR-4106**	**Pressurized Vessel**	**(-)**	**326 to 354**	**100 to 158**	**2**
8	**HSST PTSE-2**	**NUREG/CR-4888**	**Pressurized Vessel**	**(-)**	**267 tp 325**	**130 to 158**	**3**
9	**HSST TSE**	**NUREG/CR-4249**	**Thermally-Shocked Cylinder**	**(-)**	**72 to 268**	**-63 to 103**	**10**
						Total =	**183**

Table 11. Chemistry and Heat Treatment of Principal Materials: ORNL 99/27 Database

Material ID	Specification	Source	Chemistry – wt (%)										Heat Treatment
			C	P	Mn	Ni	Mo	Si	Cr	Cu	S	Al	
HSST 01	A533B Cl. 1	Mager (1970)	.22	.012	1.48	.68	.52	.25	-	-	.018	-	Note 1
HSST 02	A533B Cl. 1	Mager (1969)	.22	.012	1.48	.68	.52	.25	-	-	.018	-	Note 2
HSST 03	A533B Cl. 1	Mager (1970)	.20	.011	1.26	.56	.45	.25	.10	.13	.018	.034	Note 3
HSST 02	A533B Cl. 1	Shabbits (1969)	.22	.012	1.48	.68	.52	.25	-	-	.018	-	Note 4
HSST 01 subarc weld	A533B Cl. 1	Shabbits (1969)	.12	.014	1.35	.65	.52	.23	-	-	.012	-	Note 5
B&W subarc weldment	A533B Cl. 1	Shabbits (1969)	.10	.009	1.77	.64	.42	.36	-	-	.015	-	Note 6
PW/PH weldment	A533B Cl. 1	Mager (1969)	.09	.019	1.25	1.08	.52	.23	.05	.22	.13	.037	Note 7
MD07 European	A508 Cl. 2 Ring forging	Mager (1969)	.18	.009	1.16	.72	.51	.24	.28	-	.10	-	Note 8
-	A533B Cl. 1	Mager (1969)	.19	.012	1.37	.52	.45	.25	.13	.15	.016	.048	Note 9
72W	A533B weld	5788	.09	.006	1.66	.60	.58	.04	.27	.23	.006	-	
73W	A533B weld	5788	.10	.005	1.56	.60	.58	.04	.25	.21	.005	-	

Notes:

1.	Normalizing:	1675 °F	4 hr, air cooled
	Austentizing:	1600 °F	4 hr
	Quenching:	Water quench	
	Tempering:	1225 °F	4 hr, furnace cooled
	Stress Relief:	1150 °F	40 hr, furnace cooled
2.	Normalizing:	1675 °F	4 hr, air cooled
	Austentizing:	1600 °F	4 hr
	Quenching:	Water quench	
	Tempering:	1225 °F	4 hr, furnace cooled
	Stress Relief:	1150 °F	40 hr, furnace cooled
3.	Normalizing:	1675 °F	12 hr, air cooled
	Austentizing:	1575 °F	12 hr
	Quenching:	Water quench	
	Tempering:	1175 °F	12 hr, furnace cooled
	Stress Relief:	1125 °F	40 hr, furnace cooled
4.	Normalizing:	1675 ± 25 °F	4 hr
	Austentizing:	1520 °F – 1620 °F	4 hr
	Quenching:	Water quench.	
	Tempering:	1200 °F – 1245 °F	4 hr, air cooled
	Stress Relief:	1150 ± 25 °F	40 hr, furnace cooled to 600 °F
5.	Post Weld:	1150 ± 25 °F	12 hr
	Intermediate	1100 ± 25 °F	15 min
6.	Post Weld	1100 °F – 1150 °F	12 hr
	Intermediate	1100 °F – 1150 °F	15 min
7.		620 °C	27 hr, air cooled
8.		925 °C	5 hr
	Quenching:	Water quench	
		650 °C	3 hr, furnace cooled
		620 °C	24 hr, air cooled
9.		910 °C	8 hr
	Quenching:	Water quench	
		680 °C	10 hr, furnace cooled
		850 °C	8 hr
	Quenching:	Water quench	
		690 °C	8 hr, air cooled
		620 °C	24 hr, air cooled

5.2.5 Index Temperature RT_{NDT} – Uncertainty Classification and Quantification

Values of RT_{NDT} are uncertain both due to epistemic and aleatory causes. The *epistemic* uncertainty is due to the conservative bias implicit in the ASME NB-2331 [137] definition of RT_{NDT}, the variety of inconsistent transition temperature metrics used to define RT_{NDT}, the lack of prescription in the test methods used to define RT_{NDT}, and the fact that the *CVN* and *NDT* values used to define RT_{NDT} do not themselves measure fracture toughness. *Aleatory* uncertainties are due to material variability. It is expected that epistemic uncertainty sources outnumber aleatory ones [133]; however, this expectation alone is inadequate to classify the uncertainty in RT_{NDT} as being primarily aleatory or primarily epistemic. To make this distinction, a comparison of the RT_{NDT} index temperature to an exemplar index temperature (such as the *Master Curve* index T_0 [150]) associated with a physically motivated model of crack initiation toughness is needed.

The Master Curve index temperature T_0 [150] is estimated directly from fracture-toughness data, and, by definition, it is therefore associated with the same location on the transition temperature curve of every steel, suggesting that the sources of epistemic uncertainty that are associated with RT_{NDT} do not influence T_0. Thus, the uncertainty in T_0 is expected to be primarily aleatory, and a comparison between T_0 and RT_{NDT} values can be used to quantify the epistemic uncertainty in RT_{NDT}. The numerical difference between RT_{NDT} and T_0 has been used to quantify how far away from measured fracture-toughness data RT_{NDT} positions a model of fracture toughness for a given heat of steel [133]. Figure 35 shows a cumulative distribution function (CDF) constructed from the difference between values of RT_{NDT} and T_0 reported in the literature [151] for the RPV steels in the ORNL 99/27 database. See Appendix E for a description of the statistical procedures applied in the construction of this CDF. These data (see Table 12) demonstrate that the epistemic uncertainty in RT_{NDT} almost always produces a high estimate of the actual fracture-toughness transition temperature.

Even though it quantifies the epistemic uncertainty in RT_{NDT}, the CDF illustrated in Fig. 35 cannot be used directly in FAVOR because of inconsistencies between T_0 and the requirements of the PTS re-evaluation project. Consequently, an alternative CDF (see Fig. 36) was developed that avoids the explicit treatment of size effects and the use of elastic-plastic fracture mechanics (EPFM) toughness data, but retains the important concept from the Master Curve that the index temperature should be quantitatively linked to the measured toughness data. This alternative CDF was determined based on the temperature shift values ($\Delta RT_{epistemic}$ in Table 13) needed to make a NB-2331 RT_{NDT}-positioned K_{Ic} curve lower-bound the ASTM E-399 [136] valid K_{Ic} data for each of the 18 heats (for FAVOR, v05.1, and earlier versions) of RPV steel in the ORNL 99/27 database. See Fig. 37 for an example of this lower-bounding shift procedure for HSST Plate 02.

The number of data points taken from Table 13 for the construction of the CDF implemented in FAVOR, v06.1, for $\Delta RT_{epistemic}$ was reduced from 18 to 11. The excluded data points are highlighted in red in Table 13. These seven values were recognized as inaccurately defined during reviews of the technical basis for PTS rule revision. Consequently, the $\Delta RT_{epistemic}$ CDF based on 18 materials that is shown in Figure 36(a) is based on erroneous RT_{LB} data; it should not be used or regarded as correct. Figure 36(a) presents a comparison of the CDF applied in FAVOR, v01.1, up to FAVOR, v05.1, and the model implemented in FAVOR, v06.1 (see Figs. 36(a) and (b)).

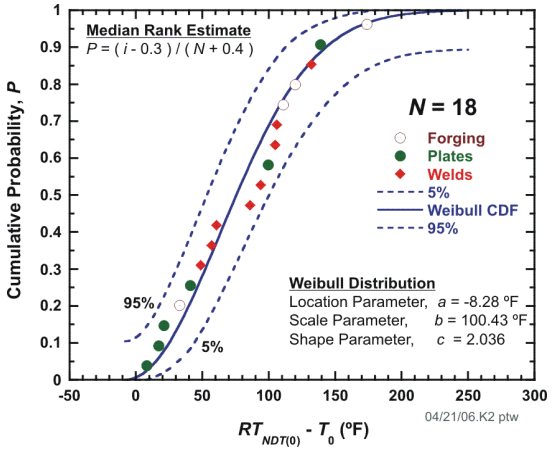

Fig. 35. Cumulative distribution function of the observed difference in $RT_{NDT(0)}$ and T_o (with a size of 1T) using data in the ORNL 99/27 database.

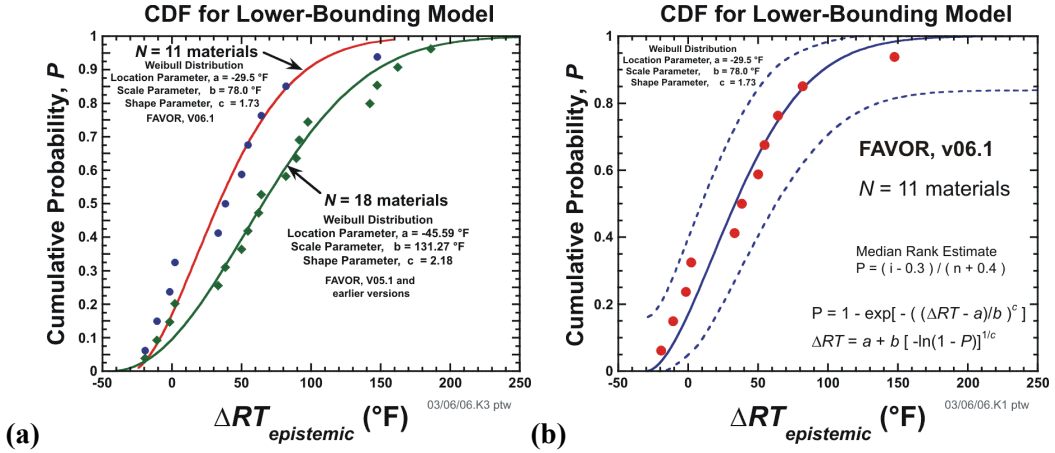

Fig. 36. Cumulative distribution function of the difference (designated as $\Delta RT_{epistemic}$) between $RT_{NDT(0)}$ and a new lower-bounding reference index designated RT_{LB}.

Table 12. Materials Used from the ORNL 99/27 K_{Ic} Extended Database

ID	Form	$RT_{NDT(0)}$ (°F)	T_0 (°F)*	$RT_{NDT(0)}$ - T_0	P	T_q (°F)**
HSST-03	Plate	20	-21	41	0.0455	26.1
HSST-02	Plate	0	-17	17	0.1104	-17.4
HSST-01	Plate	20	-1	21	0.1753	-2.9
A508 Cl. 3	Forging	-13	-46	33	0.2403	
73W	Weld	-29.2	-78	48.8	0.3052	
A533B Cl. 1	Weld	0	-57	57	0.3701	-56.7
72W	Weld	-9.4	-70	60.6	0.4351	
A533B Cl. 1	Plate	-9.4	-109	99.6	0.5000	
HSST-01	Weld	0	-105	105	0.5649	-104.4
A533B Cl. 1	Weld	-45	-151	106	0.6299	-151.5
A508 Cl. 2	Forging	51	-60	111	0.6948	-59.9
A508 Cl. 2	Forging	65	-55	120	0.7597	-5.8
A533B Cl. 1	HAZ	0	-132	132	0.8247	-132.3
A533B Cl. 1	Plate	65	-74	139	0.8896	-73.8
A508 Cl. 2	Forging	50	-124	174	0.9545	-119.3

*T_0 values calculated using ASTM E-1921 valid data.
**Provisional T_q values calculated using ASTM E-399 valid K_{Ic} data in [89].

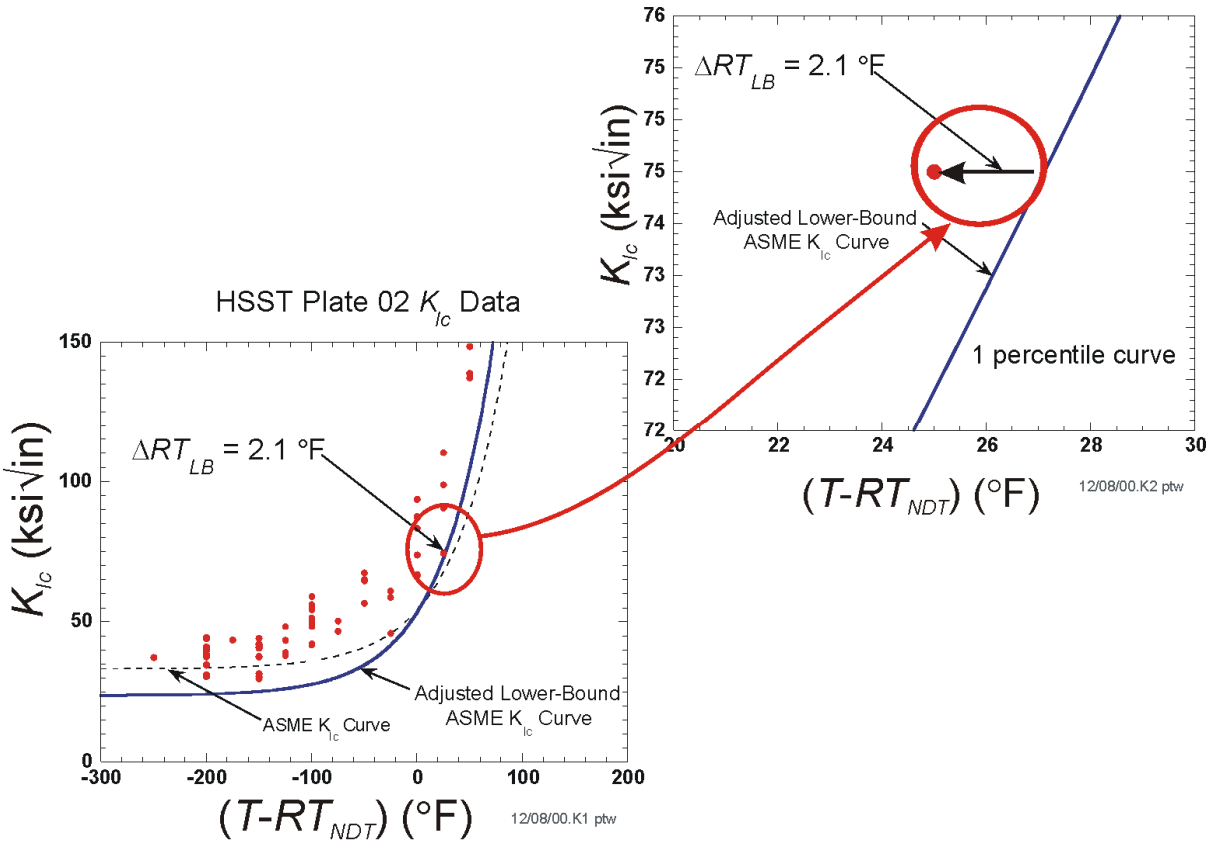

Fig. 37. The ΔRT_{LB} for HSST Plate 02. The lower-bounding transition reference temperature, RT_{LB}, was developed from 18 materials in the ORNL 99/27 database, where for each material $RT_{LB} = RT_{NDT0} - \Delta RT_{LB}$.

Table 13. Values of Lower-Bounding Reference Temperature with and without Sample-Size Adjustment: ORNL 99/27 Database

Material Description	Product Form	Sample Size, N	Reference Temperatures					Uncertainty Terms	
			$RT_{NDT(0)}$ (°F)	T_0 (°F)	RT_{LB}^{*} (°F)	*Size Correct.* (°F)	RT_{LB}^{**} (°F)	$RT_{NDT(0)} - T_0$ (°F)	$\Delta RT_{epistemic}^{**}$ (°F)
HSST 01	Weld	8	0	-105	-75.2	10.9	-64.3	105	64.3
A533 Cl. 1	Weld	8	0	-57	0	10.9	10.9	57	-10.9
HSST 01	Plate	17	20	-1	-82.4	4.6	-77.8	21	97.8
HSST 03	Plate	9	20	-21	-81.1	9.6	-71.5	41	91.5
A533 Cl. 1	Plate	13	65	-74	-127.6	6.4	-121.2	139	186.2
HSST 02	Plate	69	0	-17	-2.1	0	-2.1	17	2.1
A533B	Weld	10	-45	-151	-195.7	8.5	-187.2	106	142.2
A533B	weld/HAZ	6	0	-132	-176.9	14.5	-162.4	132	162.4
A508 Cl. 2	Forging	12	50	-124	-104.5	6.9	-97.6	174	147.6
A508 Cl. 2	Forging	9	51	-60	-8.7	9.6	0.9	111	50.1
A508 Cl. 2	forging	10	65	-55	1.9	8.5	10.4	120	54.6
HSSI 72W	weld	12	-9.4	-70	3.6	6.4	10.0	60.6	-19.4
HSSI 73W	weld	10	-29.2	-78	-76.1	8.5	-67.6	48.8	38.4
HSST 13A	plate	43	-9.4	-109	-43.5	0.9	-42.6	99.6	33.2
A508 Cl. 3	forging	6	-13	-46	-25.8	14.5	-11.3	33	-1.7
Midland Nozzle	weld	6	52	-34	-51.9	14.5	-37.4	86	89.4
Midland Beltline	weld	2	23	-71	-99.7	40.8	-58.9	94	81.9
Plate 02 4th Irr.	plate	4	0	-8	-83.8	21.5	-62.3	8	62.3

RT_{LB}^{*} = lower-bounding reference temperature without sample-size adjustment

RT_{LB}^{**} = lower-bounding reference temperature with sample-size adjustment

$$\Delta RT_{epistemic}^{**} = RT_{NDT(0)} - RT_{LB}^{**}$$

The adjusted ASME lower-bounding curve shown in Fig. 37 has the following form:

$$K_{Ic} = 23.65 + 29.56\exp\left[0.02(T - RT_{NDT})\right] \ \text{ksi}\sqrt{\text{in.}} \tag{101}$$

with $(T - RT_{NDT})$ in °F. The adjustment for sample size indicated in Table 13 assumes that Eq. (101) represents a 0.01 fractile. The $RT_{NDT(0)} - T_0$ CDF (Figs. 35 and 38) is a Weibull distribution with a flaw-size dependence

$$(RT_{NDT(0)} - T_0) \leftarrow W(a_{xT}, 100.43, 2.036)$$

$$a_{xT} = a_{1T} - \frac{1.8}{0.019}\ln\left[\frac{80\left(B_{xT}/B_{1T}\right)^{1/4} - 10}{70}\right] \ [°\text{F}]$$

$$a_{1T} = -8.28 \ °\text{F} \tag{102}$$

B_{xT} = flaw length [in.]

B_{1T} = 1.0 in.

The lower-bounding CDF, Eq. (103), quantifies the epistemic uncertainty in RT_{NDT} in a manner fully consistent with the constraints placed on the toughness models used in the PTS re-evaluation effort. In Fig. 38, we also compare this quantification of epistemic uncertainty with that based on the Master Curve. This comparison illustrates that the implicit treatment of size effects adopted when developing the alternative CDF using ASTM E-399 valid data produces a result quite similar in form to that based on the Master Curve. The similarity of the alternative CDF to the Master Curve-based CDF provides a link between the RT_{LB} concept developed to conform to the requirements of the PTS re-evaluation and the physical and empirical underpinnings of the Master Curve, thereby demonstrating that aleatory and epistemic uncertainties can be reasonably distinguished using RT_{LB} and $\Delta RT_{epistemic}$. The epistemic uncertainty in the unirradiated value of $RT_{NDT(0)}$ is estimated by sampling from the following Weibull distribution (see Appendix F for details on the development of Eq. (103)):

$$\widehat{\Delta RT}_{epistemic} \leftarrow W(-29.5, 78.0, 1.73)$$
$$\widehat{\Delta RT}_{epistemic} = -29.5 + 78.0\left[-\ln\left(1-\Phi\right)\right]^{1/1.73} \quad [°\mathrm{F}] \qquad (103)$$
$$\text{where } \Phi \leftarrow \mathrm{U}(0,1)$$

Combined with the sampled irradiation-shift term described in Sect. 5.2.2, the irradiated value of $\widehat{RT_{NDT}}$ is calculated by

$$\widehat{RT}_{NDT}(r,\ldots) = \widehat{RT}_{NDT(0)} - \widehat{\Delta RT}_{epistemic} + \widehat{\Delta RT}_{NDT}(r,\ldots) \qquad (104)$$

where $\widehat{RT}_{NDT0} \leftarrow N(\overline{RT}_{NDT0}, \sigma_{RT_{NDT0}})$ and $\widehat{RT_{NDT}}$ is a function of the position of the crack tip due to the attenuation of the fast-neutron fluence at position r in the vessel wall.

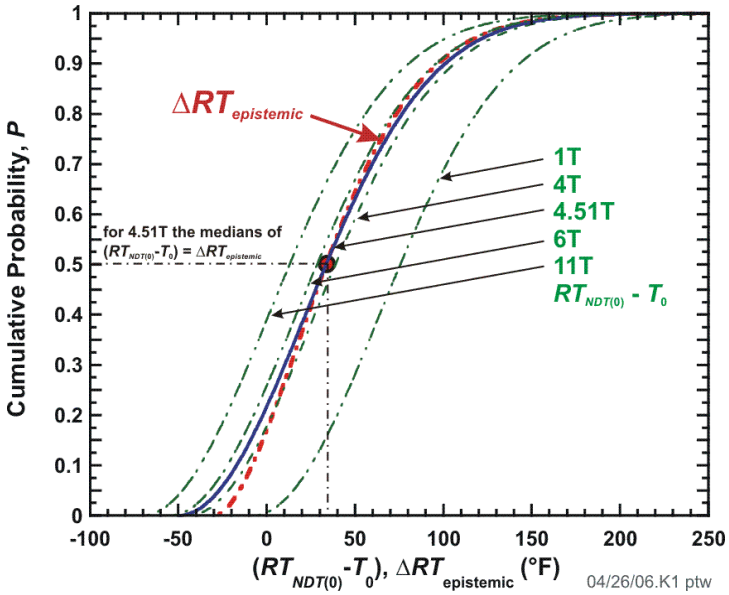

Fig. 38. Comparison of cumulative distribution functions developed for $RT_{NDT(0)}$-T_0 and $RT_{NDT(0)}$-RT_{LB} .

5.2.6 Index Temperature RT_{Arrest} – Uncertainty Classification and Quantification

To enable all commercial operators of pressurized water reactors to assess the state of their RPV relative to new PTS screening criteria without the need to make new material property measurements, the arrest fracture toughness of the RPV needs to be estimated using only currently available unirradiated $RT_{NDT(0)}$ values. These restrictions suggest that very limited information, specifically a value of $RT_{NDT(0)}$, is available to define the arrest fracture-toughness model appropriate to a particular steel in a particular RPV. Consequently, the temperature dependency and uncertainty of the arrest fracture-toughness model will either have to be demonstrated or assumed to be invariant over a wide range of conditions because sufficient information is not available to establish these features on a heat-specific basis [133].

The information presented in [133] suggests that a relevant arrest reference temperature can be defined based on (a) an index temperature that defines the position of the plane-strain crack arrest toughness, K_{Ia} , transition curve on the temperature axis and (b) a relationship between the index temperatures for the initiation and arrest fracture-toughness curves (assuming such a relationship exists). For this study, the temperature dependency of K_{Ia} data was assumed to be universal to all reactor pressure vessel steels, or, more specifically, within this class of materials the temperature dependency was assumed to be insensitive to all individual and combined effects of alloying, heat treatment (and other thermal processing), mechanical processing, and irradiation. These material variables only influence the temperature range over which a particular steel experiences a transition from brittle behavior (at low temperatures) to ductile behavior (at higher temperatures), this being quantified by a heat-specific index temperature value. Furthermore, the information presented in [133] suggests that the relationship between the index temperatures for crack initiation and crack arrest toughness is also not expected to be influenced strongly by heat-specific factors.

From [133]:

> **Crack arrest occurs when dislocations can move faster than the crack propagates, resulting in crack tip blunting and arrest. Dislocation mobility therefore controls the ability of a ferritic steel to arrest a running cleavage crack, and thus its crack arrest toughness. The atomic lattice structure is the only feature of the material that controls the temperature dependence of the material properties that are controlled by dislocation motion. Consequently, as was the case for crack initiation toughness, the temperature dependency of crack arrest toughness depends only on the short-range barriers to dislocation motion established by the BCC lattice structure. Other features that vary with steel composition, heat treatment, and irradiation include grain size/boundaries, point defects, inclusions, precipitates, and dislocation substructures. These features all influence dislocation motion, and thereby both strength and toughness, but their large inter-barrier spacing relative to the atomic scale associated with the lattice structure makes these effects completely athermal.**

This understanding suggests that the myriad of metallurgical factors that can influence absolute strength and toughness values, and thereby the transition temperature, exert no control over the temperature dependency of arrest toughness in fracture mode transition. Additionally, since K_{Ic} and K_{Ia} both depend on the ability of the material to absorb energy via dislocation motion, K_{Ic} and K_{Ia} are both expected to exhibit a similar temperature dependence.

As described in [133], a strong physical basis supports a temperature dependency in arrest fracture-toughness data that is universal to all ferritic steels; this temperature dependence has a similar functional form to that of crack-initiation toughness. Mathematically, Wallin and co-workers proposed [152,153]:

$$K_{Ia(mean)} = 30 + 70\exp\left[0.019\left(T - T_{KIa}\right)\right] \quad [\mathrm{MPa}\sqrt{\mathrm{m}}] \tag{105}$$

where $(T - T_{KIa})$ is in °C. Equation (105) describes the temperature (T) dependency of the mean arrest toughness ($K_{Ia(mean)}$). In this equation, temperature is normalized to the index temperature T_{KIa}, where T_{KIa} is defined as the temperature at which the mean arrest toughness is 100 $\mathrm{MPa}\sqrt{\mathrm{m}}$ (91 $\mathrm{ksi}\sqrt{\mathrm{in.}}$). Wallin found that a lognormal distribution having a lognormal standard deviation of 0.18 fits the extensive database used in his study.

The physical understanding of the relationship between crack initiation and crack arrest presented in [133] suggests that the temperature separation between the K_{Ic} and K_{Ia} transition curves should progressively diminish as the material is hardened (e.g. by cold work, irradiation, etc.). Available empirical evidence supports this expectation, as illustrated in Fig. 39. An exponentially decaying functional form for the mean was selected to represent these data, because this relationship had the mathematical form anticipated from physical considerations (i.e. the separation between the K_{Ic} and K_{Ia} curves diminishes as T_o increases). This nonlinear regression fit was:

$$\Delta RT_{ARREST(mean)} \equiv T_{K_{Ia}} - T_o = 44.123 \cdot \exp\left\{-0.006T_0\right\} \quad [°\mathrm{C}] \tag{106}$$

where ΔRT_{ARREST} is distributed lognormally about the mean given by Eq. (106), with an estimated log-normal standard deviation of 0.39 (see Fig. 40). Table 14 presents several reference-transition temperature indices for the steels in the ORNL 99/27 K_{Ia} database including $\overline{RT}_{Arrest}$ calculated from Eq. (106).

Table 14. ORNL 99/27 K_{Ia} Database – Reference-Transition Temperatures

Material ID	Product Form	Sample Size	RT_{NDT0} (°F)	RT_{LB} (°F)	T_0 (°F)	RT_{Arrest} (°F)	T_{KIa} (°F)
HSST-02	Plate	50	0	-2.1	-17	76.8	75.2
72W	Weld	32	-9.4	-42.6	-70	49.8	8.6
73W	Weld	26	-29.2	-67.6	-78	34.1	6.8
Midland	Weld	4	32.2	-58.9	NA	NA	NA

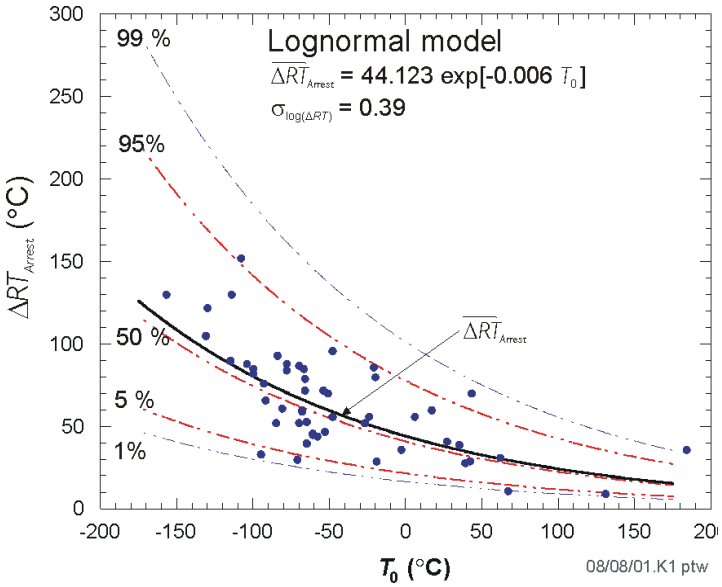

Fig. 39. Lognormal distribution of $\Delta RT_{ARREST} = T_{K_{Ia}} - T_0$ as a function of T_0

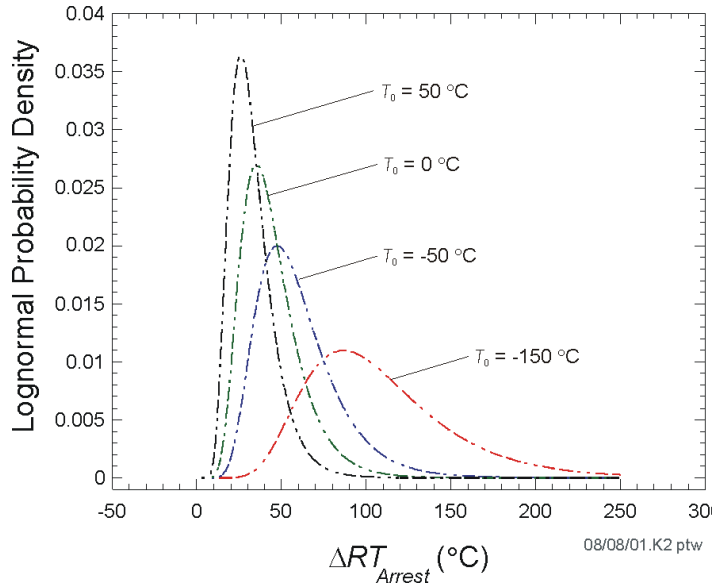

Fig. 40. Lognormal probability densities for ΔRT_{Arrest} as function of T_0.

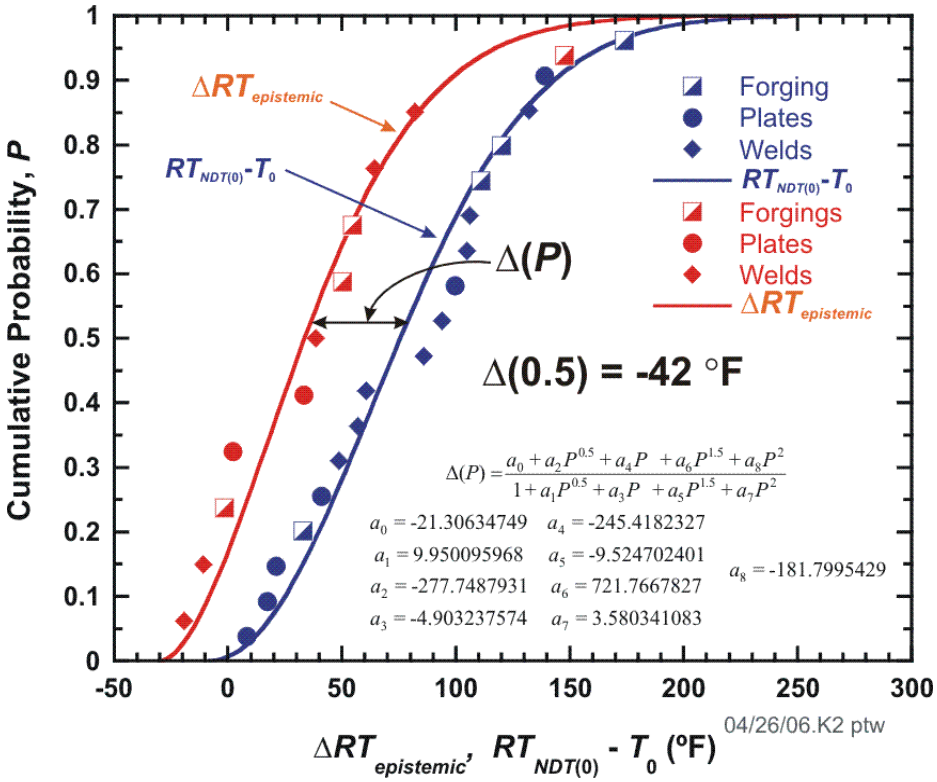

Fig. 41. Proposed adjustment to RT_{LB} arises from observed offset between $\Delta RT_{epistemic}$ CDF and $RT_{NDT} - T_0$ CDF.

An approximate connection between T_0 and the initiation reference temperature RT_{LB} can be established from the offset of -42 °F between the medians of the $\Delta RT_{epistemic}$ CDF and the $RT_{NDT(0)}$-T_0 CDF, as can be observed in Fig. 41. This observation allows us to apply Eq. (106) to develop an estimate for the epistemic uncertainty in the arrest reference temperature linked to the sampled epistemic uncertainty in the initiation reference temperature.

$$\overline{\Delta RT}_{epist-arrest} = \overline{\Delta RT}_{epistemic(\Phi)} + \Delta\left(\overline{\Phi}\right) \quad [°\mathrm{F}] \tag{107}$$

where $\overline{\Delta RT}_{epistemic}$ has been sampled previously at a probability of Φ from the distribution given by Eq. (103). For better computational efficiency, the function $\Delta(P)$ has been implemented into FAVOR, v07.1, as a curve fit based the following rational function

$$\left[\Delta RT_{epistemic} - \left(RT_{NDT(0)} - T_0\right)\right] = \Delta(P) \equiv$$

$$-29.5 + 78.0\left[-\ln(1-P)\right]^{1/1.73} + 8.28 - 100.43\left[-\ln(1-P)\right]^{1/2.036} \approx \tag{108}$$

$$\approx \frac{a_0 + a_2\sqrt{P} + a_4 P + a_6 P\sqrt{P} + a_8 P^2}{1 + a_1\sqrt{P} + a_3 P + a_5 P\sqrt{P} + a_7 P^2} \quad [°\mathrm{F}]$$

where

$a_0 = -21.30634749$ $a_3 = -4.903237574$ $a_6 = 721.7667827$

$a_1 = 9.950095968$ $a_4 = -245.4182327$ $a_7 = 3.580341083$

$a_2 = -277.7487931$ $a_5 = -9.524702401$ $a_8 = -181.7995429$

The sampled arrest reference temperature can now be calculated by

$$\widehat{RT}_{ARREST}(r,\ldots) = \widehat{RT_{NDT0}} - \widehat{\Delta RT}_{epist-arrest} + \widehat{\Delta RT}_{ARREST} + \widehat{\Delta RT_{NDT}}(r,\ldots) \tag{109}$$

where $\widehat{RT_{NDT0}}$, $\widehat{\Delta RT}_{epist-arrest}$, and $\widehat{\Delta RT_{NDT}}(r,\cdots)$ have not been re-sampled from their initiation values and $\widehat{\Delta RT}_{ARREST} \leftarrow \Lambda(\widehat{\mu}_{\ln(\Delta RT_{ARREST})}, \widehat{\sigma}_{\ln(\Delta RT_{ARREST})})$ is sampled from the following lognormal distribution:

$$\widehat{\mu}_{\ln(\Delta RT_{ARREST})} = \ln\left[\widehat{\Delta RT}_{ARREST(mean)}\right] - \frac{\widehat{\sigma}^2_{\ln(\Delta RT_{ARREST})}}{2}$$

where

$$\widehat{T_0} = \left(\widehat{RT}_{NDT_0} - \widehat{\Delta RT}_{epist-arrest} - 32\right)/1.8 \ \ [°\text{C}]$$

$$\widehat{\Delta RT}_{ARREST(mean)} = 44.122\exp\left[-0.005971 \times \widehat{T_0}\right] \ \ [°\text{C}] \tag{110}$$

$$\widehat{\sigma}_{\ln(\Delta RT_{ARREST})} = \sqrt{\ln\left\{\exp\left[0.38998^2 + 2\ln(\widehat{\Delta RT}_{ARREST(mean)})\right] - \text{var}\left(\widehat{T_0}\right)\right\} - 2\ln\left[\widehat{\Delta RT}_{ARREST(mean)}\right]}$$

where

$$\text{var}(\widehat{T_0}) = \begin{cases} (12.778)^2 & \text{for } \widehat{T_0} < -35.7 \ °\text{C} \\ 99.905972 - 1.7748073\widehat{T_0} & \text{for } -35.7 \ °\text{C} \le \widehat{T_0} \le 56 \ °\text{C} \\ 0 & \text{for } \widehat{T_0} > 56 \ °\text{C} \end{cases}$$

and $\widehat{\Delta RT}_{ARREST}$ is sampled from (see Step 11 in Sect. 5.5)

$$\widehat{\Delta RT}_{ARREST} = 1.8\exp\left[\widehat{\sigma}_{\ln(\Delta RT_{Arrest})}\widehat{Z_{P_f}} + \widehat{\mu}_{\ln(\Delta RT_{Arrest})}\right] \ \ [°\text{F}]$$

$\widehat{Z_{P_f}} \leftarrow N(0,1)$; $\widehat{Z_{P_f}}$ is the standard normal deviate corresponding to the $\widehat{P_f}$ fractile $(0 < \widehat{P_f} < 1)$ for this trial in the crack *Initiation - Growth - Arrest* model.

See Appendix F for the details of the development of Eq. (110).

5.2.7 Plane-Strain Static Cleavage Initiation Toughness – K_{Ic}

Using the K_{Ic} data in the ORNL 99/27 fracture-toughness database (see Fig. 42) and the new lower-bounding reference temperature, RT_{LB}, a statistical model based on a Weibull distribution was developed by applying the statistical procedures given in [89]. The cumulative distribution function (CDF) for the Weibull model has the following form:

$$\Pr(K_{Ic} < K_I) = \Phi_{K_{Ic}}(K_I \mid \widehat{a_{K_{Ic}}}, \widehat{b_{K_{Ic}}}) = \begin{cases} 0; & K_I \le a_{K_{Ic}} \\ 1 - \exp\left[-\left(\dfrac{K_I - a_{K_{Ic}}(\widehat{\Delta T}_{RELATIVE})}{b_{K_{Ic}}(\widehat{\Delta T}_{RELATIVE})} \right)^{c_{K_{Ic}}} \right]; & a_{K_{Ic}} < K_I < \infty \end{cases} \quad (111)$$

where the inverse CDF or percentile function is given by

$$K_{Ic}(\widehat{\Delta T}) = \widehat{a_{K_{Ic}}}(\widehat{\Delta T}) + \widehat{b_{K_{Ic}}}(\widehat{\Delta T})\left[-\ln(1 - \Phi_{K_{Ic}}) \right]^{1/c_{K_{Ic}}} \quad \text{for } 0 < \Phi_{K_{Ic}} < 1$$
$$\text{for } a \le K_{Ic} \le K_{Ic(\max)} \quad (112)$$

where the bounding value of $K_{Ic(\max)}$ is input by the user to FAVOR (typically $K_{Ic(\max)}$ = 200 ksi$\sqrt{\text{in.}}$). The parameters of the distribution are

$$a_{K_{Ic}}(\widehat{\Delta T}_{RELATIVE}) = 19.35 + 8.335\exp\left[0.02254(\widehat{\Delta T}_{RELATIVE}) \right] \text{ [ksi}\sqrt{\text{in.}}\text{]}$$
$$b_{K_{Ic}}(\widehat{\Delta T}_{RELATIVE}) = 15.61 + 50.132\exp\left[0.008(\widehat{\Delta T}_{RELATIVE}) \right] \text{ [ksi}\sqrt{\text{in.}}\text{]} \quad (113)$$
$$c_{K_{Ic}} = 4$$

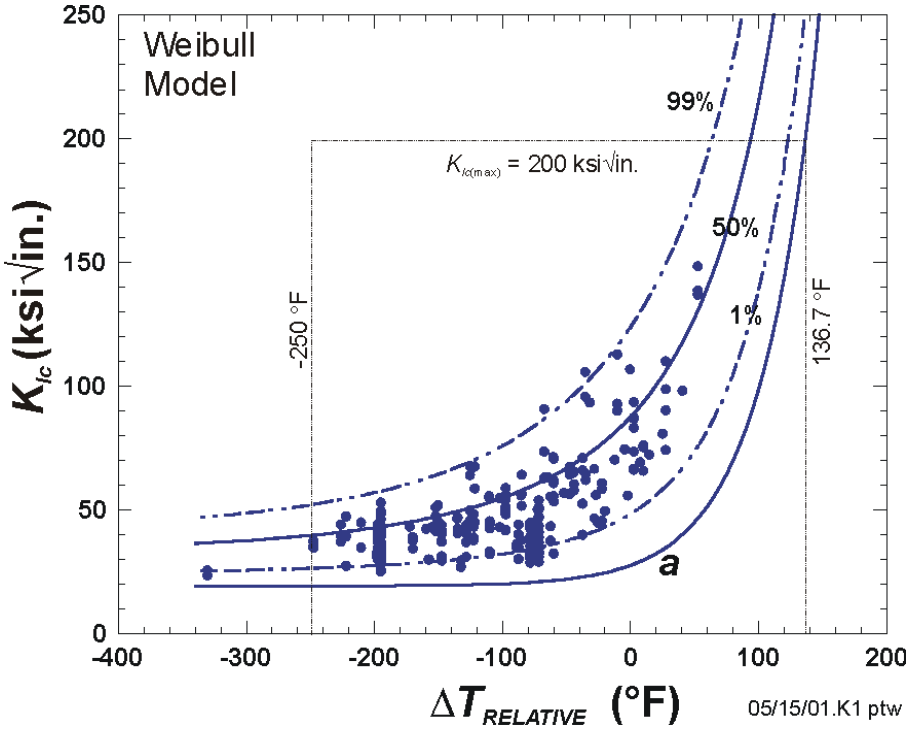

Fig. 42. Weibull statistical distribution for plane-strain cleavage initiation fracture toughness, K_{Ic}, with prescribed validity bounds. The ORNL 99/27 K_{Ic} database was used in the construction of the model.

with K_{Ic} in ksi$\sqrt{}$in and $\widehat{\Delta T_{RELATIVE}} = T(\tau) - \widehat{RT_{NDT}}(r,\cdots)$ in °F. Note that this Weibull statistical model describes the *aleatory* uncertainty in the plane-strain static initiation fracture toughness, since it is assumed that the *epistemic* uncertainty has been quantified by the sampled $\widehat{\Delta RT}_{epistemic}$ value in Eq. (103)

5.2.8 Plane-Strain Crack Arrest Toughness – K_{Ia}

Two lognormal distributions (see Fig. 43) are available in FAVOR to describe the aleatory uncertainty in the plane-strain crack arrest toughness, K_{Ia}. For a lognormal distribution with random variate, x, the cumulative distribution function is expressed by

$$\begin{aligned} \Pr\{X \le x\} &= \frac{1}{\sigma x\sqrt{2\pi}} \int_{-\infty}^{\ln(x)} \exp\left[-\left(\frac{(\xi-\mu)^2}{2\sigma^2}\right)\right] \mathrm{d}\xi = \\ \Phi\left(\frac{\ln(x)-\mu}{\sigma}\right) &= \frac{1}{\sqrt{2\pi}} \int_{-\infty}^{(\ln(x)-\mu)/\sigma} \exp\left[-\frac{\varsigma^2}{2}\right] \mathrm{d}\varsigma \end{aligned} \tag{114}$$

The function Φ can be evaluated numerically through its relation to the *error function*, erf(x), such that for a given applied stress intensity factor, K_I, and normalized temperature, $\Delta T = T\text{-}RT_{Arrest}$,

$$\Pr\left\{K_{Ia} \le K_I\right\} = \Phi_{K_{Ia}}\left(\frac{\ln(K_I) - \mu_{\ln(K_{Ia})}(\Delta T)}{\sigma_{\ln(K_{Ia})}}\right) = \frac{1}{2}\left[\mathrm{erf}\left(\frac{\ln(K_I) - \mu_{\ln(K_{Ia})}(\Delta T)}{\sigma_{\ln(K_{Ia})}\sqrt{2}}\right) + 1\right] \tag{115}$$

where $\Phi_{K_{Ia}}$ is now the cumulative probability of crack extension and the error function (a special case of the incomplete gamma function, $\Gamma_0\left(a, x^2\right)$) is defined by

$$\begin{aligned} \Gamma_0\left(0.5, x^2\right) &= \mathrm{erf}(x) = \frac{2}{\sqrt{\pi}} \int_0^x \exp(-\xi^2)\, \mathrm{d}\xi \\ \mathrm{erf}(-x) &= -\mathrm{erf}(x) \end{aligned} \tag{116}$$

The inverse CDF for the lognormal distribution allows sampling of K_{Ia} by

$$\begin{aligned} K_{Ia}(\widehat{\Phi}_{K_{Ia}}, \widehat{\Delta T}_{RELATIVE}) &= \exp\left[\sigma_{\ln(K_{Ia})} \widehat{Z}_{\Phi K_{Ia}} + \mu_{\ln(K_{Ia})}(\widehat{\Delta T}_{RELATIVE})\right] \\ \widehat{Z}_{\Phi_{K_{Ia}}} &= \text{ standard normal deviate} \\ &\qquad \text{corresponding to the } \widehat{\Phi}_{K_{Ia}} \text{ fractile} \\ \widehat{\Phi}_{K_{Ia}} &\leftarrow U(0,1) \end{aligned} \tag{117}$$

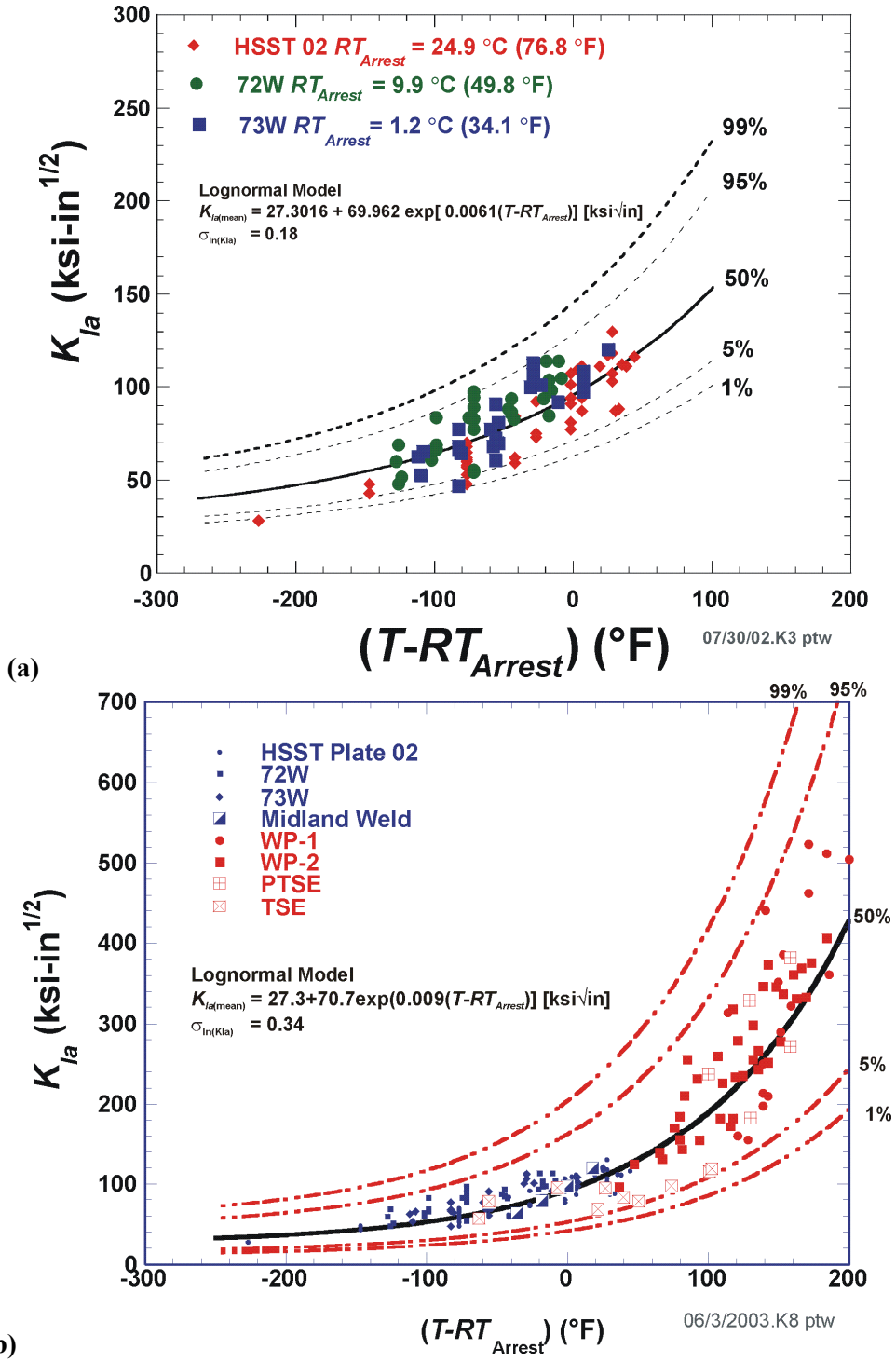

Fig. 43. Lognormal statistical distribution for plane-strain crack arrest fracture toughness, K_{Ia}, constructed using the (a) Model 1: ORNL 99/27 K_{Ia} database normalized by the arrest reference temperature, RT_{Arrest} and (b) Model 2: Extended K_{Ia} database normalized by the arrest reference temperature, RT_{Arrest}.

Model 1 is based on the ORNL 99/27 K_{Ia} database of 112 data points which were taken using CCA specimens. The parameters of the Model 1 K_{Ia} lognormal distribution, shown in Fig. 43(a), are

$$\mu_{\ln(K_{Ia})}(\widehat{\Delta T}_{RELATIVE}) = \ln\left[\bar{K}_{Ia}(\widehat{\Delta T}_{RELATIVE})\right] - \frac{\sigma^2_{\ln(K_{Ia})}}{2}$$

where

$$\sigma_{\ln(K_{Ia})} = 0.18 \tag{118}$$

$$K_{Ia(\text{mean})}(\widehat{\Delta T}_{RELATIVE}) = 27.302 + 69.962\exp\left[0.006057(\widehat{\Delta T}_{RELATIVE})\right] \quad [\text{ksi}\sqrt{\text{in.}}]$$

$$\widehat{\Delta T}_{RELATIVE} = T(r,\tau) - \widehat{RT_{Arrest}}(r,\cdots) \quad [°\text{F}]$$

The equation for the mean was developed by nonlinear regression of the data shown in Fig. 43(a). Model 1 is recommended to be used when the ductile-tearing model is not activated, and an upper bound for K_{Ia} of 200 $\text{ksi}\sqrt{\text{in.}}$ should be set in the FAVPFM input file.

Model 2 is based on the Extended K_{Ia} database of 183 data points which were taken using both CCA specimens and Large-Specimen experiments. The parameters of the Model 2 K_{Ia} lognormal distribution, shown in Fig. 43b, are

$$\mu_{\ln(K_{Ia})}(\widehat{\Delta T}_{RELATIVE}) = \ln\left[\bar{K}_{Ia}(\widehat{\Delta T}_{RELATIVE})\right] - \frac{\sigma^2_{\ln(K_{Ia})}}{2}$$

where

$$\sigma_{\ln(K_{Ia})} = 0.34 \tag{119}$$

$$K_{Ia(\text{mean})}(\widehat{\Delta T}_{RELATIVE}) = 27.302 + 70.6998\exp\left[0.008991(\widehat{\Delta T}_{RELATIVE})\right] \quad [\text{ksi}\sqrt{\text{in.}}]$$

$$\widehat{\Delta T}_{RELATIVE} = T(r,\tau) - \widehat{RT_{Arrest}}(r,\cdots) \quad [°\text{F}]$$

Model 2 will be automatically selected when the ductile-tearing model is activated, and any specified upper bound on K_{Ia} is ignored.

5.2.9 Material Chemistry – Sampling Protocols

FAVOR treats the vessel beltline as a collection of major regions of plates, forgings, and welds. These major regions are then discretized into subregions, where, within a given subregion, flaws are analyzed through Monte Carlo *realizations* of the RPV subjected to the PTS transients under study.

As input data, FAVOR requires estimated chemistry (Cu, Mn, Ni, and P) content values for each plate, forging, and weld major region used to model the beltline of the vessel. The user will, therefore, input best-heat estimates for each major region designated as HE_{Cu}, HE_{Mn}, HE_{Ni}, and HE_P in wt%. The material chemistry sampling protocols distinguish between the first flaw simulated in a subregion, designated as *Flaw*1, and all subsequent flaws in the subregion, designated as *Flawx*. The plate, forging, or weld chemistry for the set of *Flawx's* will be perturbations of the sampled *Flaw*1 chemistry for this subregion. This variation in chemistry is intended to simulate *local variability* in the subregion chemistry.

Plate and Forging Subregion Chemistry

Flaw1

The Cu, Mn, Ni, and P content (expressed in wt%) for the first flaw in a plate/forging subregion are sampled at the subregion level from the following normal distributions:

$$\begin{aligned} \widehat{Cu}_{Flaw1} &\leftarrow N(HE_{Cu}, \sigma_{Cu}) \\ \widehat{Ni}_{Flaw1} &\leftarrow N(HE_{Ni}, \sigma_{Ni}) \\ \widehat{P}_{Flaw1} &\leftarrow N(HE_P, \sigma_P) \\ \widehat{Mn}_{Flaw1} &\leftarrow N(HE_{Mn}, \widehat{\sigma}_{Mn}) \end{aligned} \tag{120}$$

where the recommended standard deviations are

$$\begin{aligned} &\sigma_{Cu} = 0.0073 \text{ wt\% for plates and forgings} \\ &\sigma_{Ni} = 0.0244 \text{ wt\% for plates and forgings} \\ &\sigma_P = 0.0013 \text{ wt\% for plates and forgings} \\ &\widehat{\sigma}_{Mn} \leftarrow \begin{cases} W(0, 0.06933, 2.4708) & \text{wt\% in plates} \\ J_{SB}(0.00163, 0.03681, 0.83358, 1.15153) & \text{wt\% in forgings} \end{cases} \end{aligned} \tag{121}$$

The triplet $(\sigma_{Cu}, \sigma_{Ni}, \sigma_P)$ is supplied by the user in the input file for the FAVPFM module and applied as constant values for all plate/forging major regions. The standard deviation for Mn, $\widehat{\sigma}_{Mn}$, is sampled for each plate/forging major region in Sampling Block 1 (once for each *RPV* trial; see Fig. 16) using distributions derived from data given in Table 15.

Table 15. Data on Mn Used to Construct Global/Local Variability Distributions

Reference	Data ID	Product Form	Type of Variability	Sample Size	Mean wt %	Standard Deviation wt %
NUREG/CR-4092	Plate 01-K	Plate	Global	9	1.356	0.0950
	Plate 01-MU	Plate	Global	3	1.403	0.0320
	Plate 02-FB	Plate	Global	3	1.49	0.0100
	Plate 03-E	Plate	Global	5	1.348	0.0520
EPRI NP-373	B, OS, F1	Forging	Local	4	0.648	0.0050
	B, 1/4, F1	Forging	Local	5	0.644	0.0050
	A, 1/2, F1	Forging	Local	5	0.636	0.0110
	A, 3/4, F1	Forging	Local	4	0.648	0.0100
	A, IS, F1	Forging	Local	4	0.65	0.0080
	All F1 Data	Forging	Global	22	0.645	0.0090
	B, OS, F2	Forging	Local	2	0.72	0.0140
	B, 1/4, F2	Forging	Local	3	0.737	0.0060
	A, 1/2, F2	Forging	Local	3	0.74	0.0170
	A, 3/4, F2	Forging	Local	3	0.76	0.0100
	All F2 Data	Forging	Global	13	0.736	0.0200
	Flux A	Weld	Global	15	1.415	0.0210
	Flux B	Weld	Global	11	1.554	0.0480
	B, OS, W	Weld	Local	10	1.548	0.0280
	B, 1/4, W	Weld	Local	9	1.494	0.0170
	A, 1/2, W	Weld	Local	6	1.445	0.0100
	A, 3/4, W	Weld	Local	4	1.423	0.0220
	A, IS, W	Weld	Local	2	1.39	0.0140
NUREG/CR-6413	A302B	Plate	Global	4	1.375	0.0370
	HSST-01	Plate	Global	16	1.392	0.0900
	HSST-02	Plate	Global	10	1.479	0.0530
	HSST-03	Plate	Global	6	1.333	0.0590
CE NPSD 944-P Rev. 2	27204-B03	Weld	Global	13	1.292	0.0380
	12008/13253-C08	Weld	Global	13	1.282	0.0780
	3P7317-T07	Weld	Global	13	1.452	0.0430
	90136-G11	Weld	Global	13	1.067	0.0340
	33A277-D08	Weld	Global	13	1.153	0.0380
	83637-N10	Weld	Global	13	1.509	0.0570
	10137-E08	Weld	Global	13	1.291	0.0480
	33A277-C19	Weld	Global	13	1.22	0.0550
	27204-B03	Weld	Local	5	1.264	0.0180
	12008/13253-C08	Weld	Local	5	1.266	0.0110
	3P7317-T07	Weld	Local	5	1.448	0.0130
	90136-G11	Weld	Local	5	1.096	0.0230
	33A277-D08	Weld	Local	5	1.162	0.0240
	83637-N10	Weld	Local	5	1.498	0.0080
	10137-E08	Weld	Local	5	1.274	0.0150
	33A277-C19	Weld	Local	5	1.184	0.0170
BAW-2220	10137	Weld	Global	20	1.132	0.0890
	21935	Weld	Global	7	1.489	0.0500
	20291/12008	Weld	Global	29	1.252	0.0790
	33A277	Weld	Global	38	1.136	0.0930
	10137	Plate	Global	12	1.259	0.0570
	21935	Plate	Global	7	1.404	0.0670
	20291/12008	Plate	Global	17	1.341	0.1010
	33A277	Plate	Global	24	1.348	0.0880

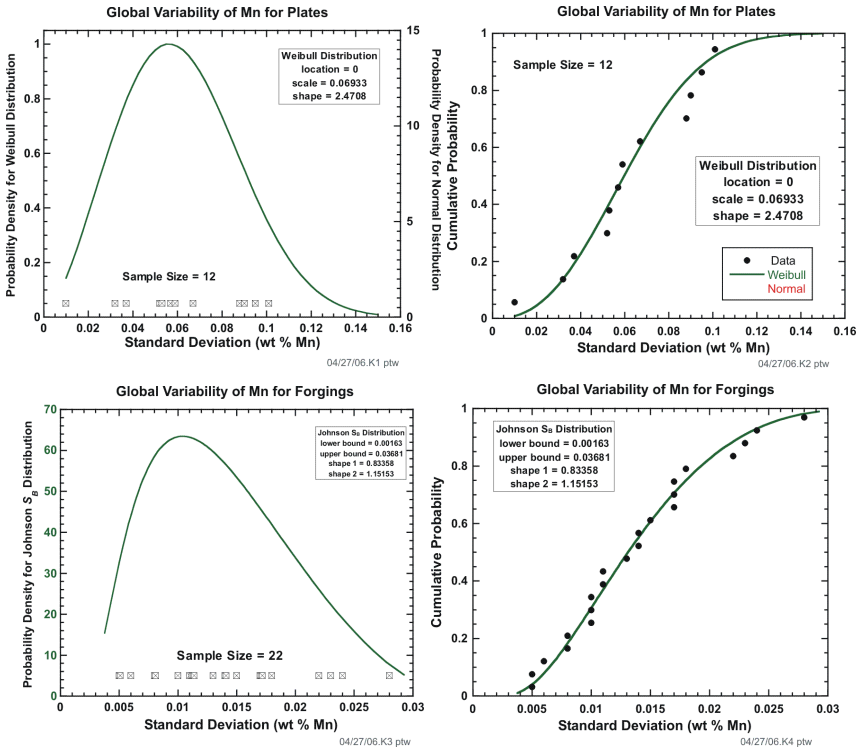

Negative values of sampled $\widehat{Cu}_{Flaw1}, \widehat{Ni}_{Flaw1}, \widehat{Mn}_{Flaw1},$ and $\widehat{P}_{Flaw1}$ are handled as nonphysical exceptions in FAVOR using the truncation protocol described in Sect. 4.3.6, with 0.0 applied as a one-sided truncation boundary.

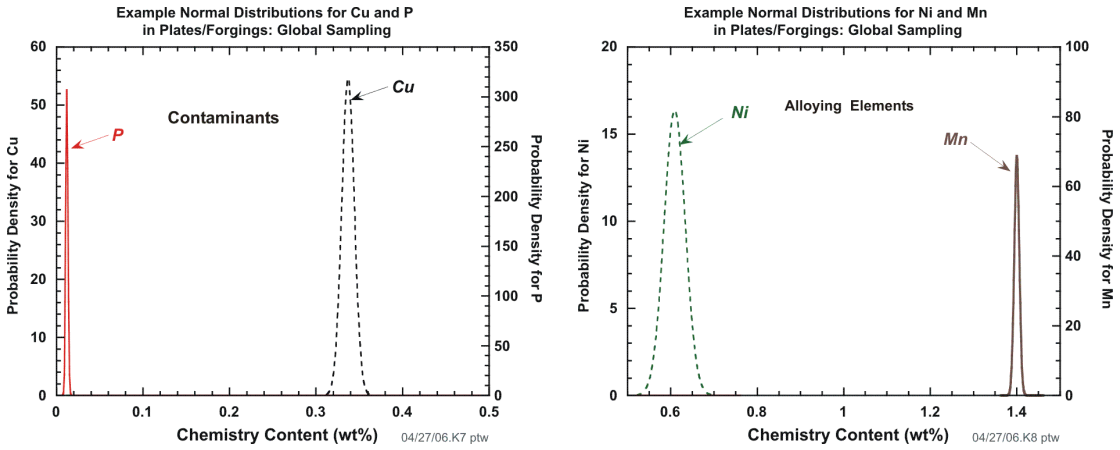

Flawx – local variability

All subsequent flaws in a given subregion should contain small local variability in Cu, Mn, Ni, and P content. This local variability is determined by sampling values from the following logistic, normal, and Johnson S_B distributions:

$$\begin{aligned}
\widehat{Cu}_{Flawx} &\leftarrow \widehat{Cu}_{Flaw1} + \widehat{\Delta_{Cu-Flawx}} \\
\widehat{Ni}_{Flawx} &\leftarrow \widehat{Ni}_{Flaw1} + \widehat{\Delta_{Ni-Flawx}} \\
\widehat{P}_{Flawx} &\leftarrow \widehat{P}_{Flaw1} + \widehat{\Delta_{P-Flawx}} \\
\widehat{Mn}_{Flawx} &\leftarrow N\left(\widehat{Mn}_{Flaw1}, \widehat{\sigma}_{Mn}\right)
\end{aligned} \tag{122}$$

$$\widehat{\Delta_{Cu-Flawx}} \leftarrow L\left(-3.89\times10^{-7}, 0.00191\right) = -3.89\times10^{-7} - 0.00191 \ln\left[\frac{1}{\widehat{\Phi}_{Cu}} - 1\right] \text{ for } \widehat{\Phi}_{Cu} \leftarrow U(0,1)$$

$$\widehat{\Delta_{Ni-Flawx}} \leftarrow L\left(-1.39\times10^{-7}, 0.00678\right) = -1.39\times10^{-7} - 0.00678 \ln\left[\frac{1}{\widehat{\Phi}_{Ni}} - 1\right] \text{ for } \widehat{\Phi}_{Ni} \leftarrow U(0,1)$$

$$\widehat{\Delta_{P-Flawx}} \leftarrow L\left(1.3\times10^{-5}, 0.000286\right) = 1.3\times10^{-5} - 0.000286 \ln\left[\frac{1}{\widehat{\Phi}_{P}} - 1\right] \text{ for } \widehat{\Phi}_{P} \leftarrow U(0,1) \tag{123}$$

$$\widehat{\sigma}_{Mn} \leftarrow J_{SB}\left(0.00163, 0.03681, 0.83358, 1.15153\right) =$$

$$= \frac{0.00163 + 0.03681 \exp\left[\dfrac{\widehat{Z}_i - 0.83358}{1.15153}\right]}{1 + \exp\left[\dfrac{\widehat{Z}_i - 0.83358}{1.15153}\right]} \text{ for } \widehat{Z}_i = \Phi^{-1}\left(\widehat{\Phi}_{Mn}\right);\ \widehat{\Phi}_{Mn} \leftarrow U(0,1)$$

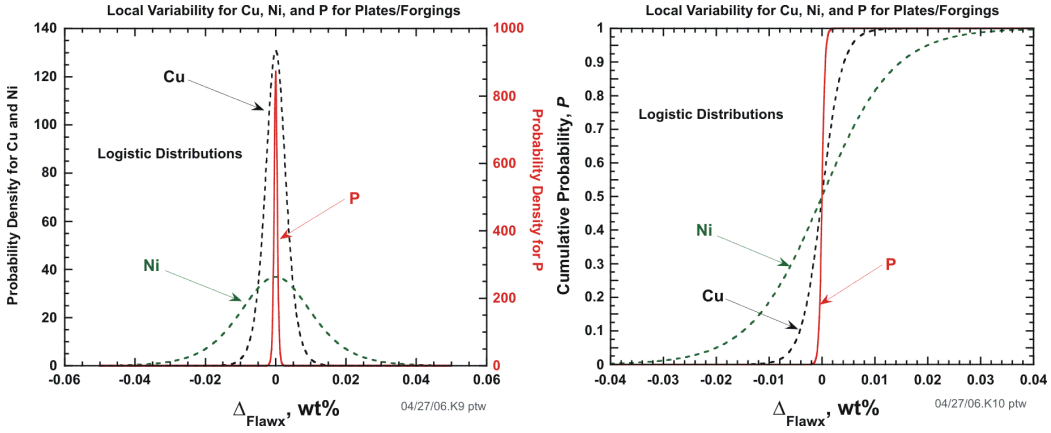

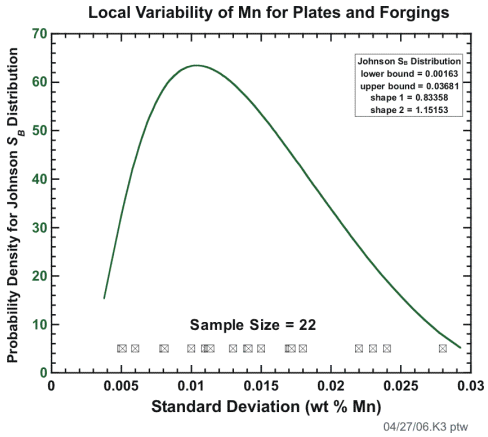

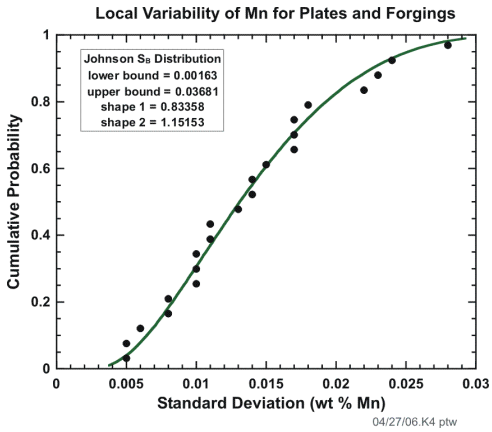

Negative values of sampled $\widehat{Cu}_{Flawx}$, $\widehat{Ni}_{Flawx}$, $\widehat{Mn}_{Flawx}$ and $\widehat{P}_{Flawx}$ are handled as nonphysical exceptions in FAVOR using the truncation protocol described in Sect. 4.3.6, with 0.0 applied as a one-sided truncation boundary.

Through-thickness sampling for plates

There is no resampling protocol for flaws growing through the thickness of plate subregions, which is consistent with the assumption that properties of the plate are homogeneous through the wall.

Weld Subregion Chemistry

Flaw1

Copper, Cu_{Flaw1}:

The Cu content for the first flaw in a weld subregion is sampled from a normal distribution with mean equal to the major-region heat estimate for Cu and a standard deviation sampled for each weld major region:

$$\begin{aligned} \widehat{Cu}_{Flaw1} &\leftarrow N(HE_{Cu}, \widehat{\sigma Cu}_{Flaw1}) \\ \widehat{\sigma Cu}_{Flaw1} &\leftarrow N\left(0.167 \times HE_{Cu},\ \min\left(0.0718 \times HE_{Cu}, 0.0185\right)\right) \end{aligned} \tag{124}$$

where HE_{Cu} is the best-heat-estimate value input for the given weld major region. To characterize global variability, the sampling for the major-region standard deviation for Cu, $\widehat{\sigma Cu}_{Flaw1}$, is done once for all major regions for each RPV trial in Sampling Block 1 (see Fig. 16).

Nickel, Ni_{Flaw1}:

Ni-addition welds (heats 34B009 and W5214)

The Ni content for the first flaw in a Ni-addition weld subregion is sampled from a normal distribution with mean equal to the heat estimate for Ni and standard deviation equal to a constant 0.162 wt%.

$$\widehat{Ni}_{Flaw1} \leftarrow N(HE_{Ni}, 0.162) \tag{125}$$

where HE_{Ni} is the best-heat-estimate value input for the given weld major region.

All other heats

The Ni content for the first flaw in a weld subregion is sampled from a normal distribution with mean equal to the heat estimate for Ni and standard deviation sampled from a normal distribution with mean equal to 0.029 wt% and standard deviation equal to 0.0165 wt%.

$$\begin{aligned} \widehat{Ni}_{Flaw1} &\leftarrow N(HE_{Ni}, \widehat{\sigma}_{Ni_{Flaw1}}) \\ \widehat{\sigma}_{Ni_{Flaw1}} &\leftarrow N(0.029, 0.0165) \end{aligned} \tag{126}$$

To characterize global variability, the sampling for the major-region standard deviation for Ni, $\widehat{\sigma}_{Ni_{Flaw1}}$, is done once for all major regions for each RPV trial in Sampling Block 1 (see Fig. 16).

Phosphorous, P_{Flaw1}:

The phosphorous content for the first flaw in a weld subregion is sampled from a normal distribution with mean equal to the input major-region heat estimate for phosphorous and standard deviation equal to 0.0013 wt %.

$$\widehat{P}_{Flaw1} \leftarrow N(HE_P, 0.0013) \tag{127}$$

Manganese, Mn_{Flaw1}:

The Mn content for the first flaw in a weld subregion is sampled from a normal distribution with mean equal to the input major-region heat estimate for Mn and a standard deviation sampled from a Weibull distribution for each weld major region:

$$\begin{aligned} \widehat{Mn}_{Flaw1} &\leftarrow N(HE_{Mn}, \widehat{\sigma}_{Mn_{Flaw1}}) \\ \widehat{\sigma}_{Mn_{Flaw1}} &\leftarrow W\left(0.01733, 0.04237, 1.83723\right) \end{aligned} \tag{128}$$

where HE_{Mn} is the best-heat-estimate value input for the given weld major region. To characterize global variability, the sampling for the major-region standard deviation for Mn, $\widehat{\sigma}_{Mn_{Flaw1}}$, is done once for all major regions for each RPV trial in Sampling Block 1 (see Fig. 16).

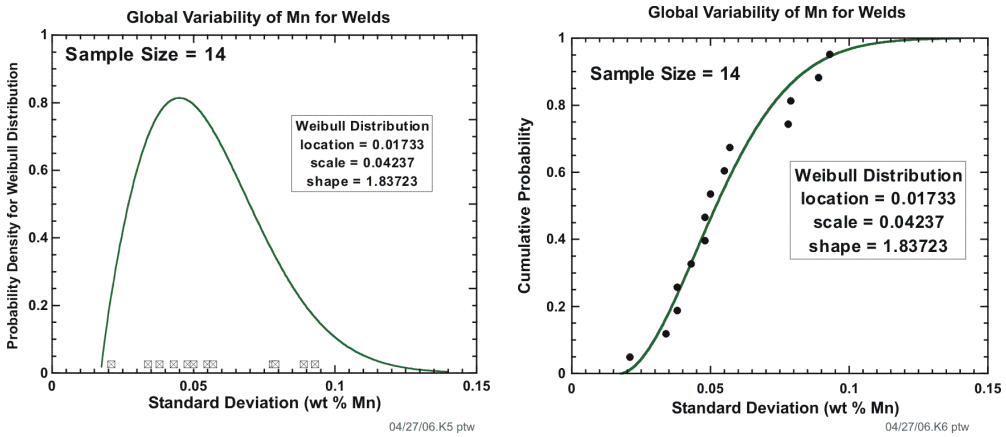

Negative values of sampled $\widehat{Cu}_{Flaw1}, \widehat{Ni}_{Flaw1}, \widehat{Mn}_{Flaw1}$, and $\widehat{P}_{Flaw1}$ are handled as nonphysical exceptions in FAVOR using the truncation protocol described in Sect. 4.3.6, with 0.0 applied as a one-sided truncation boundary.

Flawx – local variability

All subsequent flaws positioned in a given weld subregion should contain small *local variability* in Cu, Ni, Mn, and P content.

Copper, $\widehat{Cu}_{Flawx}$:

The local variability for Cu is determined by sampling a $\widehat{\Delta_{Cu}}$ value drawn from a logistic distribution with parameters $\alpha = 6.85\times10^{-8}$ and $\beta = 0.0072$ such that

$$\begin{aligned}
&\widehat{\Delta_{Cu\,Flawx}} \leftarrow L(6.85\times10^{-8}, 0.0072)\\
&\widehat{\Delta_{Cu\,Flawx}} = 6.85\times10^{-8} - 0.0072\ln\left[\frac{1}{\widehat{\Phi}_{Cu}} - 1\right] \text{ for } \widehat{\Phi}_{Cu} \leftarrow U(0,1)\\
&\widehat{Cu}_{Flawx} = \widehat{Cu}_{Flaw1} + \widehat{\Delta_{Cu\,Flawx}}
\end{aligned} \tag{129}$$

Nickel, $\widehat{Ni}_{Flawx}$:

The local variability for Ni is determined by sampling a $\widehat{\Delta_{Ni}}$ value drawn from a logistic distribution with parameters $\alpha = -0.0014$ and $\beta = 0.00647$ such that

$$\begin{aligned}
&\widehat{\Delta_{Ni\,Flawx}} \leftarrow L(-0.0014, 0.00647)\\
&\widehat{\Delta_{Ni\,Flawx}} = -0.0014 - 0.00647\ln\left[\frac{1}{\widehat{\Phi}_{Ni}} - 1\right] \text{ for } \widehat{\Phi}_{Ni} \leftarrow U(0,1)\\
&\widehat{Ni}_{Flawx} = \widehat{Ni}_{Flaw1} + \widehat{\Delta_{Ni\,Flawx}}
\end{aligned} \tag{130}$$

The same local variability samplings are applied to Ni-addition and non-Ni-addition welds.

Phosphorous, $\widehat{P}_{Flawx}$:

The local variability for phosphorous is determined by sampling a $\widehat{\Delta_P}$ value drawn from a logistic distribution with parameters $\alpha = 3.27\times10^{-6}$ and $\beta = 0.000449$.

$$\begin{aligned}
&\widehat{\Delta}_{P-Flawx} \leftarrow L(3.27\times10^{-6}, 0.000449)\\
&\widehat{\Delta}_{P-Flawx} = 3.27\times10^{-6} - 0.000449\ln\left[\frac{1}{\Phi_P} - 1\right] \text{ for } \Phi_P \leftarrow U(0,1)\\
&\widehat{P_{Flawx}} = P_{Flaw1} + \widehat{\Delta}_{Ni-Flawx}
\end{aligned} \tag{131}$$

Manganese, $\widehat{Mn}_{Flawx}$:

The local variability for manganese is determined by sampling values from the following normal and Johnson S_B distributions:

$$\begin{aligned}
\widehat{\sigma}_{Mn} &\leftarrow J_{SB}\left(0.00163, 0.03681, 0.83358, 1.15153\right)\\
\widehat{Mn}_{Flawx} &\leftarrow N\left(\widehat{Mn}_{Flaw1}, \widehat{\sigma}_{Mn}\right)
\end{aligned} \tag{132}$$

$$\widehat{\sigma}_{Mn} = \frac{0.00163 + 0.03681\exp\left[\dfrac{\widehat{Z}_i - 0.83358}{1.15153}\right]}{1 + \exp\left[\dfrac{\widehat{Z}_i - 0.83358}{1.15153}\right]} \text{ for } \widehat{Z}_i = \Phi^{-1}\left(\widehat{\Phi}_{Mn}\right);\ \widehat{\Phi}_{Mn} \leftarrow U(0,1) \tag{133}$$

$$\widehat{Mn}_{Flawx} \leftarrow N\left(\widehat{Mn}_{Flaw1}, \widehat{\sigma}_{Mn}\right)$$

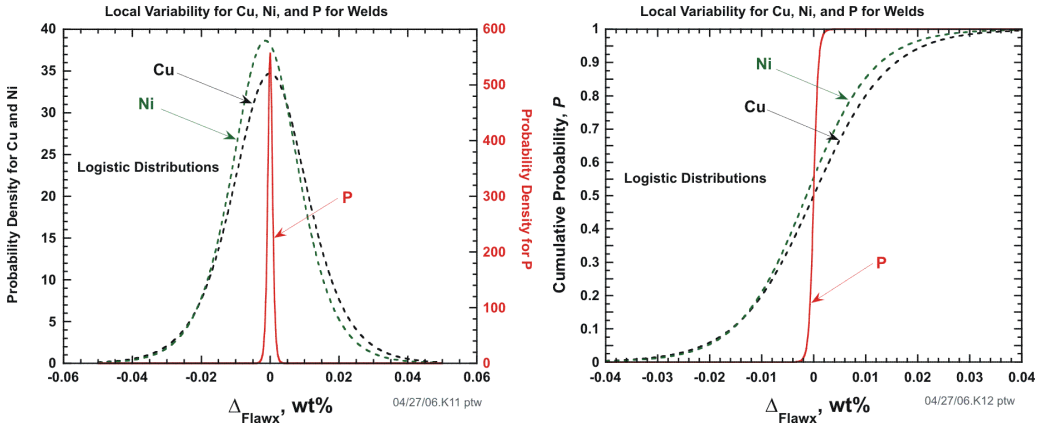

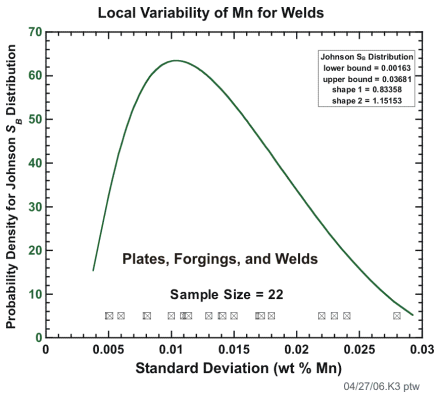

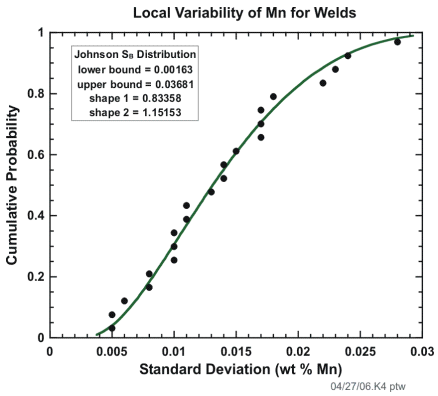

Negative values of sampled $\widehat{Cu}_{Flawx}$, $\widehat{Ni}_{Flawx}$, $\widehat{Mn}_{Flawx}$, and $\widehat{P}_{Flawx}$ are handled as nonphysical exceptions in FAVOR using the truncation protocol described in Sect. 4.3.6, with 0.0 applied as a one-sided truncation boundary.

Through-thickness re-sampling for weld layers

Due to their thickness, RPV welds were typically constructed using multiple coils of weld wire. The variability in chemistry from one coil or weld layer to another is resampled in FAVOR as a given crack grows through the wall and enters a new weld layer. The weld-layer thickness in which this variability is imposed is every 1/4T of the RPV. In general, when a flaw has initiated, the weld chemistry content is not resampled for each growth increment. However, if the inner crack tip of the flaw has moved from one 1/4T of the vessel wall thickness to an adjoining 1/4T region, then the chemistry of the weld is sampled as if the flaw had advanced into a new material.

Additional comments on chemistry sampling in forging, plate, and weld subregions

When a sampled chemistry value for the first flaw in a subregion (*for the current RPV trial*) is truncated internally by FAVPFM, the non-truncated chemistry value for *Flaw1* continues to be used as the basis for subsequent *local variability* perturbation samplings. As an example, for a given RPV trial and first flaw in a given subregion, the sampled value of Cu_{Flaw1} might be truncated back to 0.25 for Linde welds or to 0.305 for all other welds, plates, and forgings, when applying the Eason 2000 correlation [101] to calculate $\Delta RT_{NDT.}$ However, FAVPFM will utilize the non-truncated value for Cu_{Flaw1} in the determination of the local variability copper content, $\widehat{Cu}_{Flawx}$, for all subsequent flaws located in this subregion for the current RPV trial. The rationale for this procedure is that the local variability random perturbation sampled for copper, $\hat{\Delta}_{Cu-Flawx}$, as determined from its logistic distribution, could possibly be sufficiently negative such that the perturbed value of $\widehat{Cu}_{Flawx}$ might take on a value below the truncation upper bound. However, if the value of $\widehat{Cu}_{Flawx}$ should exceed the upper truncation boundary, then FAVPFM will automatically truncate back to the appropriate upper bound or Cu saturation limit.

5.3 NRC RVID2 Database

The *Reactor Vessel Integrity Database*, RVID [154] , developed following the NRC staff review of licensee responses to Generic Letter (GL) 92-01, Revision 1, provides a key source of input data for FAVOR. The most recent update of the database, RVID2 [155], was released in July of 2000. The RVID2 summarizes the properties of the reactor vessel beltline materials for each operating commercial nuclear power plant. The RVID2 includes four tables for each plant: (1) background information table, (2) chemistry data table, (3) upper-shelf energy table, and (4) pressure-temperature limits or pressurized thermal shock table. References and notes follow each table to document the source(s) of data and to provide supplemental information. Appendix D presents a selection of RVID2 data relevant to FAVOR for the four power plants included in the PTS Re-evaluation Project. As of this writing, they are: (1) Beaver Valley 1, (2) Calvert Cliffs 1, (3) Oconee 1, and (4) Palisades 1.

5.4 Flaw Characterization and Uncertainty

The method used to quantify the uncertainty in the flaw characterization is to include 1000 flaw-characterization records in each of the three data files: (1) surface-breaking flaws (2) embedded flaws in weld material, and (3) embedded flaws in plate material. The flaw-characterization file for inner surface- breaking flaws is applicable to weld and plate material. Each of these records contains separate discrete flaw-density and flaw-size distributions.

During the Monte Carlo PFM analysis, the RPV flaw-characterization data for the first stochastically generated RPV trial are taken from the first group of records, i.e., the first inner surface-breaking record, the first embedded-flaw weld material record, and the first embedded-flaw plate material record. The RPV flaw characterization for the second stochastically generated RPV trial is determined from the second group of records, etc. The RPV trials cycle through the flaw-characterization records sequentially up to 1000, and then restart at the first record.

Surface-breaking flaw density data are expressed in flaws per unit RPV-inner-surface area and weld subregion embedded flaws are flaws per unit area on the fusion line between the weld and adjacent plate subregions. These conventions are consistent with the physical model utilized by Pacific Northwest National Laboratory to derive the flaw characterization data input to FAVOR. Embedded flaws in plate regions are expressed on a volumetric basis.

Figures 44a and 44b illustrate axial and circumferential weld subregion elements, respectively. The number of flaws in each of these weld elements is calculated (internally by FAVOR) as the sum of the number of inner- surface breaking flaws and the number of embedded flaws as follows:

$$\begin{pmatrix}\text{Number of Flaws}\\ \text{in Weld Subregions}\end{pmatrix} = \rho_{SB}\left[\alpha\left(\frac{2\pi}{360}\right)R_i\, dz\, d\theta\right] + \rho_{EW}\left[2\beta dA\right] \tag{134}$$

$\alpha =$ 1 when surface-breaking flaws are located on either inner or external vessel surface only

$\alpha =$ 2 when surface-breaking flaws are located on both inner and external vessel surfaces

$\beta =$ 3/8 when embedded flaws with inner crack tip residing in either the inner or outer 3/8 of base metal thickness are included in PFM analysis

$\beta =$ 1 when all through-wall embedded flaws are included in PFM analysis

$\rho_{SB} =$ inner surface-breaking flaw density (per unit surface area - flaws/in^2)

$\rho_{EW} =$ weld embedded-flaw density (per unit weld-fusion area - flaws/in^2)

$dA =$ user-input weld-fusion area (for one side of weld) (in^2 - input by user)

$R_i =$ internal radius of RPV (in. - input by user)

$dz =$ height of subregion element (in. - input by user)

$d\theta =$ subtended angle of subregion element (degrees - input by user)

where ρ_{SB} and ρ_{EW} are summed over all flaw depths.

For axial welds, the fusion lines are on the sides of the weld, whereas for circumferential welds, the fusion lines are on the top and bottom of the welds. In the term $\left[2\beta dA\right]$, the factor of 2 accounts for the fact that the user input data is the area on one side of the fusion line whereas flaws reside in fusion lines on both sides of the welds. The β variable depends on the user-specified option regarding which flaw population is to be included in the analysis. All flaw densities are assumed to be uniform through the RPV wall thickness.

Figure 44c illustrates a plate subregion element. The number of flaws in each of these plate elements is calculated (internally by FAVOR) as the sum of the number of inner surface-breaking flaws and the number of embedded flaws as follows:

$$\begin{pmatrix}\text{Number of Flaws}\\ \text{in Plate Subregions}\end{pmatrix} = \rho_{SB}\left[\alpha\left(\frac{2\pi}{360}\right)R_i\ dz\ d\theta\right] + \rho_{EP}\left[\beta\pi\left(R_o^2 - \left(R_i + CLTH\right)^2\right)dz\left(\frac{d\theta}{360}\right)\right]$$

where

α = 1 when surface-breaking flaws are located on either inner or external vessel surface only (user-specified option)

α = 2 when surface-breaking flaws are located on both inner and external vessel surfaces (user-specified option)

β = 3/8 when embedded flaws with inner crack tip residing in either the inner or outer 3/8 of base metal thickness are included in PFM analysis

β = 1 when all through-wall embedded flaws are included in PFM analysis

ρ_{SB} = inner surface-breaking flaw density (per unit surface area - flaws/in^2)

ρ_{EP} = plate embedded-flaw density summed over all flaw depths (flaws per unit volume - flaws/in^3)

R_o = external radius of RPV (in - input by user)

R_i = internal radius of RPV (in. - input by user)

$CLTH$ = cladding thickness (in. - input by user)

dz = height of subregion element (in. - input by user)

$d\theta$ = subtended angle of subregion element (degrees - input by user)

(135)

where ρ_{SB} and ρ_{EP} are summed over all flaw depths.

Surface-Breaking Flaws

Due to the location of tensile stresses during cool-down transients, the only type of surface breaking flaws that are likely to initiate in cleavage fracture are those on the RPV inner surface; therefore, previous versions of FAVOR were assumed that all surface-breaking flaws were modeled as inner surface-breaking flaws. The FAVOR^{HT} code was designed for heat-up transients; however, it did not have the capability to model external surface-breaking flaws, because there were insufficient verified stress intensity factor influence coefficients (SIFIC(s)) available for external surface-breaking flaws.

Comprehensive databases of SIFIC(s) were generated [112] at ORNL, implemented into FAVOR, v09.1, and verified for a range of infinite- and finite-length, axially- and circumferentially-oriented external-surface breaking flaw depths. Therefore, FAVOR now has the capability to model a range of external surface-breaking flaws in addition to internal surface-breaking flaws. User-specified options are available that control the values assigned to the variable α in Eqs. (134) and (135). See ref. [2] for a detailed discussion of these user-specified options.

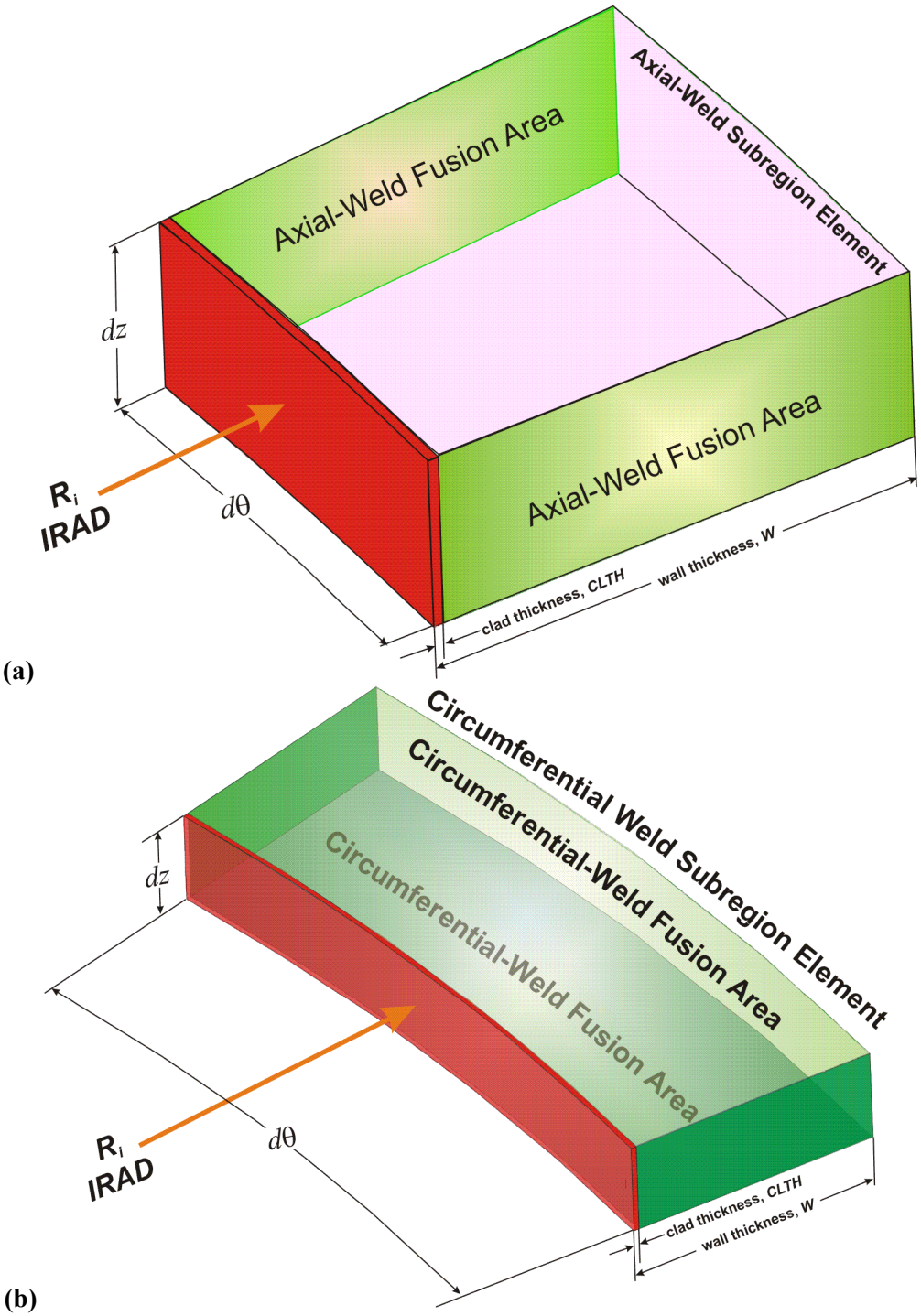

Fig. 44. Weld fusion area definitions for (a) axial-weld subregion elements and (b) circumferential subregion elements.

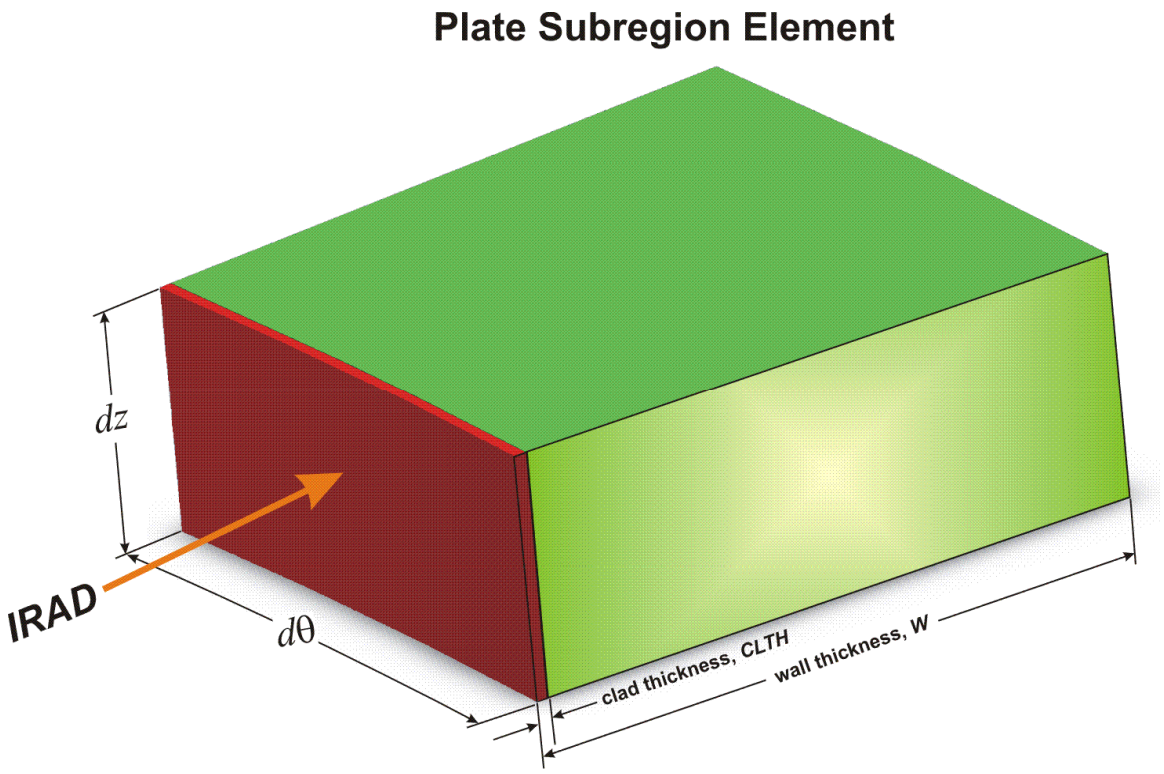

Fig. 44. (continued) (c) Plate subregion element.

Embedded Flaws

Embedded flaw are assumed to be distributed uniformly through the RPV wall thickness, but only those in a specific fractional part of the wall thickness may be applicable to a particular problem; therefore, for computational efficiency, only those embedded flaws that could initiate in cleavage fracture should be included in the analysis. For example, the PFM analysis of a cool-down transient, in which all of the embedded flaws distributed through the entire RPV wall thickness were included, would generate nearly the same solution (if sufficiently converged) as the analysis in which only those embedded flaws in the 3/8 of the base metal thickness nearest the RPV inner (wetted) surface were included because the stress distributions induced by realistic cool down transients attenuate through the RPV wall thickness such that the applied-K_I for embedded flaws in the outer 5/8 of the base metal thickness would never be sufficiently high to result in cleavage fracture. Similarly, stress distributions induced by realistic heat-up transients are such that the applied-K_I for embedded flaws in the inner 5/8 of the base metal thickness would never be sufficiently high to result in cleavage fracture.

The initial releases of FAVOR were developed for cool-down transients, therefore, for reasons of computational efficiency, it was assumed that only the embedded flaws in the 3/8 of the base metal thickness nearest the RPV inner (wetted) surface should be included in PFM analyses. Similarly, FAVOR^{HT} was developed for heat-up transients, and it was assumed that only the embedded flaws in the 3/8 of the wall thickness nearest the RPV outer surface should be included in PFM analyses.

FAVOR, v09.1, consolidated and expanded the capabilities of FAVOR and FAVOR^{HT}; therefore, user-specified options are available that control the values assigned to the variable β in Eqs. (134) and (135). See ref. [2] for a detailed discussion of these user-specified options.

5.5 Summary of Uncertainty Distributions and Sampling Protocols

Plane-Strain Static Initiation

The following uncertainty distributions and their sampling protocols have been implemented in the FAVOR code (FAVPFM) to represent (for a given flaw at a given time in the specific PTS transient under study) the epistemic and aleatory uncertainties in the plane-strain static initiation fracture-toughness values used in determining the probability of cleavage initiation:

Step 1. For plate, forging, and weld product forms, provide the following input to FAVOR:

- Provide, for *all product forms*, major-region best estimates for the means to be used in sampling at the subregion level from normal distributions for copper, HE_{Cu}, nickel, HE_{Ni}, manganese, HE_{Mn}, and phosphorous, HE_P, content.[15]
- Provide, for *plate and forging* major regions, global[16] best estimates for the standard deviations to be used in sampling at the subregion level from normal distributions for copper, σ_{Cu}, nickel, σ_{Ni}, and phosphorous, σ_P. These values of $\left(\sigma_{Cu}, \sigma_{Ni}, \sigma_P\right)$ are applied as constants for all plate/forging major regions. The standard deviation for manganese, σ_{Mn}, is sampled in *Sampling Block 1* (see Fig. 16) for each plate/forging major region from statistical distributions defined in Eq. (121). For *weld* major regions, the standard deviations are described by Eqs.(124)-(128) in Sect. 5.2.9.
- Provide, at the subregion level, a best estimate for the mean of a normal distribution to be used in sampling the fluence at the inside surface of the vessel as described by Eq. (100) in Sect. 5.2.3.
- Provide, for each major region, best estimates for the mean, $\overline{RT}_{NDT(0)}$, and the standard deviations, $\sigma_{RT_{NDT(0)}}$, of unirradiated $RT_{NDT(0)}$.
- Provide the *global* coolant temperature, T_c in °F, and RPV exposure time in EFPY, where T_c is the temperature of the coolant on the inner surface of the RPV beltline region (adjacent to the active core) at the time that the transient originates (at time = 0).
- Determine the current regulatory estimate of the mean value of the unirradiated RT_{NDT} from the Reactor Vessel Integrity Database (RVID2) [155] for the material of interest (see Appendix D).

  a) If this RT_{NDT} value was determined using either the ASME NB-2331 or MTEB 5-2 methods, designate the value of $RT_{NDT(RVID)}$ from RVID as $RT_{RTND(0)}$ and proceed directly to Step 2.

[15] Note that negative values of $\widehat{Cu}, \widehat{Ni}, \widehat{Mn},$ and $\widehat{P}$ sampled from normal distributions are handled as non-physical exceptions in FAVOR using the truncation protocol described in Sect. 4.3.6 with 0.0 as the truncation boundary.

[16] *Global* variables are fixed by product form as constants for the full RPV beltline.

b) If this RT_{NDT} value was determined using the *Generic* method, assign $\overline{RT}_{NDT(0)}$ as –8 °F for welds and 0 °F for plates and forgings; sample $\widehat{RT}_{NDT(0)} \leftarrow N(\overline{RT}_{NDT(0)}, \sigma_{RT_{NDT(0)}})$; then proceed to Step 2.

Step 2. Generate a random number, $\widehat{\Phi}$, between 0 and 1 from a uniform distribution. Use this random number to sample[17] for each major region (once for each RPV trial) a value of $\widehat{\Delta RT}_{epistemic}$ from the Weibull percentile function (inverse CDF) given by Eq. (103).

Step 3. Sample the irradiation shift, $\widehat{\Delta RT}_{NDT}$, at the subregion level by using either the Eason 2000 [101] or the Eason 2006 [134] embrittlement correlation to calculate $\widehat{\Delta T}_{30}$ from sampled values (sampled for each flaw) of neutron fluence, $\hat{f}_0(r)$; copper content, $\widehat{Cu} \leftarrow N(\overline{Cu}, \sigma_{Cu})$; nickel content, $\widehat{Ni} \leftarrow N(\overline{Ni}, \sigma_{Ni})$; manganese content, $\widehat{Mn} \leftarrow N(\overline{Mn}, \overline{\sigma_{Mn}})$; phosphorous content, $\widehat{P} \leftarrow N(\overline{P}, \sigma_P)$; and product form. The irradiation shift, $\widehat{\Delta RT}_{NDT}$, is then determined by Eq. (98) in Sect. 5.2.2.

$$\widehat{\Delta RT}_{NDT}(r,\ldots) = \begin{cases} 0.99\widehat{\Delta T_{30}}(r,\ldots) & \text{weld} \\ 1.10\widehat{\Delta T_{30}}(r,\ldots) & \text{plate and forgings} \end{cases} \tag{98}$$

where $\widehat{Cu}$ is the sampled copper content in wt%, $\widehat{Ni}$ is the sampled nickel content in wt%, $\widehat{Mn}$ is the sampled manganese content in wt%, $\widehat{P}$ is the sampled phosphorous content in wt%, $\hat{f}_0(r)$ is the sampled and then attenuated neutron fluence in n/cm^2, r is the position from the inner surface of RPV wall, $\tau_{exposure}$ is exposure time in hours (input to FAVOR in EFPY), and T_c is coolant temperature in °F. The fast- neutron fluence at the inner surface of the vessel is sampled using the protocol described by Eqs. (100) in Sect. 5.2.3. The sampled neutron fluence for the flaw is then attenuated by Eq. (99) in Sect. 5.2.3 (but not resampled) as the crack grows through the wall to produce $\widehat{f}_0(r)$.

Step 4. Calculate the sampled, irradiated value of RT_{NDT} by Eq. (104) in Sect. 5.2.5:

$$\widehat{RT}_{NDT}(r,\ldots) = \overline{RT}_{NDT(0)} - \widehat{\Delta RT}_{epistemic} + \widehat{\Delta RT}_{NDT}(r,\ldots) \tag{104}$$

where

$$\overline{RT}_{NDT(0)\text{–major-region}} = \begin{cases} \widehat{RT}_{NDT(0)} \leftarrow N(\overline{RT}_{NDT(0)}, \sigma_{RT_{NDT(0)}}) \text{ if RVID2 method is } \textit{Generic} \\ \text{Heat Estimate of } RT_{NDT(0)} \text{ if RVID2 method is NB-2331 or MTEB 5-2} \end{cases}$$

Step 5. Calculate the normalized temperature of the vessel at the current location, r, of the crack tip in the RPV wall as described in Sect. 5.2.7:

$$\widehat{\Delta T}_{RELATIVE}(r,\ldots) = T(r,\tau) - \widehat{RT}_{NDT}(r,\ldots) \tag{136}$$

[17] A curved overbar, $\widehat{X}$, indicates a sampled random variate. A braced overbar, $\overbrace{X}$, indicates that sampling has occurred in a prior step but not in the current step.

Step 6. Calculate the parameters of the Weibull distribution of the K_{Ic} Weibull statistical distribution by

$$\begin{aligned} a_{K_{Ic}}(\widehat{\Delta T}_{RELATIVE}) &= 19.35 + 8.335\exp\left[0.02254(\widehat{\Delta T}_{RELATIVE})\right] \text{ [ksi}\sqrt{\text{in.}}\text{]} \\ b_{K_{Ic}}(\widehat{\Delta T}_{RELATIVE}) &= 15.61 + 50.132\exp\left[0.008(\widehat{\Delta T}_{RELATIVE})\right] \text{ [ksi}\sqrt{\text{in.}}\text{]} \\ c_{K_{Ic}} &= 4 \end{aligned} \tag{137}$$

with K_{Ic} in ksi$\sqrt{\text{in}}$ and $\widehat{\Delta T}_{RELATIVE} = T(r,\tau) - \widehat{RT}_{NDT}(r,\ldots)$ in °F.

Note that this Weibull statistical model describes the *aleatory* uncertainty in plane-strain static initiation.

Step 7. For a given applied K_I, calculate the instantaneous conditional probability of crack initiation, $\Pr\{K_{Ic} \le K_I\}$ with *aleatory* uncertainty, from the following Weibull distribution given by Eq. (111) in Sect. 5.2.7

$$\Pr(K_{Ic} < K_I) = \widehat{cpi} = \begin{cases} 0; & K_I \le a_{K_{Ic}} \\ 1 - \exp\left[-\left(\dfrac{K_I - a_{K_{Ic}}(\widehat{\Delta T}_{RELATIVE})}{b_{K_{Ic}}(\widehat{\Delta T}_{RELATIVE})}\right)^{c_{K_{Ic}}}\right]; & K_I > a_{K_{Ic}} \end{cases} \tag{138}$$

If the flaw is determined to be in a warm-prestressing state (and the WPS option has been turned on by the user), then the conditional probability of initiation is set to zero. See Sect. 4.3.4 for a complete discussion of warm prestressing.

Plane-Strain Static Crack Arrest

Assuming that the given flaw at a given time (for the specific PTS transient under study) has a finite conditional probability of initiation that is increasing with time, the following protocol has been implemented in FAVOR as a part of the *Initiation-Growth-Arrest* (IGA) submodel (see Sect. 4.3.12) to represent the epistemic and aleatory uncertainties in plane-strain crack arrest fracture-toughness values.

Step 8. For plate, forging, and weld product forms, the following input will have been provided to FAVOR:

- Best estimates for the mean and standard deviation for normal distributions of copper, nickel, and phosphorous content, $N(\overline{Cu},\sigma_{Cu}), N(\overline{Ni},\sigma_{Ni}), N(\overline{P},\sigma_P)$ at the major region level, and best estimate for the mean major-region manganese content, $N(\overline{Mn},\widehat{\sigma}_{Mn})$ are input.[18] For copper, nickel, and phosphorous, the corresponding standard deviations $(\sigma_{Cu},\sigma_{Ni},\sigma_P)$ are constant

[18] Note that negative values of chemistry content ($\widehat{Cu},\widehat{Ni},\widehat{Mn}$ and $\widehat{P}$) sampled from normal distributions are handled as nonphysical exceptions in FAVOR using the truncation protocol described in Sect. 3.3.4 with 0 as the truncation boundary.

input data for all major region plates and forgings. The standard deviation (characterizing *global variability*) for Mn is sampled for each major plate/forging region at the point of entry into the RPV trial loop (see Sampling Block 1 in Fig. 16) from a prescribed Weibull distribution for plates and a Johnson S_B distribution for forgings (see Eqs. (121) in Sect. 5.2.9). For welds, the standard deviation simulating the *global variability* of copper, $\widehat{\sigma}_{Cu}$, is sampled from the normal distribution given by Eq. (124) for each weld major region in Sampling Block 1. For nickel-addition welds (heats 34B009 and W5214), the *global variability* applies a constant value indicated by Eq. (125), and all other heats sample in Sampling Block 1 from the normal distribution given by Eq. (126). The global variability of phosphorous in welds uses a constant value for the standard deviation by Eq. (127).

- At the subregion level, a best estimate for the mean of a normal distribution, $N(\overline{f_0}(0), \sigma_{f_0(0)})$ [19], to be used in sampling the fluence at the inside surface of the vessel as described by Eq. (100) in Sect. 5.2.3.
- Best estimate for the standard deviation, $\sigma_{RT_{NDT(0)}}$, of unirradiated RT_{NDT}.
- The coolant temperature, T_c in °F, and RPV exposure time in EFPY.
- From the initiation procedure for this flaw, the current regulatory estimate of the unirradiated RT_{NDT} will have already been determined from the Reactor Vessel Integrity Database (RVID2) [155] for the material of interest (see Appendix D) and designated as either $RT_{NDT(0)}$ if the RVID2 $RT_{NDT(u)}$ method is NB-2331 or MTEB 5-2 or sampled from a normal distribution $\widehat{RT}_{NDT(0)} \leftarrow N(\overline{RT}_{NDT(RVID)}, \sigma_{RT_{NDT(0)}})$ if the RVID2 $RT_{NDT(u)}$ method is *Generic*.

Step 9. Retrieve the value of $\widehat{\Delta RT}_{epistemic}$ and its associated *p-value*, $\widehat{\Phi}$, determined by the sampling protocol in Step 2 for the major region in which the candidate flaw resides and adjust the epistemic uncertainty in $RT_{NDT(0)}$ by applying the offset defined by Eq. (108) with Eq. (107)

$$\widehat{\Delta RT}_{epist-arrest} = \widehat{\Delta RT}_{epistemic(\Phi)} + \Delta\left(\widehat{\Phi}\right) \quad [°\text{F}] \tag{107}$$

Note that this step does not involve a resampling of $\widehat{\Delta RT}_{epistemic}$.

Step 10. Retrieve the sampled value of the irradiation shift for this flaw, $\widehat{\Delta RT}_{NDT}(r,\ldots)$, determined from Step 3 in the initiation procedure applied for this flaw at its current position in the RPV wall. Note that this step does not involve a resampling of $\widehat{\Delta RT}_{NDT}(r,\ldots)$.

Step 11. Sample $\widehat{\Delta RT}_{ARREST} \leftarrow \Lambda(\widehat{\mu}_{\ln(\Delta RT_{ARREST})}, \widehat{\sigma}_{\ln(\Delta RT_{ARREST})})$ from a lognormal distribution (see Appendix F) where

[19] Note that sampled negative values of fluence, $\widehat{f_0}(0)$, are handled as nonphysical exceptions in FAVOR using the truncation protocol described in Sect. 3.3.4 with 0 as the truncation boundary.

$$\widehat{\mu}_{\ln(\Delta RT_{ARREST})} = \ln\left[\widehat{\Delta RT}_{ARREST(mean)}\right] - \frac{\widehat{\sigma}^2_{\ln(\Delta RT_{ARREST})}}{2}$$

where

$$\widehat{T}_0 = \left(\widehat{RT}_{NDT_0} - \widehat{\Delta RT}_{epist-arrest} - 32\right)/1.8 \ \ [°\text{C}]$$

$$\widehat{\Delta RT}_{ARREST(mean)} = 44.122\exp\left[-0.005971\times\widehat{T}_0\right] \ \ [°\text{C}] \tag{139}$$

$$\widehat{\sigma}_{\ln(\Delta RT_{ARREST})} = \sqrt{\ln\left\{\exp\left[0.38998^2 + 2\ln(\widehat{\Delta RT}_{ARREST(mean)})\right] - \text{var}\left(\widehat{T}_0\right)\right\} - 2\ln\left[\widehat{\Delta RT}_{ARREST(mean)}\right]}$$

where

$$\text{var}(\widehat{T}_0) = \begin{cases} (12.778)^2 & \text{for } \widehat{T}_0 < -35.7 \ °\text{C} \\ 99.905972 - 1.7748073\widehat{T}_0 & \text{for } -35.7 \ °\text{C} \le \widehat{T}_0 \le 56 \ °\text{C} \\ 0 & \text{for } \widehat{T}_0 > 56 \ °\text{C} \end{cases}$$

$\widehat{\Delta RT}_{ARREST}$ is sampled from the lognormal percentile function and then converted into °F

$$\widehat{\Delta RT}_{ARREST} = 1.8\exp\left[\widehat{\sigma}_{\ln(\Delta RT_{Arrest})}\widehat{Z_{P_f}} + \widehat{\mu}_{\ln(\Delta RT_{Arrest})}\right] \ \ [°\text{F}]$$

$\widehat{Z_{P_f}} \leftarrow N(0,1)$; $\widehat{Z_{P_f}}$ is the standard normal deviate corresponding to the $\widehat{P_f}$ fractile $(0 < \widehat{P_f} < 1)$ for this trial in the crack *Initiation - Growth - Arrest* model.

Step 12. Calculate the estimated arrest reference temperature, $\widehat{RT}_{ARREST}$, by Eq. (109)

$$\widehat{RT}_{ARREST}(r,\ldots) = \widehat{RT}_{NDT(0)} - \widehat{\Delta RT}_{epist-arrest} + \widehat{\Delta RT}_{ARREST} + \widehat{\Delta RT}_{NDT}(r,\ldots) \tag{109}$$

Step 13. Calculate the normalized (relative to $\widehat{RT}_{ARREST}$) temperature of the vessel at the current location, *r*, in the RPV wall

$$\widehat{\Delta T}_{RELATIVE}(r,\ldots) = T(r,t) - \widehat{RT}_{ARREST}(r,\ldots) \tag{140}$$

Step 14. Calculate the lognormal mean, $\mu_{\ln(K_{Ia})}(\widehat{\Delta T}_{RELATIVE})$, of the K_{Ia} statistical distribution by Eq. (118) or Eq. (119):

$$\mu_{\ln(K_{Ia})}(\widehat{\Delta T}_{RELATIVE}) = \ln\left[K_{Ia(mean)}(\widehat{\Delta T}_{RELATIVE})\right] - \frac{\sigma^2_{\ln(K_{Ia})}}{2}$$

where

if K_{Ia}_Model is equal to 1

$$K_{Ia(\text{mean})}(\widehat{\Delta T}_{RELATIVE}) = 27.302 + 69.962\exp\left[0.006057(\widehat{\Delta T}_{RELATIVE})\right] \ \ [\text{ksi}\sqrt{\text{in.}}] \tag{118}$$

$$\sigma_{\ln(K_{Ia})} = 0.18$$

else if K_{Ia}_Model is equal to 2

$$K_{Ia(\text{mean})}(\widehat{\Delta T}_{RELATIVE}) = 27.302 + 70.6998\exp\left[0.008991(\widehat{\Delta T}_{RELATIVE})\right] \ \ [\text{ksi}\sqrt{\text{in.}}] \tag{119}$$

$$\sigma_{\ln(K_{Ia})} = 0.34$$

Step 15. Given the current value of $K_{I\text{-}initiation}$ from the initiation model, we first calculate the fractile, $\widehat{\Phi}_{K_{I-initiation}}$, associated with this value in the arrest model by

$$\widehat{\Phi}_{K_{I-initiation}} = \frac{1}{2}\left[\operatorname{erf}\left(\frac{\ln(K_{I-initiation}) - \mu_{\ln(K_{Ia})}(\widehat{\Delta T}_{RELATIVE})}{\sigma_{\ln(K_{Ia})}\sqrt{2}} \right) + 1 \right] \tag{141}$$

where $\operatorname{erf}(x) \equiv \frac{2}{\sqrt{\pi}} \int_0^x \exp(-\xi^2)\, \mathrm{d}\xi$. Using the same value of $\widehat{P_f}$ from Step 11, scale by $\widehat{\Phi}_{K_{I-initiation}}$ such that

$$\widehat{\Phi}_{K_{Ia}} = (\widehat{P_f})(\widehat{\Phi}_{K_{I-initiation}}) \tag{142}$$

With this $\widehat{\Phi}_{K_{Ia}}$ fractile, draw a value of K_{Ia} from its lognormal distribution

$$\widehat{K_{Ia}}(\Phi_{K_{Ia}}, \widehat{\Delta T}_{RELATIVE}) = \exp\left[\sigma_{\ln(K_{Ia})} \widehat{Z}_{\Phi_{K_{Ia}}} + \mu_{\ln(K_{Ia})}(\widehat{\Delta T}_{RELATIVE}) \right] \tag{143}$$

$\widehat{Z}_{\Phi_{K_{Ia}}}$ = standard normal deviate corresponding to the $\widehat{\Phi}_{K_{Ia}}$ fractile

Notes:

Note on Step 3: The current sampled value of $\widehat{\Delta T_{30}}$ is also used to estimate the effects of irradiation on the unirradiated flow stress, $\sigma_{flow(u)}$, in the crack *Initiation-Growth-Arrest* model. After each resampling of $\widehat{\Delta T_{30}}$, the flow stress is adjusted by the following relation:

$$\sigma_{flow} = \sigma_{flow(u)} + \gamma \widehat{\Delta T_{30}} \text{ where } \gamma = \begin{cases} 0.112 \text{ ksi/°F for welds} \\ 0.131 \text{ ksi/°F for plates} \end{cases}$$

This value of σ_{flow} is then used in the vessel-failure test against the pressure-induced membrane stress in the remaining ligament, checking for net-section plastic collapse.

Note on Step 11: The only random variate sampled in Step 11 is $\widehat{Z_{P_f}}$. All other variates have been sampled in previous steps.

Note on Step 15: The scaling procedure in Step 15 ensures that the initial value of K_{Ia}, calculated immediately after initiation, does not exceed the initiating value of K_I, thus ensuring an initial extension. For welds, the scaling procedure of Eq. (142) is used only in the weld layer in which the flaw originally initiated. If the flaw advances into other weld layers, then this scaling is not applied, since it is assumed that any linkage between the original initiation event and crack arrest is thereby broken.

For either an initiated ($cpi > 0$) surface-breaking or embedded flaw, the flaw is first assumed to extend to become an infinite-length flaw before it is allowed to advance through the RPV wall. It is the applied K_I of the infinite-length flaw (designated as $K_{I\text{-}initiation}$ in Step 15, Eq. (141)) that is taken as

the operative initiating K_{Ic} to establish the required scaling factor and not the applied K_I of the surface-breaking or embedded flaw at initiation. It was determined that scaling by the lower embedded-flaw K_I at initiation was an overly restrictive constraint.

6. Summary and Conclusions

This report has provided a detailed description of the theory, algorithms, methods, and correlations that have been implemented in this release of the FAVOR computer code for performing probabilistic fracture mechanics analyses of nuclear reactor pressure vessels subjected to pressurized thermal shock and other pressure-thermal events. In support of the PTS Re-evaluation Project, the following advanced technologies and new capabilities have been incorporated into FAVOR:

- **the ability to incorporate new detailed flaw-characterization distributions from NRC research (with Pacific Northwest National Laboratory, PNNL),**
- **the ability to incorporate detailed neutron fluence maps,**
- **the ability to incorporate warm-prestressing effects into the analysis,**
- **the ability to include temperature-dependencies in the thermo-elastic properties of base and cladding,**
- **the ability to include crack-face pressure loading for surface-breaking flaws,**
- **the addition of a new ductile-fracture model simulating stable and unstable ductile tearing,**
- **the addition of a new embrittlement correlation,**
- **the ability to include multiple transients in one execution of FAVOR,**
- **the ability to include input from the Reactor Vessel Integrity Database, Revision 2, (RVID2) of relevant RPV material properties,**
- **the addition of new fracture-toughness models based on extended databases and improved statistical distributions,**
- **the addition of a variable failure criterion, i.e., how far must a flaw propagate into the RPV wall for the vessel simulation to be considered as "failed" ?**
- **the addition of semi-elliptic surface-breaking and embedded-flaw models,**
- **the addition of through-wall weld stresses,**
- **the addition of base material SIFIC(s) from ASME code, Section XI, Appendix A, Article A-3000, *Method of K_I Determination*, for finite axial and circumferential flaws and infinite axial and 360° continuous circumferential flaws into the FAVOR SIFIC database, and**
- **the implementation of improved PFM methodology that incorporates modern PRA procedures for the classification and propagation of input uncertainties and the characterization of output uncertainties as statistical distributions.**

The companion report *Fracture Analysis of Vessels – Oak Ridge, FAVOR, v16.1, Computer Code: User's Guide* [2] gives complete details on input requirements and execution of FAVOR, v16.1.

References

1. T.L. Dickson, S.N.M. Malik, J.W. Bryson, and F.A. Simonen, "Revisiting the Integrated Pressurized Thermal Shock Studies of an Aging Pressurized Water Reactor," ASME PVP-Volume 388, *Fracture, Design Analysis of Pressure Vessels, Heat Exchangers, Piping Components, and Fitness for Service*, *ASME Pressure Vessels and Piping Conference*, August, 1999.

2 . T.L. Dickson, P.T. Williams, B.R.Bass, and H.B. Klasky, *Fracture Analysis of Vessels – Oak Ridge – FAVOR, v16.1, Computer Code: User's Guide,* ORNL/LTR-2016/310, Oak Ridge National Laboratory, Oak Ridge, TN, 2016.

3. A.R. Foster and R.L. Wright, Jr., *Basic Nuclear Engineering*, 2nd ed., Allyn and Bacon, Inc., Boston, 1973.

4. API 579-1/ASME FFS-1 (API 579 Second Edition) *American Petroleum Institute Practice 579 Fitness-for-Service*, June 5, 2007 (Joint standard with ASME).

5. *American Society of Mechanical Engineers Boiler and Pressure Vessel Code,* Section XI, Rules for Inservice Inspection of Nuclear Power Plant Components, Nonmandatory Appendix A, Analysis of Flaws, Article A-3000, Method for K_I Determination, American Society of Mechanical Engineers, New York, 2015.

6. R.C. Cipolla and D.R. Lee, "Stress Intensity Factor Coefficients for Circumferential ID Surface Flaws in Cylinders for Appendix A of ASME Section XI", PVP2013-97734, *Proceedings of the ASME 2013 Pressure Vessels and Piping Conference*, July 14-18, 2013, Paris, France.

7. S.X. Xu, D.A. Scarth, R.C. Cipolla, and D.R. Lee, "Closed-Form Relations for Stress Intensity Factor Influence Coefficients for Axial ID Surface Flaws in Cylinders for Appendix A of ASME Section XI", PVP2014-28222, *Proceedings of the ASME 2014 Pressure Vessels and Piping Conference*, July 20-24, 2014, Anaheim, California.

8. K. Balkey, F.J. Witt, and B.A. Bishop, *Documentation of Probabilistic Fracture Mechanics Codes Used for Reactor Pressure Vessels Subjected to Pressurized Thermal Shock Loading, Parts 1 and 2*, EPRI TR-105001, Westinghouse Electric Corporation, Pittsburgh, PA, June 1995.

9. D.L. Selby, et al., *Pressurized Thermal Shock Evaluation of the H.B. Robinson Nuclear Power Plant,* NUREG/CR-4183 (ORNL/TM-9567), September 1985.

10. *Classification of TMI Action Plan Requirements*, U.S. Nuclear Regulatory Commission, NUREG-0737, November 1980.

11. D.L. Selby, et al., *Pressurized Thermal Shock Evaluation of the Calvert Cliffs Unit 1 Nuclear Power Plant*, NUREG/CR-4022 (ORNL/TM-9408), Oak Ridge National Laboratory, Oak Ridge, TN, September 1985.

12 . T.J. Burns, et al., *Preliminary Development of an Integrated Approach to the Evaluation of Pressurized Thermal Shock as Applied to the Oconee Unit 1 Nuclear Power Plant*, NUREG/CR-3770 (ORNL/TM-9176), May 1986.

13. Policy Issue from J.W. Dircks to NRC Commissioners, *Enclosure A: NRC Staff Evaluation of Pressurized Thermal Shock, November 1982*, SECY-82-465, November 23, 1982, Division of Nuclear Reactor Regulation, U.S. Nuclear Regulatory Commission, Washington, D.C.

14. T.L. Dickson, *Review of Pressurized Thermal Shock Screening Criteria for Embrittled Pressurized Water Reactor Pressure Vessels,* ORNL/NRC/LTR-95/39, December, 1995.

15. *U.S. Code of Federal Regulations,* Title 10, Part 50, Section 50.61 and Appendix G.

16. U.S. Nuclear Regulatory Commission, Regulatory Guide 1.154 (1987), *Format and Content of Plant-Specific Pressurized Thermal Shock Safety Analysis Reports for Pressurized Water Reactors*.

17. U. S. Nuclear Regulatory Commission, Regulatory Guide 1.99, Revision 2 (1988), *Radiation Embrittlement of Reactor Vessel Materials*.

18. Proposed Rules 10CFR50.61a (RIN 3150-A101) – Alternate Fracture Toughness Requirements for Protection Against Pressurized Thermal Shock Events, *Federal Register* **72(1)**, October 3, 2007, 56275-56287.

19. M. Kirk, et al., *Technical Basis for Revision of the Pressurized Thermal Shock (PTS) Screening Limit in the PTS Rule (10 CFR 50.61)*, NUREG-1806, U.S. Nuclear Regulatory Commission, Office of Nuclear Regulatory Research, Washington, DC, August 2007.

20. M. T. Kirk and T. L. Dickson, *Recommended Screening Limits for Pressurized Thermal Shock (PTS)*, NUREG-1874, U.S. Nuclear Regulatory Commission, Office of Nuclear Regulatory Research, Washington, DC, March 2007.

21. C. E. Pugh and B. R. Bass, *A Review of Large-Scale Fracture Experiments Relevant to Pressure Vessel Integrity Under Pressurized Thermal Shock Conditions,* NUREG/CR-6699 (ORNL/TM-2000/360), Oak Ridge National Laboratory, January 2001.

22. B. R. Bass, C. E. Pugh, J. Keeney-Walker, H. Schulz, and J. Sievers, *CSNI Project for Future Analyses of Large-Scale International Reference Experiments (Project FALSIRE),* NUREG/CR-5997 (ORNL/TM-12307), Oak Ridge National Laboratory, December 1992.

23. B. R. Bass, C. E. Pugh, J. Keeney-Walker, H. Schulz, and J. Sievers, *CSNI Project for Future Analyses of Large-Scale International Reference Experiments (FALSIRE II),* NUREG/CR-6460 (ORNL/TM-13207), Oak Ridge National Laboratory, April 1996.

24. J. Sievers and B. R. Bass, "Comparative Assessment of Project FALSIRE-Results," *Journal Nucl. Engr. Des.* **152**, (1994) 19-38.

25. B. R. Bass, et al., "CSNI Project for Fracture Analysis of Large-Scale International Reference Experiments (FALSIRE II)," *Proceedings of the International Conference on Nuclear Engineering-4 (ICONE-4),* Vol. 1, Part A, American Society of Mechanical Engineers, (1996) 149-162.

26. B. R. Bass, C. E. Pugh, S. Crutzen, and R. Murgatroyd, *Relationship of NESC-1 to Other Large-Scale International Projects,* ORNL/NRC/LTR-99/20, Oak Ridge National Laboratory, Oak Ridge, TN, 1999.

27. J. G. Merkle, G. D. Whitman, and R. H. Bryan, *An Evaluation of the HSST Program Intermediate Pressure Vessel Tests in Terms of Light-Water-Reactor Pressure Vessel Safety*, ORNL/TM-5090, Oak Ridge National Laboratory, Oak Ridge, TN, November 1975.

28. G. D. Whitman, *Historical Summary of the Heavy-Section Steel Technology Program and Some Related Activities in Light-Water-Reactor Pressure Vessel Safety Research*, NUREG/CR-4489 (ORNL-6259), Oak Ridge National Laboratory, Oak Ridge, TN, March 1986.

29. R. W. Derby, et al., *Test of 6-Inch-Thick Pressure Vessels, Series 1: Intermediate Test Vessels V-1 and V-2*, ORNL-4895, Oak Ridge National Laboratory, Oak Ridge, TN, February 1974.

30. R. H. Bryan, et al., *Test of 6-Inch-Thick Pressure Vessels, Series 2: Intermediate Test Vessels V-3, V-4, and V-6*, ORNL-5059, Oak Ridge National Laboratory, Oak Ridge, TN, November 1975.

31. R. H. Bryan, et al., *Test of 6-Inch-Thick Pressure Vessels, Series 3: Intermediate Test Vessels V-7B*, NUREG/CR-0309 (ORNL/NUREG-38), Oak Ridge National Laboratory, Oak Ridge, TN, October 1978.

32. J. G. Merkle, et al., *Test of 6-Inch-Thick Pressure Vessels, Series 4: Intermediate Test Vessels V-5 and V-9 with Nozzle Corner Cracks,* ORNL/NUREG-7, Oak Ridge National Laboratory, Oak Ridge, TN, August 1977.

33. R. H. Bryan, et al., *Test of 6-Inch-Thick Pressure Vessels, Series 3: Intermediate Test Vessel V-8,* NUREG/CR-0675 (ORNL/NUREG-58), Oak Ridge National Laboratory, Oak Ridge, TN, December 1979.

34. R. H. Bryan, et al., *Pressurized-Thermal Shock Test of 6-Inch-Thick Pressure Vessel, PTSE-1: Investigations of Warm Prestressing and Upper-Shelf Arrest*, NUREG/CR-4106 (ORNL-6135), Oak Ridge National Laboratory, Oak Ridge, TN, April 1985.

35. R. H. Bryan, et al., *Pressurized Thermal Shock Test of 6-Inch-Thick Pressure Vessel PTSE-2: Investigation of Low Tearing Resistance and Warm Prestressing*, NUREG/CR-4888 (ORNL-6377), Oak Ridge National Laboratory, Oak Ridge, TN, December 1987.

36. H. Keinanen, et al., "Pressurized Thermal Shock Tests with Model Pressure Vessels Made of VVER-440 Reactor Steel," *IAEA/CSNI Specialists' Meeting on Fracture Mechanics Verification by Large-Scale Testing, Oak Ridge, Tennessee*, *October 26-29, 1992*, NUREG/CP-0131 (ORNL/TM-12413), October 1993, 275-288.

37. B. R. Bass, et al., *CSNI Project for Fracture Analyses of Large-Scale International Reference Experiments (FALSIRE II)*, NUREG/CR-6460 (ORNL/TM-13207), Oak Ridge National Laboratory, Oak Ridge, TN, April 1996.

38. L. Stumpfrock, "FALSIRE Results for NKS-3 and NKS-4," *IAEA/CSNI Specialists' Meeting on Fracture Mechanics Verification by Large-Scale Testing, Oak Ridge, Tennessee*, *October 26-29, 1992*, NUREG/CR-0131 (ORNL/TM-12413), October 1993, 151-188.

39. L. Stumpfrock, et al., "Fracture Mechanics Investigations on Cylindrical Large-Scale Specimens under Thermal-Shock Loading," *Journal of Nuclear Engineering Design* **144**, (1993) 31-44.

40. E. Morland, "Spinning Cylinder Experiments SC-I and SC-II: A Review of Results and Analyses Provided to the FALSIRE Project," *IAEA/CSNI Specialists' Meeting on Fracture Mechanics Verification by Large-Scale Testing, Oak Ridge, Tennessee*, *October 26-29, 1992*, NUREG/CR-0131 (ORNL/TM-12413), October 1993, 39-74.

41. D. J. Lacey, et al., *Spinning Cylinder Test 4: An Investigation of Transition Fracture Behavior for Surface Breaking Defects in Thick-Section Steel Specimens*, AEA Technology Report AEA TRS 4098, June 1991.

42. R. D. Cheverton, et al., "Review of Pressurized-Water-Reactor-Related Thermal Shock Studies," *Fracture Mechanics: Nineteenth Symposium (June 30-July 2, 1986)*, ASTM STP-969, American Society for Testing and Materials, (1988) 752-766.

43. R. D. Cheverton, "Thermal Shock Experiments with Flawed Clad Cylinders," *Journal of Nuclear Engineering and Design* **124**, (1990) 109-119.

44. B. R. Bass, J. Wintle, R. C. Hurst, and N. Taylor (eds), *NESC-1 Project Overview*, EUR 19051EN, European Commission, Directorate-General Joint Research Centre, Institute for Advanced Materials, Petten, The Netherlands, 2001.

45. H. Okumura, et al., "PTS Integrity Study in Japan," *Ninth International Conference on Structural Mechanics in Reactor Technology*, Vol. F, (1989) 7-12.

46. D. J. Naus, et al., *High-Temperature Crack Arrest Behavior in 152-mm-Thick SEN Wide Plates of Quenched and Tempered A533 Grade B Class 1 Steel*, NUREG/CR-5330 (ORNL-11083), Oak Ridge National Laboratory, Oak Ridge, TN, April 1989.

47. D. J. Naus, et al., *Crack-Arrest Behavior in SEN Wide Plates of Low-Upper-Shelf Base Metal Tested Under Nonisothermal Conditions: WP-2 Series*, NUREG/CR-5451 (ORNL-6584), Oak Ridge National Laboratory, Oak Ridge, TN, April 1989.

48. K. Kussmaul, R. Gillot, and T. Elenz, "Full Thickness Crack Arrest Investigations on Compact Specimens and a Heavy-Wide Plate," *IAEA/CSNI Specialists' Meeting on Fracture Mechanics Verification by Large-Scale Testing, Oak Ridge, Tennessee*, *October 26-29, 1992*, NUREG/CR-0131 (ORNL/TM-12413), October 1993, 551-572.

49. D. Moinerau, et al., "Cleavage Fracture of Specimens Containing an Underclad Crack, PVP Vol. 233, *Pressure Vessel Fracture, Fatigue and Life Management,* American Society of Mechanical Engineers, 1992.

50. J. A. Keeney, B. R. Bass, and W. J. McAfee, "Fracture Assessment of Weld Material from a Full-Thickness Clad RPV Shell Segment," *Fatigue and Fracture Mechanics, 20th Volume,* ASTM STP-1321, eds., J. H. Underwood, B. D. McDonald, and M. R. Mitchell, American Society of Materials and Testing, 1997.

51. J. A. Keeney and P. T. Williams, "Fracture Analysis of Ductile Crack Growth in Weld Material from a Full-Thickness Clad RPV Shell Segment," *Fatigue and Fracture Mechanics, 29th Volume*, ASTM STP-1332, eds. T. L. Panontin and S. D. Sheppard, American Society of Materials and Testing, 1998.

52. B. R. Bass, et al., "Evaluation of Constraint Methodologies Applied to Shallow-Flaw Cruciform Bend Specimens Tested under Biaxial Loading Conditions," PVP Vol. 365, *Proceedings of the 1998 ASME Pressure Vessel and Piping Conference,* San Diego, CA, July 1998, 11-26.

53. M. G. Morgan and M. Henrion, *Uncertainty – A Guide to Dealing with Uncertainty in Quantitative Risk and Policy Analysis*, Cambridge University Press, Cambridge, UK, 1990.

54. F.A. Simonen, S.R. Doctor, G.J. Schuster, and P.G. Heasler, "A Generalized Procedure for Generating Flaw Related Inputs for the FAVOR Code," NUREG/CR-6817, Rev. 1, U.S. Nuclear Regulatory Commission, October 2003.

55. G. J. Schuster, S. R. Doctor, S. L. Crawford, and A. F. Pardini, *Characterization of Flaws in U.S. Reactor Pressure Vessels: Density and Distribution of Flaw Indications in PVRUF*, USNRC Report NUREG/CR-6471, Vol. 1, U.S. Nuclear Regulatory Commission, Washington, D.C. (1998).

56. G. J. Schuster, S. R. Doctor, and P. G. Heasler, *Characterization of Flaws in U.S. Reactor Pressure Vessels: Validation of Flaw Density and Distribution in the Weld Metal of the PVRUF Vessel,* USNRC Report NUREG/CR-6471, Vol. 2, U.S. Nuclear Regulatory Commission, Washington, D.C. (2000).

57. G. J. Schuster, S. R. Doctor, S. L. Crawford, and A. F. Pardini, *Characterization of Flaws in U.S. Reactor Pressure Vessels: Density and Distribution of Flaw Indications in the Shoreham Vessel,* USNRC Report NUREG/CR-6471, Vol. 3, U.S. Nuclear Regulatory Commission, Washington, D.C. (1999).

58. A. M. Law and W. D. Kelton, *Simulation Modeling and Analysis*, 3rd ed., McGraw-Hill, New York, NY, (2000).

59. A. J. Brothers and S. Yukawa, "The Effect of Warm Prestressing on Notch Fracture Strength," *Journal of Basic Engineering*, *Transaction of the ASME*, Series D, **85**(1), (1963) 87-104.

60. R. W. Nichols, "The Use of Overstressing Techniques to Reduce the Risk of Subsequent Brittle Fracture: Parts 1 and 2," *British Welding Journal*, January and February 1968.

61. J. J. McGowan, "An Assessment of the Beneficial Effects of Warm Prestressing on the Fracture Properties of Nuclear Reactor Pressure Vessels Under Severe Thermal Shock," Westinghouse Electric Company, WCAP-9178, March 1978.

62. G. C. Chell, "A Theory of Warm Prestressing: Experimental Validation and the Implication for Elastic-Plastic Failure Criteria," CERL Lab Note RD/L/N78/79, September 1979.

63. G. C. Chell, "Some Fracture Mechanics Applications of Warm Prestressing to Pressure Vessels," *4th International Conference on Pressure Vessel Technology*, Paper C22/80, London, May 1980.

64. B. W. Pickles and A. Cowan, "A Review of Warm Prestressing Studies," *International Journal of Pressure Vessels and Piping* **14**, (1983) 95-131.

65. D. Lidbury and P. Birkett, "Effect of Warm Prestressing on the Transition Toughness Behaviour of an A533 Grade B Class 1 Pressure Vessel Steel," *ASTM STP 1074, Fracture Mechanics: 21st Symposium*, American Society for Testing and Materials, Philadelphia, PA, (1990) 264-285.

66. F. M. Burdekin and D. P. G. Lidbury, "Views of TAGSI on the Current Position with Regard to Benefits of Warm Prestressing," *International Journal of Pressure Vessels and Piping* **76**, (1999) 885-890.

67. H. Kordisch, R. Böschen, J. G. Blauel, W. Schmitt, and G. Nagel, "Experimental and Numerical Investigation of the Warm-Prestressing (WPS) Effect Considering Different Load Paths," *Nuclear Engineering Design* **198**, (2000) 89-96.

68. J. H. Chen, V. B. Wang, G. Z. Wang, and X. Chen, "Mechanism of Effects of Warm Prestressing on Apparent Toughness of Precracked Specimens of HSLA Steels," *Engineering Fracture Mechanics* **68**, (2001) 1669-1689.

69. W. Lefevre, G. Barbier, R. Masson, and G. Rousselier, "A Modified Beremin Model to Simulate the Warm Pre-Stress Effect," *Nuclear Engineering and Design* **216**, (2002) 27-42.

70. M. T. Kirk, "Inclusion of Warm Prestressing Effects in Probabilistic Fracture Mechanics Calculations Performed to Assess the Risk of RPV Failure Produced by Pressurized Thermal Shock Events: An Opinion," presented at the *NATO Advanced Research Workshop – Scientific Fundamentals for the Life Time Extension of Reactor Pressure Vessels*, Kiev, Ukraine, April 22-25, 2002.

71. M. T. Kirk and T. L. Dickson, "The Sensitivity of Risk-Informed Reactor Structural Integrity Analysis Results to Various Interpretations of Warm Pre-Stress," PVP2009-77127 *Proceedings of 2009 ASME Pressure Vessel and Piping Division Conference*, Prague, Czech Republic, July 27-31, 2009.

72. D. Moinereau, A. Dahl, S. Chapuliot, T. Yritzinn, Ph. Gilles, and B. Tanguy, "The Demonstration of Warm Prestress Effect in RPV Assessment: Some Experimental Results and Their Interpretation by Fracture Mechanics," presented at the *7th International ASTM/ESIS Symposium on Fatigue and Fracture Mechanics, 36th ASTM National Symposium on Fatigue and Fracture Mechanics*, November 14-16, 2007, Tampa, Florida, USA.

73. T. W. Anderson and D.A. Darling, "A Test of Goodness of Fit," *J. Am. Statist. Assoc,* **49**, (1954) 765-769.

74. M. A. Stephens, "Goodness of Fit and Some Comparisons," *J. Am. Statist. Assoc.* **69**, (1974) 730-737.

75. K. Pearson, "On a Criterion that a Given System of Deviations from the Probable in the Case of a Correlated System of Variables is Such That it can be Reasonably Supposed to Have Arisen in Random Sampling," *Phil. Mag.* **50**(5), (1900) 157-175.

76. B. W. Brown and J. Lovato, *RANLIB – A Library of Fortran Routines for Random Number Generation*, Department of Biomathematics, University of Texas, Houston, TX, 1994.

77. P. L'Ecuyer, "Efficient and Portable Combined Random Number Generators," *Communications of the ACM* **31**(6), (1988) 742-774.

78. P. L'Ecuyer and S. Cote, "Implementing a Random Number Package with Splitting Facilities." *ACM Transactions on Mathematical Software* **17**, (1991) 98-111.

79. A. Rukhin, et al., *A Statistical Test Suite for Random and Pseudorandom Number Generators for Cryptographic Applications*, NIST Special Publication 800-22, National Institute of Standards and Technology, Gaithersburg, MD, May 15, 2001.

80. G. E. P. Box and M. E. Müller, "A Note on the Generation of Random Normal Deviates," *Annals of Mathematical Statistics*, **29** (1958), 610-611.

81. M. E. Müller, "An Inverse Method for the Generation of Random Normal Deviates on Large Scale Computers," *Math. Tables Aids Comp.* **63**, (1958) 167-174.

82. M. Abramowitz and I. A. Stegun, *Handbook of Mathematical Functions*, Dover Publications, Inc., New York, (1972) 931.

83. J. H. Ahrens and U. Dieter, "Extensions of Forsythe's Method for Random Sampling from the Normal Distribution," *Math. Comput.* **27**(124), (1973) 927-937.

84. Kennedy and Gentle, *Statistical Computing*, Marcel Dekker, NY, (1980) 95.

85. N. L. Johnson, "Systems of Frequency Curves Generated by Methods of Translation," *Biometrika* **36**, (1949) 149-176.

86. J. F. Slifker and S. S. Shapiro, "The Johnson System: Selection and Parameter Estimation," *Technometrics* **22**(2), (1980) 239-246.

87. N. L. Johnson, S. Kotz, and N. Balakrishnan, *Continuous Univariate Distributions*, *Vol. 1*, 2nd ed., Houghton Mifflin, Boston (1994), p. 35.

88. EPRI Special Report, 1978, *Flaw Evaluation Procedures: ASME Section XI*, EPRI NP-719-SR, Electric Power Research Institute, Palo Alto, CA.

89. K. O. Bowman and P. T. Williams, *Technical Basis for Statistical Models of Extended K_{Ic} and K_{Ia} Fracture Toughness Databases for RPV Steels*, ORNL/NRC/LTR-99/27, Oak Ridge National Laboratory, Oak Ridge, TN, February, 2000.

90. R. D. Cheverton, et al., *Pressure Vessel Fracture Studies Pertaining to the PWR Thermal-Shock Issue: Experiment TSE-7, NUREG/CR-4304 (ORNL/TM-6177),* Oak Ridge National Laboratory*,* Oak Ridge, TN, August, 1985.

91. F. Li, *Assessment of Pressure Vessel Failure Due to Pressurized Thermal Shock with Consideration of Probabilistic-Deterministic Screening and Uncertainty Analysis,* Ph.D. Dissertation, Center for Technology Risk Studies, University of Maryland, 2001.

92. T. Fang and M. Modarres, "Probabilistic and Deterministic Treatments for Multiple Flaws in Reactor Pressure Vessel Safety Analysis," *Transactions of the 17th International Conference on Structural Mechanics in Reactor Technology (SMiRT 17),* August 17-22, 2003, Prague, Czech Republic.

93. A. L. Hiser, et al., "J-R Curve Characterization of Irradiated Low Upper Shelf Welds," NUREG/CR-3506, U. S. Nuclear Regulatory Commission, 1984.

94. D. E. McCabe, R. K. Nanstad, S. K. Iskander, D. W. Heatherly, and R. L. Swain, *Evaluation of WF-70 Weld Metal From the Midland Unit 1 Reactor Vessel*, USNRC Report NUREG/CR-5736 (ORNL/TM-13748), Oak Ridge National Laboratory, Oak Ridge, TN, November 2000.

95. J. R. Hawthorne, J.R., "Investigations of Irradiation-Anneal-Reirradiation (IAR) Properties Trends of RPV Welds: Phase 2 Final Report," NUREG-CR/5492, U. S. Nuclear Regulatory Commission, 1990.

96. *Standard Test Method for Measurement of Fracture Toughness*, ASTM E 1820-1, Annual Book of ASTM Standards 2002, Section Three, Metals Test Methods and Analytical Procedures, Volume 03.01, American Society for Testing and Materials, West Conshohocken, PA (2002).

97. M. EricksonKirk and M. T. EricksonKirk, "The Relationship Between the Transition and Upper-shelf Fracture Toughness of Ferritic Steels," *Fatigue Fract Engng Mater Struct* **29**, (2006) 1–13.

98. M. T. Kirk, B. R. Bass, T. L. Dickson, C. E. Pugh, T. Santos, and P. T. Williams, "Probabilistic Fracture Mechanics: Models, Parameters, and Uncertainty Treatment Used in FAVOR Version 04.1," U.S. Nuclear Regulatory Commission, NUREG-1807, 2006.

99. EricksonKirk, Marjorie and EricksonKirk, Mark, "An Upper-Shelf Fracture Toughness Master Curve for Ferritic Steels," *International Journal of Pressure Vessels and Piping*, **83** (2006) 571–583.

100. E. D. Eason, J. E. Wright, and G. R. Odette, "Improved Embrittlement Correlations for Reactor Pressure Vessel Steels," NUREG/CR-6551, U. S. Nuclear Regulatory Commission, Washington, DC, 1998.

101. M. T. Kirk, C. S. Santos, E.D. Eason, J.E. Wright, and G. R. Odette, "Updated Embrittlement Trend Curve for Reactor Pressure Vessel Steels," Paper No. G01-5, *Transactions of the 17th International Conference on Structural Mechanics in Reactor Technology (SMiRT 17)*, Prague, Czech Republic, August 17-22, 2003.

102. I. Guttman, S. S. Wilkes, and J. S. Hunter, *Introductory Engineering Statistics*, 3rd ed., John Wiley and Sons, In, New York, 1982, pp. 302-331.

103. M. Evans, N. Hastings, and B. Peacock, *Statistical Distributions*, 3rd ed., Wiley Series in Probability and Statistics, John Wiley and Sons, New York, 2000.

104. P. Bratley, B. L. Fox, and L. E. Schrage, *A Guide to Simulation*, 2nd ed., Springer Verlag, New York, 1987, pp. 150-151.

105. N. Siu, S. Malik, D. Bessette, R. Woods, A. Mosleh, and M. Modarres, "Treating Aleatory and Epistemic Uncertainties in Analyses of Pressurized Thermal Shock," *Proceedings of PSAM 5, International Conference on Probabilistic Safety Assessment and Management*, Osaka, Japan, (2000) 377-382.

106. R. W. Lewis, K. Morgan, H. R. Thomas, and K. N. Seetharamu, *The Finite-Element Method in Heat Transfer Analysis*, John Wiley & Sons, New York, 1996.

107. R. D. Cook, D. S. Malkus, and M. E. Plesha, *Concepts and Applications of Finite Element Analysis, 3r^{d} ed.,* John Wiley & Sons, New York, 1989.

108. M. Nifenegger, "The Proper Use of Thermal Expansion Coefficients in Finite Element Calculations," *Laboratory for Safety and Accident Research*, Paul Scherrer Institute, Würenlingen, Switzerland, 2005.

109. T.L .Dickson, W.J. McAfee, W.E. Pennell, and P.T. Williams, Evaluation of Margins in the ASME Rules for Defining the P-T Curve for an RPV, NUREG/CP-0166, Oak Ridge National Laboratory, Oak Ridge, TN, *Proceedings of the Twenty-Sixth Water Reactor Safety Meeting* , (1999) 47-72.

110. R. E. Faw and J. K. Shultis, *Fundamentals of Nuclear Science and Engineering*, CRC Press, 2002.

111. J. W. Bryson, T. L. Dickson, and J. A. Keeney, "Stress-Intensity-Factor Influence Coefficients for Axially and Circumferentially Oriented Semi-Elliptical Inner-Surface Flaws in Clad Pressure Vessels (R_i/t = 20)," ORNL/NRC/LTR-98/7, Oak Ridge National Laboratory, Oak Ridge, TN, August, 1998.

112. S. Yin, T. L. Dickson, P. T. Williams, and B. R. Bass, "Stress Intensity Factor Influence Coefficients for External Surface Flaws in Boilng Water Reactor Pressure Vessels," proceedings of *2009 ASME Pressure Vessels and Piping Conference*, PVP2009-77143, July, 2009, Prague, Czech Republic.

113. H. F. Bückner, "A Novel Principle for the Computation of Stress Intensity Factors," *Z. angew. Math. Mech.* **50**, (1970) 529-546.

114. C. B. Buchalet and W. H. Bamford, "Stress Intensity Factor Solutions for Continuous Surface Flaws in Reactor Pressure Vessels," ASTM STP 590, *Mechanics of Crack Growth*, American Society for Testing and Materials, (1976) 385-402.

115. J. Heliot, R. C. Labbens, and A. Pellissier-Tanon, "Semi-Elliptical Cracks in a Cylinder Subjected to Stress Gradients," ASTM STP 677, *Fracture Mechanics,* ed. C. W. Smith, American Society for Testing and Materials, (1979) 341-364.

116. J. J. McGowan and M. Raymund, "Stress Intensity Factor Solutions for Internal Longitudinal Semi-Elliptical Surface Flaws in a Cylinder Under Arbitrary Loadings," ASTM STP 677, *Fracture Mechanics*, ed. C. W. Smith, American Society for Testing and Materials, (1979) 365-380.

117. I. S. Raju and J. C. Newman, Jr., "Stress Intensity Factor Influence Coefficients for Internal and External Surface Cracks in Cylindrical Vessels," PVP Vol. 58, *Aspects of Fracture Mechanics in Pressure Vessels and Piping*, ASME Pressure Vessels and Piping Conference, (1982) 37-48.

118. S. K. Iskander, R. D. Cheverton, and D. G. Ball, OCA-I, A Code for Calculating the Behavior of Flaws on the Inner Surface of a Pressure Vessel Subjected to Temperature and Pressure Transients, NUREG/CR-2113 (ORNL/NUREG-84), Oak Ridge National Laboratory, Oak Ridge, TN, 1981.

119. R. D. Cheverton and D. G. Ball, *OCA-P, A Deterministic and Probabilistic Fracture Mechanics Code for Application to Pressure Vessels,* NUREG/CR-3618 (ORNL-5991), Oak Ridge National Laboratory, Oak Ridge, TN, May 1984.

120. J. W. Bryson and T. L. Dickson, "Stress-Intensity-Factor Influence Coefficients for Axial and Circumferential Flaws in Reactor Pressure Vessels," PVP Vol. 250, ASME Pressure Vessels and Piping Conference, (1993) 77-88.

121. T. L. Dickson, J. A. Keeney, and J. W. Bryson, "Validation of FAVOR Code Linear-Elastic Fracture Solutions for Finite-Length Flaw Geometries," PVP-Vol. 304, *Fatigue and Fracture Mechanics in Pressure Vessels and Piping*, ASME Pressure Vessels and Piping Conference, (1995) 51-58.

122 . J. W. Bryson and T. L. Dickson, *Stress-Intensity-Factor Influence Coefficients for Circumferentially Oriented Semielliptical Inner Surface Flaws in Clad Pressure Vessels (R_i / t = 10)*, ORNL/NRC/LTR-94/8, Oak Ridge National Laboratory, Oak Ridge, TN, April, 1994.

123. *ABAQUS Theory Manual, Version 4.8,* Hibbit, Karlson, and Sorenesen, Inc., Providence, RI, 1989.

124. S. Timoshenko, *Theory of Plates and Shells*, McGraw-Hill, New York, 1940.

125. S. Yin, T.L. Dickson, P.T. Williams, and B.R. Bass, "Verification of New Capabilities of Deterministic Load Module of FAVOR, v09.1," PVP2010-25439, *Proceedings of 2010 ASME Pressure Vessels and Piping Division Conference*, Bellevue, WA, July, 2010.

126. S. Yin, T.L. Dickson, P.T. Williams, and B.R. Bass, "Stress Intensity Factor Influence Coefficients for External Surface Flaws in Boiling Water Reactor Pressure Vessels," *Proceedings of 2009 ASME Pressure Vessels and Piping Conference*, PVP2009-77143, Prague, Czech Republic, July, 2009.

127. T. L. Dickson, B. R. Bass, and P. T. Williams, "Validation of a Linear-Elastic Fracture Methodology for Postulated Flaws Embedded in the Wall of a Nuclear Reactor Pressure Vessel," PVP-Vol. 403, *Severe Accidents and Other Topics in RPV Design*, American Society of Mechanical Engineering Pressure Vessels and Piping Conference, (2000) 145-151.

128. R.C. Cipolla, et al., Failure Analysis Associates, Computational Method to Perform the Flaw Evaluation Procedure as Specified in the ASME Code, Section XI, Appendix A, EPRI Report NP-1181, September, 1979.

129. *American Society of Mechanical Engineers Boiler and Pressure Vessel Code,* Section XI, Rules for Inservice Inspection of Nuclear Power Plant Components, Nonmandatory Appendix A, Analysis of Flaws, Article A-3000, Method for K_I Determination, American Society of Mechanical Engineers, New York, 1998.

130. T. L. Dickson, B. R. Bass, and W. J. McAfee, "The Inclusion of Weld Residual Stress In Fracture Margin Assessments of Embrittled Nuclear Reactor Pressure Vessels," PVP-Vol. 373, *Fatigue, Fracture, and Residual Stresses*, ASME Pressure Vessels and Piping Conference, (1998) 387-395.

131. J. A. Keeney, et al., *Preliminary Assessment of the Fracture Behavior of Weld Material in Full-Thickness Clad Beams*, NUREG/CR-6228 (ORNL/TM-12735), Oak Ridge National Laboratory, Oak Ridge, TN, October 1994.

132. W. E. Pennell, *Heavy-Section Steel Technology Program: Semiannual Progress Report for October 1996-March 1997*, NUREG/CR-4219 **14(1)**, (ORNL/TM-9593/V14&N1), Oak Ridge National Laboratory, Oak Ridge, TN, (1997) 36-39.

133. M. T. Kirk, B. R. Bass, T. L. Dickson, C. E. Pugh, T. Santos, and P. T. Williams, "Probabilistic Fracture Mechanics: Models, Parameters, and Uncertainty Treatment Used in FAVOR Version 04.1," U.S. Nuclear Regulatory Commission, NUREG-1807, 2006.

134. E. D. Eason, G. R. Odette, R. K. Nanstad, and T. Yamamoto, *A Physically Based Correlation of Irradiation-Induced Transition Temperature Shifts for RPV Steels*, Oak Ridge National Laboratory, ORNL/TM-2006/530, 2006.

135. R. K. Nanstad, J. A. Keeney, and D. E. McCabe, *Preliminary Review of the Bases for the K_{Ic} Curve in the ASME Code*, ORNL/NRC/LTR-93/15, Oak Ridge National Laboratory, Oak Ridge, TN, 1993.

136. *Standard Test Method for Plane-Strain Fracture Toughness of Metallic Materials,* E-399-90, Annual Book of ASTM Standards - Section 3: Metals Test Methods and Analytical Procedures, vol. 03.01, *Metals – Mechanical Testing; Elevated and Low-Temperature Tests; Metallography*, American Society for Testing and Materials, West Conshohocken, PA, 1998.

137. *ASME Boiler and Pressure Vessel Code*, Section III, Article NB-2331, American Society of Mechanical Engineers, New York, NY, (1998).

138. R. K. Nanstad, F. M. Haggag, and D. E. McCabe, *Irradiation Effects on Fracture Toughness of Two High-Copper Submerged-Arc Welds, HSSI Series 5,* USNRC Report NUREG/CR-5913 (ORNL/TM-12156/V1 and V2) Vols. 1 and 2, Oak Ridge National Laboratory, Oak Ridge, TN, October 1992.

139. D. E. McCabe, *A Comparison of Weibull and β_{Ic} Analysis of Transition Range Fracture Toughness Data,* USNRC Report NUREG/CR-5788 (ORNL/TM-11959), Oak Ridge National Laboratory, Oak Ridge, TN, January 1992.

140. T. Iawadate, Y. Tanaka, S. Ono, and J. Watanabe, "An Analysis of Elastic-Plastic Fracture Toughness Behavior for J_{Ic} Measurements in the Transition Region," *Elastic-Plastic Fracture: Second Symposium, Vol. II-Fracture Resistance Curves and Engineering Applications*, (edited by C. F. Shih and J. P. Gudas) ASTM STP 803, (1983) II531-II561.

141. D. E. McCabe, R. K. Nanstad, S. K. Iskander, and R. L. Swain, *Unirradiated Material Properties of Midland Weld WF-70,* USNRC Report NUREG/CR-6249 (ORNL/TM-12777), Oak Ridge National Laboratory, Oak Ridge, TN, October 1994.

142. J. J. McGowan, R. K. Nanstad, and K. R. Thoms, *Characterization of Irradiated Current-Practice Welds and A533 Grade B Class 1 Plate for Nuclear Pressure Vessel Service*, USNRC Report NUREG/CR-4880 (ORNL-6484/V1 and V2), Oak Ridge National Laboratory, Oak Ridge, TN, July 1988.

143. American Society for Testing and Materials, *Standard Test Method for Determining Plane-Strain Crack Arrest Toughness, K_{Ia}, of Ferritic Steels,* E 1221-88, Annual Book of ASTM Standards, Section 3: Metals Test Methods and Analytical Procedures, vol. 03.01, *Metals – Mechanical Testing; Elevated and Low-Temperature Tests; Metallography*, American Society for Testing and Materials, West Conshohocken, PA, 1998.

144. S. K. Iskander, W. R. Corwin, R. K. Nanstad, *Results of Crack-Arrest Tests on Two Irradiated High-Copper Welds,* USNRC Report NUREG/CR-5584 (ORNL/TM-11575), Oak Ridge National Laboratory, Oak Ridge, TN, December 1990.

145. S. K. Iskander, C. A. Baldwin, D. W. Heatherly, D. E. McCabe, I. Remec, and R. L. Swain, *Detailed Results of Testing Unirradiated and Irradiated Crack-Arrest Toughness Specimens from the Low Upper-Shelf Energy, High Copper Weld, WF-70,* NUREG/CR-6621 (ORNL/TM-13764) under preparation.

146. S. K. Iskander, R. K. Nanstad, D. E. McCabe, and R. L. Swain, "Effects of Irradiation on Crack-Arrest Toughness of a Low Upper-Shelf Energy, High-Copper Weld," *Effects of Radiation on Materials: 19th International Symposium, ASTM STP 1366*, M. L. Hamilton, A. S. Kumar, S. T. Rosinski, and M. L. Grossbeck, eds., American Society for Testing and Materials, to be published.

147. E. J. Ripling and P. B. Crosley, "Strain Rate and Crack Arrest Studies," *HSST 5th Annual Information Meeting*, Paper No. 9, 1971.

148. E. J. Ripling and P. B. Crosley, "Crack Arrest Studies," *HSST 6th Annual Information Meeting*, Paper No. 10, 1972.

149. R. D. Cheverton, D. G. Ball, S. E. Bolt, S. K. Iskander, and R. K. Nanstad, *Pressure Vessel Fracture Studies Pertaining to the PWR Thermal-Shock Issue: Experiments TSE-5, TSE-5A, and TSE-6,* NUREG/CR-4249 (ORNL-6163), Oak Ridge National Laboratory, Oak Ridge, TN, June 1985.

150. "Standard Test Method for Determination of Reference Temperature, T_0, for Ferritic Steels in the Transition Range," E 1921-97, Annual Book of ASTM Standards Section 3: Metals Test Methods and Analytical Procedures, vol. 03.01, *Metals – Mechanical Testing; Elevated and Low-Temperature Tests; Metallography*, American Society for Testing and Materials, West Conshohocken, PA, 1998.

151. M. Kirk, R. Lott, W. L. Server, R. Hardies, and S. Rosinski, "Bias and Precision of T_0 Values Determined Using ASTM Standard E 1921-97 for Nuclear Reactor Pressure Vessel Steels," *Effects of Radiation on Materials: 19th International Symposium, ASTM STP 1366,* M. L. Hamilton, A. S. Kumar, S. T. Rosinski, and M. L. Grossbeck, Eds., American Society for Testing and Materials, West Conshococken, PA, (2000) 143-161.

152. K. Wallin, "Master Curve Based Correlation Between Static Initiation Toughness, K_{Ic}, and Crack Arrest Toughness, K_{Ia}," presented at *24th MPA Seminar*, Stuttgart, Germany, October 8 and 9, 1998.

153. K. Wallin, "Application of the Master Curve Method to Crack Initiation and Crack Arrest," *Fracture, Fatigue, and Weld Residual Stress*, PVP Vol. 393, ASME Pressure Vessels and Piping Conference, Boston, MA, August 1-5, 1999.

154. *Reactor Vessel Integrity Database (RVID), User's Manual,* Version 1.1, U. S. Nuclear Regulatory Commission, July 1995.

155. *Reactor Vessel Integrity Database (RVID2)*, Version 2.1.1, U. S. Nuclear Regulatory Commission July 6, 2000.

Appendix A – Background and Antecedents of FAVOR

Codes Pre-Dating FAVOR

OCA-P [A1] and VISA-II [A2] are PFM computer programs that were developed at Oak Ridge National Laboratory (ORNL) and Pacific Northwest National Laboratory (PNNL), respectively, in the 1980s with NRC funding. These computer codes had the specific goal of performing PFM analyses of PTS transients. There have also been other proprietary and public-domain PTS PFM codes independently developed in the US and internationally by reactor vendors and research laboratories. The OCA-P code [A1] (and its deterministic predecessors, OCA-I [A3], and OCA-II [A4]) and the VISA II code [A2] was preceded by two earlier probabilistic computer programs developed by the NRC, specifically OCTAVIA [A5] (**O**perationally **C**aused **T**ransients **a**nd **V**essel **I**ntegrity **A**nalysis) and a second unnamed code developed by Gamble and Strosnider [A6].

OCTAVIA [A5] was developed in the mid-1970s to calculate the probability of RPV failure from operational pressure transients which can occur in a PWR vessel at low operating temperatures. OCTAVIA computed the pressure at which the vessel would fail for different-sized flaws existing in the beltline region, where only axially oriented flaws in the vessel beltline were considered. The probability of vessel failure was then calculated as the product of two factors: the probability that the maximum-sized flaw in the beltline is of a given size, and the probability that the transient would occur and would have a pressure exceeding the vessel failure pressure associated with the flaw size. The probabilities of vessel failure were summed over the various sizes to obtain the total vessel failure probability.

The code developed by Gamble and Strosnider [A6] calculated the probability of flaw-induced failure in the vessel beltline region using mathematical relationships based on linear-elastic fracture mechanics to model variable interaction and to estimate a failure rate. The RPV failure criterion was based on a comparison of the driving-force stress-intensity factor, K_I, with the static initiation toughness, K_{Ic}, of the material. Monte Carlo methods were used to simulate independently each of the several variables and model their interaction to obtain values of K_I and K_{Ic} to predict the probabilities of vessel failure. Near the end of this study, an *importance-sampling* scheme was incorporated into the computer code to increase the code's efficiency for performing calculations in the transition-temperature region and to allow greater accuracy for analyzing conditions associated with low-failure probabilities (see Appendix B of ref. [A6]).

An early version of the VISA code [A7] was used in the NRC staff evaluation of PTS as described in SECY-82-465 [A8]. VISA is a simulation model, which means that the failure probability is assessed by performing a large number of deterministic evaluations with random variables selected for various parameters. The user can specify the thermal transient with either a polynomial representation or an exponential decay model, and the pressure transient can be specified with a polynomial function. The deterministic analysis in VISA assumes linear-elastic material behavior, implying that the total maximum stresses are less than the yield strength of the material. This assumption of linear-elastic deformation response allows stress components to be added through linear superposition, and the principles of linear-elastic fracture mechanics (LEFM) can be applied. For rapid thermal transients, high stresses (potentially above the yield strength of the cladding) can occur locally at the inside surface of the vessel wall; however, acceptable stress distributions can still be obtained over the remaining section if the overstressed region is relatively thin. Stress intensity factors are calculated from influence coefficients developed by Heliot, Labbens, and Pellissier-Tanon [A9, A10].

Examples of international PFM/PTS codes include PASCAL (**P**FM **A**nalysis of **S**tructural **C**omponents in **A**ging **L**WR) [A11-A13], OPERA [A14], and PARISH (**P**robabilistic **A**ssessment of **R**eactor **I**ntegrity under pressurized thermal **SH**ock) [A15]. In addition, other PFM codes such as PRAISE [A16] and STAR6 [A17] have been developed to calculate failure probabilities considering the aged condition of RCW piping systems allowing for factors such as fatigue crack growth, stress corrosion crack growth, and changes in mechanical properties.

The above codes perform PFM/PTS analyses using Monte Carlo techniques to estimate the increase in failure probability as the vessel accumulates radiation damage over its operating life. The results of such analyses, when compared with the limit of acceptable failure probability, provide an estimate of the residual life of a reactor pressure vessel. Also results of such analyses can be used to evaluate the potential benefits of plant-specific mitigating actions designed to reduce the probability of reactor vessel failure, thus potentially extending the operating life of the vessel [A18].

First Version of FAVOR

Previous efforts at obtaining the same probabilistic solutions to a specified PTS problem using different PFM codes have met with varying degrees of success [A19-A21]. Experience with the application of OCA-P, VISA-II, and other PFM codes as well as advancements in the science of probabilistic risk assessment (PRA) over the past 15 years have provided insights into areas where the PTS PFM methodology could be improved. The FAVOR computer code was initially

developed at ORNL in the early 1990s [A22] in an effort to combine the best attributes of OCA-P and VISA-II.

Subsequent Updates of FAVOR

In the ensuing years, the NRC-funded FAVOR code has continued its advancement with the goal of providing a computational platform for incorporating additional capabilities and new developments in relevant fracture-related disciplines.

During the 1990s, an updated computational methodology developed through research and interactions among experts in the relevant disciplines of thermal-hydraulics, probabilistic risk assessment (PRA), materials embrittlement, probabilistic fracture mechanics (PFM), and inspection (flaw characterization). This updated methodology was incrementally implemented into FAVOR. As depicted in Figure A1, there have been several public releases of FAVOR between 2001 and 2015.

The evolving versions of the FAVOR computer program (through the 2015 release) performed deterministic and risk-informed PFM analyses of the structural integrity of a nuclear reactor pressure vessel (RPV) subjected to overcooling events (e.g., pressurized thermal shock accidental transients) and normal cool-down transients (e.g., reactor shutdown). The FAVOR^{HT} computer program, released in 2006, carries deterministic and probabilistic fracture analyses of a nuclear RPV subjected to heat-up events (e.g., transients associated with the start-up of reactors), though FAVOR^{HT} did not have the capability to include external surface-breaking flaws in the model.

An objective of FAVOR, v12.1, was to consolidate and expand the modeling and analysis capabilities of the previous versions of FAVOR and FAVOR^{HT} discussed above into a single computer program. As a result, FAVOR, v12.1, generalized the capability to perform deterministic and probabilistic fracture analyses of PWRs and BWRs vessels subjected to cool-down and/or heat-up transients.

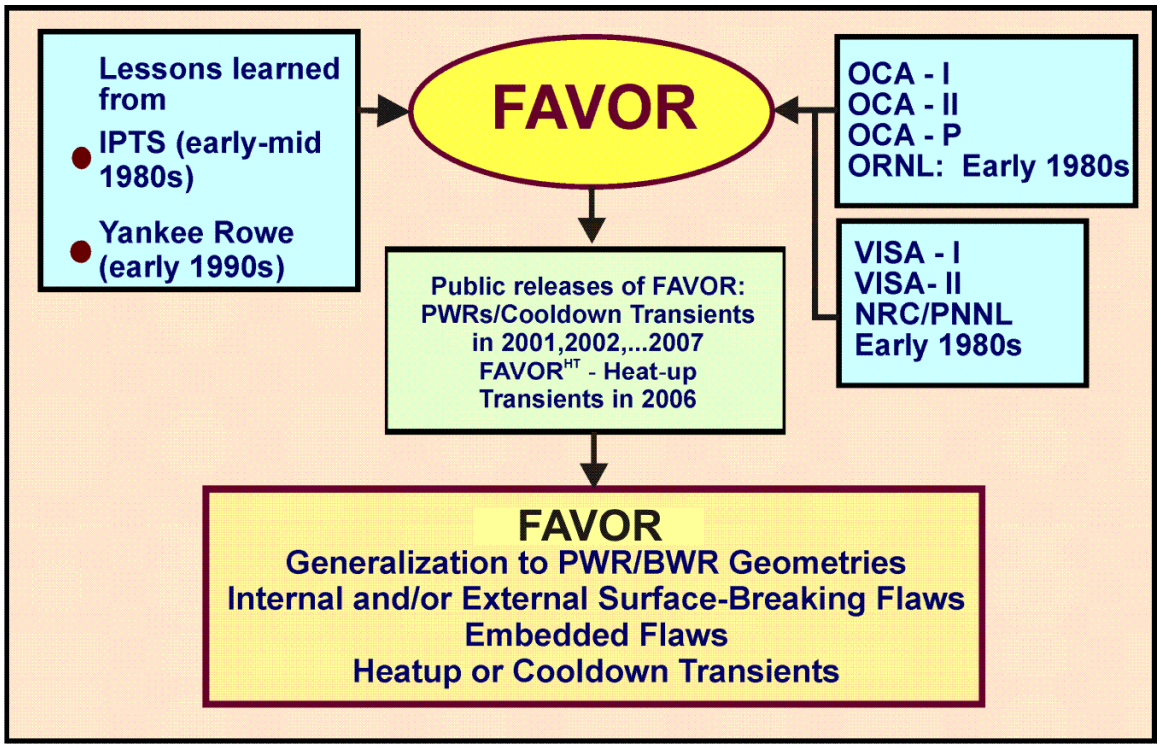

Fig. A1. Depiction of the development history of the FAVOR code from 2001 to the present release.

References to Appendix A

A1. R. D. Cheverton and D. G. Ball, *OCA-P, A Deterministic and Probabilistic Fracture Mechanics Code for Application to Pressure Vessels,* NUREG/CR-3618 (ORNL-5991), Oak Ridge National Laboratory, Oak Ridge, TN, May 1984.

A2. F. A. Simonen, et al., *VISA-II – A Computer Code for Predicting the Probability of Reactor Pressure Vessel Failure*, NUREG/CR-4486 (PNL-5775), Pacific Northwest Laboratory, Richland, Washington, March 1986.

A3. S. K. Iskander, R. D. Cheverton, and D. G. Ball, OCA-I, A Code for Calculating the Behavior of Flaws on the Inner Surface of a Pressure Vessel Subjected to Temperature and Pressure Transients, NUREG/CR-2113 (ORNL/NUREG-84), Oak Ridge National Laboratory, Oak Ridge, TN, 1981.

A4. D. G. Ball, R. D. Cheverton, J. B. Drake, and S. K. Iskander, *OCA-II, A Code for Calculating the Behavior of 2-D and 3-D Surface Flaws in a Pressure Vessel Subjected to Temperature and Pressure Transients*, NUREG/CR-3491 (ORNL-5934), Oak Ridge National Laboratory, Oak Ridge, TN, 1983.

A5. W. E. Vesely, E. K. Lynn, and F. F. Goldberg, *The Octavia Computer Code: PWR Reactor Pressure Vessel Failure Probabilities Due to Operationally Caused Pressure Transients*, NUREG-0258, U. S. Nuclear Regulatory Commission, Washington, D.C., 1978.

A6. R. M. Gamble and J. Strosnider, Jr., *An Assessment of the Failure Rate for the Beltline Region of PWR Pressure Vessels During Normal Operation and Certain Transient Conditions*, NUREG-0778, U. S. Nuclear Regulatory Commission, Washington, D.C., 1981.

A7. D. L. Stevens, F. A. Simonen, J. Strosnider, Jr., R. W. Klecker, D. W. Engel, and K. I. Johnson, *VISA – A Computer Code for Predicting the Probability of Reactor Pressure Vessel Failure*, NUREG/CR-3384, (PNL-4774), Pacific Northwest Laboratory, Richland, Washington, 1983.

A8. Policy Issue from J. W. Dircks to NRC Commissioners, *Enclosure A: NRC Staff Evaluation of Pressurized Thermal Shock, November 1982*, SECY-82-465, November 23, 1982, Division of Nuclear Reactor Regulation, U.S. Nuclear Regulatory Commission, Washington, D.C.

A9. R. Labbens, A. Pellissier-Tanon, and J. Heliot, "Practical Method for Calculating Stress-Intensity Factors Through Weight Functions," ASTM STP-590, *Mechanics of Crack Growth*, American Society for Testing and Materials, (1976) 368-384.

A10. J. Heliot, R. C. Labbens, and A. Pellissier-Tanon, "Semi-Elliptical Cracks in the Meridonal Plane of a Cylinder Subjected to Stress Gradients, Calculation of Stress Intensity Factors by the Boundary Integral Equations Method," *XIth National Symposium on Fracture Mechanics*, Blacksburg, VA, 1978.

A11. G. Yagawa, Y. Kanto, S. Yoshimura, H. Machida, and K. Shibata, "Probabilistic Fracture Mechanics Analysis of Nuclear Structural Components: A Review of Recent Japanese Activities," *Nuclear Engineering and Design* **207**, (2001) 269-286.

A12. K. Shibata, D. Kato, and Y. Li, "Development of a PFM Code for Evaluating Reliability of Pressure Components Subject to Transient Loading," *Nuclear Engineering and Design* **208**, (2001) 1-13.

A13. Y. Li, D. Kato, K. Shibata, and K. Onizawa, "Improvements to a Probabilistic Fracture Mechanics Code for Evaluating the Integrity of an RPV Under Transient Loading," *International Journal of Pressure Vessels and Piping* **78**, (2001) 271-282.

A14. M. Persoz, S. Hugonnard-Bruyere, et al., "Deterministic and Probabilistic Assessment of the Reactor Pressure Vessel Structural Integrity with a User-Friendly Software," PVP-Vol. 403, *presented at the ASME Pressure Vessels and Piping Conference*, (2000) 137-144.

A15. B. K. Dutta, H. S. Kushwaha, and V. V. Raj, "Probabilistic Assessment of Reactor Pressure Vessel Integrity Under Pressurised Thermal Shock," *International Journal of Pressure Vessels and Piping* **76**, (1999) 445-453.

A16. D. O. Harris, E. Y. Lim, et al., "Probability of Pipe Fracture in the Primary Coolant Loop of a PWR Plant," NUREG/CR-2189, 1981.

A17. R. Wilson and R. A. Ainsworth, "A Probabilistic Fracture Mechanics Assessment Procedure," SMiRT 11, vol. G, (1991) 325-330.

A18. T. L. Dickson and F. A. Simonen, "The Application of Probabilistic Fracture Analysis to Residual Life Evaluation of Embrittled Reactor Vessels," AD-Vol. 28, Reliability Technology, *American Society of Mechanical Engineers,* (1992) 43-55.

A19. B. A. Bishop, T. L. Dickson, and F. A. Simonen, *Benchmarking of Probabilistic Fracture Mechanics Analyses of Reactor Vessels Subjected to Pressurized Thermal Shock (PTS) Loading,* Research Project 2975-5, Final Report, February 1993.

A20. T. L. Dickson and R. D. Cheverton, *Review of Reactor Pressure Vessel Evaluation Report for Yankee Rowe Nuclear Power Station (YAEC No. 1735), Appendix D,* NUREG/CR-5799 (ORNL/TM-11982), Oak Ridge National Laboratory, Oak Ridge, TN, March 1992.

A21. B. R. Bass, et al., *International Comparative Assessment Study of Pressurized Thermal Shock in Reactor Pressure Vessels,* NUREG/CR-6651 (ORNL/TM-1999/231), Oak Ridge National Laboratory, Oak Ridge, TN, December 1999.

A22. T. L. Dickson, *FAVOR: A Fracture Analysis Code for Nuclear Reactor Pressure Vessels, Release 9401*, ORNL/NRC/LTR/94/1, Oak Ridge National Laboratory, Oak Ridge, TN, 1994.

Appendix B – Stress-Intensity Factor Influence Coefficients Database[20]

Table B1. Influence Coefficients for Inside Axial and Circumferential Semi-elliptical Surface Flaws: R / t =10 and a/t=0.01
Table B2. Influence Coefficients for Inside Axial and Circumferential Semi-elliptical Surface Flaws: R / t =10 and a/t=0.0184
Table B3. Influence Coefficients for Inside Axial and Circumferential Semi-elliptical Surface Flaws: R / t =10 and a/t=0.05
Table B4. Influence Coefficients for Inside Axial and Circumferential Semi-elliptical Surface Flaws: R / t =10 and a/t=0.075
Table B5. Influence Coefficients for Inside Axial and Circumferential Semi-elliptical Surface Flaws: R / t =10 and a/t=0.1
Table B6. Influence Coefficients for Inside Axial and Circumferential Semi-elliptical Surface Flaws: R / t =10 and a/t=0.2
Table B7. Influence Coefficients for Inside Axial and Circumferential Semi-elliptical Surface Flaws: R / t =10 and a/t=0.3
Table B8. Influence Coefficients for Inside Axial Semi-elliptical Surface Flaws: R / t =10 and a/t=0.5
Table B9. Influence Coefficients for Inside Circumferential Semi-elliptical Surface Flaws: R / t =10 and a/t=0.5
Table B10. Influence Coefficients for Inside Axial and Circumferential Semi-elliptical Surface Flaws: R / t =20 and a/t=0.01
Table B11. Influence Coefficients for Inside Axial and Circumferential Semi-elliptical Surface Flaws: R / t =20 and a/t=0.0255
Table B12. Influence Coefficients for Inside Axial and Circumferential Semi-elliptical Surface Flaws: R / t =20 and a/t=0.05
Table B13. Influence Coefficients for Inside Axial and Circumferential Semi-elliptical Surface Flaws: R / t =20 and a/t=0.075
Table B14. Influence Coefficients for Inside Axial and Circumferential Semi-elliptical Surface Flaws: R / t =20 and a/t=0.1
Table B15. Influence Coefficients for Inside Axial and Circumferential Semi-elliptical Surface Flaws: R / t =20 and a/t=0.2
Table B16. Influence Coefficients for Inside Axial and Circumferential Semi-elliptical Surface Flaws: R / t =20 and a/t=0.3
Table B17. Influence Coefficients for Inside Axial Semi-elliptical Surface Flaws: R / t =20 and a/t=0.5
Table B18. Influence Coefficients for Inside Circumferential Semi-elliptical Surface Flaws: R / t =20 and a/t=0.5
Table B19. Influence Coefficients for Inside Axial Infinite-Length Surface Flaws: R / t =10
Table B20. Influence Coefficients for Inside Circumferential 360° Surface Flaws: R / t =10
Table B21. Influence Coefficients for Inside Axial Infinite-Length Surface Flaws: R / t =20
Table B22. Influence Coefficients for Inside Circumferential 360° Surface Flaws: R / t =20
Table B23. Influence Coefficients for Outside Axial and Circumferential Semi-elliptical Surface Flaws: R / t =10 and a/t=0.1

[20] Starting with FAVOR, v15.3, all base material SIFIC(s) for inside surface-breaking flaws are calculated using curve fits from the ASME BPVC, Appendix A, Article A-3000 (see Appendix G). The base material inside SIFIC(s) in the FAVOR database are no longer used; however, the database SIFIC(s) for the cladding and external surface-breaking flaws continue to be applied.

Table B1. Influence Coefficients for Inside Axial and Circumferential Semi-elliptical Surface Flaws: $R_i / t = 10$ and $a / t = 0.01$

Aspect Ratio	Elliptic Angle (deg)	K_0 Uniform	K_1 Linear	K_2 Quadratic	K_3 Cubic	K_0 t_{cl}=0.25 in.	K_1 t_{cl}=0.25 in.	K_0 t_{cl}=0.156 in.	K_1 t_{cl}=0.156 in.
2:1	0.00	0.764	0.153	0.061	0.034	0.764	0.153	0.764	0.153
	2.37	0.754	0.165	0.062	0.032	0.754	0.165	0.754	0.165
	16.60	0.690	0.192	0.079	0.040	0.690	0.192	0.690	0.192
	30.80	0.669	0.264	0.127	0.069	0.669	0.264	0.669	0.264
	45.00	0.660	0.335	0.196	0.124	0.660	0.335	0.660	0.335
	59.20	0.653	0.393	0.269	0.198	0.653	0.393	0.653	0.393
	73.40	0.651	0.434	0.329	0.268	0.651	0.434	0.651	0.434
	87.60	0.649	0.463	0.366	0.310	0.649	0.463	0.649	0.463
	90.00	0.649	0.468	0.372	0.317	0.649	0.468	0.649	0.468
6:1	0.00	0.670	0.134	0.048	0.024	0.670	0.134	0.670	0.134
	2.37	0.667	0.134	0.043	0.019	0.667	0.134	0.667	0.134
	16.60	0.654	0.170	0.055	0.009	0.654	0.170	0.654	0.170
	30.80	0.741	0.269	0.109	0.029	0.741	0.269	0.741	0.269
	45.00	0.827	0.381	0.199	0.100	0.827	0.381	0.827	0.381
	59.20	0.893	0.481	0.302	0.197	0.893	0.481	0.893	0.481
	73.40	0.938	0.559	0.389	0.290	0.938	0.559	0.938	0.559
	87.60	0.970	0.594	0.435	0.341	0.970	0.594	0.970	0.594
	90.00	0.975	0.601	0.443	0.350	0.975	0.601	0.975	0.601
10:1	0.00	0.515	0.090	0.020	0.006	0.515	0.090	0.515	0.090
	2.37	0.529	0.094	0.010	0.005	0.529	0.094	0.529	0.094
	16.60	0.610	0.146	0.033	0.005	0.610	0.146	0.610	0.146
	30.80	0.762	0.258	0.060	0.019	0.762	0.258	0.762	0.258
	45.00	0.889	0.389	0.171	0.066	0.889	0.389	0.889	0.389
	59.20	0.979	0.507	0.290	0.136	0.979	0.507	0.979	0.507
	73.40	1.033	0.593	0.389	0.249	1.033	0.593	1.033	0.593
	87.60	1.064	0.635	0.439	0.307	1.064	0.635	1.064	0.635
	90.00	1.069	0.642	0.447	0.316	1.069	0.642	1.069	0.642

Table B2. Influence Coefficients for Inside Axial and Circumferential Semi-elliptical Surface Flaws: R_i/t = 10 and a/t = 0.0184

Aspect Ratio	Elliptic Angle (deg)	K_0 Uniform	K_1 Linear	K_2 Quadratic	K_3 Cubic	K_0 t_{cl}=0.25 in.	K_1 t_{cl}=0.25 in.	K_0 t_{cl}=0.156 in.	K_1 t_{cl}=0.156 in.
2:1	0.00	0.777	0.155	0.061	0.034	0.777	0.155	0.777	0.155
	2.37	0.767	0.167	0.062	0.032	0.767	0.167	0.767	0.167
	16.60	0.700	0.194	0.079	0.040	0.700	0.194	0.700	0.194
	30.80	0.677	0.266	0.127	0.069	0.677	0.266	0.677	0.266
	45.00	0.667	0.338	0.196	0.125	0.667	0.338	0.667	0.338
	59.20	0.660	0.397	0.270	0.198	0.660	0.397	0.660	0.397
	73.40	0.657	0.438	0.330	0.267	0.657	0.438	0.657	0.438
	87.60	0.654	0.467	0.366	0.310	0.654	0.467	0.654	0.467
	90.00	0.653	0.472	0.373	0.317	0.653	0.472	0.653	0.472
6:1	0.00	0.653	0.127	0.043	0.021	0.653	0.127	0.653	0.127
	2.37	0.654	0.128	0.038	0.016	0.654	0.128	0.654	0.128
	16.60	0.654	0.168	0.045	0.021	0.654	0.168	0.654	0.168
	30.80	0.758	0.271	0.099	0.026	0.758	0.271	0.758	0.271
	45.00	0.852	0.387	0.192	0.085	0.852	0.387	0.852	0.387
	59.20	0.920	0.492	0.298	0.187	0.920	0.492	0.920	0.492
	73.40	0.963	0.569	0.387	0.283	0.963	0.569	0.963	0.569
	87.60	0.994	0.609	0.434	0.335	0.994	0.609	0.994	0.609
	90.00	0.999	0.616	0.442	0.344	0.999	0.616	0.999	0.616
10:1	0.00	0.525	0.092	0.019	0.007	0.525	0.092	0.525	0.092
	2.37	0.538	0.096	0.009	0.005	0.538	0.096	0.538	0.096
	16.60	0.621	0.149	0.039	0.005	0.621	0.149	0.621	0.149
	30.80	0.777	0.262	0.050	0.022	0.777	0.262	0.777	0.262
	45.00	0.899	0.392	0.164	0.075	0.899	0.392	0.899	0.392
	59.20	0.982	0.509	0.283	0.127	0.982	0.509	0.982	0.509
	73.40	1.033	0.595	0.383	0.242	1.033	0.595	1.033	0.595
	87.60	1.063	0.637	0.433	0.300	1.063	0.637	1.063	0.637
	90.00	1.068	0.644	0.441	0.310	1.068	0.644	1.068	0.644

Table B3. Influence Coefficients for Inside Axial and Circumferential Semi-elliptical Surface Flaws: R_i/t = 10 and a/t = 0.05

Aspect Ratio	Elliptic Angle (deg)	K_0 Uniform	K_1 Linear	K_2 Quadratic	K_3 Cubic	K_0 t_{cl}=0.25 in.	K_1 t_{cl}=0.25 in.	K_0 t_{cl}=0.156 in.	K_1 t_{cl}=0.156 in.
2:1	0.00	0.779	0.155	0.061	0.034	0.708	0.184	0.636	0.205
	2.37	0.769	0.166	0.062	0.031	0.701	0.194	0.624	0.213
	16.60	0.701	0.194	0.079	0.040	0.659	0.264	0.509	0.232
	30.80	0.678	0.267	0.128	0.070	0.581	0.340	0.246	0.124
	45.00	0.668	0.339	0.199	0.126	0.326	0.188	0.159	0.083
	59.20	0.661	0.398	0.273	0.201	0.233	0.127	0.128	0.067
	73.40	0.658	0.440	0.333	0.270	0.204	0.110	0.115	0.060
	87.60	0.656	0.469	0.370	0.313	0.185	0.099	0.106	0.055
	90.00	0.655	0.474	0.377	0.320	0.182	0.097	0.104	0.054
6:1	0.00	0.655	0.128	0.043	0.021	0.631	0.151	0.576	0.176
	2.37	0.655	0.128	0.039	0.016	0.628	0.156	0.570	0.177
	16.60	0.655	0.167	0.049	0.019	0.646	0.221	0.537	0.213
	30.80	0.758	0.270	0.104	0.013	0.688	0.357	0.340	0.167
	45.00	0.851	0.386	0.197	0.091	0.494	0.263	0.271	0.138
	59.20	0.918	0.492	0.305	0.193	0.422	0.217	0.253	0.128
	73.40	0.962	0.569	0.395	0.290	0.396	0.201	0.241	0.121
	87.60	0.992	0.609	0.443	0.342	0.374	0.189	0.231	0.115
	90.00	0.997	0.616	0.450	0.351	0.370	0.186	0.229	0.115
10:1	0.00	0.523	0.092	0.021	0.005	0.533	0.119	0.496	0.149
	2.37	0.537	0.095	0.011	0.015	0.543	0.121	0.504	0.146
	16.60	0.622	0.147	0.033	0.050	0.631	0.149	0.547	0.199
	30.80	0.778	0.261	0.061	0.080	0.718	0.348	0.376	0.182
	45.00	0.898	0.391	0.171	0.065	0.550	0.286	0.349	0.156
	59.20	0.981	0.509	0.292	0.138	0.474	0.241	0.287	0.144
	73.40	1.034	0.596	0.392	0.252	0.444	0.224	0.273	0.136
	87.60	1.063	0.638	0.442	0.310	0.418	0.221	0.260	0.130
	90.00	1.068	0.645	0.450	0.320	0.414	0.221	0.257	0.128

Table B4. Influence Coefficients for Inside Axial and Circumferential Semi-elliptical Surface Flaws: $R_i/t = 10$ and $a/t = 0.075$

Aspect Ratio	Elliptic Angle (deg)	K_0 Uniform	K_1 Linear	K_2 Quadratic	K_3 Cubic	K_0 t_{cl}=0.25 in.	K_1 t_{cl}=0.25 in.	K_0 t_{cl}=0.156 in.	K_1 t_{cl}=0.156 in.
2:1	0.00	0.740	0.128	0.045	0.023	0.650	0.197	0.572	0.210
	7.03	0.737	0.147	0.055	0.028	0.629	0.220	0.529	0.217
	14.20	0.721	0.179	0.067	0.033	0.593	0.271	0.400	0.177
	35.90	0.671	0.298	0.155	0.086	0.219	0.120	0.118	0.060
	48.70	0.661	0.355	0.220	0.143	0.161	0.085	0.094	0.048
	61.50	0.656	0.404	0.285	0.212	0.137	0.071	0.081	0.042
	74.30	0.654	0.439	0.336	0.273	0.125	0.065	0.075	0.038
	87.00	0.651	0.468	0.372	0.313	0.114	0.065	0.068	0.035
	90.00	0.651	0.475	0.381	0.322	0.111	0.065	0.067	0.034
6:1	0.00	0.650	0.098	0.029	0.013	0.591	0.170	0.527	0.188
	2.37	0.635	0.104	0.031	0.013	0.571	0.180	0.495	0.179
	16.60	0.672	0.140	0.040	0.014	0.590	0.243	0.441	0.187
	30.80	0.786	0.309	0.139	0.048	0.334	0.171	0.195	0.098
	45.00	0.862	0.410	0.229	0.125	0.294	0.149	0.180	0.090
	59.20	0.918	0.501	0.326	0.219	0.275	0.138	0.170	0.085
	73.40	0.952	0.566	0.404	0.303	0.265	0.133	0.164	0.082
	87.60	0.980	0.602	0.446	0.351	0.265	0.133	0.159	0.080
	90.00	0.987	0.611	0.456	0.362	0.265	0.132	0.157	0.079
10:1	0.00	0.547	0.073	0.016	0.006	0.514	0.148	0.469	0.171
	2.37	0.551	0.074	0.016	0.003	0.514	0.145	0.458	0.131
	16.60	0.636	0.113	0.023	0.009	0.583	0.220	0.465	0.173
	30.80	0.812	0.303	0.124	0.018	0.375	0.189	0.223	0.112
	45.00	0.914	0.419	0.225	0.111	0.335	0.168	0.206	0.103
	59.20	0.982	0.522	0.332	0.216	0.310	0.156	0.193	0.096
	73.40	1.022	0.593	0.416	0.307	0.298	0.149	0.185	0.093
	87.60	1.048	0.631	0.461	0.356	0.295	0.147	0.185	0.092
	90.00	1.055	0.639	0.471	0.368	0.295	0.147	0.184	0.092

Table B5. Influence Coefficients for Inside Axial and Circumferential Semi-elliptical Surface Flaws: $R_i/t = 10$ and $a/t = 0.1$

Aspect Ratio	Elliptic Angle (deg)	K_0 Uniform	K_1 Linear	K_2 Quadratic	K_3 Cubic	K_0 t_{cl}=0.25 in.	K_1 t_{cl}=0.25 in.	K_0 t_{cl}=0.156 in.	K_1 t_{cl}=0.156 in.
2:1	0.00	0.729	0.124	0.044	0.023	0.596	0.195	0.519	0.205
	5.27	0.741	0.139	0.053	0.027	0.582	0.208	0.483	0.198
	17.10	0.722	0.230	0.096	0.048	0.366	0.213	0.168	0.086
	31.10	0.676	0.273	0.133	0.072	0.176	0.097	0.095	0.048
	45.10	0.664	0.339	0.201	0.127	0.122	0.064	0.072	0.037
	59.10	0.658	0.396	0.274	0.200	0.101	0.052	0.061	0.031
	73.10	0.655	0.436	0.333	0.268	0.091	0.047	0.056	0.028
	87.00	0.653	0.470	0.373	0.313	0.082	0.047	0.050	0.025
	90.00	0.652	0.477	0.382	0.323	0.080	0.047	0.049	0.025
6:1	0.00	0.641	0.094	0.029	0.014	0.550	0.175	0.485	0.188
	2.37	0.630	0.098	0.031	0.015	0.532	0.176	0.454	0.168
	16.60	0.701	0.196	0.067	0.015	0.427	0.232	0.211	0.108
	30.80	0.756	0.273	0.115	0.039	0.258	0.131	0.152	0.077
	45.00	0.848	0.385	0.207	0.109	0.224	0.112	0.138	0.069
	59.20	0.915	0.489	0.312	0.207	0.208	0.104	0.129	0.065
	73.40	0.958	0.565	0.402	0.302	0.200	0.100	0.125	0.062
	87.60	0.989	0.607	0.450	0.356	0.200	0.100	0.120	0.060
	90.00	0.996	0.616	0.461	0.367	0.200	0.100	0.119	0.060
10:1	0.00	0.543	0.067	0.016	0.007	0.490	0.148	0.443	0.168
	2.37	0.536	0.069	0.016	0.006	0.479	0.144	0.421	0.138
	16.60	0.670	0.175	0.047	0.027	0.443	0.220	0.229	0.117
	30.80	0.778	0.269	0.102	0.030	0.291	0.143	0.176	0.088
	45.00	0.897	0.395	0.202	0.089	0.256	0.128	0.159	0.080
	59.20	0.979	0.512	0.318	0.199	0.236	0.118	0.147	0.074
	73.40	1.029	0.597	0.416	0.302	0.226	0.113	0.141	0.071
	87.60	1.060	0.640	0.466	0.358	0.224	0.111	0.140	0.070
	90.00	1.066	0.649	0.477	0.370	0.223	0.111	0.140	0.070

Table B6. Influence Coefficients for Inside Axial and Circumferential Semi-elliptical Surface Flaws: $R_i/t = 10$ and $a/t = 0.2$

Aspect Ratio	Elliptic Angle (deg)	K_0 Uniform	K_1 Linear	K_2 Quadratic	K_3 Cubic	K_0 t_{cl}=0.25 in.	K_1 t_{cl}=0.25 in.	K_0 t_{cl}=0.156 in.	K_1 t_{cl}=0.156 in.
2:1	0.00	0.692	0.127	0.046	0.024	0.457	0.173	0.393	0.178
	19.80	0.695	0.214	0.089	0.044	0.155	0.080	0.071	0.031
	31.10	0.679	0.273	0.133	0.073	0.090	0.050	0.048	0.023
	42.50	0.671	0.332	0.192	0.120	0.061	0.031	0.038	0.019
	53.80	0.665	0.383	0.255	0.182	0.052	0.026	0.032	0.016
	65.20	0.660	0.423	0.312	0.245	0.047	0.023	0.029	0.014
	76.50	0.658	0.450	0.354	0.296	0.044	0.022	0.027	0.014
	87.90	0.656	0.475	0.384	0.329	0.041	0.021	0.025	0.013
	90.00	0.656	0.479	0.389	0.335	0.040	0.020	0.025	0.013
6:1	0.00	0.617	0.101	0.034	0.017	0.434	0.163	0.377	0.171
	2.37	0.699	0.194	0.066	0.019	0.180	0.090	0.093	0.043
	16.60	0.781	0.280	0.118	0.045	0.127	0.063	0.079	0.039
	30.80	0.856	0.375	0.195	0.101	0.116	0.058	0.072	0.036
	45.00	0.915	0.464	0.283	0.180	0.110	0.055	0.069	0.034
	59.20	0.958	0.538	0.366	0.265	0.106	0.053	0.066	0.033
	73.40	0.986	0.590	0.430	0.336	0.104	0.052	0.065	0.032
	87.60	1.010	0.619	0.464	0.373	0.102	0.051	0.064	0.032
	90.00	1.020	0.624	0.470	0.380	0.101	0.051	0.063	0.032
10:1	0.00	0.525	0.077	0.022	0.009	0.402	0.149	0.355	0.160
	2.37	0.694	0.183	0.050	0.025	0.200	0.100	0.106	0.050
	16.60	0.815	0.280	0.107	0.011	0.149	0.073	0.093	0.046
	30.80	0.915	0.387	0.190	0.083	0.137	0.068	0.085	0.043
	45.00	0.991	0.488	0.287	0.170	0.130	0.065	0.081	0.040
	59.20	1.045	0.572	0.379	0.263	0.125	0.062	0.078	0.039
	73.40	1.080	0.631	0.449	0.340	0.122	0.061	0.077	0.038
	87.60	1.103	0.660	0.483	0.378	0.120	0.060	0.075	0.037
	90.00	1.107	0.666	0.490	0.385	0.119	0.060	0.075	0.037

Table B7. Influence Coefficients for Inside Axial and Circumferential Semi-elliptical Surface Flaws: $R_i/t = 10$ and $a/t = 0.3$

Aspect Ratio	Elliptic Angle (deg)	K_0 Uniform	K_1 Linear	K_2 Quadratic	K_3 Cubic	K_0 t_{cl}=0.25 in.	K_1 t_{cl}=0.25 in.	K_0 t_{cl}=0.156 in.	K_1 t_{cl}=0.156 in.
2:1	0.00	0.723	0.127	0.048	0.026	0.404	0.188	0.334	0.176
	17.40	0.708	0.203	0.083	0.042	0.102	0.049	0.056	0.025
	29.10	0.690	0.264	0.126	0.068	0.058	0.028	0.034	0.016
	40.90	0.680	0.326	0.185	0.114	0.043	0.021	0.026	0.013
	52.60	0.673	0.381	0.251	0.177	0.036	0.018	0.022	0.011
	64.40	0.668	0.423	0.310	0.242	0.032	0.016	0.020	0.010
	76.10	0.665	0.452	0.355	0.297	0.030	0.015	0.018	0.009
	87.90	0.662	0.478	0.385	0.331	0.028	0.014	0.017	0.009
	90.00	0.662	0.482	0.391	0.337	0.027	0.014	0.017	0.009
6:1	0.00	0.665	0.112	0.041	0.022	0.380	0.181	0.315	0.167
	2.37	0.715	0.190	0.068	0.027	0.117	0.054	0.069	0.032
	16.60	0.804	0.277	0.118	0.051	0.093	0.045	0.057	0.028
	30.80	0.886	0.376	0.194	0.104	0.085	0.042	0.053	0.026
	45.00	0.951	0.470	0.284	0.182	0.081	0.040	0.050	0.025
	59.20	0.998	0.549	0.372	0.270	0.078	0.039	0.049	0.024
	73.40	1.028	0.605	0.439	0.345	0.077	0.038	0.048	0.024
	87.60	1.053	0.635	0.475	0.384	0.075	0.038	0.047	0.024
	90.00	1.058	0.640	0.481	0.391	0.075	0.037	0.047	0.023
10:1	0.00	0.562	0.085	0.029	0.014	0.344	0.168	0.290	0.153
	2.37	0.707	0.176	0.052	0.016	0.128	0.059	0.078	0.037
	16.60	0.848	0.276	0.104	0.016	0.110	0.054	0.068	0.034
	30.80	0.962	0.389	0.188	0.082	0.102	0.051	0.064	0.032
	45.00	1.051	0.498	0.288	0.169	0.098	0.049	0.062	0.031
	59.20	1.115	0.590	0.385	0.265	0.096	0.048	0.060	0.030
	73.40	1.157	0.653	0.460	0.346	0.095	0.047	0.060	0.030
	87.60	1.183	0.685	0.496	0.387	0.094	0.047	0.059	0.029
	90.00	1.187	0.691	0.503	0.394	0.094	0.047	0.059	0.029

Table B8. Influence Coefficients for Inside Axial Semi-elliptical Surface Flaws: $R_i/t = 10$ and $a / t = 0.5$

Aspect Ratio	Elliptic Angle (deg)	K_0 Uniform	K_1 Linear	K_2 Quadratic	K_3 Cubic	K_0 t_{cl}=0.25 in.	K_1 t_{cl}=0.25 in.	K_0 t_{cl}=0.156 in.	K_1 t_{cl}=0.156 in.
2:1	0.00	0.736	0.132	0.053	0.029	0.327	0.162	0.272	0.150
	15.40	0.746	0.203	0.083	0.043	0.079	0.037	0.045	0.020
	27.50	0.719	0.263	0.124	0.067	0.042	0.020	0.025	0.012
	39.60	0.704	0.327	0.183	0.112	0.029	0.014	0.018	0.009
	51.70	0.693	0.383	0.249	0.175	0.023	0.012	0.015	0.007
	63.70	0.685	0.426	0.311	0.242	0.021	0.010	0.013	0.006
	75.80	0.681	0.456	0.357	0.299	0.019	0.009	0.012	0.006
	87.90	0.676	0.483	0.389	0.334	0.018	0.009	0.011	0.006
	90.00	0.676	0.488	0.395	0.340	0.017	0.009	0.011	0.005
6:1	0.00	0.758	0.142	0.059	0.033	0.322	0.163	0.268	0.149
	2.37	0.814	0.213	0.083	0.040	0.091	0.041	0.054	0.025
	16.60	0.908	0.302	0.132	0.065	0.070	0.034	0.043	0.021
	30.80	0.998	0.405	0.208	0.116	0.065	0.032	0.040	0.020
	45.00	1.069	0.504	0.300	0.195	0.062	0.031	0.039	0.019
	59.20	1.120	0.588	0.392	0.285	0.061	0.030	0.038	0.019
	73.40	1.153	0.647	0.463	0.363	0.060	0.030	0.038	0.019
	87.60	1.182	0.679	0.500	0.404	0.059	0.029	0.037	0.018
	90.00	1.187	0.685	0.506	0.411	0.059	0.029	0.037	0.018
10:1	0.00	0.666	0.119	0.049	0.028	0.302	0.156	0.254	0.140
	2.37	0.822	0.208	0.077	0.033	0.097	0.044	0.060	0.028
	16.60	0.995	0.316	0.131	0.056	0.086	0.042	0.054	0.027
	30.80	1.138	0.440	0.216	0.112	0.083	0.041	0.052	0.026
	45.00	1.251	0.560	0.321	0.198	0.083	0.041	0.052	0.026
	59.20	1.335	0.662	0.425	0.298	0.083	0.041	0.052	0.026
	73.40	1.390	0.734	0.506	0.383	0.083	0.041	0.052	0.026
	87.60	1.423	0.770	0.546	0.427	0.083	0.041	0.052	0.026
	90.00	1.429	0.776	0.553	0.434	0.083	0.041	0.052	0.026

Table B9. Influence Coefficients for Inside Circumferential Semi-elliptical Surface Flaws: $R_i/t = 10$ and $a/t = 0.5$

Aspect Ratio	Elliptic Angle (deg)	K_0 Uniform	K_1 Linear	K_2 Quadratic	K_3 Cubic	K_0 t_{cl}=0.25 in.	K_1 t_{cl}=0.25 in.	K_0 t_{cl}=0.156 in.	K_1 t_{cl}=0.156 in.
2:1	0.00	0.741	0.134	0.054	0.030	0.324	0.162	0.269	0.151
	15.40	0.750	0.205	0.084	0.044	0.079	0.038	0.045	0.020
	27.50	0.721	0.264	0.124	0.067	0.042	0.020	0.025	0.012
	39.60	0.706	0.328	0.183	0.112	0.029	0.014	0.018	0.009
	51.70	0.698	0.384	0.250	0.175	0.024	0.012	0.015	0.007
	63.70	0.692	0.430	0.312	0.243	0.021	0.010	0.013	0.007
	75.80	0.686	0.461	0.360	0.301	0.019	0.010	0.012	0.006
	87.90	0.682	0.488	0.392	0.336	0.020	0.010	0.012	0.006
	90.00	0.682	0.493	0.398	0.343	0.020	0.009	0.013	0.006
6:1	0.00	0.727	0.132	0.053	0.030	0.315	0.161	0.262	0.147
	15.40	0.786	0.205	0.079	0.037	0.087	0.039	0.052	0.024
	27.50	0.882	0.295	0.128	0.062	0.067	0.032	0.041	0.020
	39.60	0.974	0.398	0.205	0.114	0.062	0.031	0.038	0.019
	51.70	1.049	0.499	0.298	0.193	0.060	0.030	0.037	0.019
	63.70	1.103	0.584	0.390	0.284	0.058	0.029	0.036	0.018
	75.80	1.138	0.644	0.462	0.362	0.057	0.029	0.036	0.018
	87.90	1.166	0.676	0.499	0.403	0.058	0.029	0.036	0.018
	90.00	1.171	0.682	0.506	0.410	0.058	0.029	0.036	0.018
10:1	0.00	0.616	0.101	0.040	0.023	0.291	0.152	0.247	0.138
	15.40	0.770	0.195	0.071	0.028	0.090	0.039	0.055	0.026
	27.50	0.936	0.301	0.125	0.053	0.078	0.038	0.049	0.024
	39.60	1.076	0.424	0.211	0.109	0.075	0.037	0.047	0.024
	51.70	1.190	0.544	0.315	0.196	0.075	0.037	0.047	0.023
	63.70	1.275	0.647	0.420	0.295	0.075	0.037	0.047	0.023
	75.80	1.330	0.719	0.501	0.381	0.075	0.037	0.047	0.023
	87.90	1.363	0.755	0.542	0.425	0.075	0.037	0.047	0.024
	90.00	1.368	0.762	0.549	0.433	0.075	0.037	0.047	0.024

Table B10. Influence Coefficients for Inside Axial and Circumferential Semi-elliptical Surface Flaws: $R_i/t = 20$ and $a/t = 0.01$

Aspect Ratio	Elliptic Angle	K0 Uniform	K1 Linear	K2 Quadratic	K3 Cubic	K0 .250 cld	K1 .250 cld	K0 .156 cld	K1 .156 cld
2:1	0.0	0.718	0.141	0.056	0.032	0.718	0.141	0.718	0.141
	2.4	0.708	0.153	0.058	0.030	0.708	0.153	0.708	0.153
	16.6	0.652	0.182	0.075	0.038	0.652	0.182	0.652	0.182
	30.8	0.636	0.254	0.122	0.067	0.636	0.254	0.636	0.254
	45.0	0.629	0.325	0.191	0.122	0.629	0.325	0.629	0.325
	59.2	0.626	0.383	0.264	0.195	0.626	0.383	0.626	0.383
	73.4	0.624	0.422	0.323	0.263	0.624	0.422	0.624	0.422
	87.6	0.622	0.452	0.360	0.306	0.622	0.452	0.622	0.452
	90.0	0.621	0.457	0.366	0.313	0.621	0.457	0.621	0.457
6:1	0.0	0.636	0.125	0.045	0.021	0.636	0.125	0.636	0.125
	2.4	0.636	0.131	0.044	0.019	0.636	0.131	0.636	0.131
	16.6	0.637	0.176	0.061	0.016	0.637	0.176	0.637	0.176
	30.8	0.732	0.278	0.119	0.043	0.732	0.278	0.732	0.278
	45.0	0.821	0.391	0.211	0.112	0.821	0.391	0.821	0.391
	59.2	0.892	0.491	0.313	0.207	0.892	0.491	0.892	0.491
	73.4	0.942	0.566	0.400	0.300	0.942	0.566	0.942	0.566
	87.6	0.976	0.606	0.446	0.351	0.976	0.606	0.976	0.606
	90.0	0.982	0.612	0.454	0.360	0.982	0.612	0.982	0.612
10:1	0.0	0.507	0.089	0.020	0.006	0.507	0.089	0.507	0.089
	2.4	0.519	0.095	0.013	0.005	0.519	0.095	0.519	0.095
	16.6	0.593	0.148	0.024	0.005	0.593	0.148	0.593	0.148
	30.8	0.732	0.257	0.069	0.020	0.732	0.257	0.732	0.257
	45.0	0.851	0.383	0.174	0.051	0.851	0.383	0.851	0.383
	59.2	0.945	0.498	0.290	0.143	0.945	0.498	0.945	0.498
	73.4	1.007	0.585	0.388	0.253	1.007	0.585	1.007	0.585
	87.6	1.041	0.627	0.437	0.309	1.041	0.627	1.041	0.627
	90.0	1.047	0.634	0.445	0.319	1.047	0.634	1.047	0.634

Table B11. Influence Coefficients for Inside Axial and Circumferential Semi-elliptical Surface Flaws: $R_i/t = 20$ and $a/t = 0.0255$ (not used starting with v15.1)

Aspect Ratio	Elliptic Angle	K0 Uniform	K1 Linear	K2 Quadratic	K3 Cubic	K0 .250 cld	K1 .250 cld	K0 .156 cld	K1 .156 cld
2:1	0.0	0.772	0.155	0.062	0.034	0.772	0.155	0.772	0.155
	2.4	0.762	0.166	0.063	0.032	0.762	0.166	0.762	0.166
	16.6	0.697	0.194	0.080	0.041	0.697	0.194	0.697	0.194
	30.8	0.674	0.266	0.128	0.070	0.674	0.266	0.674	0.266
	45.0	0.665	0.337	0.198	0.126	0.665	0.337	0.665	0.337
	59.2	0.658	0.396	0.272	0.200	0.658	0.396	0.658	0.396
	73.4	0.656	0.437	0.331	0.269	0.656	0.437	0.656	0.437
	87.6	0.653	0.466	0.368	0.311	0.653	0.466	0.653	0.466
	90.0	0.653	0.471	0.374	0.318	0.653	0.471	0.653	0.471
6:1	0.0	0.646	0.126	0.043	0.021	0.646	0.126	0.646	0.126
	2.4	0.646	0.125	0.038	0.016	0.646	0.125	0.646	0.125
	16.6	0.647	0.164	0.046	0.022	0.647	0.164	0.647	0.164
	30.8	0.751	0.267	0.100	0.024	0.751	0.267	0.751	0.267
	45.0	0.846	0.382	0.193	0.085	0.846	0.382	0.846	0.382
	59.2	0.918	0.488	0.300	0.188	0.918	0.488	0.918	0.488
	73.4	0.964	0.565	0.390	0.284	0.964	0.565	0.964	0.565
	87.6	0.995	0.605	0.437	0.337	0.995	0.605	0.995	0.605
	90.0	1.000	0.612	0.445	0.345	1.000	0.612	1.000	0.612
10:1	0.0	0.509	0.089	0.019	0.008	0.509	0.089	0.509	0.089
	2.4	0.523	0.088	0.011	0.006	0.523	0.088	0.523	0.088
	16.6	0.602	0.138	0.043	0.006	0.607	0.138	0.607	0.138
	30.8	0.764	0.252	0.041	0.030	0.764	0.252	0.764	0.252
	45.0	0.889	0.382	0.160	0.081	0.889	0.382	0.889	0.382
	59.2	0.977	0.501	0.281	0.122	0.977	0.501	0.977	0.501
	73.4	1.031	0.587	0.382	0.240	1.031	0.587	1.031	0.587
	87.6	1.061	0.629	0.432	0.298	1.061	0.629	1.061	0.629
	90.0	1.066	0.637	0.440	0.308	1.066	0.637	1.066	0.637

Table B12. Influence Coefficients for Inside Axial and Circumferential Semi-elliptical Surface Flaws: $R_i/t = 20$ and $a/t = 0.05$

Aspect Ratio	Elliptic Angle	K0 Uniform	K1 Linear	K2 Quadratic	K3 Cubic	K0 .250 cld	K1 .250 cld	K0 .156 cld	K1 .156 cld
2:1	0.0	0.779	0.156	0.062	0.034	0.758	0.165	0.699	0.181
	2.4	0.769	0.167	0.062	0.032	0.750	0.171	0.677	0.187
	16.6	0.702	0.194	0.079	0.041	0.702	0.207	0.545	0.218
	30.8	0.678	0.266	0.128	0.069	0.640	0.260	0.420	0.220
	45.0	0.667	0.338	0.198	0.125	0.571	0.316	0.235	0.123
	59.2	0.660	0.397	0.272	0.200	0.410	0.248	0.174	0.094
	73.4	0.658	0.439	0.332	0.270	0.299	0.172	0.152	0.082
	87.6	0.655	0.468	0.369	0.312	0.278	0.157	0.146	0.078
	90.0	0.655	0.473	0.375	0.319	0.274	0.154	0.145	0.077
6:1	0.0	0.653	0.127	0.043	0.020	0.650	0.125	0.645	0.129
	2.4	0.653	0.128	0.039	0.016	0.650	0.129	0.639	0.132
	16.6	0.654	0.168	0.049	0.019	0.653	0.165	0.602	0.159
	30.8	0.758	0.271	0.104	0.013	0.673	0.281	0.548	0.241
	45.0	0.851	0.387	0.198	0.091	0.728	0.331	0.378	0.186
	59.2	0.919	0.492	0.305	0.193	0.648	0.328	0.331	0.172
	73.4	0.962	0.569	0.395	0.289	0.550	0.288	0.321	0.164
	87.6	0.992	0.609	0.442	0.342	0.498	0.257	0.298	0.150
	90.0	0.997	0.615	0.450	0.351	0.489	0.252	0.294	0.148
10:1	0.0	0.523	0.088	0.019	0.009	0.527	0.102	0.503	0.124
	2.4	0.523	0.088	0.011	0.016	0.543	0.108	0.519	0.127
	16.6	0.609	0.138	0.044	0.053	0.634	0.153	0.599	0.151
	30.8	0.767	0.252	0.039	0.087	0.682	0.235	0.578	0.232
	45.0	0.888	0.382	0.159	0.083	0.766	0.298	0.416	0.200
	59.2	0.972	0.500	0.281	0.120	0.698	0.332	0.368	0.189
	73.4	1.025	0.586	0.381	0.238	0.606	0.312	0.362	0.183
	87.6	1.054	0.628	0.431	0.297	0.524	0.269	0.316	0.159
	90.0	1.059	0.635	0.439	0.306	0.511	0.262	0.308	0.154

Table B13. Influence Coefficients for Inside Axial and Circumferential Semi-elliptical Surface Flaws: $R_i/t = 20$ and $a/t = 0.075$

Aspect Ratio	Elliptic Angle	K0 Uniform	K1 Linear	K2 Quadratic	K3 Cubic	K0 .250 cld	K1 .250 cld	K0 .156 cld	K1 .156 cld
2:1	0.0	0.780	0.156	0.061	0.034	0.701	0.189	0.625	0.208
	2.4	0.770	0.167	0.062	0.032	0.694	0.198	0.612	0.215
	16.6	0.720	0.194	0.080	0.041	0.649	0.270	0.485	0.223
	30.8	0.679	0.267	0.128	0.070	0.526	0.313	0.220	0.104
	45.0	0.668	0.339	0.199	0.126	0.280	0.156	0.147	0.076
	59.2	0.661	0.398	0.273	0.200	0.213	0.115	0.120	0.062
	73.4	0.659	0.440	0.333	0.270	0.188	0.101	0.107	0.056
	87.6	0.656	0.469	0.370	0.313	0.171	0.091	0.098	0.051
	90.0	0.656	0.474	0.377	0.320	0.168	0.089	0.097	0.050
6:1	0.0	0.657	0.128	0.044	0.021	0.631	0.161	0.571	0.184
	2.4	0.657	0.128	0.039	0.016	0.627	0.165	0.564	0.184
	16.6	0.690	0.168	0.049	0.019	0.646	0.234	0.524	0.218
	30.8	0.761	0.271	0.104	0.013	0.651	0.354	0.312	0.155
	45.0	0.853	0.387	0.198	0.091	0.439	0.228	0.252	0.128
	59.2	0.921	0.493	0.305	0.193	0.392	0.200	0.236	0.119
	73.4	0.965	0.570	0.395	0.289	0.368	0.187	0.225	0.113
	87.6	0.995	0.610	0.443	0.342	0.348	0.176	0.214	0.108
	90.0	1.000	0.617	0.451	0.351	0.345	0.174	0.213	0.107
10:1	0.0	0.523	0.092	0.021	0.007	0.538	0.131	0.497	0.160
	2.4	0.537	0.094	0.010	0.016	0.546	0.134	0.502	0.155
	16.6	0.660	0.146	0.037	0.051	0.636	0.207	0.540	0.208
	30.8	0.779	0.259	0.055	0.083	0.687	0.354	0.346	0.170
	45.0	0.900	0.389	0.168	0.073	0.492	0.251	0.288	0.145
	59.2	0.983	0.508	0.289	0.131	0.440	0.223	0.268	0.135
	73.4	1.036	0.595	0.389	0.247	0.410	0.207	0.252	0.127
	87.6	1.066	0.637	0.439	0.305	0.386	0.195	0.239	0.120
	90.0	1.071	0.644	0.448	0.315	0.382	0.193	0.237	0.119

Table B14. Influence Coefficients for Inside Axial and Circumferential Semi-elliptical Surface Flaws: $R_i/t = 20$ and $a/t = 0.1$

Aspect Ratio	Elliptic Angle (deg)	K_0 Uniform	K_1 Linear	K_2 Quadratic	K_3 Cubic	K_0 t_{cl}=0.25 in.	K_1 t_{cl}=0.25 in.	K_0 t_{cl}=0.156 in.	K_1 t_{cl}=0.156 in.
2:1	0.000	0.743	0.129	0.045	0.023	0.658	0.197	0.579	0.210
	2.370	0.738	0.149	0.055	0.028	0.636	0.222	0.535	0.220
	16.600	0.705	0.258	0.115	0.057	0.425	0.254	0.184	0.095
	30.800	0.671	0.303	0.159	0.089	0.226	0.124	0.122	0.062
	45.000	0.661	0.358	0.223	0.147	0.168	0.088	0.098	0.050
	59.200	0.656	0.406	0.287	0.215	0.143	0.075	0.085	0.043
	73.400	0.654	0.439	0.337	0.274	0.131	0.068	0.078	0.040
	87.600	0.652	0.468	0.372	0.313	0.120	0.062	0.072	0.037
	90.000	0.652	0.475	0.381	0.323	0.117	0.061	0.070	0.036
6:1	0.000	0.657	0.100	0.030	0.014	0.599	0.170	0.534	0.188
	2.370	0.641	0.108	0.032	0.014	0.579	0.182	0.502	0.182
	16.600	0.746	0.238	0.085	0.012	0.530	0.294	0.253	0.129
	30.800	0.794	0.317	0.145	0.054	0.347	0.178	0.203	0.102
	45.000	0.869	0.417	0.235	0.130	0.308	0.156	0.188	0.095
	59.200	0.924	0.506	0.330	0.224	0.289	0.145	0.178	0.090
	73.400	0.958	0.568	0.406	0.306	0.278	0.140	0.172	0.087
	87.600	0.985	0.604	0.448	0.353	0.268	0.134	0.167	0.084
	90.000	0.992	0.613	0.458	0.364	0.265	0.133	0.165	0.083
10:1	0.000	0.554	0.075	0.017	0.006	0.476	0.171	0.476	0.171
	2.370	0.561	0.077	0.016	0.003	0.468	0.135	0.468	0.135
	16.600	0.750	0.219	0.060	0.041	0.282	0.142	0.282	0.142
	30.800	0.821	0.310	0.128	0.018	0.231	0.116	0.231	0.116
	45.000	0.923	0.425	0.229	0.113	0.216	0.108	0.216	0.108
	59.200	0.989	0.526	0.334	0.217	0.203	0.101	0.203	0.101
	73.400	1.028	0.595	0.417	0.307	0.195	0.098	0.195	0.098
	87.600	1.055	0.632	0.460	0.355	0.194	0.097	0.194	0.097
	90.000	1.061	0.641	0.471	0.367	0.311	0.155	0.194	0.097

Table B15. Influence Coefficients for Inside Axial and Circumferential Semi-elliptical Surface Flaws: $R_i/t = 20$ and $a/t = 0.2$

Aspect Ratio	Elliptic Angle (deg)	K_0 Uniform	K_1 Linear	K_2 Quadratic	K_3 Cubic	K_0 t_{cl}=0.25 in.	K_1 t_{cl}=0.25 in.	K_0 t_{cl}=0.156 in.	K_1 t_{cl}=0.156 in.
2:1	0.000	0.715	0.131	0.047	0.023	0.524	0.186	0.452	0.193
	2.370	0.718	0.188	0.072	0.036	0.327	0.135	0.166	0.066
	16.600	0.693	0.231	0.099	0.050	0.162	0.079	0.091	0.040
	30.800	0.680	0.287	0.145	0.081	0.107	0.053	0.064	0.031
	45.000	0.672	0.342	0.203	0.129	0.085	0.043	0.052	0.026
	59.200	0.666	0.390	0.263	0.190	0.073	0.037	0.045	0.023
	73.400	0.661	0.426	0.317	0.250	0.066	0.033	0.040	0.020
	87.600	0.659	0.451	0.356	0.298	0.062	0.032	0.038	0.019
	90.000	0.657	0.480	0.389	0.323	0.054	0.027	0.034	0.017
6:1	0.000	0.642	0.102	0.032	0.017	0.495	0.174	0.431	0.183
	2.370	0.680	0.150	0.045	0.026	0.343	0.130	0.180	0.073
	16.600	0.724	0.214	0.073	0.045	0.209	0.101	0.125	0.059
	30.800	0.802	0.299	0.129	0.075	0.176	0.087	0.108	0.054
	45.000	0.871	0.390	0.206	0.120	0.162	0.081	0.101	0.050
	59.200	0.926	0.475	0.291	0.186	0.154	0.077	0.096	0.048
	73.400	0.965	0.544	0.370	0.267	0.149	0.075	0.093	0.047
	87.600	0.991	0.592	0.430	0.334	0.146	0.073	0.091	0.046
	90.000	1.026	0.624	0.467	0.375	0.141	0.070	0.088	0.044
10:1	0.000	0.547	0.078	0.020	0.012	0.401	0.171	0.401	0.171
	2.370	0.635	0.126	0.021	0.021	0.188	0.072	0.188	0.072
	16.600	0.730	0.203	0.051	0.037	0.143	0.068	0.143	0.068
	30.800	0.842	0.300	0.113	0.045	0.128	0.063	0.128	0.063
	45.000	0.934	0.403	0.198	0.100	0.119	0.059	0.199	0.059
	59.200	1.004	0.499	0.292	0.190	0.113	0.056	0.113	0.056
	73.400	1.055	0.578	0.380	0.260	0.109	0.055	0.109	0.055
	87.600	1.087	0.632	0.445	0.332	0.108	0.054	0.108	0.054
	90.000	1.118	0.665	0.484	0.380	0.172	0.085	0.108	0.054

Table B16. Influence Coefficients for Inside Axial and Circumferential Semi-elliptical Surface Flaws: $R_i/t = 20$ and $a/t = 0.3$

Aspect Ratio	Elliptic Angle (deg)	K_0 Uniform	K_1 Linear	K_2 Quadratic	K_3 Cubic	K_0 t_{cl}=0.25 in.	K_1 t_{cl}=0.25 in.	K_0 t_{cl}=0.156 in.	K_1 t_{cl}=0.156 in.
2:1	0.000	0.737	0.131	0.049	0.026	0.461	0.203	0.382	0.193
	2.370	0.708	0.215	0.089	0.045	0.126	0.061	0.070	0.031
	16.600	0.691	0.274	0.133	0.073	0.078	0.038	0.046	0.022
	30.800	0.682	0.334	0.192	0.120	0.059	0.030	0.037	0.018
	45.000	0.675	0.385	0.256	0.181	0.050	0.025	0.031	0.016
	59.200	0.669	0.425	0.313	0.245	0.045	0.023	0.028	0.014
	73.400	0.667	0.453	0.356	0.297	0.042	0.021	0.026	0.013
	87.600	0.665	0.478	0.386	0.331	0.040	0.020	0.025	0.012
	90.000	0.664	0.483	0.391	0.337	0.039	0.020	0.024	0.012
6:1	0.000	0.666	0.144	0.040	0.021	0.424	0.193	0.353	0.180
	2.370	0.734	0.204	0.073	0.026	0.156	0.073	0.093	0.043
	16.600	0.821	0.291	0.125	0.052	0.129	0.063	0.079	0.039
	30.800	0.899	0.388	0.202	0.107	0.119	0.059	0.074	0.037
	45.000	0.962	0.479	0.291	0.186	0.114	0.057	0.071	0.035
	59.200	1.007	0.555	0.376	0.272	0.110	0.055	0.069	0.034
	73.400	1.037	0.608	0.441	0.344	0.108	0.054	0.068	0.034
	87.600	1.062	0.638	0.475	0.381	0.107	0.053	0.067	0.033
	90.000	1.067	0.643	0.481	0.388	0.106	0.053	0.067	0.033
10:1	0.000	0.583	0.089	0.028	0.013	0.316	0.167	0.316	0.167
	2.370	0.736	0.196	0.061	0.012	0.107	0.050	0.107	0.050
	16.600	0.869	0.296	0.118	0.031	0.095	0.047	0.095	0.047
	30.800	0.979	0.407	0.202	0.095	0.090	0.045	0.090	0.045
	45.000	1.064	0.513	0.301	0.181	0.087	0.043	0.087	0.043
	59.200	1.127	0.601	0.395	0.275	0.085	0.042	0.085	0.042
	73.400	1.168	0.662	0.467	0.354	0.084	0.042	0.084	0.042
	87.600	1.193	0.693	0.503	0.393	0.083	0.041	0.083	0.041
	90.000	1.198	0.699	0.509	0.400	0.132	0.066	0.083	0.041

Table B17. Influence Coefficients for Inside Axial Semi-elliptical Surface Flaws: R_i/t= 20 and a/t = 0.5

Aspect Ratio	Elliptic Angle (deg)	K_0 Uniform	K_1 Linear	K_2 Quadratic	K_3 Cubic	K_0 t_{cl}=0.25 in.	K_1 t_{cl}=0.25 in.	K_0 t_{cl}=0.156 in.	K_1 t_{cl}=0.156 in.
2:1	0.000	0.762	0.139	0.055	0.030	0.382	0.183	0.314	0.169
	2.370	0.748	0.210	0.087	0.044	0.096	0.046	0.054	0.024
	16.600	0.722	0.270	0.128	0.069	0.055	0.027	0.033	0.016
	30.800	0.707	0.332	0.187	0.115	0.040	0.020	0.025	0.012
	45.000	0.696	0.386	0.252	0.177	0.033	0.016	0.021	0.010
	59.200	0.688	0.429	0.312	0.243	0.029	0.015	0.018	0.009
	73.400	0.683	0.458	0.358	0.298	0.027	0.014	0.017	0.009
	87.600	0.679	0.484	0.389	0.333	0.025	0.013	0.016	0.008
	90.000	0.678	0.489	0.394	0.340	0.025	0.012	0.016	0.008
6:1	0.000	0.784	0.149	0.060	0.033	0.374	0.184	0.307	0.167
	2.370	0.827	0.222	0.086	0.040	0.119	0.055	0.071	0.034
	16.600	0.923	0.311	0.136	0.065	0.097	0.048	0.060	0.030
	30.800	1.012	0.414	0.212	0.117	0.091	0.045	0.057	0.028
	45.000	1.083	0.512	0.304	0.196	0.088	0.044	0.055	0.028
	59.200	1.133	0.594	0.394	0.285	0.086	0.043	0.054	0.027
	73.400	1.166	0.651	0.464	0.361	0.085	0.042	0.053	0.027
	87.600	1.194	0.683	0.500	0.401	0.084	0.042	0.053	0.026
	90.000	1.199	0.689	0.507	0.408	0.083	0.041	0.052	0.026
10:1	0.000	0.687	0.124	0.049	0.027	0.287	0.156	0.287	0.156
	2.370	0.842	0.217	0.078	0.030	0.081	0.039	0.081	0.039
	16.600	1.013	0.326	0.133	0.053	0.075	0.037	0.075	0.037
	30.800	1.155	0.449	0.220	0.110	0.074	0.037	0.074	0.037
	45.000	1.268	0.568	0.325	0.196	0.073	0.036	0.074	0.036
	59.200	1.351	0.669	0.427	0.295	0.073	0.036	0.073	0.036
	73.400	1.405	0.740	0.507	0.380	0.073	0.036	0.073	0.036
	87.600	1.438	0.775	0.546	0.422	0.073	0.036	0.073	0.036
	90.000	1.444	0.781	0.553	0.430	0.177	0.058	0.073	0.036

Table B18. Influence Coefficients for Inside Circumferential Semi-elliptical Surface Flaws: $R_i/t = 20$ and $a/t = 0.5$

Aspect Ratio	Elliptic Angle (deg)	K_0 Uniform	K_1 Linear	K_2 Quadratic	K_3 Cubic	K_0 0.250 cld	K_1 0.250 cld	K_0 0.156 cld	K_1 0.156 cld
2:1	0.00	0.765	0.140	0.055	0.030	0.381	0.183	0.313	0.169
	16.60	0.750	0.211	0.087	0.048	0.096	0.046	0.054	0.024
	28.50	0.723	0.270	0.128	0.069	0.055	0.027	0.033	0.016
	40.30	0.708	0.332	0.187	0.115	0.040	0.020	0.025	0.012
	52.20	0.699	0.387	0.252	0.177	0.033	0.017	0.021	0.010
	64.10	0.691	0.430	0.313	0.244	0.030	0.015	0.019	0.009
	76.00	0.685	0.460	0.359	0.299	0.028	0.014	0.017	0.009
	87.90	0.681	0.486	0.390	0.334	0.028	0.014	0.018	0.009
	90.00	0.680	0.491	0.396	0.341	0.028	0.014	0.018	0.009
6:1	0.00	0.769	0.144	0.057	0.033	0.371	0.182	0.304	0.166
	16.60	0.813	0.218	0.084	0.039	0.117	0.054	0.069	0.033
	28.50	0.909	0.308	0.134	0.064	0.095	0.046	0.059	0.029
	40.30	1.000	0.410	0.211	0.116	0.089	0.044	0.056	0.028
	52.20	1.073	0.509	0.303	0.195	0.086	0.043	0.054	0.027
	64.10	1.125	0.592	0.394	0.285	0.084	0.042	0.053	0.026
	76.00	1.159	0.650	0.464	0.361	0.083	0.041	0.052	0.026
	87.90	1.187	0.682	0.500	0.401	0.084	0.042	0.053	0.026
	90.00	1.192	0.688	0.507	0.408	0.084	0.042	0.053	0.026
10:1	0.00	0.660	0.113	0.043	0.023	0.340	0.172	0.283	0.154
	16.60	0.811	0.209	0.074	0.026	0.126	0.058	0.077	0.037
	28.50	0.978	0.317	0.129	0.050	0.114	0.056	0.071	0.035
	40.30	1.120	0.440	0.216	0.107	0.111	0.055	0.070	0.035
	52.20	1.234	0.559	0.321	0.194	0.111	0.055	0.069	0.035
	64.10	1.319	0.660	0.424	0.294	0.111	0.055	0.070	0.035
	76.00	1.374	0.731	0.504	0.378	0.111	0.055	0.070	0.035
	87.90	1.407	0.767	0.543	0.421	0.112	0.055	0.070	0.035
	90.00	1.412	0.773	0.550	0.428	0.112	0.056	0.070	0.035

Table B19. Influence Coefficients for Inside Axial Infinite-Length Surface Flaws, R_i/t= 10 (not used starting with v15.1)

Normalization: $0.1t^{1/2}K^*$

			$0.1\,t^{1/2}\,K^*$			
a′* / *a	***a/t*=0.01**	***a/t*=0.02**	***a/t*=0.03**	***a/t*=0.05**	***a/t*=0.075**	***a/t*=0.10**
0	1.434	1.029	0.846	0.667	0.565	0.511
0.0556	1.435	1.029	0.846	0.667	0.564	0.510
0.1111	1.436	1.029	0.846	0.666	0.563	0.508
0.1667	1.436	1.028	0.846	0.665	0.562	0.506
0.2222	1.438	1.029	0.846	0.665	0.561	0.505
0.2778	1.442	1.032	0.848	0.666	0.561	0.504
0.3333	1.450	1.037	0.852	0.669	0.563	0.505
0.3888	1.463	1.046	0.859	0.674	0.566	0.507
0.4444	1.482	1.058	0.869	0.682	0.571	0.511
0.500	1.509	1.077	0.884	0.693	0.580	0.517
0.5556	1.546	1.103	0.905	0.708	0.592	0.527
0.6111	1.598	1.138	0.934	0.731	0.609	0.541
0.6666	1.669	1.188	0.974	0.761	0.633	0.561
0.7222	1.768	1.258	1.031	0.804	0.668	0.590
0.7778	1.913	1.360	1.113	0.868	0.718	0.632
0.8333	2.138	1.518	1.242	0.967	0.798	0.699
0.8888	2.534	1.798	1.470	1.143	0.940	0.821
0.9166	2.878	2.041	1.668	1.294	1.064	0.927
0.9444	3.499	2.624	2.187	1.749	1.385	1.224
0.9639	5.831	4.227	3.499	2.770	2.187	1.895
0.9778	11.225	7.289	5.685	4.227	3.426	2.916
0.9889	17.493	11.662	8.746	6.414	5.102	4.373

a'/a	a/t=0.2	a/t=0.3	a/t=0.4
0	0.461	0.510	0.617
0.0552	0.457	0.502	0.602
0.1103	0.452	0.492	0.586
0.1655	0.447	0.483	0.571
0.2206	0.443	0.475	0.556
0.2757	0.439	0.466	0.542
0.3309	0.436	0.459	0.527
0.3861	0.434	0.451	0.513
0.4412	0.432	0.445	0.500
0.4963	0.433	0.440	0.488
0.5515	0.435	0.436	0.477
0.6066	0.440	0.434	0.467
0.6618	0.450	0.435	0.460
0.7169	0.464	0.440	0.456
0.7721	0.487	0.453	0.457
0.8272	0.526	0.477	0.468
0.8824	0.598	0.527	0.501
0.9118	0.665	0.577	0.538
0.9412	0.875	0.729	0.671
0.9618	1.385	1.020	0.948
0.9765	2.187	1.749	1.604
0.9882	2.916	2.478	2.187

a'/a	a/t=0.5
0	0.781
0.059	0.755
0.118	0.730
0.176	0.704
0.235	0.679
0.294	0.654
0.353	0.630
0.412	0.605
0.471	0.582
0.529	0.559
0.588	0.538
0.647	0.518
0.706	0.501
0.750	0.491
0.794	0.485
0.838	0.486
0.882	0.501
0.912	0.526
0.941	0.656
0.962	0.875
0.976	1.312
0.988	2.041

Table B19. (continued) Influence Coefficients for Inside Axial Infinite-Length Surface Flaws, R_i/t = 10 (not used starting with v15.1)

Normalization: $0.1t^{1/2}K^*$

$0.1\ t^{1/2}\ K^*$

a'/a	a/t=0.6	a'/a	a/t=0.7	a'/a	a/t=0.8	a'/a	a/t=0.9	a/t=0.95
0	1.021	0	1.35	0	1.739	0	1.952	1.902
0.0564	0.983	0.057	1.294	0.058	1.661	0.058	1.866	1.827
0.1127	0.946	0.115	1.238	0.116	1.583	0.117	1.779	1.752
0.1691	0.908	0.172	1.182	0.174	1.506	0.175	1.694	1.678
0.2255	0.871	0.229	1.127	0.232	1.428	0.233	1.608	1.604
0.2819	0.834	0.286	1.071	0.289	1.351	0.292	1.523	1.529
0.3382	0.798	0.343	1.016	0.347	1.275	0.35	1.438	1.456
0.3946	0.761	0.401	0.961	0.405	1.198	0.409	1.354	1.381
0.451	0.725	0.458	0.906	0.463	1.122	0.467	1.27	1.308
0.5074	0.69	0.515	0.852	0.521	1.047	0.526	1.186	1.234
0.5637	0.655	0.572	0.799	0.579	0.971	0.584	1.102	1.162
0.6201	0.622	0.63	0.747	0.637	0.897	0.643	1.019	1.088
0.6765	0.59	0.687	0.696	0.695	0.824	0.701	0.936	1.017
0.7328	0.561	0.744	0.648	0.753	0.752	0.759	0.854	0.947
0.7892	0.536	0.802	0.604	0.811	0.685	0.818	0.773	0.878
0.8456	0.521	0.859	0.569	0.869	0.627	0.876	0.699	0.815
0.902	0.528	0.916	0.562	0.927	0.598	0.935	0.651	0.768
0.9265	0.549	0.937	0.575	0.945	0.607	0.951	0.654	0.766
0.951	0.671	0.958	0.729	0.963	0.7	0.967	0.729	0.781
0.9681	0.933	0.973	1.02	0.976	1.02	0.979	0.875	0.826
0.9804	1.399	0.983	1.458	0.985	1.458	0.987	1.166	0.911
0.9902	2.041	0.992	2.041	0.993	2.041	0.993	1.749	1.093

Table B20. Influence Coefficients for Inside Circumferential 360° Surface Flaws, R_i/t = 10 (not used starting with v15.1)

Normalization: $10t^{3/2}K^*$

	10t $t^{1/2}$ K*					
a' / a	***a / t*=0.01**	**a/t=0.02**	**a/t=0.03**	**a/t=0.05**	**a/t=0.075**	**a/t=0.10**
0	2.255	1.616	1.325	1.036	0.867	0.771
0.0556	2.256	1.616	1.324	1.036	0.865	0.769
0.1111	2.257	1.616	1.324	1.035	0.864	0.767
0.1667	2.258	1.616	1.323	1.034	0.863	0.765
0.2222	2.260	1.617	1.324	1.035	0.862	0.764
0.2778	2.267	1.621	1.327	1.037	0.863	0.764
0.3333	2.280	1.629	1.334	1.041	0.866	0.766
0.3888	2.300	1.642	1.344	1.049	0.872	0.770
0.4444	2.329	1.662	1.361	1.061	0.880	0.777
0.5000	2.372	1.691	1.384	1.079	0.894	0.788
0.5556	2.431	1.732	1.417	1.104	0.914	0.804
0.6111	2.511	1.788	1.462	1.138	0.941	0.826
0.6666	2.623	1.866	1.526	1.187	0.979	0.859
0.7222	2.779	1.975	1.615	1.255	1.034	0.905
0.7778	3.008	2.135	1.744	1.355	1.114	0.972
0.8333	3.361	2.383	1.946	1.510	1.239	1.079
0.8888	3.986	2.823	2.305	1.786	1.462	1.271
0.9166	4.520	3.199	2.611	2.022	1.654	1.425
0.9444	6.195	3.965	3.346	2.478	1.982	1.735
0.9639	8.674	5.948	4.956	3.717	2.974	2.602
0.9778	13.630	9.913	8.054	6.195	4.956	4.337
0.9889	18.586	14.249	11.771	9.045	7.682	6.567

a'/a	**a/t=0.2**	**a/t=0.3**	**a/t=0.4**	**a'/a**	**a/t=0.5**
0	0.645	0.644	0.691	0	0.764
0.0552	0.640	0.635	0.678	0.059	0.744
0.1103	0.635	0.626	0.664	0.118	0.724
0.1655	0.630	0.617	0.651	0.176	0.704
0.2206	0.625	0.609	0.638	0.235	0.684
0.2757	0.622	0.601	0.625	0.294	0.666
0.3309	0.619	0.594	0.613	0.353	0.647
0.3861	0.618	0.588	0.602	0.412	0.630
0.4412	0.618	0.584	0.592	0.471	0.614
0.4963	0.622	0.581	0.584	0.529	0.600
0.5515	0.628	0.581	0.578	0.588	0.589
0.6066	0.639	0.584	0.574	0.647	0.580
0.6618	0.656	0.592	0.575	0.706	0.577
0.7169	0.681	0.607	0.581	0.750	0.579
0.7721	0.721	0.633	0.596	0.794	0.588
0.8272	0.784	0.678	0.626	0.838	0.608
0.8824	0.900	0.764	0.691	0.882	0.650
0.9118	1.007	0.845	0.793	0.912	0.702
0.9412	1.363	1.078	0.954	0.941	0.843
0.9618	1.921	1.487	1.301	0.962	1.115
0.9765	2.912	2.354	1.982	0.976	1.859
0.9882	3.841	3.346	2.912	0.988	2.726

Table B20. (continued) Influence Coefficients for Inside Circumferential 360° Surface Flaws, R_i/t = 10 (not used starting with v15.1)

Normalization: $10t^{3/2}K^*$

10t $t^{1/2}$ K^*							
a'/a	**a/t=0.6**	**a'/a**	**a/t=0.7**	**a'/a**	**a/t=0.8**	**a'/a**	**a/t=0.9**
0	0.852	0	0.944	0	1.028	0	1.129
0.0564	0.827	0.057	0.913	0.058	0.995	0.058	1.099
0.1127	0.802	0.115	0.883	0.116	0.962	0.117	1.070
0.1691	0.778	0.172	0.853	0.174	0.929	0.175	1.041
0.2255	0.753	0.229	0.823	0.232	0.897	0.233	1.013
0.2819	0.729	0.286	0.794	0.289	0.866	0.292	0.986
0.3382	0.706	0.343	0.766	0.347	0.835	0.350	0.959
0.3946	0.684	0.401	0.739	0.405	0.805	0.409	0.932
0.4510	0.663	0.458	0.712	0.463	0.776	0.467	0.907
0.5074	0.642	0.515	0.687	0.521	0.748	0.526	0.882
0.5637	0.624	0.572	0.663	0.579	0.721	0.584	0.857
0.6201	0.608	0.630	0.641	0.637	0.695	0.643	0.832
0.6765	0.595	0.687	0.622	0.695	0.671	0.701	0.809
0.7328	0.586	0.744	0.607	0.753	0.651	0.759	0.786
0.7892	0.586	0.802	0.600	0.811	0.636	0.818	0.767
0.8456	0.601	0.859	0.608	0.869	0.637	0.876	0.757
0.9020	0.653	0.916	0.661	0.927	0.686	0.935	0.786
0.9265	0.703	0.937	0.709	0.945	0.729	0.951	0.820
0.9510	0.867	0.958	0.855	0.963	0.880	0.967	0.892
0.9681	1.140	0.973	1.155	0.976	1.128	0.979	1.115
0.9804	1.797	0.983	1.760	0.985	1.722	0.987	1.735
0.9902	2.602	0.992	2.602	0.993	2.466	0.993	2.478

Table B21. Influence Coefficients for Inside Axial Infinite-Length Surface Flaws, R_i/t = 20 (not used starting with v15.1)

Normalization: $0.1t^{1/2}K^*$

a'/a	a/T = 0.01	a'/a	a/T = 0.02	a'/a	a/T = 0.03	a'/a	a/T = 0.05	a'/a	a/T = 0.075
0.1572	1.3734	0.1545	0.9941	0.2131	0.8034	0.2721	0.6931	0.1814	0.5871
0.2520	1.3850	0.2730	0.9935	0.4263	0.8073	0.5442	0.7064	0.3628	0.5840
0.3469	1.3991	0.3916	1.0005	0.6395	0.8503	0.8163	0.8128	0.5442	0.5952
0.4294	1.4196	0.5102	1.0237	0.6883	0.9205	0.8373	0.9789	0.6147	0.6192
0.5022	1.4519	0.5725	1.0569	0.7196	0.9604	0.8534	1.0205	0.6735	0.6418
0.5669	1.4934	0.6277	1.0942	0.7510	1.0010	0.8696	1.0663	0.7330	0.6712
0.6239	1.5454	0.6766	1.1378	0.7823	1.0496	0.8857	1.1199	0.7818	0.7128
0.6745	1.6109	0.7197	1.1890	0.8073	1.1015	0.8988	1.1768	0.8220	0.7614
0.7192	1.6881	0.7580	1.2502	0.8297	1.1591	0.9105	1.2389	0.8551	0.8194
0.7587	1.7783	0.7918	1.3215	0.8500	1.2212	0.9211	1.3054	0.8822	0.8879
0.7937	1.8841	0.8217	1.4035	0.8682	1.2897	0.9306	1.3784	0.9045	0.9673
0.8247	2.0065	0.8482	1.4974	0.8846	1.3672	0.9392	1.4606	0.9229	1.0589
0.8521	2.1476	0.8716	1.6064	0.8993	1.4530	0.9469	1.5527	0.9380	1.1649
0.8764	2.3144	0.8924	1.7317	0.9126	1.5500	0.9539	1.6539	0.9504	1.2870
0.8978	2.5088	0.9107	1.8799	0.9245	1.6573	0.9601	1.7687	0.9606	1.4294
0.9169	2.7425	0.9269	2.0546	0.9353	1.7798	0.9657	1.8978	0.9689	1.5956
0.9337	3.0295	0.9413	2.2648	0.9450	1.9196	0.9708	2.0433	0.9758	1.7928
0.9485	3.3882	0.9540	2.5284	0.9537	2.0799	0.9753	2.2128	0.9815	2.0311
0.9617	3.8597	0.9653	2.8657	0.9615	2.2688	0.9795	2.4084	0.9861	2.3239
0.9733	4.5185	0.9752	3.3249	0.9685	2.4923	0.9831	2.6408	0.9900	2.6987
0.9837	5.5374	0.9840	4.0104	0.9749	2.7692	0.9865	2.9247	0.9931	3.2010
1.0000	12.4839	0.9918	5.2382	0.9806	3.1177	0.9894	3.2771	0.9957	3.9366
		1.0000	12.4504	0.9858	3.5845	0.9921	3.7467	0.9978	5.2069
				0.9904	4.2536	0.9945	4.4058	1	12.443
				0.9945	5.3769	0.9967	5.4671		
				1.0000	12.4543	1.0000	12.4438		

a'/a	a/T = 0.1	a'/a	a/T = 0.2	a'/a	a/T = 0.3	a'/a	a/T = 0.4	a'/a	a/T = 0.5
0.2041	0.5262	0.1020	0.4691	0.0680	0.5229	0.0510	0.6420	0.0408	0.8376
0.4082	0.5215	0.2041	0.4597	0.1361	0.5109	0.1020	0.6270	0.0816	0.8179
0.4750	0.5258	0.3156	0.4505	0.2426	0.4957	0.2449	0.5982	0.2544	0.7662
0.5334	0.5326	0.4129	0.4445	0.3492	0.4780	0.3878	0.5570	0.3824	0.6942
0.5918	0.5427	0.5102	0.4421	0.4558	0.4625	0.5544	0.5155	0.5105	0.6347
0.6664	0.5588	0.6244	0.4446	0.5876	0.4494	0.6758	0.4841	0.6248	0.5815
0.7277	0.5863	0.7122	0.4582	0.6877	0.4445	0.7643	0.4706	0.7126	0.5421
0.7780	0.6203	0.7796	0.4811	0.7637	0.4507	0.8287	0.4731	0.7801	0.5179
0.8194	0.6621	0.8315	0.5142	0.8214	0.4676	0.8757	0.4904	0.8319	0.5071
0.8535	0.7126	0.8713	0.5577	0.8652	0.4950	0.9099	0.5220	0.8717	0.5083
0.8815	0.7722	0.9019	0.6123	0.8984	0.5333	0.9348	0.5683	0.9024	0.5209
0.9045	0.8417	0.9254	0.6791	0.9237	0.5831	0.9529	0.6306	0.9259	0.5448
0.9234	0.9231	0.9435	0.7597	0.9428	0.6459	0.9662	0.7107	0.9440	0.5803
0.9389	1.0180	0.9574	0.8564	0.9574	0.7233	0.9758	0.8117	0.9579	0.6286
0.9517	1.1293	0.9681	0.9723	0.9684	0.8182	0.9828	0.9378	0.9685	0.6914
0.9622	1.2610	0.9763	1.1118	0.9768	0.9343	0.9879	1.0952	0.9768	0.7715
0.9708	1.4192	0.9826	1.2813	0.9832	1.0776	0.9916	1.2937	0.9831	0.8729
0.9779	1.6124	0.9874	1.4903	0.9881	1.2565	0.9944	1.5485	0.9879	1.0029
0.9837	1.8557	0.9911	1.7537	0.9917	1.4853	0.9963	1.8874	0.9916	1.1729
0.9885	2.1744	0.9940	2.0994	0.9945	1.7904	0.9978	2.3653	0.9945	1.4053
0.9925	2.6237	0.9962	2.5801	0.9966	2.2250	0.9988	3.1132	0.9967	1.7468
0.9957	3.3301	0.9979	3.3291	0.9982	2.9255	0.9996	4.6337	0.9984	2.3319
0.9984	4.7770	0.9992	4.7983	0.9995	4.4599	1.0000	12.6847	0.9997	3.8826
1.0000	12.4534	1.0000	12.4404	1.0000	12.2947			1.0000	12.6594

Table B21. (continued) Influence Coefficients for Inside Axial Infinite-Length Surface Flaws, R_i/t = 20 (not used starting with v15.1)

Normalization: $0.1t^{1/2}K^*$

a'/a	a/T = 0.6	a'/a	a/T = 0.7	a'/a	a/T = 0.8	a'/a	a/T = 0.9	a'/a	a/T = 0.95
0.0340	1.1480	0.5714	1.0077	0.0255	2.4173	0.0227	3.1821	0.0215	3.0610
0.0680	1.1216	0.6458	0.9082	0.0510	2.3663	0.0454	3.1208	0.0430	3.0089
0.2154	1.0510	0.7201	0.8206	0.2112	2.1808	0.3329	2.7029	0.1125	2.8985
0.3628	0.9367	0.7995	0.7334	0.3507	1.8821	0.5338	2.0487	0.1792	2.7336
0.5102	0.8240	0.8565	0.6641	0.4722	1.6234	0.6743	1.5945	0.2432	2.5756
0.6492	0.7175	0.8973	0.6248	0.5779	1.3995	0.7724	1.2787	0.3047	2.4243
0.7489	0.6348	0.9265	0.6110	0.6699	1.2060	0.8410	1.0607	0.3637	2.2794
0.8203	0.5835	0.9475	0.6197	0.7500	1.0400	0.8889	0.9136	0.4204	2.1406
0.8715	0.5578	0.9625	0.6490	0.7934	0.9233	0.9029	0.8393	0.4748	2.0076
0.9082	0.5538	0.9732	0.6990	0.8367	0.8449	0.9152	0.8121	0.5271	1.8800
0.9344	0.5692	0.9809	0.7705	0.8830	0.7683	0.9274	0.7893	0.5772	1.7576
0.9533	0.6034	0.9865	0.8657	0.9162	0.7109	0.9443	0.7641	0.6254	1.6402
0.9668	0.6565	0.9904	0.9879	0.9400	0.6833	0.9573	0.7507	0.6716	1.5275
0.9765	0.7303	0.9933	1.1421	0.9571	0.6820	0.9673	0.7510	0.7160	1.4193
0.9834	0.8274	0.9953	1.3357	0.9693	0.7046	0.9750	0.7675	0.7586	1.3155
0.9884	0.9518	0.9968	1.5796	0.9780	0.7499	0.9809	0.8014	0.7995	1.2158
0.9919	1.1102	0.9978	1.8890	0.9843	0.8183	0.9854	0.8517	0.8387	1.1204
0.9945	1.3122	0.9986	2.2945	0.9888	0.9114	0.9889	0.9190	0.8764	1.0296
0.9963	1.5734	0.9991	2.8471	0.9920	1.0318	0.9916	1.0051	0.9126	0.9448
0.9976	1.9218	0.9995	3.6603	0.9944	1.1836	0.9936	1.1118	0.9474	0.8712
0.9986	2.4131	0.9998	5.0518	0.9960	1.3725	0.9952	1.2425	0.9546	0.8380
0.9992	3.1782	1.0000	12.6885	0.9972	1.6059	0.9964	1.4025	0.9618	0.8331
0.9997	4.7048			0.9981	1.8956	0.9974	1.5976	0.9690	0.8343
1.0000	12.6606			0.9987	2.2575	0.9981	1.8383	0.9751	0.8431
				0.9991	2.7161	0.9986	2.1406	0.9800	0.8629
				0.9994	3.3167	0.9991	2.5294	0.9839	0.8928
				0.9996	4.1429	0.9994	3.0568	0.9871	0.9341
				0.9998	5.3565	0.9996	3.8257	0.9897	0.9874
				1.0000	12.3011	0.9998	5.1467	0.9918	1.0537
						1.0000	12.6930	0.9934	1.1342
								0.9948	1.2309
								0.9959	1.3462
								0.9968	1.4833
								0.9975	1.6473
								0.9981	1.8444
								0.9985	2.0829
								0.9989	2.3819
								0.9992	2.7635
								0.9995	3.2744
								0.9997	4.0155
								0.9998	5.2608
								1.0000	12.6977

Table B22. Influence Coefficients for Inside Circumferential 360° Surface Flaws, R_i/t = 20 (not used starting with v15.1)

Normalization: $10t^{3/2}K^*$

a'/a	a/T = 0.01	a'/a	a/T = 0.02	a'/a	a/T = 0.03	a'/a	a/T = 0.05	a'/a	a/T = 0.075
0.1156	1.1120	0.1735	0.7682	0.3197	0.6143	0.4082	0.5357	0.2721	0.4454
0.2313	1.1132	0.3469	0.7738	0.6395	0.6516	0.8163	0.6074	0.5442	0.4506
0.3469	1.1192	0.4304	0.7858	0.6785	0.7193	0.8340	0.7605	0.6415	0.4759
0.4173	1.1308	0.5043	0.8035	0.7131	0.7465	0.8517	0.7902	0.7388	0.5090
0.4812	1.1490	0.5696	0.8256	0.7477	0.7790	0.8694	0.8274	0.7813	0.5464
0.5394	1.1719	0.6275	0.8540	0.7823	0.8192	0.8834	0.8649	0.8171	0.5807
0.5923	1.2008	0.6787	0.8896	0.8016	0.8566	0.8962	0.9061	0.8474	0.6191
0.6404	1.2382	0.7240	0.9327	0.8197	0.8906	0.9079	0.9499	0.8729	0.6634
0.6842	1.2835	0.7641	0.9834	0.8367	0.9259	0.9185	0.9978	0.8944	0.7147
0.7241	1.3368	0.7995	1.0432	0.8526	0.9644	0.9281	1.0525	0.9126	0.7735
0.7603	1.4003	0.8309	1.1132	0.8675	1.0082	0.9369	1.1134	0.9279	0.8404
0.7932	1.4755	0.8587	1.1958	0.8815	1.0571	0.9448	1.1808	0.9408	0.9169
0.8232	1.5622	0.8832	1.2935	0.8946	1.1123	0.9520	1.2575	0.9517	1.0050
0.8505	1.6673	0.9049	1.4111	0.9069	1.1743	0.9587	1.3444	0.9609	1.1067
0.8753	1.7920	0.9242	1.5547	0.9184	1.2456	0.9647	1.4439	0.9687	1.2254
0.8980	1.9461	0.9412	1.7366	0.9292	1.3264	0.9701	1.5587	0.9752	1.3664
0.9185	2.1377	0.9563	1.9746	0.9394	1.4227	0.9751	1.6934	0.9807	1.5361
0.9371	2.3834	0.9696	2.3098	0.9489	1.5360	0.9796	1.8559	0.9854	1.7456
0.9541	2.7263	0.9814	2.8313	0.9578	1.6750	0.9837	2.0563	0.9894	2.0184
0.9696	3.2320	0.9918	3.8594	0.9661	1.8481	0.9874	2.3121	0.9927	2.3857
0.9837	4.1227	1.0000	9.5945	0.9739	2.0784	0.9908	2.6611	0.9955	2.9377
1.0000	9.6321			0.9813	2.3984	0.9939	3.1778	0.9978	3.9401
				0.9881	2.9037	0.9967	4.0822	1	9.5611
				0.9945	3.8933	1.0000	9.5753		
				1.0000	9.5929				

a'/a	a/T = 0.1	a'/a	a/T = 0.2	a'/a	a/T = 0.3	a'/a	a/T = 0.4	a'/a	a/T = 0.5
0.2041	0.3962	0.1020	0.3336	0.0680	0.3440	0.0510	0.3840	0.0408	0.4443
0.4082	0.3935	0.2041	0.3278	0.1361	0.3374	0.1020	0.3763	0.0816	0.4355
0.5000	0.3985	0.2755	0.3233	0.2415	0.3289	0.1837	0.3660	0.2469	0.4123
0.5918	0.4088	0.3469	0.3206	0.3469	0.3196	0.2653	0.3539	0.4122	0.3773
0.6794	0.4258	0.5205	0.3184	0.5323	0.3094	0.4739	0.3335	0.5791	0.3452
0.7484	0.4526	0.6481	0.3246	0.6651	0.3063	0.6233	0.3141	0.6987	0.3238
0.8027	0.4867	0.7419	0.3405	0.7603	0.3145	0.7304	0.3081	0.7844	0.3160
0.8454	0.5292	0.8108	0.3666	0.8285	0.3337	0.8072	0.3140	0.8458	0.3202
0.8791	0.5808	0.8614	0.4029	0.8774	0.3635	0.8622	0.3307	0.8898	0.3356
0.9056	0.6420	0.8986	0.4498	0.9124	0.4044	0.9017	0.3579	0.9213	0.3616
0.9265	0.7141	0.9259	0.5083	0.9376	0.4574	0.9299	0.3962	0.9439	0.3988
0.9430	0.7984	0.9460	0.5800	0.9555	0.5240	0.9502	0.4466	0.9601	0.4482
0.9559	0.8971	0.9608	0.6671	0.9685	0.6065	0.9647	0.5107	0.9718	0.5115
0.9661	1.0128	0.9717	0.7726	0.9777	0.7079	0.9751	0.5911	0.9801	0.5909
0.9742	1.1494	0.9796	0.9004	0.9843	0.8322	0.9826	0.6911	0.9861	0.6901
0.9805	1.3122	0.9855	1.0561	0.9891	0.9853	0.9879	0.8158	0.9903	0.8139
0.9855	1.5086	0.9898	1.2483	0.9925	1.1758	0.9917	0.9727	0.9934	0.9696
0.9894	1.7520	0.9930	1.4887	0.9949	1.4154	0.9945	1.1737	0.9956	1.1698
0.9925	2.0594	0.9953	1.7995	0.9967	1.7274	0.9964	1.4397	0.9972	1.4349
0.9949	2.4674	0.9970	2.2190	0.9979	2.1508	0.9979	1.8141	0.9983	1.8073
0.9969	3.0556	0.9983	2.8338	0.9988	2.7720	0.9989	2.3965	0.9991	2.3882
0.9984	4.0225	0.9992	3.8883	0.9995	3.8327	0.9996	3.5447	0.9997	3.5442
1.0000	9.5578	1.0000	9.5017	1.0000	9.3453	1.0000	9.5956	1.0000	9.5307

Table B22. (continued) Influence Coefficients for Inside Circumferential 360° Surface Flaws, R_i/t = 20 (not used starting with v15.1)

Normalization: $10t^{3/2}K^*$

a'/a	a/T = 0.6	a'/a	a/T = 0.7	a'/a	a/T = 0.8	a'/a	a/T = 0.9	a'/a	a/T = 0.95
0.0340	0.5193	0.0292	0.6003	0.0255	0.6696	0.0227	0.7146	0.0215	0.7664
0.0680	0.5092	0.0583	0.5892	0.0510	0.6586	0.0454	0.7057	0.0430	0.7598
0.2891	0.4699	0.2293	0.5499	0.2840	0.6007	0.3265	0.6426	0.1183	0.7440
0.5102	0.4066	0.4004	0.4866	0.5170	0.5045	0.6077	0.5383	0.1937	0.7211
0.6492	0.3603	0.5714	0.4263	0.7500	0.4153	0.8889	0.4423	0.2691	0.6987
0.7489	0.3360	0.6458	0.3868	0.7934	0.3701	0.9082	0.4050	0.3444	0.6767
0.8203	0.3258	0.7201	0.3650	0.8367	0.3595	0.9274	0.4074	0.4198	0.6552
0.8715	0.3280	0.7995	0.3461	0.8801	0.3528	0.9467	0.4158	0.4952	0.6339
0.9082	0.3416	0.8565	0.3367	0.9120	0.3549	0.9609	0.4347	0.5705	0.6130
0.9344	0.3662	0.8973	0.3389	0.9355	0.3661	0.9713	0.4626	0.6459	0.5922
0.9533	0.4022	0.9265	0.3528	0.9527	0.3872	0.9789	0.5016	0.7213	0.5715
0.9668	0.4505	0.9475	0.3780	0.9653	0.4185	0.9845	0.5526	0.7966	0.5507
0.9765	0.5127	0.9625	0.4147	0.9746	0.4603	0.9887	0.6169	0.8720	0.5307
0.9834	0.5912	0.9732	0.4638	0.9815	0.5139	0.9917	0.6962	0.9474	0.5172
0.9884	0.6893	0.9809	0.5268	0.9865	0.5808	0.9939	0.7927	0.9528	0.5221
0.9919	0.8120	0.9865	0.6057	0.9902	0.6630	0.9956	0.9088	0.9582	0.5267
0.9945	0.9668	0.9904	0.7035	0.9929	0.7633	0.9968	1.0481	0.9636	0.5337
0.9963	1.1656	0.9933	0.8240	0.9949	0.8857	0.9976	1.2153	0.9691	0.5434
0.9976	1.4293	0.9953	0.9731	0.9964	1.0356	0.9983	1.4156	0.9747	0.5578
0.9986	1.7997	0.9968	1.1589	0.9974	1.2204	0.9988	1.6567	0.9793	0.5796
0.9992	2.3752	0.9978	1.3931	0.9982	1.4532	0.9991	1.9493	0.9832	0.6059
0.9997	3.5215	0.9986	1.6985	0.9988	1.7535	0.9994	2.3071	0.9863	0.6382
1.0000	9.4860	0.9991	2.1132	0.9992	2.1608	0.9996	2.7560	0.9889	0.6776
		0.9995	2.7222	0.9996	2.7544	0.9997	3.3267	0.9910	0.7247
		0.9998	3.7624	0.9998	3.7688	0.9998	4.1021	0.9927	0.7803
		1.0000	9.4614	1.0000	9.1286	1.0000	9.3761	0.9942	0.8458
								0.9953	0.9230
								0.9963	1.0142
								0.9971	1.1227
								0.9977	1.2526
								0.9983	1.4118
								0.9987	1.6111
								0.9991	1.8677
								0.9994	2.2230
								0.9996	2.7596
								0.9998	3.7410
								1.0000	9.3592

Table B23. Influence Coefficients for Outside Axial and Circumferential Semi-elliptical Surface Flaws: R_i/t 10 and a/t = 0.1

Aspect Ratio = 2:1					Aspect Ratio = 6:1					Aspect Ratio = 10:1				
Φ	K0 (Uniform)	K1 (Linear)	K2 (Quad)	K3 (Cubic)	Φ	K0 (Uniform)	K1 (Linear)	K2 (Quad)	K3 (Cubic)	Φ	K0 (Uniform)	K1 (Linear)	K2 (Quad)	K3 (Cubic)
0.0	0.6625	0.1033	0.0399	0.0210	0.0	0.6072	0.0815	0.0284	0.0141	0.0	0.4769	0.0536	0.0163	0.0073
5.4	0.7067	0.1409	0.0522	0.0268	2.8	0.6161	0.0928	0.0308	0.0149	4.9	0.4885	0.0687	0.0188	0.0079
11.5	0.6870	0.1690	0.0627	0.0309	14.8	0.6362	0.1492	0.0495	0.0212	10.4	0.5121	0.0915	0.0252	0.0098
21.0	0.6642	0.2156	0.0898	0.0441	21.1	0.6744	0.1913	0.0709	0.0311	20.3	0.6433	0.1628	0.0543	0.0214
29.2	0.6529	0.2577	0.1239	0.0660	30.7	0.7229	0.2589	0.1160	0.0575	29.3	0.7357	0.2393	0.0991	0.0457
38.5	0.6420	0.3022	0.1690	0.1015	44.5	0.8221	0.3743	0.2119	0.1302	39.5	0.8186	0.3305	0.1686	0.0942
49.2	0.6390	0.3510	0.2275	0.1569	52.0	0.8632	0.4328	0.2705	0.1834	49.2	0.8907	0.4167	0.2464	0.1590
61.1	0.6330	0.3936	0.2880	0.2235	60.1	0.8978	0.4883	0.3320	0.2450	61.7	0.9632	0.5151	0.3493	0.2588
70.0	0.6320	0.4182	0.3256	0.2691	73.9	0.9471	0.5641	0.4216	0.3425	70.9	0.9938	0.5664	0.4098	0.3241
79.8	0.6326	0.4368	0.3548	0.3060	84.5	0.9933	0.6215	0.4861	0.4125	81.2	1.0188	0.6049	0.4564	0.3766
90.0	0.6328	0.4439	0.3664	0.3210	90.0	0.9829	0.6136	0.4803	0.4084	90.0	1.0238	0.6148	0.4693	0.3918

Table B24. Influence Coefficients for Outside Axial and Circumferential Semi-elliptical Surface Flaws: R_i/t = 10 and a/t = 0.2

Aspect Ratio = 2:1					Aspect Ratio = 6:1					Aspect Ratio = 10:1				
Φ	K0 (Uniform)	K1 (Linear)	K2 (Quad)	K3 (Cubic)	Φ	K0 (Uniform)	K1 (Linear)	K2 (Quad)	K3 (Cubic)	Φ	K0 (Uniform)	K1 (Linear)	K2 (Quad)	K3 (Cubic)
0.0	0.6982	0.1105	0.0430	0.0228	0.0	0.6233	0.0895	0.0325	0.0165	0.0	0.5279	0.0624	0.0205	0.0099
4.7	0.7306	0.1430	0.0532	0.0276	4.0	0.6308	0.1049	0.0357	0.0175	4.1	0.5090	0.0713	0.0213	0.0098
10.7	0.7084	0.1705	0.0631	0.0312	16.7	0.6602	0.1667	0.0583	0.0257	11.6	0.5949	0.1125	0.0331	0.0137
21.3	0.6836	0.2243	0.0939	0.0460	21.0	0.6867	0.1949	0.0731	0.0327	19.1	0.6536	0.1622	0.0540	0.0219
31.9	0.6920	0.2909	0.1468	0.0807	31.6	0.7712	0.2793	0.1277	0.0649	30.8	0.7801	0.2640	0.1139	0.0547
40.4	0.6770	0.3301	0.1909	0.1181	44.7	0.8560	0.3863	0.2186	0.1348	41.5	0.8903	0.3680	0.1932	0.1113
49.5	0.6709	0.3721	0.2433	0.1691	54.0	0.9051	0.4574	0.2906	0.2010	51.2	0.9760	0.4594	0.2755	0.1810
58.0	0.6738	0.4119	0.2956	0.2250	60.4	0.9319	0.5001	0.3382	0.2491	61.6	1.0361	0.5442	0.3650	0.2682
71.5	0.6474	0.4297	0.3365	0.2799	73.1	0.9718	0.5656	0.4165	0.3346	69.9	1.0620	0.5928	0.4235	0.3317
81.3	0.6450	0.4437	0.3603	0.3108	87.2	0.9903	0.5984	0.4585	0.3837	80.0	1.0851	0.6312	0.4710	0.3856
90.0	0.6436	0.4472	0.3669	0.3198	90.0	0.9892	0.5984	0.4591	0.3846	90.0	1.0927	0.6442	0.4875	0.4049

Table B25. Influence Coefficients for Outside Axial and Circumferential Semi-elliptical Surface Flaws: R/t = 10 and a/t = 0.3

Aspect Ratio = 2:1					Aspect Ratio = 6:1					Aspect Ratio = 10:1				
Φ	K0 (Uniform)	K1 (Linear)	K2 (Quad)	K3 (Cubic)	Φ	K0 (Uniform)	K1 (Linear)	K2 (Quad)	K3 (Cubic)	Φ	K0 (Uniform)	K1 (Linear)	K2 (Quad)	K3 (Cubic)
0.0	0.7164	0.1146	0.0450	0.0240	0.0	0.6555	0.1011	0.0386	0.0202	0.0	0.3365	0.0384	0.0143	0.0075
4.7	0.7473	0.1472	0.0552	0.0287	2.1	0.6906	0.1145	0.0421	0.0218	4.3	0.5460	0.0832	0.0270	0.0132
10.7	0.7244	0.1750	0.0650	0.0323	11.3	0.6860	0.1509	0.0521	0.0246	12.0	0.6816	0.1375	0.0430	0.0189
21.3	0.7035	0.2310	0.0967	0.0473	20.9	0.7441	0.2127	0.0814	0.0375	19.7	0.7380	0.1913	0.0671	0.0288
31.9	0.6937	0.2895	0.1457	0.0801	31.8	0.8249	0.2992	0.1380	0.0710	31.6	0.8795	0.3028	0.1339	0.0662
40.4	0.6850	0.3325	0.1918	0.1186	42.1	0.8943	0.3845	0.2086	0.1239	42.5	1.0195	0.4313	0.2326	0.1376
49.9	0.6810	0.3749	0.2448	0.1703	51.3	0.9506	0.4597	0.2816	0.1883	51.2	1.0994	0.5204	0.3152	0.2091
59.7	0.6754	0.4145	0.3004	0.2312	60.6	1.0218	0.5474	0.3721	0.2759	62.2	1.1291	0.5821	0.3886	0.2856
71.3	0.6618	0.4381	0.3431	0.2854	74.4	1.0415	0.5971	0.4385	0.3529	71.1	1.1732	0.6385	0.4523	0.3534
79.8	0.6588	0.4497	0.3636	0.3125	86.4	1.0562	0.6236	0.4729	0.3933	80.6	1.2008	0.6765	0.4976	0.4043
90.0	0.6565	0.4541	0.3722	0.3244	90.0	1.0555	0.6243	0.4742	0.3951	90.0	1.2072	0.6877	0.5120	0.4214

Table B26. Influence Coefficients for Outside Axial and Circumferential Semi-elliptical Surface Flaws: R_i/t = 10 and a/t = 0.4

Aspect Ratio = 2:1					Aspect Ratio = 6:1					Aspect Ratio = 10:1				
Φ	K0 (Uniform)	K1 (Linear)	K2 (Quad)	K3 (Cubic)	Φ	K0 (Uniform)	K1 (Linear)	K2 (Quad)	K3 (Cubic)	Φ	K0 (Uniform)	K1 (Linear)	K2 (Quad)	K3 (Cubic)
0.0	0.7563	0.1255	0.0501	0.0269	0.0	0.7439	0.1252	0.0502	0.0270	0.0	0.4241	0.0606	0.0238	0.0128
5.3	0.7789	0.1599	0.0607	0.0317	1.7	0.7616	0.1347	0.0525	0.0280	4.0	0.5946	0.1002	0.0357	0.0184
11.4	0.7529	0.1877	0.0708	0.0354	10.4	0.7465	0.1668	0.0603	0.0299	11.2	0.7148	0.1502	0.0512	0.0243
20.8	0.7292	0.2362	0.0987	0.0486	20.2	0.8029	0.2286	0.0888	0.0421	19.1	0.8070	0.2111	0.0764	0.0345
29.1	0.7299	0.2870	0.1377	0.0730	30.4	0.8897	0.3128	0.1417	0.0724	30.7	0.9783	0.3322	0.1465	0.0728
38.4	0.7003	0.3260	0.1815	0.1086	40.1	0.9654	0.3966	0.2080	0.1202	41.2	1.0952	0.4420	0.2314	0.1342
49.0	0.6987	0.3791	0.2447	0.1684	50.8	1.0243	0.4825	0.2917	0.1935	49.5	1.1812	0.5293	0.3093	0.1998
60.9	0.6873	0.4215	0.3072	0.2381	60.5	1.0793	0.5544	0.3679	0.2684	61.5	1.2767	0.6361	0.4173	0.3034
69.8	0.6721	0.4366	0.3376	0.2779	70.6	1.1187	0.6119	0.4350	0.3407	70.6	1.3197	0.6894	0.4781	0.3687
79.5	0.6567	0.4428	0.3560	0.3049	84.9	1.1458	0.6549	0.4887	0.4025	80.4	1.3552	0.7318	0.5269	0.4228
90.0	0.6551	0.4484	0.3660	0.3184	90.0	1.1454	0.6570	0.4921	0.4069	90.0	1.3729	0.7492	0.5461	0.4438

Table B27. Influence Coefficients for Outside Axial and Circumferential Semi-elliptical Surface Flaws: R_i/t = 10 and a/t = 0.5

Aspect Ratio = 2:1					Aspect Ratio = 6:1					Aspect Ratio = 10:1				
Φ	K0 (Uniform)	K1 (Linear)	K2 (Quad)	K3 (Cubic)	Φ	K0 (Uniform)	K1 (Linear)	K2 (Quad)	K3 (Cubic)	Φ	K0 (Uniform)	K1 (Linear)	K2 (Quad)	K3 (Cubic)
0.0	0.7613	0.1295	0.0523	0.0282	0.0	0.7944	0.1455	0.0606	0.0332	0.0	0.5244	0.0861	0.0352	0.0192
4.6	0.8139	0.1657	0.0639	0.0337	2.7	0.8419	0.1644	0.0659	0.0357	4.0	0.6759	0.1243	0.0472	0.0251
10.4	0.7876	0.1916	0.0728	0.0369	10.5	0.8300	0.1935	0.0731	0.0373	11.4	0.8027	0.1765	0.0638	0.0317
21.6	0.7549	0.2484	0.1051	0.0521	20.3	0.8948	0.2586	0.1032	0.0504	21.7	0.9550	0.2679	0.1045	0.0498
31.7	0.7353	0.3017	0.1510	0.0830	31.0	0.9834	0.3467	0.1594	0.0830	30.3	1.0965	0.3651	0.1611	0.0812
40.3	0.7269	0.3439	0.1962	0.1206	41.4	1.0651	0.4381	0.2333	0.1375	40.6	1.2288	0.4808	0.2480	0.1428
49.7	0.7162	0.3857	0.2490	0.1719	50.5	1.1285	0.5157	0.3068	0.2014	49.1	1.3298	0.5681	0.3226	0.2042
58.3	0.7046	0.4188	0.2974	0.2251	61.0	1.1887	0.5952	0.3913	0.2845	61.2	1.4477	0.6900	0.4418	0.3161
71.0	0.7059	0.4621	0.3609	0.3001	71.8	1.2309	0.6559	0.4623	0.3615	70.4	1.5094	0.7546	0.5112	0.3887
81.4	0.6860	0.4620	0.3725	0.3205	80.0	1.2497	0.6848	0.4980	0.4023	80.3	1.5537	0.8015	0.5633	0.4455
90.0	0.6850	0.4660	0.3796	0.3300	90.0	1.2548	0.6959	0.5130	0.4204	90.0	1.5744	0.8203	0.5835	0.4674

Table B28. Influence Coefficients for Outside Axial and Circumferential Semi-elliptical Surface Flaws: R_i/t = 20 and a/t = 0.1

Aspect Ratio = 2:1					Aspect Ratio = 6:1					Aspect Ratio = 10:1				
Φ	K0 (Uniform)	K1 (Linear)	K2 (Quad)	K3 (Cubic)	Φ	K0 (Uniform)	K1 (Linear)	K2 (Quad)	K3 (Cubic)	Φ	K0 (Uniform)	K1 (Linear)	K2 (Quad)	K3 (Cubic)
0.0	0.6919	0.1113	0.0429	0.0227	0.0	0.5023	0.0784	0.0277	0.0137	0.0	0.1918	0.0152	0.0048	0.0023
3.9	0.7084	0.1348	0.0506	0.0263	5.7	0.5173	0.0940	0.0319	0.0152	5.3	0.5177	0.0708	0.0202	0.0086
12.1	0.6805	0.1711	0.0644	0.0318	16.1	0.5119	0.1256	0.0440	0.0196	11.3	0.5329	0.0997	0.0281	0.0108
21.1	0.6548	0.2126	0.0894	0.0442	22.6	0.5912	0.1680	0.0642	0.0293	21.3	0.6157	0.1645	0.0567	0.0227
31.1	0.6475	0.2640	0.1311	0.0717	31.3	0.6510	0.2237	0.0990	0.0495	31.0	0.7411	0.2512	0.1083	0.0519
42.1	0.6520	0.3233	0.1910	0.1209	45.1	0.7408	0.3202	0.1757	0.1058	40.7	0.8261	0.3390	0.1757	0.0996
47.9	0.6347	0.3437	0.2193	0.1487	52.5	0.7618	0.3627	0.2187	0.1443	47.7	0.8667	0.3966	0.2290	0.1441
60.7	0.6196	0.3848	0.2813	0.2180	60.6	0.8075	0.4146	0.2704	0.1930	60.7	0.9581	0.5088	0.3421	0.2511
67.8	0.6954	0.4666	0.3639	0.3000	75.7	0.8474	0.4774	0.3424	0.2689	70.6	0.9834	0.5602	0.4052	0.3204
74.8	0.6548	0.4487	0.3609	0.3077	82.6	0.8625	0.4959	0.3632	0.2916	81.6	1.0127	0.6023	0.4554	0.3767
90.0	0.6077	0.4386	0.3676	0.3257	90.0	0.8727	0.5056	0.3734	0.3023	90.0	1.0142	0.6097	0.4661	0.3899

Table B29. Influence Coefficients for Outside Axial and Circumferential Semi-elliptical Surface Flaws: $R_i/t = 20$ and $a/t = 0.2$

Aspect Ratio = 2:1					Aspect Ratio = 6:1					Aspect Ratio = 10:1				
Φ	K0 (Uniform)	K1 (Linear)	K2 (Quad)	K3 (Cubic)	Φ	K0 (Uniform)	K1 (Linear)	K2 (Quad)	K3 (Cubic)	Φ	K0 (Uniform)	K1 (Linear)	K2 (Quad)	K3 (Cubic)
0.0	0.6951	0.1100	0.0427	0.0226	0.0	0.5729	0.0887	0.0323	0.0163	0.0	0.3212	0.0386	0.0130	0.0063
4.3	0.7199	0.1387	0.0517	0.0268	5.7	0.5784	0.1057	0.0362	0.0176	5.2	0.5322	0.0768	0.0238	0.0110
11.5	0.6946	0.1717	0.0640	0.0316	16.1	0.5836	0.1440	0.0507	0.0228	11.4	0.6234	0.1170	0.0339	0.0139
19.2	0.6749	0.2096	0.0851	0.0414	20.4	0.6099	0.1683	0.0628	0.0284	20.8	0.6759	0.1767	0.0611	0.0252
30.6	0.6582	0.2675	0.1315	0.0709	31.3	0.7177	0.2505	0.1120	0.0563	30.2	0.7854	0.2621	0.1119	0.0534
39.9	0.6516	0.3141	0.1798	0.1104	45.1	0.8052	0.3538	0.1967	0.1197	39.7	0.8572	0.3450	0.1761	0.0985
50.0	0.6442	0.3575	0.2340	0.1628	50.0	0.8289	0.3881	0.2300	0.1490	46.6	0.9431	0.4217	0.2391	0.1480
61.0	0.6420	0.3982	0.2909	0.2257	60.6	0.8705	0.4528	0.2990	0.2159	58.0	1.0037	0.5127	0.3336	0.2374
68.8	0.6418	0.4205	0.3246	0.2661	75.6	0.9129	0.5195	0.3766	0.2989	70.5	1.0540	0.5900	0.4228	0.3322
81.2	0.6396	0.4417	0.3595	0.3108	82.5	0.9319	0.5410	0.4006	0.3250	80.3	1.0760	0.6267	0.4681	0.3836
90.0	0.6397	0.4466	0.3675	0.3213	90.0	0.9338	0.5465	0.4081	0.3339	90.0	1.0832	0.6391	0.4839	0.4021

Table B30. Influence Coefficients for Outside Axial and Circumferential Semi-elliptical Surface Flaws: $R_i/t = 20$ and $a/t = 0.3$

Aspect Ratio = 2:1					Aspect Ratio = 6:1					Aspect Ratio = 10:1				
Φ	K0 (Uniform)	K1 (Linear)	K2 (Quad)	K3 (Cubic)	Φ	K0 (Uniform)	K1 (Linear)	K2 (Quad)	K3 (Cubic)	Φ	K0 (Uniform)	K1 (Linear)	K2 (Quad)	K3 (Cubic)
0.0	0.7180	0.1153	0.0452	0.0241	0.0	0.6331	0.1037	0.0396	0.0207	0.0	0.4320	0.0570	0.0208	0.0107
4.3	0.7404	0.1440	0.0541	0.0282	5.7	0.6355	0.1213	0.0435	0.0218	4.4	0.6016	0.0907	0.0307	0.0153
11.5	0.7141	0.1772	0.0664	0.0329	16.1	0.6455	0.1625	0.0587	0.0271	9.7	0.6607	0.1224	0.0380	0.0172
21.9	0.6891	0.2299	0.0978	0.0485	22.6	0.7211	0.2111	0.0827	0.0385	20.6	0.7468	0.1971	0.0707	0.0308
30.5	0.6749	0.2736	0.1343	0.0724	31.3	0.7880	0.2760	0.1242	0.0628	31.1	0.8625	0.2931	0.1286	0.0633
39.8	0.6680	0.3208	0.1835	0.1125	45.1	0.8605	0.3774	0.2107	0.1291	39.2	0.9324	0.3676	0.1857	0.1034
49.9	0.6598	0.3649	0.2385	0.1657	52.5	0.8875	0.4258	0.2602	0.1741	51.1	1.0571	0.4878	0.2900	0.1898
60.9	0.6755	0.4217	0.3099	0.2416	60.6	0.9413	0.4845	0.3191	0.2304	61.6	1.1257	0.5762	0.3818	0.2785
68.7	0.6781	0.4481	0.3486	0.2876	75.6	0.9918	0.5566	0.4021	0.3192	69.8	1.1529	0.6251	0.4405	0.3423
81.0	0.6628	0.4589	0.3749	0.3253	82.5	1.0025	0.5741	0.4237	0.3438	80.0	1.1810	0.6656	0.4893	0.3971
90.0	0.6586	0.4595	0.3788	0.3318	90.0	1.0046	0.5797	0.4313	0.3529	90.0	1.1897	0.6791	0.5061	0.4168

Table B31. Influence Coefficients for Outside Axial and Circumferential Semi-elliptical Surface Flaws: $R_i/t = 20$ and $a/t = 0.4$

Aspect Ratio = 2:1					Aspect Ratio = 6:1					Aspect Ratio = 10:1				
Φ	K0 (Uniform)	K1 (Linear)	K2 (Quad)	K3 (Cubic)	Φ	K0 (Uniform)	K1 (Linear)	K2 (Quad)	K3 (Cubic)	Φ	K0 (Uniform)	K1 (Linear)	K2 (Quad)	K3 (Cubic)
0.0	0.7469	0.1232	0.0490	0.0263	0.0	0.7034	0.1237	0.0495	0.0266	0.0	0.6558	0.0971	0.0377	0.0201
4.3	0.7676	0.1518	0.0577	0.0303	5.7	0.7036	0.1415	0.0532	0.0277	4.3	0.6522	0.1104	0.0391	0.0201
11.5	0.7387	0.1845	0.0697	0.0348	16.1	0.7085	0.1827	0.0684	0.0329	9.3	0.6909	0.1369	0.0462	0.0224
19.2	0.7155	0.2224	0.0907	0.0444	22.6	0.7841	0.2326	0.0935	0.0450	19.9	0.8102	0.2161	0.0796	0.0362
30.5	0.6951	0.2807	0.1377	0.0743	31.3	0.8516	0.2987	0.1361	0.0702	28.9	0.9351	0.3046	0.1304	0.0638
39.9	0.7013	0.3372	0.1931	0.1185	45.1	0.9493	0.4093	0.2269	0.1387	38.8	1.0453	0.4064	0.2046	0.1141
49.9	0.6868	0.3794	0.2483	0.1728	52.5	0.9786	0.4595	0.2782	0.1852	51.6	1.1793	0.5337	0.3160	0.2071
60.9	0.6820	0.4197	0.3062	0.2376	60.6	1.0304	0.5192	0.3390	0.2439	60.4	1.2420	0.6119	0.3969	0.2853
68.7	0.6792	0.4417	0.3407	0.2795	75.6	1.0752	0.5899	0.4225	0.3342	71.0	1.2963	0.6801	0.4731	0.3659
81.2	0.6733	0.4612	0.3750	0.3244	82.5	1.0840	0.6048	0.4414	0.3562	81.7	1.3321	0.7235	0.5235	0.4219
90.0	0.6739	0.4667	0.3837	0.3356	90.0	1.0876	0.6099	0.4479	0.3639	90.0	1.3384	0.7328	0.5350	0.4353

Table B32. Influence Coefficients for Outside Axial and Circumferential Semi-elliptical Surface Flaws: $R_i/t = 20$ and $a/t = 0.5$

Aspect Ratio = 2:1					Aspect Ratio = 6:1					Aspect Ratio = 10:1				
Φ	K0 (Uniform)	K1 (Linear)	K2 (Quad)	K3 (Cubic)	Φ	K0 (Uniform)	K1 (Linear)	K2 (Quad)	K3 (Cubic)	Φ	K0 (Uniform)	K1 (Linear)	K2 (Quad)	K3 (Cubic)
0.0	0.7802	0.1327	0.0534	0.0288	0.0	0.7743	0.1719	0.0665	0.0349	0.0	0.5804	0.0963	0.0395	0.0216
4.2	0.8030	0.1603	0.0619	0.0327	5.7	0.7841	0.1676	0.0659	0.0351	4.2	0.6882	0.1285	0.0490	0.0261
10.8	0.7718	0.1896	0.0721	0.0364	16.1	0.8088	0.2131	0.0825	0.0409	9.0	0.7217	0.1517	0.0555	0.0283
20.4	0.7404	0.2367	0.0988	0.0489	20.4	0.8432	0.2421	0.0968	0.0475	19.4	0.8998	0.2420	0.0919	0.0436
31.1	0.7186	0.2910	0.1441	0.0784	31.3	0.9438	0.3294	0.1510	0.0788	31.2	1.0778	0.3652	0.1636	0.0835
39.7	0.7117	0.3376	0.1917	0.1169	45.1	1.0453	0.4428	0.2441	0.1492	38.0	1.1698	0.4408	0.2183	0.1209
49.2	0.7201	0.3927	0.2546	0.1759	52.5	1.0864	0.4984	0.2987	0.1980	50.2	1.3221	0.5720	0.3290	0.2109
59.2	0.6917	0.4156	0.2977	0.2270	60.6	1.1311	0.5557	0.3590	0.2570	61.9	1.4258	0.6842	0.4408	0.3173
70.1	0.6902	0.4486	0.3477	0.2870	75.6	1.1740	0.6252	0.4415	0.3466	70.9	1.4758	0.7420	0.5048	0.3851
81.8	0.6741	0.4573	0.3703	0.3196	82.5	1.1830	0.6404	0.4608	0.3690	80.6	1.5134	0.7850	0.5536	0.4389
90.0	0.6625	0.4521	0.3687	0.3206	90.0	1.1887	0.6479	0.4698	0.3792	90.0	1.5226	0.7978	0.5693	0.4570

Table B33. Influence Coefficients for Outside Axial Infinite-Length Surface Flaws: R_i/t= 10

Normalization: $0.1t^{1/2}K^*$

a'/a	a/T = 0.01	a'/a	a/T = 0.02	a'/a	a/T = 0.03	a'/a	a/T = 0.05	a'/a	a/T = 0.075
0.1214	1.4179	0.1111	1.0404	0.1111	0.8570	0.1111	0.6771	0.1000	0.5720
0.2274	1.4182	0.2222	1.0387	0.2222	0.8555	0.2222	0.6752	0.2000	0.5696
0.3333	1.4238	0.3333	1.0410	0.3333	0.8571	0.3333	0.6758	0.3775	0.5688
0.3930	1.4360	0.4189	1.0505	0.4421	0.8665	0.4423	0.6823	0.5161	0.5785
0.4489	1.4529	0.4946	1.0687	0.5338	0.8878	0.5343	0.6980	0.6241	0.6016
0.5013	1.4751	0.5616	1.0946	0.6112	0.9191	0.6118	0.7217	0.7085	0.6381
0.5505	1.5036	0.6209	1.1290	0.6765	0.9615	0.6773	0.7540	0.7743	0.6877
0.5966	1.5404	0.6734	1.1729	0.7316	1.0152	0.7325	0.7952	0.8256	0.7505
0.6397	1.5849	0.7198	1.2263	0.7781	1.0804	0.7791	0.8454	0.8656	0.8276
0.6802	1.6385	0.7609	1.2905	0.8173	1.1582	0.8184	0.9056	0.8969	0.9205
0.7182	1.7038	0.7973	1.3666	0.8504	1.2500	0.8515	0.9770	0.9212	1.0318
0.7538	1.7818	0.8294	1.4566	0.8783	1.3580	0.8795	1.0613	0.9403	1.1648
0.7872	1.8748	0.8579	1.5632	0.9019	1.4856	0.9031	1.1613	0.9551	1.3248
0.8184	1.9872	0.8831	1.6909	0.9217	1.6370	0.9230	1.2808	0.9667	1.5186
0.8477	2.1264	0.9054	1.8456	0.9385	1.8194	0.9398	1.4256	0.9757	1.7575
0.8752	2.3002	0.9251	2.0375	0.9526	2.0428	0.9540	1.6048	0.9828	2.0601
0.9009	2.5249	0.9425	2.2822	0.9645	2.3260	0.9659	1.8342	0.9883	2.4579
0.9250	2.8307	0.9580	2.6113	0.9746	2.6988	0.9760	2.1417	0.9925	3.0167
0.9477	3.2777	0.9716	3.0833	0.9831	3.2245	0.9845	2.5880	0.9959	3.8942
0.9689	4.0228	0.9837	3.8617	0.9902	4.0621	0.9917	3.3391	0.9985	5.7059
0.9888	5.7151	0.9944	5.6233	0.9963	5.8053	0.9978	5.1760	1.0000	15.3431
1.0000	15.3969	1.0000	15.3509	1.0000	15.3461	1.0000	14.9059		

a'/a	a/T = 0.1	a'/a	a/T = 0.2	a'/a	a/T = 0.3	a'/a	a/T = 0.4	a'/a	a/T = 0.5
0.1618	0.5162	0.1667	0.4599	0.1667	0.5018	0.1481	0.6022	0.1889	0.7506
0.3031	0.5115	0.3333	0.4459	0.3333	0.4748	0.2963	0.5611	0.3778	0.6677
0.4444	0.5127	0.5225	0.4372	0.5226	0.4501	0.4444	0.5219	0.5726	0.5871
0.5740	0.5244	0.6581	0.4428	0.6582	0.4379	0.6022	0.4863	0.7064	0.5262
0.6735	0.5501	0.7553	0.4644	0.7554	0.4419	0.7152	0.4635	0.7984	0.4955
0.7500	0.5878	0.8249	0.5017	0.8251	0.4614	0.7962	0.4588	0.8616	0.4898
0.8087	0.6382	0.8748	0.5545	0.8750	0.4960	0.8542	0.4706	0.9051	0.5058
0.8539	0.7015	0.9106	0.6240	0.9108	0.5457	0.8959	0.4978	0.9349	0.5424
0.8886	0.7787	0.9362	0.7119	0.9364	0.6119	0.9257	0.5404	0.9554	0.6000
0.9153	0.8715	0.9546	0.8210	0.9548	0.6965	0.9470	0.5995	0.9695	0.6803
0.9358	0.9819	0.9678	0.9550	0.9680	0.8025	0.9624	0.6768	0.9792	0.7862
0.9515	1.1133	0.9772	1.1186	0.9774	0.9339	0.9733	0.7748	0.9859	0.9223
0.9636	1.2690	0.9840	1.3186	0.9842	1.0962	0.9812	0.8975	0.9905	1.0948
0.9729	1.4555	0.9888	1.5641	0.9890	1.2979	0.9868	1.0502	0.9936	1.3129
0.9801	1.6810	0.9923	1.8687	0.9925	1.5510	0.9909	1.2407	0.9958	1.5896
0.9855	1.9557	0.9948	2.2538	0.9950	1.8748	0.9938	1.4805	0.9972	1.9461
0.9898	2.3014	0.9966	2.7514	0.9968	2.3023	0.9959	1.7892	0.9983	2.4174
0.9930	2.7485	0.9979	3.4266	0.9981	2.9025	0.9973	2.1998	0.9990	3.0710
0.9955	3.3655	0.9988	4.4176	0.9990	3.8367	0.9984	2.7786	0.9994	4.0586
0.9974	4.2982	0.9994	6.1279	0.9996	5.6774	0.9992	3.6887	0.9998	5.8650
0.9989	6.0007	1.0000	15.3387	1.0000	14.9026	0.9997	5.5716	1.0000	15.3757
1.0000	15.3753					1.0000	15.3393		

Table B33. Influence Coefficients for Outside Axial Infinite-Length Surface Flaws: R_i/t= 10 (continued)

Normalization: $0.1t^{1/2}K^*$

a'/a	a/T = 0.6	a'/a	a/T = 0.7	a'/a	a/T = 0.8	a'/a	a/T = 0.9	a'/a	a/T = 0.95
0.3148	0.9337	0.2437	1.2767	0.3130	1.6184	0.3668	1.8234	0.2877	1.8550
0.6296	0.7244	0.4127	1.0666	0.5299	1.2400	0.6211	1.3231	0.5011	1.5161
0.7456	0.5923	0.5299	0.9231	0.6804	0.9827	0.7975	0.9818	0.6594	1.2677
0.8252	0.5444	0.6111	0.8256	0.7847	0.8097	0.9198	0.7569	0.7769	1.0842
0.8800	0.5255	0.6786	0.7544	0.8229	0.7182	0.9352	0.6757	0.8640	0.9486
0.9176	0.5315	0.7460	0.6924	0.8611	0.6738	0.9506	0.6713	0.9287	0.8520
0.9434	0.5600	0.8136	0.6346	0.8980	0.6361	0.9637	0.6798	0.9766	0.8129
0.9612	0.6106	0.8632	0.5924	0.9252	0.6152	0.9734	0.7074	0.9794	0.8531
0.9734	0.6844	0.8997	0.5712	0.9451	0.6132	0.9804	0.7513	0.9816	0.8707
0.9818	0.7836	0.9265	0.5691	0.9598	0.6298	0.9856	0.8146	0.9838	0.8918
0.9876	0.9121	0.9462	0.5843	0.9705	0.6644	0.9895	0.8983	0.9860	0.9189
0.9915	1.0751	0.9607	0.6162	0.9785	0.7167	0.9923	1.0043	0.9880	0.9523
0.9943	1.2797	0.9713	0.6649	0.9843	0.7881	0.9943	1.1350	0.9898	0.9953
0.9961	1.5359	0.9792	0.7315	0.9886	0.8801	0.9959	1.2940	0.9913	1.0431
0.9974	1.8586	0.9849	0.8183	0.9917	0.9959	0.9970	1.4856	0.9926	1.0982
0.9983	2.2688	0.9891	0.9282	0.9940	1.1393	0.9978	1.7149	0.9937	1.1624
0.9989	2.7997	0.9922	1.0660	0.9957	1.3161	0.9984	1.9901	0.9947	1.2360
0.9993	3.5195	0.9945	1.2387	0.9969	1.5346	0.9988	2.3197	0.9956	1.3206
0.9996	4.5507	0.9962	1.4572	0.9979	1.8071	0.9992	2.7160	0.9963	1.4179
0.9998	6.2177	0.9974	1.7395	0.9985	2.1532	0.9994	3.1965	0.9969	1.5306
1.0000	15.3764	0.9983	2.1162	0.9990	2.6065	0.9996	3.7856	0.9975	1.6619
		0.9990	2.6556	0.9994	3.2317	0.9997	4.5239	0.9980	1.8162
		0.9995	3.5271	0.9997	4.1816	0.9998	7.3907	0.9984	2.0025
		0.9998	5.4220	0.9999	5.9366	0.9999	6.7304	0.9987	2.2285
		1.0000	15.3416	1.0000	14.9062	1.0000	15.1053	0.9990	2.5135
								0.9993	2.8882
								0.9995	3.4153
								0.9997	4.2472
								0.9999	5.9255
								1.0000	15.1111

Table B34. Influence Coefficients for Outside Circumferential 360° Surface Flaws: $R_i/t = 10$

Normalization: $10t^{3/2}K^*$

a'/a	a/T = 0.01	a'/a	a/T = 0.02	a'/a	a/T = 0.03	a'/a	a/T = 0.05	a'/a	a/T = 0.075
0.1111	2.1128	0.1111	1.6282	0.0864	1.3567	0.1259	1.0713	0.1445	0.8981
0.2222	2.1228	0.2222	1.6268	0.1728	1.3552	0.2519	1.0677	0.2889	0.8935
0.3333	2.1407	0.3333	1.6309	0.2593	1.3543	0.3778	1.0707	0.4358	0.8967
0.4182	2.1712	0.4418	1.6481	0.3802	1.3587	0.4795	1.0855	0.5529	0.9197
0.4933	2.2231	0.5333	1.6910	0.4822	1.3816	0.5653	1.1157	0.6461	0.9592
0.5597	2.2902	0.6105	1.7526	0.5682	1.4202	0.6377	1.1574	0.7203	1.0168
0.6186	2.3752	0.6756	1.8353	0.6408	1.4770	0.6988	1.2126	0.7794	1.0928
0.6705	2.4820	0.7305	1.9409	0.7021	1.5528	0.7503	1.2824	0.8265	1.1871
0.7166	2.6096	0.7769	2.0687	0.7537	1.6472	0.7937	1.3670	0.8639	1.3013
0.7574	2.7597	0.8160	2.2206	0.7973	1.7615	0.8304	1.4675	0.8938	1.4379
0.7934	2.9356	0.8490	2.3984	0.8341	1.8975	0.8613	1.5861	0.9175	1.6001
0.8253	3.1385	0.8768	2.6069	0.8651	2.0587	0.8874	1.7258	0.9365	1.7932
0.8535	3.3760	0.9003	2.8514	0.8913	2.2500	0.9095	1.8908	0.9515	2.0243
0.8785	3.6561	0.9201	3.1400	0.9134	2.4775	0.9280	2.0877	0.9636	2.3044
0.9006	3.9906	0.9368	3.4839	0.9320	2.7531	0.9437	2.3256	0.9731	2.6496
0.9201	4.3927	0.9509	3.9021	0.9477	3.0919	0.9569	2.6197	0.9807	3.0867
0.9374	4.8957	0.9628	4.4220	0.9610	3.5215	0.9681	2.9948	0.9868	3.6661
0.9528	5.5427	0.9729	5.0954	0.9722	4.0906	0.9775	3.4970	0.9916	4.4886
0.9663	6.4272	0.9813	6.0126	0.9816	4.9001	0.9854	4.2222	0.9955	5.8145
0.9783	7.7488	0.9884	7.3921	0.9896	6.2066	0.9921	5.4337	0.9985	8.7068
0.9889	10.0987	0.9945	9.8899	0.9963	9.0139	0.9978	8.3418	1.0000	23.8523
1.0000	24.0349	1.0000	23.9962	1.0000	23.9702	1.0000	23.9167		

a'/a	a/T = 0.1	a'/a	a/T = 0.2	a'/a	a/T = 0.3	a'/a	a/T = 0.4	a'/a	a/T = 0.5
0.1111	0.8050	0.1667	0.6789	0.1111	0.6930	0.1528	0.7463	0.1889	0.8390
0.2222	0.7994	0.3333	0.6593	0.2222	0.6690	0.3056	0.6973	0.3778	0.7517
0.3333	0.7963	0.4768	0.6489	0.3333	0.6468	0.5027	0.6474	0.5726	0.6740
0.4767	0.8006	0.5898	0.6535	0.4890	0.6252	0.6440	0.6146	0.7064	0.6166
0.5896	0.8241	0.6788	0.6717	0.6086	0.6146	0.7453	0.6090	0.7984	0.6169
0.6785	0.8634	0.7489	0.7031	0.7005	0.6202	0.8179	0.6269	0.8616	0.6358
0.7485	0.9198	0.8040	0.7477	0.7711	0.6407	0.8699	0.6662	0.9051	0.6812
0.8037	0.9935	0.8475	0.8055	0.8254	0.6754	0.9072	0.7266	0.9349	0.7533
0.8471	1.0848	0.8817	0.8778	0.8671	0.7244	0.9339	0.8095	0.9554	0.8537
0.8813	1.1953	0.9087	0.9662	0.8991	0.7885	0.9530	0.9171	0.9695	0.9859
0.9082	1.3276	0.9299	1.0731	0.9238	0.8692	0.9667	1.0531	0.9792	1.1549
0.9294	1.4852	0.9466	1.2023	0.9427	0.9690	0.9766	1.2229	0.9859	1.3680
0.9461	1.6729	0.9598	1.3590	0.9572	1.0914	0.9836	1.4340	0.9905	1.6351
0.9593	1.8981	0.9702	1.5512	0.9684	1.2415	0.9887	1.6972	0.9936	1.9702
0.9696	2.1713	0.9783	1.7913	0.9770	1.4271	0.9923	2.0296	0.9958	2.3942
0.9778	2.5087	0.9848	2.1006	0.9836	1.6606	0.9949	2.4585	0.9972	2.9385
0.9842	2.9375	0.9898	2.5189	0.9887	1.9625	0.9968	3.0324	0.9983	3.6567
0.9893	3.5057	0.9938	3.1327	0.9926	2.3718	0.9981	3.8525	0.9990	4.6507
0.9933	4.3150	0.9970	4.1884	0.9956	2.9733	0.9990	5.1768	0.9994	6.1565
0.9964	5.6259	0.9994	7.0856	0.9979	4.0091	0.9997	8.1075	0.9998	8.9055
0.9989	8.5435	1.0000	23.5571	0.9996	6.8766	1.0000	23.1039	1.0000	18.9594
1.0000	23.7940			1.0000	23.3302				

Table B34. Influence Coefficients for Outside Circumferential 360° Surface Flaws: R_i/t = 10 (continued)

Normalization: $10t^{3/2}K^*$

a'/a	a/T = 0.6	a'/a	a/T = 0.7	a'/a	a/T = 0.8	a'/a	a/T = 0.9	a'/a	a/T = 0.95
0.1898	0.9313	0.3056	0.9925	0.2524	1.1145	0.2958	1.2388	0.6266	1.3739
0.3796	0.8220	0.6111	0.7948	0.4442	0.9498	0.5206	1.0584	0.8537	1.1490
0.5046	0.7405	0.6627	0.6996	0.5899	0.8367	0.6914	0.9391	0.9360	1.0868
0.6296	0.6823	0.7143	0.6738	0.7006	0.7601	0.8211	0.8583	0.9658	1.0979
0.7456	0.6376	0.7989	0.6477	0.7847	0.7107	0.9198	0.8198	0.9766	1.1516
0.8252	0.6099	0.8585	0.6253	0.8090	0.6873	0.9275	0.8233	0.9789	1.1960
0.8800	0.6362	0.9004	0.6512	0.8333	0.6771	0.9352	0.8276	0.9813	1.2200
0.9176	0.6770	0.9300	0.6886	0.8777	0.6730	0.9429	0.8341	0.9836	1.2483
0.9434	0.7438	0.9508	0.7489	0.9102	0.6712	0.9506	0.8467	0.9860	1.2904
0.9612	0.8387	0.9655	0.8341	0.9342	0.7102	0.9621	0.8766	0.9882	1.3485
0.9734	0.9641	0.9758	0.9461	0.9518	0.7547	0.9710	0.9110	0.9902	1.4049
0.9818	1.1251	0.9831	1.0891	0.9647	0.8181	0.9778	0.9945	0.9918	1.5136
0.9876	1.3274	0.9882	1.2679	0.9742	0.9019	0.9830	1.0774	0.9932	1.6118
0.9915	1.5798	0.9918	1.4898	0.9812	1.0087	0.9870	1.1789	0.9943	1.7239
0.9943	1.8934	0.9943	1.7644	0.9863	1.1414	0.9901	1.3026	0.9953	1.8529
0.9961	2.2835	0.9961	2.1052	0.9901	1.3048	0.9924	1.4506	0.9961	2.0006
0.9974	2.7719	0.9974	2.5318	0.9928	1.5045	0.9943	1.6274	0.9968	2.1706
0.9983	3.3916	0.9982	3.0755	0.9949	1.7489	0.9957	1.8375	0.9974	2.3665
0.9989	4.1946	0.9989	3.7878	0.9964	2.0495	0.9967	2.0874	0.9979	2.5945
0.9993	5.2736	0.9993	4.7682	0.9975	2.4243	0.9976	2.3857	0.9983	2.8616
0.9996	6.8185	0.9996	6.2323	0.9983	2.9014	0.9982	2.7452	0.9987	3.1790
0.9998	9.3326	0.9998	8.8603	0.9989	3.5302	0.9987	3.1841	0.9990	3.5627
1.0000	18.7798	1.0000	18.6058	0.9993	4.4078	0.9991	3.7306	0.9992	4.0407
				0.9996	5.7708	0.9994	4.4301	0.9994	4.6559
				0.9999	8.4499	0.9996	5.3744	0.9996	5.4961
				1.0000	18.4340	0.9997	6.7510	0.9998	6.7536
						0.9999	9.0997	0.9999	9.0332
						1.0000	18.2706	1.0000	18.1986

Table B35. Influence Coefficients for Outside Axial Infinite-Length Surface Flaws: R_i/t= 20

Normalization: $0.1t^{1/2}K^*$

a'/a	a/T = 0.01	a'/a	a/T = 0.02	a'/a	a/T = 0.03	a'/a	a/T = 0.05	a'/a	a/T = 0.075
0.1263	1.3469	0.1156	1.0302	0.1156	0.8553	0.1380	0.6756	0.1517	0.5716
0.2364	1.3512	0.2312	1.0283	0.2313	0.8533	0.2759	0.6740	0.3034	0.5686
0.3468	1.3614	0.3469	1.0311	0.3469	0.8550	0.4138	0.6784	0.4578	0.5722
0.4048	1.3788	0.4304	1.0418	0.4532	0.8652	0.5286	0.6937	0.5783	0.5896
0.4591	1.3986	0.5042	1.0612	0.5428	0.8873	0.6212	0.7223	0.6723	0.6198
0.5100	1.4241	0.5696	1.0880	0.6184	0.9195	0.6960	0.7621	0.7456	0.6630
0.5578	1.4559	0.6274	1.1236	0.6822	0.9628	0.7563	0.8139	0.8028	0.7192
0.6026	1.4950	0.6786	1.1686	0.7360	1.0173	0.8051	0.8777	0.8474	0.7886
0.6445	1.5433	0.7239	1.2231	0.7814	1.0831	0.8444	0.9543	0.8823	0.8726
0.6838	1.5990	0.7640	1.2883	0.8197	1.1615	0.8762	1.0449	0.9094	0.9728
0.7207	1.6673	0.7994	1.3645	0.8520	1.2531	0.9019	1.1510	0.9306	1.0919
0.7553	1.7463	0.8308	1.4544	0.8792	1.3608	0.9226	1.2754	0.9472	1.2327
0.7877	1.8401	0.8586	1.5606	0.9022	1.4871	0.9393	1.4209	0.9601	1.4009
0.8181	1.9541	0.8831	1.6866	0.9217	1.6360	0.9528	1.5926	0.9701	1.6021
0.8465	2.0900	0.9049	1.8383	0.9380	1.8144	0.9637	1.7973	0.9780	1.8481
0.8732	2.2602	0.9241	2.0244	0.9518	2.0304	0.9725	2.0431	0.9841	2.1520
0.8981	2.4752	0.9412	2.2602	0.9635	2.3007	0.9796	2.3475	0.9889	2.5434
0.9218	2.7633	0.9562	2.5684	0.9733	2.6478	0.9853	2.7357	0.9926	3.0699
0.9437	3.1684	0.9696	3.0016	0.9816	3.1242	0.9900	3.2525	0.9955	3.8377
0.9644	3.8153	0.9813	3.6754	0.9886	3.8383	0.9937	3.9987	0.9978	5.1601
0.9835	5.0853	0.9917	4.9976	0.9945	5.1216	0.9967	5.2431	1.0000	12.6594
1.0000	12.7060	1.0000	12.6985	1.0000	12.6924	1.0000	12.6879		

a'/a	a/T = 0.1	a'/a	a/T = 0.2	a'/a	a/T = 0.3	a'/a	a/T = 0.4	a'/a	a/T = 0.5
0.1263	0.5175	0.1735	0.4653	0.1735	0.5156	0.0884	0.6402	0.2056	0.8074
0.2366	0.5135	0.3469	0.4503	0.3469	0.4859	0.1769	0.6137	0.3581	0.7194
0.3469	0.5118	0.5322	0.4415	0.5323	0.4596	0.2653	0.5874	0.5105	0.6468
0.4991	0.5161	0.6649	0.4475	0.6651	0.4465	0.4739	0.5450	0.6248	0.5869
0.6160	0.5338	0.7601	0.4694	0.7603	0.4500	0.6233	0.4994	0.7126	0.5466
0.7059	0.5640	0.8283	0.5071	0.8285	0.4692	0.7304	0.4761	0.7801	0.5217
0.7749	0.6068	0.8772	0.5603	0.8774	0.5035	0.8072	0.4717	0.8319	0.5102
0.8280	0.6622	0.9122	0.6302	0.9124	0.5533	0.8622	0.4840	0.8717	0.5110
0.8688	0.7310	0.9373	0.7186	0.9375	0.6196	0.9017	0.5121	0.9024	0.5232
0.9001	0.8143	0.9553	0.8280	0.9555	0.7044	0.9299	0.5563	0.9259	0.5467
0.9242	0.9141	0.9682	0.9620	0.9684	0.8105	0.9502	0.6175	0.9440	0.5820
0.9427	1.0331	0.9774	1.1253	0.9777	0.9418	0.9647	0.6979	0.9579	0.6300
0.9569	1.1745	0.9840	1.3237	0.9843	1.1036	0.9751	0.8003	0.9685	0.6926
0.9678	1.3438	0.9888	1.5648	0.9891	1.3036	0.9826	0.9293	0.9768	0.7724
0.9762	1.5474	0.9922	1.8613	0.9925	1.5530	0.9879	1.0915	0.9831	0.8737
0.9827	1.7958	0.9946	2.2290	0.9949	1.8671	0.9917	1.2967	0.9879	1.0035
0.9876	2.1054	0.9964	2.6927	0.9967	2.2765	0.9945	1.5608	0.9916	1.1734
0.9915	2.5013	0.9976	3.2976	0.9979	2.8327	0.9964	1.9109	0.9945	1.4053
0.9944	3.0366	0.9985	4.1276	0.9988	3.6491	0.9979	2.4037	0.9967	1.7463
0.9966	3.8108	0.9992	5.3602	0.9994	5.0438	0.9989	3.1720	0.9984	2.3293
0.9984	5.1461	1.0000	12.6576	1.0000	12.6841	0.9996	4.6883	0.9997	3.8709
1.0000	12.6585					1.0000	12.2953	1.0000	12.6858

Table B35. Influence Coefficients for Outside Axial Infinite-Length Surface Flaws: R_i/t= 20 (continued)

Normalization: $0.1t^{1/2}K^*$

a'/a	a/T = 0.6	a'/a	a/T = 0.7	a'/a	a/T = 0.8	a'/a	a/T = 0.9	a'/a	a/T = 0.95
0.2007	1.1014	0.1688	1.5917	0.2144	2.2890	0.2752	2.9514	0.2917	2.9371
0.4014	0.9422	0.3043	1.3960	0.3864	1.8918	0.4794	2.2820	0.5082	2.2862
0.4966	0.8263	0.4131	1.2397	0.5246	1.5750	0.6308	1.7885	0.6687	1.8063
0.5918	0.7539	0.5004	1.1150	0.6354	1.3224	0.7432	1.4240	0.7878	1.4506
0.7029	0.6781	0.5705	1.0158	0.7245	1.1219	0.8265	1.1558	0.8762	1.1882
0.7839	0.6138	0.6268	0.9371	0.7959	0.9642	0.8884	0.9620	0.9417	0.9971
0.8429	0.5751	0.6735	0.8739	0.8256	0.8678	0.9342	0.8312	0.9903	0.9377
0.8858	0.5582	0.7201	0.8178	0.8516	0.8179	0.9404	0.7803	0.9914	1.0709
0.9171	0.5603	0.7668	0.7633	0.8775	0.7737	0.9475	0.7717	0.9923	1.1083
0.9399	0.5799	0.8233	0.7062	0.9061	0.7312	0.9546	0.7659	0.9931	1.1518
0.9565	0.6165	0.8661	0.6574	0.9280	0.7006	0.9629	0.7637	0.9940	1.2027
0.9686	0.6709	0.8987	0.6284	0.9449	0.6871	0.9697	0.7709	0.9947	1.2570
0.9774	0.7445	0.9234	0.6169	0.9579	0.6900	0.9753	0.7864	0.9953	1.3168
0.9839	0.8401	0.9422	0.6212	0.9678	0.7084	0.9799	0.8115	0.9958	1.3807
0.9885	0.9617	0.9565	0.6404	0.9755	0.7418	0.9837	0.8468	0.9963	1.4517
0.9919	1.1153	0.9673	0.6744	0.9814	0.7906	0.9868	0.8925	0.9968	1.5306
0.9944	1.3106	0.9755	0.7238	0.9859	0.8558	0.9894	0.9497	0.9972	1.6195
0.9962	1.5629	0.9817	0.7900	0.9893	0.9393	0.9915	1.0195	0.9976	1.7189
0.9976	1.8992	0.9865	0.8753	0.9920	1.0438	0.9932	1.1042	0.9979	1.8297
0.9985	2.3753	0.9901	0.9830	0.9941	1.1733	0.9946	1.2058	0.9982	1.9555
0.9992	3.1257	0.9928	1.1190	0.9956	1.3339	0.9958	1.3288	0.9985	2.0967
0.9997	4.6586	0.9949	1.2916	0.9969	1.5351	0.9968	1.4787	0.9987	2.2622
1.0000	12.6607	0.9964	1.5145	0.9978	1.7914	0.9975	1.6643	0.9989	2.4558
		0.9976	1.8144	0.9985	2.1308	0.9982	1.9004	0.9991	2.6848
		0.9986	2.2443	0.9990	2.6055	0.9987	2.2125	0.9993	2.9655
		0.9992	2.9426	0.9995	3.3488	0.9992	2.6520	0.9994	3.3186
		0.9998	4.4879	0.9998	4.8121	0.9995	3.3526	0.9996	3.7825
		1.0000	12.6624	1.0000	12.4474	0.9998	4.7917	0.9997	4.4405
						1.0000	12.4558	0.9998	5.4831
								1.0000	12.4681

Table B36. Influence Coefficients for Outside Circumferential 360° Surface Flaws: $R_i/t = 20$

Normalization: $10t^{3/2}K^*$

a'/a	a/T = 0.01	a'/a	a/T = 0.02	a'/a	a/T = 0.03	a'/a	a/T = 0.05	a'/a	a/T = 0.075
0.0884	0.9212	0.1156	0.7587	0.1156	0.6466	0.1030	0.5163	0.1156	0.4360
0.1769	0.9306	0.2312	0.7599	0.2313	0.6466	0.2061	0.5161	0.2313	0.4343
0.2653	0.9404	0.3469	0.7644	0.3469	0.6491	0.3092	0.5167	0.3469	0.4341
0.3306	0.9512	0.4414	0.7748	0.4531	0.6571	0.4122	0.5205	0.4663	0.4379
0.3919	0.9661	0.5230	0.7950	0.5427	0.6752	0.5194	0.5303	0.5644	0.4497
0.4494	0.9846	0.5935	0.8220	0.6184	0.7005	0.6075	0.5502	0.6451	0.4675
0.5032	1.0073	0.6546	0.8572	0.6822	0.7341	0.6800	0.5772	0.7113	0.4920
0.5538	1.0364	0.7072	0.9016	0.7360	0.7767	0.7394	0.6121	0.7658	0.5236
0.6011	1.0727	0.7527	0.9544	0.7814	0.8279	0.7884	0.6555	0.8106	0.5623
0.6455	1.1152	0.7921	1.0168	0.8197	0.8889	0.8286	0.7075	0.8474	0.6087
0.6871	1.1660	0.8260	1.0896	0.8520	0.9599	0.8617	0.7688	0.8777	0.6636
0.7259	1.2260	0.8553	1.1744	0.8792	1.0434	0.8889	0.8407	0.9026	0.7286
0.7626	1.2977	0.8806	1.2734	0.9022	1.1411	0.9112	0.9248	0.9230	0.8056
0.7967	1.3835	0.9026	1.3892	0.9217	1.2561	0.9296	1.0235	0.9399	0.8973
0.8288	1.4864	0.9215	1.5288	0.9380	1.3940	0.9447	1.1402	0.9537	1.0078
0.8590	1.6148	0.9379	1.6961	0.9518	1.5608	0.9571	1.2791	0.9650	1.1443
0.8874	1.7798	0.9520	1.9042	0.9635	1.7697	0.9673	1.4484	0.9744	1.3167
0.9138	1.9971	0.9642	2.1709	0.9733	2.0364	0.9757	1.6598	0.9820	1.5455
0.9384	2.3073	0.9748	2.5345	0.9816	2.4040	0.9825	1.9299	0.9884	1.8705
0.9619	2.8028	0.9839	3.0741	0.9886	2.9538	0.9882	2.3033	0.9935	2.3957
0.9835	3.8248	0.9917	4.0237	0.9945	3.9444	0.9929	2.8676	0.9978	3.5422
1.0000	9.7845	1.0000	9.7816	1.0000	9.7746	0.9967	3.8932	1.0000	9.7259
						1.0000	9.7621		

a'/a	a/T = 0.1	a'/a	a/T = 0.2	a'/a	a/T = 0.3	a'/a	a/T = 0.4	a'/a	a/T = 0.5
0.1735	0.3897	0.1735	0.3367	0.1735	0.3501	0.1327	0.3952	0.2061	0.4479
0.3469	0.3871	0.3469	0.3271	0.3469	0.3317	0.2653	0.3726	0.4122	0.3976
0.5203	0.3911	0.5205	0.3220	0.5323	0.3166	0.4739	0.3451	0.5791	0.3568
0.6477	0.4095	0.6481	0.3277	0.6651	0.3121	0.6233	0.3230	0.6987	0.3325
0.7413	0.4401	0.7419	0.3433	0.7603	0.3191	0.7304	0.3150	0.7844	0.3227
0.8102	0.4837	0.8107	0.3691	0.8285	0.3375	0.8072	0.3195	0.8458	0.3255
0.8607	0.5404	0.8614	0.4050	0.8774	0.3667	0.8622	0.3352	0.8898	0.3398
0.8979	0.6111	0.8986	0.4516	0.9124	0.4071	0.9017	0.3616	0.9213	0.3650
0.9252	0.6971	0.9259	0.5098	0.9375	0.4596	0.9299	0.3993	0.9439	0.4017
0.9453	0.8006	0.9460	0.5813	0.9555	0.5259	0.9502	0.4491	0.9601	0.4506
0.9600	0.9245	0.9608	0.6683	0.9684	0.6081	0.9647	0.5129	0.9718	0.5134
0.9709	1.0720	0.9717	0.7735	0.9777	0.7092	0.9751	0.5929	0.9801	0.5925
0.9788	1.2482	0.9796	0.9013	0.9843	0.8333	0.9826	0.6925	0.9860	0.6913
0.9847	1.4586	0.9855	1.0570	0.9891	0.9862	0.9879	0.8170	0.9903	0.8149
0.9890	1.7115	0.9898	1.2487	0.9925	1.1766	0.9917	0.9738	0.9934	0.9705
0.9922	2.0180	0.9930	1.4895	0.9949	1.4160	0.9945	1.1748	0.9956	1.1702
0.9945	2.3931	0.9953	1.8001	0.9967	1.7279	0.9964	1.4409	0.9972	1.4345
0.9962	2.8561	0.9970	2.2208	0.9979	2.1512	0.9979	1.8147	0.9983	1.8068
0.9974	3.4611	0.9983	2.8381	0.9988	2.7723	0.9989	2.3969	0.9991	2.3861
0.9984	4.2784	0.9992	3.8949	0.9994	3.8329	0.9996	3.5449	0.9997	3.5286
1.0000	9.7134	1.0000	9.6677	1.0000	9.6415	1.0000	9.3011	1.0000	9.5506

Table B36. Influence Coefficients for Outside Circumferential 360° Surface Flaws: R_i/t = 20 (continued)

Normalization: $10t^{3/2}K^*$

a'/a	a/T = 0.6	a'/a	a/T = 0.7	a'/a	a/T = 0.8	a'/a	a/T = 0.9	a'/a	a/T = 0.95
0.2551	0.5112	0.3296	0.5710	0.4192	0.6132	0.3185	0.6979	0.2878	0.8154
0.5102	0.4280	0.5199	0.4656	0.6613	0.4659	0.5410	0.5833	0.4930	0.7290
0.6492	0.3713	0.6297	0.4101	0.8010	0.3918	0.6965	0.5089	0.6393	0.6712
0.7489	0.3440	0.6749	0.3841	0.8189	0.3678	0.8052	0.4597	0.7436	0.6311
0.8203	0.3317	0.7201	0.3703	0.8367	0.3637	0.8812	0.4299	0.8180	0.6030
0.8715	0.3326	0.7995	0.3535	0.8801	0.3588	0.9342	0.4207	0.8710	0.5836
0.9082	0.3452	0.8565	0.3424	0.9120	0.3600	0.9444	0.4297	0.9088	0.5714
0.9344	0.3691	0.8973	0.3435	0.9355	0.3705	0.9546	0.4397	0.9357	0.5663
0.9533	0.4046	0.9265	0.3565	0.9527	0.3909	0.9644	0.4556	0.9549	0.5695
0.9668	0.4524	0.9475	0.3810	0.9653	0.4215	0.9720	0.4800	0.9686	0.5828
0.9765	0.5143	0.9625	0.4172	0.9746	0.4629	0.9781	0.5101	0.9784	0.6093
0.9834	0.5925	0.9732	0.4659	0.9815	0.5162	0.9828	0.5478	0.9854	0.6539
0.9884	0.6905	0.9810	0.5285	0.9865	0.5827	0.9866	0.5941	0.9903	0.7220
0.9919	0.8131	0.9865	0.6072	0.9902	0.6647	0.9895	0.6498	0.9913	0.7807
0.9945	0.9675	0.9904	0.7047	0.9929	0.7648	0.9918	0.7159	0.9922	0.8081
0.9963	1.1664	0.9933	0.8250	0.9949	0.8869	0.9937	0.7941	0.9931	0.8419
0.9976	1.4298	0.9953	0.9739	0.9964	1.0365	0.9951	0.8862	0.9939	0.8770
0.9986	1.8001	0.9968	1.1594	0.9974	1.2217	0.9962	0.9951	0.9945	0.9154
0.9992	2.3780	0.9978	1.3947	0.9982	1.4540	0.9971	1.1243	0.9951	0.9557
0.9997	3.5282	0.9986	1.6993	0.9988	1.7549	0.9978	1.2788	0.9957	1.0006
1.0000	9.4861	0.9991	2.1136	0.9992	2.1615	0.9984	1.4660	0.9962	1.0507
		0.9995	2.7225	0.9996	2.7582	0.9988	1.6969	0.9967	1.1065
		0.9998	3.7731	0.9998	3.7821	0.9992	1.9913	0.9971	1.1705
		1.0000	9.4419	1.0000	9.2372	0.9994	2.3832	0.9975	1.2413
						0.9996	2.9446	0.9978	1.3224
						0.9998	3.8765	0.9981	1.4146
						1.0000	9.1967	0.9984	1.5235
								0.9987	1.6520
								0.9989	1.8029
								0.9991	1.9941
								0.9993	2.2405
								0.9995	2.5672
								0.9997	3.0602
								0.9998	3.9188
								1.0000	9.1956

Table B37. Influence Coefficients for Inside Axial and Circumferential Semi-elliptical Surface Flaws: $R_i/t = 20$ and $a / t = 0.0184$

Aspect Ratio	Elliptic Angle(deg)	K0-base Uniform	K1-base Linear	K2-base Quadratic	K3-base Cubic	K0-clad 0.250 cld	K1-clad 0.250 cld	K0-clad 0.156 cld	K1-clad 0.156 cld
2:1	90	0.638	0.465	0.370	0.316	0.638	0.465	0.638	0.465
6:1	90	0.992	0.612	0.449	0.352	0.992	0.612	0.992	0.612
10:1	90	1.057	0.636	0.442	0.313	1.057	0.636	1.057	0.636

Table B38. Influence Coefficients for Inside Infinite Axial Surface Flaws: $R_i/t = 10$

Depth a/t	K0-base Uniform	K1-base Linear	K2-base Quadratic	K3-base Cubic	K0-clad .250 cld	K1-clad .250 cld	K0-clad .156 cld	K1-clad .156 cld
0.010	1.0719	0.6336	0.4778	0.3948	1.0576	0.6280	1.0442	0.6225
0.020	1.0802	0.6559	0.4999	0.4165	1.0547	0.6404	0.8857	0.4804
0.035	1.0964	0.6567	0.5000	0.4163	0.7824	0.4112	0.4554	0.2289
0.050	1.1095	0.6640	0.5054	0.4208	0.5213	0.2630	0.3182	0.1591
0.075	1.0818	0.6244	0.4622	0.3759	0.3524	0.1769	0.2228	0.1140
0.100	1.1168	0.6438	0.4771	0.3886	0.2732	0.1368	0.1734	0.0887
0.200	1.2960	0.7252	0.5305	0.4298	0.1710	0.0855	0.1092	0.0558
0.300	1.5592	0.8317	0.5936	0.4738	0.1529	0.0760	0.0959	0.0478
0.400	1.9328	0.9758	0.6753	0.5287	0.1596	0.0793	0.1001	0.0499
0.500	2.5216	1.2031	0.8046	0.6158	0.1851	0.0920	0.1161	0.0579
0.600	3.2328	1.4672	0.9521	0.7148	0.2162	0.1075	0.1355	0.0676
0.700	4.2766	1.8423	1.1521	0.8417	0.2655	0.1320	0.1663	0.0829
0.800	5.5496	2.2891	1.3830	0.9827	0.3193	0.1589	0.1996	0.0995
0.900	6.6356	2.7273	1.6372	1.1543	0.3396	0.1691	0.2119	0.1057
0.950	6.9510	2.9762	1.8292	1.3080	0.3131	0.1560	0.1952	0.0974

Table B39. Influence Coefficients for Inside 360º Continuous Circumferential Surface Flaws: $R_i/t = 10$

Depth a/t	K0-base Uniform	K1-base Linear	K2-base Quadratic	K3-base Cubic	K0-clad .250 cld	K1-clad .250 cld	K0-clad .156 cld	K1-clad .156 cld
0.010	1.0829	0.6413	0.4830	0.3979	1.0543	0.6274	1.0566	0.6309
0.020	1.0985	0.6528	0.4921	0.4053	1.0634	0.6394	0.8896	0.4833
0.035	1.1037	0.6566	0.4954	0.4084	0.7821	0.4114	0.4552	0.2289
0.050	1.1026	0.6530	0.4916	0.4047	0.5168	0.2605	0.3161	0.1580
0.075	1.1193	0.6617	0.4977	0.4094	0.3445	0.1722	0.2130	0.1063
0.100	1.1382	0.6707	0.5036	0.4139	0.2631	0.1311	0.1635	0.0816
0.200	1.2441	0.7148	0.5301	0.4327	0.1528	0.0764	0.0950	0.0474
0.300	1.3917	0.7730	0.5635	0.4551	0.1270	0.0651	0.0772	0.0385
0.400	1.5773	0.8442	0.6034	0.4813	0.1171	0.0595	0.0717	0.0357
0.500	1.8005	0.9288	0.6500	0.5118	0.1157	0.0589	0.0709	0.0354
0.600	2.0593	1.0265	0.7040	0.5469	0.1197	0.0618	0.0722	0.0360
0.700	2.3546	1.1412	0.7684	0.5891	0.1201	0.0606	0.0741	0.0370
0.800	2.7045	1.2897	0.8559	0.6486	0.1236	0.0629	0.0756	0.0377
0.900	3.2984	1.5796	1.0411	0.7815	0.1260	0.0631	0.0783	0.0391
0.950	4.1456	2.0410	1.3626	1.0302	0.1357	0.0659	0.0871	0.0435

Table B40. Influence Coefficients for Inside Infinite Axial Surface Flaws: $R_i/t = 20$

Depth a/t	K0-base Uniform	K1-base Linear	K2-base Quadratic	K3-base Cubic	K0-clad .250 cld	K1-clad .250 cld	K0-clad .156 cld	K1-clad .156 cld
0.010	1.0404	0.6037	0.4475	0.3638	1.0320	0.6002	1.0238	0.5970
0.020	1.0654	0.6263	0.4691	0.3848	1.0426	0.6172	1.0196	0.6069
0.035	1.0668	0.6245	0.4665	0.3818	1.0100	0.5993	0.6573	0.3372
0.050	1.0572	0.6116	0.4538	0.3700	0.7634	0.3982	0.4491	0.2254
0.075	1.0996	0.6404	0.4773	0.3904	0.4947	0.2483	0.3045	0.1519
0.100	1.1347	0.6585	0.4907	0.4017	0.3814	0.1902	0.2369	0.1181
0.200	1.3187	0.7396	0.5429	0.4407	0.2395	0.1189	0.1501	0.0747
0.300	1.5991	0.8516	0.6081	0.4857	0.2176	0.1080	0.1368	0.0681
0.400	2.0117	1.0100	0.6971	0.5450	0.2317	0.1149	0.1457	0.0725
0.500	2.6262	1.2390	0.8231	0.6274	0.2706	0.1342	0.1702	0.0847
0.600	3.5729	1.5837	1.0092	0.7469	0.3390	0.1681	0.2131	0.1060
0.700	5.0789	2.1228	1.2959	0.9289	0.4504	0.2236	0.2831	0.1408
0.800	7.4602	2.9616	1.7372	1.2058	0.6211	0.3084	0.3894	0.1939
0.900	10.2223	3.9577	2.2687	1.5437	0.7839	0.3893	0.4902	0.2441
0.950	10.5648	4.1983	2.4488	1.6861	0.7396	0.3677	0.4617	0.2300

Table B41. Influence Coefficients for Inside 360º Continuous Circumferential Surface Flaws: $R_i/t = 20$

Depth a/t	K0-base Uniform	K1-base Linear	K2-base Quadratic	K3-base Cubic	K0-clad .250 cld	K1-clad .250 cld	K0-clad .156 cld	K1-clad .156 cld
0.010	1.0197	0.5841	0.4284	0.3454	1.0113	0.5806	1.0031	0.5774
0.020	1.0502	0.6119	0.4552	0.3712	1.0276	0.6029	1.0046	0.5926
0.035	1.0035	0.5653	0.4094	0.3264	0.9459	0.5396	0.6530	0.3347
0.050	1.0297	0.5866	0.4289	0.3448	0.7587	0.3957	0.4462	0.2240
0.075	1.0630	0.6100	0.4491	0.3634	0.4885	0.2454	0.3003	0.1499
0.100	1.0943	0.6288	0.4641	0.3767	0.3731	0.1862	0.2313	0.1153
0.200	1.2754	0.7345	0.5485	0.4515	0.2211	0.1100	0.1382	0.0689
0.300	1.4605	0.8079	0.5906	0.4799	0.1858	0.0923	0.1164	0.0580
0.400	1.7028	0.9011	0.6430	0.5147	0.1794	0.0891	0.1125	0.0560
0.500	2.0059	1.0152	0.7064	0.5561	0.1852	0.0920	0.1162	0.0578
0.600	2.3703	1.1513	0.7811	0.6048	0.1970	0.0979	0.1235	0.0615
0.700	2.7847	1.3081	0.8676	0.6613	0.2101	0.1044	0.1315	0.0655
0.800	3.2344	1.4892	0.9721	0.7315	0.2189	0.1089	0.1368	0.0682
0.900	3.8255	1.7770	1.1570	0.8651	0.2207	0.1099	0.1378	0.0687
0.950	4.4720	2.0716	1.3229	0.9646	0.2320	0.1157	0.1448	0.0723

Appendix C – Listings of K_{Ic} And K_{Ia} Extended Databases

Table C1 – Static Initiation Toughness K_{Ic} Extended Database

Table C2 - Crack Arrest Toughness K_{Ia} ORNL 99/27 Database

Table C3. Crack Arrest Toughness K_{Ia} Extended K_{Ia} Database – Large Specimen Data

Table C1. Static Initiation Toughness K_{Ic} Extended Database

Material	Reference Source	Specimen ID	Type No.	Orientation	T (°F)	RT_{NDT} (°F)	$T - RT_{NDT}$ (°F)	K_{Ic} (ksi√in)
HSST 01	Shabbits	1T-C(T)	1		-200	0	-200	46.6
subarc	(1969)	1T-C(T)	1		-175	0	-175	55.8
weldment		4T-C(T)	4		-150	0	-150	56.1
		4T-C(T)	4		-125	0	-125	61.1
		4T-C(T)	4		-100	0	-100	96.0
		4T-C(T)	4		-75	0	-75	90.3
		4T-C(T)	4		-75	0	-75	93.1
		6T-C(T)	6		-50	0	-50	72.6
A533B Class 1	Shabbits	1T-C(T)	1		-200	0	-200	35.1
subarc	(1969)	1T-C(T)	1		-200	0	-200	45.2
weldment		1T-C(T)	1		-320	0	-320	25.9
		1T-C(T)	1		-320	0	-320	23.7
		4T-C(T)	4		-100	0	-100	55.2
		4T-C(T)	4		-50	0	-50	71.6
		4T-C(T)	4		-25	0	-25	105.9
		8T-C(T)	8		0	0	0	113.1
HSST 01	Mager (1969)	1T-C(T)	1	RW	-150	20	-170	43.9
		1T-C(T)	1	RW	-150	20	-170	39.4
		1T-C(T)	1	RW	-150	20	-170	31.3
		1T-C(T)	1	RW	-150	20	-170	47.3
		1T-C(T)	1	RW	-150	20	-170	50.4
		1T-C(T)	1	RW	-150	20	-170	41.2
		1T-C(T)	1	RW	-150	20	-170	54.0
		1T-C(T)	1	RW	-150	20	-170	50.9
		1T-C(T)	1	RW	-150	20	-170	35.5
		1T-C(T)	1	RW	-150	20	-170	33.2
		1T-C(T)	1	RW	-150	20	-170	37.2
		1T-C(T)	1	RW	-150	20	-170	37.1
		1T-C(T)	1	RW	-150	20	-170	37.1
		1T-C(T)	1	RW	-150	20	-170	34.7
		1T-C(T)	1	RW	-150	20	-170	35.0
		1T-C(T)	1	RW	-150	20	-170	32.6
		1T-C(T)	1	RW	-150	20	-170	29.4
HSST 03	Mager (1969)	1T-C(T)	1	RW	-150	20	-170	44.0
		1T-C(T)	1	RW	-150	20	-170	31.4
		1T-C(T)	1	RW	-150	20	-170	39.3
		1T-C(T)	1	RW	-150	20	-170	31.3
		1T-C(T)	1	RW	-150	20	-170	33.0
		1T-C(T)	1	RW	-150	20	-170	38.1
		1T-C(T)	1	RW	-150	20	-170	31.1
		1T-C(T)	1	RW	-150	20	-170	44.9
		1T-C(T)	1	RW	-150	20	-170	39.4
A533B Class 1	Mager (1969)	1X-WOL	1	RW	-320	65	-385	31.6
		1T-WOL	1	RW	-320	65	-385	32.5
		1X-WOL	1	RW	-250	65	-315	40.9
		1X-WOL	1	RW	-250	65	-315	37.1
		1X-WOL	1	RW	-250	65	-315	44.0
		1T-WOL	1	RW	-250	65	-315	40.8
		1T-WOL	1	RW	-250	65	-315	31.2
		1X-WOL	1	RW	-200	65	-265	30.6

Material	Reference Source	Specimen ID	Type No.	Orientation	T (°F)	RT_{NDT} (°F)	$T - RT_{NDT}$ (°F)	K_{Ic} (ksi√in)
		1X-WOL	1	RW	-200	65	-265	29.0
		1T-WOL	1	RW	-200	65	-265	35.6
		1T-WOL	1	RW	-200	65	-265	42.8
		2T-WOL	2	RW	-150	65	-215	46.9
		2T-WOL	2	RW	-150	65	-215	66.9
HSST 02	Mager (1969)	1X-WOL	1	RW	-200	0	-200	30.5
		1X-WOL	1	RW	-200	0	-200	37.5
		1X-WOL	1	RW	-200	0	-200	41.0
		1T-WOL	1	RW	-200	0	-200	31.2
		1T-WOL	1	RW	-200	0	-200	30.8
		1T-WOL	1	RW	-175	0	-175	43.5
		1X-WOL	1	RW	-150	0	-150	29.7
		1X-WOL	1	RW	-150	0	-150	31.5
		1X-WOL	1	RW	-150	0	-150	41.2
		1X-WOL	1	RW	-150	0	-150	30.5
		1X-WOL	1	RW	-125	0	-125	39.1
		1T-WOL	1	RW	-125	0	-125	48.3
		1T-WOL	1	RW	-125	0	-125	43.4
		1T-WOL	1	RW	-125	0	-125	38.1
		2T-WOL	2	RW	-100	0	-100	51.4
		2T-WOL	2	RW	-100	0	-100	59.0
		2T-WOL	2	RW	-100	0	-100	56.2
		2T-WOL	2	RW	-100	0	-100	50.2
		2T-WOL	2	RW	-50	0	-50	65.1
		2T-WOL	2	RW	-50	0	-50	65.0
		2T-WOL	2	RW	-50	0	-50	67.5
		2T-WOL	2	RW	-50	0	-50	65.0
		1X-WOL	1	RW	-250	0	-250	37.3
		1X-WOL	1	RW	-200	0	-200	44.0
		1X-WOL	1	RW	-200	0	-200	34.6
		1X-WOL	1	RW	-200	0	-200	39.9
		1X-WOL	1	RW	-200	0	-200	38.5
		1T-C(T)	1	RW	-150	0	-150	42.1
		1T-C(T)	1	RW	-150	0	-150	37.7
		1T-C(T)	1	RW	-150	0	-150	40.7
		1T-C(T)	1	RW	-100	0	-100	42.2
		1T-C(T)	1	RW	-100	0	-100	48.5
		1T-C(T)	1	RW	-100	0	-100	48.5
		1T-C(T)	1	RW	-75	0	-75	50.3
		1T-C(T)	1	RW	-75	0	-75	46.6
		1T-C(T)	1	RW	-100	0	-100	54.8
		1T-C(T)	1	RW	-100	0	-100	54.4
		2T-WOL	2	RW	-50	0	-50	56.7
		2T-WOL	2	RW	0	0	0	66.4
		2T-WOL	2	RW	0	0	0	93.7
		2T-WOL	2	RW	0	0	0	83.4
A533B Class 1 weld	Mager (1969)	1X-WOL	1		-320	-45	-275	29.7
		1X-WOL	1		-320	-45	-275	27.2
		1X-WOL	1		-250	-45	-205	37.6
		1X-WOL	1		-250	-45	-205	37.8
		1T-WOL	1		-250	-45	-205	43.6
		2T-WOL	2		-250	-45	-205	55.6
		1T-WOL	1		-225	-45	-180	40.1
		1T-WOL	1		-225	-45	-180	52.8

Material	Reference Source	Specimen ID	Type No.	Orientation	T (°F)	RT_{NDT} (°F)	$T - RT_{NDT}$ (°F)	K_{Ic} (ksi√in)
		2T-WOL	2		-225	-45	-180	66.2
		2T-WOL	2		-200	-45	-155	70.7
A533B Class 1	Mager (1969)	1X-WOL	1		-320	0	-320	30.3
weld-HAZ		1X-WOL	1		-250	0	-250	35.2
		1X-WOL	1		-250	0	-250	40.4
		1T-WOL	1		-250	0	-250	30.5
		1T-WOL	1		-250	0	-250	44.2
		2T-WOL	2		-200	0	-200	71.2
A508 Class 2	Mager (1969)	1X-WOL	1		-320	50	-370	39.6
European		1X-WOL	1		-320	50	-370	27.5
Forging		1T-WOL	1		-320	50	-370	47.5
“ring forging”		1X-WOL	1		-250	50	-300	43.2
		1X-WOL	1		-250	50	-300	47.9
		1X-WOL	1		-250	50	-300	41.6
		1T-WOL	1		-250	50	-300	51.3
		1T-WOL	1		-200	50	-250	55.0
		2T-WOL	2		-200	50	-250	43.3
		2T-WOL	2		-150	50	-200	57.2
		2T-WOL	2		-125	50	-175	56.2
		2T-WOL	2		-100	50	-150	56.0
HSST 02	Shabbits	6T-C(T)	6	RW	25	0	25	98.9
	(1969)	6T-C(T)	6	RW	25	0	25	74.5
		6T-C(T)	6	RW	25	0	25	90.5
		6T-C(T)	6	RW	0	0	0	73.9
		6T-C(T)	6	RW	0	0	0	66.9
		11T-C(T)	11	RW	50	0	50	148.6
		10T-C(T)	10	RW	50	0	50	137.3
		10T-C(T)	10	RW	50	0	50	139.0
		4T-C(T)	4	RW	0	0	0	87.2
		4T-C(T)	4	RW	-25	0	-25	61.0
		4T-C(T)	4	RW	-25	0	-25	58.7
		4T-C(T)	4	RW	-25	0	-25	45.9
		10T-C(T)	10	RW	0	0	0	87.5
		10T-C(T)	10	RW	25	0	25	110.3
		1T-C(T)	1	RW	-250	0	-250	37.3
		1T-C(T)	1	RW	-200	0	-200	44.4
		1T-C(T)	1	RW	-200	0	-200	34.6
		1T-C(T)	1	RW	-200	0	-200	39.9
		1T-C(T)	1	RW	-200	0	-200	34.8
		1T-C(T)	1	RW	-150	0	-150	44.1
		1T-C(T)	1	RW	-150	0	-150	37.4
		1T-C(T)	1	RW	-150	0	-150	41.8
		1T-C(T)	1	RW	-100	0	-100	48.3
		1T-C(T)	1	RW	-100	0	-100	48.3
		1T-C(T)	1	RW	-100	0	-100	41.9
		2T-C(T)	2	RW	-100	0	-100	49.7
		2T-C(T)	2	RW	-50	0	-50	64.6
		2T-C(T)	2	RW	-50	0	-50	64.7
A508 Class 2	unpublished	2T-C(T)	2		-150	51	-201	52.2
	outside of	2T-C(T)	2		-150	51	-201	45.5
	EPRI NP-719-SR	2T-C(T)	2		-125	51	-176	46.0
		2T-C(T)	2		-125	51	-176	64.3
		2T-C(T)	2		-125	51	-176	50.0
		4T-C(T)	4		-25	51	-76	45.0

Material	Reference Source	Specimen ID	Type No.	Orientation	T (°F)	RT_{NDT} (°F)	$T - RT_{NDT}$ (°F)	K_{Ic} (ksi√in)
		6T-C(T)	6		0	51	-51	107.0
		2T-C(T)	2		-125	51	-176	45.6
		2T-C(T)	2		-125	51	-176	68.0
A508 Class 2	unpublished	2T-C(T)	2		-75	65	-140	52.0
	outside of	2T-C(T)	2		-75	65	-140	64.6
	EPRI NP-719-SR	2T-C(T)	2		-75	65	-140	56.6
		2T-C(T)	2		-25	65	-90	64.7
		2T-C(T)	2		-25	65	-90	62.4
		8T-C(T)	8		35	65	-30	81.0
		2T-C(T)	2		-125	65	-190	47.2
		2T-C(T)	2		-125	65	-190	40.9
		2T-C(T)	2		-125	65	-190	42.5
		2T-C(T)	2		-125	65	-190	42.5
HSSI Weld	NUREG/CR-	1T-C(T)	1	T-L	-238	-9.4	-228.6	35.09
72W	5913	1T-C(T)	1	T-L	-238	-9.4	-228.6	35.45
		1T-C(T)	1	T-L	-238	-9.4	-228.6	37.82
		1T-C(T)	1	T-L	-149.8	-9.4	-140.4	42.55
		1T-C(T)	1	T-L	-112	-9.4	-102.6	45.09
		2T-C(T)	2	T-L	-112	-9.4	-102.6	58.73
		2T-C(T)	2	T-L	-112	-9.4	-102.6	67.64
		2T-C(T)	2	T-L	-58	-9.4	-48.6	63.27
		4T-C(T)	4	T-L	-58	-9.4	-48.6	73.82
		4T-C(T)	4	T-L	-58	-9.4	-48.6	90.91
		4T-C(T)	4	T-L	-22	-9.4	-12.6	93.45
		4T-C(T)	4	T-L	5	-9.4	14.4	74.64
HSSI	NUREG/CR-	1T-C(T)	1	T-L	-238	-29.2	-208.8	34.64
73W	5913	1T-C(T)	1	T-L	-238	-29.2	-208.8	37.82
		1T-C(T)	1	T-L	-238	-29.2	-208.8	38.18
		1T-C(T)	1	T-L	-238	-29.2	-208.8	39.45
		2T-C(T)	2	T-L	-112	-29.2	-82.8	58.18
		2T-C(T)	2	T-L	-112	-29.2	-82.8	60.64
		2T-C(T)	2	T-L	-112	-29.2	-82.8	65.55
		2T-C(T)	2	T-L	-58	-29.2	-28.8	66.09
		4T-C(T)	4	T-L	-58	-29.2	-28.8	75.55
		4T-C(T)	4	T-L	-58	-29.2	-28.8	76.45
HSST Plate 13	NUREG/CR-	1T-C(T)	1	L-T	-103	-9.4	-93.6	32.64
	5788 (A533B	2T-C(T)	2	L-T	-103	-9.4	-93.6	55.82
	Plate 13A)	4T-C(T)	4	L-T	-103	-9.4	-93.6	53.73
		4T-C(T)	4	L-T	-103	-9.4	-93.6	62.09
		4T-C(T)	4	L-T	-103	-9.4	-93.6	70.82
		½T-C(T)	0.5	L-T	-238	-9.4	-228.6	25.36
		½T-C(T)	0.5	L-T	-238	-9.4	-228.6	26.18
		½T-C(T)	0.5	L-T	-238	-9.4	-228.6	29.27
		½T-C(T)	0.5	L-T	-238	-9.4	-228.6	29.45
		½T-C(T)	0.5	L-T	-238	-9.4	-228.6	30.18
		½T-C(T)	0.5	L-T	-238	-9.4	-228.6	31.00
		½T-C(T)	0.5	L-T	-238	-9.4	-228.6	32.82
		½T-C(T)	0.5	L-T	-238	-9.4	-228.6	33.82
		½T-C(T)	0.5	L-T	-238	-9.4	-228.6	36.00
		½T-C(T)	0.5	L-T	-238	-9.4	-228.6	36.36
		1T-C(T)	1	L-T	-238	-9.4	-228.6	32.09
		1T-C(T)	1	L-T	-238	-9.4	-228.6	33.73
		1T-C(T)	1	L-T	-238	-9.4	-228.6	34.27
		1T-C(T)	1	L-T	-238	-9.4	-228.6	34.91

Material	Reference Source	Specimen ID	Type No.	Orientation	T (°F)	RT_{NDT} (°F)	$T - RT_{NDT}$ (°F)	K_{Ic} (ksi√in)
		1T-C(T)	1	L-T	-238	-9.4	-228.6	35.09
		1T-C(T)	1	L-T	-238	-9.4	-228.6	36.00
		1T-C(T)	1	L-T	-238	-9.4	-228.6	37.45
		1T-C(T)	1	L-T	-238	-9.4	-228.6	37.45
		1T-C(T)	1	L-T	-238	-9.4	-228.6	39.55
		1T-C(T)	1	L-T	-238	-9.4	-228.6	39.73
		1T-C(T)	1	L-T	-238	-9.4	-228.6	40.36
		1T-C(T)	1	L-T	-238	-9.4	-228.6	42.36
		1T-C(T)	1	L-T	-238	-9.4	-228.6	43.73
		1T-C(T)	1	L-T	-238	-9.4	-228.6	46.45
		1T-C(T)	1	L-T	-238	-9.4	-228.6	49.55
		1T-C(T)	1	L-T	-238	-9.4	-228.6	49.64
		2T-C(T)	2	L-T	-238	-9.4	-228.6	30.09
		2T-C(T)	2	L-T	-238	-9.4	-228.6	33.00
		2T-C(T)	2	L-T	-238	-9.4	-228.6	36.55
		2T-C(T)	2	L-T	-238	-9.4	-228.6	37.00
		2T-C(T)	2	L-T	-238	-9.4	-228.6	39.36
		2T-C(T)	2	L-T	-238	-9.4	-228.6	39.91
		2T-C(T)	2	L-T	-238	-9.4	-228.6	40.91
		2T-C(T)	2	L-T	-238	-9.4	-228.6	41.45
		2T-C(T)	2	L-T	-238	-9.4	-228.6	42.18
		2T-C(T)	2	L-T	-238	-9.4	-228.6	46.45
		2T-C(T)	2	L-T	-238	-9.4	-228.6	48.64
		2T-C(T)	2	L-T	-238	-9.4	-228.6	53.18
A508 Class 3	Iwadate, et al.	Bx2B	1	NA	-238	-13	-225	37.29
	ASTM STP	Bx2B	1	NA	-238	-13	-225	39.89
	803	Bx2B	1	NA	-238	-13	-225	44.22
		Bx2B	4	NA	-166	-13	-153	43.36
		Bx2B	4	NA	-76	-13	-63	63.30
		Bx2B	3	NA	-4	-13	9	69.37
Midland Nozzle	NUREG/CR-	1T-C(T)	1		-58	52	-110	49.81
Course Weld	6249	1T-C(T)	1		-148	52	-200	45.63
		1T-C(T)	1		-148	52	-200	44.63
		1T-C(T)	1		-148	52	-200	42.81
		1T-C(T)	1		-148	52	-200	33.45
		1T-C(T)	1		-148	52	-200	32.36
Midland Beltline	NUREG/CR-	1T-C(T)	1		-148	23	-171	36.45
	6249	1T-C(T)	1		-148	23	-171	34.91
Plate 02 4th Irr.	NUREG/CR-	1T-C(T)	1	T-L	-148	0	-148	38.09
Series	4880, 1988	1T-C(T)	1	T-L	-139	0	-139	33.45
	Plate 02	1T-C(T)	1	T-L	-139	0	-139	39.27
	(68-71W)	1T-C(T)	1	T-L	-139	0	-139	40.09

References for Table C1

EPRI Special Report, 1978, *Flaw Evaluation Procedures: ASME Section XI*, EPRI NP-719-SR, Electric Power Research Institute, Palo Alto, CA.

W. O. Shabbits, W. H. Pryle, and E. T. Wessel, *Heavy Section Fracture Toughness Properties of A533, Grade B, Class-1 Steel Plate and Submerged Arc Weldments*, HSST Technical Report 6, WCAP-7414, December 1969.

T. R. Mager, F. O. Thomas, and W. S. Hazelton, *Evaluation by Linear Elastic Fracture Mechanics of Radiation Damage to Pressure Vessel Steels,* HSST Technical Report 5, WCAP-7328, Revised, October 1969.

T. R. Mager, *Fracture Toughness Characterization Study of A533, Grade B, Class-1 Steel*, HSST Technical Report 10, WCAP-7578, October 1970.

R. K. Nanstad, F. M. Haggag, and D. E. McCabe, *Irradiation Effects on Fracture Toughness of Two High-Copper Submerged-Arc Welds, HSSI Series 5,* USNRC Report NUREG/CR-5913 (ORNL/TM-12156/V1 and V2) Vol. 1 and 2, Oak Ridge National Laboratory, Oak Ridge, TN, October 1992.

D. E. McCabe., *A Comparison of Weibull and β_{Ic} Analysis of Transition Range Fracture Toughness Data,* USNRC Report NUREG/CR-5788 (ORNL/TM-11959), Oak Ridge National Laboratory, Oak Ridge, TN, January 1992.

T. Iawadate, Y. Tanaka, S. Ono, and J. Watanabe, "An Analysis of Elastic-Plastic Fracture Toughness Behavior for J_{Ic} Measurements in the Transition Region," *Elastic-Plastic Fracture: Second Symposium, Vol. II-Fracture Resistance Curves and Engineering Applications*, ASTM STP 803, (1983) II531-II561.

D. E. McCabe, R. K. Nanstad, S. K. Iskander, R. L. Swain, *Unirradiated Material Properties of Midland Weld WF-70,* USNRC Report NUREG/CR-6249 (ORNL/TM-12777), Oak Ridge National Laboratory, Oak Ridge, TN, October 1994.

J. J. McGowan, R. K. Nanstad, and K. R. Thoms, *Characterization of Irradiated Current-Practice Welds and A533 Grade B Class 1 Plate for Nuclear Pressure Vessel Service*, USNRC Report NUREG/CR-4880 (ORNL-6484/V1 and V2), Oak Ridge National Laboratory, Oak Ridge, TN, July 1988.

Table C2. Crack Arrest Toughness K_{Ia} ORNL 99/27 Database

Material	Reference Source	Specimen ID	Size No.	Orientation	T (°F)	RT_{NDT} (°F)	T-RT_{NDT} (°F)	K_{Ia} (ksi√in)
HSST-02	EPRI NP	CCA	1.4	L-T	-150	0	-150	28.0
HSST-02	719-SR	CCA	1	L-T	-70	0	-70	43.0
HSST-02	Ripling (1971)	CCA	2	L-T	-70	0	-70	48.0
HSST-02		CCA	2	L-T	-70	0	-70	43.0
HSST-02		CCA	1	L-T	0	0	0	68.0
HSST-02		CCA	1	L-T	0	0	0	58.0
HSST-02		CCA	1	L-T	0	0	0	48.0
HSST-02		CCA	1	L-T	0	0	0	57.0
HSST-02		CCA	1	L-T	0	0	0	62.0
HSST-02		CCA	1.3	L-T	0	0	0	58.0
HSST-02		CCA	1.3	L-T	0	0	0	60.0
HSST-02		CCA	1.3	L-T	0	0	0	65.0
HSST-02		CCA	1.6	L-T	0	0	0	60.0
HSST-02		CCA	1.6	L-T	0	0	0	58.0
HSST-02		CCA	2	L-T	0	0	0	53.0
HSST-02		CCA	2	L-T	0	0	0	58.0
HSST-02		CCA	2	L-T	0	0	0	70.0
HSST-02		CCA	2	L-T	0	0	0	57.0
HSST-02		CCA	3	L-T	0	0	0	57.0
HSST-02		CCA	3	L-T	0	0	0	61.0
HSST-02		CCA	2	L-T	22	0	22	68.0
HSST-02		CCA	1.4	L-T	35	0	35	59.0
HSST-02		CCA	1.6	L-T	35	0	35	84.0
HSST-02		CCA	2	L-T	35	0	35	62.0
HSST-02		CCA	1.4	L-T	50	0	50	92.0
HSST-02		CCA	2	L-T	50	0	50	73.0
HSST-02		CCA	3	L-T	50	0	50	75.0
HSST-02		CCA	1	L-T	75	0	75	94.0
HSST-02		CCA	1.6	L-T	75	0	75	107.0
HSST-02		CCA	2	L-T	75	0	75	77.0
HSST-02		CCA	2	L-T	75	0	75	81.0
HSST-02		CCA	2	L-T	75	0	75	91.0
HSST-02		CCA	2	L-T	75	0	75	102.3
HSST-02		CCA	2	L-T	80	0	80	109.0
HSST-02		CCA	2	L-T	83	0	83	87.0
HSST-02		CCA	3	L-T	83	0	83	94.0
HSST-02		CCA	3	L-T	83	0	83	107.0
HSST-02		CCA	3	L-T	83	0	83	111.0
HSST-02		CCA	2	L-T	96	0	96	111.0
HSST-02		CCA	2	L-T	102	0	102	117.0
HSST-02		CCA	1.8	L-T	105	0	105	118.0
HSST-02		CCA	2	L-T	105	0	105	103.0
HSST-02		CCA	2	L-T	105	0	105	107.0
HSST-02		CCA	3	L-T	105	0	105	130.0
HSST-02		CCA	2	L-T	107	0	107	87.0
HSST-02		CCA	2	L-T	110	0	110	88.0
HSST-02		CCA	2	L-T	110	0	110	88.0
HSST-02		CCA	1.1	L-T	112	0	112	112.0
HSST-02		CCA	2	L-T	115	0	115	111.0
HSST-02		CCA	1.1	L-T	121	0	121	116.0
72W	NUREG/CR-5584	CCA		Crack	-77.8	-10	-68	60.1

Material	Reference Source	Specimen ID	Size No.	Orientation	T (°F)	RT_{NDT} (°F)	T-RT_{NDT} (°F)	K_{Ia} (ksi√in)
72W		CCA		runs	-76	-10	-66	48.2
72W		CCA		in	-76	-10	-66	69.2
72W		CCA		welding	-74.2	-10	-64.2	51.9
72W		CCA		direction	-52.6	-10	-42.6	61.0
72W		CCA			-52.6	-10	-42.6	64.6
72W		CCA			-49	-10	-39	66.4
72W		CCA			-49	-10	-39	67.3
72W		CCA			-49	-10	-39	69.2
72W		CCA			-49	-10	-39	83.7
72W		CCA			-25.6	-10	-15.6	83.7
72W		CCA			-22	-10	-12	54.6
72W		CCA			-22	-10	-12	55.5
72W		CCA			-22	-10	-12	77.4
72W		CCA			-22	-10	-12	82.8
72W		CCA			-22	-10	-12	89.2
72W		CCA			-22	-10	-12	94.6
72W		CCA			-22	-10	-12	97.4
72W		CCA			3.2	-10	13.2	88.3
72W		CCA			5	-10	15	85.5
72W		CCA			5	-10	15	85.5
72W		CCA			5	-10	15	86.5
72W		CCA			5	-10	15	93.7
72W		CCA			6.8	-10	16.8	82.8
72W		CCA			28.4	-10	38.4	93.7
72W		CCA			30.2	-10	40.2	113.8
72W		CCA			32	-10	42	84.6
72W		CCA			32	-10	42	97.4
72W		CCA			32	-10	42	103.7
72W		CCA			33.8	-10	43.8	98.3
72W		CCA			39.2	-10	49.2	113.8
72W		CCA			41	-10	51	104.7
73W	NUREG/CR-5584	CCA		Crack	-77.8	-30	-47.8	62.8
73W		CCA		runs	-76	-30	-46	52.8
73W		CCA		in	-74.2	-30	-44.2	65.5
73W		CCA		welding	-49	-30	-19	47.3
73W		CCA		direction	-49	-30	-19	66.4
73W		CCA			-49	-30	-19	68.3
73W		CCA			-49	-30	-19	77.4
73W		CCA			-47.2	-30	-17.2	64.6
73W		CCA			-25.6	-30	4.4	77.4
73W		CCA			-23.8	-30	6.2	68.3
73W		CCA			-22	-30	8	61.0
73W		CCA			-22	-30	8	72.8
73W		CCA			-22	-30	8	91.0
73W		CCA			-20.2	-30	9.8	70.1
73W		CCA			-20.2	-30	9.8	81.0
73W		CCA			3.2	-30	33.2	100.1
73W		CCA			5	-30	35	106.5
73W		CCA			5	-30	35	111.9
73W		CCA			5	-30	35	112.8
73W		CCA			10.4	-30	40.4	102.3
73W		CCA			23	-30	53	91.9
73W		CCA			41	-30	71	97.4
73W		CCA			41	-30	71	101.9

Material	Reference Source	Specimen ID	Size No.	Orientation	T (°F)	RT_{NDT} (°F)	T-RT_{NDT} (°F)	K_{Ia} (ksi√in)
73W		CCA			41	-30	71	102.8
73W		CCA			41	-30	71	108.3
73W		CCA			59	-30	89	120.1
MW15JC	NUREG/CR-6621	CCA		Crack	-4	32.2	-36.2	63.7
MW15JB*r*		CCA		runs	14	32.2	-18.2	79.0
MW15JE*r1*		CCA		in welding	32	32.2	-0.2	97.1
MW15JF		CCA		direction	50	32.2	17.8	119.7

References for Table C2

EPRI Special Report, 1978, *Flaw Evaluation Procedures: ASME Section XI*, EPRI NP-719-SR, Electric Power Research Institute, Palo Alto, CA.

E. J. Ripling and P. B. Crosley, "Strain Rate and Crack Arrest Studies," *HSST 5th Annual Information Meeting*, Paper No. 9, 1971.

S. K. Iskander, W. R. Corwin, R. K. Nanstad, *Results of Crack-Arrest Tests on Two Irradiated High-Copper Welds,* USNRC Report NUREG/CR-5584 (ORNL/TM-11575), Oak Ridge National Laboratory, Oak Ridge, TN, December 1990.

S. K. Iskander, C. A. Baldwin, D. W. Heatherly, D. E. McCabe, I. Remec, and R. L. Swain, *Detailed Results of Testing Unirradiated and Irradiated Crack-Arrest Toughness Specimens from the Low Upper-Shelf Energy, High Copper Weld, WF-70,* NUREG/CR-6621 (ORNL/TM-13764) under preparation.

S. K. Iskander, R. K. Nanstad, D. E. McCabe, and R. L. Swain, "Effects of Irradiation on Crack-Arrest Toughness of a Low Upper-Shelf Energy, High-Copper Weld," *Effects of Radiation on Materials: 19th International Symposium, ASTM STP 1366*, M. L. Hamilton, A. S. Kumar, S. T. Rosinski, and M. L. Grossbeck, eds., American Society for Testing and Materials, 2000.

Table C3. Crack Arrest Toughness K_{Ia} Extended K_{Ia} Database – Large Specimen Data

Material Test No.	Reference Source	T (°F)	RT_{NDT} (°F)	T-RT_{NDT} (°F)	K_{Ia} (ksi-in$^{1/2}$)
WP 1.2A	NUREG/CR-4930	-9.4	143.6	153.0	385.81
WP 1.2B		-9.4	197.6	207.0	623.29
WP 1.3		-9.4	129.2	138.6	213.83
WP 1.4B		-9.4	140.0	149.4	352.14
WP 1.5A		-9.4	132.8	142.2	210.19
WP 1.5B		-9.4	161.6	171.0	463.15
WP 1.6A		-9.4	129.2	138.6	250.23
WP 1.6B		-9.4	176.0	185.4	361.24
WP 1.7A	NUREG/CR-5330	-9.4	141.8	151.2	290.26
WP 1.7B		-9.4	190.4	199.8	505.00
WP 1.8A		-9.4	104.0	113.4	313.92
WP 1.8B		-9.4	131.0	140.4	440.40
WP 1.8C		-9.4	174.2	183.6	512.28
WP CE-1		-31.0	96.8	127.8	154.69
WP CE-2A		-31.0	107.6	138.6	198.36
WP CE-2B		-31.0	127.4	158.4	322.11
WP CE-2C		-31.0	140.0	171.0	524.11
SP 1.3	Smirt 10 Vol F, p 37	-9.4	111.2	120.6	160.15
WP 2.1A	NUREG/CR-5451	140.0	176.0	36.0	96.45
WP 2.1B		140.0	204.8	64.8	139.22
WP 2.1D		140.0	221.0	81.0	143.77
WP 2.1E		140.0	233.6	93.6	154.69
WP 2.1F		140.0	257.0	117.0	182.89
WP 2.1H		140.0	275.0	135.0	266.61
WP 2.1I		140.0	293.0	153.0	337.58
WP 2.1J		140.0	305.6	165.6	369.43
WP 2.2A		140.0	248.0	108.0	182.89
WP 2.2B		140.0	264.2	124.2	235.67
WP 2.2C		140.0	271.4	131.4	255.69
WP 2.2D		140.0	282.2	142.2	252.05
WP 2.2E		140.0	287.6	147.6	345.77
WP 2.2F		140.0	302.0	162.0	331.21
WP 2.2G		140.0	323.6	183.6	405.82
WP 2.3A		140.0	206.6	66.6	131.03
WP 2.3B		140.0	222.8	82.8	211.10
WP 2.3D		140.0	231.8	91.8	232.03
WP 2.3F		140.0	258.8	118.8	234.76
WP 2.4B		140.0	186.8	46.8	124.66
WP 2.4C		140.0	215.6	75.6	171.06
WP 2.4D		140.0	224.6	84.6	255.69
WP 2.4E		140.0	249.8	109.8	226.57
WP 2.4F		140.0	260.6	120.6	279.34
WP 2.4G		140.0	278.6	138.6	346.68
WP 2.4H		140.0	300.2	160.2	361.24
WP 2.5B		140.0	219.2	79.2	155.60
WP 2.5C		140.0	255.2	115.2	172.88
WP 2.5D		140.0	275.0	135.0	243.86
WP 2.5E		140.0	291.2	151.2	278.43
WP 2.5F		140.0	309.2	169.2	333.03
WP 2.6A		140.0	219.2	79.2	185.62
WP 2.6B		140.0	239.0	99.0	235.67
WP 2.6C		140.0	246.2	106.2	260.24
WP 2.6D		140.0	257.0	117.0	318.47
WP 2.6F		140.0	271.4	131.4	298.45
WP 2.6G		140.0	282.2	142.2	373.98
WP 2.6H		140.0	312.8	172.8	375.80
PTSE1B	NUREG/CR-4106	196.3	326.3	130.0	182.80
PTSE1C		196.3	354.2	157.9	271.97
PTSE2A	NUREG/CR-4888	167.0	267.1	100.1	237.85
PTSE2B		167.0	296.2	129.2	329.03
PTSE2C		167.0	325.2	158.2	381.53
TSE4	NUREG/CR-4249	167.0	267.8	100.8	115.56
TSE5-1		152.6	96.8	-55.8	78.25
TSE5-2		152.6	179.6	27.0	94.63
TSE5-3		152.6	192.2	39.6	83.71
TSE5A-1		50.0	71.6	21.6	69.15
TSE5A-2		50.0	100.4	50.4	78.25
TSE5A-3		50.0	123.8	73.8	97.36
TSE5A-4		50.0	152.6	102.6	118.29
TSE6-1		152.6	89.6	-63.0	57.32
TSE6-2		152.6	145.4	-7.2	95.54

References for Table C3

D. J. Naus, et al., *High-Temperature Crack Arrest Behavior in 152-mm-Thick SEN Wide Plates of Quenched and Tempered A533 Grade B Class 1 Steel*, NUREG/CR-5330 (ORNL-11083), Oak Ridge National Laboratory, Oak Ridge, TN, April 1989.

D. J. Naus, et al., *Crack-Arrest Behavior in SEN Wide Plates of Low-Upper-Shelf Base Metal Tested Under Nonisothermal Conditions: WP-2 Series*, NUREG/CR-5451 (ORNL-6584), Oak Ridge National Laboratory, Oak Ridge, TN, April 1989.

R. H. Bryan, et al., *Pressurized-Thermal Shock Test of 6-Inch-Thick Pressure Vessel, PTSE-1: Investigations of Warm Prestressing and Upper-Shelf Arrest*, NUREG/CR-4106 (ORNL-6135), Oak Ridge National Laboratory, Oak Ridge, TN, April 1985.

R. H. Bryan, et al., *Pressurized Thermal Shock Test of 6-Inch-Thick Pressure Vessel PTSE-2: Investigation of Low Tearing Resistance and Warm Prestressing*, NUREG/CR-4888 (ORNL-6377), Oak Ridge National Laboratory, Oak Ridge, TN, December 1987.

R. D. Cheverton, D. G. Ball, S. E. Bolt, S. K. Iskander, and R. K. Nanstad, *Pressure Vessel Fracture Studies Pertaining to the PWR Thermal-Shock Issue: Experiments TSE-5, TSE-5A, and TSE-6,* NUREG/CR-4249 (ORNL-6163), Oak Ridge National Laboratory, Oak Ridge, TN, June 1985.

Appendix D – Summary of RVID2 Data for Use in FAVOR Calculations

Product Form	Heat	Beltline	$\sigma_{flow(u)}$ [ksi]	$RT_{NDT(u)}$ [°F]			Composition[2]				$USE_{(u)}$ [ft-lb]
				$RT_{NDT(u)}$ Method	$RT_{NDT(u)}$ Value	$\sigma_{(u)}$ Value	Cu	Ni	P	Mn	
Beaver Valley 1, (Designer: Westinghouse, Manufacturer: CE) Coolant Temperature = 547°F, Vessel Thickness = 7-7/8 in.											
PLATE	C4381-1	INTERMEDIATE SHELL B6607-1	83.8	MTEB 5-2	43	0	0.14	0.62	0.015	1.4	90
	C4381-2	INTERMEDIATE SHELL B6607-2	84.3	MTEB 5-2	73	0	0.14	0.62	0.015	1.4	84
	C6293-2	LOWER SHELL B7203-2	78.8	MTEB 5-2	20	0	0.14	0.57	0.015	1.3	84
	C6317-1	LOWER SHELL B6903-1	72.7	MTEB 5-2	27	0	0.2	0.54	0.01	1.31	80
LINDE 1092 WELD	305414	LOWER SHELL AXIAL WELD 20-714	75.3	Generic	-56	17	0.337	0.609	0.012	1.44	98
	305424	INTER SHELL AXIAL WELD 19-714	79.9	Generic	-56	17	0.273	0.629	0.013	1.44	112
LINDE 0091 WELD	90136	CIRC WELD 11-714	76.1	Generic	-56	17	0.269	0.07	0.013	0.964	144
Oconee 1, (Designer and Manufacturer: B&W) Coolant Temperature = 556°F, Vessel Thickness = 8.44-in.											
FORGING	AHR54 (ZV2861)	LOWER NOZZLE BELT	(4)	B&W Generic	3	31	0.16	0.65	0.006	(5)	109
PLATE	C2197-2	INTERMEDIATE SHELL	(4)	B&W Generic	1	26.9	0.15	0.5	0.008	1.28	81
	C2800-1	LOWER SHELL	(4)	B&W Generic	1	26.9	0.11	0.63	0.012	1.4	81
	C2800-2	LOWER SHELL	69.9	B&W Generic	1	26.9	0.11	0.63	0.012	1.4	119
	C3265-1	UPPER SHELL	75.8	B&W Generic	1	26.9	0.1	0.5	0.015	1.42	108
	C3278-1	UPPER SHELL	(4)	B&W Generic	1	26.9	0.12	0.6	0.01	1.26	81
LINDE 80 WELD	1P0962	INTERMEDIATE SHELL AXIAL WELDS SA-1073	79.4	B&W Generic	-5	19.7	0.21	0.64	0.025	1.38	70
	299L44	INT./UPPER SHL CIRC WELD (OUTSIDE 39%) WF-25	(4)	B&W Generic	-7	20.6	0.34	0.68	(3)	1.573	81
	61782	NOZZLE BELT/INT. SHELL CIRC WELD SA-1135	(4)	B&W Generic	-5	19.7	0.23	0.52	0.011	1.404	80
	71249	INT./UPPER SHL CIRC WELD (INSIDE 61%) SA-1229	76.4	ASME NB-2331	10	0	0.23	0.59	0.021	1.488	67
	72445	UPPER/LOWER SHELL CIRC WELD SA-1585	(4)	B&W Generic	-5	19.7	0.22	0.54	0.016	1.436	65
	8T1762	LOWER SHELL AXIAL WELDS SA-1430	75.5	B&W Generic	-5	19.7	0.19	0.57	0.017	1.48	70
	8T1762	UPPER SHELL AXIAL WELDS SA-1493	(4)	B&W Generic	-5	19.7	0.19	0.57	0.017	1.48	70
	8T1762	LOWER SHELL AXIAL WELDS SA-1426	75.5	B&W Generic	-5	19.7	0.19	0.57	0.017	1.48	70

Product Form	Heat	Beltline	$\sigma_{flow(u)}$ [ksi]	$RT_{NDT(u)}$ [°F]			Composition[2]				$USE_{(u)}$ [ft-lb]
				$RT_{NDT(u)}$ Method	$RT_{NDT(u)}$ Value	$\sigma_{(u)}$ Value	Cu	Ni	P	Mn	
Palisades, (Designer and Manufacturer: CE) Coolant Temperature = 532°F, Vessel Thickness = 8½ in.											
PLATE	A-0313	D-3803-2	(4)	MTEB 5-2	-30	0	0.24	0.52	0.01	1.35	87
	B-5294	D-3804-3	(4)	MTEB 5-2	-25	0	0.12	0.55	0.01	1.27	73
	C-1279	D-3803-3	(4)	ASME NB-2331	-5	0	0.24	0.5	0.011	1.293	102
	C-1279	D-3803-1	74.7	ASME NB-2331	-5	0	0.24	0.51	0.009	1.293	102
	C-1308A	D-3804-1	(4)	ASME NB-2331	0	0	0.19	0.48	0.016	1.235	72
	C-1308B	D-3804-2	(4)	MTEB 5-2	-30	0	0.19	0.5	0.015	1.235	76
LINDE 0124 WELD	27204	CIRC. WELD 9-112	76.9	Generic	-56	17	0.203	1.018	0.013	1.147	98
LINDE 1092 WELD	34B009	LOWER SHELL AXIAL WELD 3-112A/C	76.1	Generic	-56	17	0.192	0.98	(3)	1.34	111
	W5214	LOWER SHELL AXIAL WELDS 3-112A/C	72.9	Generic	-56	17	0.213	1.01	0.019	1.315	118
	W5214	INTERMEDIATE SHELL AXIAL WELDS 2-112 A/C	72.9	Generic	-56	17	0.213	1.01	0.019	1.315	118

Notes:

(1) Information taken from the July 2000 release of the NRCs Reactor Vessel Integrity (RVID2) database.

(2) These composition values are as reported in RVID2 for Cu, Ni, and P and as in RPVDATA for Mn. In FAVOR calculations these values should be treated as the central tendency of the Cu, Ni, P, and Mn distributions.

(3) No values of phosphorus are recorded in RVID2 for these heats. A generic value of 0.012 should be used, which is the mean of 826 phosphorus values taken from the surveillance database used by Eason et al. to calibrate the embrittlement trend curve.

(4) No strength measurements are available in PREP4 for these heats [PREP]. A value of 77 ksi should be used, which is the mean of other flow strength values reported in this Appendix.

(5) No values of manganese strength in RPVDATA for these heats [ref]. A generic value of 0.80 should be used, which is the mean value of manganese for forgings taken from the surveillance database used by Eason et al. to calibrate the embrittlement trend curve.

References:

RVID2 U.S. Nuclear Regulatory Commission Reactor Vessel Integrity Database, Version 2.1.1, July 6, 2000.

PREP PREP4: Power Reactor Embrittlement Program, Version 1.0," EPRI, Palo Alto, CA: 1996. SW-106276

RPVDATA T. J. Griesbach, and J.F. Williams, “User’s Guide to RPVDATA, Reactor Vessel Materials Database,” Westinghouse Energy Systems Business Unit, WCAP-14616, 1996.

Appendix E – Statistical Point-Estimation Techniques for Weibull Distributions

The three parameters for the Weibull distributions of $RT_{NDT} - T_0$ and ΔRT_{LB} were calculated using a combination of two point-estimation procedures, *Maximum Likelihood* and the *Method of Moments*. The parameters to estimate are the location parameter, *a*, of the random variate, the scale parameter, *b*, of the random variate, and the shape parameter, *c*.

Maximum likelihood estimators for the shape parameter c' and the scale parameter b' can be derived from the likelihood function, *L*, for the Weibull distribution. The Weibull density is given by

$$w(\Delta RT \,|\, a,b,c) = \frac{c}{b} y^{c-1} \exp\left(-y^c\right), \quad \text{for} \quad (y = (\Delta RT - a)/b, \Delta RT > a,\ b,c > 0) \tag{E1}$$

and the corresponding likelihood function is the joint density (see Ref.[E1]) (given the location parameter, *a*)

$$L(b,c \,|\, \Delta RT, a) = \prod_{i=1}^{N} \frac{c}{b}\left(\frac{\Delta RT_{(i)} - a}{b}\right)^{c-1} \exp\left[-\left(\frac{\Delta RT_{(i)} - a}{b}\right)^{c}\right] \tag{E2}$$

The maximum likelihood (*ML*) estimators for the scale, b', and shape parameters, c', are defined as the unique values of (b', c') that maximize the joint probability that the *N* members of the sample set all come from the same parent population. The *ML* estimators are, therefore, calculated by finding the stationary point of Eq. (E2). Upon taking the logarithm of Eq. (E2), the derivatives with respect to the individual parameters (b', c') are set to zero. The resulting *ML* estimator for the shape parameter, c', is found by solving iteratively for c' in the following nonlinear equation

$$\frac{\partial(\ln(L(c')))}{\partial c'} = \frac{\sum_{i=1}^{N} (\Delta RT_{(i)} - a)^{c'} \ln(\Delta RT_{(i)} - a)}{\sum_{i=1}^{N} (\Delta RT_{(i)} - a)^{c'}} - \frac{1}{N}\sum_{i=1}^{N} \ln(\Delta RT_{(i)} - a) - \frac{1}{c'} = 0 \tag{E3}$$

Upon obtaining a solution for c', the *ML* estimator for the scale parameter, b', follows directly from

$$\frac{\partial(\ln(L))}{\partial b'} = b' - \left[\sum_{i=1}^{N} \frac{\left(\Delta RT_{(i)} - a\right)^{c'}}{N} \right]^{\frac{1}{c'}} = 0 \tag{E4}$$

For the *ML* point estimators for (b', c'), the location parameter, *a*, was assumed given. The *Method of Moments* (*MM*) can now be applied to provide a point estimate for the location parameter, a^*. In the *Method of Moments*, the sample moments are used as estimators for the population moments. The *MM* point estimator for the scale parameter, b^*, is (given the shape parameter, *c*),

$$b^* = \sqrt{m_2 / [\Gamma(1+2/c) - \Gamma^2(1+1/c)]} \tag{E5}$$

where m_2 is the second moment of the sample about the sample mean and Γ is Euler's gamma function. The *MM* estimator for the location parameter, a^*, follows from

$$a^* = m_1' - b^* \Gamma(1+1/c) \tag{E6}$$

where m_1' is the 1st crude moment of the sample (the sample mean) and the sample moments are defined by

$$\begin{aligned} m_1' &= \sum_{i=1}^{N} \frac{\Delta RT_{NDT(i)}}{N} \\ m_2 &= \sum_{i=1}^{N} \frac{\left(\Delta RT_{NDT}(i) - m_1'\right)^2}{N} \end{aligned} \tag{E7}$$

From Ref. [B.2], a moment estimator for the shape parameter, c^*, also exists

$$c^* = \frac{4.104683 - 1.148513\sqrt{b_1} + 0.44326(\sqrt{b_1})^2 - 0.053025(\sqrt{b_1})^3}{\sqrt{b_1} + 1.139547} \tag{E8}$$

where $\sqrt{b_1}$ is the sample skewness. However, for sample sizes as small as 20, there will be a high level of uncertainty in the (a^*, b^*, c^*) estimates derived from c^* (Ref. [B.2]).

The three parameters for the Weibull distribution of ΔRT were estimated through the following iterative sequence:

1) For the discrete set $(\Delta RT_{(i)}, i = 1, N)$, calculate the sample moments, (m_1', m_2) from Eqs. (E7).
2) Select a trial value for the location parameter, a_{trial} where $a_{trial} < \min(\Delta RT_{(i)}, i = 1, 2, \ldots N)$.
3) Calculate *ML* estimates for (c', b') from Eqs. (E3)-(E4) by letting $a = a_{trial}$.

4) Calculate MM estimates for (a^*, b^*) from Eqs. (E5)-(E6) by letting $c = c'$ as determined in Step 3.

5) Calculate a relative deviation between the trial a_{trial} and the MM estimate of a^* from Step 4 by

$$\delta = \frac{a_{trial} - a^*}{a_{trial}} \tag{E9}$$

6) Given $\varepsilon_{tolerance}$, as a pre-selected convergence tolerance, if $\delta > \varepsilon_{tolerance}$, then select a new trial location parameter, a_{trial}, and repeat Steps 3-6 until convergence, defined as $\delta \le \varepsilon_{tolerance}$.

Upon convergence, there will be two triplets (a_{trial}, b', c') and (a^*, b^*, c') where in general $a_{trial} \approx a^*$ and $b' \neq b^*$ although b' was typically close to b^* in this study. The triplet (a^*, b', c') was taken as the converged estimate for the parameters of the Weibull distribution for ΔRT.

References

E1. A. Ghosh, "A FORTRAN Program for Fitting Weibull Distribution and Generating Samples," *Computers & Geosciences* **25**, (1999) 729-738.

E2. K. O. Bowman and P. T. Williams, *Technical Basis for Statistical Models of Extended K_{Ic} and K_{Ia} Fracture Toughness Databases for RPV Steels*, ORNL/NRC/LTR-99/27, Oak Ridge National Laboratory, Oak Ridge, TN, February 2000.

Appendix F – Development of Stochastic Models for $\Delta RT_{epistemic}$ and ΔRT_{arrest}

F.1 Stochastic Model for $\Delta RT_{epistemic}$

F.1.1 Initial Weibull Model for $\Delta RT_{epistemic}$

Initially, the epistemic uncertainty in the unirradiated value for $RT_{NDT\text{o}}$ was modeled by a continuous 3-parameter Weibull distribution of the form

$$f_W(\Delta RT \mid a,b,c) = \frac{c}{b}\left(\frac{\Delta RT - a}{b}\right)^{c-1} \exp\left[-\left(\frac{\Delta RT - a}{b}\right)^{c}\right], \qquad \left(\Delta RT > a,\ \ (b,c) > 0\right)$$
$$\Pr\left(X \le \Delta RT\right) = F_W(\Delta RT \mid a,b,c) = P = 1 - \exp\left[-\left(\frac{\Delta RT - a}{b}\right)^{c}\right],\ \left(\Delta RT > a,\ \ (b,c) > 0\right) \tag{F1}$$

where f_W is the probability density function (PDF), F_W is the cumulative distribution function (CDF), and *a, b,* and *c* are the location, scale, and shape parameters, respectively, of the Weibull distribution. In FAVOR, the epistemic uncertainty term is sampled using the inverse CDF

$$\Delta RT = a + b\left[-\ln\left(1-P\right)\right]^{\frac{1}{c}}; \quad 0 < P < 1 \tag{F2}$$

where *P* is randomly sampled from a uniform distribution on the open interval (0,1). The *epistemic* uncertainty in $RT_{NDT(\text{u})}$ can then be reduced by

$$RT_{LB} = RT_{NDT(\text{u})} - \Delta RT \tag{F3}$$

Using a combination of the *Maximum Likelihood* and *Method of Moments* point-estimation procedures (as described in Appendix E), the following values were determined for the three Weibull parameters in Eqs. (F1) and (F2):

$$\begin{aligned} a &= -40.02\ ^\circ\text{F} \\ b &= \ 124.88\ ^\circ\text{F} \\ c &= \ 1.96 \end{aligned} \tag{F4}$$

based on the sample ($N = 18$) given in Table 8 and repeated in Table F1.

Table F1. $\Delta RT_{epistemic}$ **Ranked Data with Order-Statistic Estimates of** ***P***

i	ΔRT_i, (°F)	$\boldsymbol{P}_i$	ln(- ln(1 - $\boldsymbol{P}_i$))
1	-19.4	0.03804	-3.24970
2	-10.9	0.09239	-2.33364
3	-1.7	0.14674	-1.84080
4	2.1	0.20109	-1.49387
5	33.2	0.25543	-1.22093
6	38.4	0.30978	-0.99223
7	50.1	0.36413	-0.79239
8	54.6	0.41848	-0.61229
9	62.3	0.47283	-0.44594
10	64.3	0.52717	-0.28898
11	81.9	0.58152	-0.13796
12	89.4	0.63587	0.01019
13	91.5	0.69022	0.15861
14	97.8	0.74457	0.31100
15	142.2	0.79891	0.47251
16	147.6	0.85326	0.65186
17	162.4	0.90761	0.86782
18	186.2	0.96196	1.18449

Sample	
mean =	70.67
variance =	3669.77
stdv =	60.58

$P_i = (i - 0.3)/(n + 0.4)$

From the following asymptotic relations for the mean and variance of a Weibull distribution,

$$\mu = a + b\,\Gamma\left(1 + \frac{1}{c}\right)$$
$$\sigma^2 = b^2\left[\Gamma\left(1 + \frac{2}{c}\right) - \Gamma^2\left(1 + \frac{1}{c}\right)\right] \quad , \tag{F5}$$
$$\Gamma(x) = \int_0^\infty t^{x-1} e^{-t}\,dt$$

the mean and variance for the Weibull model for $\Delta RT_{epistemic}$ compared to the corresponding sample estimators are:

Model	Sample
$\mu = 70.70$ °F	$m_1' = 70.67$ °F
$\sigma^2 = 3473.65$	$s^2 = 3669.77$
$\sigma = 58.94$ °F	$s = 60.58$ °F

F.1.2 New Model Developed Using Orthogonal Distance Regression (ODR)

The initial statistical model for $\Delta RT_{epistemic}$ was developed using point-estimation procedures that did not take into account any uncertainty in the data sample of Table F1. An analytical procedure, called *orthogonal distance regression* (ODR), can be employed to solve the *errors-in-variables* problem in which uncertainties are assumed to exist in the data. The computational procedure implemented into the software package, ODRPACK [F1], can be used to fit a model equation to data using orthogonal distance regression.

The explicit ODR problem is defined as follows. Let $(x_i, y_i), i = 1, 2, \ldots n$ be an observed set of data. Assume that the values y_i are a (possibly nonlinear) function of x_i and a set of unknown parameters $\beta \in \Re^p$, where both y_i and x_i contain the uncertainties, $\varepsilon_i^* \in \Re^1$ and $\delta_i^* \in \Re^1$, respectively. The superscript "*" denotes an actual but unknown value. The observed value, y_i, can be expressed in terms of a *model equation*

$$y_i + \varepsilon_i^* = f_i\left(x_i + \delta_i^* \left| \left\{\beta_k^*\right\}\right.\right); \quad \left(i = 1, 2, \ldots n\right) \tag{F6}$$

for some actual values of the parameter vector $\left(\left\{\beta_k^*\right\}; k = 1, 2, \ldots p\right)$. The variables y_i are sometimes referred to as the *dependent* or *response* variables, and x_i are the *independent* (*regressor* or *explanatory*) variables.

The explicit *orthogonal distance regression* problem approximates $\left\{\beta^*\right\}$ by finding the estimate $\left\{\beta\right\}$ for which the sum of the squares of the *n* orthogonal distances from the curve $f(x\,; \left\{\beta\right\})$ to the *n* data points is minimized [F1]. This can be accomplished by the following minimization problem

$$\min_{\beta, \delta, \varepsilon} \sum_{i=1}^{n} \left(\varepsilon_i^2 + \delta_i^2\right) \tag{F7}$$

subject to the constraints

$$y_i = f_i\left(x_i + \delta_i \left| \left\{\beta\right\}\right.\right) - \varepsilon_i \qquad i = 1, 2, \ldots n. \tag{F8}$$

Since the constraints are linear in ε_i, they and thus ε_i can be eliminated from the minimization problem, obtaining

$$\min_{\{\beta\}, \{\delta\}} \sum_{i=1}^{n} \left(\left[f_i\left(x_i + \delta_i \left| \left\{\beta\right\}\right.\right) - y_i \right]^2 + \delta_i^2 \right) \tag{F9}$$

The algorithm implemented in ODRPACK uses the Levenberg-Marquardt *trust region* method to iteratively solve the nonlinear minimization problem of Eq. (F9).

Derivation of the Model Equation Form

To proceed, the form of the problem-specific model equation must be derived. The CDF in Eq.(F1) can be rewritten as

$$\begin{aligned} P &= 1-\exp\left[-\left(\frac{\Delta RT-a}{b}\right)^c\right] \\ 1-P &= \exp\left[-\left(\frac{\Delta RT-a}{b}\right)^c\right] \\ -\ln(1-P) &= \left(\frac{\Delta RT-a}{b}\right)^c \\ \ln\left[-\ln(1-P)\right] &= c\ln(\Delta RT-a)-c\ln(b) \end{aligned} \tag{F10}$$

The location parameter, *a*, is related to the scale, *b*, and shape, *c*, parameters through its *moment estimator*

$$a \approx m_1' - b\,\Gamma\left(1+\frac{1}{c}\right) \tag{F11}$$

where m_1' is the 1st crude moment of the sample (or sample mean). The use of the Eq. (F11) as a constraint in the model equation forces the mean of the resulting Weibull model to be identical to the sample mean, m_1'. Introducing Eq. (F11) into Eq. (F10), the final form of the nonlinear model equation is

$$y_i = \beta_1 \ln\left[x_i - m_1' + \beta_2\,\Gamma\left(1+\frac{1}{\beta_1}\right)\right] - \beta_1\ln(\beta_2);\ (i=1,2,\ldots n)$$

where (F12)

$$\left(\{\beta\}=\begin{Bmatrix}\beta_1\\ \beta_2\end{Bmatrix}=\begin{Bmatrix}c\\ b\end{Bmatrix};\quad \{x_i\}=\{\Delta RT_{(i)}\};\{y_i\}=\left\{\ln\left[-\ln(1-P_i)\right]\right\}\right)$$

Values for P_i can be estimated by ranking the data in Table F1 and applying the median-rank order statistic

$$P_i \approx \frac{i-0.3}{n+0.4} \tag{F13}$$

ODRPACK iteratively solves for the solution vector $\begin{Bmatrix} \beta_1 \\ \beta_2 \\ \delta_1 \\ \delta_2 \\ \vdots \\ \delta_n \end{Bmatrix}_{n+2}$

The results of the ODRPACK analysis are presented in Table F2. In summary, the ODR analysis produced the following estimates for the Weibull model for $\Delta RT_{epistemic}$:

Location Parameter, a =	-45.586	95% Confidence Intervals
Scale Parameter, b =	130.899 ± 10.259	109.15 to 152.65
Shape Parameter, c =	1.855 ± 0.227	1.374 to 2.337
ΔRT_{ODR} =	$-45.586 + 130.899\left[-\ln\left(1-P\right)\right]^{\frac{1}{1.855}}$;	$0 < P < 1$
Sample Mean, m_1' =	70.67	
Weibull Mean, μ =	70.667	
Sample Stdv, s =	60.58	
Weibull Stdv, σ =	65.036	
Sample Variance, s^2 =	3669.77	
Weibull Variance, σ^2 =	4229.692	

The 95% confidence intervals for the two parameters $\beta_1 = c$ and $\beta_2 = b$ are calculated by ODRPACK using $\beta_k \pm t_{(0.975,\mu)}\sigma_{\beta_k}$ where $t_{(0.975,\mu)}$ is the appropriate value for constructing a two-sided confidence interval using Student's *t* distribution with μ degrees of freedom. The computational procedure used by ODRPACK to calculate the standard deviations for the parameters, σ_{β_k}, is given in [F2]. See Fig. F1 for a comparison of the initial Weibull model and the model produced by the ODR analysis. The application of ODR has resulted in an increase in the Weibull model's standard deviation from 58.94 °F to 65.04 °F compared to the sample's standard deviation of 60.58 °F.

Table F2. ODRPACK Results of ODR Analysis of $\Delta RT_{epistemic}$ Model Equation

```
*****************************************************
* ODRPACK VERSION 2.01 OF 06-19-92 (DOUBLE PRECISION) *
*****************************************************

    ODR Analysis of DRTLB Weibull Model Parameters

   BETA(1) = c >> Shape Parameter
   BETA(2) = b >> Scale Parameter

   a = M1 - b*Gamma[1 + 1/c]

 *** INITIAL SUMMARY FOR FIT BY METHOD OF ODR ***

 --- PROBLEM SIZE:
           N =    18          (NUMBER WITH NONZERO WEIGHT =    18)
          NQ =     1
           M =     1
          NP =     2          (NUMBER UNFIXED =     2)

 --- CONTROL VALUES:
         JOB = 00010
             = ABCDE, WHERE
                      A=0 ==> FIT IS NOT A RESTART.
                      B=0 ==> DELTAS ARE INITIALIZED TO ZERO.
                      C=0 ==> COVARIANCE MATRIX WILL BE COMPUTED USING
                              DERIVATIVES RE-EVALUATED AT THE SOLUTION.
                      D=1 ==> DERIVATIVES ARE ESTIMATED BY CENTRAL
DIFFERENCES.
                      E=0 ==> METHOD IS EXPLICIT ODR.
       NDIGIT =    16          (ESTIMATED BY ODRPACK)
       TAUFAC =     1.00D+00

 --- STOPPING CRITERIA:
        SSTOL =     1.49D-08   (SUM OF SQUARES STOPPING TOLERANCE)
       PARTOL =     3.67D-11   (PARAMETER STOPPING TOLERANCE)
        MAXIT =    50          (MAXIMUM NUMBER OF ITERATIONS)

 --- INITIAL WEIGHTED SUM OF SQUARES        =   1.15671908D+00
         SUM OF SQUARED WEIGHTED DELTAS     =   0.00000000D+00
         SUM OF SQUARED WEIGHTED EPSILONS   =   1.15671908D+00

 *** ITERATION REPORTS FOR FIT BY METHOD OF ODR ***


         CUM.                 ACT. REL.   PRED. REL.
  IT.   NO. FN     WEIGHTED   SUM-OF-SQS   SUM-OF-SQS              G-N
 NUM.    EVALS   SUM-OF-SQS    REDUCTION    REDUCTION  TAU/PNORM  STEP
 ----   ------  -----------  -----------  -----------  ---------  ----

    1      12  5.36253D-01   5.3640D-01   5.3739D-01  1.333D-01   YES
    2      19  5.33419D-01   5.2849D-03   4.2184D-03  4.265D-02   YES
    3      26  5.33152D-01   4.9976D-04   3.9259D-04  1.461D-02   YES
    4      33  5.33130D-01   4.1577D-05   3.2561D-05  4.323D-03   YES
    5      40  5.33128D-01   3.2902D-06   2.5746D-06  1.224D-03   YES
    6      47  5.33128D-01   2.5647D-07   2.0064D-07  3.423D-04   YES
    7      54  5.33128D-01   1.9907D-08   1.5572D-08  9.542D-05   YES
    8      61  5.33128D-01   1.5432D-09   1.2072D-09  2.657D-05   YES
```

Table F2. ODRPACK Results of ODR Analysis of $\Delta RT_{epistemic}$ Model Equation (continued)

```
*** FINAL SUMMARY FOR FIT BY METHOD OF ODR ***

 --- STOPPING CONDITIONS:
        INFO =     1 ==> SUM OF SQUARES CONVERGENCE.
       NITER =     8          (NUMBER OF ITERATIONS)
        NFEV =    67          (NUMBER OF FUNCTION EVALUATIONS)
       IRANK =     0          (RANK DEFICIENCY)
       RCOND =     1.20D-01   (INVERSE CONDITION NUMBER)
       ISTOP =     0          (RETURNED BY USER FROM SUBROUTINE FCN)

 --- FINAL WEIGHTED SUMS OF SQUARES       =    5.33127879D-01
        SUM OF SQUARED WEIGHTED DELTAS   =    7.67684538D-04
        SUM OF SQUARED WEIGHTED EPSILONS =    5.32360195D-01

 --- RESIDUAL STANDARD DEVIATION          =    1.82539016D-01
        DEGREES OF FREEDOM               =    16

 --- ESTIMATED BETA(J), J = 1, ..., NP:

           BETA        S.D. BETA     ---- 95%  CONFIDENCE INTERVAL ----

 1   1.85530498D+00     2.2706D-01     1.37390691D+00 TO  2.33670305D+00
 2   1.30899017D+02     1.0259D+01     1.09149592D+02 TO  1.52648443D+02

 --- ESTIMATED EPSILON(I) AND DELTA(I,*), I = 1, ..., N:

        I    EPSILON(I,1)      DELTA(I,1)

        1  2.62841903D-01 -1.86361603D-02
        2 -1.29977011D-01  6.95094427D-03
        3 -1.86382404D-01  7.87802505D-03
        4 -3.79012096D-01  1.47415688D-02
        5  2.78865897D-01 -6.56742977D-03
        6  1.68817068D-01 -3.72942044D-03
        7  2.10949482D-01 -4.09035239D-03
        8  1.16154880D-01 -2.15105581D-03
        9  8.71915578D-02 -1.49943300D-03
       10 -3.56507199D-02  6.01915026D-04
       11  8.89342397D-02 -1.29426169D-03
       12  4.68465281D-02 -6.43875329D-04
       13 -7.29122682D-02  9.86768713D-04
       14 -1.41925842D-01  1.83636941D-03
       15  1.97009129D-01 -1.94642622D-03
       16  7.02764840D-02 -6.74910438D-04
       17 -8.73096746D-03  7.78822029D-05
       18 -1.24381318D-01  9.95579717D-04
```

F.1.3. Final Stochastic Model for $\Delta RT_{epistemic}$ in FAVOR

The epistemic uncertainty in $RT_{NDT(u)}$ is estimated in FAVOR by

$$\Delta RT_{epistemic} = RT_{NDT(u)} - RT_{LB} \tag{F14}$$

where $RT_{NDT(u)}$ is the unirradiated reference nil-ductility transition temperature and RT_{LB} is a new temperature index developed for FAVOR analyses. If we assume that $RT_{NDT(u)}$ and RT_{LB} are statistically independent and, therefore, uncorrelated, then the variance of $\Delta RT_{epistemic}$ is

$$\text{var}(\Delta RT_{epistemic}) = \text{var}(RT_{NDT}) + \text{var}(RT_{LB}) \tag{F15}$$

where the $\text{cov}\left(RT_{NDT(u)} RT_{LB}\right)$ has been assumed to be zero. The statistical model developed for $\Delta RT_{epistemic}$ using the ODR procedure contains the following four sources of uncertainty

1. Measurement uncertainty and material variability in $RT_{NDT(u)}$, $\sigma^2_{(1)}$
2. Measurement uncertainty and material variability in RT_{LB}, $\sigma^2_{(2)}$
3. Model uncertainty in $RT_{NDT(u)}$, $\sigma^2_{(3)}$
4. Model uncertainty in RT_{LB}, $\sigma^2_{(4)}$

such that the components of the variances for $RT_{NDT(u)}$ and RT_{LB} are the following:

$$\begin{aligned} \text{var}(RT_{NDT(u)}) &= \sigma^2_{(1)} + \sigma^2_{(3)} \\ \text{var}(RT_{LB}) &= \sigma^2_{(2)} + \sigma^2_{(4)} \end{aligned} \tag{F16}$$

Therefore, the variance (uncertainty) in the ODR-developed Weibull distribution for $\Delta RT_{epistemic}$ can be expressed as

$$\sigma^2_{\Delta RT} = \sigma^2_{(1)} + \sigma^2_{(2)} + \sigma^2_{(3)} + \sigma^2_{(4)} = 4229.69 \tag{F17}$$

As a result of the sampling protocols in FAVOR, the uncertainties associated with sources (1) and (2) have already been accounted for at the point in FAVOR where $\Delta RT_{epistemic}$ is sampled. The Weibull model for $\Delta RT_{epistemic}$ can be revised such that it reflects the uncertainties associated with sources (3) and (4) only, specifically

$$\sigma^2_{\Delta RT(rev)} = \sigma^2_{(3)} + \sigma^2_{(4)} = \sigma^2_{\Delta RT} - \sigma^2_{(1)} - \sigma^2_{(2)} \tag{F18}$$

Two cases were examined:

Case 1:

$$\sigma_{(1)}^2 = (23°\text{F})^2$$
$$\sigma_{(2)}^2 = 0$$

Case 2:

$$\sigma_{(1)}^2 = (23°\text{F})^2$$
$$\sigma_{(2)}^2 = (23°\text{F})^2$$

The required adjustments to the Weibull model for $\Delta RT_{epistemic}$ can be calculated by solving the following nonlinear system of equations

$$\begin{aligned} \mu_{\Delta RT} - a - b\Gamma\left(1+\frac{1}{c}\right) &= 0 \\ \sigma_{\Delta RT(rev)}^2 - b^2\left[\Gamma\left(1+\frac{2}{c}\right) - \Gamma^2\left(1+\frac{1}{c}\right)\right] &= 0 \end{aligned} \tag{F19}$$

for the new parameters *b* and *c*, where $\mu_{\Delta RT} = 70.67$ °F and the location parameter for the ODR-developed model, *a* = -45.586 °F, remain fixed. Equations (F19) are the asymptotic relations for the mean and variance of a Weibull distribution.

Case 1:

$$\sigma_{\Delta RT(rev)}^2 = \sigma_{\Delta RT}^2 - \sigma_{(1)}^2 - \sigma_{(2)}^2$$
$$\sigma_{\Delta RT(rev)}^2 = 4229.692 - 23^2 - 0 = 3700.692$$
$$\sigma_{\Delta RT(rev)} = 60.83\ °\text{F}$$

The solutions for (*b*,*c*) are

$$b = 131.18\ °\text{F}$$
$$c = 1.998$$

Case 2:

$$\sigma^2_{\Delta RT(rev)} = \sigma^2_{\Delta RT} - \sigma^2_{(1)} - \sigma^2_{(2)}$$
$$\sigma^2_{\Delta RT(rev)} = 4229.692 - 23^2 - 23^2 = 3171.692$$
$$\sigma_{\Delta RT(rev)} = 56.32\ °\text{F}$$

The solutions for (*b,c*) are

$$b = 131.27\ °\text{F}$$
$$c = 2.177$$

See Fig. F2 for a comparison of the ODR-derived model with the revised models of Cases 1 and 2. Figure F3 compares the CDF of the initial Weibull model to that of Case 2 with emphasis placed on the lower-left tail. Note that Case 2 produces a more negative $\Delta RT_{epistemic}$ adjustment than the initial model for cumulative probabilities less than approximately 3.5%. A comparison between the ODR-derived model and Case 2 is shown in Fig. F4. For cumulative probabilities less than approximately 60%, Case 2 produces more positive values of $\Delta RT_{epistemic}$ than the ODR model.

In summary the revised Weibull models for Cases (1) and (2) are:

Summary:

Case 1:

$$\Delta RT_{(rev)} = -45.586 + 131.18\left[-\ln\left(1-P\right)\right]^{\frac{1}{1.998}};\quad 0 < P < 1$$

Case 2:

$$\Delta RT_{(rev)} = -45.586 + 131.27\left[-\ln\left(1-P\right)\right]^{\frac{1}{2.177}};\quad 0 < P < 1$$

Case 2 was selected for implementation into FAVOR.

F.2. Stochastic Model for ΔRT_{arrest} in FAVOR

F.2.1 Initial Model for ΔRT_{arrest}

The initial stochastic model developed for FAVOR to describe the statistical distribution of $\Delta RT_{arrest} = T_0 - T_{K_{Ia}}$ was based on a lognormal distribution (see Fig. F5) with the parameters

$$\begin{aligned} &\overline{\Delta RT}_{arrest} = \mu(T_0) = 44.123\exp(-0.006\,T_0); \quad T_0[^\circ c] \\ &\sigma^2_{\log} = 0.39^2 = 0.1521 \text{ (constant)} \end{aligned} \tag{F20}$$

The asymptotic relations for the log-mean and variance of the model are:

$$\begin{aligned} &\mu_{\log}(T_0) = \ln\left[\mu(T_0)\right] - \frac{\sigma^2_{\log}}{2} \\ &\text{var}(\Delta RT_{arrest}) = \sigma^2(T_0) = \omega(\omega-1)\exp\left[2\mu_{\log}(T_0)\right]; \quad \omega = \exp(\sigma^2_{\log}) \end{aligned} \tag{F21}$$

The initial model was derived from an ordinary least squares regression analysis using the log-transformed data shown in Table F3.

F.2.2 Model Developed Using Orthogonal Distance Regression (ODR)

The ORDPACK program was used to reanalyze the following model equation

$$\ln(\overline{\Delta RT}_{arrest}) = \beta_1 T_0 + \beta_2 \tag{F22}$$

where, upon reversing the log-transformation, the mean value for ΔRT_{arrest} is

$$\overline{\Delta RT}_{arrest} = \exp(\beta_2)\exp\left(\beta_1 T_0\right) \tag{F23}$$

The results of the ODR analysis are presented in Table F4 with the following ODR estimates for the model parameters:

$$\begin{aligned} &\beta_1 = -0.00597110744 \pm 0.00082458 \\ &\beta_2 = 3.78696343 \pm 0.065299 \\ &\exp(\beta_2) = 44.12221645 \pm 2.908036613 \end{aligned} \tag{F24}$$

$$\begin{aligned} &\overline{\Delta RT}_{arrest} = 44.1222\exp(-0.00597 T_0); \quad [^\circ\text{C}] \\ &\sigma_{\log} = 0.389987535; \quad \sigma^2_{\log} = 0.1520903 \end{aligned}$$

Table F3. Data Used in the Development of the ΔRT_{arrest} Model

N	T_0 (°C)	T_{KIa} (°C)	T_{KIa} - T_0 (°C)	ln(T_{KIa} - T_0)
1	-114	16	130	4.8675
2	131	140	9	2.1972
3	-66	13	79	4.3694
4	-78	6	84	4.4308
5	-104	-16	88	4.4773
6	-108	44	152	5.0239
7	43	113	70	4.2485
8	-20	60	80	4.3820
9	-71	-41	30	3.4012
10	-66	6	72	4.2767
11	-84	9	93	4.5326
12	-21	65	86	4.4543
13	-53	-6	47	3.8501
14	-54	18	72	4.2767
15	62	93	31	3.4340
16	-65	-12	53	3.9703
17	-100	-15	85	4.4427
18	-130	-8	122	4.8040
19	-100	-18	82	4.4067
20	-27	25	52	3.9512
21	-78	10	88	4.4773
22	-115	-25	90	4.4998
23	-68	-9	59	4.0775
24	-70	17	87	4.4659
25	-65	-25	40	3.6889
26	-51	19	70	4.2485
27	17	77	60	4.0943
28	-48	48	96	4.5643
29	-92	-26	66	4.1897
30	-70	-18	52	3.9512
31	-81	-20	61	4.1109
32	-157	-27	130	4.8675
33	67	78	11	2.3979
34	-84	9	93	4.5326
35	-67	18	85	4.4427
36	-58	-14	44	3.7842
37	35	74	39	3.6636
38	39	67	28	3.3322
39	-61	-15	46	3.8286
40	6	62	56	4.0254
41	-61	-16	45	3.8067
42	-48	8	56	4.0254
43	-24	32	56	4.0254
44	-19	10	29	3.3673
45	-85	-33	52	3.9512
46	-131	-26	105	4.6540
47	-3	33	36	3.5835
48	-95	-62	33	3.4965
49	-93	-17	76	4.3307
50	-68	-8	60	4.0943
51	184	220	36	3.5835
52	42	71	29	3.3673
53	27	68	41	3.7136

Table F4. ODRPACK Results of ODR Analysis of ΔRT_{arrest} Model Equation

```
*******************************************************
* ODRPACK VERSION 2.01 OF 06-19-92 (DOUBLE PRECISION) *
*******************************************************

    ODR Analysis of DARTarrest Lognormal Model

   BETA(1) = slope
   BETA(2) = intercept of log-transformed data

   LN(DRTarrest) = BETA(1)*T0 + BETA(2)

   DRTArrest = EXP(BETA(2))*EXP(BETA(1)*T0)


*** DERIVATIVE CHECKING REPORT FOR FIT BY METHOD OF ODR ***


    FOR RESPONSE  1 OF OBSERVATION     1

                            USER
                         SUPPLIED     RELATIVE    DERIVATIVE
      DERIVATIVE WRT        VALUE   DIFFERENCE    ASSESSMENT

           BETA(  1)    -1.57D+02     4.25D-07    VERIFIED
           BETA(  2)     1.00D+00     7.87D-08    VERIFIED
         DELTA( 1, 1)    -5.84D-03     4.30D-07    VERIFIED

    NUMBER OF RELIABLE DIGITS IN FUNCTION RESULTS          16
       (ESTIMATED BY ODRPACK)

    NUMBER OF DIGITS OF AGREEMENT REQUIRED BETWEEN
    USER SUPPLIED AND FINITE DIFFERENCE DERIVATIVE FOR
    USER SUPPLIED DERIVATIVE TO BE CONSIDERED VERIFIED      4

    ROW NUMBER AT WHICH DERIVATIVES WERE CHECKED            1

      -VALUES OF THE EXPLANATORY VARIABLES AT THIS ROW

         X( 1, 1)  -1.57000000D+02
*******************************************************
* ODRPACK VERSION 2.01 OF 06-19-92 (DOUBLE PRECISION) *
*******************************************************


*** INITIAL SUMMARY FOR FIT BY METHOD OF ODR ***

--- PROBLEM SIZE:
          N =    53          (NUMBER WITH NONZERO WEIGHT =    53)
         NQ =     1
          M =     1
         NP =     2          (NUMBER UNFIXED =     2)

--- CONTROL VALUES:
        JOB = 00020
            = ABCDE, WHERE
                     A=0 ==> FIT IS NOT A RESTART.
                     B=0 ==> DELTAS ARE INITIALIZED TO ZERO.
                     C=0 ==> COVARIANCE MATRIX WILL BE COMPUTED USING
                             DERIVATIVES RE-EVALUATED AT THE SOLUTION.
                     D=2 ==> DERIVATIVES ARE SUPPLIED BY USER.
                             DERIVATIVES WERE CHECKED.
                             RESULTS APPEAR CORRECT.
                     E=0 ==> METHOD IS EXPLICIT ODR.
     NDIGIT =    16          (ESTIMATED BY ODRPACK)
     TAUFAC =     1.00D+00
```

Table F4. ODRPACK Results of ODR Analysis of ΔRT_{arrest} Model Equation (continued)

```
--- STOPPING CRITERIA:
       SSTOL =     1.49D-08   (SUM OF SQUARES STOPPING TOLERANCE)
      PARTOL =     3.67D-11   (PARAMETER STOPPING TOLERANCE)
       MAXIT =    50          (MAXIMUM NUMBER OF ITERATIONS)

--- INITIAL WEIGHTED SUM OF SQUARES        =   7.76381810D+00
        SUM OF SQUARED WEIGHTED DELTAS     =   0.00000000D+00
        SUM OF SQUARED WEIGHTED EPSILONS   =   7.76381810D+00

*** ITERATION REPORTS FOR FIT BY METHOD OF ODR ***


        CUM.                  ACT. REL.   PRED. REL.
 IT.  NO. FN     WEIGHTED   SUM-OF-SQS   SUM-OF-SQS              G-N
NUM.   EVALS   SUM-OF-SQS    REDUCTION    REDUCTION  TAU/PNORM  STEP
----  ------  -----------  -----------  -----------  ---------  ----

   1      15  7.75660D+00   9.2916D-04   9.2766D-04  3.063D-02   YES
   2      16  7.75660D+00   1.7592D-08   1.7540D-08  5.224D-05   YES
   3      17  7.75660D+00   6.0973D-13   6.0818D-13  1.064D-06   YES


*** FINAL SUMMARY FOR FIT BY METHOD OF ODR ***

--- STOPPING CONDITIONS:
        INFO =     1 ==> SUM OF SQUARES CONVERGENCE.
       NITER =     3          (NUMBER OF ITERATIONS)
        NFEV =    17          (NUMBER OF FUNCTION EVALUATIONS)
        NJEV =     4          (NUMBER OF JACOBIAN EVALUATIONS)
       IRANK =     0          (RANK DEFICIENCY)
       RCOND =     1.02D-01   (INVERSE CONDITION NUMBER)
       ISTOP =     0          (RETURNED BY USER FROM SUBROUTINE FCN)

--- FINAL WEIGHTED SUMS OF SQUARES       =    7.75660416D+00
        SUM OF SQUARED WEIGHTED DELTAS   =    2.76544656D-04
        SUM OF SQUARED WEIGHTED EPSILONS =    7.75632762D+00

--- RESIDUAL STANDARD DEVIATION          =    3.89987535D-01
        DEGREES OF FREEDOM               =   51

--- ESTIMATED BETA(J), J = 1, ..., NP:

            BETA          S.D. BETA     ---- 95%  CONFIDENCE INTERVAL ----

   1  -5.97110744D-03     8.2458D-04    -7.62651413D-03 TO -4.31570076D-03
   2   3.78696343D+00     6.5299D-02     3.65587019D+00 TO  3.91805666D+00
   2a  44.1222164         1.06747815    38.70118385     TO 50.30259469
```

Table F4. ODRPACK Results of ODR Analysis of ΔRT_{arrest} Model Equation (continued)

```
--- ESTIMATED EPSILON(I) AND DELTA(I,*), I = 1, ..., N:

        I    EPSILON(I,1)      DELTA(I,1)

        1 -1.43102053D-01 -8.54477100D-04
        2 -8.47788261D-02 -5.06223103D-04
        3 -2.40805066D-01 -1.43787185D-03
        4 -2.61679548D-02 -1.56251554D-04
        5 -3.99850519D-01 -2.38754864D-03
        6 -5.92016383D-01 -3.53499080D-03
        7 -6.93757401D-02 -4.14249691D-04
        8 -5.85749970D-02 -3.49757341D-04
        9 -2.26442691D-02 -1.35211263D-04
       10  8.57680493D-01  5.12129857D-03
       11  1.15426669D-02  6.89224532D-05
       12  1.46645341D-01  8.75634434D-04
       13  3.43251602D-01  2.04959067D-03
       14 -2.44054340D-01 -1.45727360D-03
       15 -2.44054340D-01 -1.45727360D-03
       16  1.59743570D-01  9.53845309D-04
       17 -1.78100642D-01 -1.06345728D-03
       18 -2.24618999D-01 -1.34122318D-03
       19  8.09685804D-01  4.83471734D-03
       20 -2.60957867D-01 -1.55820631D-03
       21  2.53688183D-01  1.51479827D-03
       22  1.15457172D-01  6.89406666D-04
       23  9.86506532D-02  5.89053212D-04
       24 -2.55614517D-01 -1.52630061D-03
       25 -1.88384618D-01 -1.12486396D-03
       26 -9.56061927D-02 -5.70874424D-04
       27  2.04786195D-01  1.22279946D-03
       28  4.86188622D-01  2.90308234D-03
       29  3.22548084D-01  1.92596784D-03
       30  3.44526207D-01  2.05720147D-03
       31  3.49085578D-01  2.08442594D-03
       32 -1.67256927D-01 -9.98708341D-04
       33  2.53275489D-01  1.51233403D-03
       34 -1.56999738D-01 -9.37461609D-04
       35 -4.90754110D-01 -2.93034334D-03
       36  4.82231733D-02  2.87945535D-04
       37 -3.06028247D-03 -1.82732618D-05
       38 -9.50782960D-02 -5.67722299D-04
       39 -5.41971290D-01 -3.23616640D-03
       40 -4.75624102D-01 -2.84000050D-03
       41  5.33099631D-01  3.18319281D-03
       42  2.21349919D-01  1.32170317D-03
       43 -2.74205133D-01 -1.63730709D-03
       44 -4.08875384D-01 -2.44143703D-03
       45 -8.78254100D-02 -5.24414570D-04
       46 -8.55839285D-02 -5.11030452D-04
       47  2.21877816D-01  1.32485529D-03
       48  1.68875063D-01  1.00837040D-03
       49 -7.18263826D-01 -4.28882729D-03
       50 -1.72318244D-02 -1.02892998D-04
       51  9.88968694D-01  5.90523394D-03
       52  8.07494984D-01  4.82163573D-03
       53 -8.95207363D-01 -5.34537537D-03
```

Comparison of Eqs. (F20) with Eqs. (F24) indicates that the ODR analysis produced essentially the same model as resulted from the ordinary least squares analysis (see Fig. F6).

F.2.3 Final Model for ΔRT_{arrest}

The variance of $\Delta RT_{arrest} = T_0 - T_{K_{Ia}}$ is

$$\text{var}(\Delta RT_{arrest}) = \text{var}(T_0) + \text{var}(T_{K_{Ia}}) - 2\,\text{cov}(T_0 T_{K_{Ia}}) \tag{F25}$$

In the absence of data to the contrary, we assume the statistical independence of T_0 and T_{KIa} such that $\text{cov}(T_0 T_{K_{Ia}}) = 0$, and Eq. (F25) becomes

$$\text{var}(\Delta RT_{arrest}) = \text{var}(T_0) + \text{var}(T_{K_{Ia}}) \tag{F26}$$

The variance of both the initial and ODR lognormal model is a decreasing function of increasing T_0

$$\begin{aligned} \text{var}(\Delta RT_{arrest(ODR)}) &= \sigma^2_{ODR}(T_0) \\ &= \exp(0.38998^2) \times \left[\exp(0.38998^2) - 1\right] \times \exp\left[2\ln\left[\mu(T_0)\right] - 0.38998^2\right] \end{aligned} \tag{F27}$$

as shown in Fig. F7. By $T_0 \approx$ 56 °C, $\text{var}(\Delta RT_{arrest}) = (12.78\ ^\circ\text{C})^2$.

The variance for T_0 has been accounted for in a separate sampling protocol prior to the sampling of ΔRT_{arrest}, and the statistical model for ΔRT_{arrest} should, therefore, reflect only the remaining variance in $T_{K_{Ia}}$. If we assume that the $\text{var}(T_0) = (23\,^\circ\text{F})^2 = (12.778\ ^\circ\text{C})^2$, then

$$\begin{aligned} &\text{var}(\Delta RT_{arrest(rev)}) = \text{var}(T_{K_{Ia}}) = \text{var}(\Delta RT_{arrest}) - \text{var}(T_0) \\ &\text{var}(\Delta RT_{arrest(rev)}) = \sigma^2_{rev}(T_0) = \\ &\left\{\exp(0.38998^2) \times \left[\exp(0.38998^2) - 1\right] \times \exp\left[2\mu_{\log}(T_0)\right]\right\} - \text{var}(T_0) = \\ &\qquad \exp\left[\sigma^2_{\log}(T_0)_{rev}\right] \times \left\{\exp\left[\sigma^2_{\log}(T_0)_{rev}\right] - 1\right\} \times \exp\left[2\mu_{\log}(T_0)_{rev}\right] \end{aligned} \tag{F28}$$

where

$$\mu_{\log}(T_0)_{rev} = \ln\left[\mu(T_0)\right] - \frac{\sigma^2_{\log}(T_0)_{rev}}{2}$$

and $\mu(T_0)$ remains a fixed function of T_0. Solving Eq. (F28) for $\sigma^2_{\log}(T_0)_{rev}$ results in

$$\sigma^2_{\log}(T_0)_{rev} = \ln\left\{\exp\left[0.38998^2 + 2\ln(\mu(T_0)\right] - \text{var}(T_0)\right\} - 2\ln\left[\mu(T_0)\right] \tag{F29}$$

and solving for $\text{var}(\Delta RT_{arrest(rev)}) = \sigma^2(T_0)_{rev}$ gives

$$\sigma^2(T_0)_{rev} = \exp\left[\sigma^2_{\log}(T_0)_{rev}\right] \times \left\{\exp\left[\sigma^2_{\log}(T_0)_{rev}\right] - 1\right\} \times \exp\left\{2\ln\left[\mu(T_0)\right] - \sigma^2_{\log}(T_0)_{rev}\right\} \tag{F30}$$

However, as noted earlier and indicated in Fig. F7, at $T_0 \approx 56$ °C, $\text{var}(\Delta RT_{arrest}) = \text{var}(T_0) = (12.78\ ^\circ\text{C})^2$ which would produce $\sigma^2(T_0)_{rev} = 0$. In order to prevent a nonphysical zero variance at this point, the assumed constant value of $\text{var}(T_0)$ can be replaced by the following function with a transition region:

$$\text{var}(T_0) = \begin{cases} (12.778)^2 & \text{for } T_0 < -35.7\ ^\circ\text{C} \\ 99.905972 - 1.7748073 T_0 & \text{for } -35.7\ ^\circ\text{C} \le T_0 \le 56\ ^\circ\text{C} \\ 0 & \text{for } T_0 > 56\ ^\circ\text{C} \end{cases} \tag{F31}$$

Figure F7 plots Eq. (F30) as the final model variance with Eq. (F31) used in Eq. (F29) to produce the final log-variance as a function of T_0. Figure F8 compares the 1% and 99% percentiles of the ODR and final models for ΔRT_{arrest}.

Summary of Stochastic Model for ΔRT_{arrest}

The lognormal model for ΔRT_{arrest} is, therefore,

$$\overline{\Delta RT}_{arrest} = \mu(T_0) = 44.122 \exp(-0.005971 T_0); \quad T_0[^\circ\text{C}]$$
$$\sigma_{\log}(T_0)_{rev} = \sqrt{\ln\left\{\exp\left[0.38998^2 + 2\ln(\mu(T_0))\right] - \text{var}\left(T_0\right)\right\} - 2\ln\left[\mu(T_0)\right]}$$
where
$$\text{var}(T_0) = \begin{cases} (12.778)^2 & \text{for } T_0 < -35.7\ ^\circ\text{C} \\ 99.905972 - 1.7748073 T_0 & \text{for } -35.7\ ^\circ\text{C} \le T_0 \le 56\ ^\circ\text{C} \\ 0 & \text{for } T_0 > 56\ ^\circ\text{C} \end{cases} \tag{F32}$$

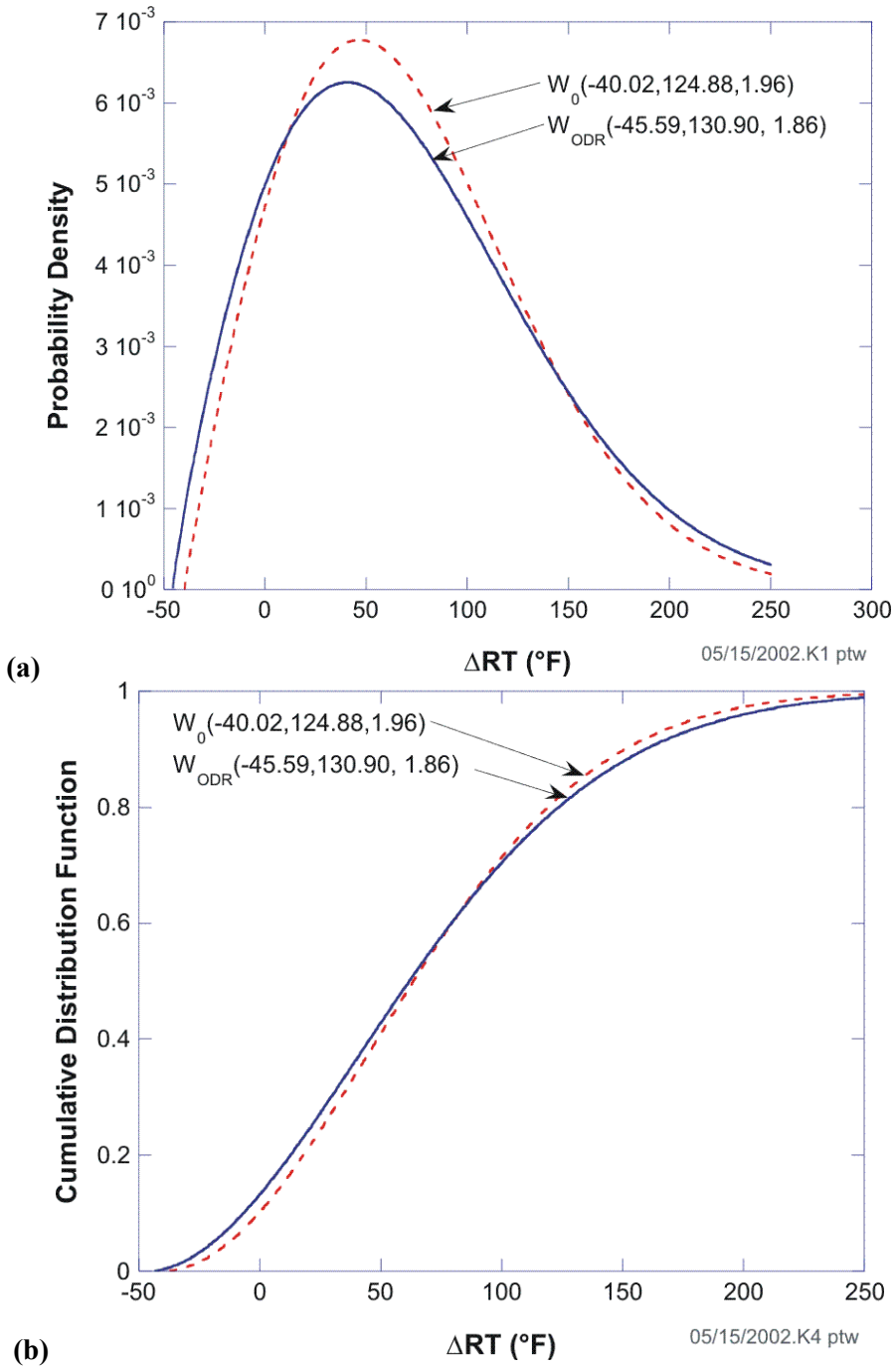

Fig. F1. Comparison of the initial Weibull model, W_0, for $\Delta RT_{epistemic}$ with the ODR model: (a) probability density functions and (b) cumulative distribution functions.

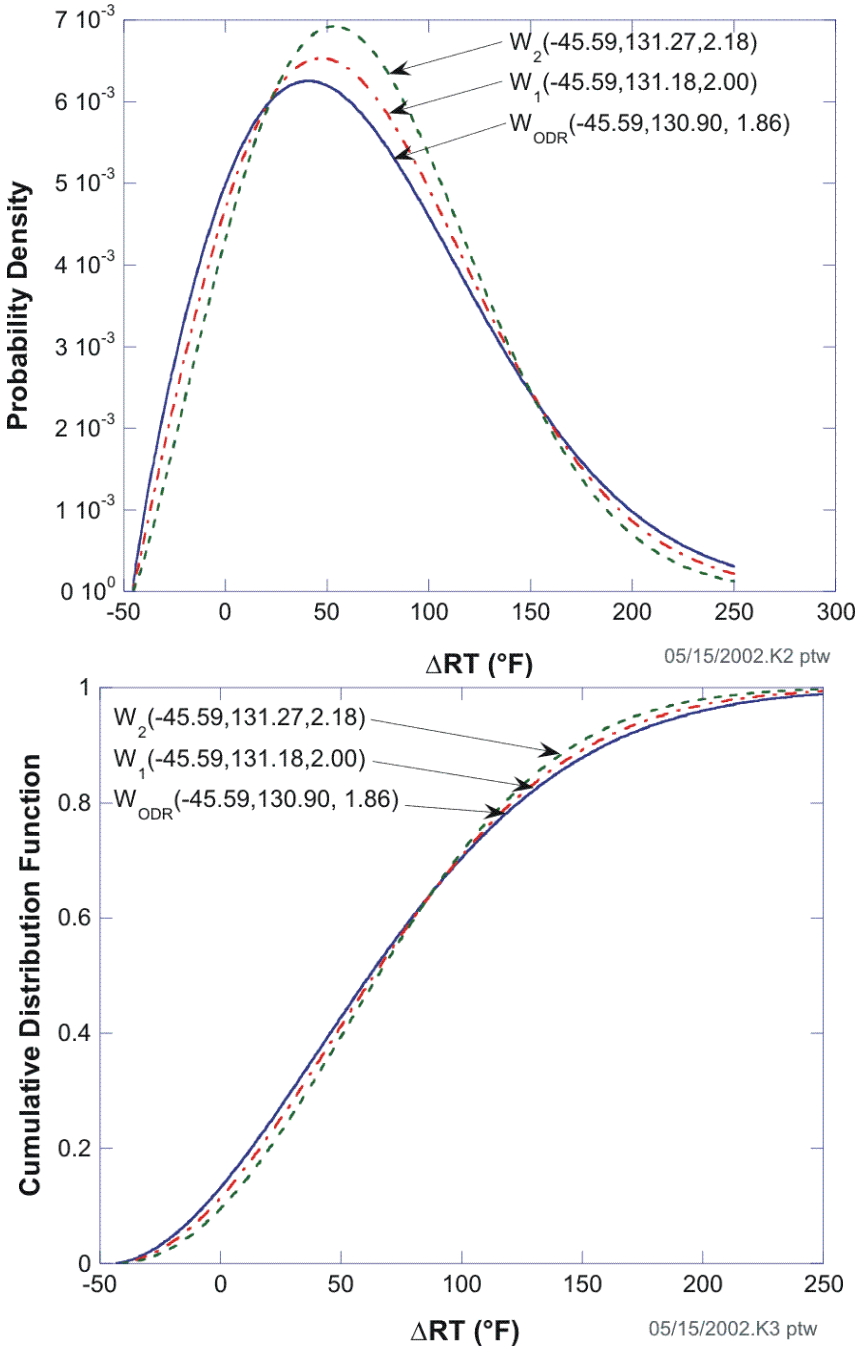

Fig. F2. Comparison of ODR Weibull model, W_{ODR}, for $\Delta RT_{epistemic}$ with the models for Case 1 (W_1) and Case 2 (W_2): (a) probability density functions and (b) cumulative distribution functions.

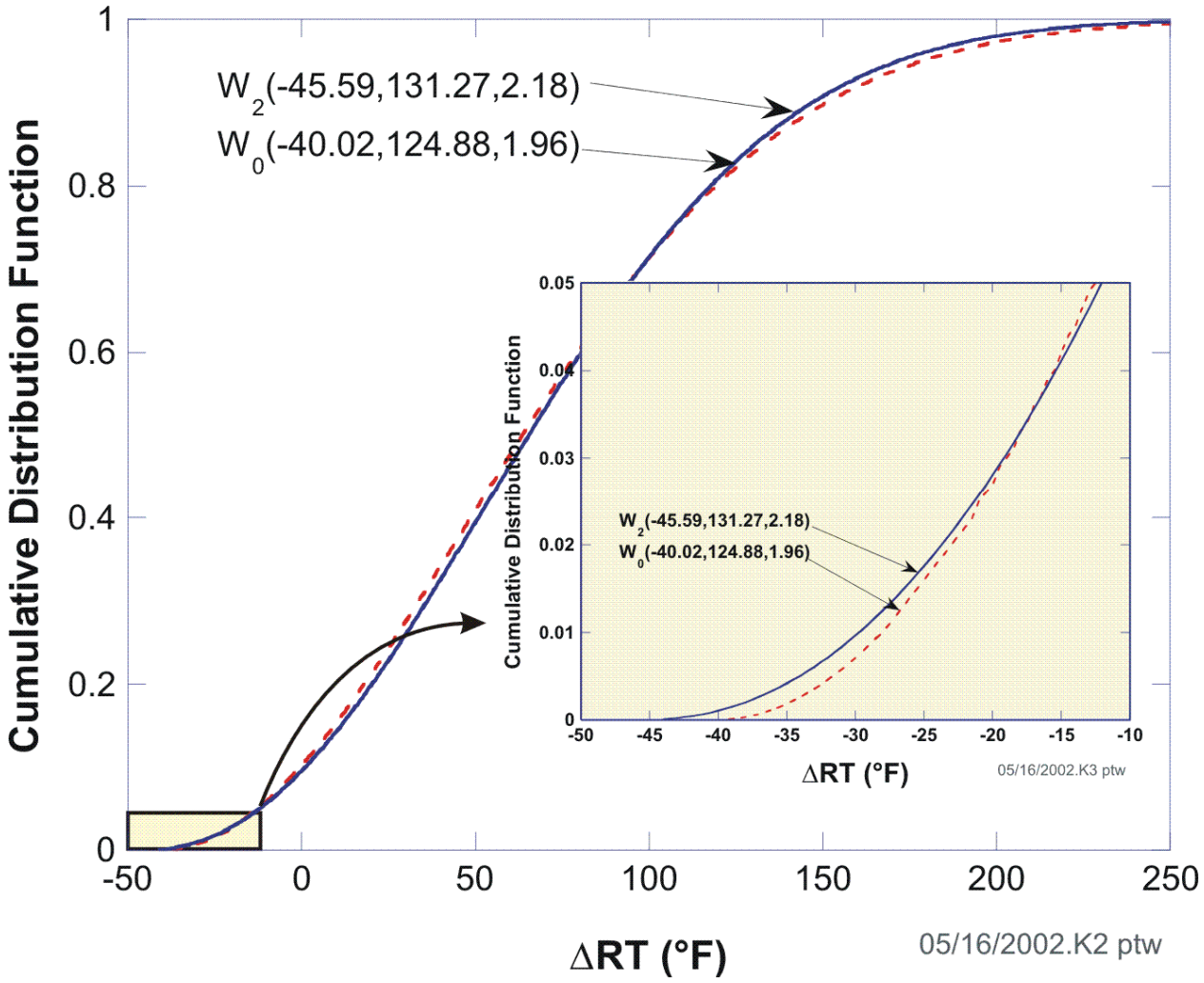

Fig. F3. Comparison of initial model in FAVOR, W_0, with Case 2, W_2.

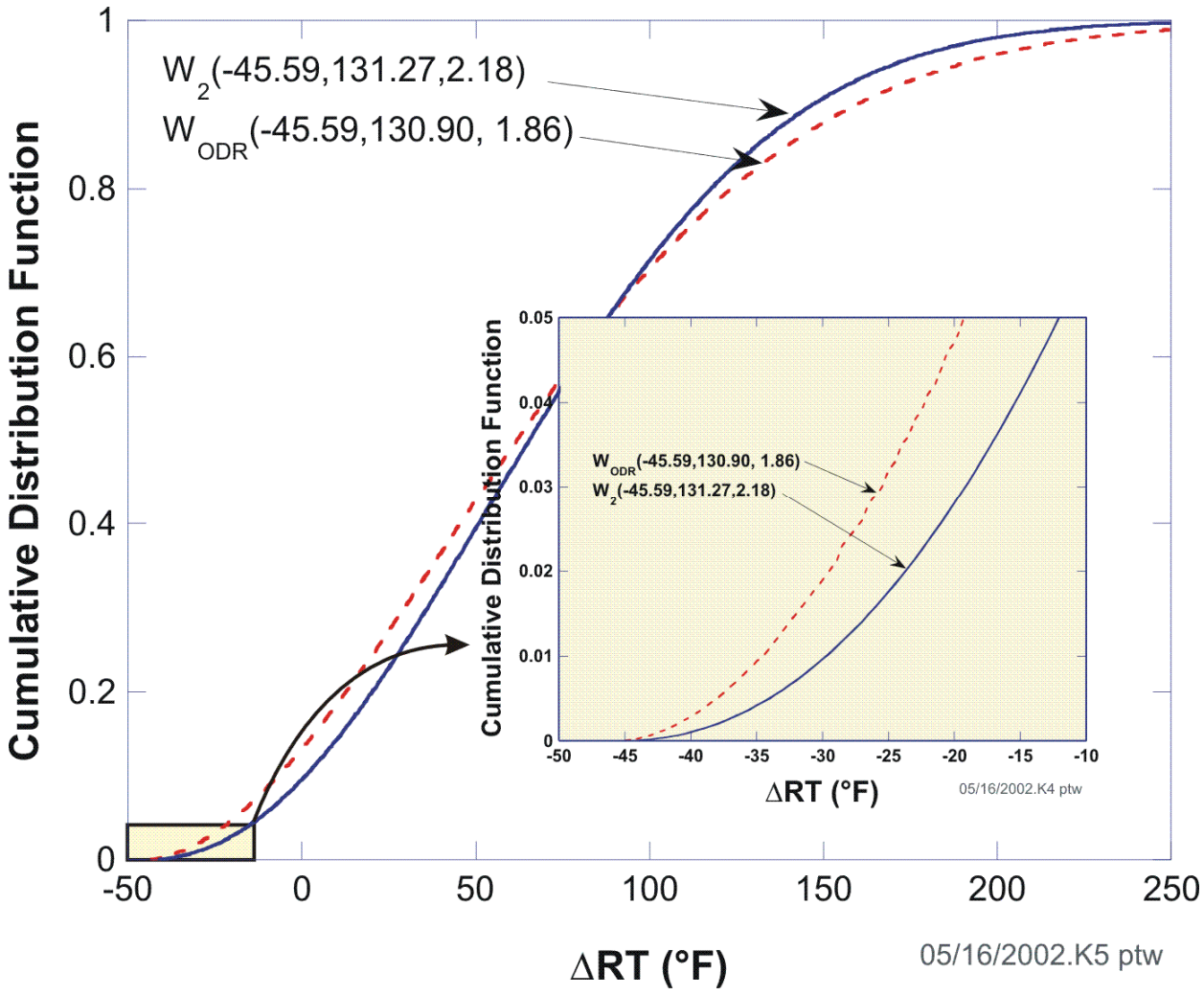

Fig. F4. Comparison of ODR model, W_{ODR}, with Case 2, W_2.

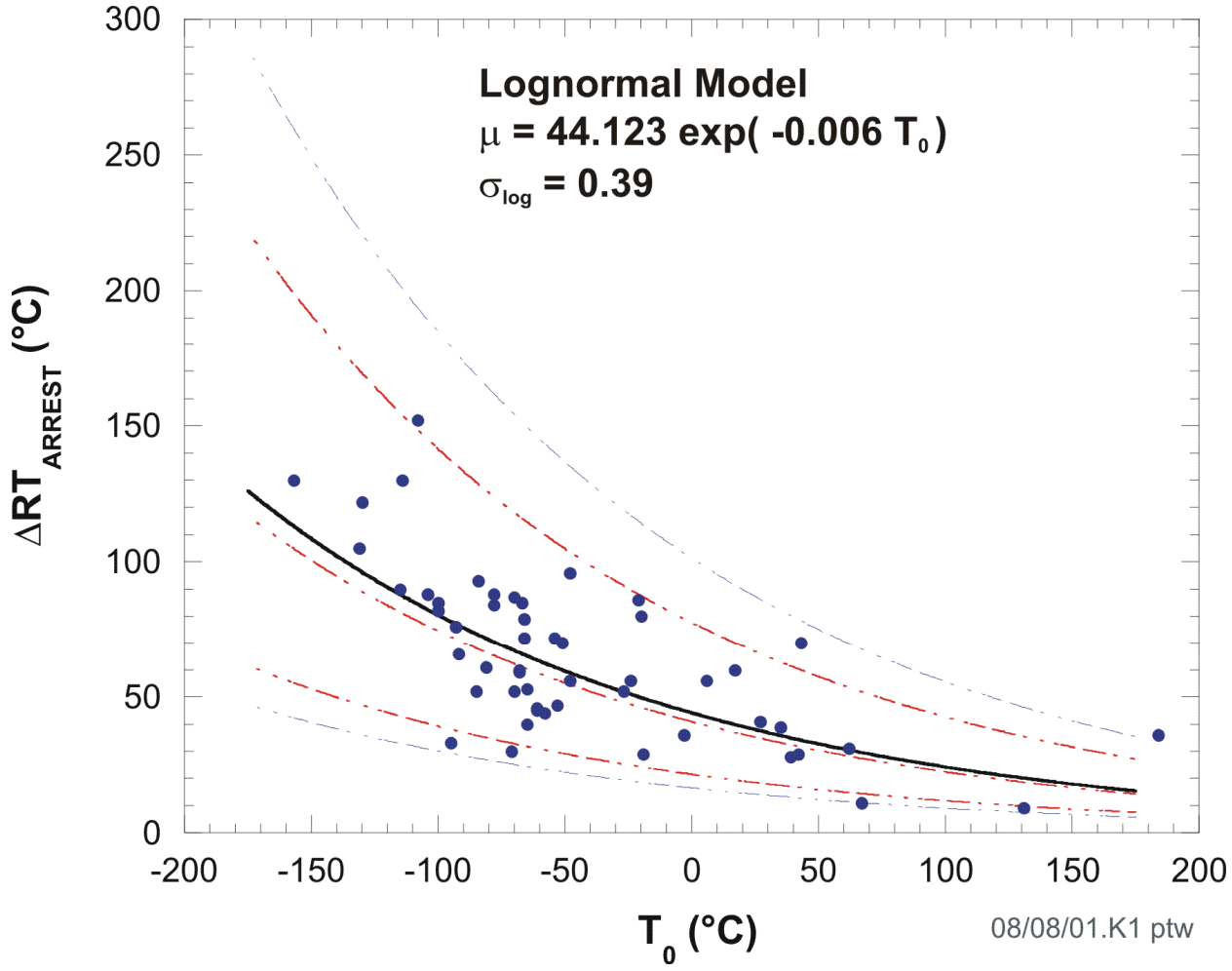

Fig. F5. Data used to develop the lognormal statistical model for ΔRT_{arrest} as a function of T_0.

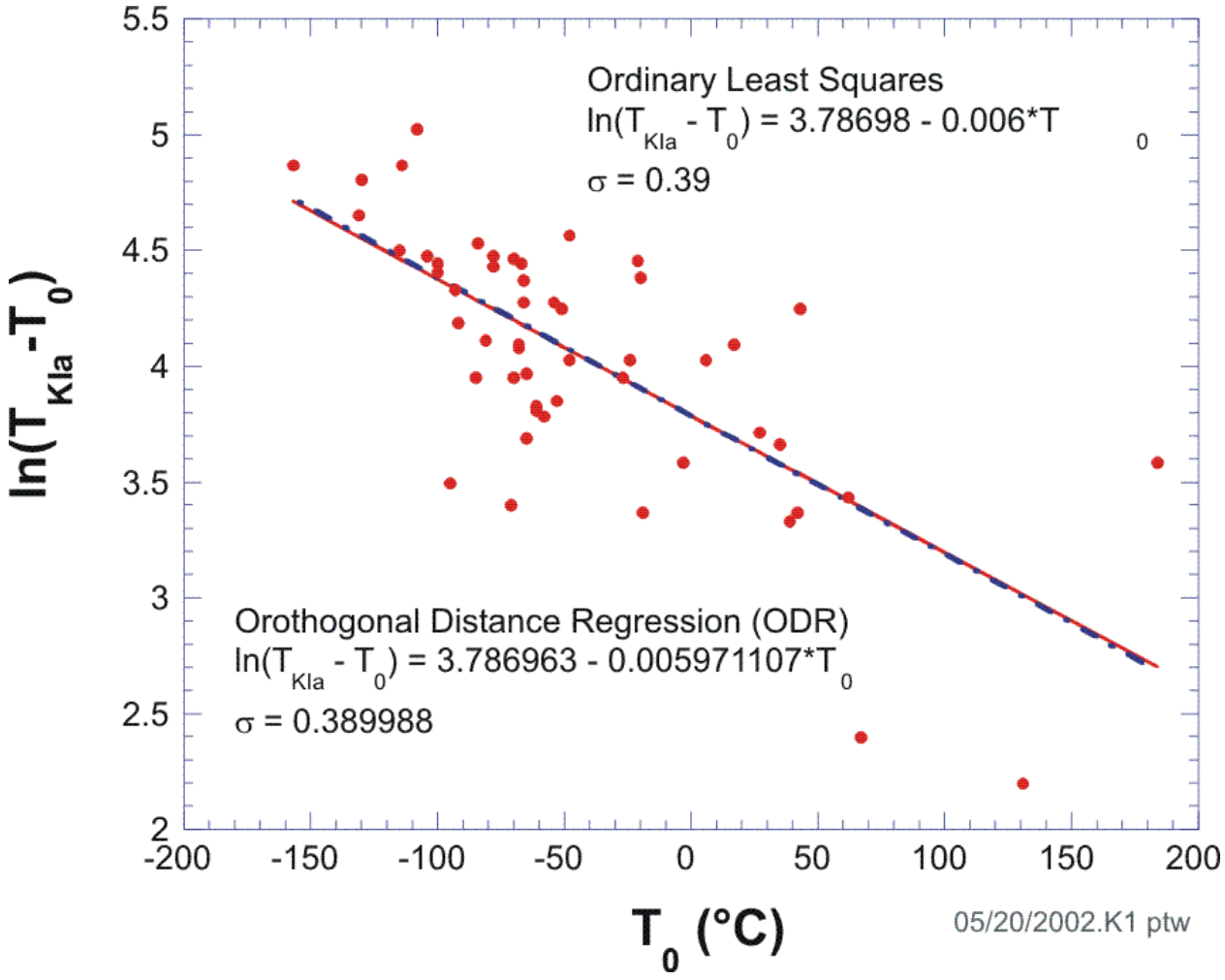

Fig. F6. Model developed from ODR analysis of log-transformed data.

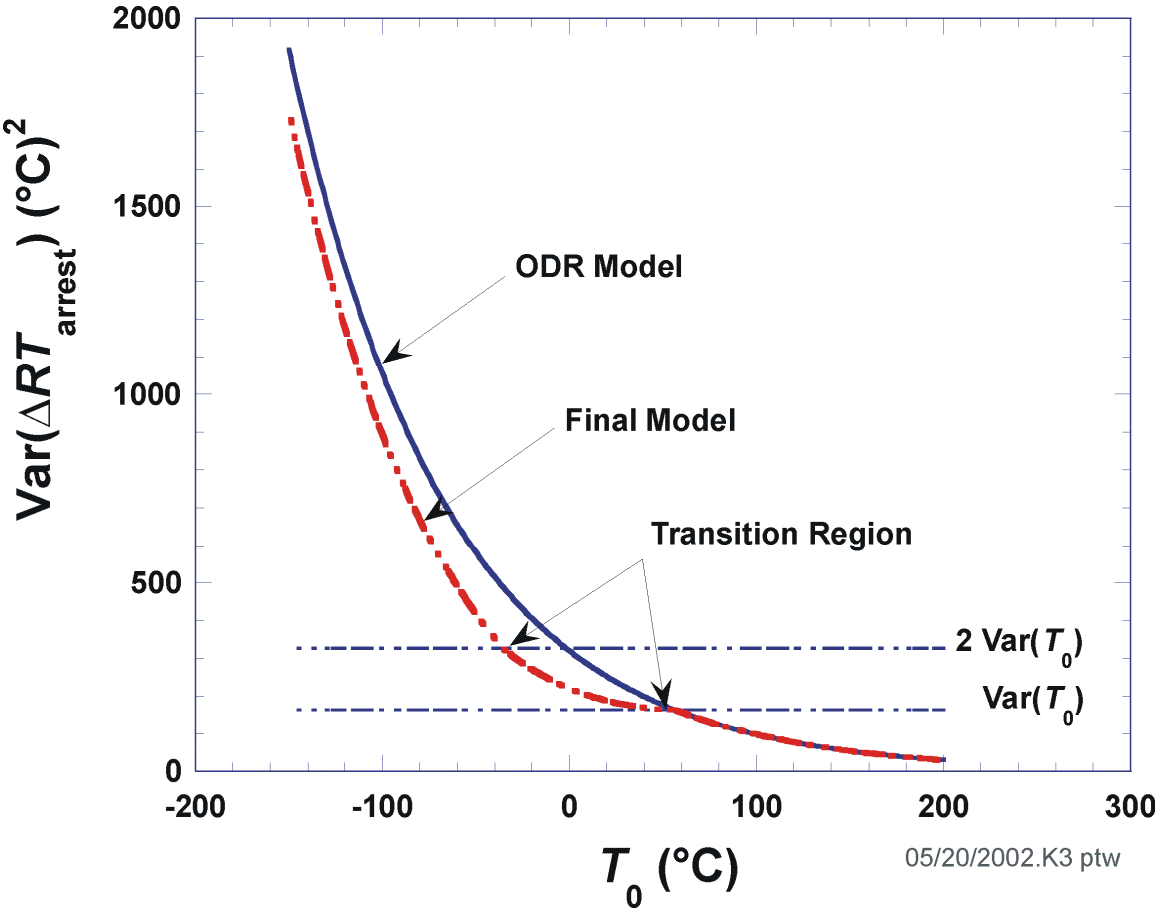

Fig. F7. Variance of ODR model compared to final model.

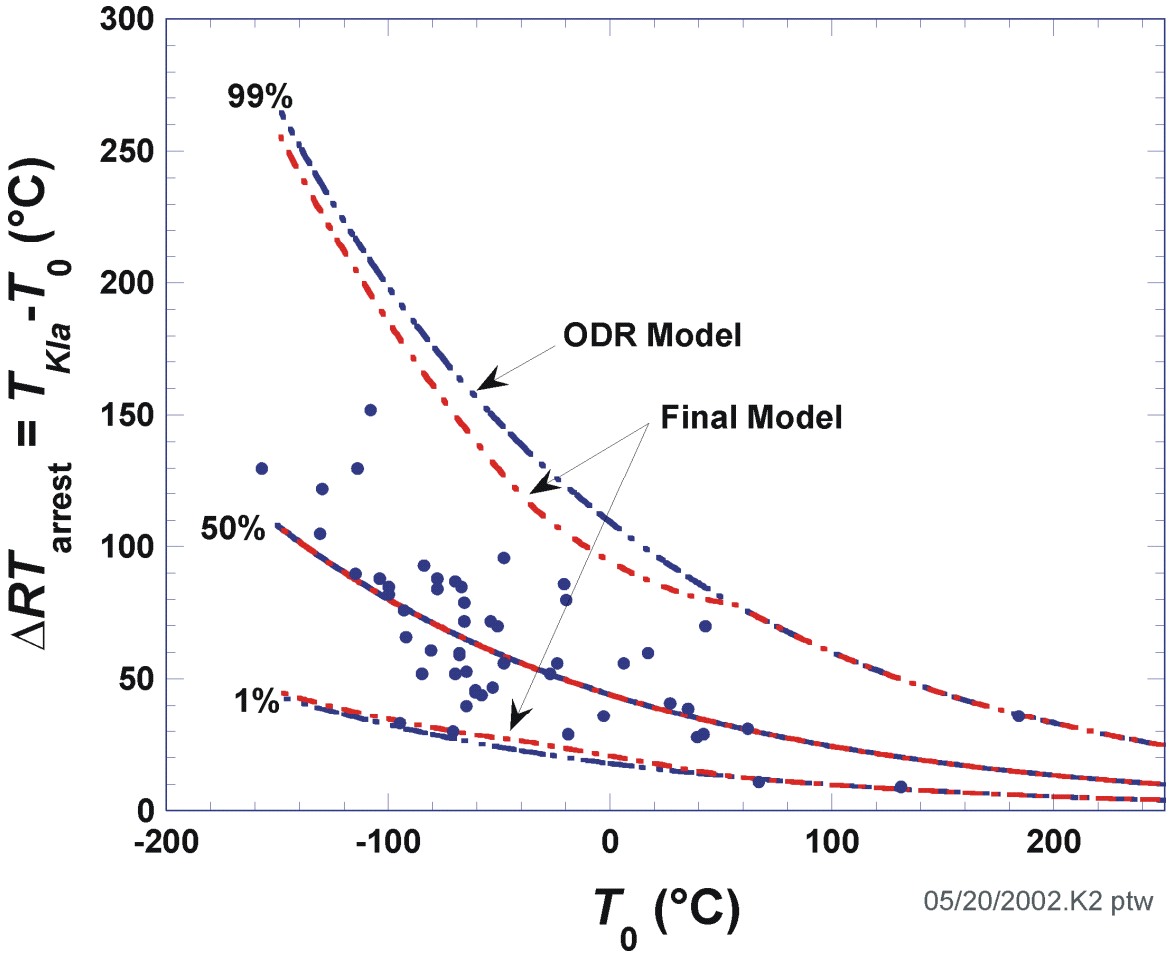

Fig. F8. Comparison of ODR model with final model.

REFERENCES

F1. P. T. Boggs, R. H. Byrd, J. E. Rogers, R. B. Schnabel, *User's Reference Guide for ODRPACK Version 2.01: Software for Weighted Orthogonal Distance Regression*, NISTIR 92-4834, National Institute of Standards and Technology, Gaithersburg, MD, 1992.

F2. P. T. Boggs and J. E. Rogers, "The Computation and Use of the Asymptotic Covariance Matrix for Measurement Error Models," Internal Report 89-4102, Applied and Computational Mathematics Division, National Institute of Standards and Technology, Gaithersburg, MD, 1990.

Appendix G – Verification and Validation Studies

Introduction

The FAVOR code has been subjected to both internal ORNL and external independent verification and validation studies throughout its development lifecycle. The procedures and processes that have been used to ensure that FAVOR meets its software requirements are summarized below.

ORNL Internal Procedures and Controls: At the time of its initial release in 2001, FAVOR was being developed under the aegis of the Software Quality Assurance (SQA) program at ORNL. Subsequent releases of FAVOR were subjected to periodic internal SQA audits; in all cases, the FAVOR code was judged to be in compliance with ORNL SQA procedures and requirements. As the ORNL consensus standard, the Laboratory's SQA Program is registered to and compliant with the ISO 9001:2008 standard. In 2012, a formal ORNL SQA exemption[21] was granted to FAVOR due to the fact that the FAVOR software was being developed and maintained with funding from the US NRC. The NRC support required that FAVOR be compliant with the terms and conditions of NRC Management Directive 11.7 [G12], which requires that all software development, modification, or maintenance follow the general guidance provided in NUREG/BR-0167 [G13]. ASME Guides and Standards for Verification and Validation (V&V) studies [G14-G15] and other references [G16-G17] have provided more specific guidance (specific to scientific computing applications) during the development of FAVOR.

Previous Verification and Validation Studies: A comprehensive listing of reports and papers covering the history of verification and validation efforts for FAVOR, up to v12.1, is presented in Table G1. This list includes both internal studies carried out by the FAVOR development team at ORNL and external studies performed by independent subject-matter experts in the field of structural integrity assessments with specialization in the requirements of nuclear reactor power plant components.

Verification Studies of Inside Surface-Breaking Flaw Models: As part of the development of the FAVOR, v15.3, release, the entire FAVOR database of SIFIC(s) for infinite axial and 360° continuous circumferential internal surface-breaking flaws, was regenerated using the same scheme employed for finite-length, semi-elliptical internal surface-breaking flaws. See

[21] An exemption from the ORNL SQA Process can be granted, as stated in the ORNL Software Quality Assurance Exemptions Exhibit 3, to "software that is developed for a non-DOE application in accordance with the sponsor's SQA requirements."

Section 5.1.3.2 for a detailed description of that methodology which explicitly models the clad layer. The revised SIFIC database is given in Tables B38 – B41 of Appendix B of this report. Motivation for this change is due to the fact that the original SIFIC database for infinite axial and 360° continuous circumferential internal surface-breaking flaws was generated in the early 1980s using a technique that did not explicitly account for the effects of cladding. The revised SIFIC database now includes cladding effects for infinite flaws that are consistent with the technique used for finite-length flaws.

Closed-form curve fits based on tabular influence coefficient data from API 579-1/ASME FFS-1 (2007 edition) [G1] for both infinite and finite axial flaws and 360° continuous and finite circumferential flaws (base material only[22]) were developed by the ASME Working Group on Flaw Evaluation (WGFE) for the ASME Boiler and Pressure Vessel Code 2015 (BPVC), Section XI, Appendix A, Article A-3000, *Method of K_I Determination*, Subsections A-3531 and A-3550 [G2]. These curve fits [G3, G4] were implemented into the FAVLoad , v15.3, release. In addition, a new Fortran subroutine (*get_A3000_SIFICs*) was developed and installed in the FAVLoad code, where the required inputs are the R_i/t ratio for the RPV under study, the flaw orientation (*axial* or *circumferential*) , and an array of normalized flaw depths, a/t. The subroutine returns an array of SIFIC(s) corresponding to the input array of a/t values, where R_i is the inner radius of the RPV, t is the wall thickness of the RPV (at the beltline and inclusive of the cladding layer), and a is the flaw depth relative to the inside surface of the RPV.

These curve fits have the following form (using the notational conventions of ref. [G2]):

For both axial and circumferential orientations, the Mode I stress intensity factor, K_I , is

$$K_I = \sum_{j=0}^{4} A_j G_j \left(\frac{\pi a}{Q} \right)^{1/2} \tag{G1}$$

where

a = crack depth

G_j = stress-intensity influence coefficients (SIFIC(s)) for base material (ferritic steel)

Q = flaw shape parameter = $\Phi - q_y$

[22] Including the effects of the stainless steel cladding requires the separate determination of SIFIC(s) for the cladding layer. The A-3000 solutions do not address this bi-material effect.

$\Phi = 1 + 4.593(a/\ell)^{1.65}$, where $\ell = 2c$ = flaw length and ($\Phi = 1$ for infinite flaws)

q_y = the plastic zone correction factor (= 0; not used in FAVOR)

A_j = coefficients of a polynomial representation of the opening mode stress distribution across the crack face (= *hoop stress* profile for axial flaw orientation; = *axial stress* profile for circumferential flaw orientation) of the form

$$\sigma(x) = A_0 + A_1\left(\frac{x}{a}\right) + A_2\left(\frac{x}{a}\right)^2 + A_3\left(\frac{x}{a}\right)^3 + A_4\left(\frac{x}{a}\right)^4 \qquad \text{(G2)}$$

where x is the distance from the inside surface of the vessel with positive moving towards the crack tip. In FAVOR, a cubic polynomial, rather than the quartic polynomial of Eq. (G2), is fitted to the stress distribution; therefore, the coefficient $A_4 \equiv 0$.

As discussed in ref. [G3], the G_j coefficients represent uniform, linear, quadratic, and cubic stress terms for the distribution of stress acting on the opening Mode I of the flaw crack face. The tabular SIFIC data available in ref. [G1] are the source for these curve fits. Only the G_0 and G_1 SIFIC terms were fitted; the remaining G_2 and G_3 SIFIC(s) were obtained using the weight function approach described in ref. [G5]. For the crack front at the deepest point in the through-thickness direction, the G_j coefficients are given by

$$\begin{aligned} G_0 &= Y_0 \\ G_1 &= Y_1 \\ G_2 &= \frac{2}{35}\frac{\sqrt{2\Phi}}{\pi} - \frac{1}{6}Y_0 + Y_1 \\ G_3 &= \frac{52}{525}\frac{\sqrt{2\Phi}}{\pi} - \frac{1}{5}Y_0 + \frac{9}{10}Y_1 \end{aligned} \qquad \text{(G3)}$$

Infinite Axial Flaws – Inside Surface

For infinite axial inside surface flaws, the Y_0 and Y_1 coefficients (G_2 and G_3 follow from Eqs. G3) are:

$$Y_0 = a_0 + a_1\left(\frac{a}{t}\right)^2 + a_2\left(\frac{a}{t}\right)^4 + a_3\left(\frac{a}{t}\right)^6$$

$$a_0 = 1.11 - 0.0415\left(\frac{t}{R_i}\right)^{0.5} + 1.168\left(\frac{t}{R_i}\right) - 4.428\left(\frac{t}{R_i}\right)^{1.5} + 6.129\left(\frac{t}{R_i}\right)^2 - 2.824\left(\frac{t}{R_i}\right)^{2.5}$$

$$a_1 = 7.258 - 1.375\left(\frac{t}{R_i}\right)^{0.5} - 83.04\left(\frac{t}{R_i}\right) + 322.75\left(\frac{t}{R_i}\right)^{1.5} - 457.5\left(\frac{t}{R_i}\right)^2 + 213.3\left(\frac{t}{R_i}\right)^{2.5}$$

$$a_2 = -13.591 - 1.834\left(\frac{t}{R_i}\right)^{0.5} + 804.6\left(\frac{t}{R_i}\right) - 3250.4\left(\frac{t}{R_i}\right)^{1.5} + 4543.5\left(\frac{t}{R_i}\right)^2 - 2083\left(\frac{t}{R_i}\right)^{2.5}$$

$$a_3 = 44.5 + 12.85\left(\frac{t}{R_i}\right)^{0.5} - 1845\left(\frac{t}{R_i}\right) + 6778.6\left(\frac{t}{R_i}\right)^{1.5} - 8987\left(\frac{t}{R_i}\right)^2 + 3996.8\left(\frac{t}{R_i}\right)^{2.5}$$

$$Y_1 = b_0 + b_1\left(\frac{a}{t}\right)^2 + b_2\left(\frac{a}{t}\right)^4 + b_3\left(\frac{a}{t}\right)^6$$

$$b_0 = 0.679 - 0.0274\left(\frac{t}{R_i}\right)^{0.5} + 0.499\left(\frac{t}{R_i}\right) - 1.839\left(\frac{t}{R_i}\right)^{1.5} + 2.548\left(\frac{t}{R_i}\right)^2 - 1.183\left(\frac{t}{R_i}\right)^{2.5}$$

$$b_1 = 2.759 - 0.781\left(\frac{t}{R_i}\right)^{0.5} - 26.71\left(\frac{t}{R_i}\right) + 105.95\left(\frac{t}{R_i}\right)^{1.5} - 152.22\left(\frac{t}{R_i}\right)^2 + 71.523\left(\frac{t}{R_i}\right)^{2.5}$$

$$b_2 = -4.828 + 0.182\left(\frac{t}{R_i}\right)^{0.5} + 271.78\left(\frac{t}{R_i}\right) - 1116.1\left(\frac{t}{R_i}\right)^{1.5} + 1574.3\left(\frac{t}{R_i}\right)^2 - 725.55\left(\frac{t}{R_i}\right)^{2.5}$$

$$b_3 = 15.4 + 4.297\left(\frac{t}{R_i}\right)^{0.5} - 638.3\left(\frac{t}{R_i}\right) + 2362.4\left(\frac{t}{R_i}\right)^{1.5} - 3147.7\left(\frac{t}{R_i}\right)^2 + 1404.4\left(\frac{t}{R_i}\right)^{2.5}$$

(G4)

Finite Semi-Elliptical Axial Flaws – Inside Surface

Reference G4 presents curve fits for finite axial semi-elliptical surface flaws (see Fig. G1) for a selected range of (R_i/t) values. To provide a suitable range for FAVOR to interpolate over (t / R_i), the curve fits for (R_i/t = 5, 10, 20, and 60) were implemented into FAVOR, v15.3.

$R_i/t = 5$ for Point 1 (deepest point)

$$Y_0 = a_0 + a_1\left(\frac{a}{t}\right)^{0.5} + a_2\left(\frac{a}{t}\right) + a_3\left(\frac{a}{t}\right)^3$$

$$a_0 = 1.153 - 0.8897\left(\frac{a}{c}\right) + 2.387\left(\frac{a}{c}\right)^{1.5} - 2.599\left(\frac{a}{c}\right)^2 + 0.9924\left(\frac{a}{c}\right)^{2.5}$$

$$a_1 = -1.145 + 2.549\left(\frac{a}{c}\right) + 8.51\left(\frac{a}{c}\right)^{1.5} - 22.05\left(\frac{a}{c}\right)^2 + 12.11\left(\frac{a}{c}\right)^{2.5}$$

$$a_2 = 3.402 - 20.3\left(\frac{a}{c}\right) + 20.23\left(\frac{a}{c}\right)^{1.5} + 8.67\left(\frac{a}{c}\right)^2 - 11.96\left(\frac{a}{c}\right)^{2.5}$$

$$a_3 = 3.229 - 42.71\left(\frac{a}{c}\right) + 106.7\left(\frac{a}{c}\right)^{1.5} - 102.7\left(\frac{a}{c}\right)^2 + 35.59\left(\frac{a}{c}\right)^{2.5}$$

$$Y_1 = b_0 + b_1\left(\frac{a}{t}\right)^{0.5} + b_2\left(\frac{a}{t}\right) + b_3\left(\frac{a}{t}\right)^{2.5}$$

$$b_0 = 0.7026 - 0.4167\left(\frac{a}{c}\right) + 4.042\left(\frac{a}{c}\right)^2 - 6.903\left(\frac{a}{c}\right)^{2.5} + 3.315\left(\frac{a}{c}\right)^3$$

$$b_1 = -0.449 + 4.929\left(\frac{a}{c}\right) - 44.82\left(\frac{a}{c}\right)^2 + 78.85\left(\frac{a}{c}\right)^{2.5} - 38.55\left(\frac{a}{c}\right)^3$$

$$b_2 = 1.197 - 13.08\left(\frac{a}{c}\right) + 105.2\left(\frac{a}{c}\right)^2 - 178.9\left(\frac{a}{c}\right)^{2.5} + 85.61\left(\frac{a}{c}\right)^3$$

$$b_3 = 1.082 - 3.018\left(\frac{a}{c}\right) - 13.75\left(\frac{a}{c}\right)^2 + 41.33\left(\frac{a}{c}\right)^{2.5} - 25.56\left(\frac{a}{c}\right)^3$$

(G5)

$R_i/t = 10$ for Point 1 (deepest point)

$$Y_0 = a_0 + a_1\left(\frac{a}{t}\right)^{0.5} + a_2\left(\frac{a}{t}\right) + a_3\left(\frac{a}{t}\right)^3$$

$$a_0 = 1.168 - 0.2108\left(\frac{a}{c}\right)^{0.5} + 0.1971\left(\frac{a}{c}\right) - 0.1101\left(\frac{a}{c}\right)^{1.5}$$

$$a_1 = -0.4291 - 3.247\left(\frac{a}{c}\right)^{0.5} + 8.116\left(\frac{a}{c}\right) - 4.495\left(\frac{a}{c}\right)^{1.5}$$

$$a_2 = 2.014 + 4.155\left(\frac{a}{c}\right)^{0.5} - 15.41\left(\frac{a}{c}\right) + 9.366\left(\frac{a}{c}\right)^{1.5}$$

$$a_3 = 10.13 - 44.04\left(\frac{a}{c}\right)^{0.5} + 61.87\left(\frac{a}{c}\right) - 27.94\left(\frac{a}{c}\right)^{1.5}$$

$$Y_1 = b_0 + b_1\left(\frac{a}{t}\right)^{0.5} + b_2\left(\frac{a}{t}\right)^{1.5} + b_3\left(\frac{a}{t}\right)^3$$

$$b_0 = 0.7019 - 0.4004\left(\frac{a}{c}\right) + 3.861\left(\frac{a}{c}\right)^2 - 6.577\left(\frac{a}{c}\right)^{2.5} + 3.155\left(\frac{a}{c}\right)^3$$

$$b_1 = -0.07093 - 0.6874\left(\frac{a}{c}\right) + 4.366\left(\frac{a}{c}\right)^2 - 6.056\left(\frac{a}{c}\right)^{2.5} + 2.402\left(\frac{a}{c}\right)^3$$

$$b_2 = 0.9797 - 1.272\left(\frac{a}{c}\right) - 11.49\left(\frac{a}{c}\right)^2 + 26.1\left(\frac{a}{c}\right)^{2.5} - 14.23\left(\frac{a}{c}\right)^3$$

$$b_3 = 1.843 - 27.52\left(\frac{a}{c}\right) + 216.9\left(\frac{a}{c}\right)^2 - 356.8\left(\frac{a}{c}\right)^{2.5} + 165.6\left(\frac{a}{c}\right)^3$$

(G6)

$R_i/t = 20$ for Point 1 (deepest point)

$$Y_0 = a_0 + a_1\left(\frac{a}{t}\right)^{0.5} + a_2\left(\frac{a}{t}\right)^{1.5} + a_3\left(\frac{a}{t}\right)^{3}$$

$$a_0 = 1.163 - 0.1762\left(\frac{a}{c}\right)^{0.5} + 0.1056\left(\frac{a}{c}\right) - 0.05611\left(\frac{a}{c}\right)^{2} + 0.007524\left(\frac{a}{c}\right)^{3}$$

$$a_1 = 0.99 - 8.514\left(\frac{a}{c}\right)^{0.5} + 15.29\left(\frac{a}{c}\right) - 14.25\left(\frac{a}{c}\right)^{2} + 6.454\left(\frac{a}{c}\right)^{3}$$

$$a_2 = -2.719 + 37.71\left(\frac{a}{c}\right)^{0.5} - 74.55\left(\frac{a}{c}\right) + 72.88\left(\frac{a}{c}\right)^{2} - 33.16\left(\frac{a}{c}\right)^{3}$$

$$a_3 = 18.38 - 104.3\left(\frac{a}{c}\right)^{0.5} + 163.2\left(\frac{a}{c}\right) - 135.3\left(\frac{a}{c}\right)^{2} + 57.98\left(\frac{a}{c}\right)^{3}$$

$$Y_1 = b_0 + b_1\left(\frac{a}{t}\right)^{0.5} + b_2\left(\frac{a}{t}\right) + b_3\left(\frac{a}{t}\right)^{1.5}$$

$$b_0 = 0.7049 - 0.7887\left(\frac{a}{c}\right) + 2.51\left(\frac{a}{c}\right)^{1.5} - 2.307\left(\frac{a}{c}\right)^{2} + 0.6204\left(\frac{a}{c}\right)^{3}$$

$$b_1 = 2.656 - 81.49\left(\frac{a}{c}\right) + 239.75\left(\frac{a}{c}\right)^{1.5} - 214.34\left(\frac{a}{c}\right)^{2} + 53.38\left(\frac{a}{c}\right)^{3}$$

$$b_2 = -10.51 + 308.34\left(\frac{a}{c}\right) - 909.47\left(\frac{a}{c}\right)^{1.5} + 815.64\left(\frac{a}{c}\right)^{2} - 204.02\left(\frac{a}{c}\right)^{3}$$

$$b_3 = 11.22 - 295.96\left(\frac{a}{c}\right) + 862\left(\frac{a}{c}\right)^{1.5} - 768.1\left(\frac{a}{c}\right)^{2} + 190.97\left(\frac{a}{c}\right)^{3}$$

(G7)

$R_i/t = 60$ for Point 1 (deepest point)

$$Y_0 = a_0 + a_1\left(\frac{a}{t}\right) + a_2\left(\frac{a}{t}\right)^{1.5} + a_3\left(\frac{a}{t}\right)^{2.5}$$

$$a_0 = 1.094 + 0.01\left(\frac{a}{c}\right)^{-0.5} - 0.06\left(\frac{a}{c}\right)$$

$$a_1 = 3.383 - 0.004\left(\frac{a}{c}\right)^{-2} + 0.723\left(\frac{a}{c}\right)^{-1} - 3.757\left(\frac{a}{c}\right)^{-0.5} - 0.527\left(\frac{a}{c}\right)$$

$$a_2 = -11.13 + 0.012\left(\frac{a}{c}\right)^{-2} - 2.136\left(\frac{a}{c}\right)^{-1} + 11.4\left(\frac{a}{c}\right)^{-0.5} + 2.346\left(\frac{a}{c}\right)$$

$$a_3 = 8.249 - 0.012\left(\frac{a}{c}\right)^{-2} + 1.891\left(\frac{a}{c}\right)^{-1} - 8.503\left(\frac{a}{c}\right)^{-0.5} - 1.88\left(\frac{a}{c}\right)$$

$$Y_1 = b_0 + b_1\left(\frac{a}{t}\right)^{0.5} + b_2\left(\frac{a}{t}\right)^{1.5} + b_3\left(\frac{a}{t}\right)^{3}$$

$$b_0 = 0.67 + 0.004\left(\frac{a}{c}\right)^{-0.5} + 0.066\left(\frac{a}{c}\right)^{1.5}$$

$$b_1 = -0.047 + 0.016\left(\frac{a}{c}\right)^{-1} - 0.084\left(\frac{a}{c}\right)^{-0.5} + 0.068\left(\frac{a}{c}\right)^{1.5}$$

$$b_2 = -0.654 - 0.127\left(\frac{a}{c}\right)^{-1} + 0.942\left(\frac{a}{c}\right)^{-0.5} - 0.015\left(\frac{a}{c}\right)^{1.5}$$

$$b_3 = 0.309 + 0.164\left(\frac{a}{c}\right)^{-1} - 0.649\left(\frac{a}{c}\right)^{-0.5} + 0.129\left(\frac{a}{c}\right)^{1.5}$$

(G8)

360° Circumferential Flaws – Inside Surface

For 360° circumferential flaws, the Y_0 and Y_1 coefficients are, for $j = 0,1$; $0 \le a/t \le 0.8$; and $1 \le R_i/t \le 100$:

$$Y_j = m_1 + m_2\left(\frac{a}{t}\right) + m_3 \ln\left(\frac{R_i}{t}\right) + m_4\left(\frac{a}{t}\right)^2 + m_5\left(\ln\left(\frac{R_i}{t}\right)\right)^2 + m_6\left(\frac{a}{t}\right)\ln\left(\frac{R_i}{t}\right) + m_7\left(\frac{a}{t}\right)^3 + m_8\left(\ln\left(\frac{R_i}{t}\right)\right)^3 + m_9\left(\frac{a}{t}\right)\left(\ln\left(\frac{R_i}{t}\right)\right)^2 + m_{10}\left(\frac{a}{t}\right)^2 \ln\left(\frac{R_i}{t}\right) \quad \text{(G9)}$$

The m coefficients are presented in Table G2.

Finite Semi-Elliptical Circumferential Flaws – Inside Surface

Reference G3 presents curve fits for finite circumferential semi-elliptical surface flaws (see Fig. G2) for a selected range of (R_i/t) values. To provide a suitable range for FAVOR to interpolate over (t / R_i), the curve fits for (R_i/t = 5, 10, 20, and 60) were implemented into FAVOR, v15.3.

$R_i/t = 5$ for Point 1 (deepest point)

$$Y_0 = \frac{\left[m_1 + m_2\left(\frac{a}{t}\right) + m_3\left(\frac{a}{\ell}\right) + m_4\left(\frac{a}{\ell}\right)^2 + m_5\left(\frac{a}{\ell}\right)^3\right]}{\left[1 + m_6\left(\frac{a}{t}\right) + m_7\left(\frac{a}{\ell}\right) + m_8\left(\frac{a}{\ell}\right)^2 + m_9\left(\frac{a}{\ell}\right)^3\right]}$$

$$Y_1 = \frac{\left[m_1 + m_2\left(\frac{a}{t}\right) + m_3\left(\frac{a}{\ell}\right) + m_4\left(\frac{a}{\ell}\right)^2\right]}{\left[1 + m_5\left(\frac{a}{t}\right) + m_6\left(\frac{a}{\ell}\right)\right]} \quad \text{(G10)}$$

$R_i/t = 10$ for Point 1 (deepest point)

$$Y_0 = \frac{\left[m_1 + m_2\left(\frac{a}{t}\right) + m_3\left(\frac{a}{\ell}\right) + m_4\left(\frac{a}{\ell}\right)^2 + m_5\left(\frac{a}{\ell}\right)^3\right]}{\left[1 + m_6\left(\frac{a}{t}\right) + m_7\left(\frac{a}{\ell}\right) + m_8\left(\frac{a}{\ell}\right)^2 + m_9\left(\frac{a}{\ell}\right)^3\right]}$$

$$Y_1 = \frac{\left[m_1 + m_2\left(\frac{a}{t}\right) + m_3\left(\frac{a}{\ell}\right) + m_4\left(\frac{a}{\ell}\right)^2\right]}{\left[1 + m_5\left(\frac{a}{t}\right) + m_6\left(\frac{a}{\ell}\right)\right]} \quad \text{(G11)}$$

R_i/t = 20 for Point 1 (deepest point)

$$Y_0 = \frac{\left[m_1 + m_2\left(\frac{a}{t}\right) + m_3\left(\frac{a}{\ell}\right) + m_4\left(\frac{a}{\ell}\right)^2 + m_5\left(\frac{a}{\ell}\right)^3 \right]}{\left[1 + m_6\left(\frac{a}{t}\right) + m_7\left(\frac{a}{\ell}\right) + m_8\left(\frac{a}{\ell}\right)^2 \right]}$$

$$Y_1 = \frac{\left[m_1 + m_2\left(\frac{a}{t}\right) + m_3\left(\frac{a}{\ell}\right) + m_4\left(\frac{a}{\ell}\right)^2 \right]}{\left[1 + m_5\left(\frac{a}{t}\right) + m_6\left(\frac{a}{\ell}\right) \right]} \qquad \text{(G12)}$$

R_i/t = 60 for Point 1 (deepest point)

$$Y_0 = \frac{\left[m_1 + m_2\left(\frac{a}{t}\right) + m_3\left(\frac{a}{\ell}\right) + m_4\left(\frac{a}{\ell}\right)^2 + m_5\left(\frac{a}{\ell}\right)^3 \right]}{\left[1 + m_6\left(\frac{a}{t}\right) + m_7\left(\frac{a}{\ell}\right) + m_8\left(\frac{a}{\ell}\right)^2 \right]}$$

$$Y_1 = \frac{\left[m_1 + m_2\left(\frac{a}{t}\right) + m_3\left(\frac{a}{\ell}\right) + m_4\left(\frac{a}{\ell}\right)^2 \right]}{\left[1 + m_5\left(\frac{a}{t}\right) + m_6\left(\frac{a}{\ell}\right) \right]} \qquad \text{(G13)}$$

The *m* coefficients for Eqs. (G10)-(G13) are presented in Table G3.

Interpolating on (t/R_i)for Finite Semi-Elliptical Axial and Circumferential Flaws – Inside Surface

For both axial and circumferential finite semi-elliptical flaws, curve fits are available for discrete values of R_i/t = 5, 10, 20, and 60. To interpolate within this range of $5 \le R_i / t \le 60$, the recommended interpolant is (t / R_i). A monotone piecewise cubic Hermite interpolation scheme [G6-G8] has been implemented in FAVOR for this purpose. The following provides a summary of this procedure.

Monotone Piecewise Cubic Hermite Interpolation Algorithm

The procedure assumes that the data to be interpolated are at least locally monotone, either monotonically increasing or decreasing. Let $\pi : (t/R_i)_{\min} = x_1 < x_2 < \cdots < x_n = (t/R_i)_{\max}$ be a partition of the interval $I = \left[(t/R_i)_{\min}, (t/R_i)_{\max}\right]$, and let $\left\{ f_j : j = 1,2,\cdots,n \right\}$ be a given set of *monotone* data values ($Y_{0(j)}$ or $Y_{1(j)}$) at the partition points (knots); i.e., we assume that either $f_j \le f_{j+1}\left(j = 1,2,\cdots,n-1\right)$ or $f_j \ge f_{j+1}\left(j = 1,2,\cdots,n-1\right)$. Construct on π a piecewise cubic function $p(x) \in \mathbb{C}^1(I)$ such that

$$p(x_j) = f_j, \quad \text{where } j = 1, 2, \ldots, n \tag{G14}$$

and $p(x)$ is monotone. Within each subinterval $I_j = [x_j, x_{j+1}]$, $p(x)$ is a cubic polynomial represented by

$$p(x) = f_j H_1(x) + f_{j+1} H_2(x) + d_j H_3(x) + d_{j+1} H_4(x) \tag{G15}$$

where $d_k = p'(x_k)$, $k = j, j+1$ are the first derivatives of f at the knots, and $H_1(x)$, $H_2(x)$, $H_3(x)$, and $H_4(x)$ are cubic Hermite basis functions for the interval I_j with the form

$$\begin{aligned} H_1(x) &= \phi\left[\frac{x_{j+1} - x}{h_j}\right], \qquad H_2(x) = \phi\left[\frac{x - x_j}{h_j}\right], \\ H_3(x) &= -h_j\, \psi\left[\frac{x_{j+1} - x}{h_j}\right], \quad H_4(x) = h_j\, \psi\left[\frac{x - x_j}{h_j}\right], \end{aligned} \tag{G16}$$

where

$$\begin{aligned} h_j &= x_{j+1} - x_j \\ \phi(t) &= 3t^2 - 2t^3 \\ \psi(t) &= t^3 - t^2 \end{aligned}$$

A method for estimating the first derivatives, $d_k = p'(x_k)$, at the knots is given in ref. [G7]. Let $\Delta_j \equiv (f_{j+1} - f_j)/(x_{j+1} - x_j)$ and, as above, $h_j = x_{j+1} - x_j$, then

$$d_j = D(\Delta_{j-1}, \Delta_j, h_{j-1,}, h_j), \quad j = 1, \cdots, n-1 \tag{G17}$$

where the *D*-function is defined by

$$D(\Delta_{j-1}, \Delta_j, h_{j-1}, h_j) \equiv \begin{cases} \dfrac{\Delta_{j-1}\Delta_j}{\alpha\Delta_j + (1-\alpha)\Delta_{j-1}} & \text{if } \Delta_{j-1}\Delta_j > 0 \\ 0 & \text{otherwise,} \end{cases}$$

and (G18)

$$\alpha \equiv \frac{h_{j-1} + 2h_j}{3(h_{j-1} + h_j)}$$

The above algorithm has been coded into Fortran in the open source PCHIP [G6] numerical package, available from the *netlib.org* open-source software repository, and implemented into FAVOR.

Verification of the Implementation of A-3000 Curve Fits into FAVOR

Three stages of both unit and integrated testing of the implementation of Article A-3000 curve fits into FAVOR were applied in this verification study: **Stage 1**: comparison of FAVOR-calculated SIFIC(s) (G_0, G_1, G_2, G_3) using the A-3000 curve fits to corresponding tabulated values in ref. [G9] for the axial orientation and ref. [G2] for the circumferential orientation, **Stage 2**: comparison of the SIFIC(s) in the FAVOR SIFIC database to A-3000 calculated SIFIC(s), and **Stage 3**: comparison of FAVOR K_I time-history solutions to Abaqus solutions for a selected test matrix.

Stage 1: Comparison to Tabulated Values of SIFIC(s) (G_0, G_1, G_2, G_3) – Unit Tests

Reference [G9] presents values for axial SIFIC(s) (G_0, G_1, G_2, G_3) in Tables A-3650-1 to A-3650-8; SIFIC(s) for circumferential flaws are tabulated in Tables A-3630-1 to A-3630-8 in ref. [G2]. For the flaw geometries given in these tables, the corresponding FAVOR-generated SIFIC(s) were calculated by applying the A-3000 curve fits implemented into FAVLoad. The results of that comparison are presented in Table G4 for inside axially-oriented flaws and Table G5 for inside circumferentially-oriented flaws. These solutions are also presented graphically in Fig. G3(a) for axial flaws and in Fig. G3(b) for circumferential flaws. These comparisons indicate the FAVOR implementation matches the tabulated SIFIC values out to at least 3 significant figures.

Stage 2: Comparison of FAVOR SIFIC Database to A-3000 SIFIC(s) – Unit Tests

The influence coefficients, calculated by Eqs. (G3-G8), are compared in Figs. G4 – G6 to the SIFIC(s) independently calculated (using finite-element models) by the FAVOR development team at ORNL for the v15.3 release. In general, there is good agreement between the new ORNL SIFIC(s) and the influence coefficients calculated using the new A-3000 equations.

Stage 3: Benchmarking FAVOR K_I Time Histories to Independent Finite Element Solutions Using Abaqus, v6.14-1 [G10] – Integrated Tests

The benchmarking exercise comparing FAVOR K_I time histories to independent Abaqus solutions was based on the test case matrix shown in Table G6. Solutions for 27 cases were generated which cover a range of vessel curvature, (R_i/t), orientation (axial or circumferential), flaw aspect ratio ($2c/a$), normalized flaw depth, (a/t), cladding layer thickness, t_{clad}, and RPV wall thickness, t.

Figures of Merit for Stage 3 – RMSD and *Sup Norm* of the Percent Deviation from the Abaqus Solution

This study employs the root-mean-square deviation (RMSD) statistic as its primary *figure of merit*. The RMSD [G11] is a frequently applied measure of the differences between values predicted by a model or *estimator* and the values observed by a designated *exemplar* which produces the assumed standard solutions. For the purposes of this study, FAVOR plays the role of the *estimator*, and Abaqus, v16.4-1 [G10], represents the *exemplar*. The RMSD can be viewed as the sample standard deviation of the differences between the predicted and observed values. Serving to aggregate the errors in predictions for individual time steps into a single measure of predictive power that covers the complete transient, the RMSD is a good measure of accuracy when comparing different models for a particular variable but not between variables, because RMSD is scale-dependent. The variable for comparison in this study is the stress-intensity factor calculated at each time step in the transient. For a given transient, flaw type, flaw orientation, and vessel geometry, the RMSD produces a good quantitative measure of predictive accuracy when comparing solutions from FAVOR, v12.1, to solutions from FAVOR, v16.1, for a specific test case. Comparing the RMSD statistic between different cases should be done with caution, however, since due to its scale-dependency RMSD is a more *qualitative*, rather than a *quantitative*, measure when applied across the test matrix.

The starting point in the Stage 3 verification analysis is to calculate the percent deviation of the FAVOR K_I with respect to the Abaqus K_I for each time step, k, in the case transient ($\Delta K_{I(k)}$,see Eq. (G19)). These values are calculated for two versions of FAVOR, v12.1 and v16.1, within the same test case, where the transient loading, flaw size, orientation, and vessel geometry are fixed.

$$\Delta K_{I(k)} = \left(\frac{K_{I-Abaqus(k)} - K_{I-FAVOR(k)}}{K_{I-Abaqus(k)}} \right) \times 100\% \text{ for each time step } k \tag{G19}$$

These individual deviations are then combined for the full transient by applying Eq. (G20).

$$\text{RMSD} = \sqrt{\frac{\sum_{k=1}^{n} \Delta K_{I(k)}^2}{n}} \quad [\%] \; ; \; n = \text{ number of time steps} \tag{G20}$$

The results of this analysis will be two statistics for each test case: $\text{RMSD}_{\text{v12.1}}$ and $\text{RMSD}_{\text{v16.1}}$.

The second figure of merit in this study is the *sup norm*, $\|\Delta K_I\|_\infty$, (also known as the supremum, infinity, uniform, or max norm) of the percent deviation of FAVOR from the Abaqus K_I solution. This statistic is defined by

$$\|\Delta K_I\|_\infty = \max\left(\left|\Delta K_{I(1)}\right|, \left|\Delta K_{I(2)}\right|, \ldots, \left|\Delta K_{I(n)}\right|\right);\ n = \text{ number of time steps} \tag{G21}$$

As for the RMSD, two statistics will be calculated for each case: $\|\Delta K_I\|_{\infty(\text{v12.1})}$ and $\|\Delta K_I\|_{\infty(\text{v16.1})}$.

Model Geometries and Transient Conditions

Table G6 and Figs. G7 – G11 present the model types, flaw orientations, flaw geometries, and vessel geometries for the 2D and 3D models employed in this study. The applied temperature and pressure histories for three cool-down transients are given in Fig. G12. The thermal-hydraulic conditions for the two PTS transients used in the study are described in Figs. G13-G15.

Results and Conclusions

As a qualitative measure of predictive accuracy, the RMSD and $\|\Delta K_I\|_\infty$ statistics for the 27 cases in the Test Matrix are presented for both circumferential and axial orientations in Table G6. For very shallow flaws ($a/t < 0.05$), the solutions from FAVOR, v16.1, appear to demonstrate an improvement in predictive accuracy relative to FAVOR, v12.1; however, the cautionary notice concerning comparing results across the test matrix is still in effect. These results should, when combined with a visual inspection of the plotted results for each case, be viewed as approximate and qualitative.

The individual solutions for the 27 cases in the test matrix are given in Figs. G17-G29. For both the RMSD and $\|\Delta K_I\|_\infty$ statistics, a smaller value indicates a higher degree of predictive accuracy.

The primary objective of the effort to expand and rework FAVOR's inside surface-breaking flaw models (finite and infinite flaws with axial and circumferential orientations) was to improve the predictive accuracy of the applied stress-intensity factor calculations for very shallow flaws, where in prior releases of FAVOR (up to and including v12.1) cladding effects had not been explicitly addressed for infinite flaws. The results of this exercise, with accompanying verification calculations, indicate that this objective has been met.

The decision was taken by the FAVOR development team to implement the A-3000 curve fits in FAVOR and apply them to finite and infinite axial and finite and 360° circumferential inside surface-breaking flaws for the base material SIFIC(s). This decision was driven by the added-value provided for FAVOR of having access to closed-form solutions that are functions of flaw

orientation (axial or circumferential), normalized flaw depth, a/t, and normalized vessel curvature, R_i/t, for infinite flaws. For finite semi-elliptical flaws, curve fits are available at discrete values of R_i/t as functions of flaw orientation (axial or circumferential), normalized flaw depth, a/t, and aspect ratio, $2c/a = \ell/a$. These A-3000 equations remove the need to carry out interpolations within the FAVOR SIFIC database for the base material influence coefficients. The requirement to interpolate within the look-up tables for the cladding SIFIC(s), however, remains.

In FAVOR, v16.1, additional work was carried out to improve the internal consistency of the cladding SIFIC(s) for finite internal semi-elliptical flaws. The emphasis was placed on very shallow flaws with normalized flaw depths of $a/t < 0.2$.

References for Appendix G

G1. API 579-1/ASME FFS-1 (API 579 Second Edition) *American Petroleum Institute Practice 579 Fitness-for-Service*, June 5, 2007 (Joint standard with ASME).

G2. *American Society of Mechanical Engineers Boiler and Pressure Vessel Code,* Section XI, Rules for Inservice Inspection of Nuclear Power Plant Components, Nonmandatory Appendix A, Analysis of Flaws, Article A-3000, Method for K_I Determination, American Society of Mechanical Engineers, New York, 2015.

G3. R.C. Cipolla and D.R. Lee, "Stress Intensity Factor Coefficients for Circumferential ID Surface Flaws in Cylinders for Appendix A of ASME Section XI", PVP2013-97734, *Proceedings of the ASME 2013 Pressure Vessels and Piping Conference*, July 14-18, 2013, Paris, France.

G4. S.X. Xu, D.A. Scarth, R.C. Cipolla, and D.R. Lee, "Closed-Form Relations for Stress Intensity Factor Influence Coefficients for Axial ID Surface Flaws in Cylinders for Appendix A of ASME Section XI", PVP2014-28222, *Proceedings of the ASME 2014 Pressure Vessels and Piping Conference*, July 20-24, 2014, Anaheim, California.

G5. R.C. Cipolla and D.R. Lee, "Technical Basis for Equations for Stress Intensity Factor Coefficients in ASME Section XI Appendix A," *Proceedings of the ASME 2004 Pressure Vessels and Piping Conference*, July 25-29, 2004, San Diego, California, Vol. 480, pp. 301-312.

G6. F. N. Fritsch, "PCHIP – Piecewise Cubic Hermite Interpolation – SLATEC Package," LLNL, 1992, obtained from *netlib.org* open-source numerical library.

G7. F. N. Fritsch and R. E. Carlson, "Monotone Piecewise Cubic Interpolation," *SIAM J. Numer. Anal.* **17**(2), (1980) 238-246.

G8. F. N. Fritsch and J. Butland, "A Method for Constructing Local Monotone Piecewise Cubic Interpolants," *SIAM J. Sci. Stat. Comput.* **5**(2), (1984) 300-304.

G9. S. Xu, D.R. Lee, D.A. Scarth, R.C. Cipolla, "Proposed Axial ID Flaw Equations for Implementation into Article A-3000 Rewrite," Record 14-1546, Rev. 1, January 27, 2015.

G10. *ABAQUS, Version 6.14-1,* Dassault Systemes Simulia Corp., Providence, RI, 2015.

G11. R. J. Hyndman and A. B. Koehler "Another Look at Measures of Forecast Accuracy," *International Journal of Forecasting* **22** (4), (2006) 679-688.

G12. Management Directive 11.7, "NRC Procedures for Placement and Monitoring of Work With the U.S. Department of Energy (DOE)," Part Xl, "Standard Terms and Conditions, Software Development, Page X1-18," U.S. Nuclear Regulatory Commission, Washington, February 17, 2000.

G13. NUREG/BR-0167, "Software Quality Assurance Program and Guidelines," U.S. Nuclear Regulatory Commission, Washington, February 1993.

G14. ASME, 2006, *Guide for Verification and Validation in Computational Solid Mechanics*, ASME V&V 10-2006, The American Society of Mechanical Engineers, New York, NY.

G15. ASME, 2009, *Standard for Verification and Validation in Computational Fluid Dynamics and Heat Transfer*, ASME V&V 20-2009, The American Society of Mechanical Engineers, New York, NY.

G16. P.J. Roache, *Fundamentals of Verification and Validation in Computational Science and Engineering*, Hermosa Publishers, Albuquerque, NM, 2009.

G17. W.L. Oberkampf and C.J. Roy, *Verification and Validation in Scientific Computing*, Cambridge University Press, 2010.

Table G1. Historical FAVOR Verification and Validation Studies

Year	Citation Title / Conference	Authors	Report No.	Comments
1995	Validation of FAVOR Code Linear Elastic Fracture Solutions for Finite-Length Flaw Geometries	T.L. Dickson	PVP-Vol. 304	Early study of surface-
	Fatigue and Fracture Mechanics in Pressure Vessels and Piping			breaking flaws
1999	Comparison of Embedded-Flaw K_I-Factors: FAVOR Implementation of ASME	B.R. Bass, et al.	ORNL/NRC/LTR-99/264	Embedded flaws
	Section XI-Appendix A Methodology versus Three-Dimensional Finite Element Solutions			initial verification
2000	Verification of a Linear-Elastic Fracture Methodology for Postulated Flaws Embedded	T.L. Dickson, B.R. Bass,	PVP-Vol. 403	Embedded flaws
	Embedded in the Wall of a Nuclear Reactor Pressure Vessel	P.T. Williams		verification study
	Severe Accidents and Other Topics in RPV Design, Proceedings of the ASME			
	Pressure Vessels and Piping Conference, pp. 145-151			
2001	A Comparison of Fracture Mechanics Methodologies for Postulated Flaws Embedded in the	T.L. Dickson, B.R. Bass,	PVP-Vol. 430	Embedded flaws
	Wall of a Nuclear Reactor Pressure Vessel	P.T. Williams		verification study
	Pressure Vessel and Piping Design Analysis, pp. 277-284			
2003	INNEL Test Activities - Task II (A) and (B) - Validation of Embrittlement Parameter Sampling	C. Gentillon, D. Knudson,	INNEL Letter Report	verification study
		W. Gaylean		of parameter sampling
2003	Materials Reliability Program: Validation and Verification of FAVOR, v02.4 (MRP-90)	R. Gamble, B. Bishop	EPRI Report 1007826	statistical sampling
	PFM Computational Algorithms and Associated Sampled Variables			verification study
2004	Verification and Validation of the FAVOR Code – Deterministic Load Variables	B.R. Bass, T.L. Dickson,	ORNL/NRC/LTR-4/11	Full verification study
		P.T. Williams, A.-V. Phan,		of deterministic solutions
		K.L. Kruse		
2004	Validation of the Treatment of Flaw Related Inputs by the FAVOR Code	F. Simonen	PNNL Letter Report	verification study
2004	INEEL Test Activities: Validation of Unirradiated Upper-Shelf Energy Embrittlement	C. Gentillon, D. Knudson,	INNEL Letter Report	statistical sampling
	Parameter Sampling	W. Gaylean		verification study
2004	Materials Reliability Program: Validation and Verification of FAVOR, v03.1 (MRP-125)	R. Gamble, B. Bishop	EPRI Report 101953	statistical sampling
	PFM Computational Algorithms and Associated Sampled Variables (MRP-125)			verification study
2004	FAVOR Code Versions 2.4 and 3.1, Verification and Validation Summary Reports	S.N.M. Malik	NUREG-1795	summary
2004	Assessment of Large-Scale Pressurized Thermal Shock Experiments Using the	T.L. Dickson,	PVP-Vol.481	validation study with
	FAVOR Fracture Mechanics Code	M.T. EricksonKirk		experimental data
	RPV Integrity and Fracture Mechanics, pp. 31-37			
2009	Stress Intensity Factor Influence Coefficients for External Surface Flaws in	S. Yin, T.L. Dickson,	PVP2009-77143	verification study
	Boiling Water Reactor Pressure Vessels	P.T. Williams, B.R. Bass		of external surface-
	Proceedings of 2009 ASME Pressure Vessels and Piping Conference			breaking flaws
2009	A Generalization of the FAVOR Code to Include BWR Geometries and Heat-Up Transients	T.L. Dickson, S. Yin,	PVP2009-77106	verification study
	Proceedings of 2009 ASME Pressure Vessels and Piping Conference	P.T. Williams		
2010	Verification of New Capabilities of Deterministic Load Module of FAVOR 09.1	S. Yin, T.L. Dickson,	PVP2010-25439	verification study
	Proceedings of PVP2010: 2010 ASME Pressure Vessels and Piping Conference	P.T. Williams, B.R. Bass		
2010	Sensitivity Studies of the Probabilistic Fracture Mechanics Model Used in FAVOR	M. EricksonKirk, T. Dickson,	NUREG-1808	verification study
		T. Mintz, F. Simonen		statistical sampling
2011	Verification and Validation of the FAVOR Version 09.1 Code	T. Wilt, G. Adams,	SwRI Report	Full V&V Study
	Center for Nuclear Waste Regulatory Analyses, San Antonio, Texas	F. Simonen		

Table G2. Coefficients for 360° Circumferential Inside Surface Flaw Equation

Coefficients	Y_0	Y_1
m_1	1.07130E+00	6.48814E-01
m_2	1.52135E-01	1.75457E-01
m_3	9.77012E-02	4.34760E-02
m_4	-3.35553E-01	-3.58231E-01
m_5	-2.14289E-02	-8.42949E-03
m_6	-3.46308E-01	-1.40864E-01
m_7	9.51292E-01	6.06585E-01
m_8	-1.20085E-05	-1.54100E-04
m_9	8.99698E-02	3.65687E-02
m_{10}	1.00469E+00	3.46561E-01

Table G3. Coefficients for Finite Semi-Elliptical Circumferential Inside Surface Flaw Equations

Coefficients	$R_i/t = 1$		$R_i/t = 3$		$R_i/t = 5$		$R_i/t = 10$	
	Y_0	Y_1	Y_0	Y_1	Y_0	Y_1	Y_0	Y_1
m_1	1.10889E+00	6.85352E-01	1.15125E+00	6.98772E-01	1.11343E+00	7.09517E-01	1.09199E+00	6.91614E-01
m_2	-1.25394E+00	-1.50548E-01	-8.82425E-01	-6.58620E-01	-4.57201E-01	-5.50839E-01	-6.34066E-02	-3.74200E-01
m_3	5.97485E-01	-1.72245E-01	1.93364E-01	1.79846E-01	6.41084E-01	1.06038E+00	3.93480E+00	2.51851E+00
m_4	4.86147E-01	7.36887E-02	2.03438E+00	1.28738E+00	3.30691E+01	9.68824E-01	4.07522E+01	1.07367E+00
m_5	2.89649E-01	1.40103E+00	5.18324E-01	9.94781E-01	-5.29889E-01	-1.00092E+00	-6.35645E+01	-9.25019E-01
m_6	-9.07933E-01	-3.15954E-01	-9.75983E-01	-9.79754E-01	-8.75031E-01	2.16603E+00	-8.17658E-01	4.24183E+00
m_7	6.68014E-01	7.86514E-01	2.46237E+00	2.42710E+00	8.80344E-01	NA	3.75120E+00	NA
m_8	NA	-1.69966E+00	NA	NA	3.08549E+01	NA	3.83982E+01	NA
m_9	NA	1.63055E+00	NA	NA	-4.89480E-01	NA	-5.79021E+01	NA
m_{10}	NA	-1.23433E+00	NA	NA	NA	NA	NA	NA

Coefficients	$R_i/t = 20$		$R_i/t = 60$		$R_i/t = 100$	
	Y_0	Y_1	Y_0	Y_1	Y_0	Y_1
m_1	1.09357E+00	6.96626E-01	1.08043E+00	6.88471E-01	1.06719E+00	6.93887E-01
m_2	1.84693E-01	-2.54857E-01	3.80354E-01	-1.82010E-01	5.05303E-01	-1.76885E-01
m_3	6.31565E+00	3.73189E+00	7.18740E+00	5.48211E+00	7.55482E+00	4.35984E+00
m_4	2.04554E+01	1.59309E+00	3.56638E+01	1.19796E+00	1.14005E+01	2.93971E+00
m_5	-2.07996E-01	-8.84114E-01	-6.37988E+00	-9.14096E-01	-8.73938E-01	-9.21967E-01
m_6	-8.22268E-01	6.28557E+00	-8.76588E-01	8.48290E+00	7.40188E+00	7.23332E+00
m_7	6.21895E+00	NA	7.07112E+00	NA	1.19984E+01	1.88388E+00
m_8	1.99526E+01	NA	3.15701E+01	NA	NA	NA
m_9	NA	NA	NA	NA	NA	NA
m_{10}	NA	NA	NA	NA	NA	NA

Table G4. Benchmarking the FAVOR Implementation of A-3000 Curve Fits for Axial Surface-Breaking Flaws

Flaw Geometry						FAVOR Implementation A-3000				ASME BPVC Tabulated SIFIC(s)				A-3000
2c/a	orient.	a	t	R/t	a/t	G0	G1	G2	G3	G0	G1	G2	G3	Tables
2	axial	0	8.5	5	0	1.044	0.740	0.606	0.527	1.044	0.740	0.606	0.527	A-3650-3
2	axial	1.7	8.5	5	0.2	1.041	0.729	0.596	0.518	1.041	0.729	0.596	0.518	A-3650-3
2	axial	3.4	8.5	5	0.4	1.051	0.734	0.599	0.520	1.051	0.734	0.599	0.520	A-3650-3
2	axial	5.1	8.5	5	0.6	1.072	0.749	0.610	0.529	1.072	0.749	0.610	0.529	A-3650-3
2	axial	6.8	8.5	5	0.8	1.110	0.774	0.629	0.544	1.110	0.774	0.629	0.544	A-3650-3
2	axial	0	8.5	10	0	1.044	0.741	0.607	0.528	1.044	0.741	0.607	0.528	A-3650-5
2	axial	1.7	8.5	10	0.2	1.045	0.728	0.594	0.516	1.045	0.728	0.594	0.516	A-3650-5
2	axial	3.4	8.5	10	0.4	1.061	0.735	0.599	0.519	1.061	0.735	0.599	0.519	A-3650-5
2	axial	5.1	8.5	10	0.6	1.081	0.750	0.611	0.529	1.081	0.750	0.611	0.529	A-3650-5
2	axial	6.8	8.5	10	0.8	1.105	0.774	0.630	0.545	1.105	0.774	0.630	0.545	A-3650-5
2	axial	0	8.5	20	0	1.044	0.740	0.606	0.527	1.044	0.740	0.606	0.527	A-3650-7
2	axial	1.7	8.5	20	0.2	1.045	0.728	0.594	0.516	1.044	0.728	0.594	0.516	A-3650-7
2	axial	3.4	8.5	20	0.4	1.063	0.737	0.600	0.520	1.063	0.737	0.600	0.520	A-3650-7
2	axial	5.1	8.5	20	0.6	1.087	0.754	0.613	0.531	1.087	0.754	0.613	0.531	A-3650-7
2	axial	6.8	8.5	20	0.8	1.112	0.777	0.632	0.547	1.112	0.777	0.632	0.547	A-3650-7
4	axial	0	8.5	5	0	1.078	0.699	0.550	0.467	1.078	0.699	0.550	0.467	A-3650-3
4	axial	1.7	8.5	5	0.2	1.067	0.679	0.532	0.452	1.067	0.679	0.532	0.452	A-3650-3
4	axial	3.4	8.5	5	0.4	1.127	0.693	0.536	0.452	1.127	0.693	0.536	0.452	A-3650-3
4	axial	5.1	8.5	5	0.6	1.218	0.734	0.562	0.471	1.218	0.734	0.562	0.471	A-3650-3
4	axial	6.8	8.5	5	0.8	1.345	0.804	0.611	0.509	1.345	0.804	0.611	0.509	A-3650-3
4	axial	0	8.5	10	0	1.079	0.699	0.550	0.467	1.079	0.699	0.550	0.467	A-3650-5
4	axial	1.7	8.5	10	0.2	1.076	0.684	0.536	0.454	1.076	0.684	0.536	0.454	A-3650-5
4	axial	3.4	8.5	10	0.4	1.143	0.713	0.554	0.467	1.143	0.713	0.554	0.467	A-3650-5
4	axial	5.1	8.5	10	0.6	1.225	0.754	0.581	0.488	1.225	0.754	0.581	0.488	A-3650-5
4	axial	6.8	8.5	10	0.8	1.320	0.801	0.612	0.511	1.319	0.801	0.612	0.511	A-3650-5
4	axial	0	8.5	20	0	1.078	0.699	0.550	0.467	1.078	0.699	0.550	0.467	A-3650-7
4	axial	1.7	8.5	20	0.2	1.079	0.684	0.535	0.453	1.079	0.684	0.535	0.453	A-3650-7
4	axial	3.4	8.5	20	0.4	1.155	0.719	0.558	0.470	1.155	0.719	0.563	0.470	A-3650-7
4	axial	5.1	8.5	20	0.6	1.240	0.758	0.582	0.488	1.240	0.758	0.582	0.488	A-3650-7
4	axial	6.8	8.5	20	0.8	1.307	0.796	0.609	0.509	1.307	0.796	0.609	0.509	A-3650-7
8	axial	0	8.5	5	0	1.098	0.687	0.532	0.447	1.098	0.687	0.532	0.447	A-3650-3
8	axial	1.7	8.5	5	0.2	1.109	0.674	0.516	0.432	1.109	0.674	0.516	0.432	A-3650-3
8	axial	3.4	8.5	5	0.4	1.264	0.724	0.541	0.447	1.264	0.724	0.541	0.447	A-3650-3
8	axial	5.1	8.5	5	0.6	1.494	0.816	0.595	0.483	1.494	0.816	0.595	0.483	A-3650-3
8	axial	6.8	8.5	5	0.8	1.818	0.953	0.677	0.542	1.818	0.953	0.677	0.542	A-3650-3

Table G5. Benchmarking the FAVOR Implementation of A-3000 Curve Fits for Circumferential Surface-Breaking Flaws

Flaw Geometry						FAVOR Implementation A-3000				ASME BPVC Tabulated SIFIC(s)				A-3000
2c/a	orient.	a	t	R/t	a/t	G0	G1	G2	G3	G0	G1	G2	G3	Tables
2	circ	0	8.5	5	0	1.014	0.711	0.583	0.508	1.014	0.711	0.583	0.508	A-3630-3
2	circ	1.7	8.5	5	0.2	1.044	0.729	0.595	0.517	1.044	0.729	0.595	0.517	A-3630-3
2	circ	3.4	8.5	5	0.4	1.078	0.750	0.611	0.529	1.078	0.750	0.611	0.529	A-3630-3
2	circ	5.1	8.5	5	0.6	1.117	0.777	0.631	0.546	1.117	0.777	0.631	0.546	A-3630-3
2	circ	6.8	8.5	5	0.8	1.161	0.812	0.659	0.569	1.161	0.812	0.659	0.569	A-3630-3
2	circ	0	8.5	10	0	1.012	0.711	0.583	0.508	1.012	0.711	0.583	0.508	A-3630-5
2	circ	1.7	8.5	10	0.2	1.042	0.730	0.597	0.519	1.042	0.730	0.597	0.519	A-3630-5
2	circ	3.4	8.5	10	0.4	1.075	0.752	0.614	0.532	1.075	0.752	0.614	0.532	A-3630-5
2	circ	5.1	8.5	10	0.6	1.109	0.777	0.633	0.548	1.109	0.777	0.633	0.548	A-3630-5
2	circ	6.8	8.5	10	0.8	1.146	0.806	0.656	0.567	1.146	0.806	0.656	0.567	A-3630-5
2	circ	0	8.5	20	0	1.027	0.715	0.584	0.508	1.027	0.715	0.584	0.508	A-3630-7
2	circ	1.7	8.5	20	0.2	1.050	0.734	0.599	0.520	1.050	0.734	0.599	0.520	A-3630-7
2	circ	3.4	8.5	20	0.4	1.074	0.755	0.616	0.534	1.073	0.755	0.616	0.534	A-3630-7
2	circ	5.1	8.5	20	0.6	1.098	0.777	0.635	0.550	1.098	0.777	0.635	0.550	A-3630-7
2	circ	6.8	8.5	20	0.8	1.124	0.803	0.656	0.567	1.124	0.803	0.656	0.567	A-3630-7
4	circ	0	8.5	5	0	1.054	0.672	0.527	0.448	1.054	0.672	0.527	0.448	A-3630-3
4	circ	1.7	8.5	5	0.2	1.096	0.690	0.538	0.455	1.096	0.690	0.538	0.455	A-3630-3
4	circ	3.4	8.5	5	0.4	1.146	0.714	0.554	0.468	1.146	0.714	0.554	0.468	A-3630-3
4	circ	5.1	8.5	5	0.6	1.204	0.749	0.579	0.487	1.204	0.749	0.579	0.487	A-3630-3
4	circ	6.8	8.5	5	0.8	1.275	0.803	0.621	0.521	1.275	0.803	0.621	0.521	A-3630-3
4	circ	0	8.5	10	0	1.057	0.674	0.529	0.449	1.057	0.674	0.529	0.449	A-3630-5
4	circ	1.7	8.5	10	0.2	1.106	0.700	0.547	0.463	1.106	0.700	0.547	0.463	A-3630-5
4	circ	3.4	8.5	10	0.4	1.160	0.733	0.571	0.481	1.160	0.733	0.571	0.481	A-3630-5
4	circ	5.1	8.5	10	0.6	1.221	0.773	0.601	0.506	1.221	0.773	0.601	0.506	A-3630-5
4	circ	6.8	8.5	10	0.8	1.288	0.825	0.641	0.539	1.288	0.825	0.641	0.539	A-3630-5
4	circ	0	8.5	20	0	1.038	0.673	0.531	0.452	1.038	0.673	0.531	0.452	A-3630-7
4	circ	1.7	8.5	20	0.2	1.096	0.701	0.549	0.466	1.095	0.701	0.549	0.466	A-3630-7
4	circ	3.4	8.5	20	0.4	1.158	0.734	0.572	0.483	1.158	0.734	0.572	0.483	A-3630-7
4	circ	5.1	8.5	20	0.6	1.227	0.772	0.599	0.504	1.227	0.772	0.599	0.504	A-3630-7
4	circ	6.8	8.5	20	0.8	1.303	0.818	0.632	0.530	1.303	0.818	0.632	0.530	A-3630-7
8	circ	0	8.5	5	0	1.074	0.675	0.523	0.440	1.074	0.675	0.523	0.440	A-3630-3
8	circ	1.7	8.5	5	0.2	1.147	0.698	0.534	0.447	1.147	0.698	0.534	0.447	A-3630-3
8	circ	3.4	8.5	5	0.4	1.242	0.732	0.552	0.458	1.242	0.732	0.552	0.458	A-3630-3
8	circ	5.1	8.5	5	0.6	1.372	0.786	0.585	0.481	1.372	0.786	0.585	0.481	A-3630-3
8	circ	6.8	8.5	5	0.8	1.558	0.886	0.654	0.534	1.558	0.886	0.654	0.534	A-3630-3

Table G6. Test Matrix for Benchmarking FAVOR Inside Surface-Breaking Flaws with Abaqus K_I Time Histories

Case No.	R_i/t	Orient.	$2c/a$	a/t	Clad t_{clad}	Thickness* t	Inside R_i	Flaw Depth, a	Actual R_i/t	RPV Type	Cool Down Rate	RMSD** v12.1	RMSD** v16.1	sup norm*** v12.1	sup norm*** v16.1
	(-)	(-)	(-)	(-)	(inches)	(inches)	(inches)	(inches)	(-)	(-)	(°F/hr)	(%)	(%)	(%)	(%)
1	10	axial	∞	0.0350	0.156	8.5	86	0.2975	10.118	PWR	50	3.18	2.80	3.45	4.52
2	10	axial	∞	0.0350	0.25	8.5	86	0.2975	10.118	PWR	50	4.86	2.45	10.57	2.95
3	10	axial	∞	0.5000	0.156	8.5	86	4.2500	10.118	PWR	50	3.24	0.63	6.56	0.89
4	10	axial	∞	0.5000	0.25	8.5	86	4.2500	10.118	PWR	50	4.99	0.74	10.05	1.05
5	10	circ.	360°	0.0350	0.156	8.5	86	0.2975	10.118	PWR	50	6.36	1.96	11.67	4.70
6	10	circ.	360°	0.0350	0.25	8.5	86	0.2975	10.118	PWR	50	4.61	2.54	10.94	6.51
7	10	circ.	360°	0.5000	0.156	8.5	86	4.2500	10.118	PWR	50	4.93	0.69	11.23	1.32
8	10	circ.	360°	0.5000	0.25	8.5	86	4.2500	10.118	PWR	50	7.53	1.07	16.74	1.94
9	20	axial	∞	0.0350	0.156	6.125	126.4	0.2144	20.637	BWR	50	7.57	2.25	8.94	3.71
10	20	axial	∞	0.0500	0.25	6.125	126.4	0.3063	20.637	BWR	50	2.40	2.28	3.95	3.88
11	20	axial	∞	0.0750	0.25	6.125	126.4	0.4594	20.637	BWR	50	0.73	1.48	1.00	2.81
12	20	axial	∞	0.1000	0.25	6.125	126.4	0.6125	20.637	BWR	50	0.64	1.37	1.19	2.24
13	20	circ.	360°	0.0350	0.156	6.125	126.4	0.2144	20.637	BWR	50	7.35	3.21	7.35	5.47
14	20	circ.	360°	0.0500	0.156	6.125	126.4	0.3063	20.637	BWR	50	0.42	2.26	0.89	3.86
15	20	circ.	360°	0.0750	0.156	6.125	126.4	0.4594	20.637	BWR	50	0.13	1.33	0.42	2.44
16	20	circ.	360°	0.1000	0.156	6.125	126.4	0.6125	20.637	BWR	50	0.12	1.17	0.48	2.14
17	10	circ.	360°	0.0300	0.156	8.5	86	0.2550	10.118	PWR	50	5.80	3.06	9.09	8.20
18	20	circ.	360°	0.0300	0.156	6.125	126.4	0.1838	20.637	BWR	50	8.95	4.36	9.83	5.57
19	15	circ.	360°	0.0350	0.156	8.427	126.4	0.2949	15.000	BWR	50	7.02	5.39	14.77	11.85
20	20	axial	6	0.1000	0.25	6.125	126.4	0.6125	20.637	BWR	50	2.62	4.27	5.34	5.94
21	20	axial	6	0.1000	0.25	6.125	126.4	0.6125	20.637	BWR	PTS 007	5.23	6.64	14.46	17.12
22	20	axial	6	0.5000	0.25	6.125	126.4	3.0625	20.637	BWR	PTS 007	4.49	6.99	9.83	16.24
23	20	axial	6	0.2500	0.25	6.125	126.4	1.5313	20.637	BWR	PTS 109	2.27	1.26	5.18	4.24
24	15	axial	6	0.1000	0.25	7.12	106.5	0.7120	14.958	BWR	PTS 109	3.13	4.23	10.41	6.19
25	15	axial	6	0.1000	0.25	7.12	106.5	0.7120	14.958	BWR	PTS 007	3.33	5.37	15.43	19.82
26	10	circ.	6	0.0300	0.25	8.75	86	0.2625	9.829	PWR	50	5.36	3.60	12.05	6.02
27	10	circ.	6	0.0300	0.25	8.75	86	0.2625	9.829	PWR	PTS 007	3.99	6.36	19.47	24.70

*RPV wall thickness inclusive of clad thickness

**RMSD - root mean square deviation of percent deviation of FAVOR K_I solution from Abaqus K_I solution.

***supremum (sup norm) of deviations covering the full transient

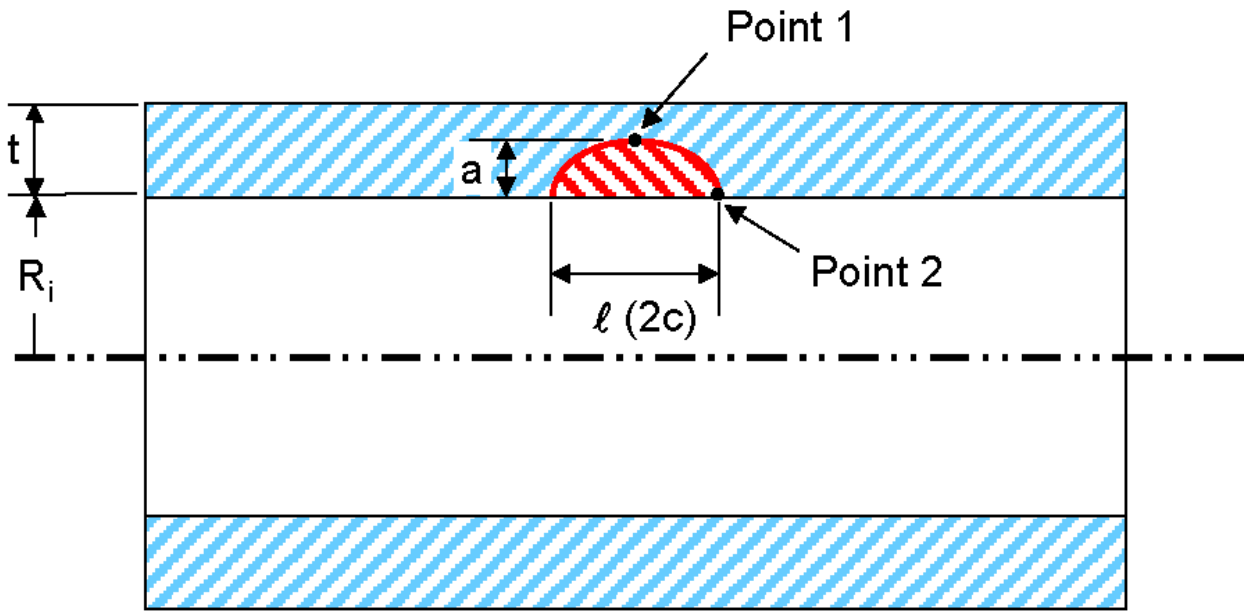

Fig. G1.Finite semi-elliptical inside surface flaw with an axial orientation (with base material only).

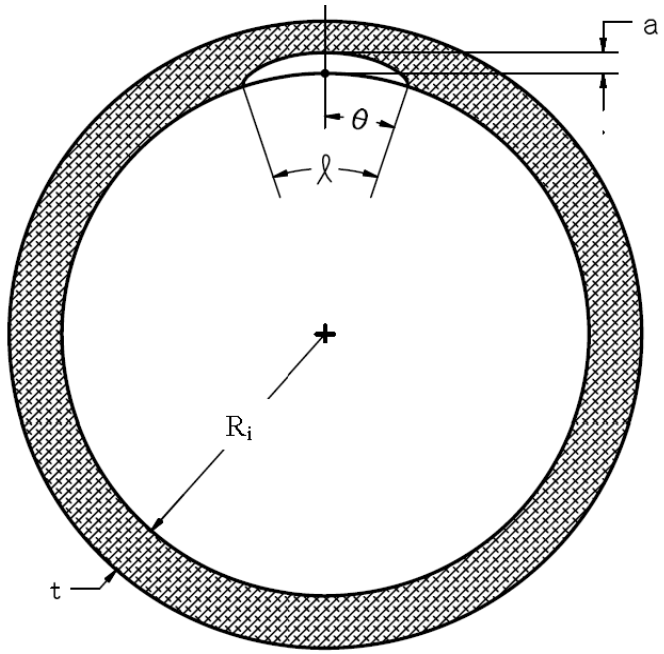

Fig. G2.Finite semi-elliptical inside surface flaw with a circumferential orientation (with base material only).

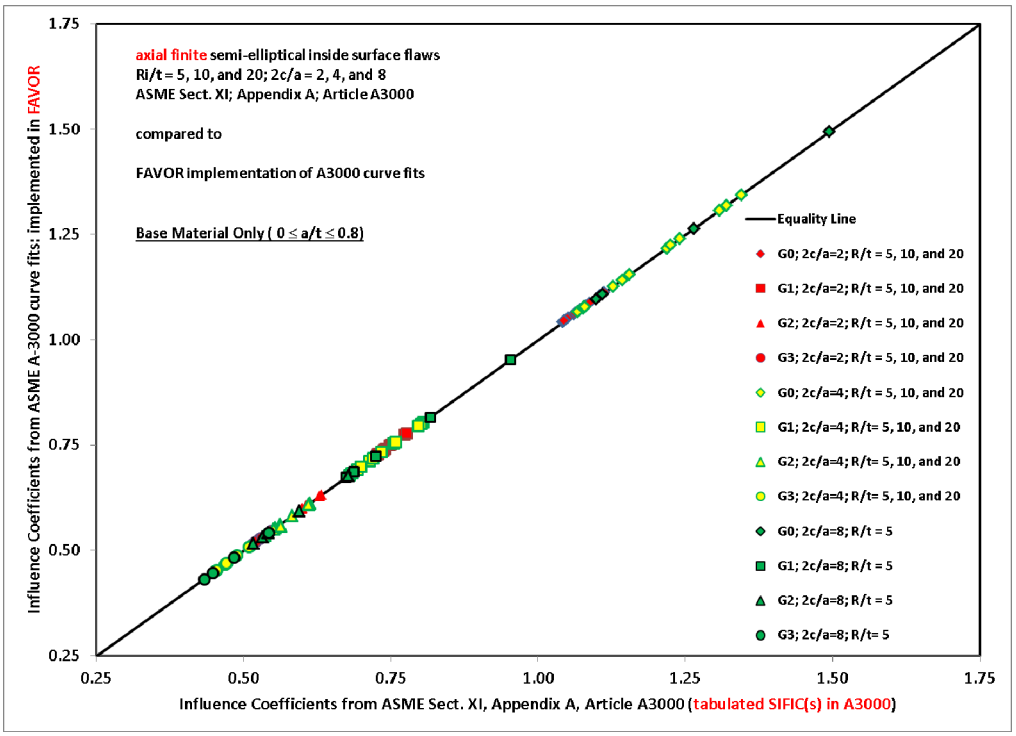

(a)

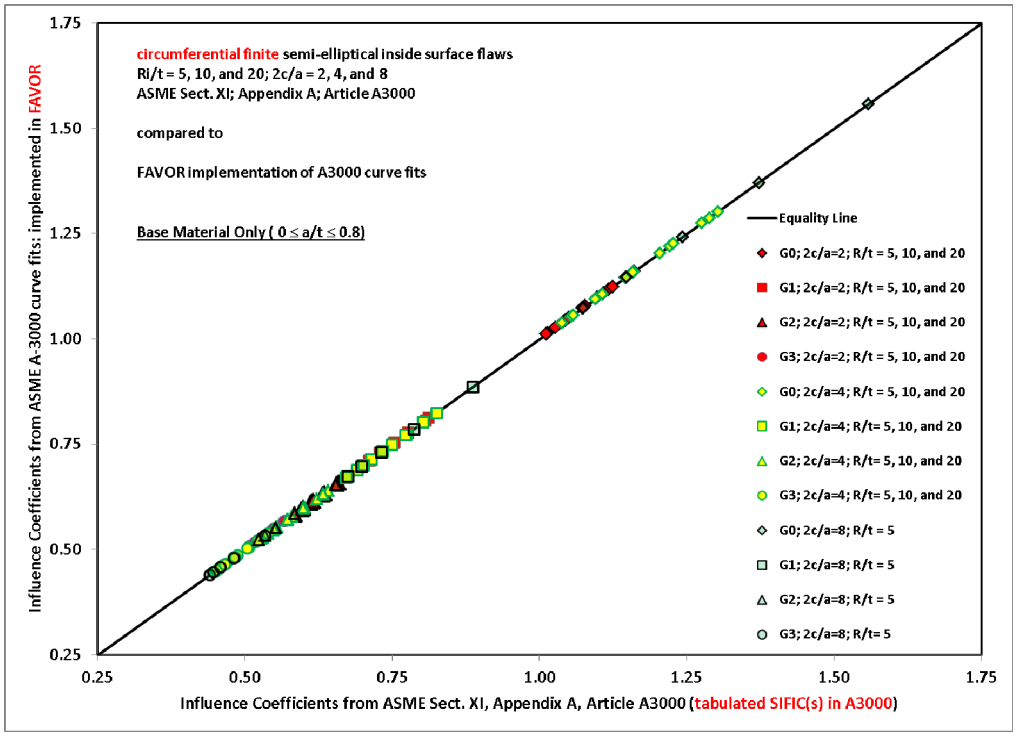

(b)

Fig. G3. Comparison of influence coefficients calculated by FAVOR using ASME A-3000 curve fits to SIFIC(s) tabulated in ASME BPVC A-3000: (a) axial inside semi-elliptical flaws and (b) circumferential inside semi-elliptical flaws.

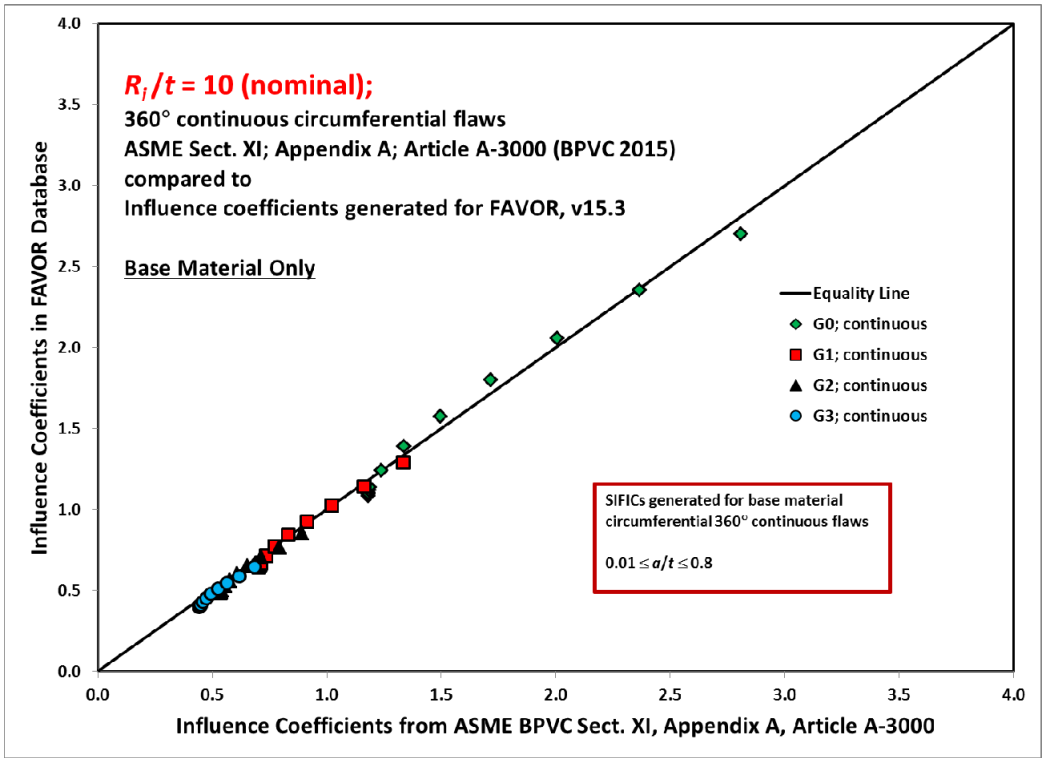

(a)

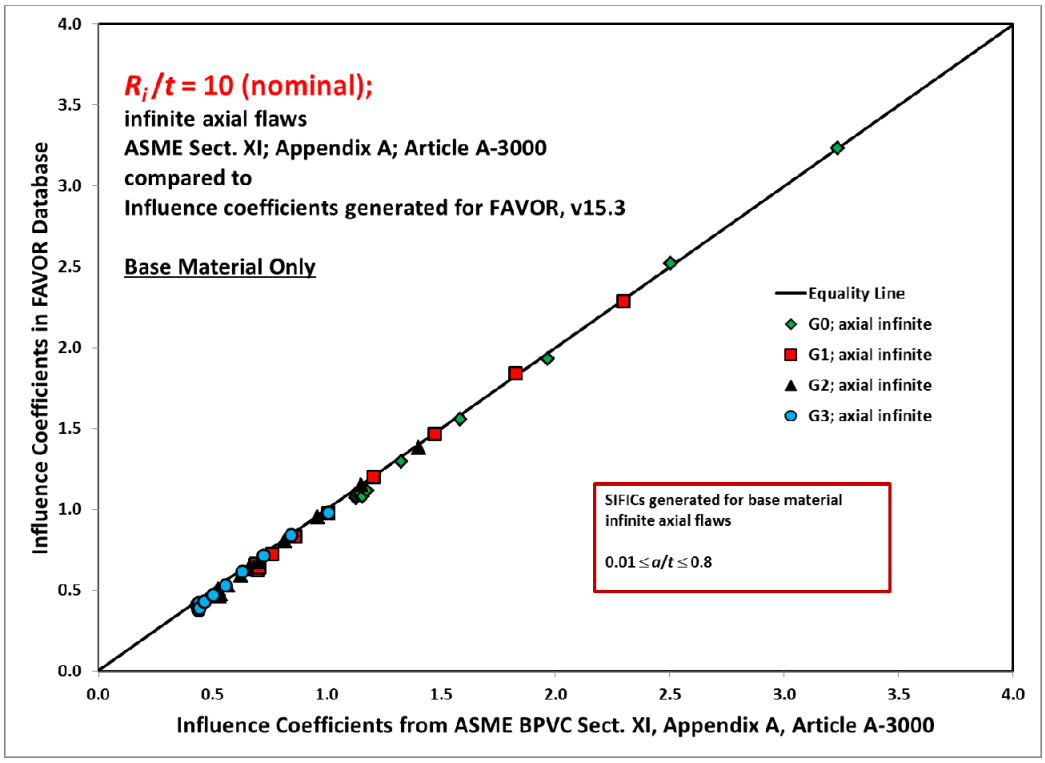

(b)

Fig. G4. Comparison of influence coefficients calculated independently by ORNL for v15.3 to closed-form curve fits available in ASME, Section XI, Article A-3000 for a R_i/t = 10 with (a) continuous 360° circumferential flaws and (b) infinite axial flaws.

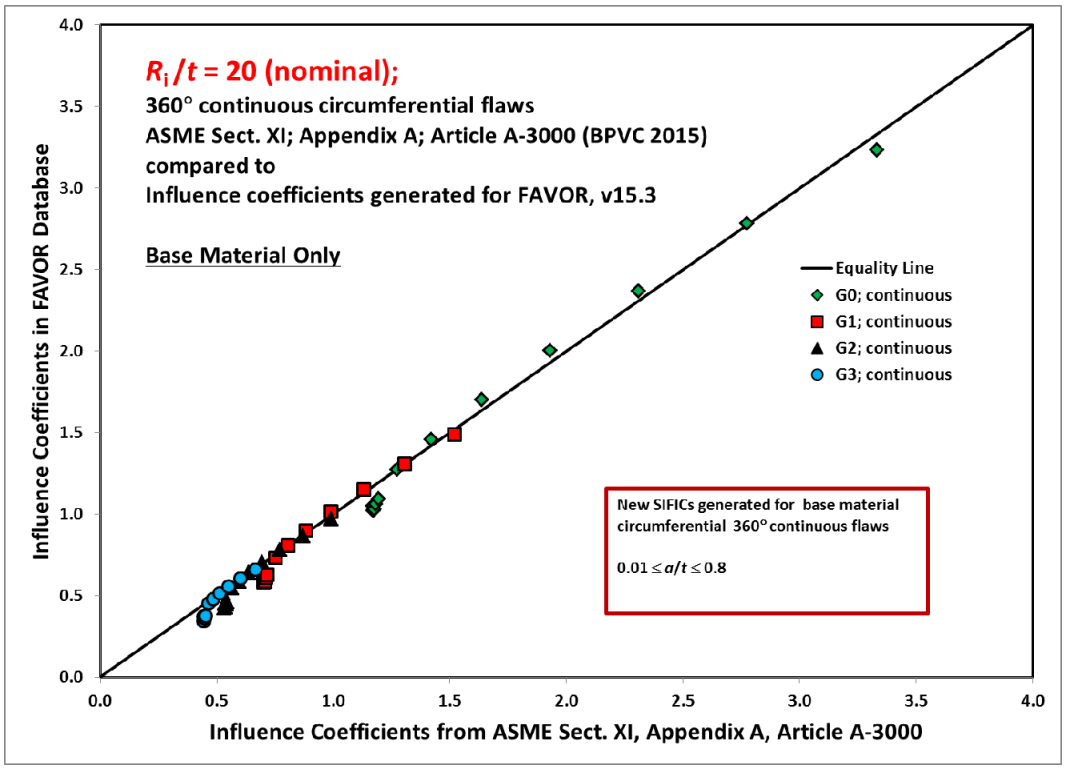

(a)

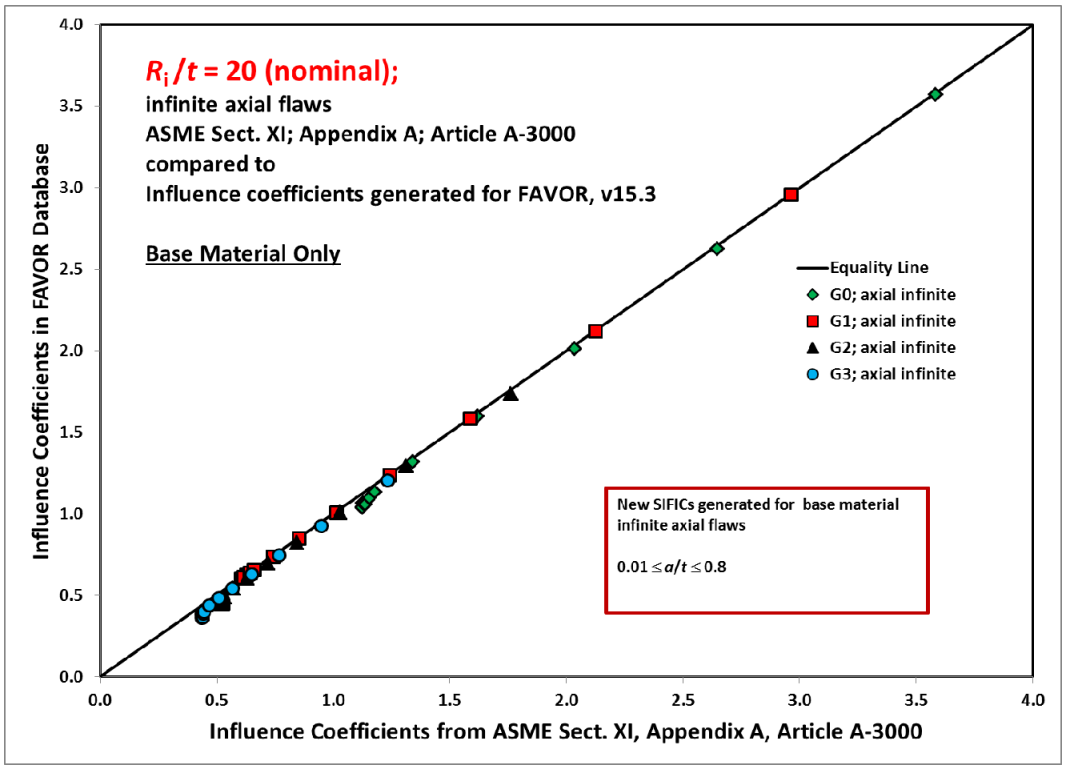

(b)

Fig. G5. Comparison of influence coefficients calculated independently by ORNL for v15.3 to closed-form curve fits available in ASME, Section XI, Article A-3000 for a R_i/t = 20 with (a) continuous 360° circumferential flaws and (b) infinite axial flaws.

(a)

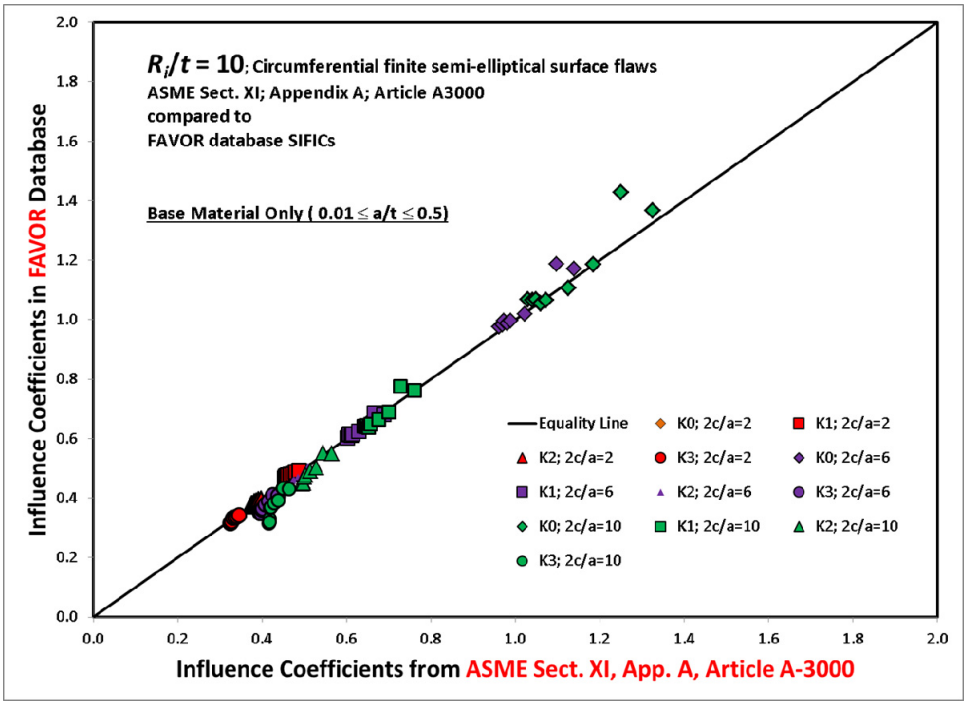

(b)

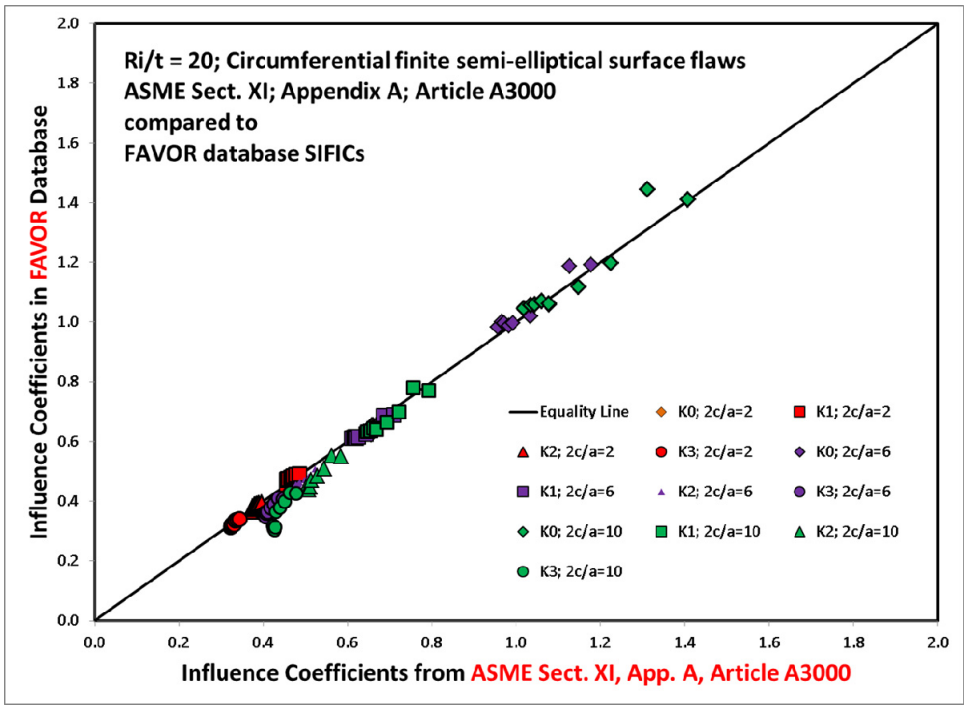

Fig. G6. Comparison of influence coefficients calculated independently by ORNL from FEM models for v15.3 to closed-form curve fits available in ASME, Section XI, Article A-3000 for circumferential flaws with (a) R_i/t = 10 and (b) R_i/t = 20.

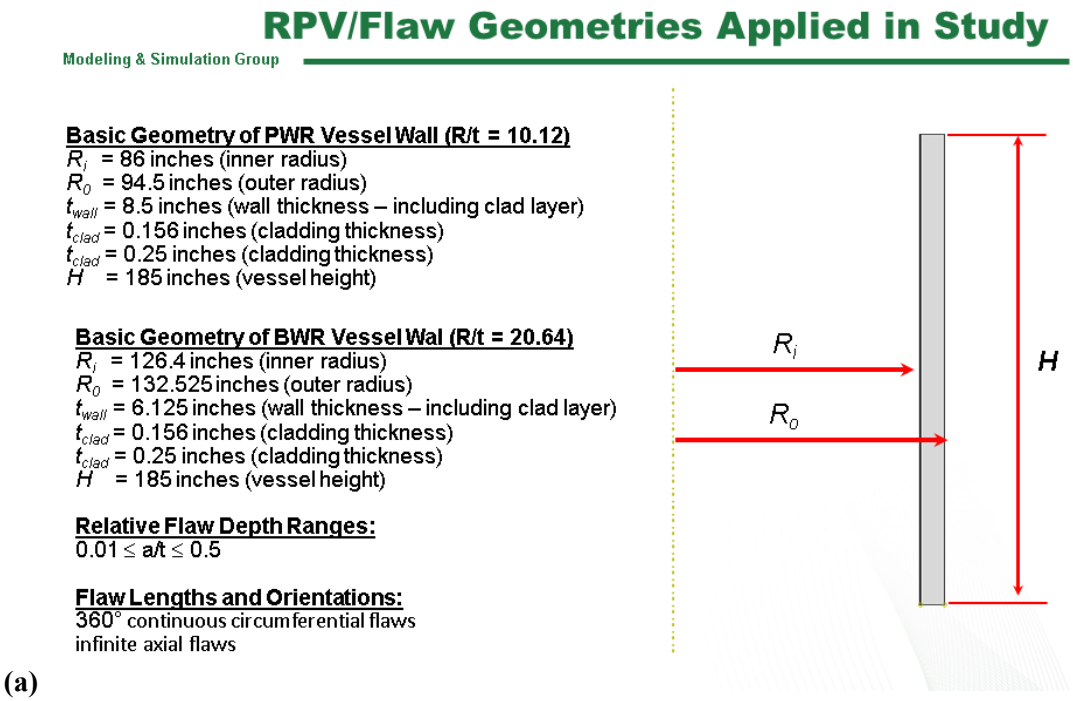

(a)

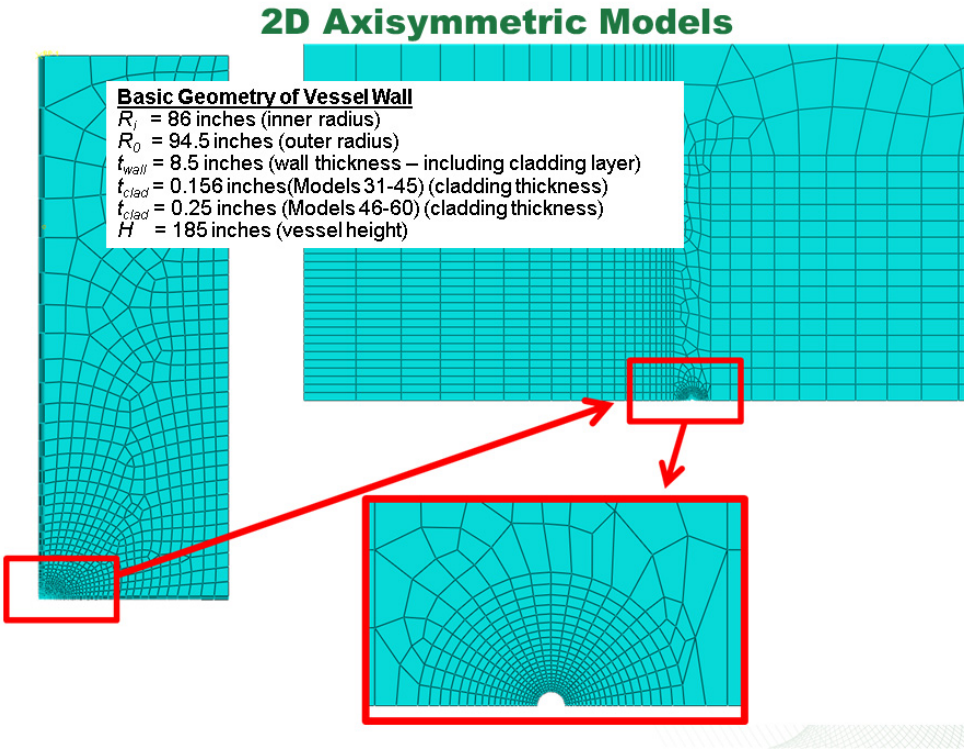

(b)

Fig. G7. Finite element models for 2D axisymmetric 360° continuous circumferential orientation flaws on inside of vessel: (a) geometry and (b) typical meshing of model.

2D model of continuous 360° inner surface circumferential flaw

2D axisymmetric model with circ. crack (a/t = 0.03) and applied internal pressure with end-cap load. Generalized Plane Strain with boundary conditions at top and symmetry plane at the bottom. The crack-face is unconstrained and free to deform.

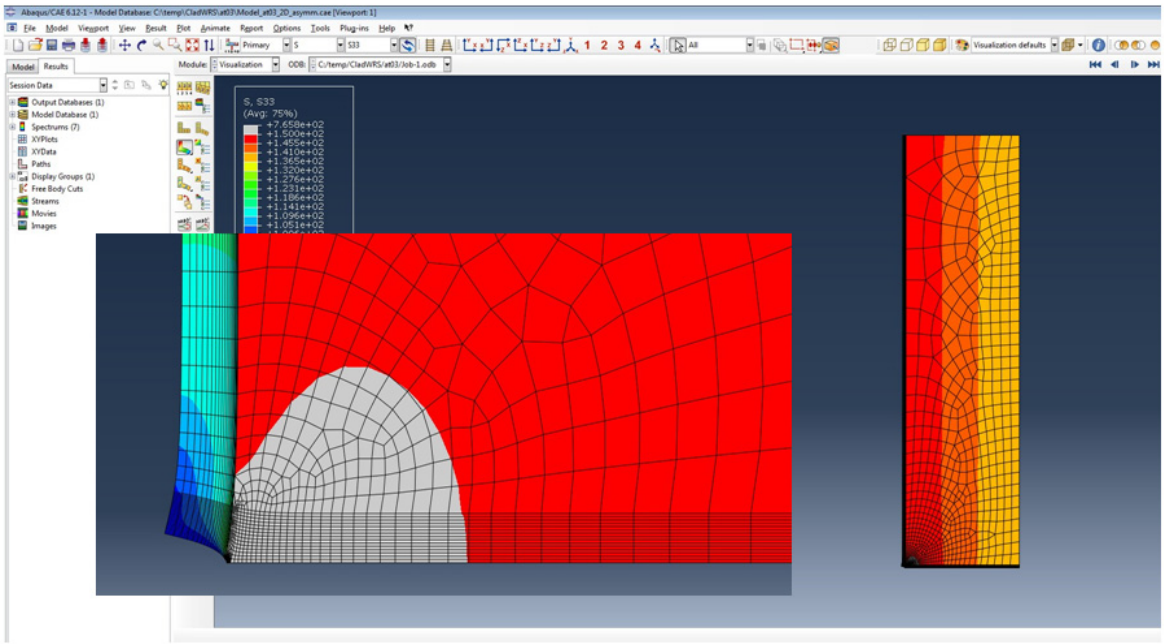

Fig. G8. Finite element models for 2D axisymmetric 360° continuous circumferential semi-elliptical flaw on inside of vessel.

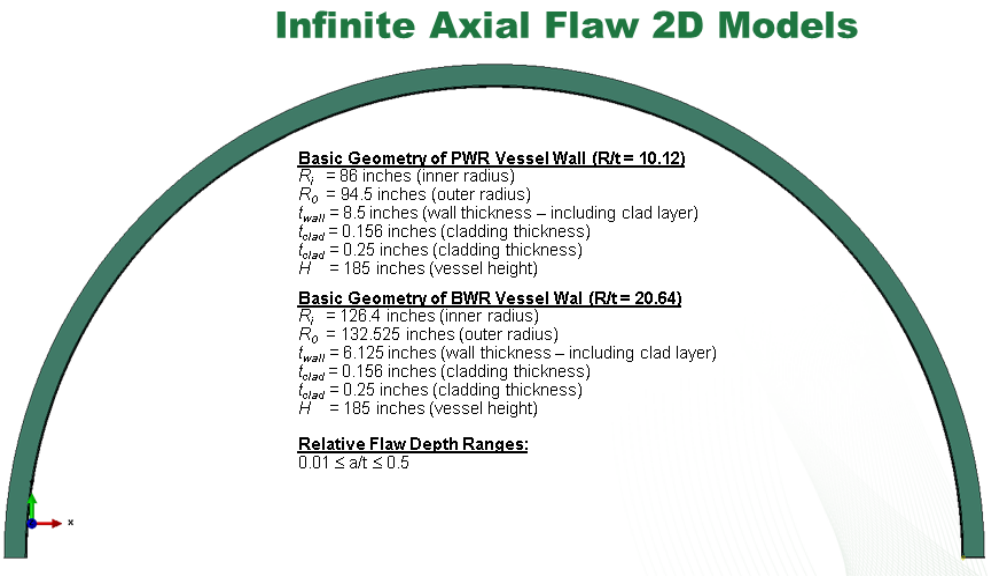

(a)

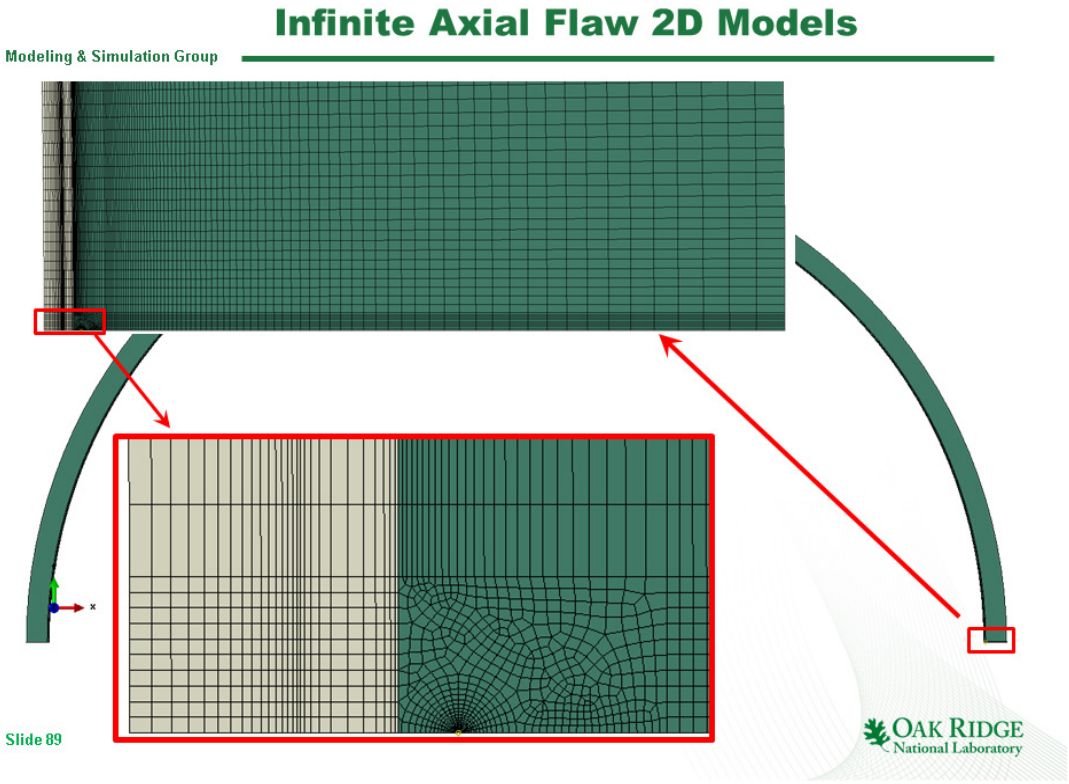

(b)

Fig. G9. Finite element models for infinite 2D flaws on inside surface of vessel with axial orientation: (a) geometry and (b) typical meshing of model.

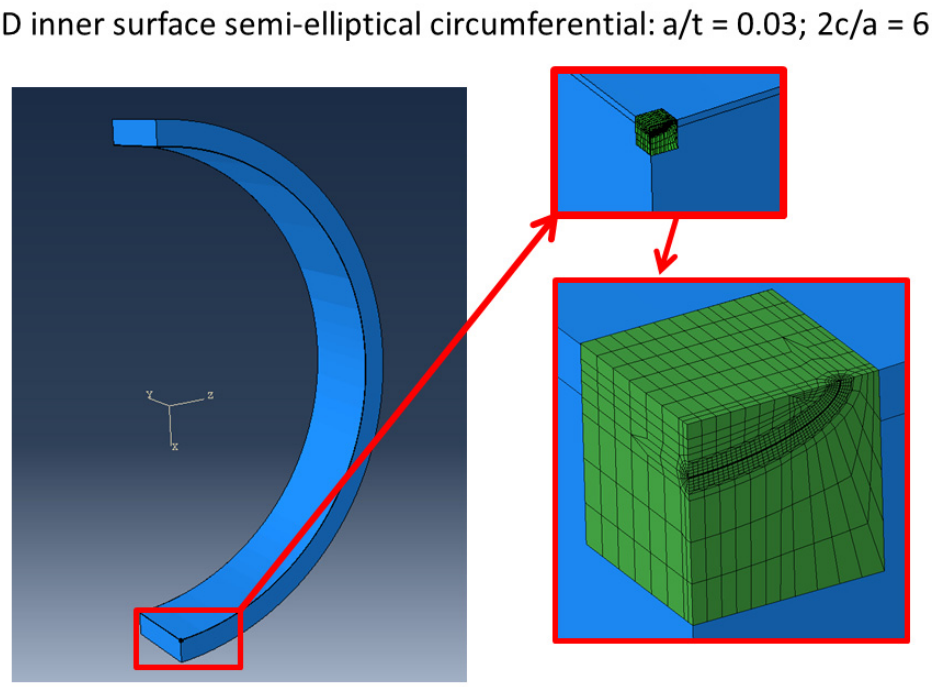

(a)

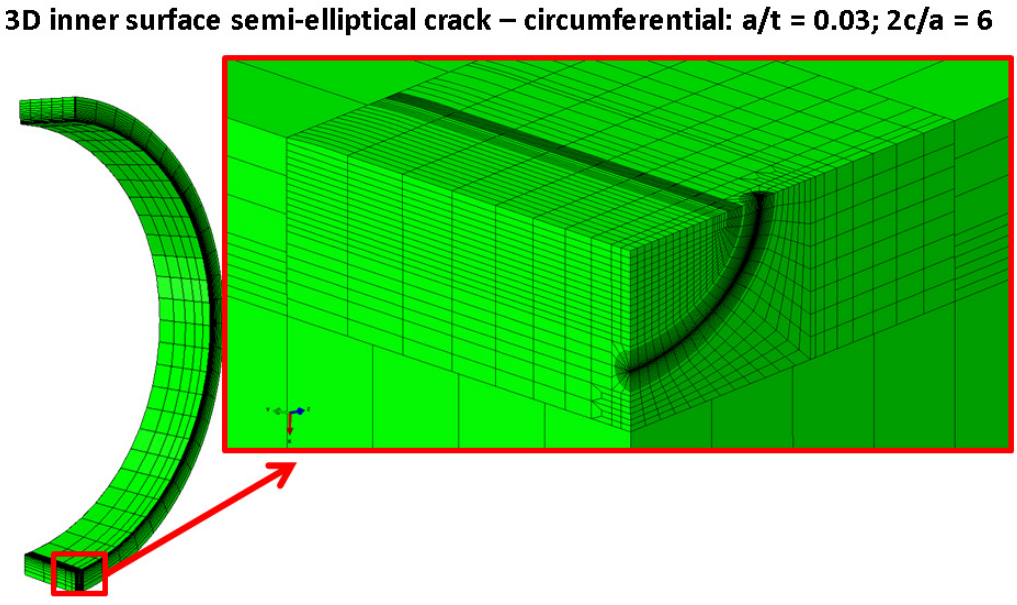

(b)

Fig. G10. Finite element models for 3D finite, inner surface, semi-elliptical flaws with circumferential orientation: (a) global model and (b) details of meshing the flaw.

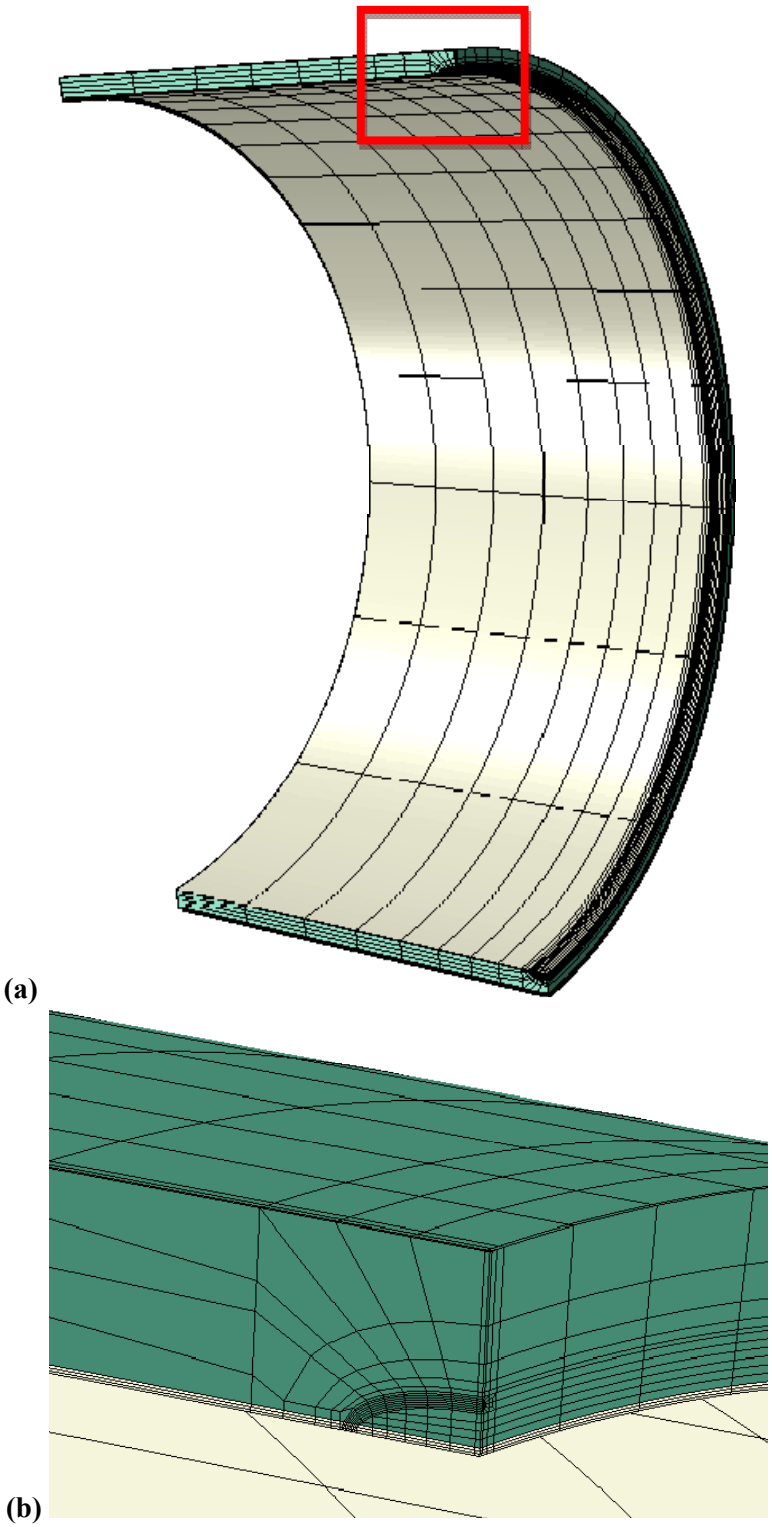

Fig. G11. Finite element models for 3D finite, inner surface, semi-elliptical flaws with axial orientation: (a) global model and (b) details of meshing the flaw.

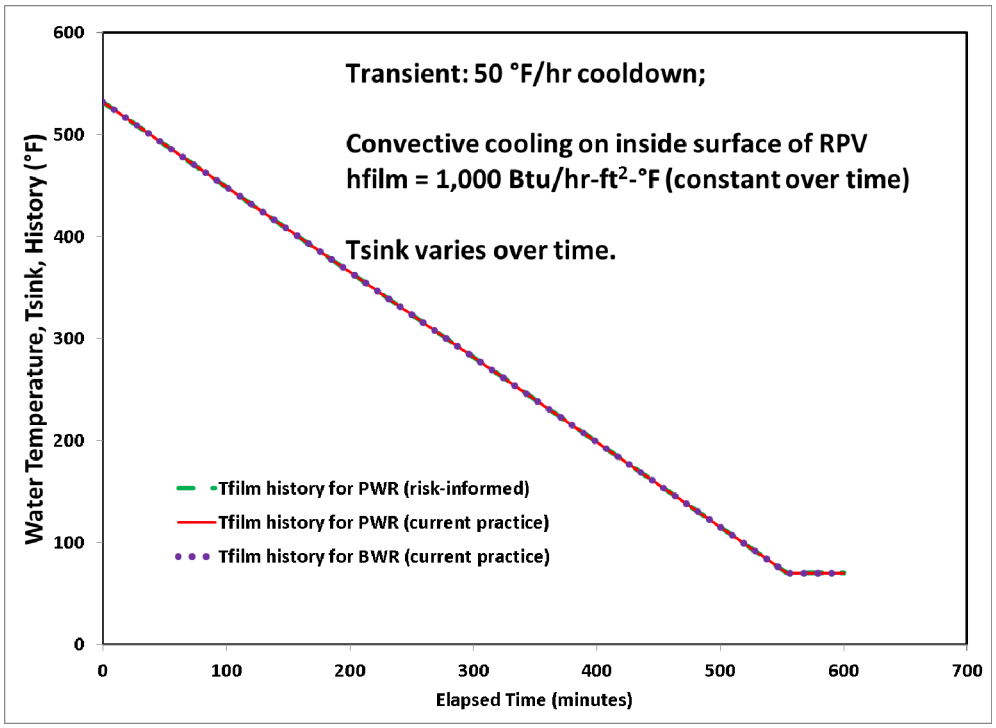

(a)

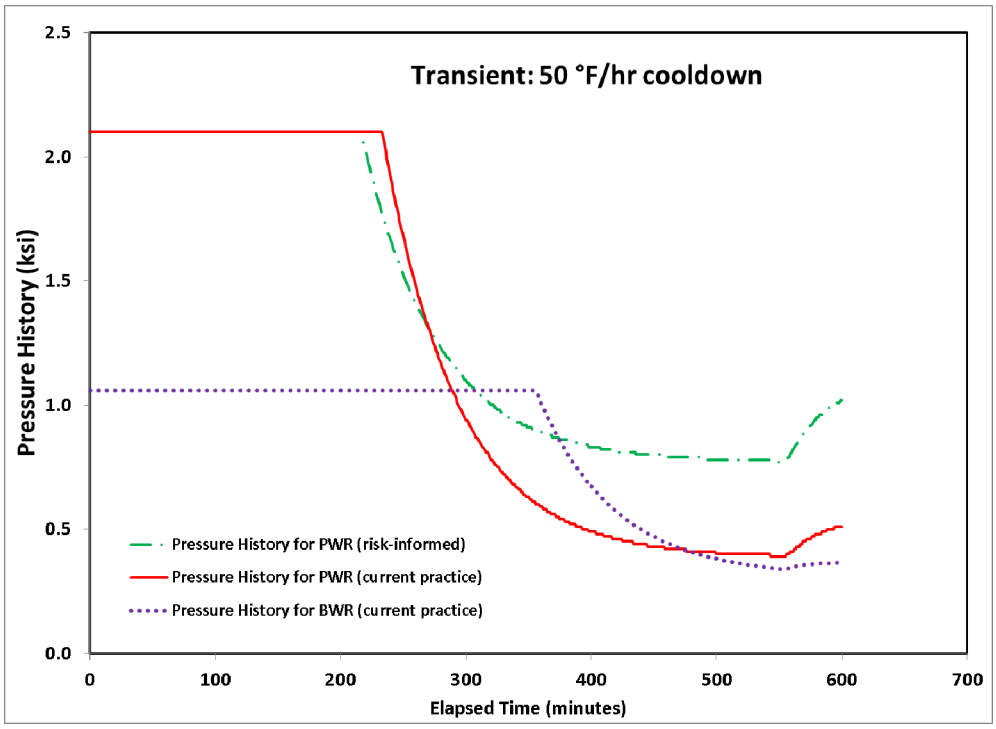

(b)

Fig. G12. Thermal boundary conditions and pressure loadings for three methods to calculate the required pressure history: (a) input temperature and film coefficient histories and (b) resulting pressure history for a cooldown transient using PWR (risk-informed method), PWR (current practice), and BWR (current practice).

(a)

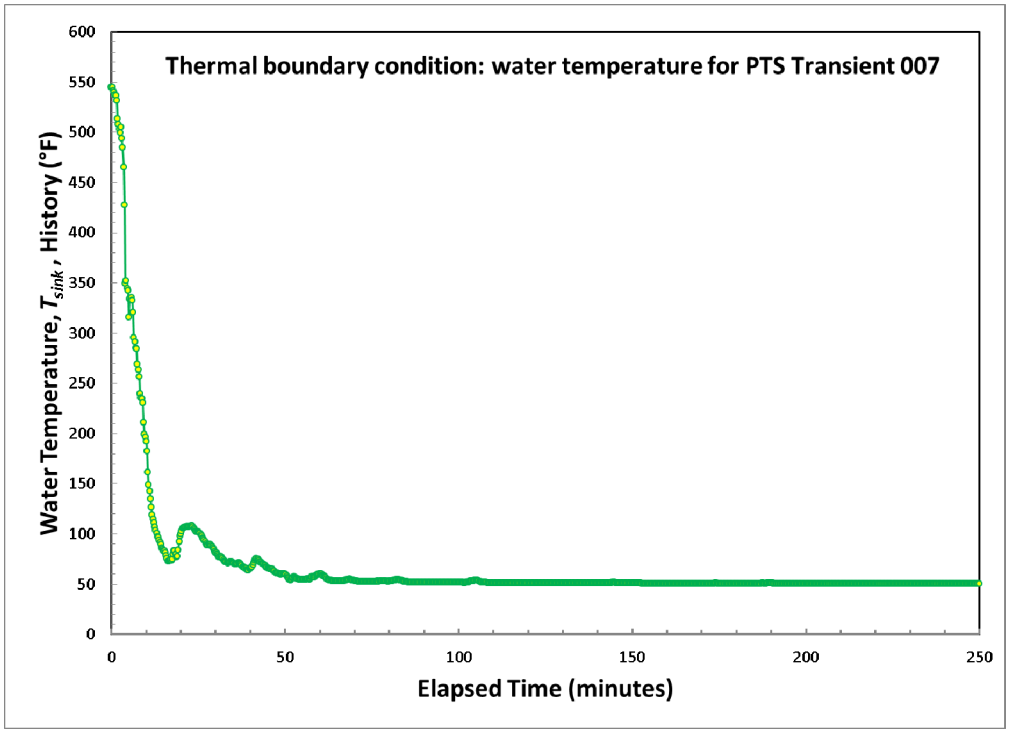

(b)

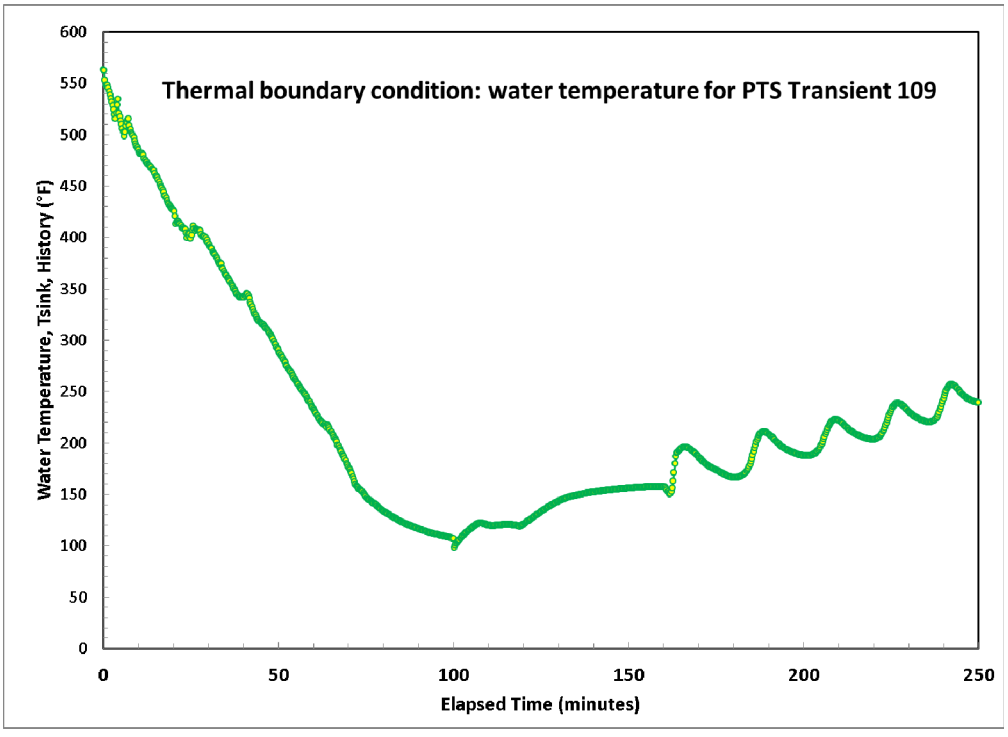

Fig. G13. Thermal boundary condition: input water temperature (T_{sink}) for PTS Transients 007 and 109.

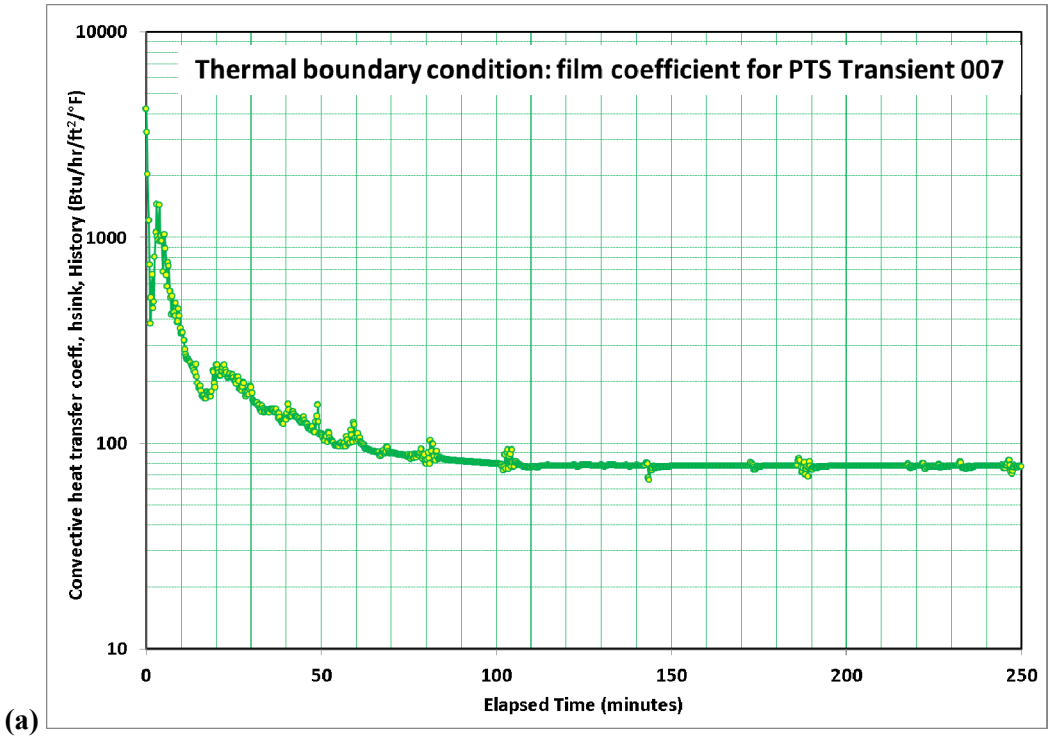

(a)

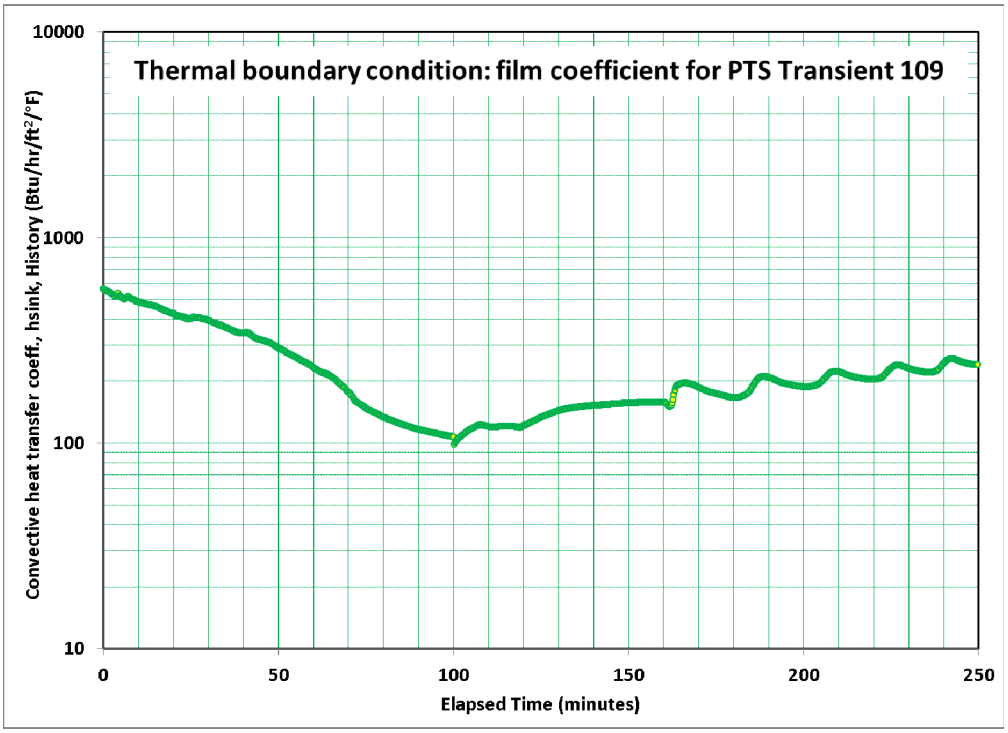

(b)

Fig. G14. Thermal boundary condition input for inner surface: heat transfer coefficients (film coefficient, h_{sink}) for PTS Transients (a) 007 and (b) 109.

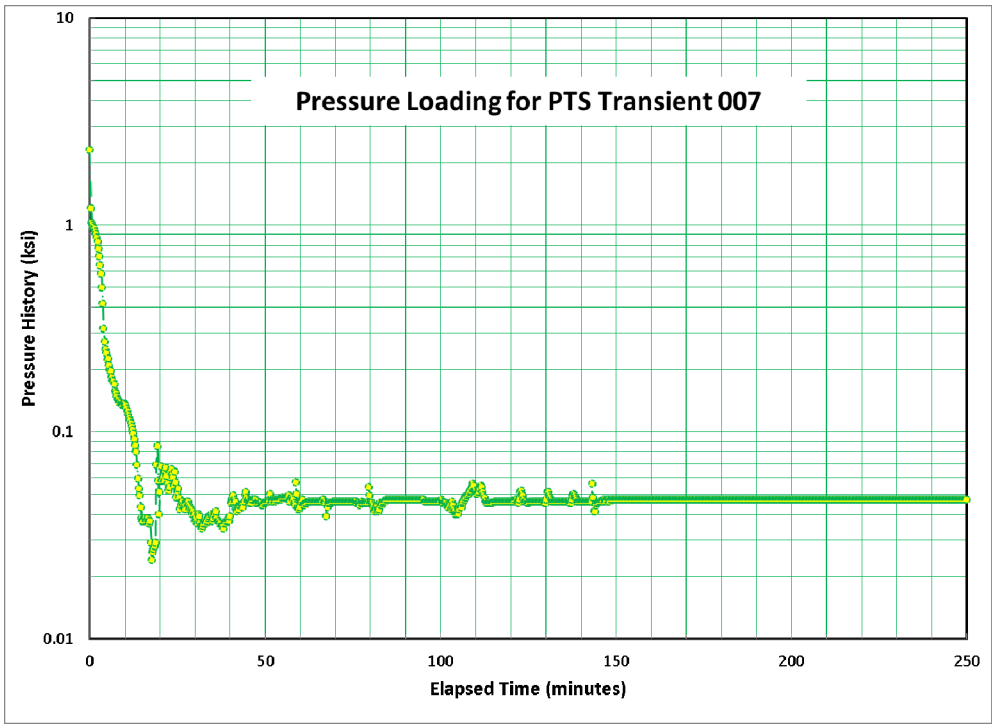

(a)

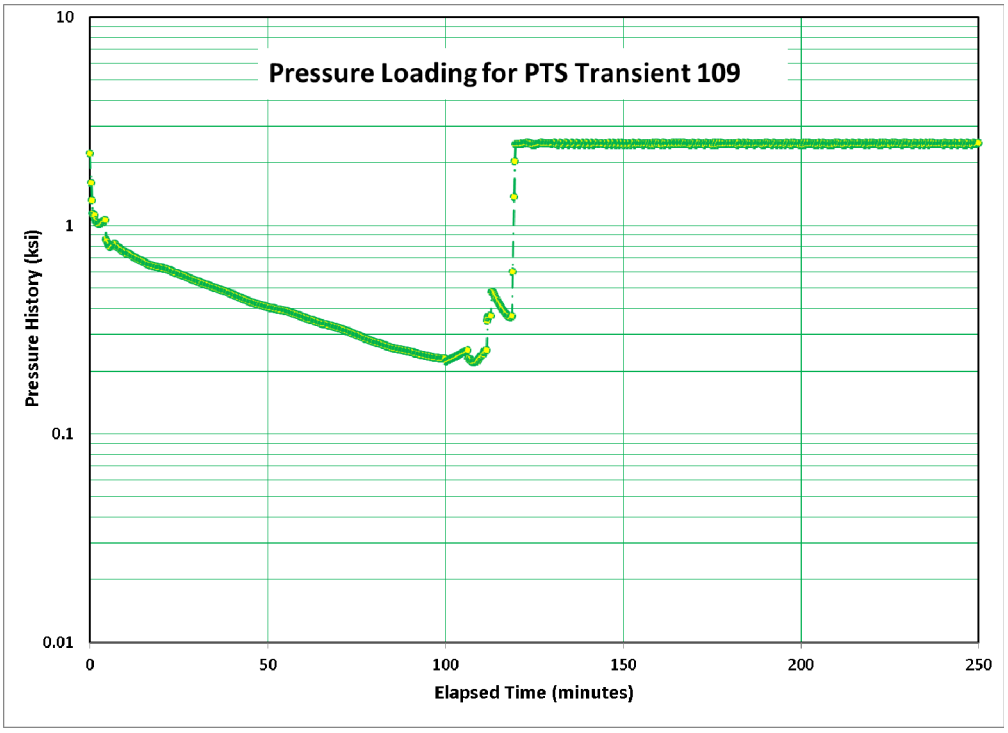

(b)

Fig. G15. Pressure loading input: water pressure applied to inside surface of the vessel: PTS Transients (a) 007 and (b) 109.

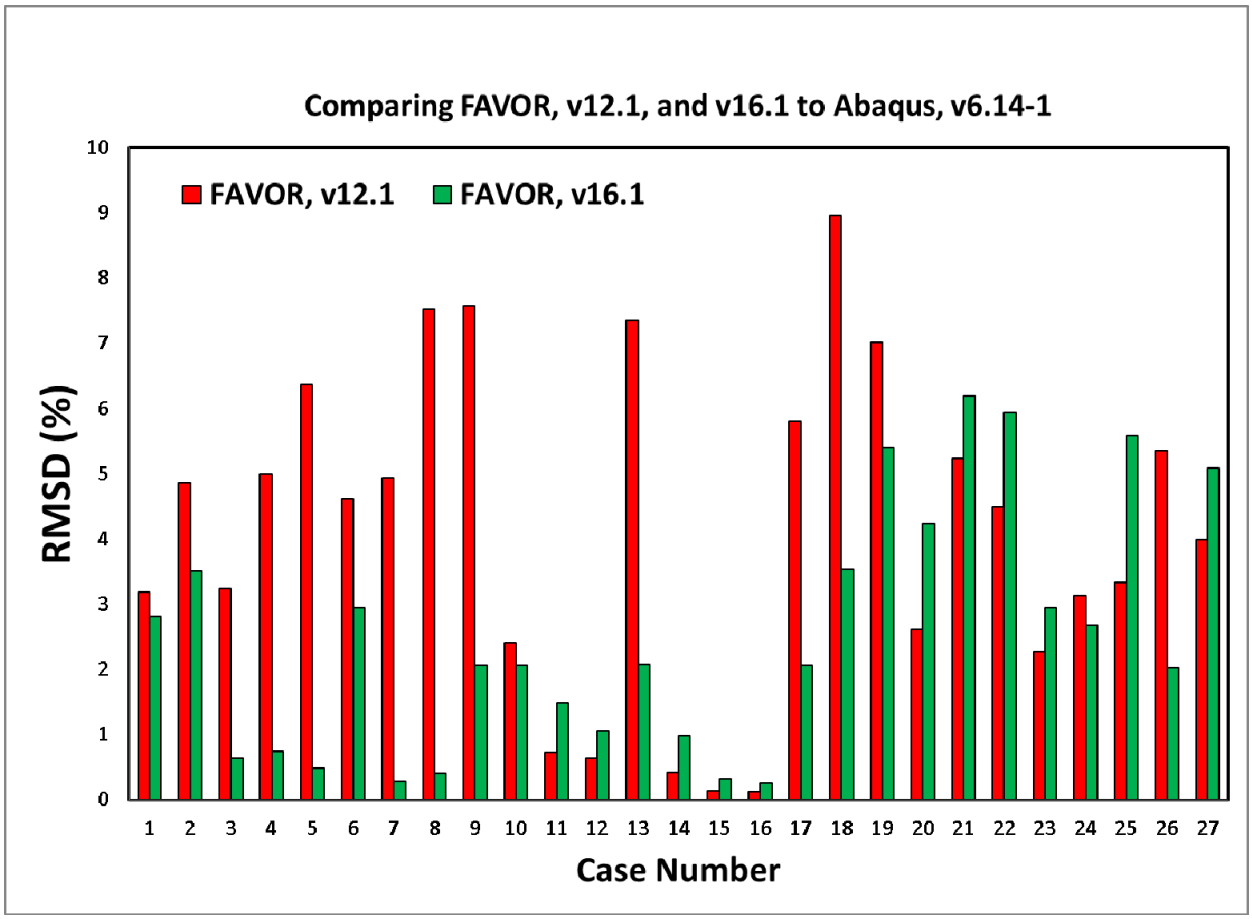

Fig. G16. RMSD statistics for all cases in Test Matrix.

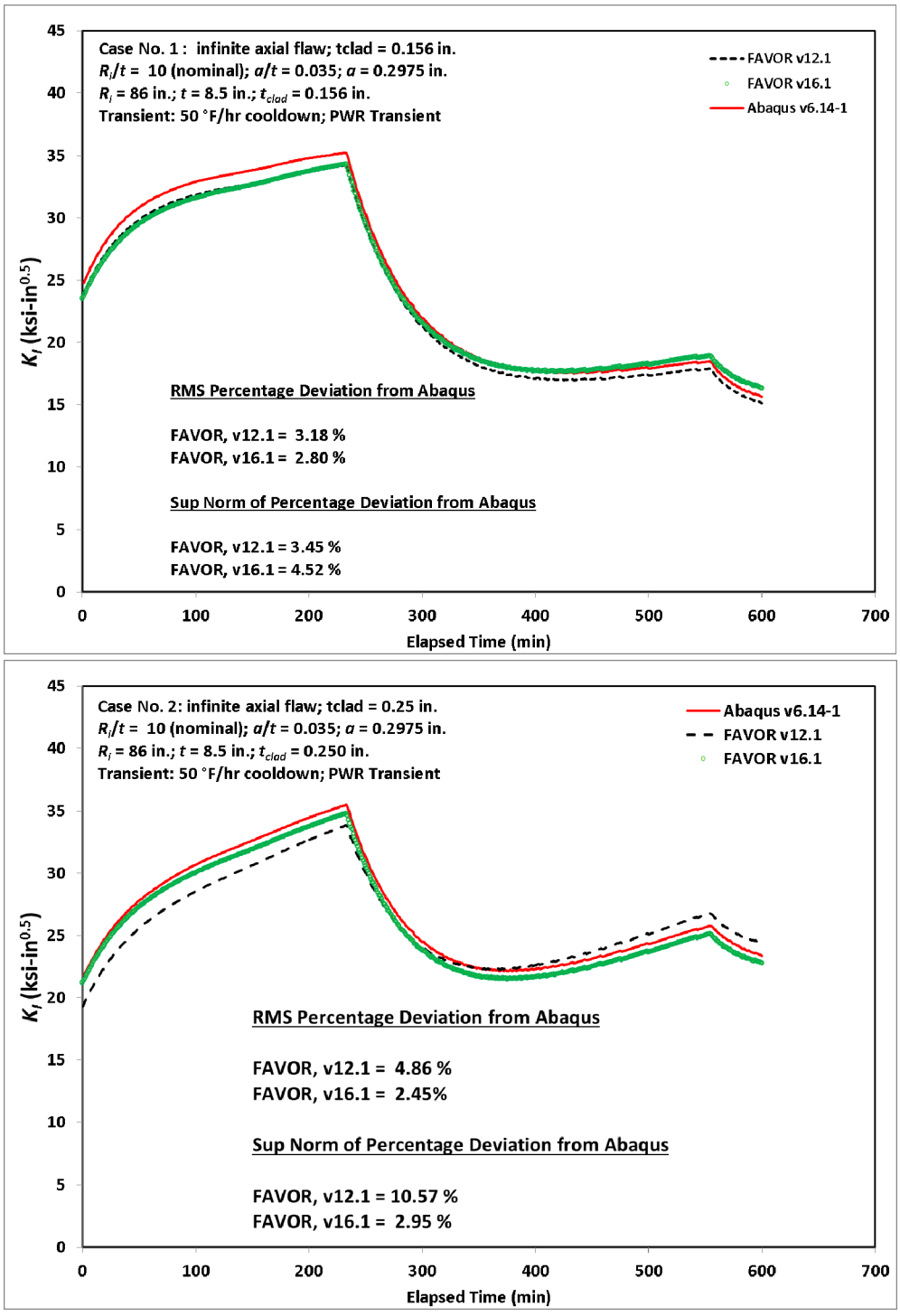

Fig. G17. Applied K_I histories for Cases 1 and 2.

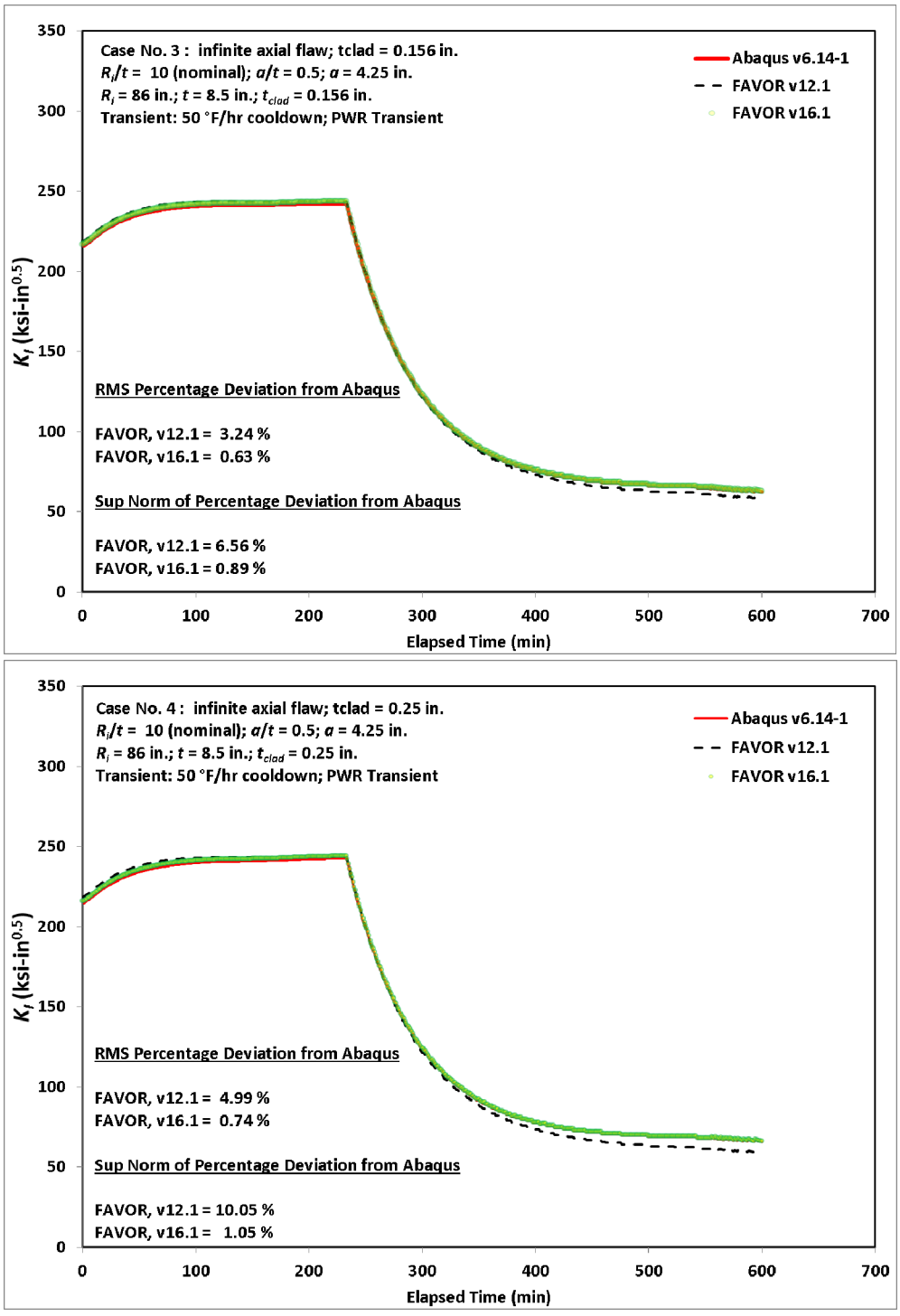

Fig. G18. Applied K_I histories for Cases 3 and 4.

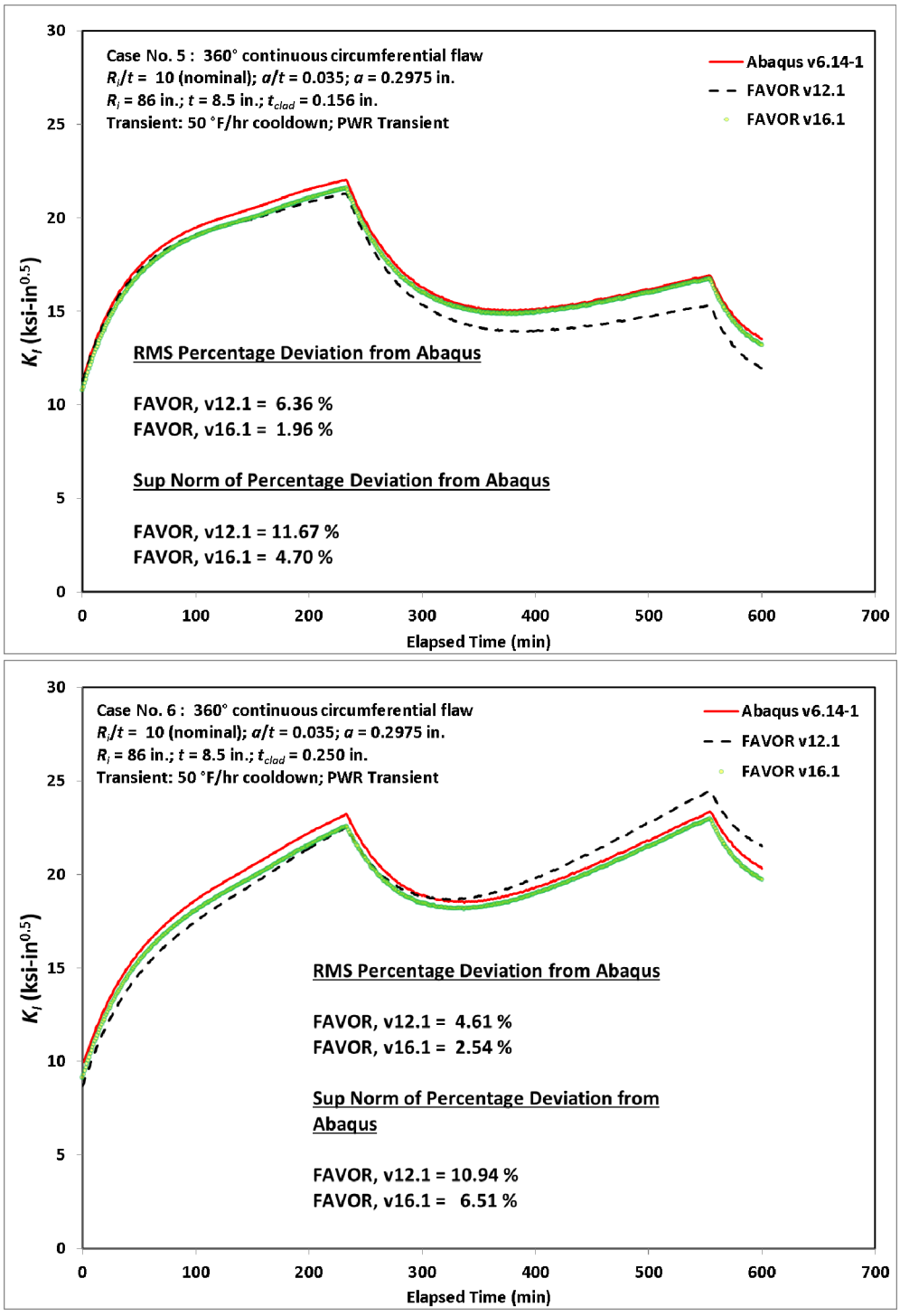

Fig. G19. Applied K_I histories for Cases 5 and 6.

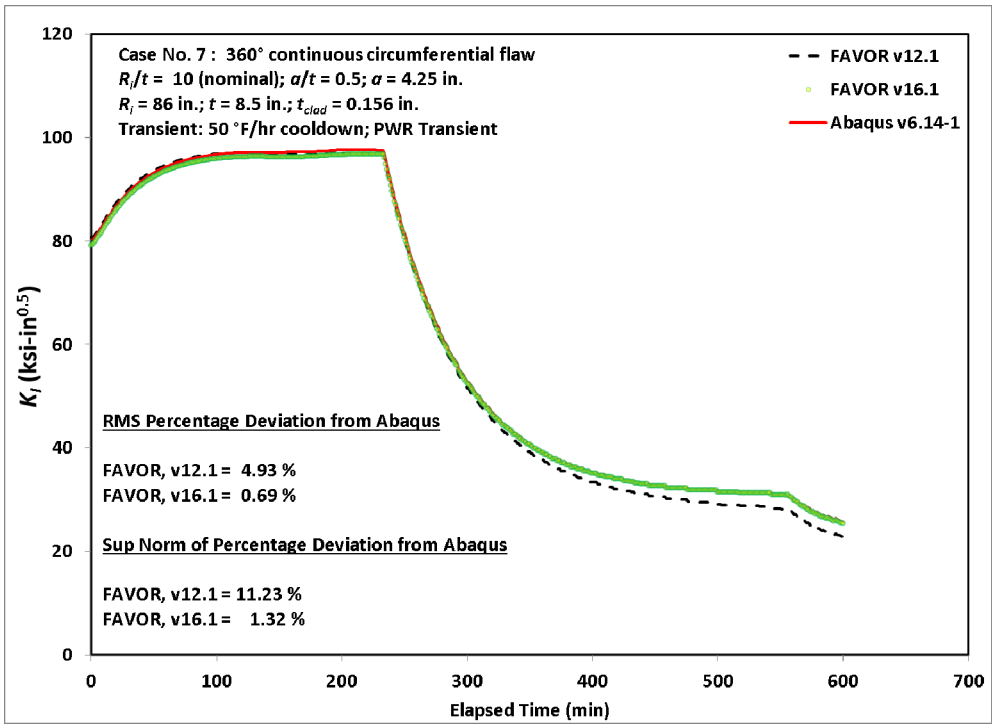

(a)

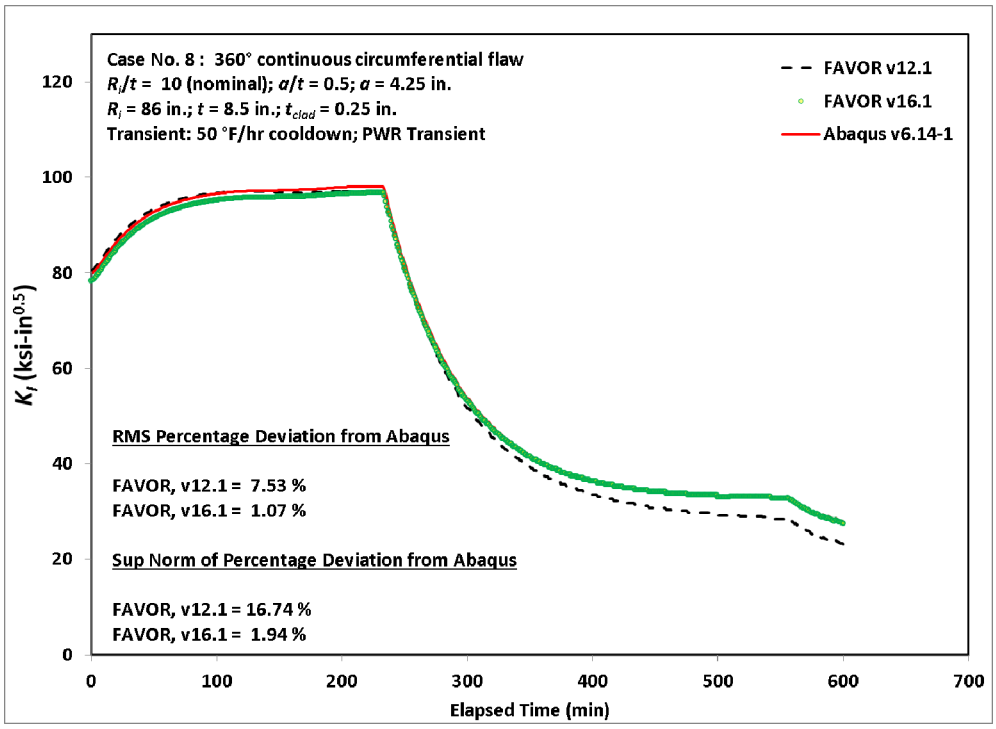

(b)

Fig. G20. Applied K_I histories for Cases 7 and 8.

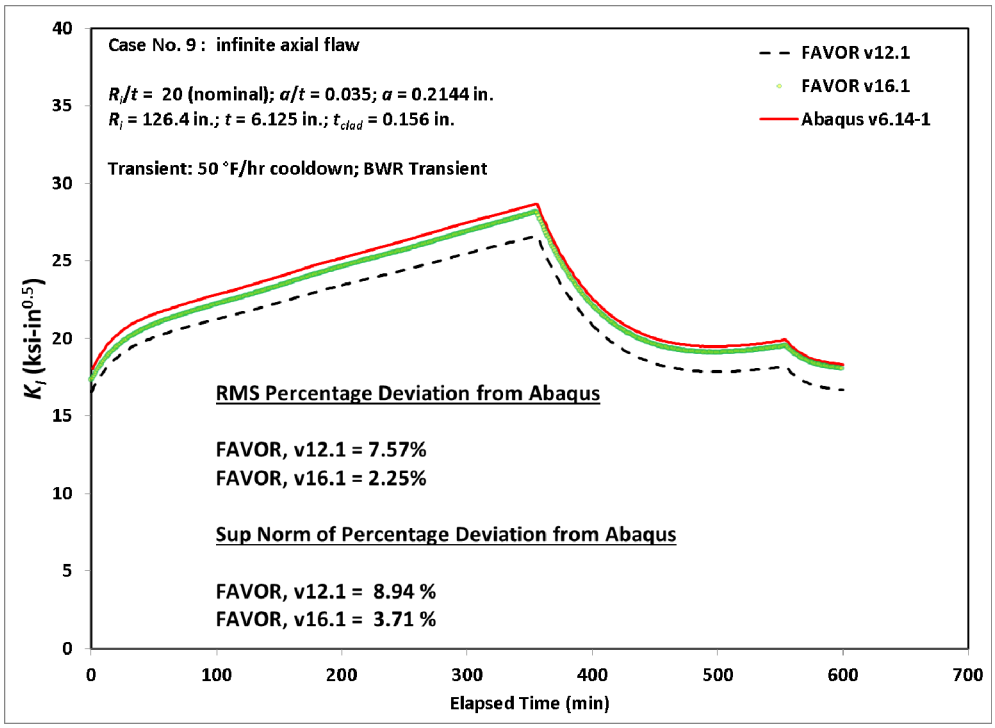

(a)

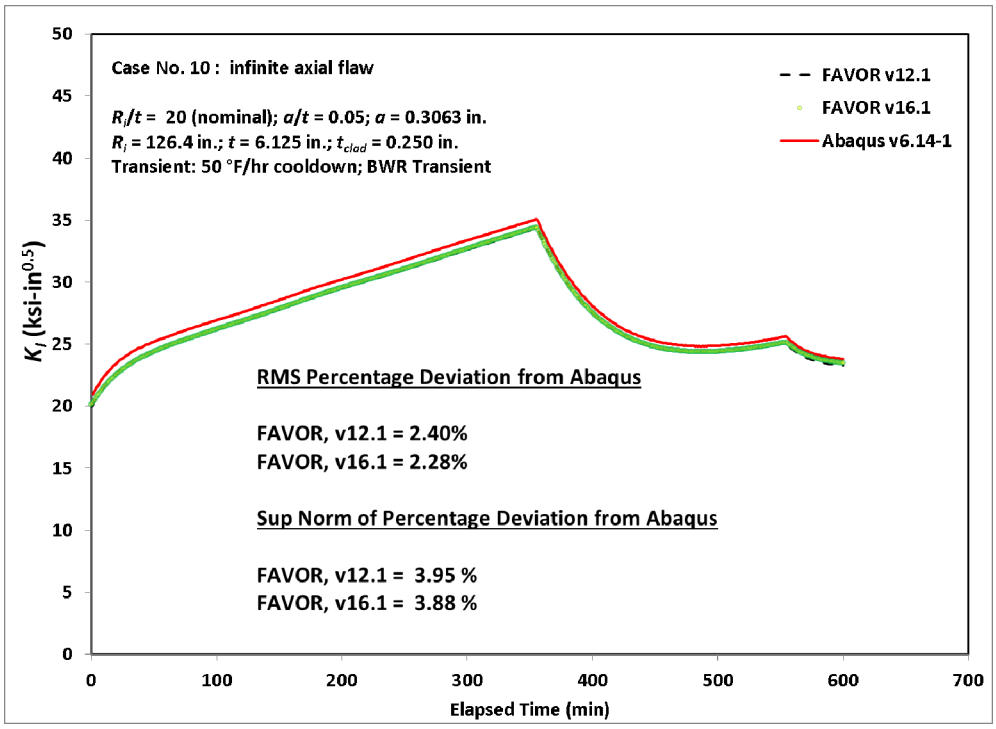

(b)

Fig. G21. Applied K_I histories for Cases 9 and 10.

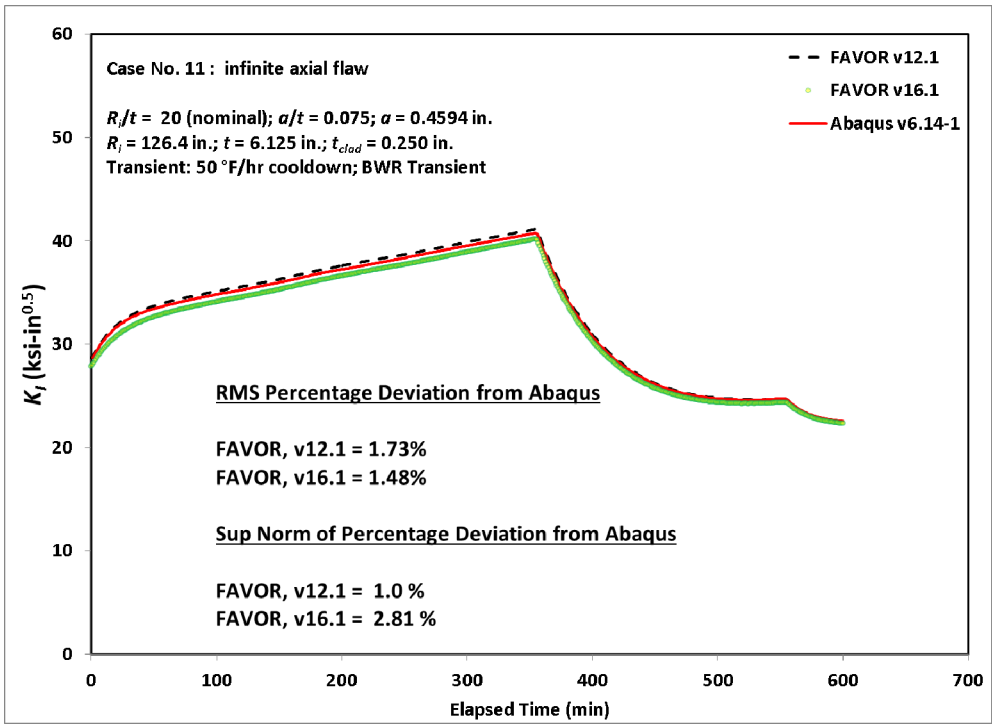

(a)

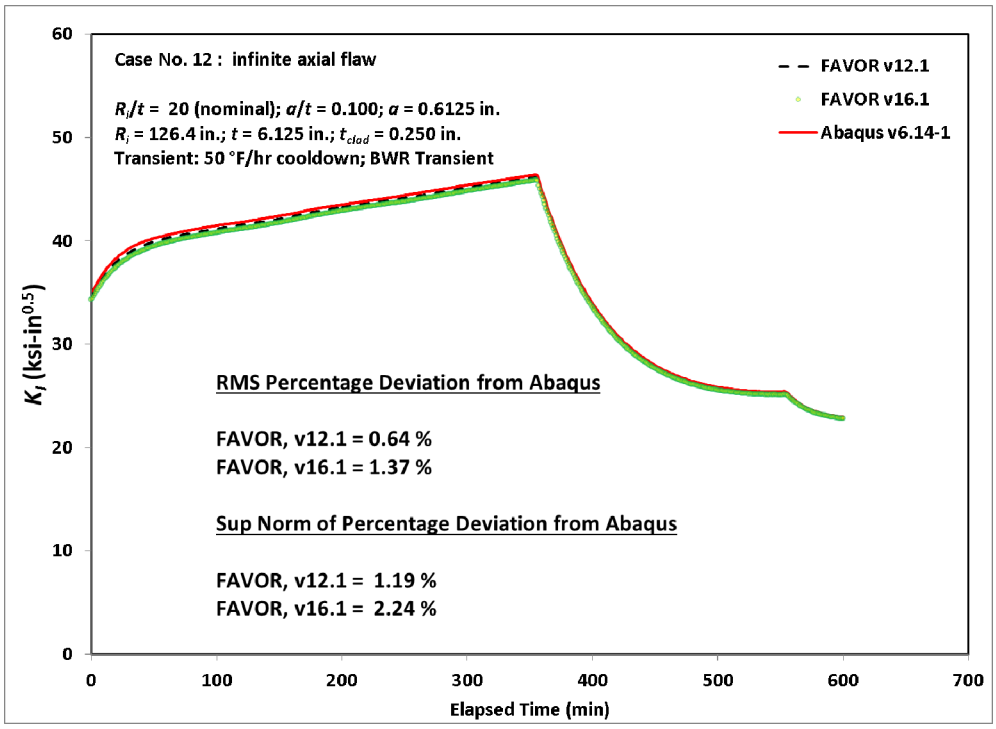

(b)

Fig. G22. Applied K_I histories for Cases 11 and 12.

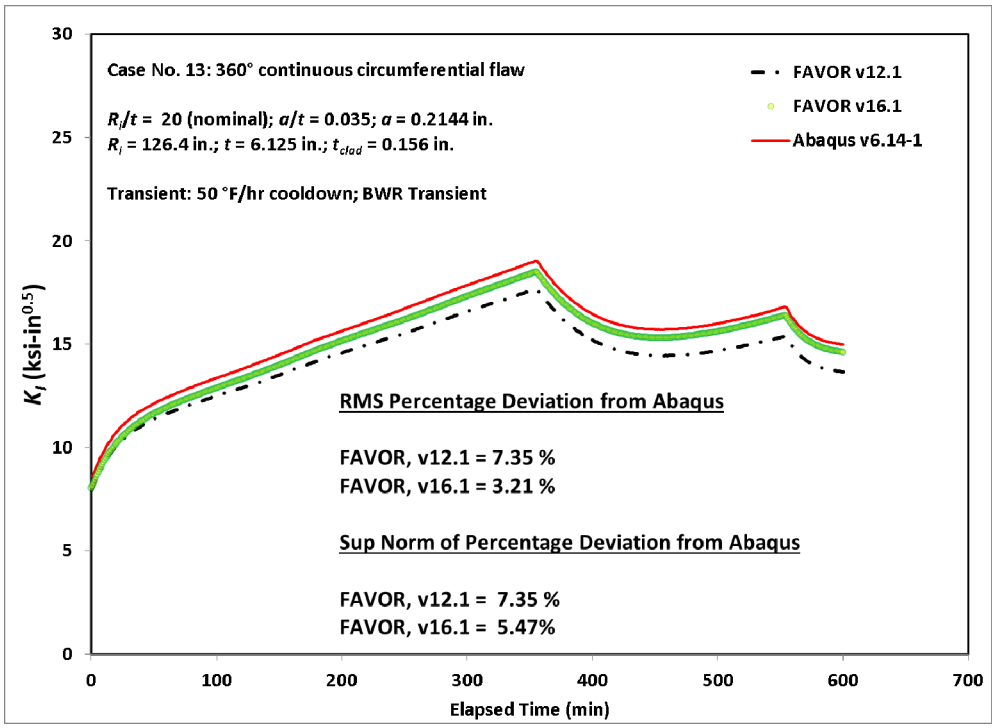

(a)

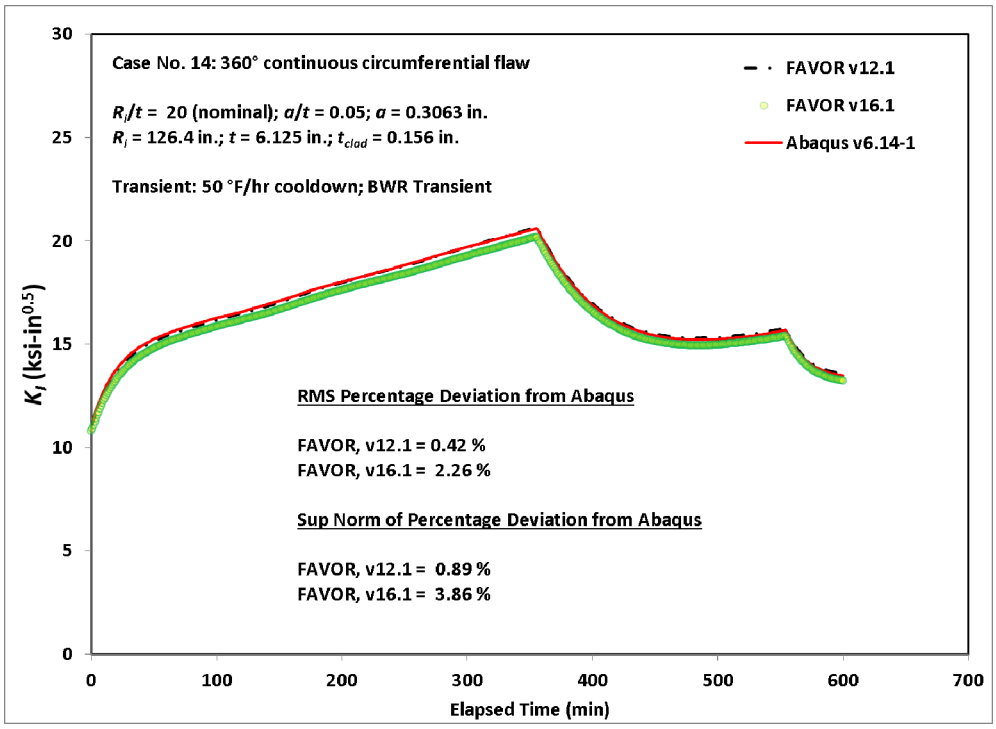

(b)

Fig. G23. Applied K_I histories for Cases 13 and 14.

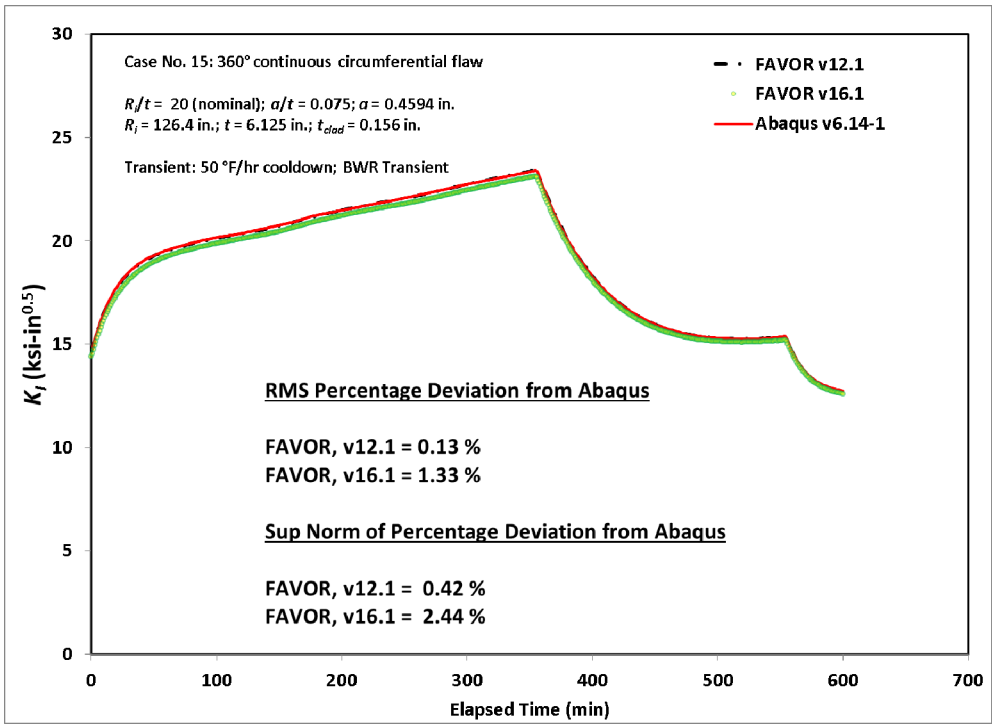

(a)

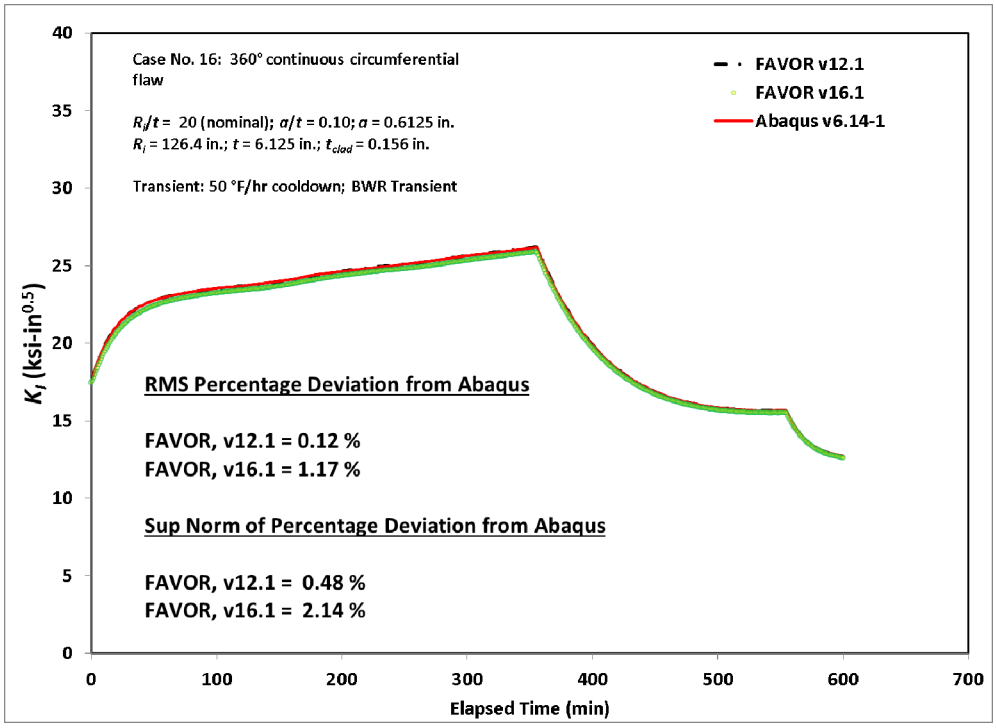

(b)

Fig. G24. Applied K_I histories for Cases 15 and 16.

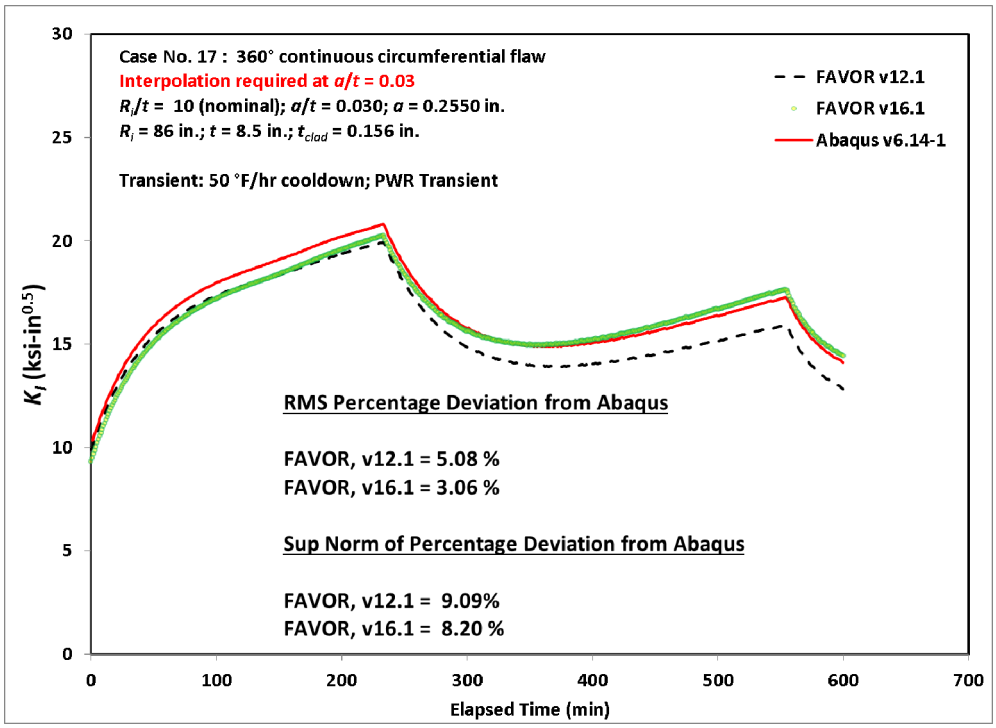

(a)

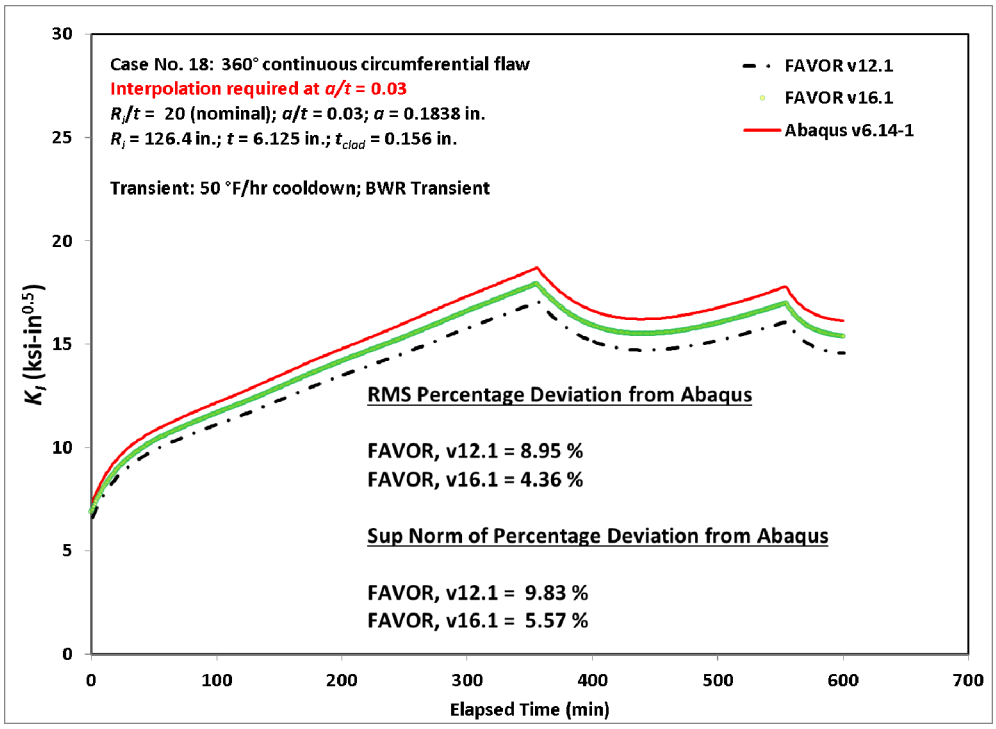

(b)

Fig. G25. Applied K_I histories for Cases 17 and 18.

(c)

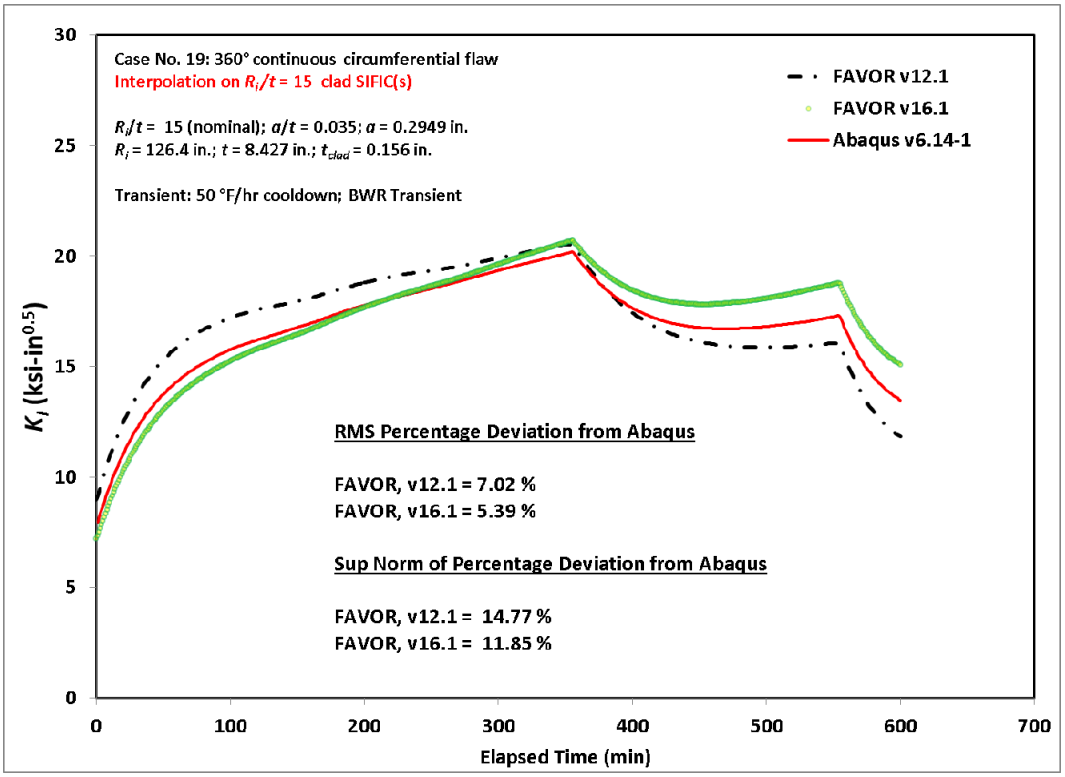

Fig. G25. (continued) Applied K_I histories for Case 19.

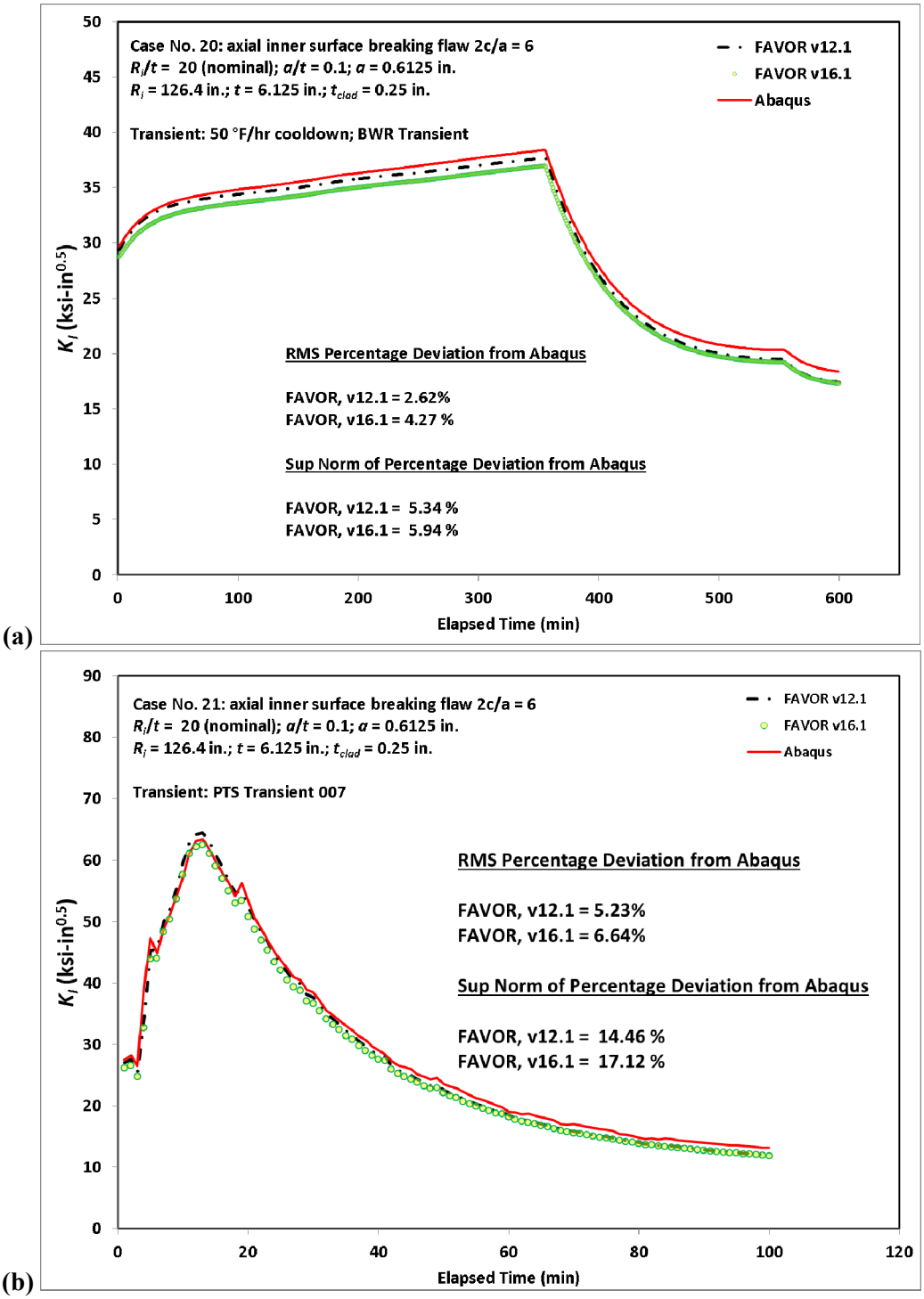

Fig. G26. Applied K_I histories for Cases 20 and 21.

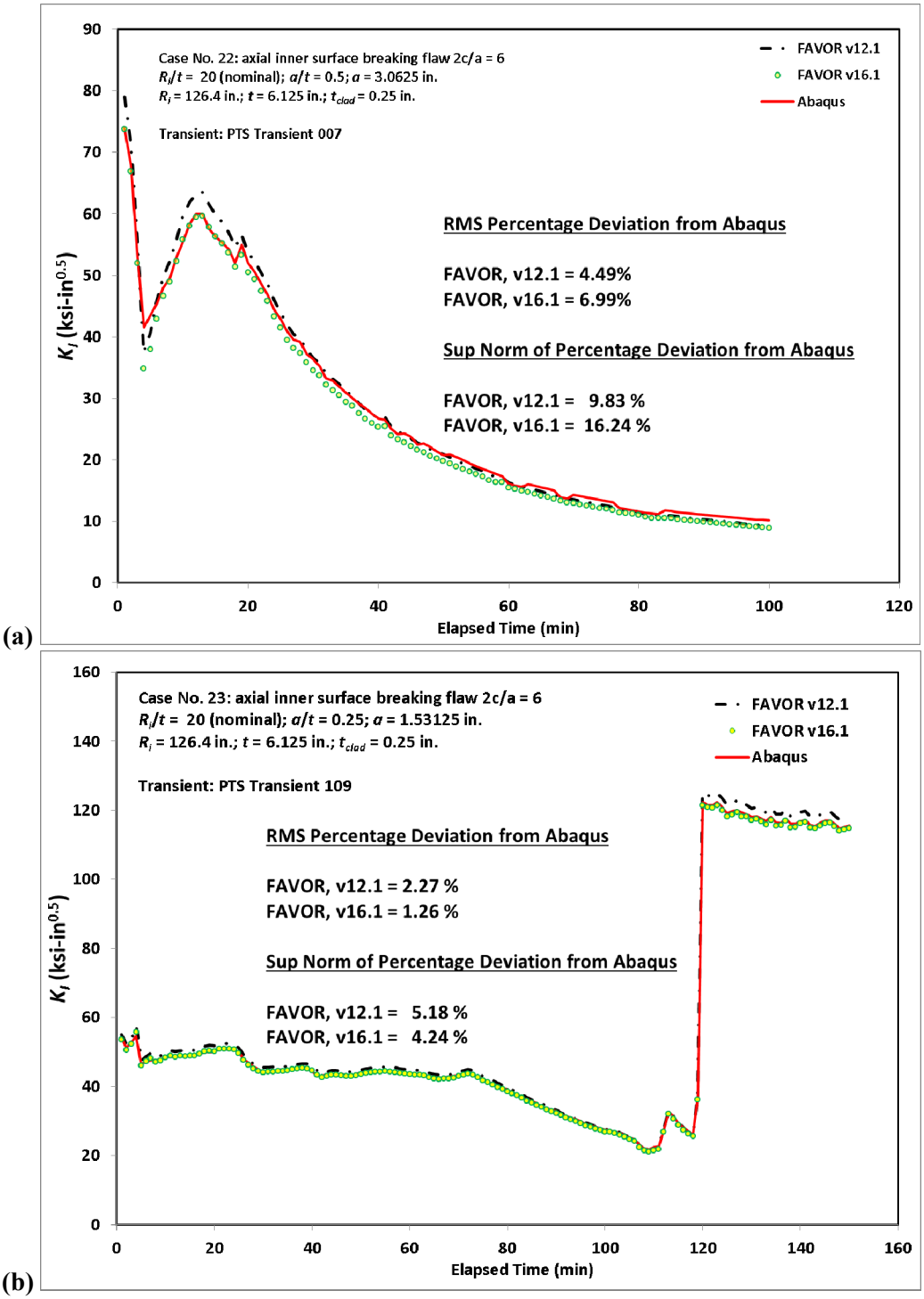

Fig. G27. Applied K_I histories for Cases 22 and 23.

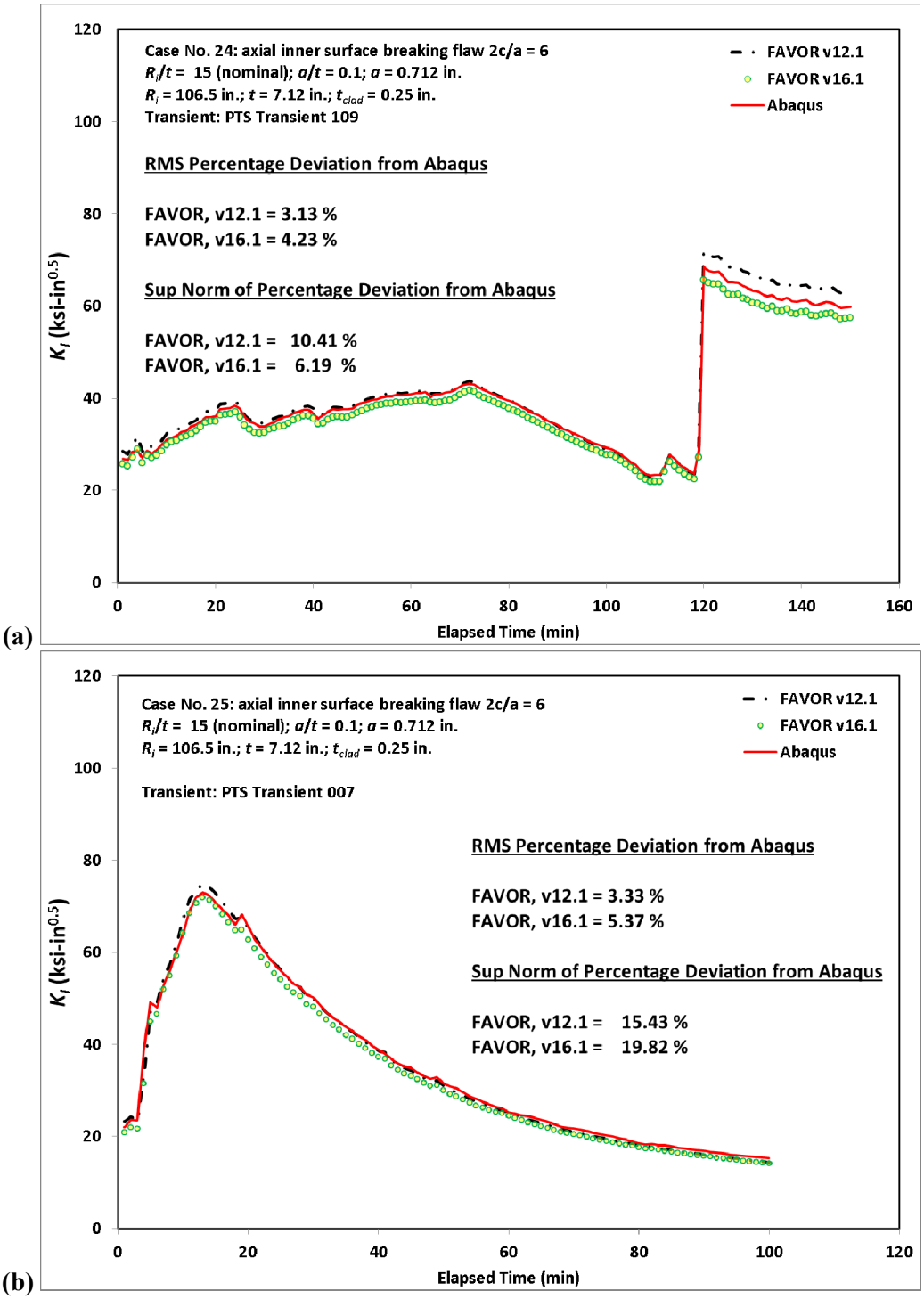

Fig. G28. Applied K_I histories for Cases 24 and 25.

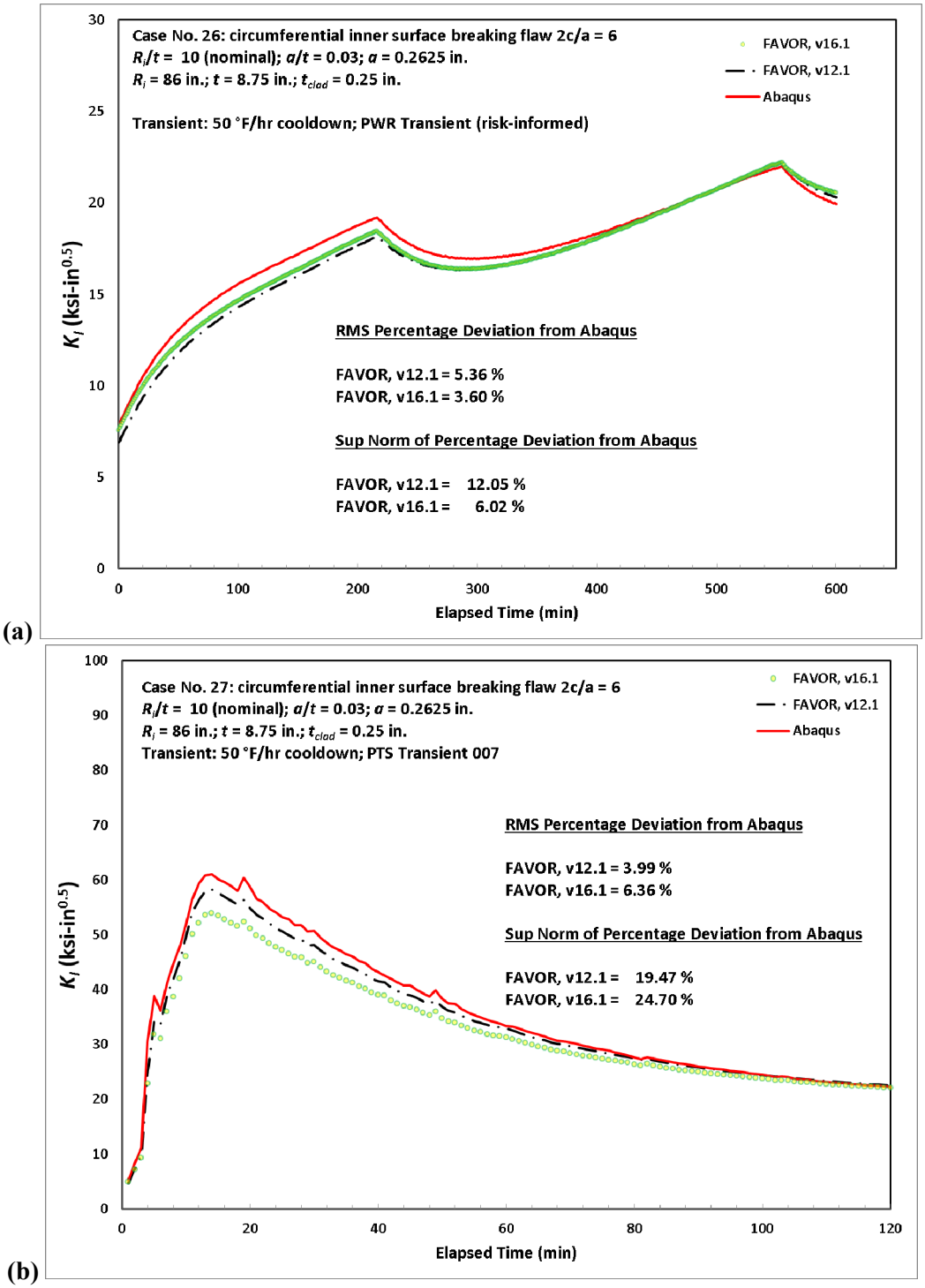

Fig. G29. Applied K_I histories for Cases 26 and 27.

Appendix H – As-Found Flaw FAVPFM Version 20.1

H.1 Introduction

The FAVOR code, specifically the FAVPFM subcode, was developed using the VFLAW (References [1], [2], [3], and [4]) based approach on flaw characterization of RPVs. VFLAW was developed at the Pacific Northwest National Laboratory (PNNL). The technical basis for VFLAW is based on flaw data obtained from the destructive examination of RPV materials [1]. VFLAW provides statistical distributions of the number and the geometry of flaws that could exist in a reactor pressure vessel (RPV). This application has been useful in the generic evaluation of surface, plate, and weld flaws in RPVs, particularly in the PTS reevaluation. More recently, an approach was developed to evaluate a large number of quasi-laminar flaws identified by ultrasonic inspection of the Doel 3 and Tihange 2 RPV lower and upper core shells (Reference [5]). A modified version of FAVPFM was developed to perform a conservative deterministic evaluation of these Doel 3 and Tihange 2 RPV flaws (Note that this modification to FAVOR 16.1 was not released). Because concerns with these flaws could be resolved with this conservative deterministic analysis, a probabilistic fracture mechanics (PFM) evaluation was not required. Because future RPV examinations may require PFM analysis to support decisions on continued plant operation with newly identified flaws, an as-found flaw version of FAVPFM (Version 20.1) has been developed. This as-found flaw FAVOR code is designed to assess identified flaws from in-service inspections where specific and unique flaw characterizations are identified.

H.2 FAVPFM As-Found Flaw Design Description

FAVOR version 16.1 and earlier FAVOR versions used flaw characterization data input generated by the VFLAW computer code. VFLAW generates three flaw files that are used to provide flaw characterization data that is input into PFM analyses performed by FAVPFM. These files specify statistical distributions of flaw densities and geometries. One file characterizes the number of and geometry of surface breaking flaws in plate and weld material; a second file characterizes embedded flaws in weld material, and a third file characterizes embedded flaws in plate or forging material.

The dependence of FAVOR upon VFLAW for performing PFM analyses is a legacy of the PTS Re-evaluation Project [7], which required that FAVOR be compatible with VFLAW.

Because the VFLAW code does not allow for FAVOR analyses of actual flaws that may be identified during RPV in-service inspections, an alternative method(s) for inputting as found flaw data into FAVOR PFM analyses was developed perform PFM analyses for flaws that may be found in non-destructive RPV examinations (NDE). This is the objective of the development of the "as-found flaw" version of FAVOR is to allow FAVOR to be used to access whether flaws found during in-service RPV examinations present any concerns with continued plant operations and whether these flaws need to be repaired to ensure safety of continued plant operation.

The as-found flaw analysis capability was added as an option to FAVOR version 16.1 to create FAVOR version 20.1. FAVOR version 20.1 is backwards compatible with version 16.1 and FAVOR 20.1 can perform analysis of flaws files generated by VFLAW and produce the same results for these analyses FAVOR version 16.1.

To maintain consistency with the previous naming convention used for earlier versions of FAVOR, the name of this new version of FAVOR, which maintains backward compatibility with FAVOR 16.1, and includes an option to perform PFM analyses for "as-found flaws", will be called FAVOR 20.1. This means it is the first version of FAVOR released in the year 2020.

H.3 The IPFLAW Variable

The user-input variable IPFLAW (flaw population) in the FAVPFM input dataset will be used to activate the as-found flaw option of FAVPFM. In the 16.1 version of FAVOR, IPFLAW =1, 2, or 3 defines the flaw population to be used in PFM analyses as follows:

IPFLAW = 1: All surface breaking flaws are assumed to be on the inner surface of the RPV. Only those embedded flaws in the 3/8th of the base metal nearest the RPV inner (wetted) surface are included in the analyses and they are uniformly distributed. This option is meant for cool-down transients based on the assumption that external surface breaking flaws and embedded flaws beyond the inner 3/8th of the base metal are primarily in compressive stress fields during cool-down transients and would therefore would never initiate in fracture.

IPFLAW = 2: All surface breaking flaws are assumed to be on the external surface of the RPV. Only those embedded flaws in the 3/8th of the base metal nearest the RPV outer surface are included in the analyses and they are uniformly distributed. This option is meant for heat-up transients based on the assumption that internal surface breaking flaws and embedded flaws in the inner 3/8th of the base metal are primarily in compressive stress fields during heat-up transients and would therefore would never initiate in fracture. It has since been found that this is not necessarily always a valid assumption as internal surface breaking flaws can also initiate very early in some cases during some heat-up transients.

IPFLAW = 3: Results in double the number of surface breaking flaws in either of the above options. Half are internal and half are external of surface breaking flaws. Embedded flaws are uniformly distributed thru the entire wall thickness and results in (8/3) as many embedded flaws as either of the above options. This option can be used for any case; however, was primarily designed for the hydrostatic test load condition, which consists of both a heat-up and cool-down phase. This option requires more computational time to perform a PFM analysis; however, there are no questions regarding "what if" all possible flaws had been included in the analysis.

In the 20.1 version of FAVOR, IPFLAW = 1,2, or 3, FAVPFM will continue to prompt the user for three flaw characterization files discussed above and will generate identical solutions as the 16.1 version of FAVOR thus providing backward compatibility.

If **IPFLAW = 4**, FAVPFM will prompt the user for a single flaw file which characterizes the "as-found flaws" which, in the general case, can be any combination of surface breaking flaws / embedded flaws / material / flaw orientation. For IPFLAW=4, FAVPFM will generate PFM solutions for the set of as-found flaws.

H.4 Methodology

The FAVOR PFM Monte Carlo looping structure starting from the outer loop is: RPV trial, flaws, transients, and transient time steps. If the IPFLAW = 4 option with FAVPFM version 20.1, each RPV contains all of the as-found flaws (of specified geometry and location) subjected to the transient included in the FAVLoad transient analysis provided as input to FAVPFM.

Design Objective: *Modify FAVPFM such that it calculates (and appropriately stores) T(t) and $K_I(t)$ for each of the as-found flaw geometries, subjected to each transient included in the analysis, prior to entering the PFM Monte Carlo loop. This strategy would use the cubic spline to transform the existing FAVLoad solutions to the appropriate locations and geometries to conform with the as-found flaw specification. It is important to note that the FAVLoad module would not require any modifications.*

Code Design Approach: Once the PFM Monte Carlo loop is entered, for each flaw, the RT_{NDT} at the appropriate crack tip is calculated by sampling (from the appropriate RPV subregion) neutron fluence, chemistry, and un-irradiated RT_{NDT}. The same T(t) and $K_I(t)$ would is always used for analysis of a given flaw ID.

Subroutines TMPTIP, AMNK99, AMNKSE, and KEMB (previously developed for application in the deterministic minimization option) will be applied to calculate T(t) and $K_I(t)$ for each of the as-found flaw geometries, subjected to each transient included in the analysis, prior to entering the PFM Monte Carlo loop.

Subroutine TMPTIP applies cubic spline fit to calculate T(t) at the appropriate crack tip for each flaw subjected to each transient.

Subroutine AMNK99 applies cubic spline fit to calculate $K_I(t)$ for infinite length axially and circumferential internal and external surface breaking flaws that reside in plate or weld material.

Subroutine AMNKSE applies cubic spline fit to calculate $K_I(t)$ at the appropriate crack tip for finite length semi-elliptical internal and external surface breaking flaws that reside in plate and weld material.

Subroutine KEMB calculates $K_I(t)$ at the appropriate crack tip for an embedded flaw of specified depth, aspect ratio, and location of inner crack tip. Note that the computational methodology implemented in FAVOR for calculating Mode I stress-intensity factors, K_I , for embedded flaws is the EPRI NP-1181 analytical interpretation of the ASME Section XI-Appendix A model for embedded flaws. A full discussion is presented in Section 5.1.3.5.

Code Design Objectives: Therefore, the development of the IPFLAW=4 option of FAVOR 20.1 consists of the following:

1. Continue to read in FAVPFM input file which contains embrittlement model, FAVLoad output file, and a single flaw file (and storing appropriately) that contains data that sufficiently describes each as-found flaw as follows: (1) unique flaw ID number, (2) type of flaw (ISB, ESB or embedded), (3) subregion number in which the flaw resides, (4) flaw orientation (axial or circumferential), (5) flaw depth, (6) flaw aspect ratio, and (7) the location of inner crack tip (applicable only if the flaw is embedded).

    a. A new Subroutine, RDFOUND, is required to read in the user specified flaw file. In addition, a new Module, Marks, is required to allow the use of as-found flaw input and internal process data within the processing of the various called subroutines.

    b. Required changes to the main FAVPFM program, subroutine FILE_INIT to open and allocate new units for the as-found flaw input file and echo as-found flaw file are required.

2. Modify FAVPFM such that it makes the necessary calls to subroutines TMPTIP, AMNK99, AMNKSE, and KEMB to calculate and appropriately store the T(t) and KI(t) for each flaw depending on specified flaw type (ISB, ESB, or embedded) and its location (weld or plate). This looping structure would be executed one time and would be located prior to entry in the PFM Monte Carlo looping structure.

3. Modify FAVPFM such that the correct characteristics (orientation, weld or plate, subregion number, etc.) are attributed to each flaw such that the correct K_I time history is assigned during the PFM analysis.

4. Maintain continuity within FAVPFM such that it would continue to propagate a flaw that initiated in cleavage fracture thru the wall to determine if it eventually propagated thru the RPV wall to failure or resulted in a stable crack arrest.

5. Modify the FAVPFM output reports such that CPI and CPF are allocated to the list of as-found flaws as opposed to the generic categories 1, 2, and 3 flaws, as has been done by previous versions of FAVOR.

6. Modify the Content of RTNDT.out file generated during PFM analysis:

Table 1 contains an abbreviated output of the RTNDT Summary for All Major Regions portion of the RTNDT.out file generated during a PFM analysis.

This PFM analysis used the simplified (13 major regions / 13 subregions) embrittlement map for Palisades at 60 EFPY subjected to a LOCA transient and an as found flaw file with 5254 flaws. This PFM analysis had 1000 RPV trials; therefore, there were 5254 x 1000 = 5,254,000 flaws in the PFM analysis.

The RTNDT Summary for all major regions provides the (1) range of values of crack tip RTNDT generated during the PFM analysis and (2) those values of RTNDT that contribute to the CPI. For the example in Table 1, the values of crack tip RTNDT generated in this PFM analysis ranged from -206 F to 383 F. The smallest value of RTNDT for which a flaw had CPI > 0 was 176 F.

The RTNDT Summary for All Major Regions has 7 columns as follows:

Column 1 – value of crack tip RTNDT

Column 2 – number of flaws during the PFM analysis that had this RTNDT

Column 3 - % of total number of flaws that had this value of RTNDT (PDF)

Column 4 – sum of column 3 (CDF)

Column 5 – number of flaws during PFM analysis with this RTNDT and CPI > 0

Column 6 - % of flaws with this RTNDT and CPI > 0 (PDF)

Column 7 – sum of column 6 (CDF)

Figure 1 graphically illustrates some of the data from the RTNDT Major Region Summary. The lower (blue) curve in Figure 1 is column 3 plotted as a function of column 1; it is a probability distribution function (PDF) of the total number of flaws as a function of crack tip RTNDT.

Each of the other three curves in Figure 1 is column 6 plotted as a function of column 1 for whatever transient (or transients) were included in the PFM analysis; they are probability distribution functions (PDFs) of the total number of flaws as a function of RTNDT for which CPI > 0. The PFM analysis that generated the PDF data for the LOCA transient (column 6) contained only the LOCA transient. Similarly, the PFM analysis that generated the PDF data (column 6) for the re-pressurization transient contained only that transient. The PFM analysis that generated the PDF data (column 6) for the re-pressurization and LOCA transient contained both transients.

Figure 2 graphically illustrates column 7 plotted as a function of column 1; it is a cumulative distribution function (CDF) - which is the integration (summation) of column 6 for the LOCA transient.

Table H.1: Example of Abbreviated RTNDT Summary for All Major Regions (generated in RTNDT.out)

LOCA Transient – AFF 5254 flaws – 1000 RPV trials

1	2	3	4	5	6	7
RTNDT	Number of all flaws	% of number of flaws PDF	CDF Sum of PDF All flaws	Number of flaws with CPI > 0	% of number of flaws with CPI > 0 PDF	CDF Sum of PDF For flaws with CPI > 0
-206	1	0	0	0	0	0
-201	1	0	0	0	0	0
-200	1	0	0	0	0	0
			⋮			
150	30074	0.572	38.182	0	0	0
151	30753	0.585	38.768	0	0	0
152	30968	0.589	39.357	0	0	0
153	30919	0.588	39.945	0	0	0
154	31227	0.594	40.54	0	0	0
155	31168	0.593	41.133	0	0	0
			⋮			
174	33232	0.633	52.808	0	0	0
175	33384	0.635	53.443	0	0	0
176	33260	0.633	54.076	5	5.00E-03	5.00E-03
177	33467	0.637	54.713	11	0.012	0.017
178	33472	0.637	55.351	26	0.028	0.046
			⋮			
250	13909	0.265	94.082	1283	1.403	49.021
251	13273	0.253	94.335	1184	1.295	50.316
252	13154	0.25	94.585	1213	1.327	51.643
253	12480	0.238	94.823	1131	1.237	52.879
254	11987	0.228	95.051	1161	1.27	54.149
255	11665	0.222	95.273	1169	1.278	55.427
256	11377	0.217	95.49	1060	1.159	56.587
			⋮			
308	704	0.013	99.838	205	0.224	96.414
309	655	0.012	99.851	194	0.212	96.626
310	617	0.012	99.863	170	0.186	96.812

311	538	0.01	99.873	185	0.202	97.015
312	525	0.01	99.883	156	0.171	97.185
			:			
381	1	0.00	100.00	1	0.00	100.00
382	1	0.00	100.00	0	0.00	100.00
383	4	0.00	100.00	4	4.00e-3	100.00

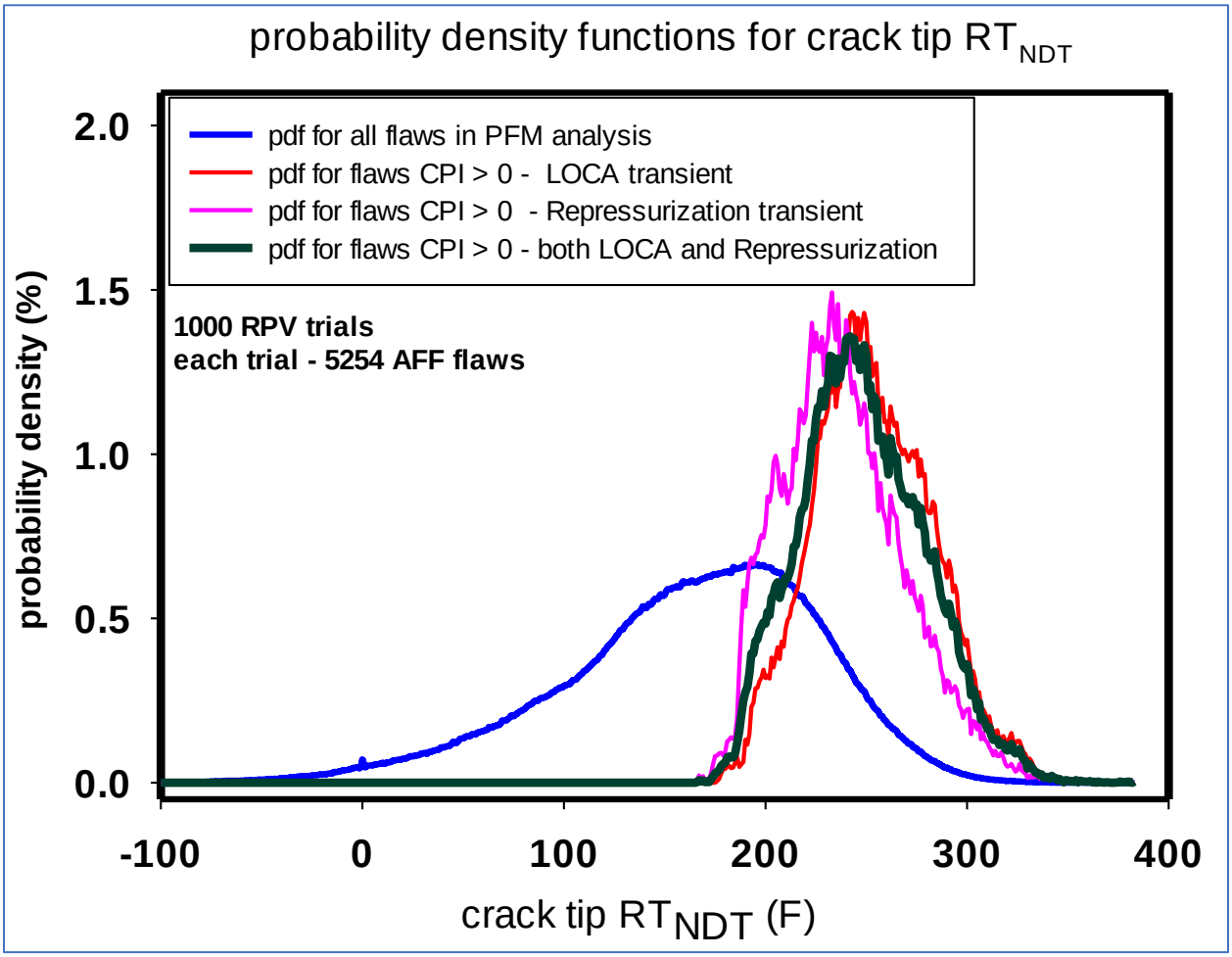

Figure H. 1: Probability Density Function Distribution for Crack Tip RT_{NDT}

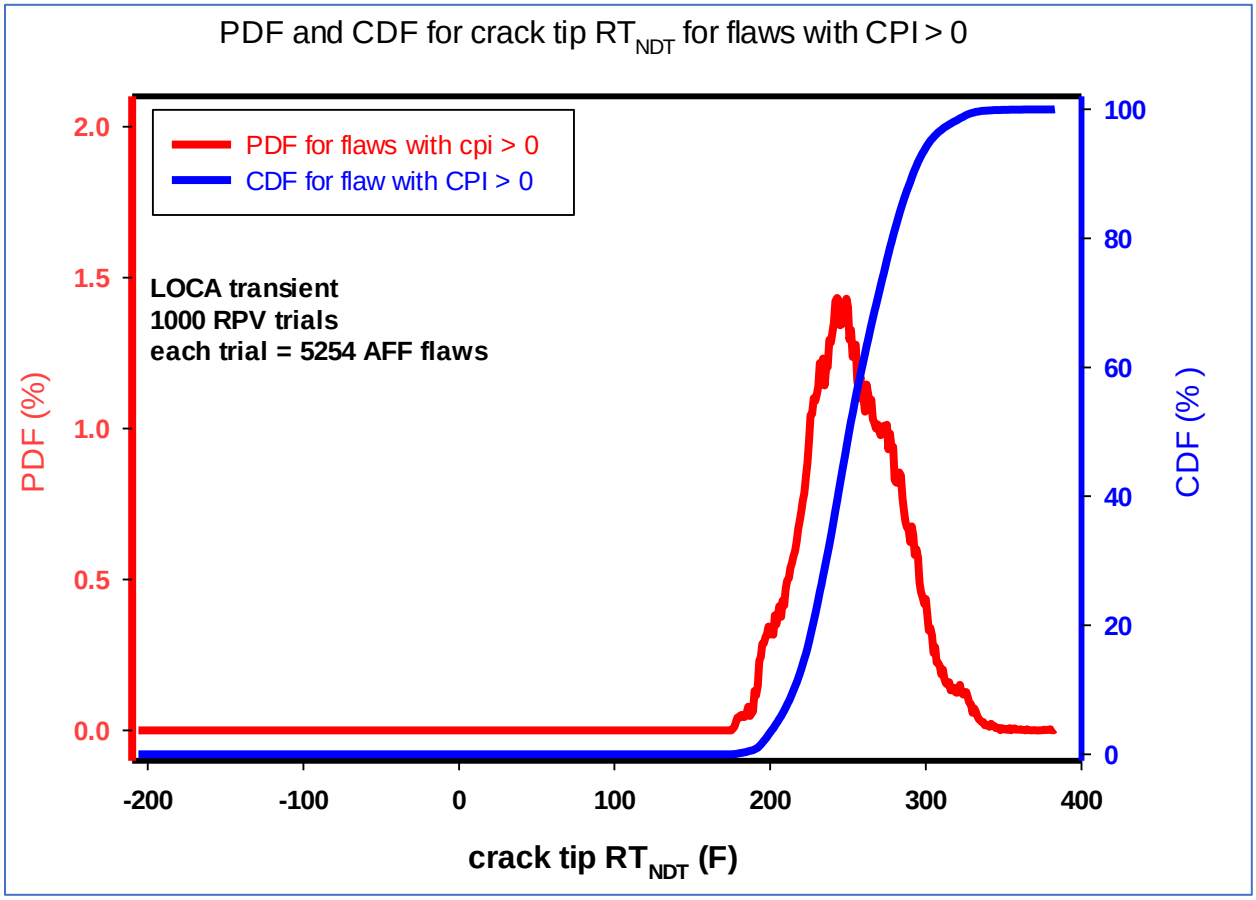

Figure H. 2: Probability and Cumulative Density Function Distributions for Flaws with CPI > 0 as a Function of Crack Tip RT_{NDT}

H.5 Verification and Validation Strategy

Verification and Validation Studies: The V&V selected cases focused on assessing the capability of FAVPFM to meet the requirements of the initial design intent (software requirements document in the formal SQA process). That is, to correctly read in the user as-found flaw data and accurately process the input data to correctly calculate the various process variables (such as axial and hoop stresses, temperature at the crack tip, RTNDT, applied KI, and KIc) using the currently available correlations within FAVPFM to correctly calculate the CPI and CPF for each flaw and for the integrated flaw population. These verification cases test appropriate internal sequencing of calculations are performed for various internal surface breaking flaws and embedded flaws used in the probabilistic fracture mechanics analyses. In addition, a series of test cases demonstrate that input filters checked the user input against acceptable ranges of values to assure that FAVPFM performs within its defined capabilities. Filters were added for subregion number flaw orientation, flaw depth, aspect ratio, and embedded flaw locations).

As background, an initial approach to verify the 20.1 version of FAVPFM was discussed at the FAVOR Developers Course held at the USNRC in September 2019. Verification of the 20.1 of FAVOR had the following two components:

If IPFLAW = 1, 2, or 3, the 20.1 version of FAVOR should generate identical PFM (CPI and CPF) solutions as generated by the 16.1 version of FAVOR for the same input files, thus providing backward compatibility. This verifies that the additional coding in FAVPFM (to accommodate the IPFLAW=4 as-found flaw option) does not impact the IPFLAW=1, 2, or 3 solutions.

If IPFLAW = 4, for a specified flaw geometry or a combination of flaw geometries, FAVPFM should generate nearly identical solutions as the 16.1 version for the same problem. To verify this, in many cases, this will require making modifications to the 16.1 version of FAVPFM (and re-compilation) to ensure that the identical problem is being solved, particularly for any case involving embedded flaws. This will be discussed more below.

The developer will design problems with appropriate transient(s), flaw geometries (and corresponding flaw files), and RPV beltline definitions as required for all verifications. The TRACE option could be helpful to accomplish this. Also, this could require inserting write statements into FAVPFM to generate information regarding the aspect ratios and location of inner crack tip of embedded flaws, as will be required to execute the identical flaw geometry when using the IPFLAW=1 option of the 16.1 version of FAVOR.

The first phase of testing was is described below. This testing focused on four types of embedded flaws as follows:

- single as-found axial embedded flaw in weld,
- single as-found axial embedded flaw in plate,
- single as-found circumferential embedded flaw in weld, and

- single as-found circumferential embedded flaw in plate.

Verification of solutions of CPI and CPF for these single flaws is a necessary first step prior to consideration of verifications of various combinations of embedded flaws (multiple flaws in each RPV trial). These four cases may be thought of as building blocks for verification for more complicated combinations of embedded flaws.

Verification of various combinations of embedded flaws (different depths, aspect ratios, orientation, and location of inner crack tip) will be successfully completed prior to verification of surface breaking flaws.

The final verification will focus on a general specification of as-found flaws, i.e., any arbitrary combination of surface breaking and embedded flaws (number of flaws, orientations, aspect ratio, and location of inner crack tip, in embrittlement maps containing multiple subregions) subjected to multiple transients.

The first phase verification is documented below.

H.6 First Phase Verification

The results of the verification of a single-embedded flaw for different permutations of material (weld or plate) and orientation are in Table H. 2.

The single embedded flaw could reside in weld material or plate material. Those flaws that reside in weld material are subjected to loads that include the thru wall weld residual stress whereas the load imposed on flaws that reside in plate material do not include the thru wall weld residual stress. The flaw orientation could be axially and circumferentially oriented.

FiguresFigure H. 3 andFigure H. 3 illustrate the two transients utilized in this verification: a LOCA transient and a re-pressurization transient. These were chosen because the LOCA is a thermally driven transient whereas the re-pressurization transient is primarily pressure driven.

The single embedded flaw has the following geometry: depth of 1.3125 inch (0.15t), an aspect ratio of 6, and the inner crack tip is located 0.30 inches from the wetted inner surface. The large flaw is chosen to achieve well converged solutions with a relatively small number of RPV trials.

Figures H.5 to H.8 illustrate the K_I time histories of this flaw geometry subjected to the LOCA and re-pressurization transients. These figures provide insight into the consistency of the results.

Figure H. 5 illustrates the K_I time histories (of this flaw geometry subjected to these two transients) if the flaw is axially oriented and resides in weld material.

Figure H. 6 illustrates the K_I time histories (of this flaw geometry subjected to these two transients) if the flaw is axially oriented and resides in plate material.

Figure H. 7 illustrates the KI time histories (of this flaw geometry subjected to these two transients) if the flaw is circumferentially oriented and resides in weld material.

Figure H. 8 illustrates the K_I time histories (of this flaw geometry subjected to these two transients) if the flaw is circumferentially oriented and resides in plate material.

Columns 7-8 of Table H. 2: Verification of PFM analysis of single flaw subjected to Single and Multiple Transientscontains the PFM results (CPI and CPF) generated by the 20.1 version of FAVPFM when IPFLAW = 4, i.e., when the flaw data is read into FAVPFM in a single "as-found flaw" characterization file.

Columns 9-10 (last two columns) contain the PFM results (CPI and CPF) generated by the 16.1 version of FAVOR when it is modified as required to solve the identical problem.

The PFM solutions (CPI and CPF) for FAVPFM 20.1 (IPFLAW = 4) are in excellent agreement with PFM solutions obtained for FAVPFM 16.1 (IPFLAW = 1). This provides the verification that we are seeking, i.e., the IPFLAW=4 option of FAVOR 20.1 generates essentially the same PFM solutions as the 16.1 version of FAVOR, provided it has been modified as is necessary to solve the identical problem.

In a regular 16.1 FAVPFM analysis, flaw aspect ratio and the thru wall location of the inner crack tip (xinner) are sampled from statistical distributions and would therefore be different for each flaw. Therefore, for all cases 1-12, the 16.1 version of FAVPFM (IPFLAW=1) must be modified such that these two flaw geometry variables remain constant (aspect ratio = 6 xinner = 0.3).

In a regular 16.1 FAVPFM analysis, for embedded flaws in weld material, the orientation is that of the weld, i.e., axial welds have axial embedded flaws and circumferential welds have circumferential flaws. The orientation of weld material is input as part of the embrittlement map; therefore, for cases 1-3 and 7-9, no code modifications are required for flaw orientation.

In 16.1 FAVPFM (IPFLAW=1), for embedded flaws in plate material, the orientation alternates between axial and circumferential orientation; therefore, for cases 4-6 and 10-12, modifications must be made to FAVPFM 16.1 (IPFLAW=1) so that the orientation remains constant as is required to compare to FAVPFM 20.1 (IPFLAW=4).

In 16.1 FAVPFM (IPFLAW=1), the flaw depth is determined from the flaw file that characterizes embedded flaws in weld material; therefore, no modifications are necessary.

Cases 3, 6, 9, and 12 provide verification that identical PFM solutions are obtained for a given flaw geometry / orientation / material for one transient or multiple transients, that all flaw characteristics are preserved thru the transient looping.

Table H. 2: Verification of PFM analysis of single flaw subjected to Single and Multiple Transients

Weld and Plate - Axial and Circumferential Orientation
WPS included in Model

Case	No Transients	Transient Description	# of flaws	Orient	Weld / Plate	IPFLAW = 4 (20.1)		IPFLAW = 1 (16.1)	
						CPI	CPF	CPI	CPF
1	1	LOCA	1	ax	w	**2.95e-2**	**1.78e-3**	**2.98e-2**	**1.76e-3**
2	1	REPR	1	ax	w	**8.65e-3**	**8.02e-3**	**8. 66e-3**	**8.02e-3**
3	2	LOCA and REPR	1	ax	w	**2.95e-3** **8.65e-3**	**1.78e-3** **8.02e-3**	**2.98e-2** **8.66e-3**	**1.76e-3** **8.02e-3**
4	1	LOCA	1	ax	P	**5.44e-3**	**1.29e-3**	**5.55e-3**	**1.97e-3**
5	1	REPR	1	ax	P	**8.37e-4**	**8.37e-4**	**8.39e-4**	**8.39e-4**
6	2	LOCA and REPR	1	ax	P	**5.44e-3** **8.37e-4**	**1.29e-3** **8.37e-4**	**5.55e-3** **8.39e-4**	**1.97e-3** **8.39e-4**
7	1	LOCA	1	cir	w	**2.98e-2**	**2.76e-7**	**3.02e-2**	**3.25e-7**
8	1	REPR	1	cir	w	**8.32e-9**	**1.14e-10**	**8.51e-9**	**8.63e-11**
9	2	LOCA and REPR	1	cir	w	**2.98e-2** **8.32e-9**	**2.76e-7** **1.14e-10**	**3.02e-2** **8.51e-9**	**3.25e-7** **8.63e-11**
10	1	LOCA	1	cir	P	**5.52e-3**	**4.77e-8**	**5.64e-3**	**5.51e-8**
11	1	REPR	1	cir	P	**0.00e-0**	**0.00e-0**	**0.00e-0**	**0.00e-0**
12	2	LOCA and REPR	1	cir	P	**5.52e-3** **0.00e-0**	**4.77e-8** **0.00e-0**	**5.64e-3** **0.00e-0**	**5.51e-8** **0.00e-0**

Notes (1) Each of the above PFM analyses were executed for 10k RPV trials.

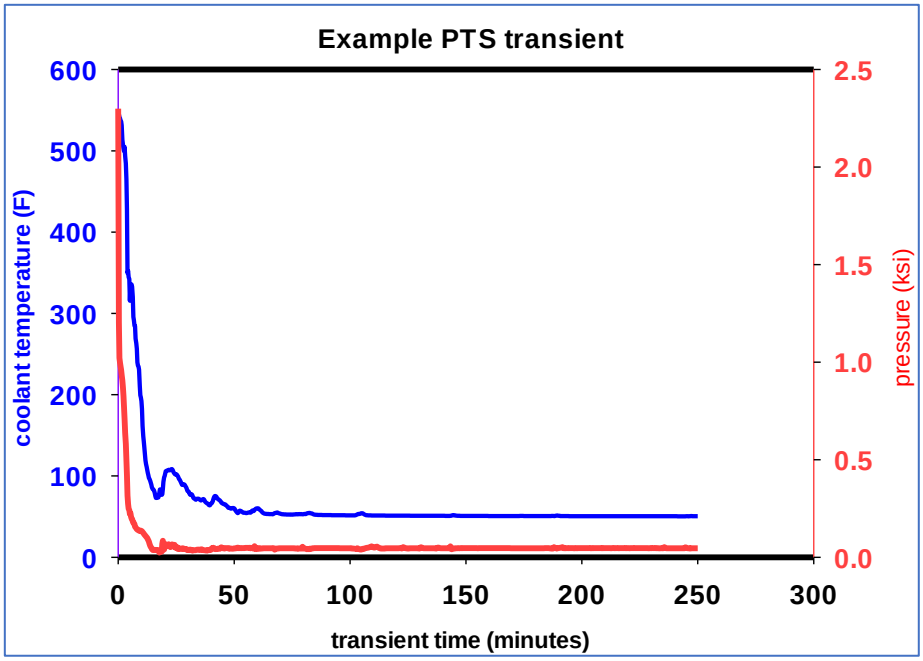

Figure H. 3: Thermally driven LOCA transient

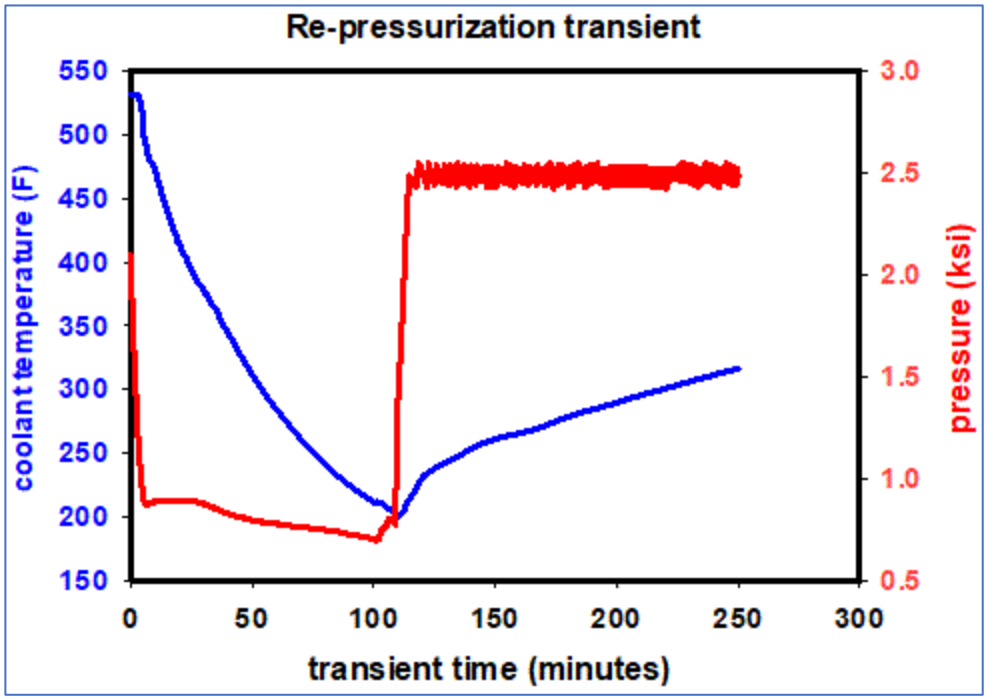

Figure H. 4: Pressure-driven Re-pressurization Transient

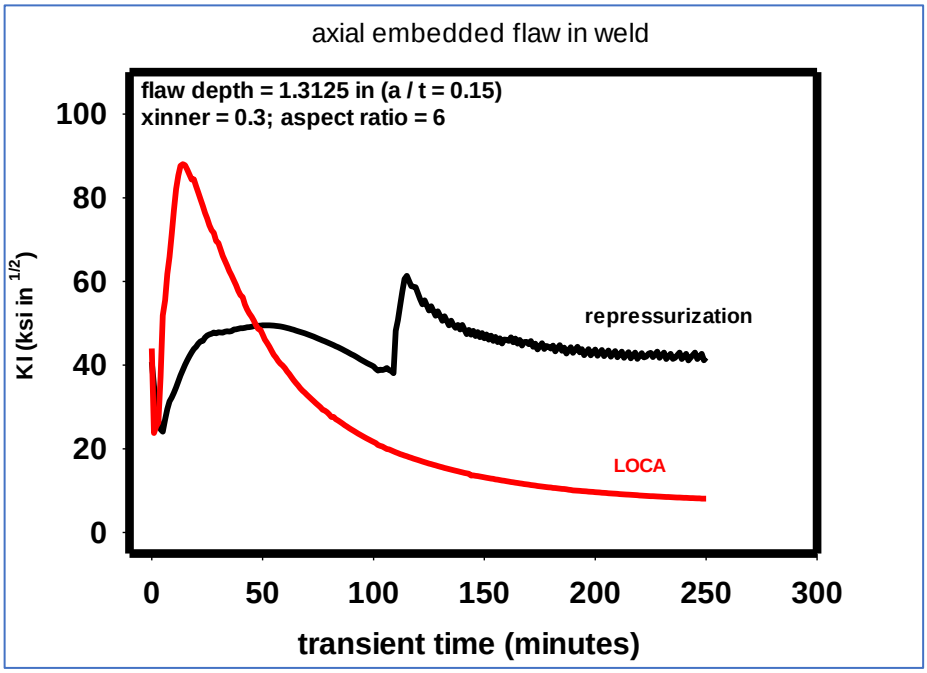

Figure H. 5: K_I Time Histories of Axially Oriented Embedded Flaw in Weld Material

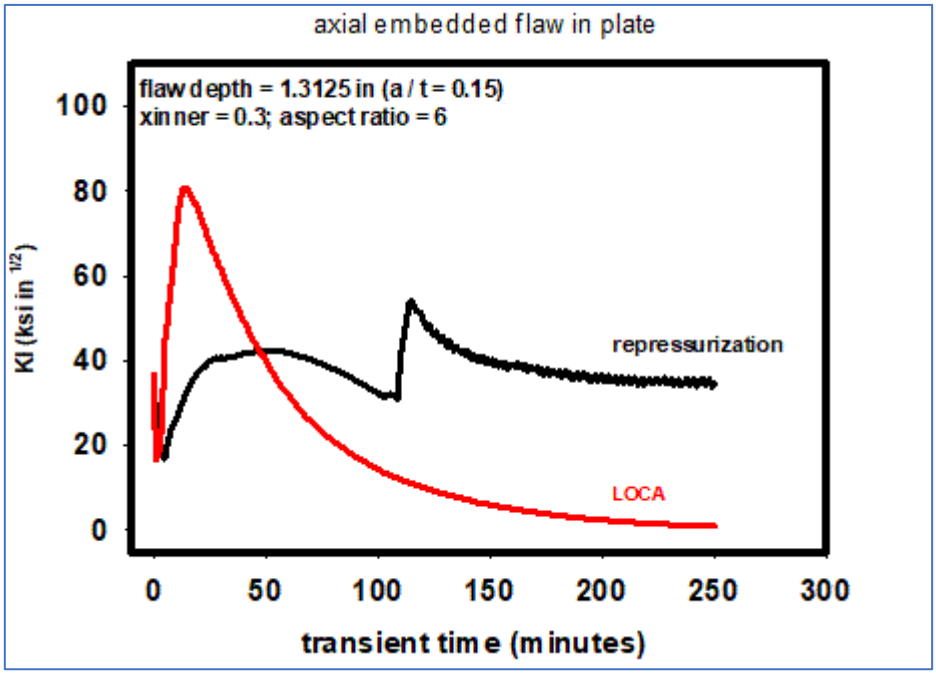

Figure H. 6: K_I Time Histories of Axially Oriented Embedded Flaw in Plate Material

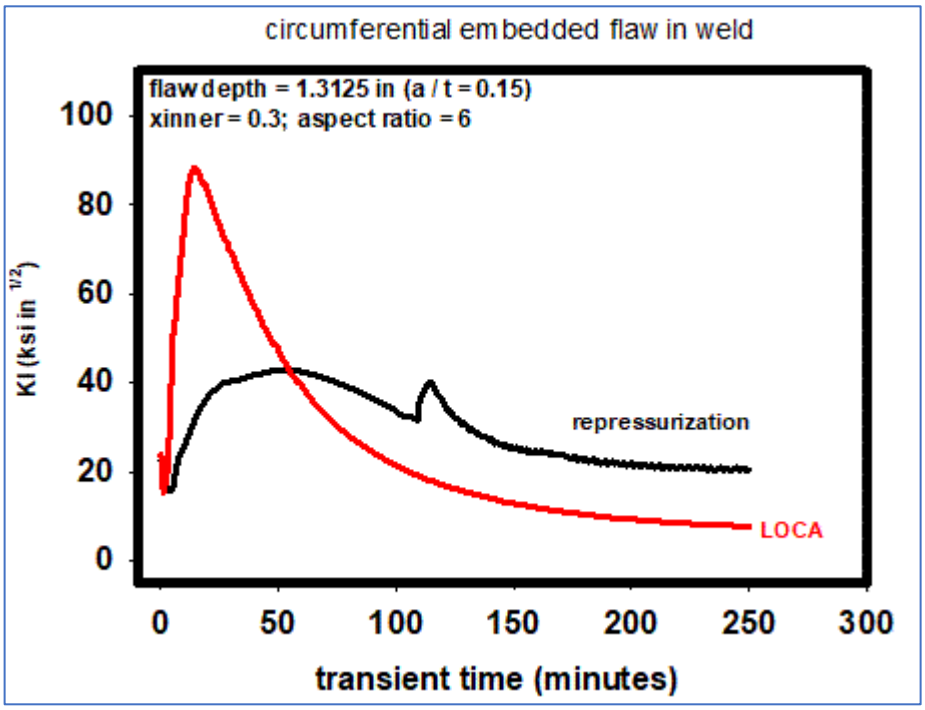

Figure H. 7: K_I Time Histories of Circumferentially Oriented Embedded Flaw in Weld Material

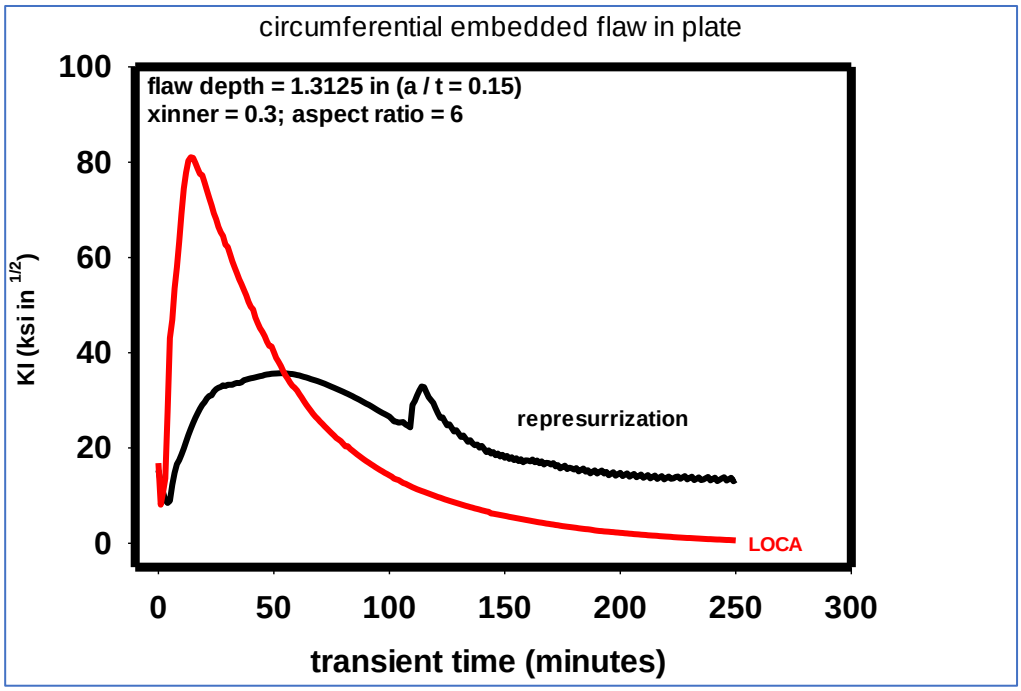

Figure H. 8: K_I Time Histories of Circumferentially Oriented Embedded Flaw in Plate Material

Table H. 3: As-Found Flaw Input File

UFLAW Unique Flaw ID Number	Flaw Type(1)	Subregion In which flaw resides	Orientation(2)	Depth(3) (inches)	Aspect(3) Ratio	Radial(4) Location (inches)
1	ISB	-	1	-	-	-
2	ESB	-	2	-	-	-
:	emb	-	1	-	-	-
:	:	-	-	-	-	-
N	:	-	-	-	-	-

(1) ISB – internal surface breaking flaw; ESB – external surface breaking flaw; emb – embedded flaw
(2) Orientation: 1 = axial; 2 = orientation
(3) See Figures 1-4
(4) Location of inner crack tip of embedded flaw relative to wetted inner surface

- In-service inspection results are typically based on ASME flaw dimensional terminology which needs to be converted to FAVOR based input. As-found flaws as described herein are related to those found in non-destructive examinations and have been characterized per ASME code, ASME Boiler and Pressure Vessel Code – Rules for Inservice Inspection of Nuclear Power Plant Components [8]. The following sections of the ASME code can assist users to provide flaw specifications into the new FAVPFM module:
    - IWA-3300, Flaw Characterization,
    - IWB-3600, Analytical Evaluation of Planar Flaws,
    - Nonmandatory Appendix A, Analytical Evaluation of Flaws, and
    - Nonmandatory Appendix G, Fracture Toughness Criteria for Protection Against Failure.
    - ASME Code Case N-848 [9].

The above referenced ASME sections layout the requirements on how to characterize and analyze flaws discovered in NDE of reactor vessels, particularly flaw characterization, multiple flaws, and proximity rules to other flaws. The current FAVOR code and associated modules do not take actual NDE surveillance data as direct input. The geometry of flaws assumed within the current v16.1 of FAVOR assume elliptical geometry, axial or circumferential, and discrete aspect ratios, whereas in reality, flaws found in surveillances are not exactly elliptical, axial, or circumferential, nor have a simple aspect ratio. Therefore, the translation from these NDE discovered flaws require a translation based on the ASME code or newly developed method to evaluate any geometry and type of flaw (e.g., surface, or embedded), and orientation. The user must interpret the NDE results and characterize the flaws according to the ASME code. An example application of this transformation is described in Appendix A of Reference [6].

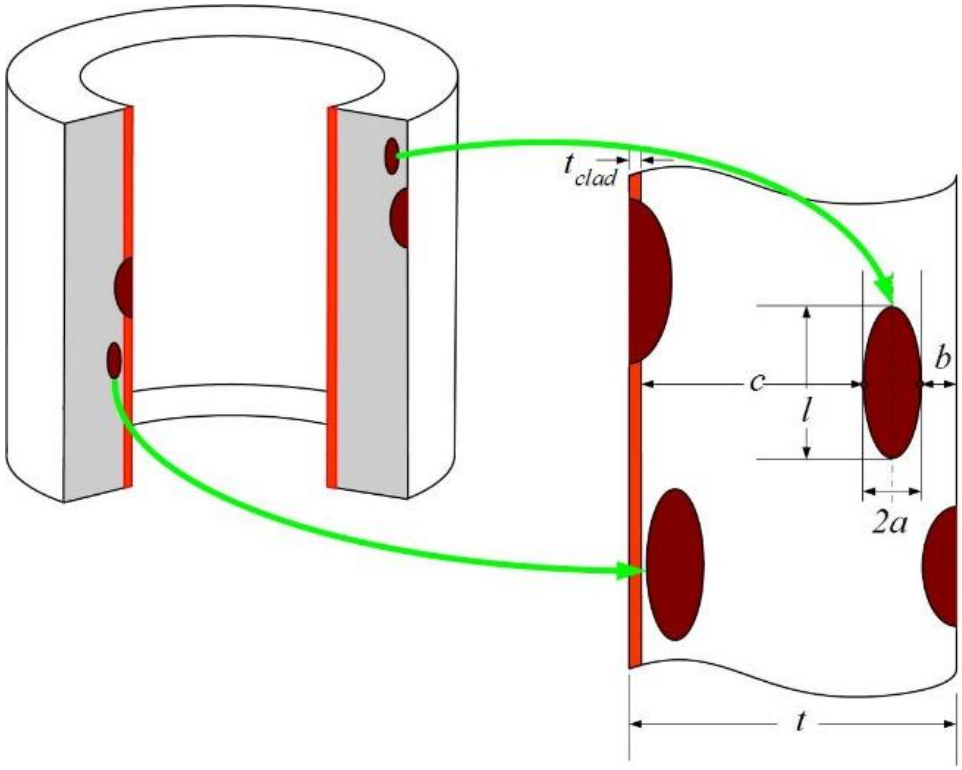

Figure H. 9: Illustration of Axially Oriented ISB, ESB, and Embedded Flaws

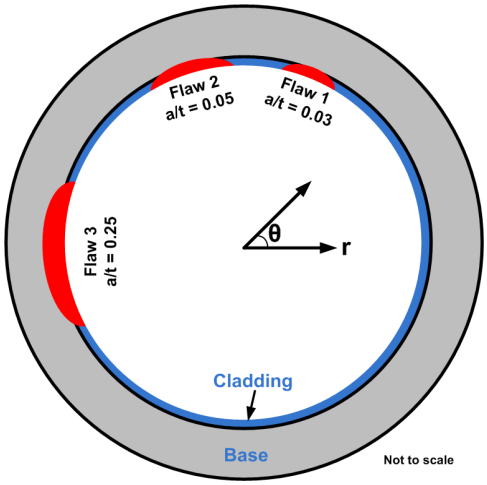

Figure H. 10: Illustration of Circumferentially Oriented ISB Flaws

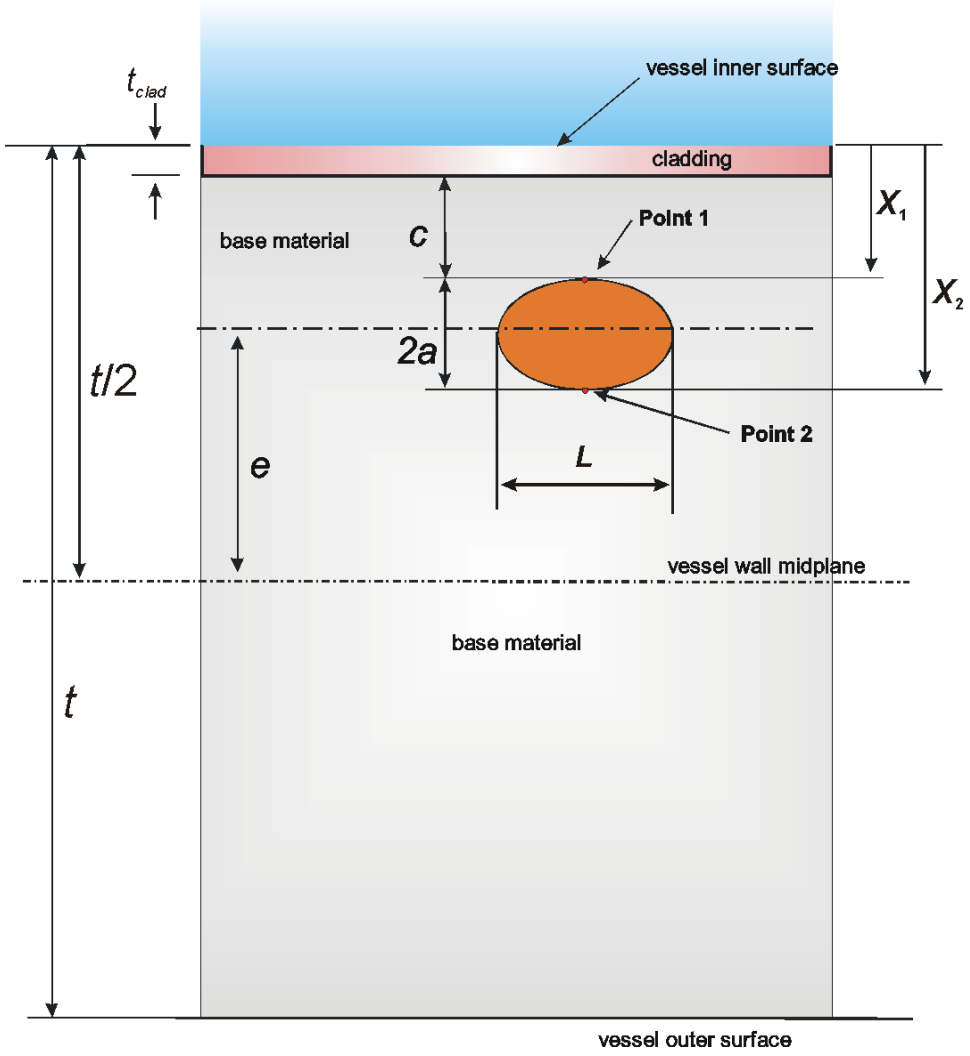

Figure H. 11: Illustration of Embedded Flaw - Inner Half of RPV Wall Thickness : Depth = 2a, Aspect Ratio = L / 2a, Distance of Inner Crack Tip from Wetted Inner Surface = X_1 = c + t_{clad}

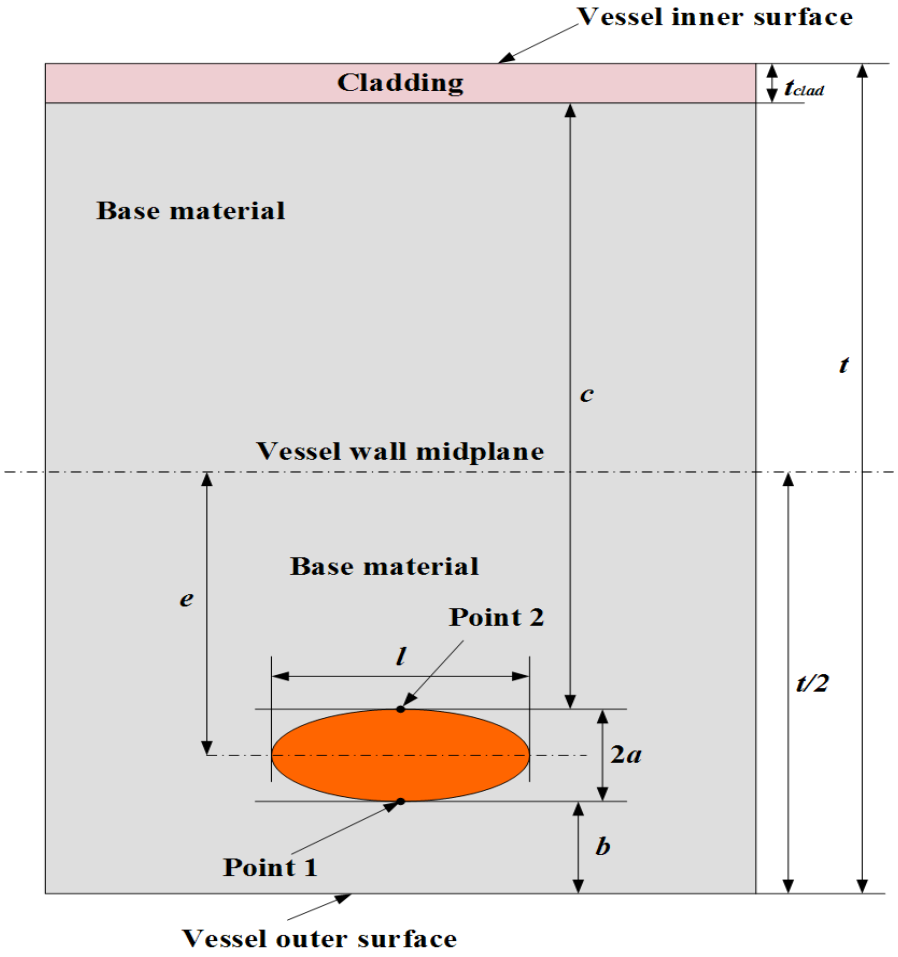

Figure H. 12: Illustration of Embedded Flaw - Outer Half of RPV Wall Thickness : Depth = 2a, Aspect Ratio = l / 2a, Distance of Inner Crack Tip from Wetted Inner Surface = $c + t_{clad}$

H.1References

[1] G. J. Schuster, S. R. Doctor, S. L. Crawford and A. F. Pardini, "Characterization of Flaws in U.S. Reactor Pressure Vessels: Density and Distribution of Flaw Indications in PVRUF, USNRC Report NUREG/CR-6471, Vol. 1," U.S. Nuclear Regulatory Commission, Washington, DC, 1998.

[2] G. J. Schuster, S. R. Doctor and P. G. Heasler, "Characterization of Flaws in U.S. Reactor Pressure Vessels: Validation of Flaw Density and Distribution in the Weld Metal of the PVRUF Vessel, USNRC Report NUREG/CR-6471, Vol. 2," U.S. Nuclear Regulatory Commission, Washington, DC, 2000.

[3] G. J. Schuster, S. R. Doctor, S. L. Crawford and A. F. Pardini, "Characterization of Flaws in U.S. Reactor Pressure Vessels: Density and Distribution of Flaw Indications in the Shoreham Vessel, USNRC Report NUREG/CR-6471, Vol. 3," U.S. Nuclear Regulatory Commission, Washington, DC, 1999.

[4] F. A. Simonen, S. R. Doctor, G. J. Schuster and P. G. Heasler, "A Generalized Procedure for Generating Flaw-Related Inputs for the FAVOR Code, USNRC Report NUREG/CR-6817, Rev. 1," U.S. Nuclear Regulatory Commission, Washington, D.C., 2013.

[5] B. R. Bass, T. L. Dickson, S. B. Gorti, H. B. Klasky, R. K. Nanstad, M. A. Sokolov and P. T. WIlliams, "ORNL Evaluation of Electrabel Safety Cases for Doel 3 / Tihange 2: Final Report (R1)," Oak Ridge National Laboratory (ORNL), Oak Ridge, TN, 2015.

[6] B. R. Bass, T. L. Dickson, S. B. Gorti, H. B. Klasky, R. K. Nanstad, M. A. Sokolov and P. T. WIlliams, "ORNL Evaluation of ELectrabel Safety Cases for Doel 3 / Tihange 2: Final Report (R1)," Oak Ridge National Laboratory (ORNL), Oak Ridge, TN, 2015.

[7] P. T. Williams, T. L. Dickson, B. R. Bass and H. B. Klasky, "ORNL/LTR-2016/309: Fracture Analysis of Vessels – Oak Ridge FAVOR, v16.1, Computer Code: Theory and Implementation of Algorithms, Methods, and Correlations (ML16273A033)," Oak Ridge National Laboratory (ORNL), Oak Ridge, TN, August 2016.

[8] American Society of Mechanical Engineers (ASME), ASME Boiler and Pressure Vessel Code – Section XI Rules for Inservice Inspection of Nuclear Power Plant Components, Two Park Avenue, New York, New York, USA.: ASME, 2017.

[9] American Society of Mechanical Engineers (ASME), Alternative Characterization Rules for Quasi-Laminar Flaws," ASME Boiler and Pressure Vessel Code, Case N-848, Section XI, Division 1, April 30, 2015, New York, New York: ASME, 2015.

[10] A. Dyszel and P. A. C. Raynaud, "FAVOR Software Quality Assurance Plan (SQAP)," U.S. Nuclear Regulatory Commission, Washington, DC, 2020.

[11] P. T. Williams, T. L. Dickson, B. R. Bass and H. B. Klasky, "ORNL/TM-2016/310: Fracture Analysis of Vessels - Oak Ridge, v16.1, Computer Code User's Guide (ML16273A034)," Oak Ridge National Laboratory (ORNL), Oak Ridge, TN, August 2016.

[12] NUREG/BR-0167: Software Quality Assurance Program and Guidelines (ML012750471), Washington, DC: U.S. Nuclear Regulatory Commission, 1993.

[13] American Society of Mechanical Engineers (ASME), "ASME V&V 10-2006: Guide for Verification and Validation in Computational Solid Mechanics," ASME, New York, NY, December 2006, reaffirmed 2016.

[14] A. Dyszel, T. L. Disckson, M. L. Smith and P. Raynaud, "TLR-RES/DE/CIB-2020-001: Compilation of Software Quality Assurance and Verification and Validation Documentation for the Fracture Analysis of Vessels - Oak Ridge (FAVOR) Software Product (ML20017A171)," U.S. Nuclear Regulatory Commission, Washington, DC, 2020.

[15] A. Ayszel, T. L. Dickson, M. Smith and P. Raynaud, "TLR-RE/DE/CIB-2020-002: Assessment of V&V Efforts of Fracture Analysis of Vessels – Oak Ridge (FAVOR) Software Product – Version 16.1 (ML20017A170)," U.S. Nuclear REgulatory Commission, Washington, DC, USA, 2020.

[16] American Society of Mechanical Engineers (ASME), ASME NQA-1-2015: Quality Assurance Requirements for Nuclear Facility Applications, New York, NY: ASME, 2015.

[17] U.S. Nuclear Regulatory Commission, *10 CFR Part 50: Domestic Licensing of Production and Utilization Facilities*, Washington, DC: U.S. NRC, 2020.

[18] U.S. Nuclear Regulatory Commission, *Regulatory Guide 1.28: Quality Assurance Program Criteria (Design and Construction), Revision 5*, Washington, DC: U.S. Nuclear Regulatory Commission, October 2017.

[19] U.S. Nuclear Regulatory Commission, *Regulatory Guide 1.152: Criteria for Use of Computers in Safety Systems of Nuclear Power Plants, Revision 3*, Washington, DC: U.S. Nuclear Regulatory Commission, July 2011.

[20] A. Dyszel and P. A. C. Raynaud, "FAVOR Configuration Management and Maintenance Plan (CMMP) - Draft," U.S. Nuclear Regulatory Commission, Washington, DC, 2020.